Eulerian modeling and simulation of two-phase flows in solid rocket motors taking into account size polydispersion and droplet trajectory crossing

Valentin Dupif

NNT : 2018SACLC050

Thèse de doctorat

Modélisation et simulation de l'écoulement diphasique dans les moteurs-fusées à propergol solide par des approches eulériennes polydispersées en taille et en vitesse

Thèse de doctorat de l'Université Paris-Saclay
préparée à CentraleSupélec

École doctorale n°574 École Doctorale de Mathématique Hadamard (EDMH)
Spécialité de doctorat : Mathématiques aux interfaces

Thèse présentée et soutenue à Gif-sur-Yvette, le 22 Juin 2018, par

VALENTIN DUPIF

Composition du Jury :

Stéphane CLAIN Professeur des Universités, Universidade do Minho, Portugal	Président
Christophe BERTHON Professeur des Universités, Université de Nantes, France	Rapporteur
Olivier SIMONIN Professeur des Universités, Institut National Polytechnique de Toulouse, France	Rapporteur
Clinton P.T. GROTH Professeur des Universités, University of Toronto, Canada	Examinateur
Marc MASSOT Professeur des Universités, École Polytechnique, France	Directeur de thèse
Joël DUPAYS Ingénieur de Recherche, ONERA, France	Co-directeur de thèse
Frédérique LAURENT Chargée de Recherche CNRS, CentraleSupélec, France	Co-directrice de thèse
Jean-Michel DUPAYS Ingénieur de Recherche CNRS, CentraleSupélec, France	Invité

Remerciements

> I know the tendency of the human mind
> to do anything rather than think.
>
> James Clerk Maxwell, Inaugural lecture
> at King's College, London, October 1860

Financé par l'ONERA, ce travail n'aurait pas pu être mené à terme sans le soutien du DMPE (précédemment DEFA) et de leurs directeurs successifs Mohammed HABIBALLAH puis Pierre MILLAN ainsi que de Yves FABIGNON, chef de l'unité MPF (et précédemment PRS). Les travaux de recherches s'inscrivent aussi dans la continuité de la collaboration de longue date entre l'ONERA et l'École Centrale Paris (désormais CentraleSupélec) ainsi que plus récemment avec la laboratoire CMAP de l'École Polytechnique qui ont fourni un environnement enrichissant à ces travaux. Je remercie également l'équipe du CRF du Sandia National Laboratory de Livermore et plus particulièrement Joseph C. OEFELEIN, Marco ARIENTI et mon prédécesseur François DOISNEAU pour m'avoir accueilli pendant un mois entre avril et mai 2016.

Dans cet environnement complexe en perpétuel mouvement où l'inscription à l'école doctorale (initialement à l'École Centrale Paris puis à l'EDMH au sein du collège doctoral de Paris-Saclay) satisfait parfaitement le second principe fondamentale de l'administration[1], mon équipe d'encadrement à su tenir bon. Tout d'abord, je remercie mon directeur de thèse Marc MASSOT, qui bien que passé de l'EM2C au CMAP et qu'ayant changé de statut à l'ONERA, a toujours gardé une infaillible passion pour la recherche, une motivation inébranlable, une rigueur sans faille et une machine à café dans son bureau. Il n'aurait pas non plus été possible de finir sans l'expertise spatiale de mon encadrant ONERA Joël DUPAYS et les solutions analytiques introuvables de ma co-directrice Frédérique LAURENT, imbattable en méthodes de moments. Leur soutien technique et moral a été précieux durant ces années de labeur. Je remercie aussi l'ensemble du jury qui, venant parfois de très loin, m'a fait l'honneur d'être présent à ma soutenance.

Cette thèse a aussi été l'occasion d'échanges scientifiques et de rencontres amicales aux seins des laboratoires dans lesquels j'ai eu la chance de travailler. Ils sont malheureusement trop nombreux pour être nommés de manière exhaustive. Tout d'abord à l'ONERA, où j'ai été accueilli chaleureusement. J'ai passé de bon moments entre les chercheurs capables de synthétiser des décennies de recherches en aérospatiale et les thésards découvrant les aléas quotidiens de la recherche. J'ai aussi eu le plaisir de passer une bonne partie de cette thèse au coté des membres du bureau 6310 A à Châtenay-Malabry: Davy avec qui nous avons eu des discussions viriles au

[1] L'entropie de la paperasse ne peut diminuer au cours du temps.

sujet de MUSCL autour de tasses de thé, Théa qui nous rappelait notre absurdité mais aussi Quentin, Abigail, Lantao, Lorella, Nicolas et Chris qui ont fait vivre ce bureau. Il ne faut pas non plus oublier les autres membre de l'EM2C, dont les membres de l'équipe math avec Aymeric, Adamet Matthieu, les spécialistes en acoustique Lionel et Aurélien, les membres administratifs du labo toujours là en cas de besoin mais aussi Jean-Michel DUPAYS (frangin de Joël) que j'ai beaucoup embêté avec mes problèmes d'informatique. Enfin, je ne pourrai oublier les thésards de l'équipe math que j'ai côtoyés, qu'ils soient aujourd'hui docteurs accomplis (Alaric, Macole, Florence et Mohamed) ou toujours en train de se poser des questions existentielles (David, Pierre, Quentin, Marc-Arthur, Ruben, Roxane et Laurent).

La vie de thésard ne s'arrêtant pas à la recherche, je tiens aussi à remercier ma famille qui m'a soutenu et qui est venue en nombre à ma soutenance, certains ayant fait un long trajet. Il ne faut pas non plus oublier mes amis personnels, parmi lesquels beaucoup d'INSAïens rouennais échoués en Ile-de-France ou partis en vadrouille en province, mais également ceux aux histoires plus particulières comme Bibi (que je n'appellerai pas par son vrai nom ici) ou Tournesol.

Contents

List of Tables

List of Figures

Glossary

I_{sp} loss difference between idealistic performances of a rocket and the its effective I_{sp}. 21, 22, 44

SSPRK Runge-Kutta (RK) time integration scheme fulfilling Stong Stability Preserving (SSP) condition. 120, 121, 130, 147, 182, 235, 261

δ-shock Dirac delta function in density coupled a velocity discontinuity, produced by the MK closure when Particle Trajectory Crossings (PTC) occur. 3, 64, 81, 286, 289, 291

ACACIA Solver of CEDRE managing conduction thermal transfer in solids. 227

ASTRE Radiative heat transfer solver of CEDRE, based on Monte-Carlo methods. 227

block structured mesh mesh composed of a set of structured meshes connected with each others. 143

cell-based AMR the cells are organized in a tree data structure in which each internal node has can be subdivided to contain a set of smaller cells through a refinement process. 143–145

CHARME Multi-species Navier-Stokes solver of CEDRE, including turbulent and combustion models. 227, 228

coarse graining modeling process consisting in coarsening underlying systems containing a large number of variables while preserving dissipative properties and a well-defined mathematical structure. 67

dense flow disperse flow where the particle dynamic is mostly controlled by collisions. 35

deterministic scale scale at which the modeling is complete enough to be considered as an exact replica of the physical problem aimed at being reproduced. 36–38, 68

dilute flow the particle dynamic is mostly driven by carrier fluid forces. 35, 68, 72

disperse flow Two-phase flow where a phase, called the disperse phase, is not materially connected but under the form of agglomerates of matter. 2, 5, 34, 53, 56–59, 62, 82

ensemble averaging averaging procedure based of the statistical convergence of a large number of realization (Drew and Passman 2006). 33, 38, 56, 58, 69

EPICEA Graphical interface of CEDRE. 229

EPINETTE Preprocessing module of CEDRE. 229

EXPLORE Post-processing module of CEDRE. 229

FILM Thin liquid layer solver of CEDRE, based on shallow-water equations. 227

flow density mass density of the mixture inside the control volume it occupies. 33

four-way coupling two-way coupling flow with significant direct interactions between the components of the disperse phase. 40, 44

granular flow disperse flow where the inter-particle mean distance is equal to a few particle diameters, particles cannot be treated independently and the assumption of negligible volume fraction may failed at being fulfilled. 35, 44

hybrid mesh mesh composed of a set of structured meshes and unstructured meshes connected with each others. 143, 144

large scale PTC PTC where the particle velocity distribution is composed of a finite number of discrete velocities. 76

mass density mass density of a phase inside the control volume occupied by the entire mixture. 32

mass fraction fraction of mass belonging to a phase inside a control volume. 33, 40, 42

material density mass density of an isolated and pure phase. 32

moderately dense spray dilute flow with significant condensed spray mass fraction. 35, 69

moment space ensemble of moments sets that are a positive measure of a position Number Density Function (NDF) (see Definition 2.1). 62, 73

mono-class models considering a unique discrete droplet size. 65

monodisperse flow Disperse flow composed of particles or droplets of an identical size. 65, 69, 108, 111

multi-class composition of independent mono-classes models, thus representing a several discrete sizes. 65–67, 69, 108–110, 116, 126, 228, 231

multi-fluid discretization of the spray in the size phase space based on a kinetic approach firstly formalized in (Laurent and Massot 2001). 102, 117, 227, 228

number density number of agglomerates of a phase scattered inside the control volume. 32, 75, 105, 125

one-way coupling flow with significant action of the carrier phase on the carried phase and negligible backward effects. 40, 55, 81, 109, 111, 126

PEUL Stochastic Lagrangian solver of CEDRE for turbulent combustion and complex chemistry. 227

point particle particle of negligible volume. 36, 37, 44, 57–60, 68, 69

point-particle DNS DNS of a disperse flow where the agglomerate of matter has been modeled as point particles. 59

polykinetic existence of several particle velocity at the same point caused by PTC, see also velocity polydispersion. 40, 64, 102

Raptor CFD code developed at Sandia by J.C. Oefelein for LES of energetic applications. 257, 261, 263

REA Radiative heat transfer solver of CEDRE, based on the discrete ordinate method. 227

realizability realizability is a condition fulfilled when the set of moment studied belongs to the moment space (see Definition 2.1) and thus are the moment of a physically plausible, positive semi-definite, phase space distribution function. 53, 75, 84, 107, 128, 132, 167, 177, 239, 289, 292

realizable scheme numerical method ensuring the conservation of the realizability conditions through a time step. 128

realization deterministic solution among an ensemble of possible events. 33, 37, 58

reconciliation determination of the same systems of governing equations through two or more distinct procedure. 36, 69

sectional approach discretization of the size phase space. 66

semi-kinetic level integration the Williams-Boltzmann Equation on the all the dimensions of the phase space except the size component, the equations are thus conditioned by size. 102

separate flow Two-phase flow where, at the scale of interest, the interface separate the phases in a singular way. 34, 37, 68

SPARTE Lagrangian solver of CEDRE for disperse phase. 227, 280

spatial averaging averaging procedure based of the integral of a quantity over a control volume (Crowe et al. 2011). 33, 38, 43, 54, 56, 58

SPIREE Eulerian multi-fluid solver of CEDRE for disperse phase. 227, 228

Spray A Spray injection test case with specific geometry and operating conditions proposed by Sandia National Laboratories. 258–260, 309, 310, 312

statistical PTC lowly organized PTC composed of a continuous distribution of the particle velocity. 76, 77, 81

statistical scale scale at which the modeling relies on a statistical description of a deterministic scale. 36–38, 68

stochastic Lagrangian Lagrangian approach where tracked particles are stochastic sample of the disperse phase. 60, 68–70

structured mesh mesh relying on a regular connectivity between cell that is implicit such that information can be stored in memory through multidimensional arrays. 143, 144, 147

three-way coupling two-way coupling where the disturbance of the fluid locally affects other particle's motion. 40

two-way coupling flow with significant reciprocal action of the carrier and carried phases. 40, 42, 43, 56, 60, 81, 109, 110, 129, 259, 289, 292, 294

unstructured mesh mesh relying on an irregular connectivity between cells that has to be explicitly described. 132, 143–145, 186, 199, 203, 226

velocity polydispersion non-uniform particle velocity distribution caused by PTC, see also polykinetic. 40

volume fraction fraction of volume occupied by a phase inside the control volume. 32, 53, 54, 82

Acronyms

I_{sp} Specific Impulse. 14, 15, 17–19, 22, 291

ACBMM Algebraic Closure-Based Moment Method. 62, 63, 67, 68, 70

ADN Ammonium Dinitramide $NH_4N(NO_2)_2$. 15

AG Anisotropic Gaussian. 64–66, 68, 69, 71, 76–87, 89, 94, 98, 99, 101–103, 109, 111, 115, 116, 122, 125, 126, 175, 176, 181, 201, 203, 204, 213, 216, 217, 219–221, 228, 231, 232, 235, 237, 244, 248, 252, 257, 261–264, 266, 270, 276–281, 284, 286, 289–292, 294, 295, 309–312

AGd degenerated Anisotropic Gaussian. 94, 99, 232, 248, 270

ALE Arbitrary Lagrangian-Eulerian. 137

AMR Adaptive Mesh Refinement. 138, 144

AN Ammonium Nitrate (NH_4NO_3). 15

AP Asymptotic Preserving. 252

AP Ammonium Perchlorate NH_4ClO_4. 15, 16

API Application Programming Interface. 234, 290

AV Artificial Viscosity. 160, 162, 177, 185, 231, 232, 235, 239, 240, 257, 266–269, 276

AX Azimuthally axi-symmetric Anisotropic Gaussian. 94, 232, 234, 248, 251, 270–273, 284, 286, 287

BGK Bhatnagar-Gross-Krook. 77

CAD Computer-Aided Design. 229

CEDRE Calcul d'Ecoulements (Diphasiques) (Réactifs) pour l'Energétique. 4, 6, 225–231, 234, 236, 237, 245, 274, 276, 279, 280, 282, 290–293, 295

CENO Centered Essentially Non-Oscillatory. 183

CFD Computational Fluid Dynamic. 4, 6, 137, 225, 226, 231, 239, 291, 292

CFL stability condition name after the scientists that analyzed the problem (Courant, Friedrichs, and Lewy 1928), stands for "Courant–Friedrichs–Lewy". 120, 128, 140, 154, 156, 159, 161, 163, 179, 182, 195, 201–204, 239, 251, 252, 254, 255, 260

CMAP Centre de Mathématiques APpliquées. 6

CPU Central Processing Unit. 162, 229, 234, 255

CQMOM Conditional Quadrature Method Of Moments. 64, 68

CRF Combustion Research Facility. 257

CSVM Coupled Size Velocity Moments. 63, 68

CWIPI Coupling With Interpolation Parallel Interface. 229

DG Discontinuous Galerkin. 132, 137, 139, 183

DMCS Direct Monte-Carlo Simulation. 60, 68, 69

DMPE Multi-Physics for Energetics Department, stand for the French 'Département Multi-Physique pour l'Énergétique'. 226

DNS Direct Numerical Simulation. 16, 17, 68

DPS deterministic simulation where every particles are tracked in the domain of interest, stands for "Discrete particle Simulation". 59, 60, 68, 69

DQMOM Direct Quadrature Method Of Moments. 64, 66, 68

EAP Etage d'Accélération à Poudre. 20

EEM Eulerian Equilibrium Model. 55, 62, 68

EG Equivalent Gas. 55, 68, 70, 284, 286

EIT Extended Irreversible Thermodynamic. 55

ELED Essentially Local Extrema Diminishing. 182, 183

ELSA Eulerian-Lagrangian Spray Atomization. 54, 68

ELV Expendable Launch Vehicle. 20

EM2C Energétique Moléculaire et Macroscopique, Combustion. 2, 6

EMSM Eulerian Multi-Size Moment. 66–69

ENO Essentially Non-Oscillatory. 182, 183

EOS Equation Of State. 56, 79, 185, 227

EQMOM Extended Quadrature Method Of Moments. 64, 68, 71, 76

FD Finite Difference. 132–136, 139, 153, 155–157, 162, 167, 171, 179, 204, 210, 231

FE Finite Element. 136, 137

FEM Finite Element Method. 132, 135–137, 139, 153, 167, 206, 207, 210

FFT Fast Fourier Transform. 278, 282

FORTRAN FORmula TRANslator. 4, 231–233, 296

FV Finite Volume. 131, 132, 134, 135, 137–139, 141, 142, 145, 147, 149, 153, 159, 161, 167, 169, 179, 183, 191, 203, 205, 209–212, 227, 228, 231, 234, 249

HDF5 Hierarchical Data Format version 5. 232, 233

hetero-PTC PTC between particles of distinct size because of their differences of inertia. 40, 44, 66

HIT Homogeneous Isotropic Turbulence. 40, 43, 82, 83

HLL Harten, Lax, van Leer. 131, 172–175, 184, 186, 187, 190, 199–202, 220, 221, 228, 252, 290, 295

HLLC HLL-Contact. 173, 174, 185, 228, 274

HLLE Harten, Lax, van Leer-Einfeldt. 173–175, 184–186, 203, 239, 245, 248, 250, 252, 261, 285

HLLEM HLLE-Modified. 174, 175, 183, 184, 186

HMX Composed of cyclotetramethylenetetranitramine. Stands for "High Melting point eXplosive". 15

homo-PTC PTC between particles of similar size because of their common large inertia. 40, 44

HPC High Performance Computing. 226, 261

HTPB hydroxyl-terminated polybutadiene. 15

ICBM Intercontinental ballistic missile. 19

IG Isotropic Gaussian. 64, 78, 81, 82, 261, 263, 309–311

ITHAC Acoustic magnitude increase caused by a combustion process. Acronym stand for the french "Instabilté THermo-ACoustique". 28, 292

IUSTI Institut Universitaire des Systèmes Thermiques Industriels. 2, 232

KBMM Kinetic-Based Moment Methods. 3, 64, 67–72, 77, 81, 88, 294

KFVS Kinetic Flux Vector Splitting. 175

LED Local Extrema Diminishing. 141, 156, 160, 163, 177, 182, 191, 192, 194–197, 202–204, 239, 240, 276

LES Large Eddy Simulation. 53, 62, 226, 227, 231

LRE Liquid Rocket Engine. 17–20, 226, 292

MEF Mesoscopic Eulerian Formalism. 62

MF Multi-Fluid. 2, 3, 66–69, 105, 108, 109, 289, 292, 294

MG Multi-Gaussian. 68, 80

MK monokinetic. 64, 66, 68, 69, 75, 76, 81–83, 86, 87, 101, 102, 109, 111, 116, 122, 125, 131, 176, 181, 228, 231, 249, 261, 263, 264, 266, 270–277, 279–281, 284, 286, 291, 309–311

MOMIC Method Of Moments with Interpolative Closure. 66, 68

MOOD Multi-dimensional Optimal Order Detection. 183

MPI Message Passing Interface. 229, 234, 261

MUSCL Monotonic Upwind Scheme for Conservation Laws. 3, 131, 132, 145, 176–178, 180–182, 191, 194, 202, 203, 207, 213, 227, 228, 232, 234, 235, 238–243, 245, 257, 258, 261, 263, 266–270, 274, 276, 277, 281, 285, 290, 291, 295

MUSIG MUltiple SIze Group. 66, 67

NDF Number Density Function. 57–59, 61, 63–66, 69, 73–75, 77, 78, 80, 81, 102, 103, 108, 176

NUMA Non Uniform Memory Architecture. 234

ODE Ordinary Differential Equation. 59, 115, 117, 119, 121, 133

ONERA Office National d'Études et de Recherches Aérospatiales. 2, 4, 6, 159, 162, 225, 226, 231, 234, 293, 295

OpenMP Open Multi-Processing. 4, 234, 260, 290

OSM One Size Moment. 66–68, 105–107, 254, 255

PDE Partial Differential Equation. 115, 117, 119, 132, 140, 209, 210

PDF Probability Density Function. 58, 63

PGD system of equation deduced from the monokinetic (MK) assumption, stands for "Pressureless Gas Dynamic". 75, 77, 84, 86, 87, 95, 99, 140, 162, 166, 169, 171, 172, 176, 203, 216, 218

PPM Piecewise Parabolic Method. 182

PTC existence of various particles in the same neighborhood with distinct velocities. 40, 42, 43, 60, 64, 71, 75, 77, 81, 82, 94, 99, 181, 249, 250, 263, 266, 267, 270, 272, 273, 280, 286, 289, 290, 309

PTF Thermal protection place on the propellant grain for operating issues. Stand for the french "Protection Thermique de Face". 26, 29

QBMM Quadrature-Based Moment Methods. 64, 71, 76, 81

QKS Quadrature Kinetic Scheme. 4–6, 122, 126, 128, 235, 238, 252, 290, 291, 294, 295

QMOM Quadrature Method Of Moments. 66, 68, 122

QUICK Quadratic Upwind Interpolation. 180, 196

RANS Reynolds Average Navier-Stokes. 53, 226, 227

RK Runge-Kutta. 120, 121, 130, 133, 147, 182, 228, 235, 261

RUE RUM Kinetic Energy. 62

RUM Random-Uncorrelated-Motion. 62

SIERRA Simulation Instationnaire d'Ecoulements et Régimes Réputés Acoustiques. 4, 6, 225, 231–237, 239, 245, 260–266, 274, 276, 277, 279–281, 283, 290, 291, 293, 295, 296

SLBM Submarine Launch Ballistic Missile. 19, 20

SP Stochastic Parcel. 59, 60, 68, 69

SRM Solid Rocket Motor. 1–6, 9, 11, 13–21, 23–29, 31, 37–40, 42, 44, 46, 47, 53, 62, 67, 69, 71, 82, 87, 109, 118, 122, 129, 159, 204, 209, 219, 226, 231, 244, 257, 261, 266, 273, 281, 283, 289–292

SSP Stong Stability Preserving. 120, 121, 130, 147, 182, 235, 261

TSM Two Size Moment. 66–69, 101, 103, 106, 108, 111, 115, 122, 124, 125, 234, 235, 252, 254, 255, 284, 286, 287, 290–292, 295

TVD Total Variation Diminishing. 120, 141, 156, 162, 163, 165, 166, 176, 179, 180, 182, 194, 195

UDMH unsymmetrical dimethylhydrazine. 17

VSA Vortex shedding taking place downstream a sharp angle of the grain. Acronym stands for the french "Vortex Shedding d'Angle". 25, 27, 29, 257, 273, 274, 277, 279–281, 283, 285, 286

VSO Vortex shedding generated behind a obstacle. Acronym stands for the french "Vortex Shedding d'Obstacle". 26, 27, 29

VSP Vortex shedding generated by the intrinsic hydrodynamic instability of a Taylor-Culick flow. Acronym stands for the french "Vortex Shedding Parietal". 26, 27, 29

WBE Williams-Boltzmann Equation. 65, 66, 69, 71, 72, 110

WENO Weighted Essentially Non-Oscillatory. 183

XDMF eXtensible Data Model and Format. 233

ZDES Zonal-Detached-Eddy simulation. 227

Introduction

I can feel, something happening
That I've never felt before
Hopeless dreaming will start
Dragging me away from heavens door

Chase & Status and Plan B, End Credits

For a wide family of industrial and environmental applications, there is a great interest in understanding two-phase flows constituted of droplets carried by a fluid. Such cases can be observed in many propulsion devices including sprays for automotive and aircraft engines but also rocket motors using either liquid or solid fuel. A great concern for that field is to be able to evaluate the influence of these droplets on the gaseous carrier phase in which they are suspended, while taking into account the inhomogeneous properties of this disperse phase. In practice, the droplets contained in a mixture possess different sizes with diameters often scattered over several order of magnitude. Obviously, large and small droplets do not have the same dynamics and can interact with each others, through coalescence and break-up, influencing even more the disperse phase and their carrier fluid. Understanding the dynamics of two-phase disperse flows to predict the behavior and performances of propulsion systems is both a challenging and a critical task that have interested generations of engineers and researchers. We place the presented work in this large class of industrial issues and focus on the specific case of solid rocket propulsion.

Among the space propulsion technologies, Solid Rocket Motors (SRMs) are known for their reliability, high trust and ability to be stored during a long period of time. Because of their relatively low cost, such engines are valuable options for the first stages of present and future space launchers (Guery et al. 2010). The presence of aluminum oxide (Al_2O_3) residues and smokes in the internal flow of SRMs have a great impact on the behavior of these engines. Caused by the introduction of aluminum powder in the propellant grain to increase the motor performances, their presence influences greatly the physical characteristics of the combustion products. Often representing up to more than 30% of the burnt mixture weight and still under a condensed form despite the extreme temperature, this polydisperse spray of alumina droplets has been shown to have a sensitive impact on the engine stability. The thrust oscillations may result from very complex interactions between acoustic waves, that propagate in the confined volume of the chamber, the spray and various transient or unsteady processes. Among those are, for instance, the unsteady propellant combustion (Culick and Yang 1992), flow instabilities either developing downstream some discontinuities of the internal geometry (Brown et al. 1981) or generated by a pure, intrinsic hydrodynamic instability of the flow injected from a lateral wall (Casalis, Avalon, and Pineau 1998), the distributed combustion of aluminum droplets (Gallier and Godfroy 2009a), or a combination of several of these factors (Kuentzmann 1995). The

impact of the condensed phase on the nozzle efficiency is clearly negative while it is generally more complex and ambiguous on pressure oscillations, especially when vortex shedding driven oscillations is developing. Since the size and velocity of the particles have a major impact on the dynamics of instabilities through the coupling of the particles to the surrounding gas, the local distribution of the spray, in terms of both size and velocity, is a key parameter to be taken into account for such applications. As a consequence, both damping and driving mechanisms may be observed depending on various factors (Dupays et al. 2008). Solid propulsion applications, where disperse flow occurs, are specific because the interaction between both phases is significant and because the carried phase remains under the structure of droplets all across the engine. In that context, the understanding not only of the gaseous carrier phase flow but also of the droplet behavior is a key issue to be able to foresee hydro-acoustics phenomena in the early development of SRMs and thus avoid deleterious effects on launcher ballistics and payload.

In that context, a long term effort has been provided by the Office National d'Études et de Recherches Aérospatiales (ONERA) to improve the knowledge of the internal flow of SRMs. Due to the harsh conditions existing inside these engines however, measurement possibilities are limited and simulations are often mandatory to understand the underlying physics driving SRMs behavior. As a consequence, along the years, ONERA has been continually developing numerical and experimental tools to investigate the physical phenomena associated with solid rocket propulsion (Fabignon et al. 2016). This duality between experimental and numerical investigations is a key point in investigating the internal flow since the understanding of the physics often requires information that can be only acquired from experiments, as the characteristic of the propellant surface combustion, or that can be exclusively obtained by numerical simulation, as the topology of the internal flow. Moreover, this issue is even more problematic since there exists only a few number of parameters on which it is possible to compare experiments and simulations to validate the chosen methodologies. This work takes place in the numerical side of this approach where the challenge is to design reliable models for both the carrier and the disperse phase to conduct always more predictive simulations while improving associated numerical methods in terms of robustness and accuracy.

To model the behavior aluminum oxide droplets and their impact on the flow inside SRMs, a wide variety of solution has been proposed over the years and can be classified in two main categories, the Lagrangian (Sabnis 2003; Dupays, Wey, and Fabignon 2001) and the Eulerian methods (Simoes 2006; Sachdev, Groth, and Gottlieb 2005; Doisneau et al. 2013). While the first class of methods aims at tracking particles or realizations along the flow, the second approach closes the problem in the same fixed referential as the carrier phase. More specifically, it is possible to design models based on a kinetic approach with high abilities to treat droplet polydispersion and that are well suited for the disperse flow conditions encounter in SRM. Therefore, a long-term effort has been conducted by ONERA in order to develop that class of Eulerian models, which can describe properly spray polydispersion and related dynamics including evaporation, heating, two-way coupling, as well as break-up and coalescence. This effort has been conducted first in collaboration with IUSTI then with the EM2C laboratory over the last decade. There has been an increasing interest for the Multi-Fluid (MF) models, originally developed for spray applications (Laurent and Massot 2001; Chaisemartin 2009; Fox, Laurent, and Massot 2008) and that are designed with the intent of providing governing equations with well-posed mathematical properties to treat size polydispersion. Based on a size discretization of the phase space, generally combined with moment methods, from low order to high order as in (Laurent, Sibra, and Doisneau 2016; Vié, Laurent, and Massot 2013), these models have been successfully integrated for industrial configurations (Doisneau et al. 2013; Sibra et al. 2017;

Emre et al. 2015; Essadki 2018).

However, Eulerian methods intrinsically possess their own issues. Most of these methods only take into account the average velocity of the particles to describe their convection, preventing any droplet trajectory crossing and create in such case a Dirac delta function in density, also called δ-shock (Chaisemartin 2009; Kah 2010). This specificity has been observed for long and revealed to be challenging for numerical methods (Bouchut, Jin, and Li 2003; Daniel et al. 1993; Saurel, Daniel, and Loraud 1994; Chaisemartin 2009). Using high order moment methods in velocity, either with algebraical closures (Fevrier, Simonin, and Squires 2005; Simoes 2006; Masi and Simonin 2012) or quadrature (Fox 2008a; Chalons, Kah, and Massot 2012; Yuan and Fox 2011), it is possible to take into account the missing local velocity dispersion of the droplet and make possible the existence of droplet trajectory crossings. More recently and still relying on high order moment methods, it has been proposed to enabled the possibility to take into account statistical droplet trajectory crossing based on a multi-variate Gaussian closure (Vié, Doisneau, and Massot 2015). Inspired from the work conducted for rarefied gas flow (Levermore and Morokoff 1998; Berthon 2006a; Groth and McDonald 2009), such choice is motivated by the need of ensuring the well-posed mathematical properties of the system of equations describing the disperse phase but also by the necessity to take into account anisotropic velocity distribution (Simoes 2006; Masi and Simonin 2012). By enabling the existence of several velocities at each spatial point, such advance extends the validity range of the MF models to particles of higher inertia. However, until the presented contribution, such an ability to treat two-phase disperse flow thanks to that new closure was restricted to academic configurations (Vié, Doisneau, and Massot 2015; Sabat 2016). This specific point is at the center of the conducted work, which aim at enabling the use of this velocity dispersion for industrial configurations. More specifically, it has been managed to provide a model, based on kinetic closure, able to treat both size and velocity dispersions thanks to high order moment in both of these phase space.

Taking into account local velocity dispersion have already been done for SRM applications (Simoes 2006; Sachdev, Groth, and Gottlieb 2007), but we propose here to do so using the multi-variate Gaussian closure (Vié, Doisneau, and Massot 2015) and relying on the mathematical structure of the governing equations. This is why, we focus our interest on a KBMM approach (Vié, Doisneau, and Massot 2015) instead of other methods (Vié et al. 2012). The specific choice of the multi-variate Gaussian form of the velocity distribution and the affine reconstruction in size ensure the hyperbolicity of the system of equations but also the existence of an entropy equation and the realizability of the moments of the kinetic equation we working with. Therefore, it is proposed to rely on these well-posed mathematical properties to design efficient resolution strategies.

The main presented contributions are associated with the design of numerical methods dedicated to the resolution of the newly proposed systems of equations modeling the disperse phase. We separate them in two categories of methods: those associated with the transport of the droplets in the physical space and those associated with drag, heat transfer and evaporation, that is a transport in the phase space. In both cases the realizability of the schemes, their ability to ensure a physically consistent solution and thus the existence of a positive number density distribution, is a key issue that has to be fulfilled. More than that, care is taken to ensure the second order of accuracy of these schemes. Ensuring either the realizability or second order of accuracy is not an issue in itself, however, there are difficulties when combining the two for the condition faced in the SRM. Indeed, singularities such as stiff source terms, shocks, δ-shocks, droplet free or null velocity dispersion area are challenging for the numerical methods while

they are often observed in the configurations we are interested in. Solutions are proposed for that purpose along the manuscript.

In the case of transport schemes, we based our approach on the MUSCL multislope methods, as designed in (Le Touze, Murrone, and Guillard 2015) and originally developed in (Buffard and Clain 2010; Clauzon 2008), that are able to maintain the realizability even at the boundaries of the open of the admissible state. Contributing particularly to the development of Riemann solvers, limiters and reconstruction variables (Berthon 2005), it has been possible to propose a numerical method adapted for general unstructured meshes and that is proved realizable. These methods are to be compared with those used during the 90's and that need to rely on case dependent artificial dissipation for stability issues (Lupoglazoff and Vuillot 1992a; Dupays 1996). Despite the efficiency of these centered numerical methods, they needed case dependent-parameters that required human intervention to be set up. Significant differences can be observed using new generations of schemes, as in this work, for SRM configurations. Indeed, the accurate resolution of the disperse phase alone is able to change the solution obtained for the same model. Additionally, this class of methods has been extended to axisymmetric framework (Clain, Rochette, and Touzani 2010) to be able to consider realistic configuration at low cost. This extension, far from being marginal, reveals that standard strategies fail to solve the physics we are interested in, because of resolution issues associated both with the closure of the model and the numerical schemes. The singularities observed in this framework, and more specifically in the neighborhood of the symmetry axis, are essentially the consequence of the specific characteristics of the multi-variate closure chosen in the conditions of two-phase flows (Dupif et al. 2018a). An original solution is proposed for that issue and tested on SRM cases.

In the phase space, the Quadrature Kinetic Scheme (QKS), as proposed in (Laurent, Sibra, and Doisneau 2016; Sibra et al. 2017), is extended to take into account a new velocity closure while maintaining the robustness and second order of accuracy. The original objective of the method is to treat simultaneous drag, evaporation and heat exchange in order to accurately solve their combined effects. Using both realizable schemes in the physical and phase spaces, it is proposed not only to treat academic configurations (Boileau et al. 2016) but also to analyze genuine SRM configurations. Doing so, it is possible to witness the evolutions of quality of Computational Fluid Dynamic (CFD) resolution, thanks to both models and numerical methods, from the 90's up to today (Dupif et al. 2015b, 2016).

The final goal of the proposed work is to integrate the new models and numerical strategy in the CFD platform of ONERA for energetics CEDRE (Refloch et al. 2011). Due to the complexity of the architecture of CEDRE, it has however been chosen to integrate first the proposed strategy in the in-house code SIERRA, originally design in the 90's specifically for the sole purpose of solid rocket propulsion. Re-writing the code to adapt it to new standards, this task has permitted to test ahead from the CEDRE integration the new strategies but also to assess an original way to implement the solver. Through that development process, the object oriented capabilities of the todays FORTRAN compilers have been investigated and OpenMP parallelizations methods have been tested. This contribution therefore exhibits the future abilities of the CEDRE code in which the proposed resolution strategy can find application in other contexts. For now, thanks to the collaboration with C. Le Touze (Le Touze, Murrone, and Guillard 2015), the new closure has been experimentally integrated in CEDRE. Further features including the axisymmetry, the boundary conditions and the QKS method still remain to be integrated and may open the way for predictive large scale simulations of SRMs (Fabignon et al. 2016) using the new elements designed in the Ph.D. thesis.

As a consequence, it is proposed through this manuscript to design model and numerical methods relevant for SRM applications while taking care to satisfy fundamental mathematical properties. Thanks to this development starting from elementary contribution and aiming at industrial issues, it is possible to observe the consequences of the combinations of numerical methods and governing equations on the physical interpretation that can be obtained from the SRM simulations. Therefore, focusing on the objective of predicting the internal flow of SRM with the highest accuracy and reliability possible, the main contributions, given here-after, are:

- The derivation of a closure for two-phase disperse flow able to treat both velocity and size polydispersion,
- The design of realizable numerical schemes able to solve this system of equations able to operate on general unstructured mesh,
- The extension of the derivation and the numerical strategy to the 2D axisymmetric framework that includes the development of a specific boundary condition for the axis of symmetry,
- The comparison of two generations of schemes on test cases directly associated with solid rocket propulsion,
- The physical analysis of instabilities in 2D and 2D axisymmetric configurations.

This manuscript is divided in 3 parts and 11 chapters. Part I is dedicated to models describing two-phase disperse flow in the conditions of the internal flow of SRMs. More specifically, Chapter 1 presents the characteristic of SRMs, the current issues of that technology, the development conducted to understand their unsteady behavior and the researches conducted today in that field. In this first chapter, it is thus aimed at giving to the reader an overview of the treated problematics and basic knowledge of solid rocket propulsion but also to detail the encountered order of magnitudes and the flow topology that we aims at modeling. Chapter 2 provides a review of the description of the two-phase disperse flows, first from a general approach and then focusing on the models based on a kinetic description of the droplets, which are able to represent droplet trajectory crossing. This chapter describes the phenomena that can be encountered in two-phase flows and models for the evolutions of droplets are given. Considering the flow conditions described in Chapter 1, it is proposed to retain and develop Eulerian models based on moment methods. Chapter 3 proposes to derive the model associated with both the carrier and the carried phases. From an original approach, the governing equations of the gas and the droplets are presented thanks to the same derivation, in both Cartesian and axisymmetric frameworks. Discussing the fundamental differences in treating the carrier and the carried phases through that approach, the mathematical properties of these systems of equations are detailed. Finally, Chapter 4 completes the model by coupling the phases one to another and introducing the size polydispersion. As a consequence, a closure, able to model both velocity and size polydispersions thanks to high order moment methods, is proposed for an accurate modeling of the internal flows of SRMs.

Part II focuses on the numerical methods chosen for the resolution of the derived models. Chapter 5 first proposed a high level strategy to couple the systems of equations thanks to operator splitting and robust time integration methods. More particularly, the end of the chapter focuses on a realizable QKS able to treat simultaneously drag, heat transfer and evaporation to couple

the systems in an efficient way. Then, Chapter 6 is dedicated to the design of a class of numerical methods, for the transport operator which is at the core of the thesis. It is aimed at creating schemes, that are proved realizable, without neglecting the need for accuracy, even at the border of the open set of admissible states. Working on general unstructured meshes, these developments are extended to 2D axisymmetric framework while conserving the realizability property. Chapter 7 completes the previous chapter by tackling the problem of the boundary conditions. Aside the description of standard methods, a new methodology to treat the symmetry axis in axisymmetric simulation is proposed.

Finally, Part III proposes to exhibit the new abilities developed through this work thanks to these new model and numerical methods. First, Chapter 8 describes the CFD codes used for that purpose. The abilities of CEDRE and SIERRA as well as their advantages are detailed. Chapter 9 is dedicated to the assessment of the quality of implementation of the numerical methods on academic problems. The abilities and performances of the schemes for the transport of the gas, of the particles and for the coupling through the QKS are tested. Then, in Chapter 10, we focus on the evaluation of the numerical methods in complex conditions. While exhibiting characteristics close to real applications, several fictitious test cases are presented enabling to observe the effect of the numerical strategies proposed in an applied context. Finally in Chapter 11, the simulation of an unsteady SRM experimentally fired is proposed. Through this last case, the consequences of the evolution proposed of the modeling can be observed on real applications.

During this thesis, results of the work detailed in this manuscript has been presented during several international conferences:

Boileau, M., J. Lagarde, V. Dupif, F. Laurent, and M. Massot. 2016. “Two-size moment Eulerian multi-fluid method describing the statistical trajectory crossing: modeling and numerical scheme”. In *9th International Conference on Multiphase Flow, ICMF*. Available at https://hal.archives-ouvertes.fr/hal-01543507. Firenze, Italy.

Dupif, V., M. Massot, J. Dupays, and F. Laurent. 2017a. “A robust multislope MUSCL method formulation for two-phase flow simulations inside solid rocket motors”. In *8ème Congrès SMAI*. Ronce-les-Bains, France.

Dupif, V., M. Massot, J. Dupays, F. Laurent, and C. Le Touze. 2015b. “Influence of numerical methods on the simulation of the steady and unsteady two-phase flow in solid rocket motors”. In *6th European Conference for Aeronautics and Space Sciences, EUCASS*. Krakow, Poland.

– . 2016. “On the influence of the numerical strategy on the predictive character of an Euler-Euler model for two-phase flow simulations in solid rocket motor instabilities”. In *9th International Conference on Multiphase Flow, ICMF*. Firenze, Italy.

– . 2017b. “A robust and accurate MUSCL multislope scheme for particle laden flow: application to solid rocket motor instabilities”. In *3rd International Conference on Numerical Methods in Multiphase Flows, ICNMMF-III*. Tokyo, Japan.

Including a poster

Dupif, V., M. Massot, J. Dupays, and F. Laurent. 2015a. “Eulerian models and related numerical schemes and parallel implementation for the simulation of polydisperse two-phase flows in solid rocket motors”. In *SimRace, International conference on numerical methods and High Performance Computing for industrial fluid flows*. Rueil-Malmaison, France.

Moreover, the developments proposed are to be submitted to international journals with review committee:

Dupif, V., J. Dupays, A. Larat, and M. Massot. 2018a. "Accurate and robust numerical strategy for axisymmetric Eulerian modeling of particles laden flows of moderate inertia". *To be submitted to Journal of Computational Mathematics, SMAI-JCM.*

Dupif, V., M. Massot, J. Dupays, and F. Laurent. 2018b. "Euler-Euler simulation of an unsteady solid rocket motors with size polydispersion and local velocity dispersion". *To be submitted to Journal of Propulsion and Power, JPP.*

Dupif, V., M. Massot, J. Dupays, F. Laurent, and C. Le Touze. 2018c. "Predictive character of Euler-Euler model and numerical strategy for two-phase flow simulations of solid rocket motor instabilities". *To be submitted to Journal of Computational Physics, JCP.*

This Ph.D. thesis has been funded by the ONERA and advised by Marc Massot, Frédérique Laurent and Joël Dupays. The financial and material support from EM2C all along the Ph.D. thesis and the support from the Sandia National Laboratory of Livermore during the scientific exchange of 2016 are greatly acknowledged. This work has been conducted in collaboration with the applied mathematics team of the EM2C laboratory of CentraleSupélec and the CMAP laboratory of the École polytechnique.

Part I

Two phase flow modeling in solid rocket motors

Chapter 1

Rocket propulsion using solid propellant

> Did you ever heard the expression "It's not rocket science"?
>
> An acquaintance of mine

This chapter is dedicated to the description of the application systems on which this PhD thesis is focused, Solid Rocket Motors (SRMs). Despite being one of the oldest rocket propulsion technology, its use is still envisioned for future space launchers and military applications (Guery et al. 2010). This chapter is dedicated to the description of the concept of rocket propulsion and more precisely to rocket motors using solid fuel. Their abilities and the research currently carried out in that field are discussed in order to position the present contribution. To do so, this chapter is divided into three sections. First the basics of rocket propulsion and the standard structure of a SRM are presented to familiarize the reader with solid propulsion. Section 2 is devoted to the description of the technologies designed along the years to improve the SRMs and provide their current abilities. Ultimately, the final section reviews the technological issues faced today by SRMs and highlights the improvements aimed to be achieved in this work.

1.1 Description of solid rocket motors

1.1.1 A brief history of the concept

The first rocket devices have obscure origins but were based on black powder making the solid rocket engines the oldest rocket propulsion systems. The first written trace of such devices can be tracked back to the late XIIth or begin XIIIth century in China (Chase 2003) where the idea to use rockets as weapons quickly arise. This technology reached Europe around 1250 A.D. through Arabic scientists in a book called "Liber Ignium" (Book of Fire) and Hassan Al-Rammah, who designed the first rocket-driven torpedo circa 1280 A.D. Although being invented after the rocket, the gun technology improved so much in the following centuries that rockets

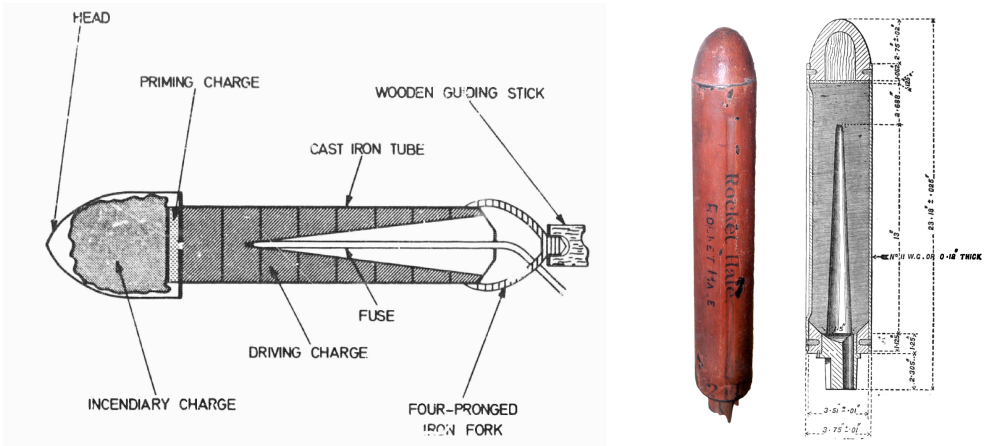

(a) Sketch of XIXth century rockets (Williams, Barrère, and Huang 1969)

(b) Hall rocket

Figure 1.1: *Rockets from the XIXth century*

fell into disuse.

The principle however reappeared in India during the Mysorean wars in the 1780's and 1790's, causing heavy damage to the british colonial troops. With up to 2 km range (Narasimha 1985), the Mysorean rocket get the attention of British militaries that reverse-engineered and improved the principle. This led to the design of the Congreve rocket in 1804 and the Hall rocket in 1855. As presented in Figure 1.1, these nozzleless rockets were composed of a tube filled with black powder placed behind a payload and attached to a stick used to guide the object at launch. Due to a great improvement of the firearms in the second half of the XIXth century, rockets fell again into disuse for the military applications but continued to exist in the fireworks industry.

At the beginning of the XXth century, ambition for space travel arises and serious work for space propulsion appeared through the pioneers Ziolkowski (Ziolkovski 1903) in Russia, Esnault-Pelterie (Esnault-Pelterie 1913) in France and Oberth (Oberth 1923) in Germany only to cite the most famous ones. These pioneers were the first to put mathematics on the subject of space travel. But, because of the technological gap needed to reach the space at that time, these works were mostly seen as science fiction. These pioneers only considered liquid propellant since, before the 1930's, solid propellant mostly refers to black powder industry and lacks of performances. As reported by Ley (Ley 1935), until then, there was a great lack of knowledge of the physics of the internal ballistic of these engines even from the well established rocket industry. Basic features as the exit gas velocity were unknown and the efficiency reached by these technologies was still far from the theoretical expectation.

Goddard (Goddard 1920), another pioneer in the US, considered that solid rocket could be used for space travel under several conditions including an improvement of the propellant material and the use of a de Laval nozzle. Starting from these considerations, Goddard successfully test the first solid rocket motor using double-base propellant during the world war I (see Figure 1.2a). Thanks to the de Laval nozzle, he was able to improve the rocket performances, literally skyrocketing from 2 % to 63 % the thermal energy transformed in thrust. Other researchers came independently to the same conclusion (Malina 1968) creating a basic concept that did not change through years.

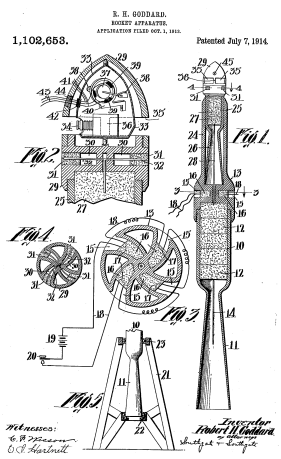

(a) Two-stage SRM pattent from Goddard (1914)

(b) First SRM assisted take-off using GALCIT propellant the August 12, 1941

Figure 1.2: *US rockets using solid propellant during the first half of the XXth century*

The solid rocket motors were considered, in the scientist community, for space launcher only after the world war II and the appearance of the GALCIT propellant developed by the Jet Propulsion Laboratory which demonstrated both the efficiency and the safety of the technology for assisted aircraft take-off (see Figure 1.2b). Thus, all around the world, scientists began independently to improve the SRMs technology, process and knowledge (Andrepont and Felix 1994; Davenas 1995; DeLuca 2017).

1.1.2 SRM structure

Modern solid rocket motors are in general composed of 4 main elements as presented Figure 1.3:

- The propellant grain constituted of the energetic material used for propulsion,
- An igniter with a charge able to ignite the grain,
- A casing containing the propellant grain and constituting the combustion chamber,
- A de Laval nozzle accelerating the burned gas to a supersonic velocity.

As any rocket motor, the objective of the engine is to provide thrust by ejecting the combustion products at high velocity. The burnt gas is expended through the de Laval nozzle at a supersonic speed while keeping the combustion chamber under a high pressure typically range from 3 to 25 MPa (Barrere et al. 1960). With a burning temperature lying around $3500\,K$, these operating conditions inside the motor explain the presence of a thermal protection to ensure the motor integrity during the time of flight.

Despite nozzleless configurations remain investigated (Gany and Aharon 1999) in order to di-

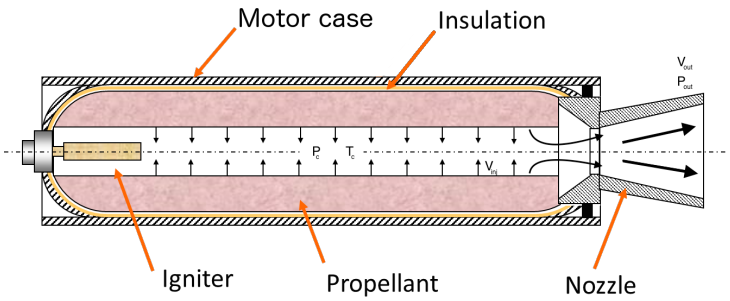

Figure 1.3: *Schematic structure of a modern solid rocket motor (adapted from www.narom.no)*

minish the weight and the length of the engine, this concept is still being used in the majority of SRMs today. During the XXth century, most of the performance enhancement were obtained through the use of new propellants and the lightening of the structure.

1.1.3 Ideal performances of solid rocket motors

1.1.3.1 Thrust

Applying the second Newton law on the motor presented Figure 1.3, it is possible to determine the thrust $\boldsymbol{F}$ depending on the mass flux $\dot{m}_{out}$ ejected at the velocity v_{out} through the nozzle of outlet surface A_s with an exit static pressure P_{out} in an environment at a pressure P_{ext} by:

$$\boldsymbol{F} = \dot{m}_{out} v_{out} + (P_{out} - P_{ext})\, A_s. \tag{1.1}$$

The performance of rocket engines is mostly driven by the ejection velocity. The combustion products are accelerated by the convergent-divergent nozzle from a negligible velocity to a supersonic speed thanks to the expansion of the gas maintained at high pressure in the combustion chamber. Knowing the total pressure in the chamber P_c, the exit velocity is a classical result (Larson and Wertz 1992; Gossant 1993; Williams, Barrère, and Huang 1969) for the isentropic expansion of a perfect gas:

$$v_{out} = \sqrt{\frac{2 T_c r_g \gamma}{\gamma - 1}\left[1 - \left(\frac{P_{out}}{P_c}\right)^{\frac{\gamma-1}{\gamma}}\right]}, \tag{1.2}$$

where T_c is the total temperature inside the chamber, r_g the specific perfect gas constant and γ the specific heat ratio.

From the observation of the equation (1.2), it is obvious that the combustion temperature is one of the most important parameter since it is directly related to the energy released. Together with the thermodynamic properties of the combustion products, the flame temperature remains

roughly constant for a given propellant depending on the operating conditions. Therefore, assuming no-change in the nozzle geometry, the thrust can be modulated only by the mass flux ejected $\dot{m}_{out}$ and the combustion chamber pressure.

1.1.3.2 Internal ballistics

For steady-state conditions, the mass flow ejected is equal to the mass flow injected $\dot{m}_{in}$ in the combustion chamber that can be directly deduced from the burning surface A_{grain} of the propellant grain and the combustion velocity v_{comb}. Such combustion velocity is generally approximated by a Vieille (or Saint-Robert) law such that $v_{comb} = a_{prop} P_c^{n_{prop}}$, where a_{prop} and n_{prop} are constant data associated to a propellant composition. Moreover, using a choked nozzle, the mass outflow is also determined by the combustion chamber pressure in addition to the surface at the throat A_t. It is therefore possible to determine the pressure inside an SRM starting from a mass conservation equation.

$$\dot{m}_{in} = A_{grain} a_{prop} P_c^{n_{prop}}, \qquad \dot{m}_{out} = \frac{P_c A_t}{C^*}, \tag{1.3}$$

$$P_c = \left(\frac{A_{grain}}{A_t} C^* a_{prop} \right)^{\frac{1}{1-n_{prop}}}, \qquad C^* = \left(\frac{\gamma+1}{2} \right)^{\frac{\gamma+1}{2(\gamma-1)}} \sqrt{\frac{r_g T_c}{\gamma}}. \tag{1.4}$$

where C^* is the characteristic velocity, here expressed for a perfect gas, and n_{prop} have in practice to remain in $[0, 1[$ to avoid an unsteady behavior or a time diverging pressure curve, leading to the destruction of the device.

Equation (1.3) shows that both mass flux and chamber pressure are actually linked and equation (1.4) shows that these can be handled by the surface ratio A_{grain}/A_t alone. As a consequence, for a given propellant, the thrust modulation of a SRM is only managed by the burning surface of the grain. Moreover, once started, the combustion of the propellant grain cannot be stopped in industrial configuration. Therefore, the thrust curve have to be determined during the SRM 's design through the grain geometry and cannot be changed afterwards. Some examples of grain cross-sections and their corresponding thrust curves are presented Figure 1.4.

1.1.3.3 Establishing performance for launchers

The performance of a space launcher cannot be only summed up to the thrust of the rocket engines and since a rocket losses weight by providing thrust, the resulting acceleration depends on the time of flight. Therefore, it is more convenient to observe the maximum velocity increase ΔV that can theoretically be achieved. Assuming a constant thrust and ejected mass flow one

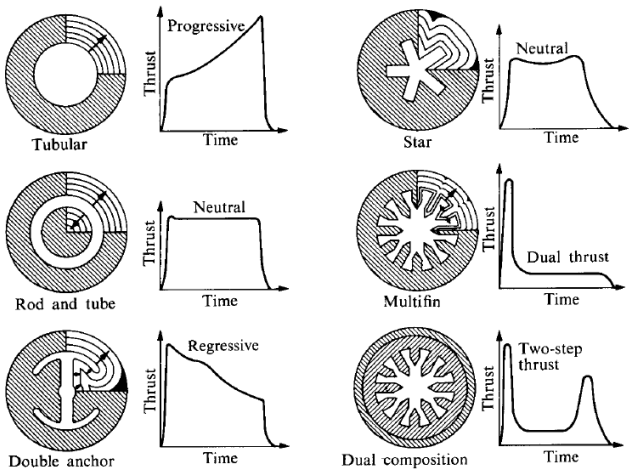

(a) Cross section geometries and associated thrust (Hill and Peterson 1992)

(b) Sub-scale motor propellant grain star geometry ©ONERA

Figure 1.4: *Examples of propellant grain cross sections*

can deduce the velocity increase of a rocket that can be put under the form:

$$\Delta V = g_0 I_{sp} \ln\left(\frac{m_{init}}{m_{final}}\right), \qquad I_{sp} = \frac{\boldsymbol{F}}{g_0 \dot{m}_{out}} \tag{1.5}$$

where g_0 is the gravitational acceleration at sea level, m_{init} and m_{final} are the initial and final mass of the launcher and finally I_{sp} is the Specific Impulse.

In ideal conditions, the Specific Impulse (I_{sp}) can be deduced from the equations used until here to describe the internal ballistics. In practice, more complex modeling, taking into account chemical reactions (see for example (Gordon and McBride 1994)) or helped from empirical relations, have to be used. Despite a simplified approach, equation (1.5) separates two distinct aspects of the performance of a space launcher:

- The mass ratio between the beginning and the end of the launch, which is related to the launcher structure.
- The thrust provided related to the mass of propellant ejected and summed up in the term I_{sp}.

The first aspect depends on the mass of the payload on the one hand and on the mass of the rocket motor structure compare to the mass of propellant embedded on the other hand. The second aspect combines the key to understand the technological choices made in the design of SRMs and the technical issue appearing consequently.

1.2 Solid rocket motor technology

1.2.1 Usual technologies

In this section, we concentrate on the technical description and theoretical performance of SRMs and compare with other rocket propulsion technologies.

1.2.1.1 Propellant composition

Among the elements composing a SRM, the propellant is the key element providing the energy to the engine. Several possibilities of energetic materials exist and have been improved over the centuries.

1.2.1.1.1 Usual formulations Basically, solid propellants are a mixture of solid oxidizer and reductants selected to maximize the gas volume generated and the burning temperature without any external supply. Unlike gunpowder used in firearms and explosives which have a similar composition, the solid propellant is compacted such that the grain can burn slowly without leading to an uncontrolled explosion. Several formulas of propellant exist and their composition has been improved through the time in term of specific impulse and operational capability:

Black powder: Mixing of nitrate (typically KNO_3), charcoal and sulfur. Still used in model rocketry, the specific impulse of these engines does not exceed 100 s.

Double-base: Propellant based on nitrocellulose and nitroglycerin with a typical specific impulse lying around 230 s.

Composite: Powdered oxidizer and often metal reductant intimately mixed and hold together by a binder that can also react as fuel. Typical mixtures include approximately 68 % of Ammonium Perchlorate NH_4ClO_4 (AP), 20 % aluminum powder (Al) and 12 % of various ingredient mostly including hydroxyl-terminated polybutadiene (HTPB) binder. Using such propellant, the specific impulse can reach up to 300 s. Other mixture based on Boron instead of aluminum or using other binder or oxidizer can be envisioned.

New propellant: New propellants generally aim at increasing the efficiency by introducing highly energetic materials such as HMX in the composite propellant binder. An I_{sp} increase from 10 to 20 seconds is expected.

Green propellant: New formulations taking into account the atmospheric pollution caused by SRMs. For example, this can be achieved by replacing the AP by a mixture of Ammonium Nitrate (NH_4NO_3) (AN) and Ammonium Dinitramide $NH_4N(NO_2)_2$ (ADN) (Wingborg and Calabro 2016) to avoid the production of hydrochloric acid.

Aside these fundamental components, additives are generally introduced in small quantities to the compositions described above in order to, for instance, enhance the ignition of the grain,

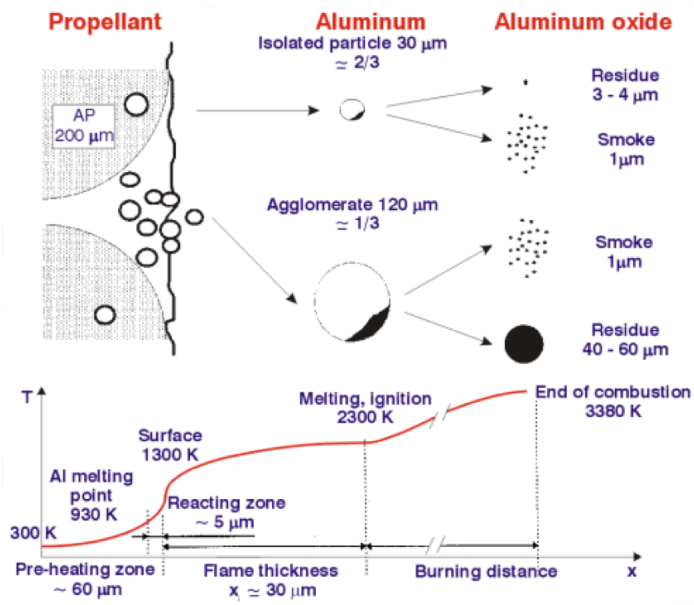

Figure 1.5: *Aluminum combustion process for the Ariane 5 propellant (Fabignon et al. 2003)*

improve the combustion velocity and stability, the resilience to external stress and reduce the aging for a more efficient storage. More information on the composition of solid propellant can be found in (Beckstead et al. 2007).

1.2.1.1.2 Aluminum particles A metalized powder is generally introduced in the propellant to increase the flame temperature. The specific combustion process of these particles is a critical issue for today SRMs that is still not completely mastered (see Section 1.3.4). As presented in Figure 1.5, aluminum particles do not burn directly at the grain surface but rather further away. Released from the grain, they react in contact with the oxidizing gas generated by the pyrolysis of the AP particles. The distance at which the droplet combustion stops is directly linked to their size. They can either burn quickly close to the surface or end their combustion further away in the chamber. The other reactants are consumed directly after the decomposition of the grain, in a thin layer above the propellant surface such that only the reaction of aluminum is clearly specific. In practice, a complete size distribution of the aluminum powder is to be considered with diameters ranging from several hundreds of nanometers to few hundreds of micrometer. From the combustion of such grain, aluminum oxide droplet resulting from the aluminum powder oxidation appears in the burnt mixture despite the extreme temperature taking place in the combustion chamber.

However, the determination of the size distribution of the droplet leaving the surface is a complex task since it generally does not correspond to the initial aluminum particle size distribution. As a matter of fact, as represented Figure 1.5, aluminum particles tends to agglomerate at the surface before creating bigger droplets. To determine such distribution, experimental investigations (see Figure 1.6b) and more recently Direct Numerical Simulation (DNS) of the propellant surface (see Figure 1.6a) are privileged. After this initial combustion, the resulting aluminum oxide droplets size distribution continue to evolves through coalescence in the chamber and break-up in the nozzle (Doisneau 2013).

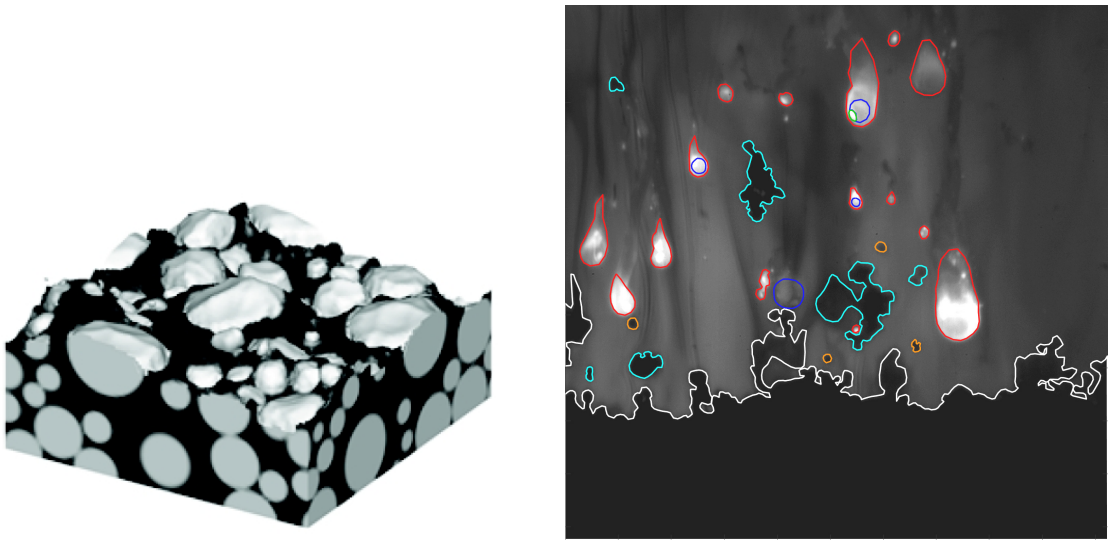

(a) DNS simulation of the propellant regression (Fabignon et al. 2016)

(b) Experimental strioscopie and automatic image analysis (courtesy R. Devillers and M. Nugue)

Figure 1.6: *Composite propellant surface combustion investigation methods*

These condensed combustion products do not participate to the expansion process and produce entropy due to drag and heat transfer lags with the carrier gas such that the theoretical performance improvement expected is never reached. The use of small particles is to be privileged for performance issues but the resulting aluminum oxide size distribution is not guaranty to be smaller because of the aggomerate process at the surface and safety concern can arise while using nanometric particles (DeLuca et al. 2010).

1.2.1.2 Comparison with other rocket technologies

1.2.1.2.1 Liquid rocket engine Rocket propulsion using liquid propellant generally hold a high specific impulse. Liquid Rocket Engines (LREs) using liquid oxygen and liquid hydrogen are known to have a typical specific impulse of 450 s, the highest among the industrial chemical rocket motors. Kerosene or liquid methane are also considered instead of liquid hydrogen to reduce structure weight and size thanks to an higher density of the reactants and lower cryogenic constraint, despite a lower I_{sp}. Moreover LREs have a more complex structure and many mechanical moving parts endure extreme external stresses. As a consequence, these engines have a higher cost and are privileged for main propulsion or upper stages.

Contrarily to SRMs, the thrust of LREs can be modulated. However, due to the low temperature at which the propellant have to be kept, high efficient cryogenic propellants cannot be stored during a long period of time, which cause space launchers to be filled only the eve of the launch. Other storable liquid reactants with performance comparable to SRMs, such as N_2O_4 and unsymmetrical dimethylhydrazine (UDMH) can be found in motor with restarting abilities. These are generally considered for satellites and upper stages of rockets to place payloads on expected trajectories and orbits.

1.2.1.2.2 Hybrid rocket engine Hybrid rocket engines aim at increasing the I_{sp} of the SRMs while being able to modulate the thrust without reaching the technical complexity of a LRE. To do so, an oxidizer tank is attached to a combustion chamber containing a grain with an adapted composition and geometry. The result is known to achieve mid-way performances between SRMs and LREs in theory and experiments (Lestrade et al. 2016). However, this technology did not until today found an industrial application (Maggi et al. 2012).

1.2.1.2.3 Gelled propellant rocket motor With propellant under a gelled state, the objective is to combine the advantages of SRMs and LREs. Unlike hybrid rocket engine, it is essentially aimed to be achieved by combining safety and storage abilities of SRMs and thrust modulation capability of LREs (Ciezki, Naumann, and Weiser 2010; Naumann et al. 2011). Since the specific impulse of these engines remain however under the efficiency of composite solid rocket motor, they are currently not envisioned for space propulsion but rather for military tactical applications.

1.2.1.2.4 Nuclear rocket propulsion Instead of using chemical energy, atomic energy can be envisioned. Two main options exist to do so:

- Using nuclear energy to heat up a gas, which is accelerated through a nozzle as for chemical rockets,
- Using small nukes to provide thrust thanks to nuclear explosions,

While the first option would achieve an I_{sp} close to $1000\,s$, the second principle would reach several tens of thousand seconds. However, for safety reasons and due to the atomic pollution that would be caused by the nuclear energy, such propulsion technologies remain at theoretical state.

1.2.1.2.5 Electrically powered spacecraft propulsion With the same idea of using a non-chemical energy source to provide thrust, electricity is used to ionize particles, typically the component of a Xenon gas, and ejecting them at high velocity. Such engines are already operational with a I_{sp} of several thousand of seconds but with a thrust that do not exceed a Newton. Since this propulsion technology cannot lift-off any payload, it is only used today on satellites to correct their trajectories or to propel probes once they have left the earth attraction.

1.2.2 Solid Rocket Motors nowadays

Solid rocket motors are therefore not the most efficient technologies and the absence of thrust modulation is their main drawback. However, their storage abilities, the high thrust they can provide and their low cost relatively to the aforementioned technologies made them relevant technologies for current and future applications.

(a) Milan ER **(b)** Exocet MM40

Figure 1.7: *Examples of tactical missiles at launch (source: MBDA)*

1.2.2.1 Tactical military applications

As explained in section 1.1.1 solid rocket motor were originally used for military purposes. Solid rocket motors can be found in many tactical weapon systems and used for various purposes depending on the device. While safety is essential for man-portable systems (see Figure 1.7a) and justified the used of double-based propellants, performance and composite propellants are privileged for anti-missile systems. SRM are employed in the great majority of supersonic air-to-air as well as surface-to-air missiles. In the case of subsonic cruise missile, SRMs are only used as starting booster, as for the Exocet for example (see Figure 1.7b), and small turbo engines provide an higher efficiency during the cruise.

Safety and stealth are primary requirement for such devices. Therefore, for these systems the engine performance is generally not the top priority and is put in concurrence with other military aspects.

1.2.2.2 Strategic military applications

The case of nuclear deterrence requires different qualities. The performances of the engine becomes a key parameter alongside with stealth in order to strike long range targets compared to tactical applications. While liquid propulsion can be an interesting option in the case of intercontinental ballistic missiles (ICBMs) launched from the ground, solid propulsion remains the privileged technology for submarine launch Ballistic missiles (SLBMs). This is the case of the M51 missile used by the French oceanic deterrence forces. With three stages contained in a $12\,m$ high case and a weight of approximately 50 tons, the system can reach target $10,000\,km$ away (see Figure 1.8). Providing a thrust close to $1800\,kN$ the SLBMs developed by ArianeGroup reach a cruise speed of 19 km/s outside the atmosphere. Its American equivalent, the Trident II, shares similar characteristics. Moreover, underwater launches require specific conception and modeling.

1.2.2.3 Space launcher application

Since the I_{sp} of SRMs are relatively low compared to LREs, these are mostly used as first stage boosters to lead the launcher quickly outside the atmosphere where LREs of the main and/or upper stages provide a higher efficiency. Thanks to the high thrust provided, this choice is able

(a) Relative size of M45 and M51 (adapted from ©Marine nationale)

(b) M51 test launcher from submarine

Figure 1.8: *Illustration of SLBM use in french deterrence forces*

(a) **(b)** **(c)** **(d)** **(e)** **(f)** **(g)** **(h)** **(i)** **(j)** **(k)**

Figure 1.9: *Examples of current ELV at lift-off, from left to right: Soyouz, VEGA, Long-March 3B, Falcon9, H-IIB, Zenit, Atlas-V, Delta IV medium, Proton, GSLV-Mk3 and Ariane 5*

to minimize the ΔV losses due to the self suspension of the launcher and the aerodynamics drag while being a low cost option compared to LREs. Such choice has been conducted for european launchers since Ariane 3 and remain unchanged for the development of Ariane 6. This configuration has also be retained by other space agency such as for the American launchers Atlas V and Delta IV Medium or the japanese H-II (see Figure 1.9). Other options are possible such as full LRE configurations (Delta IV Heavy, Falcon 9, Soyouz, Proton or Zenit) or mostly SRM configurations (VEGA, Taurus or Minotaur) with their pro and cons.

While they provide most of the thrust during the lift-off, SRMs are characterized by a large size and high length to radius ratio. For example the Ariane 5 solid rocket booster, namely the P230, is 31.6 m high and 3.05 m wide and contain each almost 237 tons of propellant. The two boosters of the first stage (the Etage d'Accélération à Poudre (EAP)) provides more than 90 % of the thrust at the lift-off. Since the construction of a single propellant grain of this size is a complex task, the grain is divided in three segments that are separated by thermal protections that have the objective of both limiting the heat transfer between the blocks and mastering the thrust profile provided by the engine. However, the presence of these thermal protections disturbs the internal flow and can lead to unsteady process. The QM-1 from Orbital ATK tested in 2015, is composed of five segments and faces similar problematics.

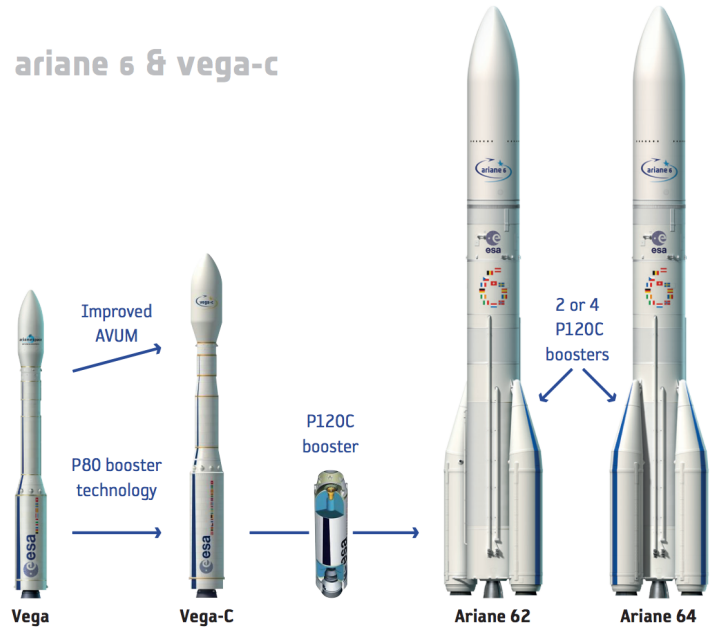

Figure 1.10: *The P120c: common motor for VEGA C and Ariane 6 (©esa)*

To avoid such problem, the P80 designed for VEGA as well as the P120c under development for Ariane 6 and VEGA C (see Figure 1.10) are composed of a single grain of shorter length compared to the P230. However, as discussed Section 1.3.3, this choice did not completely erase it, at least for the P80 motor. At the end, SRMs for space launcher and strategic military applications have similar sizes and structures while sharing a close aim in terms of performances.

1.3 Improving the knowledge on SRMs

A significant number of problematics can arise and impact the reliability of the engine. This section aims at providing an overview of the issues that SRMs are submitted to and point out the importance of the condensed phase in these problematics. Flow instabilities leading to thrust oscillations are the remarkable phenomena to be investigated in this work and are therefore detailed more specifically.

1.3.1 Critical issues in the design of SRMs

1.3.1.1 Performance losses

The internal ballistic detailed Section 1.1.3.2 provides an idealistic description of the behavior of the SRMs. Due to the complexity of real motor and the full physics involved, the unfavorable gap between these idealistic performances and the reality are referred as I_{sp} losses. Several phenomena cause such losses. For non-metalized propellant the following phenomena are generally considered (Kuentzmann 1973):

Chemical losses: Losses produced by a deviation to chemical equilibrium, when the combustion is uncompleted or during quick expansion in the nozzle that prevent low temperature recombination of the combustion product.

Wall frictions losses: The interaction of the flow with the structure especially important in the nozzle. That friction produces entropy that negatively affects the total pressure and thus diminishes the ability of the nozzle to transform thermal energy into kinetic energy.

Heat transfer losses: The propulsion flow can lose energy due to thermal transfer with the outside through walls and heat transfer. Due to the high velocity reached in the nozzle, that effect is more important in this area, remarkably at the throat.

Jet divergence losses: Due to multi-dimensional effects, the propulsive jet is ejected with small opening angle. This sensibly reduces the thrust obtained compared to mono-dimensional analysis.

In the case of composite propellant, the presence of condensed particles in the internal flow clearly impact the I_{sp} losses described above and more specifically the chemical losses. Moreover, since the droplets have a finite size and a lag exists between their velocity and the one of carrier gas, as well as for the temperature, the following effects can be remarked:

Drag effect: The drag effect between the gas and the droplets does not affect directly the thrust since the momentum of the mixture remains the same. However the entropy generated by the drag reduces the total pressure similarly to the wall frictions losses. As a consequence a part of the thermal energy can no more be transformed into kinetic energy through the expansion process.

Heat transfer lag: Unlike the gaseous phase, the condensed phase cannot expands and thus directly contributes to the decrease of the velocity of the mixture. However, through the heating of its surrounding gas, the condensed phase contributes to the thrust. The I_{sp} losses caused be the heat transfer lag is due to the incomplete transfer of energy from the disperse phase to the carrier gas. Entropy produced by this thermal process also contributes to the I_{sp} losses.

In the case where a two phase flow is to be considered, the I_{sp} losses are assessed by comparing the effective thrust with the one deduced from the assumption an equivalent gas (see Section 2.3.1.3) which is used as reference. In practice, these losses are greatly impacted by the size of the particles and the smaller they are, the closest they remain in equilibrium with the gas and thus generate a limited loss. In practice, while the two-phase I_{sp} losses cause a typical decrease of 4 % to 6 % of the I_{sp} (Bandera, Maggi, and DeLuca 2009), the loss unrelated to the disperse phase are contained in a 2 % of the optimal I_{sp}. Two-phase I_{sp} losses are thus dominant and roughly represent 15 s of I_{sp} for composite propellants compare to double-base formulations for instance but are greatly compensated by the gain in performance obtained by the introduction of the metalized reductant.

1.3.1.2 Operating concerns

The performance topic does not concentrate every issue regarding SRMs. As discussed through the text safety is another fundamental aspect but more generally, the reliable and smooth functioning of the motor are key features to be master. Among the most critical known issues, the following ones are detailed:

Slag accumulation: Depending on the internal geometry condensed droplets can be partly trapped into the aft-end of the combustion chamber (Cesco 1997; Godfroy and Guéry 1997; Villedieu et al. 2000). This is typically the case of SRMs using a submerged nozzle, like the P230 where the accumulated mass reaches approximately two tons at the end of their flight. In addition to a loss of performance due to the mass unused for propulsion, the phenomenon may be able to unbalance the launcher and erode the structure.

Transient stages: During the pressurization of the combustion chamber, during significant change of the grain geometry or for the tail-off, at the end of the combustion, transient processes can affect the behavior of a SRM. These phenomena are purely unsteady without being cyclic and therefore require specific analysis.

Grain ignition: Due to unsteady heat transfers, the ignition process requires a specific knowledge. The consideration of the internal flow is not sufficient, radiative heat transfer and the properties of both the propellant and the internal structure need to be considered.

Radiative heat transfer: The high temperature of the flow leads to an important heat transfer caused by radiations. Such emissions are an issue in the ejected gas, the plume, since it can heat up cryogenic tanks in the case of civilian launchers or increase the signature of military devices.

Pressure oscillations: In real SRMs, the pressure is not homogeneous as the internal ballistic analysis Section 1.1.3.2 may let think. In practice, an unsteady pressure can be observed and directly affects the thrust that becomes unsteady. Approximate relations between the thrust and pressure oscillations can be found in (Blomshield 2007). Such effect can lead in the worst case scenario to erratic behavior, but if the magnitude is maintained under an acceptable level, deleterious effect can be contained or avoided.

While being fundamental for the slag accumulation, the condensed phase play a key role in the other phenomena. Since the behavior of the plume rely on specific expertise, the presented work is focused on the other phenomena, mostly related to the internal flow of solid rocket motors.

1.3.2 Characteristics of the internal flow of SRMs

1.3.2.1 Taylor-Culick flow

The internal flow of a SRM presents a few specificities that are rarely encountered in other field. The internal geometry of a SRM can be roughly summed up by a semi-infinite tube where fluid is injected from the lateral wall as represented in Figure 1.11. This parietal injection is

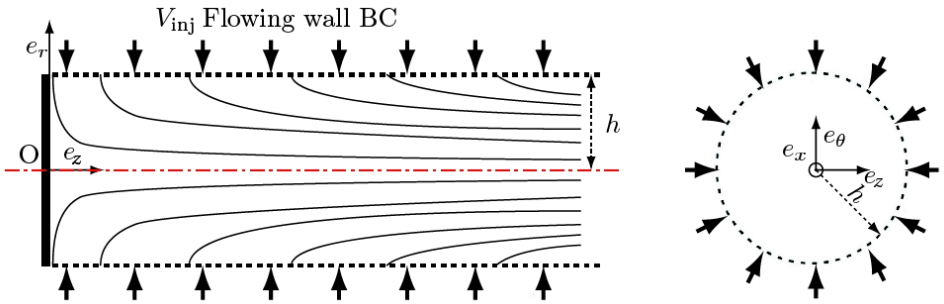

Figure 1.11: *Taylor-Culick flow representation*

rather uncommon in other fields and has thus been particularly studied for Solid Rocket Motors. For low-Mach regimes and inviscid flow, an analytic solution has been found by Taylor (Taylor 1956) and by Culick (Culick 1966) as a preliminary task to characterize linear acoustics waves in SRMs. The solution for incompressible mean flows yields:

$$\begin{cases} u_z &= v_{inj}\pi\frac{z}{h}\cos\left(\frac{\pi}{2h^2}r^2\right), \\ u_r &= -\frac{v_{inj}h}{r}\sin\left(\frac{\pi}{2h^2}r^2\right), \\ u_\theta &= 0. \end{cases} \qquad P = P_0 - \left[\frac{\pi^2 z^2}{2h^2} + \frac{h^2}{r^2}\sin^2\left(\frac{\pi}{2h^2}r^2\right)\right]\rho v_{inj} \tag{1.6}$$

where $r \in]0, h]$ and $z \in \mathbb{R}$ are the position coordinates, u_z, u_r and u_θ are the mean velocities, ρ the fluid density, P the pressure and P_0 the reference pressure.

The solution has been slightly improved over the time by taking into account full-Mach regimes (Clavin 1996; Majdalani 2007) or more complex cases (Griffond 2001; Griffond and Casalis 2001; Majdalani, Vyas, and Flandro 2001; Majdalani and Van Moorhem 2001). However, many limits remain like the absence of nozzle, the consideration of a single phase or rotation symmetries among others.

1.3.2.2 A multi-scale problem

Another particularity of SRMs is the presence of a wide range of Mach regimes from very subsonic in the chamber to clearly supersonic in the divergent of the nozzle. With an acoustic velocity roughly equal to $1000\,m/s$ and a mean velocity inside the chamber generally lying under $100\,m/s$ for large SRMs, the approximation of incompressible flow for the mean velocity field inside the chamber, away from the nozzle, is rather fair. Therefore, depending on the size of the engine, droplets can thus stay from few tens of millisecond to few hundreds of them in average. Including the particle relaxation with the gas, the combustion and typical eddy revolution times, the typical characteristic times of the phenomena encountered in the internal flow range on several orders of magnitude as presented in Table 1.1. It appears that while some phenomena occur on clearly distinct time scales, others are significantly close and may interacts with each other according to both the disperse and carrier phases.

Table 1.1: *Typical time scales in a P230 motor*

Small droplet relaxation time	$1\,\mu s$	First acoustic period	$50\,ms$
Small droplet combustion time	$0.1\,ms$	Large eddy revolution time	$50\,ms$
Large droplet relaxation time	$10\,ms$	Significant regression time	$1\,s$
Large droplet combustion time	$100\,ms$	Operating time	$120\,s$

1.3.3 Hydrodynamic instabilities

Since no moving mechanical part composes SRMs, aside for flight control devices, unsteady processes can be caused by purely hydrodynamic instabilities taking place in the internal flow. These can exist under various forms and are more likely to appear and develop in large motors since such phenomena have time to grow. It is critical to anticipate and soften these unsteadiness in order to reduce the stress applied to the payload during the launch.

These phenomena do not involve any feature related to the combustion of the propellant and can be studied experimentally through cold gas configurations and therefore several investigation campaigns using optic diagnotic have been conducted (Ugurtas et al. 2000; Regert and Planquart 2015). When solid propellant is used as for real applications, data are however limited due to the harsh conditions in the combustion chamber. Experimental results thus generally consist only in well placed pressure sensors to match the ballistic and track instabilities (Dupays 1996; Anthoine 2000) together with ultrasonic sensors to follow surface regression (Cauty 2000; Traineau and Kuentzmann 1986).

1.3.3.1 Acoustic ambiance

Due to their confined combustion chamber and the chocked nozzle, SRMs are likely to produce unsteady behavior often locked on acoustic modes of their internal cavity. As a result, the generation of purely hydrodynamic and periodic phenomena can by amplified by the acoustic ambiance if both characteristic frequencies match.

The first axial modes are roughly equal to $\frac{ak}{2L}$ where k is an integer, a the sound velocity in the internal flow and L the length between the head-end and the throat, but have to be adapted considering the choked nozzle (Lupoglazoff and Vuillot 1992b). For large SRMs, such frequencies are problematic since, mostly locked on the first acoustic mode of the chamber, they are generally close to the elastic modes of the structure. In the case of small SRMs, acoustic modes have an higher frequency and are more likely to interact with combustion processes.

1.3.3.2 Angle Vortex Shedding (VSA)

Among the large scale hydrodynamic instabilities, vortex shedding refers to periodic detachment of coherent structures responsible for thrust oscillations. In the case of Angle Vortex Shedding (VSA), these are generated by sharp angle taking place on the propellant grain, generally at the edge of a propellant segment (see Figure 1.12a). This singularity creates downstream an inflexion point in the axial velocity profile, which degenerates in convective instabilities

developing toward the nozzle according to Rayleigh's theorem (Charru 2011).

The phenomenon has been investigated through numerical and experimental investigations, at ONERA especially on the C1x (Vuillot 1995) but also elsewhere (Morfouace and Tissier 1995; Kourta 1999) and remains the subject of investigations (Dupif et al. 2015b, 2016).

1.3.3.3 Obstacle Vortex Shedding (VSO)

The presence of thermal protection rings (PTF) in large motor can also disturb the internal flow through the appearance of coherent structures downstream this obstacle as shown in Figure 1.12b. Since such feature appears in segmented SRMs, it was largely investigated (Brown et al. 1981; Vuillot, Tissier, and De Amicis 1996; Vetel 2001) The fluid-structure interaction causing the Obstacle Vortex Shedding (VSO) is strongly coupled such that it can modify the structure of the PTF or cause the flapping of this element (Regert and Planquart 2015).

1.3.3.4 Parietal Vortex Shedding (VSP)

For long Solid Rocket Motor, a third kind of hydrodynamic instability can appear due to the parietal injection of the burnt gases through the lateral walls as represented Figure 1.12c. In the case of the P230, the major role of Parietal Vortex Shedding (VSP) was proven from numerical (Lupoglazoff and Vuillot 1996) and experimental (Traineau et al. 1997) studies. Such phenomena in that case is coupled to VSO but the obtained instability magnitude cannot be explained without taking into account VSP.

Modeling the interior of a SRMs by a Taylor-Culick flow (see Section 1.3.2.1), it is possible to theoretically predict the occurrence of this phenomena (Varapaev and Yagodkin 1969; Casalis, Avalon, and Pineau 1998; Griffond, Casalis, and Pineau 2000). It appears that starting for a length to internal radius ratio of $\frac{x^*}{r} = 8$ such instability emerges and degenerates to turbulence fluctuation after $\frac{x^*}{r} = 13$ approximately. Such phenomenon contributed to the will of reducing the length of SRM boosters for Ariane 6.

1.3.3.5 Turbulence

While turbulence is generally required to enhance flame combustion, it is generally wished to avoid it in aerodynamics in order to prevent unsteadiness and vibrations. In the combustion chamber of SRMs, turbulence is mostly unwanted despite it is known that breaking coherent structure can reduce the magnitude of instabilities (Gallier, Godfroy, and Plourde 2004). However, as explained here-above, such phenomenon naturally appears in long motors and transient flow have to be considered (Beddini 1981). Independently from the nature of the vortex shedding, the coherent structures generated break along the internal flow if they are not ejected from the engine before. Such features create needs for proper modeling and simulations (Kourta 1999; Dupuy 2012).

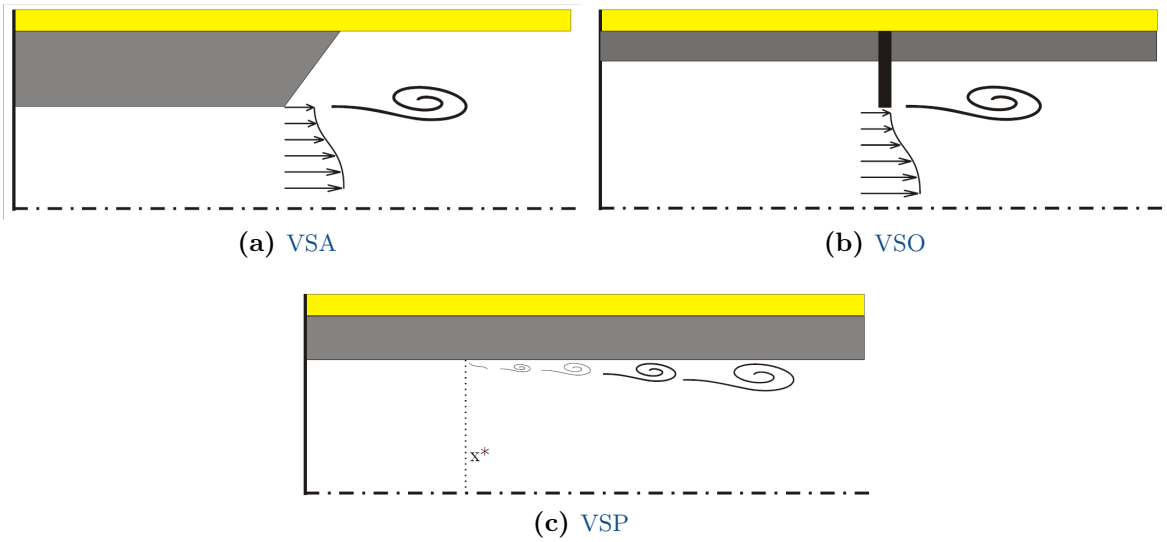

(a) VSA **(b)** VSO

(c) VSP

Figure 1.12: *Sketches of vortex shedding phenomena (Simoes 2003) in SRMs*

1.3.3.6 Inert disperse phase effect

Hydrodynamic instabilities described until here can be observed by considering the gaseous phase alone. In general, the presence of particles does not suppress these instabilities but modifies their behavior. Aside combustion effect, significant phenomena occur due the momentum and heat exchanges between the phases caused by drag and thermal conduction. Composed of gas and droplet, the mixture has a distinct behavior compared to the isolated gas, which is significant when the particle to gas mass ratio is not negligible, like in SRMs. Typically, the traveling wave velocity is modified and a dispersion of acoustic waves can either be observed while amplitude of the oscillation can either be increased or smeard (Temkin and Dobbins 1966).

Stimulated by acoustic waves, vortex shedding can also be either damped or excited depending on the involved characteristic frequencies. It explains the relevance of the inert phase for VSA, VSO and VSP. Moreover, this does not affect uniformly the flow since the droplets can either be naturally concentrated on privileged areas when the flow is organized or be scattered by turbulent fluctuations. Such heterogeneity of the particle density distribution increases the complexity of the flow and causes the acoustic velocity to depend on the position in the chamber. Aside acoustic phenomena, the droplet mass loading increases locally the inertia of the flow thanks to mutual interaction. This behavior is greatly dependent on the size of the particles and thus the full size polydispersion of the spray should be considered in practice.

As a consequence, the presence of particles in the internal flow of SRMs interacts with other hydrodynamic instabilities with the ability to modify significantly their behavior through complex processes. An efficient modeling of both phases and their two-way coupling interaction (Doisneau et al. 2014) is therefore necessary to describe the flow instabilities.

1.3.4 Unsteady combustion

The combustion process inside the chamber can impact the stability of the motor in several ways as related in (Blomshield 2007). Among them, two main processes can appear and be coupled to the acoustic ambiance. Firstly by playing a significant role in the combustion of the droplets burning in the internal flow away from the grain and secondly by modifying the combustion velocity of the propellant.

1.3.4.1 Thermo-acoustic instabilities (ITHAC)

The burning process of aluminum away from the propellant surface is known to have an effect on the oscillation observed (Lupoglazoff et al. 2000; Ballereau et al. 2003) and is still the subject of active studies (Sibra 2015). The unsteady heat release produced by the combustion of the particles is impacted by the pressure and velocity perturbations caused by the acoustic waves. Depending on the frequency, this can greatly exacerbate the pressure oscillation magnitude.

This elaborated scenario meets common features with the Rijke's tube (Rijke 1859) and has been purposely studied for aluminum combustion in (Raun and Beckstead 1993). Until today, such process, referred as Thermo-acoustic instabilities (ITHAC), has been observed numerically (Gallier and Godfroy 2009b) locked on the first acoustic mode of the chamber and is suspected to occur in the P230, despite it is not the main cause of unsteadiness. The reduction of hydrodynamic instabilities in the P80 may however have let place for this phenomenon to be dominant (Gallier and Godfroy 2009a).

1.3.4.2 Propellant combustion instability

Unlike the ITHAC, this phenomena is directly linked to the surface regression dynamics of the propellant and has been experimentally observed in early motors (Price 1984). Submitted to a periodic excitation, the propellant provides an unsteady response (Kuentzmann 1991; Vuillot and Lupoglazoff 1996; Lupoglazoff and Vuillot 1999). While for low frequency the regression law remains valid, high frequencies disturbs the temperature profile through the propellant surface and impacts its transfer function. Such behavior deeply depends on the composition of the grain and for composite propellant for instance, such property is linked to the packing (Buckmaster et al. 2005). Instabilities of this kind have a typical frequency standing around $1\,kH_z$ and therefore are unlikely to couple with acoustics modes of large SRMs.

1.3.5 Mapping the instabilities

In actual SRMs, an instability generally does not exist alone, several of the conditions presented here-above can occur simultaneously depending on the size of the motor, its geometry and the propellant composition. As explained through this chapter, the acoustic ambiance is likely to be coupled with instabilities. The presence of a condensed phase in the combustion product disturbs these coupling and can either damp or exacerbate the pressure oscillations.

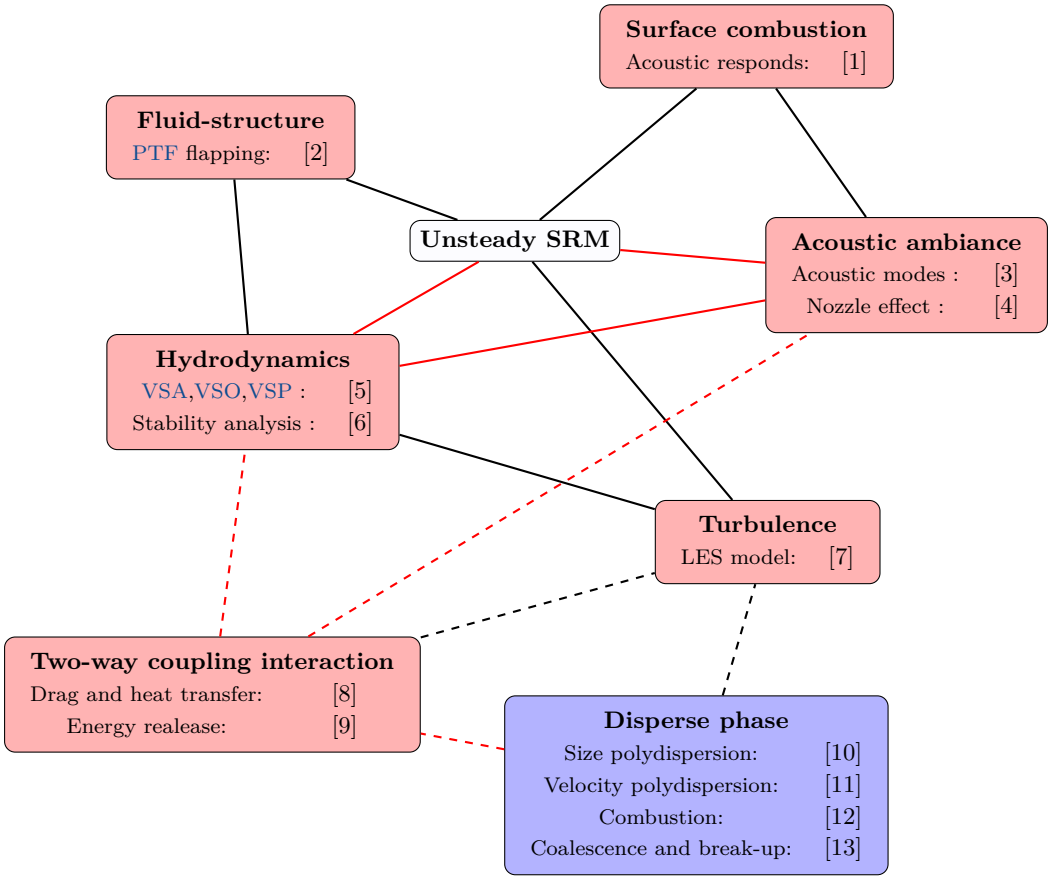

Figure 1.13: *Causality map of phenomena related to trust oscillation investigations (solid lines: hydrodynamic interactions, dashed lines: disperse phase effects, red lines: effects studied through this thesis, see Table 1.2 for references)*

In the case of the presented manuscript, only the applications linked to thrust oscillations are considered. A mapping of the element detailed until here and their interaction is proposed in Figure 1.13 and phenomena targeted through this work are indicated. Obviously, this representation does not exhibit all the possible effects but stresses the main known physical interactions encountered in SRMs and leading to thrust oscillations. In this work, the efforts are concentrated on the modeling of the disperse phase and the two way interaction with the carrier gas. Such features mostly impact the thrust oscillations through the modification of the acoustic ambiance and the vortex shedding, which are themselves coupled with each others. Considering the high particle to gas mass ratio encountered in SRMs, the modeling of the disperse phase is a critical issue in order to predict unsteady behaviors.

Table 1.2: *References of Figure 1.13*

Block	Reference number	Reference
Surface combustion	[1]	Buckmaster et al. 2005
Fluid-structure	[2]	Regert and Planquart 2015
Acoustic ambiance	[3]	Barrere et al. 1960
	[4]	Marble and Candel 1977
Hydrodynamics	[5]	Lupoglazoff and Vuillot 1999
	[6]	Casalis, Avalon, and Pineau 1998
Turbulence	[7]	Dupuy 2012

Two-way coupling	[8]	Temkin and Dobbins 1966
	[9]	Raun and Beckstead 1993
Disperse phase	[10]	Laurent, Sibra, and Doisneau 2016
	[11]	Simoes 2006
	[12]	Sibra 2015
	[13]	Doisneau et al. 2013

Chapter 2

Two-phase flow modeling strategies

> The thesis that no model can be perfect
> is at the root of the physical theory.
>
> R. V. Jones, The theory of practical joking - its relevance to physics

Dedicated to the physics of two-phase flows, this chapter exhibits the modeling possibilities for the disperse phase and aims at a priori determining the best-suited models to describe the internal flow of Solid Rocket Motors (SRMs). If the investigations are focused on that specific application field, the developed models can find a use for various applications including automotive and aeronautic spray injection, fluidized bed and bubble flows among others. However, due to the presence of a disperse phase of a neglected volume fraction almost everywhere from the grain to the nozzle exit and because of the heavy particle to gas mass fraction, SRMs are the playing ground for the development of specific classes of models. The chapter is therefore divided as follow. Section 1 is dedicated to the description of the phenomenological features characterizing the flow and the multi-scale nature of the problem. The specific aspects of solid rocket motors and the characteristics of the internal flow allow model reductions that are clarified. Section 2 describes the modeling of an isolated droplet in the flow, such that the full resolution of droplet and its surrounding gas can be substituted by this simplified description. Finally, section 3 exhibits the variety of solutions existing to model particle laden flows. Discussing the pro and cons of each solution, a class of methods is selected for further investigation and enhancement.

2.1 A Multiscale problem

Based on a great literature, two-phase flows can be classified in several categories and exhibit complex behaviors. Mostly based on a specific application as explained in (Ishii and Hibiki 2010), a great variety of models has been designed in order to describe physical specific effects. We propose here to firstly specify the various phenomena and scales characterizing two-phase flows. Through such process, it is possible to reduce the dimension and complexity of the model

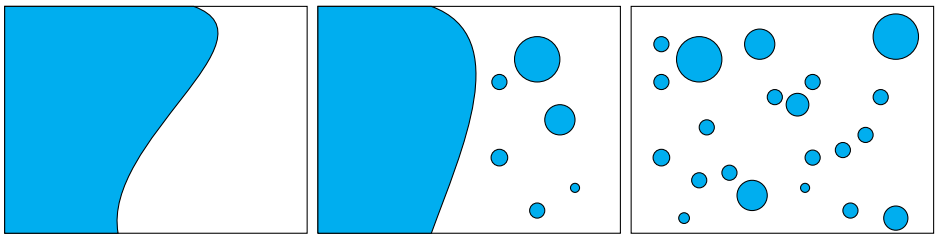

(a) separate **(b)** hybride **(c)** disperse

Figure 2.1: *Typical control volumes in two-phase flows, carrier phase in white and carried phase in cyan*

according to the application field targeted in this manuscript.

2.1.1 Modeling scale

2.1.1.1 Flow topology

2.1.1.1.1 Definition of multi-phase flows Multi-phase flows (Crowe et al. 2011; Ishii and Hibiki 2010; Zaichik, Alipchenkov, and Sinaiski 2008) can be encountered in a wide variety of engineering systems and natural phenomena. It involves several components called *phases* separated by *interfaces*. Without being exhaustive, issues concerning multi-phase flows are critical for environmental control, as air conditioners or pollutant collectors, for biological systems, as cardiovascular system, to the prediction of geo-meteorological phenomena, like sedimentation or formation and motion of rain droplets, or also for power systems, as nuclear power plants, automotive spray injection and rocket engines using either liquid or solid propellant as studied here. Such applications can involve gas-liquid, gas-solid, solid-liquid or immiscible-liquid mixture and sometimes mixture of more than two phases.

Independently from the states of the material involved in the flow, quantities that are locals according to a control volume, as represented in Figure 2.1, can be described:

- material density: mass density of an isolated and pure phase. It can be mathematically described for a phase i as $\check{M}_i = \frac{\overline{M}_i^{\mathcal{V}}}{\mathcal{V}_i}$, where $\overline{M}_i^{\mathcal{V}}$ is the mass of the phase i contained in the control volume of interest and $\mathcal{V}_i$ the volume it occupies,

- mass density: mass density of a phase inside the control volume occupied by the entire mixture. It can be mathematically described for a mixture as $\rho_i = \frac{\overline{M}_i^{\mathcal{V}}}{\sum_j \mathcal{V}_j}$,

- number density: number of agglomerates of a phase scattered inside the control volume. It can be mathematically described for a mixture as $n_i = \frac{N_{i,agg}}{\sum_j \mathcal{V}_j}$, where $N_{i,agg}$ is the number of agglomerates of the phase i in the control volume,

- volume fraction: fraction of volume occupied by a phase inside the control volume. It can be mathematically described for a phase i as $\alpha_i = \frac{\mathcal{V}_i}{\sum_j \mathcal{V}_j}$,

- mass fraction: fraction of mass belonging to a phase inside a control volume. It can be mathematically described for a phase i as $Y_i = \frac{\rho_i}{\sum_j \rho_j}$,

- flow density: mass density of the mixture inside the control volume it occupies. It can be mathematically described for a mixture as $\rho = \sum_i \rho_i$

ρ, ρ_i and n_i are obtained through a spatial averaging on the control volume $\mathcal{V} = \sum_j \mathcal{V}_j$. In order to describe these values at a point, we define such local quantity ϕ as the limit of its integral value $\Phi(\mathcal{V})$ on a volume $\mathcal{V}$ centered on the position $\boldsymbol{x}$ when the volume vanish. Mathematically, this corresponds to:

$$\phi(\boldsymbol{x}) = \lim_{\mathcal{V}\to 0} \frac{\Phi(\mathcal{V})}{\mathcal{V}} \tag{2.1}$$

Such process necessarily assume that the phases are represented as a continuum or that there exists a minimal control volume $\mathcal{V}^0$ sufficiently small to be considered as a point (Crowe et al. 2011). In order to overcome these issues, it is possible to proceed to an average based on a large number of *realizations*, defining a realization as a deterministic solution among an ensemble of possible events. Stating now that $\Phi(\mathcal{V}, \mu)$ is the realizations of $\Phi(\mathcal{V})$ occurring with a probability $\mathrm{d}m(\mu)$, this ensemble averaging (Drew and Passman 2006) takes the expression:

$$\phi(\boldsymbol{x}) = \lim_{\mathcal{V}\to 0} \frac{\int \Phi(\mathcal{V}, \mu)\mathrm{d}m(\mu)}{\mathcal{V}} \tag{2.2}$$

In a given context, these definitions can be seen as equivalent, but their meaning actually differ. These averaged quantities are critical in order to describe the flow of interest from a macroscopic or statistical point of view and are key feature to evaluate the regime of a two-phase flow. However, as observed by several authors including (Ishii and Hibiki 2010; Kocamustafaogullari 1971) among others, multiphase flows and more specifically two-phase flows should rather be classified according to the geometry of the interface separating the phases.

2.1.1.1.2 Interface The geometry of the interface between phases can take a large variety of structures from simple spherical form to the most complex arrangements. Physically, the interface is generally, even implicitly, modeled as a discrete time-dependent boundary. As detailled in (Delhaye 1974), its dynamic is driven by a jump condition characterizing the transition from a phase to another. The accurate description of the mass and energy transfer through the interface thus becomes a critical topic, even conceptually (Delhaye 2001). One can refer to (Ishii and Hibiki 2010) among others for a more detailed description of the subject.

For the cases studied here, only a few parameters are detailed for the reminder in order to describe two-phase flows from a phenomenological point of view. Assuming a gas-liquid flow,

one can define the hydrodynamic and aerodynamic Weber numbers as:

$$\mathrm{We}_L^l = \frac{\check{M}_l L \|\boldsymbol{u}_l - \boldsymbol{u}_g\|_2^2}{\sigma_{lg}}, \qquad \mathrm{We}_L^a = \frac{\check{M}_g L \|\boldsymbol{u}_l - \boldsymbol{u}_g\|_2^2}{\sigma_{lg}} \tag{2.3}$$

where $\check{M}_l$ and $\check{M}_g$ are the material densities of the liquid and gaseous phase, $\boldsymbol{u}_l$ and $\boldsymbol{u}_g$ their velocities, σ_{lg} is the surface tension between the phases and L is the characteristic length of the studied case.

For the description of two-phase flows, the Weber numbers play for interfaces a role analog to the Reynolds number in the case of turbulence. In a given context, these values summarize the competition between the convective forces of a phase or the other and the surface tensions. The complexity of the interface shape between two fluids is directly linked to this non-dimensional number. The higher the Weber number, the more chaotic the interface becomes until an eventual break-up.

2.1.1.1.3 Separate flows The notion of separate flows can define, in the literature, two different cases. On the one hand, separate flows can refer to cases where the interface shape is complex and none of the phases has a remarkable geometry. Such case can occur when the bulk kinetic energy is significant compared to interfacial energy and therefore when the Weber number is high. On the other hand, such terms also describe free surface, film and annular pipe flows. In (Crowe 2005), it is suggested that a two-phase flow is said *separated* when both phases are separated by a contact line, suggesting that each phase is materially connected in its entirety. Such definition can also fit the case of an isolated droplet, component of a disperse flow, and excludes possibilities of agglomerates detaching from a liquid core. We therefore suggest, introducing a scale at which the flows is observed, that to be said separated, the instantaneous interface curvature have to be significantly large in comparison to the scales of interest.

Such cases, where the interface have a key role and the phases have a equivalent status, can occur in many engineering systems and are the subject of extensive researches. The dynamics of separate flows is critical in the field of oil-extraction or in nuclear power-plant for instance. The rendering of complex phenomena at phase interface and the determination of its detailed shape is of utmost importance since, interacting together, they drive the mass and energy transfer significantly acting on the dynamic of the flow. In the case of pipe flow with evaporation for instance, a full chart, including churn, plug and slug flow regimes among others, has been built to witness the wide observable phenomenology.

The combined description of the flow in a phase or at the interface constitutes the most general case theoretically able to describe any flow at the price, most of the time, of a great complexity. For specific cases, the resolution of the small scales is however not mandatory and can be described in a simplified way.

2.1.1.1.4 Disperse flows Disperse flows, that are extensively studied through this manuscript, are flows in which one phase, the disperse phase, is not materially connected (Crowe et al. 2011). This disperse phase constituted of small agglomerates of matter is embedded in the carrier phase

that occupied most of the volume. In the case where the existence of agglomerates of matter is fulfilled and the assumption of negligible volume is not, the flow is said to be dense.

Usually, these disperse bubbles, droplets or particles will be modeled as spherical, but this constraint is not mandatory. The shape of the interface of each agglomerate needs to have a much simpler geometry than for separate flows such that it can be described with a finite number of parameters. Additionally, thanks to this simplified description of the situation or treatment of the problem, the interaction between the carrier and carried phases can be modeled instead of being fully resolved.

Several specific categories of particle laden flows can be observed:

- Granular flow: disperse flow where the inter-particle mean distance is equal to a few particle diameters, particles cannot be treated independently and the assumption of negligible volume fraction may failed at being fulfilled. Such situation is not unusual in fluidized bed for instance,
- Dense flow: disperse flow where the particle dynamic is mostly controlled by collisions. This is the case for granular flows, but can remain true for fully negligible volume fractions as well,
- Moderately dense spray: dilute flow with significant condensed spray mass fraction, i.e. $Y_c = \mathcal{O}(1)$,
- Dilute flow: the particle dynamic is mostly driven by carrier fluid forces, typically drag and lift.

Identically as for separate flows, the subject of disperse flow has been widely investigated, see (Crowe et al. 2011; Sirignano 1999; Zaichik, Alipchenkov, and Sinaiski 2008) for a broader view of the field.

The definition of moderately dense spray perfectly fits the characteristics encountered inside solid rocket motors. Using simple, but fair, assumptions[1], to obtain an order of magnitude, a number density of $1.7 \cdot 10^5$ particles per cubic centimeters and an aluminum oxide volume fraction of $7.1 \cdot 10^{-4}$ can be computed. Moreover, because of the dissipative effect of the carried gas, the behavior of these droplets in a common neighborhood is fairly similar, especially for the smallest ones. In addition, since the material density of the disperse phase is high compared to the carrier gas, the volume fraction of the aluminum droplet remains usually negligible whereas the mass fraction remains significant.

2.1.1.1.5 Case of spray injection The specific case of primary injection can be observed in automotive, aeronautic and liquid rocket engines among others. Stored under a liquid state in a tank, the fuel is converted into droplets during the injection and atomization process. Such process, represented in Figure 2.2, involves an area where the phases are separated and an area

[1] Aluminum oxide particles ($\rho_{Al_2O_3} = 2800\, kg.m^3$) having a uniform radius ($r_p = 10\, \mu m$) dispersed in gas combustion products ($r_g = 287\, J/kg/K$) at a pressure of $50\, bar$ and a temperature of $3500\, K$ with a mass ratio $\frac{\rho_{Al_2O_3}}{\rho_{gas}} = 0.4$

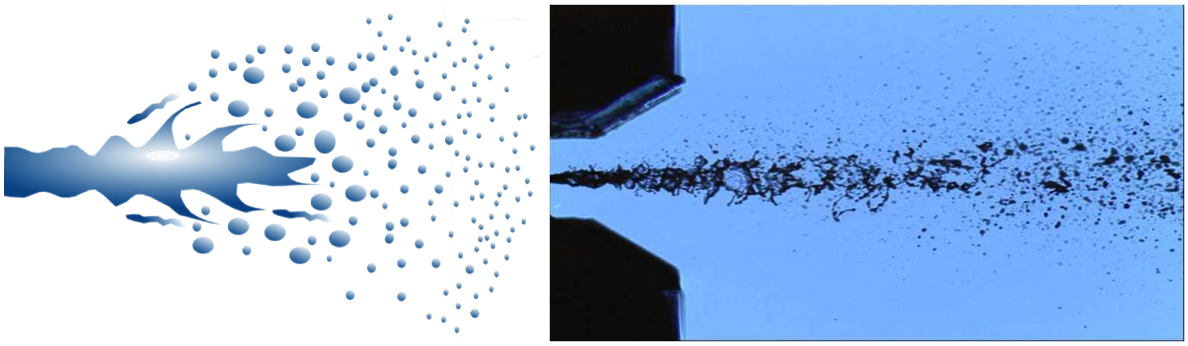

(a) Sketch of spray injection **(b)** Experiment visualization of spray injection (©Coria)

Figure 2.2: *Spray injection*

where the liquid appears as a disperse phase. It is a complex task to represent this transition from separate to disperse flow where primary break-up occurs and agglomerates are detached from the injected liquid core. Several ways to achieve the link between both regimes have been proposed until now:

- Proceed to an interface tracking until droplets are sufficiently small to be modeled as a point particle (Ling, Zaleski, and Scardovelli 2015; Arienti et al. 2012; Herrmann 2010) (see Section 2.1.1.2.2),
- Generating the disperse phase from knowledge and analysis of the separate phase geometry (Lebas et al. 2009),
- Increasing the accuracy of the disperse phase description leading to a reconciliation of the model with the separate phase description and provide an unified model (Essadki et al. 2017; Drui 2017).

Achieving to represent both regimes with the same model in a unique simulation while being predictive is a hot topic that did not find a satisfying solution yet. The presence of a wide range of scales, with both separate and disperse flow regimes, to be resolved in the same application remains a major issue for both modeling and simulation.

2.1.1.2 Specific observation scales

Two-phase flows are multi-scales by nature (Hoef and Sint Annaland 2004). The relations between small and large scales need to be well defined in order to establish a link between the microscopic and macroscopic levels. We propose here to review, at a conceptual level, the assumptions related to model reduction strategies used to model particle laden flows.

2.1.1.2.1 Deterministic versus statistical scales In many cases, the knowledge of the exact solution of a two-phase flow is not necessary. Typically, for engineering purpose, only relevant macroscopic observable are needed. Therefore, as a foreword to this section the notions of *deterministic scale* and *statistical scale* are introduced. The difference between these notions

is completely implicit to the observer and thus depend on the phenomena to be modeled.

- deterministic scale: scale at which the modeling is complete enough to be considered as an exact replica of the physical problem aimed at being reproduced,
- statistical scale: scale at which the modeling relies on a statistical description of a deterministic scale, detailed information is thus lost and the metric enable to all the scales.

In order to link these notions to the context of two-phase flows, the deterministic scale, or at least the ultimate replica of the reality, is the scale at which the model has to be able to represent the mixture as a separate flow. This includes the continuous descriptions of both the carrier and the carried fluid as well as the interface between them. In contrast, the statistical scale is the scale of the same flow able to describe the system of interest without the significant complexity of its deterministic representation. For disperse flows, this requires a sufficient number of particles or realizations. As a consequence, taking advantage of the assumed flow characteristics, the detailed and complex description is thrown over and replaced by a simplified description of the fluid-particle and particle-particle interactions that relies on a finite number of continuous field and/or parameters.

2.1.1.2.2 Concept of point particle The notion of point particle is fundamental while modeling the disperse phase. The objective is no more to represent the particle as an agglomerate of matter but to approximate it as a discrete object without effective volume to which attributes are associated [2]. As a consequence, the interactions between a droplet of the disperse phase and the carrier phase is no more to be resolved but is modeled. Typically, it supposes that only the exchange of momentum between the particle and its surrounding medium is considered and additional carrier fluid disturbance due to the trail behind the droplet is neglected. The same behavior is to be observed for each interaction between the carrier and carried phases. Various models able to describe the behavior of droplets are proposed in Section 2.2.

The approximation of point particles is not necessarily a transition for a deterministic scale to a statistical scale in itself. The droplet model can be accurate enough such that almost no information is lost.

2.1.1.2.3 Change of scale The introduction of the point particle concept is, in itself, a first transition from a microscopic scale to a macroscopic scale. However, the notions of microscopic, mesoscopic and macroscopic scales are often subject of controversy and strongly depends on the field of application. For the sake of simplicity, while describing the disperse phase in SRMs, these terms refer along the manuscript to the following features:

Microscopic level Fluid-fluid or fluid-solid description of the mixture able to represent each particle and its surrounding, point particle assumption can be stated at this level if the approximation is accurate enough,

Mesoscopic level Statistical description of a group of particles, the uniqueness of each particle

[2] Volume, or more generally size, can be an attribute but is only involve, as a parameter, in the coupling between phases or collision integral

is dropped and a ensemble averaging is applied,

Macroscopic level Fluid description of the disperse phase, the group of particles is locally described through a finite set of fields.

From another point of view, the microscopic level could have referred to the molecular level, as for the kinetic theory of gases, and the macroscopic level refers to the behavior of the combustion chamber of a SRM. This explain the introduction of the notions of *deterministic scale* and *statistical scale*, that actually refer to the proper transition from a scale to another with information loss or more precisely a entropy hierarchy. Such process can be applied several time successively (Grmela 2010). Therefore, the microscopic level as described above is the deterministic scale in the presented case but is also already a statistical scale considering molecular dynamics.

The existence of an intermediate level, called mesoscopic, is however not mandatory and subject to discussion since its only reason to exist is to articulate the relation between a microscopic level and a macroscopic level. Its advantage is to let explicitly appear a statistical distribution of the problem before approximating it. There is a global consensus on the necessity of detaining a well known link between the scales. However, the accurate description of such link is rarely conducted (Öttinger 2009).

2.1.1.2.4 Scale of interest According to (Crowe et al. 2011) roughly 10^4 at least entities are necessary in a control volume to rely on a spatial averaging. Starting from the same consideration as in Section 2.1.1.1.4, it appears that for the disperse phase of SRM applications, such control volume is roughly a cube of $4\,mm$ edge length. Such volume can be considered as a point if it is much smaller than the flow system.

Smaller control volumes can still be taken into account but that fine discrete behavior cannot be rendered. Therefore, phenomenon modeled by this continuum equation under such scale are not necessary false. For example, thin combustion layer smaller than this minimal control volume can be solved in a simulation as in (Sibra 2015). In this context, the flame front can be resolved from a statistical point of view, through an ensemble averaging or a filtering process. In other words, droplet temperature or size fields can be solved, however, the distinction of a droplet to another cannot be achieved, even for control volume smaller than the droplet size.

In the case of gas dynamic, this volume will be a $0.1\,\mu m$ edge length cube. Such size is clearly small considering the application system. However, very small droplets with diameters under the micrometer can be significantly impacted by Brownian effects due to the surrounding gas which require specific modeling (Doisneau 2013).

2.1.2 Characteristic features of disperse flows

In view of the disperse phase characteristics inside SRMs, we propose here to exhibit some significant attributes of two-phase disperse flows.

2.1.2.1 Size polydispersion

A disperse flow is rarely composed of droplets of the same size. Far from it, most sprays possess droplets of sizes that can, in the context of solid propulsion, be spread over several order of magnitude in terms of diameter as discussed Section 1.2.1.1.2. It is of utmost importance to treat size polydispersion since particles of distinct size have unalike behavior in term of inertia, clustering or evaporation/combustion among others.

Usually, sprays inside SRMs are approximated through a log-normal distribution such as follows:

$$f(S) = \frac{1}{\sqrt{2\pi}\sigma_0} \exp\left[-\frac{1}{2}\left(\frac{\ln(S) - \ln(\bar{S})}{\sigma_0}\right)\right] \tag{2.4}$$

where $\bar{S}$ the average size and σ_0 the variance are parameters of the distribution.

Depending on the case or on the data experimentally obtained, such distribution can represent a number or mass frequency and can depend on the diameter, surface or another well chosen size parameter. Inside a system, this distribution can be dynamic and influenced by dilatation or evaporation process, when each particle size vary due to mass exchange with the carrier fluid. In addition, inert phenomena can also influence the size distribution due to the inertia of the spray. Typically, large particles can be quickly ejected from a vortex whereas small particles remain inside it.

Here, we shall thus make the difference between the terms *particle* and *droplet* regarding the evolution of their size distribution in the flow. Despite the usual associated definition the term particle to solid and droplet to liquid, it is preferred here to associate the term *droplets* when the flux in the size phase space is not null, because of evaporation for instance (see Section 2.2) and to *particles* otherwise. Since aluminum oxide smokes and residues can be either liquid or solid depending on the flame temperature and the position in the motor, this new distinction is preferred. Confusion between both terms is maintained to refer to model and phenomena that does or does not involve flux in the size phase space.

2.1.2.2 Droplet inertia and velocity polydispersion

The kinematic behavior of a particle mostly depends on its size. Large particles are barely influenced by the surrounding flow and have ballistic trajectories whereas the smallest ones act as tracers and follow the carrier fluid kinematic. Such phenomena are driven by the kinetic inertia of a particle on the one hand and by the viscous effect of the carrier phase on the other hand. In this context, the particle kinetic is driven by the Stokes number that can be defined under the following form:

$$\mathrm{St} = \frac{\tau_{\boldsymbol{u}}}{\tau_g} \tag{2.5}$$

where $\tau_{\boldsymbol{u}}$ is the response time of the velocity of a droplet (see Section 2.2.1.1) and τ_g is the characteristic time of the carrier fluid.

The convective time of the carrier phase is often associated to a strain rate. Whereas it can be chosen to take this strain rate local, it is generally preferable to link this value to a specific case as for the Taylor-Green vortices (Chaisemartin 2009) or the HIT (Sabat 2016). Generally, the Stokes number is scaled again relatively to a critical Stokes Stc where Particle Trajectory Crossings (PTC) begin to occur.

Because of the non-null response time of the particles belonging to a spray, particle trajectories can cross (Chaisemartin 2009) and distinct velocities can be observed in the vicinity of the same point. More precisely, we associate the term PTC to the existence of various particles in the same neighborhood with distinct velocities. PTC is a critical feature for two-phase flows since the disperse phase becomes polykinetic and a non-unique velocity distribution (velocity polydispersion) appears when such phenomena occur. As a consequence, the disperse flow complexity greatly increases when PTC appears (Csanady 1963; Squires and Eaton 1991b).

Moreover we make the distinction between heterogeneous PTC (hetero-PTC) and homogeneous PTC (homo-PTC). The first is caused by the difference of inertia between particles of distinct size and related to size polydispersion. The second one is related to particles of the same or of similar size but that cross each others due to significant inertia and to their independence to the carrier phase. The last phenomenon is the key feature studied in this manuscript, where the goal is to manage homo-PTC thanks to Eulerian model.

2.1.2.3 Phase kinematic interaction

Another essential aspect tackled in this work concerns the interaction between both phases. According to the literature on this subject, four cases can be observed:

- One-way coupling: flow with significant action of the carrier phase on the carried phase and negligible backward effects, this corresponds to disperse phase of very small volume and mass fraction,
- Two-way coupling: flow with significant reciprocal action of the carrier and carried phases, this corresponds to disperse phase of small volume fraction but significant mass fraction,
- Three-way coupling: two-way coupling where the disturbance of the fluid locally affects other particle's motion,
- Four-way coupling: two-way coupling flow with significant direct interactions between the components of the disperse phase.

The Figure 2.3 illustrate theses cases according to particle flow regimes and link them to the categories of particle laden flows described Section 2.1.1.1.4.

Because of the large aluminum oxide mass fraction inside SRMs, the flow will be considered as two-way coupling in this manuscript. As discussed in Chapter 1 such effects significantly

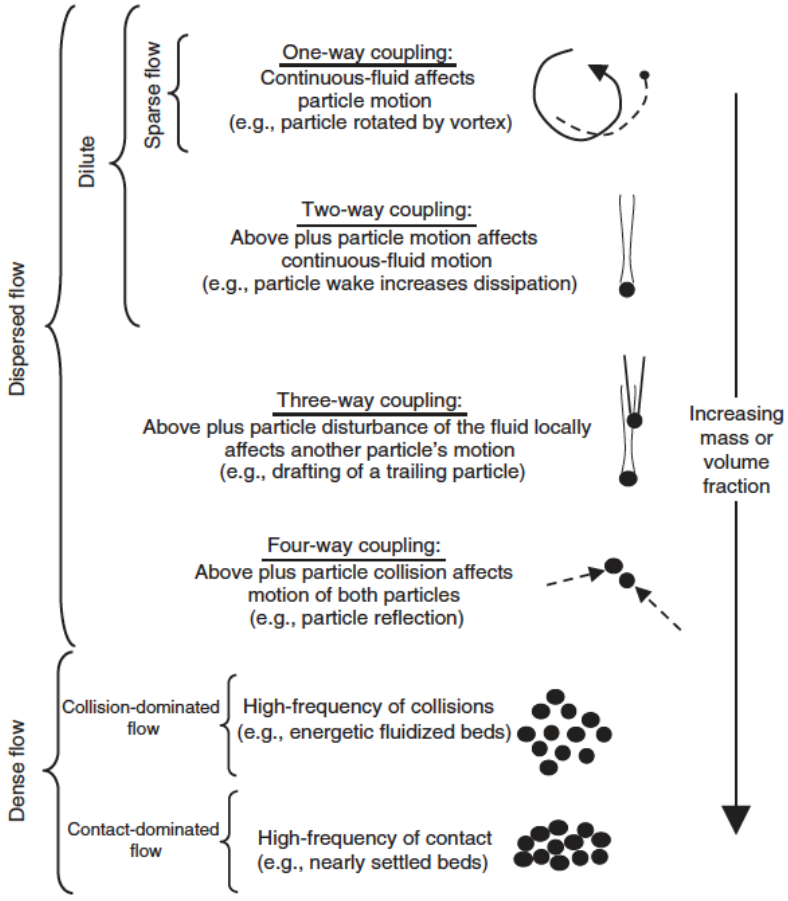

Figure 2.3: *Particle laden flow conditions based on various interphase and intraphase couplings (Crowe 2005)*

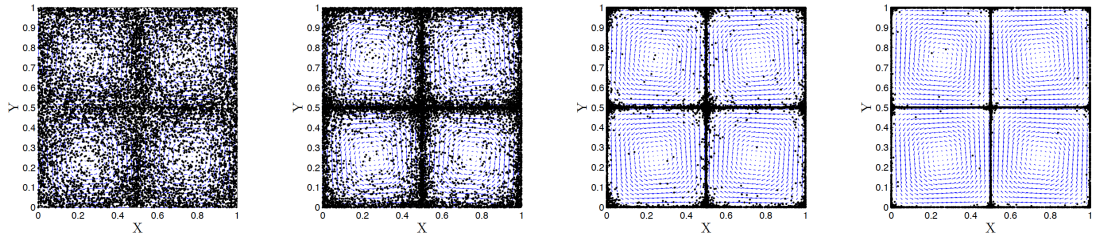

(a) Low Stokes number St = 0.03 < Stc

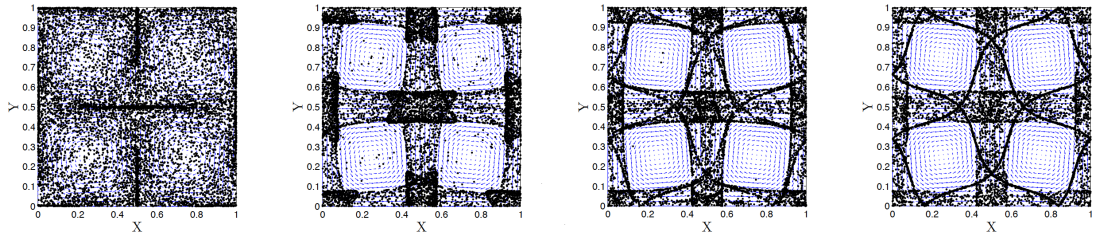

(b) High Stokes number St = 0.3 > Stc

Figure 2.4: *Lagrangian simulation of particles of low and high inertia in Taylor-Green vortices starting from a homogeneous filling (Chaisemartin 2009). Non-dimensioned time of pictures from left to right:* $t = 0.5$, $t = 1.25$, $t = 2.75$ *and* $t = 4$

impact SRMs behavior. Aside from the action of the particles on the mean carrier flow, the mutual action of the phases can significantly impact the propagation of acoustic waves in the mixture. Such phenomena is driven by the acoustic Stokes number defined as:

$$\mathrm{St_a} = \omega \tau_{\boldsymbol{u}} \tag{2.6}$$

where ω is the circular or angular acoustic frequency.

As shown in (Temkin and Dobbins 1966), due to two-way coupling, an acoustic wave can be either attenuated or amplified depending on $\mathrm{St_a}$ and the thermodynamic properties of the mixture.

2.1.2.4 Segregation

Depending on the flow topology, the particles are concentrated in clusters or are scattered inside the flow. As analyzed in (Squires and Eaton 1991a; Druzhinin 1995), the mass fraction of particles decreases at the vortex centers and increases near hyperbolic stagnation points (uniform strain and null vorticity). This behavior is significant for convective Stokes number close to a critical value where particles have sufficient inertia to leave vortex centers but barely enough to produce PTC. For large Stokes number, the particle paths tend to merge on preferred trajectories (Maxey 1987). The example of particle movement inside Taylor-Green vortices (Chaisemartin 2009) is a good example of such processes as it can be seen Figure 2.4.

To measure this phenomenon from a macroscopic scale, we observe the distribution of the

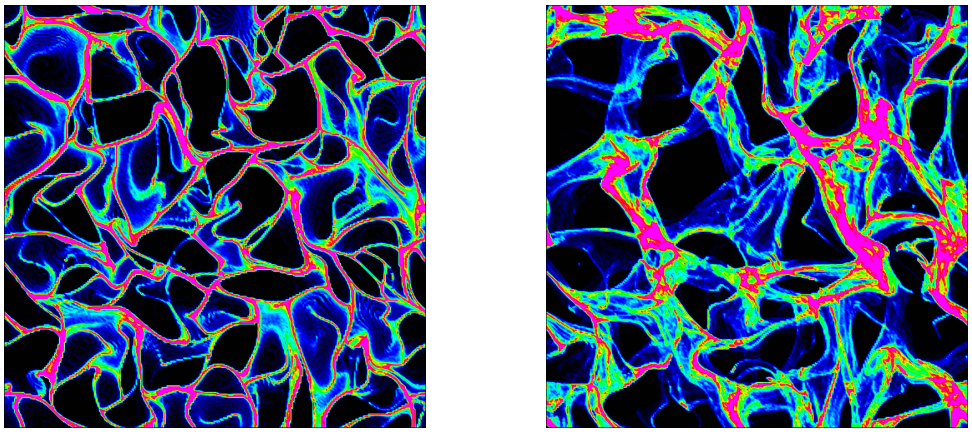

(a) St = 0.8 **(b)** St = 4.2

Figure 2.5: *Lagrangian simulation of particle and low and high inertia in frozen HIT (Sabat 2016)*

number density over a control volume. The segregation as defined in (Sabat 2016) leads to:

$$G_{pp}^{\Delta} = \frac{\langle n^2 \rangle}{\langle n \rangle^2} \tag{2.7}$$

where n is the number density field and the operator $\langle \cdot \rangle$ is the spatial averaging of a quantity over the domain Δ.

2.1.2.5 Particles in turbulence

The dynamics of particles in a turbulent flow is a highly complex topic. Because of the presence of eddies in the carrier phase, the particles are scattered in a chaotic way inside the flow according their Stokes number, scaled here on the kolmogorov time scale (Snyder and Lumley 1971; Simonin, Fevrier, and Lavieville 2002; Sabat 2016). It is observed in these conditions that the segregation is the highest for St = 1 where particles quickly form clusters. For St > 1, particles leave the smallest vortices and their behavior is driven by vortices of larger size. Such kind of behavior can be observed in the case of frozen HIT on Figure 2.5 where one can find similar behavior with Figure 2.4 in terms of segregation, with preferential path, concentration area and scattering due to carrier phase strain and PTC.

Including the possibility of two-way coupling, the behavior of turbulence has been observed to be modified (Elghobashi and Truesdell 1993; Boivin, Simonin, and Squires 2000). The energy dissipation process can be greatly impacted by the presence of particles. Moreover, in specific cases, phenomena of turbulence is observed to be generated from rest by the presence of particles (Zamansky et al. 2014).

2.1.2.6 Collision, break-up and coalescence

The consideration of four-way coupling effects have also been proven important (Doisneau 2013; Doisneau et al. 2013) for SRMs due to the impact of coalescence on size polydispersion. The droplet size can change because of collisions or because of the hydrodynamical stress caused by the carrier phase. Depending on the case, the first phenomenon can lead to the coalescence of two small droplets in a unique bigger one or to more complex phenomena (see Section 2.2.1.5 for more details). The second shatters a big droplet into smaller one through a process called secondary break-up (see Section 2.2.1.4), to make the distinction with primary break-up where droplets are detaching from a liquid core. Both can be observed in spray injection (see Section 2.1.1.1.5).

For SRMs, unlike for granular flows where the dynamic is mostly driven by elastic collisions between particles, collisions affect essentially the internal flow through its impact on the size distribution that itself influences the flow. Inside the chamber, droplets coalesce due to both homo-PTC and hetero-PTC and disturb acoustic waves according the local size distribution modification. At the level of the nozzle however, because of the high drift velocity magnitude, large droplets explode and reduce the average droplet size which helps at reducing I_{sp} losses. Considering the complexity of such phenomena, especially at the microscopic scale for disperse flows, it is preferable to model it rather than to solve it.

2.2 Droplet modeling

Starting from the assumption of point particles, this section proposes several models able to describe the dynamic of such objects. Assumed to be carried by a viscous gas modeled by a Navier-Stokes equation, several distinct phenomena can be observed and modeled. These can be considered either for particles alone or considering group effects. A review of the relevant droplet models for solid propulsion is given in this section.

2.2.1 Isolated droplets in the flow

The physics to be resolved around a single aluminum droplet in combustion is rich as illustrated in Figure 2.6. Drag, thermal conduction, thermal radiation, combustion or hydrodynamic stress among other lead to mass, momentum and energy exchanges between the carrier and carried phases that have to be taken into account. Due to the wide involved phenomenology, the effort is focused on the relevant models for the internal flows of SRM.

2.2.1.1 Drag forces

This variation of the droplet velocity caused by the surrounding gas can be sum up as a simple exchange of momentum and associated kinetic energy. The information on the detailed flow pattern around the droplet is replaced by the expression of a force applied on the particle. The

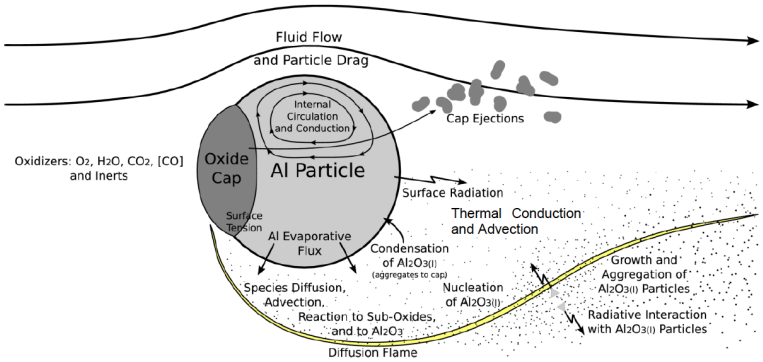

Figure 2.6: *Representation of the physical phenomena involved in the combustion of an aluminum droplet (Washburn et al. 2010)*

drag force is driven by the particulate Reynolds number that takes the following form:

$$\mathrm{Re}_p = \frac{\rho_g d_p \|\boldsymbol{u}_g - \boldsymbol{u}_p\|_2}{\mu_g}, \tag{2.8}$$

where ρ_g is the density of the surrounding gas, μ_g its dynamical viscosity, d_p is the particle diameter and $\boldsymbol{u}_g - \boldsymbol{u}_p$ is the drift velocity of the particle in the carrier phase.

For small Reynolds numbers, in the Stokes regime where the viscous forces are dominant compared to the convective effects, the drag force per unit of mass applied by a fluid on a sphere has the following analytical expression:

$$\boldsymbol{F}^{\mathrm{St}} = \frac{\boldsymbol{u}_g - \boldsymbol{u}_p}{\tau_{\boldsymbol{u}}}, \qquad \tau_{\boldsymbol{u}} = \frac{\rho_g d_p^2}{18\mu_g}, \tag{2.9}$$

where $\tau_{\boldsymbol{u}}$ is the drag force relaxation time.

This result due to Stokes (Stokes 1846) only takes into account viscous effects. A more detailed formulation first analyzed by Basset (Basset 1888), Boussinesq (Boussinesq 1885) and Oseen (Oseen 1927) is able to separate the Stokes drag from three other effects that are the Froude-Krylov force (action from a pressure gradient), the virtual mass (unsteady deflection of the surrounding fluid) and the history term, also named Boussinesq-Basset force (lag of the boundary layer). An extension of these effects for low-Mach limit compressible flow is given in (Parmar, Haselbacher, and Balachandar 2011).

These theoretical values have however to be corrected for Reynolds numbers larger than 1 when non-linear effects occur. Hypothesis used to determine the flow around the sphere at low Reynolds are no more valid. Starting from experimental analysis, the correction due to Schiller

and Naumann (Schiller and Naumann 1935) gives:

$$\boldsymbol{F}^{SN} = \boldsymbol{F}^{\mathrm{St}} \left(1 + 0.15\mathrm{Re}_p^{0.687}\right), \tag{2.10}$$

Formula (2.10) remains valid for $\mathrm{Re}_p \leq 10^3$ which is sufficient for the internal flow of a SRM since, according to (Doisneau 2013), the Reynolds number do not exceed 500, even in the nozzle.

Despite being sufficient in most situations, as for the internal flow of SRMs, the expression given above can find several limits. For instance, one can remark that the expressions of the drag given until now does not depend on the carrier phase density. As a consequence, a force remain applied on the particle in vacuum, which is an issue for high altitude plume simulations and one can refer to (Henderson 1976) for a specific correction. Moreover, assumption that droplets or particles are spherical can be overridden (Hölzer and Sommerfeld 2008) and is not opposed to the assumption of point particle. For conclusion, the chosen drag model needs to be adapted to the physical situation to be solved.

2.2.1.2 Heat transfer

Complementary to momentum exchanges, the droplets can also exchange thermal energy with the carrier phase by conduction/convection heating and radiation.

2.2.1.2.1 Heat conduction In the Stokes regime, because of the prevalence of the viscous effects, the conduction terms find an analytic solution that yields per unit of mass:

$$H^{\mathrm{St}} = C_{p,l}\frac{T_g - T_p}{\tau_T}, \text{ with } \tau_T = \frac{3}{2}P_r\frac{C_{p,l}}{C_{p,g}}\tau_{\boldsymbol{u}}, \tag{2.11}$$

where τ_T is the thermal relaxation time

For larger Reynolds numbers, a correction term needs to be applied. Ranz and Marshall (Ranz and Marshall 1952) proposed a correction that is still a standard today, for higher Reynolds number ($\mathrm{Re}_p < 10^5$) assuming a Prandlt number between 0.6 and 380:

$$H^{RM} = H^{\mathrm{St}} \left(1 + 0.3\mathrm{Re}_p^{1/2}P_r^{1/3}\right), \tag{2.12}$$

where P_r is the Prandtl number of the carrier phase.

In some cases, an equivalent expression to (2.12) is preferred:

$$H^{RM} = \sqrt{\pi} S^{1/2} \lambda_g \mathrm{Nu}_c \left(T_g - T_p\right), \qquad \mathrm{Nu}_c = 2 + 0.6 \mathrm{Re}_p^{1/2} P_r^{1/3}, \tag{2.13}$$

where λ_g is the thermal conductivity of the carrier phase, S the surface of the particle and Nu_c the Nusselt number.

Other models can be found in (Will, Kruyt, and Venner 2017) and the references within. For SRM applications, this model appears to be sufficient for the internal flow but, similarly to the drag models presented above, can be unrealistic for plume simulation.

2.2.1.2.2 Radiative heat transfer According to (Burt and Boyd 2005), in the case of plume simulation, the radiative heat transfer is clearly dominant starting from a few meters after the nozzle exit. While the heat transfer is mostly driven by convection in the nozzle due to the large drift velocity, such prevalence in the combustion chamber can still be questioned (Duval 2002). For the studied sprays, the heat convection prevails but cannot be proved to overwhelm by several order of magnitude the radiations through a simplified analysis. This subject, important for the propellant combustion and during the grain ignition phase, is of great complexity and therefore still actively studied (Binauld 2018). However, heat transfers through radiations are neglected for this work since they are not prevalent and the effort is focused on the resolution of hydro-acoustic instabilities (see Section 1.3.3).

2.2.1.3 Evaporation

The evaporation is generally defined as a mass transfer $\dot{m}_p$ between the phases associated to a heat transfer. Depending on the situation, it can be useful to rely not on the mass transfer but on the droplet surface change rate R_s. The relation between both thus is:

$$\dot{m}_p = \mathrm{d}_t \frac{\rho_l S^{3/2}}{6\sqrt{\pi}} = \frac{\rho_l S^{1/2}}{4\sqrt{\pi}} \mathrm{d}_t S = \frac{\rho_l S^{1/2}}{4\sqrt{\pi}} R_s. \tag{2.14}$$

The determination of the evaporation can be a complex task relying on the thermodynamic properties and on chemistry in the case of combustion. In practice however, simplified law can be used to model it.

2.2.1.3.1 Thermal conduction driven evaporation In the case of a droplet evaporating in its own vapor, the mass transfer is fully driven by the thermal flux between the phase (Williams 1985). Introducing the thermal Spalding B_T this evaporation model can be written

under the following form:

$$\dot{m}_p = \pi d_p \frac{\lambda_g}{C_{p,g}} \mathrm{Nu}_c \ln\left(1 + B_T\right), \qquad B_T = \frac{C_{p,l}\left(T_g - T_p\right)}{L_v}, \tag{2.15}$$

where L_v is the specific latent heat of evaporation.

In this model, the heat transfered from the gas to the droplet is used only to sustain the phase change so that such process occurs at a constant droplet temperature $T_{p,sat}$ and thus $Q_p = \dot{m}_p L_v$.

2.2.1.3.2 Species diffusion driven evaporation For more general multicomponent flows, as detailed in (Sirignano 2010) for instance, the evaporation is driven by the diffusion of the droplet component in the carrier phase. The mass transfer in these conditions can be written:

$$\dot{m}_p = \pi d_p \frac{\mu_g}{P_r} \mathrm{Nu}_c \ln\left(1 + B_M\right), \qquad B_M = \frac{Y_{A,s} - Y_{A,\infty}}{1 - Y_{A,s}}, \tag{2.16}$$

Such evaporation process will by itself create a temperature difference with the carrier phase because of the latent heat. Thus the mass flux (2.16) needs to be corrected in order to take into account thermal conduction process. Additionally, another correlation is needed to take into account the convection of the droplet. To such purpose, we present here the model proposed in (Abramzon and Sirignano 1989), and widely used in the literature. The thermal flux is then rewritten:

$$\dot{m}_p = \pi d_p \rho_g \overline{D}_g Sh^* \ln\left(1 + B_M\right), \qquad Sh^* = 2 + \frac{Sh_0 - 2}{F_M(B_M)}, \tag{2.17}$$

where $\overline{D}_g$ is the diffusion coefficient of the droplet material in the carrier phase, Sh^* the corrected Sherwood number, Sh_0 the standard Sherwood number and F_M the correction function.

These two last terms are given by the relations:

$$Sh_0 = 2 + 0.552 \mathrm{Re}_p^{1/2} Sc^{1/3}, \qquad F_M(B_M) = (1 + B_M)^{0.7} \frac{\ln\left(1 + B_M\right)}{B_M}, \tag{2.18}$$

where $Sc = \frac{\mu_g}{\rho_g \overline{D}_g}$ is the Schmidt number.

Finally, the thermal flux from the droplet to the gas in this context takes the form:

$$H_p = \dot{m}_p \left[\frac{C_{p,l}\left(T_g - T_p\right)}{B_T^*} - L_v \right], \tag{2.19}$$

where a correction loop, detailed in the original paper, is required to evaluate the corrected thermal Spalding B_T^* and take into account coupled thermal and diffusion driven evaporation process.

2.2.1.3.3 d^n combustion law Because of the complex physics involved, the evaporation laws can reach a high complexity as presented above. In the context of combustion of aluminum, the complexity of the laws giving $\dot{m}_p$ and H_p is even more increased. We restrict here the presentation of the combustion model to the so-called d^n law. This combustion law introduces a minimal, amount of parameters namely the initial diameter d_0, the diameters of the residues d_{res}, the combustion time τ_{comb} and an exponent n. The combustion time, depending on the surrounding gas composition, can be obtained from (Beckstead 2002), for example, while the others are fixed parameters. Starting from a droplet mass conservation law, the resulting mass flux yields:

$$\dot{m}_p = \frac{Sh_0\pi}{4n}\rho_l \frac{d_0^n - d_{res}^n}{\tau_{comb}} d_p^{3-n}. \tag{2.20}$$

In this situation, the heat flux depends on the chemical properties of the mixture and the dynamic of the droplet. Thus the gas temperature is obtained by the appropriate definition of the enthalpy of the aluminum oxide and of the combustion products. Such description is not given here but more details and proposition on aluminum combustion modeling can be found in (Sibra 2015).

2.2.1.4 Secondary break-up

The secondary break-up is the phenomenon that tears apart a droplet because of the shear stress caused by the surrouding gas. Properly explained in (Hsiang and Faeth 1995), the droplet surface disturbance together with the surface tension create a pressure disequilibrium inside the droplet leading to the droplet break-up under a finite time span. The occurrence of such event on a droplet is driven by the aerodynamic Weber number (2.3) based on the diameter of the studied droplet, which leads to:

$$\mathrm{We}^a = \frac{\rho_g d_p \|\boldsymbol{u}_l - \boldsymbol{u}_g\|_2^2}{\sigma_{lg}}. \tag{2.21}$$

The determination of the critical Weber number We_c^a is derived from the knowledge of the surface topology. A correlation obtained in (Pilch and Erdman 1987) simplifies the problem to:

$$\mathrm{We}_c^a = 12\left(1 + 0.77\mathrm{Oh}^{1.6}\right), \qquad \mathrm{Oh} = \frac{\mu_l}{\sqrt{\sigma_{lg}\rho_l d_p}}, \tag{2.22}$$

where Oh is the Ohnesorge number and μ_l the droplet material dynamical viscosity.

In addition to the critical Weber number, the typical break-up time τ_{bu} allows the definition of the break-up frequency $\nu_{bu} = \tau_{bu}^{-1}$. As suggested in (Ranger and Nicholls 1968), such break-up time can be adimensionned by a characteristic time τ_0 relative to the momentum velocity propagation and defined as:

$$\tau_0 = \frac{d_p}{\|\boldsymbol{u}_g - \boldsymbol{u}_p\|_2} \frac{\rho_l}{\rho_g}. \tag{2.23}$$

It was suggest in (Ranger and Nicholls 1968) that $\tau_{bu} \approx 5\tau_0$, however such estimation can be improved as in (Nigmatulin 1990):

$$\tau_{bu} = \frac{6\left(1 + 1.5\mathrm{Oh}^{0.74}\right)}{\left(\ln(\mathrm{We}^a)\right)^{0.25}}. \tag{2.24}$$

Details on the droplets generated by break-up can be found in (Pilch and Erdman 1987; Hsiang and Faeth 1993; Gelfand 1996; Shraiber, Podvysotsky, and Dubrovsky 1996).

2.2.1.5 Collision

By colliding, particles and droplets can change their trajectories or coalesce, obviously influencing the dynamics of the spray. In the case of solid particles, binary collisions generally lead to elastic rebounds that can be easily modeled. In the case of liquid droplets, the collisions can have additional consequences. The effect of binary collisions between a big and a small droplets are presented on Figure 2.7 briefly described hereafter. These mostly depend on two parameters, the collision Weber number We_{coll}^l and the impact parameter b:

$$\mathrm{We}_{coll}^l = \frac{\rho_g r_b \|\boldsymbol{u}_s - \boldsymbol{u}_b\|_2^2}{\sigma_{lg}}, \qquad b = \frac{I}{r_s + r_b}, \tag{2.25}$$

where $\boldsymbol{u}_s$ and $\boldsymbol{u}_b$ are the velocities of the small and the big droplets respectively, r_s and r_b their radii and I the distance between the droplet barycenter trajectories.

Therefore, $b = 0$ describes a frontal collision and $b = 1$ a skimming collision. According to (Ashgriz and Poo 1990), put aside strong collisions leading to the explosions of the droplets, three kinds of regimes can be observed depending to these parameters:

- $b < b_1(\mathrm{We}_{coll}^l, \frac{r_s}{r_b})$: separation by reflection,

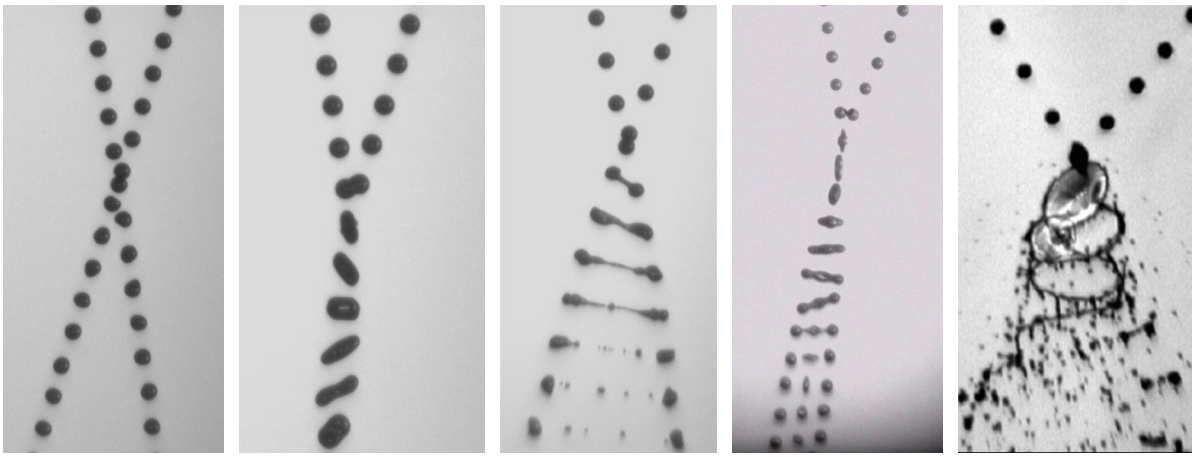

(a) Rebound **(b)** Coalescence **(c)** Separation by stretching **(d)** Separation by reflection **(e)** Bursting

Figure 2.7: *Existing regimes of binary collision (Foissac et al. 2010)*

- $b > b_2(\mathrm{We}^l_{coll}, \frac{r_s}{r_b})$: separation by stretching,
- $b \in \left[b_1(\mathrm{We}^l_{coll}, \frac{r_s}{r_b}), b_2(\mathrm{We}^l_{coll}, \frac{r_s}{r_b})\right]$ coalescence.

In the case of the separation, the exchange of mass between the droplets can be neglected which leads to:

$$\begin{cases} r'_s = r_s, \\ r'_b = r_b. \end{cases} \tag{2.26}$$

where the $'$ indicate the state of the droplets after collision.

Also no evolution of the scalar conservative quantities can be observed. In addition, for droplet reflecting, the velocities of the droplets remain unchanged.

$$\begin{cases} \boldsymbol{u}'_s = \boldsymbol{u}_s, \\ \boldsymbol{u}'_b = \boldsymbol{u}_b. \end{cases} \tag{2.27}$$

While in the case of stretching, the resulting droplet velocities are:

$$\begin{cases} \boldsymbol{u}'_s = \boldsymbol{u}_s - \frac{2r_b^3}{r_b^3+r_s^3}\left((\boldsymbol{u}_s - \boldsymbol{u}_b)\cdot\overrightarrow{\boldsymbol{n}}\right)\overrightarrow{\boldsymbol{n}}, \\ \boldsymbol{u}'_b = \boldsymbol{u}_b + \frac{2r_s^3}{r_b^3+r_s^3}\left((\boldsymbol{u}_s - \boldsymbol{u}_b)\cdot\overrightarrow{\boldsymbol{n}}\right)\overrightarrow{\boldsymbol{n}}. \end{cases} \tag{2.28}$$

where $\overrightarrow{\boldsymbol{n}} = \frac{\boldsymbol{u}_s - \boldsymbol{u}_b}{\|\boldsymbol{u}_s - \boldsymbol{u}_b\|_2}$ is the normal vector of the relative velocity.

In the case of coalescence, droplets merge in a new one detaining the conserved quantities of both droplets conserved quantities. Thus neglecting the relative kinetic energy dissipated by viscous effect and surface tension variation, one can obtain:

$$\begin{cases} m' = m_s + m_b, \\ m'\boldsymbol{u}' = m_s\boldsymbol{u}_s + m_b\boldsymbol{u}_b, \\ m'h' = m_s h_s + m_b h_b. \end{cases} \tag{2.29}$$

where the m are the masses and the h are the thermal enthalpies.

Such simplified approach does not take into account all the corrections that have to be used in practice. For example, due to aerodynamic effects droplets can *dodge* each other avoiding collisions. We refer to (Qian and Law 1997; Dufour 2005; Hylkema 1999; Rabe 2009) and the reference within for more details on the droplet collisions and their modeling.

2.2.2 Droplets group dynamic

Aside their individual interaction with the gas, the droplets can interact between each others and affect the dynamic of the group inside a given control volume. As a consequence, the interaction between the carrier and carried phase cannot always be restricted to the sum of the individual gas-droplet interactions. Such effect can be caused by the direct interaction of the droplet with each others through the carrier phase.

2.2.2.1 Drag correction

Because of the significant volume fraction α_l of the droplets inside the disperse flow, the drag trail of droplet disturbs the flow seen by another and thus modify the average drag coefficient. As observed in (Rusche and Issa 2000), several strategies are possible. One can multiply the drag force by a correction coefficient (Kumar and Hartland 1985) or by modifying the relative viscosity (Ishii and Zuber 1979) for example. Taking the drag force correction proposed in (Rusche and Issa 2000) for example, the average drag $\overline{\boldsymbol{F}}$ on a droplet of the group yield:

$$\overline{\boldsymbol{F}} = \left[\exp(K_1\alpha_l) + \alpha_l^{K_2}\right]\boldsymbol{F}, \tag{2.30}$$

where α_l is the volume fraction of liquid and parameters K_1 and K_2 are fitted depending on the nature of the disperse flow.

In the case of droplet flows, the original paper gives:

$$K_1 = 2.10 \qquad K_2 = 0.249. \tag{2.31}$$

2.2.2.2 Turbulence

Finally, we quickly discuss here the case of turbulence. Such subject is highly complex and many strategies have been proposed to consider such aspects for Reynolds Average Navier-Stokes (RANS) and Large Eddy Simulation (LES) modeling with a wide variety of approaches (see (Simonin, Fevrier, and Lavieville 2002; Zaichik, Simonin, and Alipchenkov 2009; Fede, Simonin, and Villedieu 2015) among others). As discussed in Section 2.1.2.5, the effect of turbulence leads to an increase of the segregation of the particles. Also the modeling introduces the need of a description of the transport of the particles by the fluctuating field but also of the collision cause by it (Zaichik, Simonin, and Alipchenkov 2003). It is thus necessary to rely on a statistical approach to model these flows (Zaichik, Alipchenkov, and Sinaiski 2008). For the work presented in this manuscript, we refer to the developments provided by Sabat (Sabat 2016; Sabat et al. 2018) that are today the closest to the contribution given here.

2.3 Disperse flow modeling

As explained in the previous section, the modeling of two-phase flows is a complex task that is strongly influenced by the field of application. Since simulations of SRMs are aimed, we focus the discussion on moderately dense disperse flows. Methods specifically designed to be operative for both separate phase and disperse flow regimes are not tackled here since it is out of concerns for the application targeted. Such review is not exhaustive but focused on the main approaches that have been developed until today. Discussing of two-phase flow model with an increasing level of complexity, this peculiarities of the models are stressed on issues of physical representativity and realizability.

2.3.1 Continuum mechanics approaches

For the derivation of disperse phase models, we propose at first not to rely on the form of the disperse phase, composed of an ensemble of agglomerate of matter. Instead, assuming the continuous description of both phases and either spatial or ensemble averaging, it is possible to derived a hierarchy of models. These do not necessarily rely on the assume structure of the disperse flow.

2.3.1.1 Two fluid averaged model

The most general approach considered here for the modeling of two coexisting fluids takes into account the conservation of mass, momentum and energy for each phase to which is added an equation for the volume fraction able to describe the interface. Proceeding to a spatial averaging one can obtain a model detaining seven equations. The first model of this class has been derived in (Baer and Nunziato 1986) to model gas-solid front propagation in explosives (see (Kah 2010) and the reference therein). Also other approaches replace the volume fraction equation by a surface density equation (Ishii and Hibiki 2010), that is the base of the Eulerian-Lagrangian Spray Atomization (ELSA) formalism (Vallet and Borghi 1999; Lebas et al. 2005;

Lebas et al. 2009).

Most issues of these models arise from the description of the interface since this element is only coarsely known because of the spatial averaging. However in some case, as proposed in (Ishii and Hibiki 2010) for bubbly flows, the equation describing the interfaces can be override which leads to the six-equation model that follow:

$$\left\{\begin{array}{lll}
\partial_t \alpha_g \check{M}_g & +\mathrm{div}\left(\alpha_g \check{M}_g \boldsymbol{u}_g\right) & = \Gamma_{gl}, \\
\partial_t \alpha_g \check{M}_g \boldsymbol{u}_g & +\mathbf{div}\left(\alpha_g \check{M}_g \boldsymbol{u}_g \otimes \boldsymbol{u}_g + \alpha_g p_g \mathbb{I}\right) & = \mathbf{div}\left(\alpha_g \boldsymbol{\Pi}_g\right) + \boldsymbol{F}_{gl}, \\
\partial_t \alpha_g \check{M}_g E_g & +\mathrm{div}\left(\alpha_g \check{M}_g E_g \boldsymbol{u}_g + \alpha_g p_g \boldsymbol{u}_g\right) & = \mathrm{div}\left(\alpha_g \boldsymbol{q}_g\right) + \mathrm{div}\left(\alpha_g \boldsymbol{\Pi}_g \cdot \boldsymbol{u}_g\right), \\
 & & \quad + H_{gl} + (\boldsymbol{u}_g - \boldsymbol{u}_p) \cdot \boldsymbol{F}_{gl}, \\
\partial_t \alpha_l \check{M}_l & +\mathrm{div}\left(\alpha_l \check{M}_l \boldsymbol{u}_g\right) & = \Gamma_{lg}, \\
\partial_t \alpha_l \check{M}_l \boldsymbol{u}_p & +\mathbf{div}\left(\alpha_l \check{M}_l \boldsymbol{u}_p \otimes \boldsymbol{u}_p + \alpha_l p_l \mathbb{I}\right) & = \mathrm{div}\left(\alpha_l \boldsymbol{\Pi}_l\right) + \boldsymbol{F}_{lg}, \\
\partial_t \alpha_l \check{M}_l E_p & +\mathrm{div}\left(\alpha_l \check{M}_l E_p \boldsymbol{u}_g + \alpha_l p_l \boldsymbol{u}_g\right) & = \mathrm{div}\left(\alpha_l \boldsymbol{q}_l\right) + \mathrm{div}\left(\alpha_l \boldsymbol{\Pi}_l \cdot \boldsymbol{u}_g\right), \\
 & & \quad + H_{gl} + (\boldsymbol{u}_g - \boldsymbol{u}_p) \cdot \boldsymbol{F}_{lg},
\end{array}\right. \tag{2.32}$$

where p_i, $\boldsymbol{\Pi}_i$, $\boldsymbol{q}_i$ are the internal pressures, stresses and heat flux of each phase, Γ_i, $\boldsymbol{F}_{ij}$ and H_{gl} are the mass, momentum and energy exchanges, E_i are the total energies and the remaining terms are already defined Section 2.1.1.1.1.

For our case of interest, one can observe that $\alpha_l \ll 1$ and $\alpha_g \approx 1$ due to the diluted character of the flow. Moreover, due to the existence of the disperse flow under the form of droplets and some additional conditions (Nigmatulin 1990), the internal stress, pressure and heat flux can be neglected. From such assumptions, a diluted two-fluid model can be deduced from (2.32):

$$\left\{\begin{array}{lll}
\partial_t \rho_g & +\mathrm{div}\left(\rho_g \boldsymbol{u}_g\right) & = 0 \\
\partial_t \rho_g \boldsymbol{u}_g & +\mathbf{div}\left(\rho_g \boldsymbol{u}_g \otimes \boldsymbol{u}_g + p_g \mathbb{I}\right) & = \mathbf{div}\left(\boldsymbol{\Pi}_g\right) + \boldsymbol{F}_{gl} \\
\partial_t \rho_g E_g & +\mathrm{div}\left(\rho_g E_g \boldsymbol{u}_g + p_g \boldsymbol{u}_g\right) & = \mathrm{div}\left(\boldsymbol{q}_g\right) + \mathrm{div}\left(\boldsymbol{\Pi}_g \cdot \boldsymbol{u}_g\right) \\
 & & \quad + H_{gl} + (\boldsymbol{u}_g - \boldsymbol{u}_p)\boldsymbol{F}_{gl} \\
\partial_t \rho_l & +\mathrm{div}\left(\rho_l \boldsymbol{u}_g\right) & = 0 \\
\partial_t \rho_l \boldsymbol{u}_p & +\mathbf{div}\left(\rho_l \boldsymbol{u}_p \otimes \boldsymbol{u}_p\right) & = \boldsymbol{F}_{lg} \\
\partial_t \rho_l e_p & +\mathrm{div}\left(\rho_l e_p \boldsymbol{u}_g\right) & = H_{gl}
\end{array}\right. \tag{2.33}$$

where e_p is the internal energy of the particles.

To ultimately close the system, additional assumptions on the equations of state and droplet sizes are required in order to evaluate the exchange terms (see Section 2.2) and the internal stress, pressure and heat flux inside the carrier phase. Similar approaches to the one presented have been used by (Temkin and Dobbins 1966) for acoustic wave interactions with a spray of spherical particles and by (Jackson and Davidson 1983) for strongly two-way coupled flows. Moreover, a link between this macroscopic approach and a statistical one, as discussed Section 2.3.4.3.2, has been established in (Laurent and Massot 2001).

This straightforward derivation is however not mandatory. As studied in (Lebon, Lhuillier, and

Palumbo 2007) based on Extended Irreversible Thermodynamic (EIT) (Casas-Vázquez, Lebon, and Jou 2010), it is possible to consider p_l, $\mathbf{\Pi}_l$ and $\boldsymbol{q}_l$ as internal variables with meanings that differ from the ones of the gas. Such process is not followed in this manuscript despite similitudes can be observed with the selected governing equations.

2.3.1.2 Linearized lag

When the Stokes number is sufficiently small, the particles velocity is strongly correlated to the local carrier fluid topology. Therefore, the consideration of a whole system of equations dedicated to the particle field dynamics is not necessary. As proposed in (Ferry and Balachandar 2001, 2002) under the name of Eulerian Equilibrium Model (EEM), the local particle velocity field can be reconstructed thanks to a Taylor expansion of the drag force according to the local carrier phase velocity gradient and temperature gradient (Ferry and Balachandar 2005). Other expansions considering two-way coupling were conducted (Druzhinin 1994, 1995) but including a partial knowledge of the flow but the approach has been essentially designed for one-way coupling flows.

2.3.1.3 Equivalent Gas

Under the condition of fast relaxation process, the mixture can be modeled as a single fluid. Since particles are considered to be in a permanent thermal and dynamical equilibrium with the carrier phase, mass, momemtum and energy of the mixture called here Equivalent Gas (EG) are the following:

$$\left\{\begin{array}{lll} \rho & = \check{M}_g\alpha_g & +\check{M}_l\alpha_l, \\ \rho\boldsymbol{u}_m & = \check{M}_g\alpha_g\boldsymbol{u}_g & +\check{M}_l\alpha_l\boldsymbol{u}_l, \\ \rho e_m & = \check{M}_g\alpha_g e_g & +\check{M}_l\alpha_l e_l. \end{array}\right. \tag{2.34}$$

where the index m stand for mixture.

The dynamics of these variables are driven, as for a standard gas, by the following conservation equations:

$$\left\{\begin{array}{lll} \partial_t\rho & +\mathrm{div}\left(\rho\boldsymbol{u}_m\right) & = 0, \\ \partial_t\rho\boldsymbol{u}_m & +\mathbf{div}\left(\rho\boldsymbol{u}_m\otimes\boldsymbol{u}_m\right) & = -\mathbf{grad}\left(p_m\right)+\mathbf{div}\left(\mathbf{\Pi}_m\right), \\ \partial_t\rho e_m & +\mathrm{div}\left(\rho e_m\boldsymbol{u}_m\right) & = -\mathrm{div}\left(p_m\boldsymbol{u}_m\right)+\mathrm{div}\left(\boldsymbol{q}_m\right)+\mathrm{div}\left(\mathbf{\Pi}_m\cdot\boldsymbol{u}_m\right). \end{array}\right. \tag{2.35}$$

The Equation Of State (EOS) of such mixture differs from the one of a pure fluid and more especially from the carrier phase due to two-way coupling effects. It remains however possible

to establish an EOS for that mixture based on the model of perfect gases:

$$p_m = \rho_m \frac{R}{M_m} T_m = \rho_m \left(\gamma_m - 1\right) \left[E_m - \frac{\boldsymbol{u}_m \cdot \boldsymbol{u}_m}{2}\right], \tag{2.36}$$

where the Molar mass M_m and thermal capacities has been modified such that:

$$M_m = \frac{1}{\sum_{i\in\{g,l\}} n_i} \sum_{i\in\{g,l\}} M_i n_i, \qquad c_{p,m} = \sum_{i\in\{g,l\}} c_{p,i} Y_i, \tag{2.37}$$

where the n_i are the molar densities.

As a consequence, compared to the gas alone, both the heat capacity ratio and the speed of sound are diminished and their expressions yield:

$$c_m = \sqrt{\gamma_m \frac{R}{M_m} T_m}, \qquad \gamma_m = \frac{c_{p,m}}{c_{p,m} - \frac{R}{M_m}}, \tag{2.38}$$

The equilibrium assumption is equivalent to the existence of infinitely small droplet which, according to Section 1.2.1.1.2, defines a maximum in terms of performances. However, due to the absence of lag between the phases, many features, especially relative to acoustic waves damping and dispersion cannot be solved.

2.3.2 A kinetic modeling

The approach previously presented rely on a spatial averaging. Taking only into account disperse flows, it is possible to represent the disperse phase as a continuum by proceeding to an ensemble averaging.

2.3.2.1 The Liouville equation for disperse flows

Directly inspired for the kinetic theory of gases (see (Pottier 2007) among other), it is first considered that each agglomerate of the disperse phase can be modeled as a point particle. For the needs of two-phase flows, each droplet i possesses a velocity $\boldsymbol{u}_{p,i}$, a size $S_{p,i}$ and an enthalpy $h^{th}_{p,i}$. The disperse phase can thus be gathered in a NDF representing the N_p droplets appearing in a system:

$$f = f(t, \boldsymbol{x}_{p,1}, S_{p,1}, \boldsymbol{u}_{p,1}, h^{th}_{p,1} \ldots \boldsymbol{x}_{p,N_p}, S_{p,N_p}, \boldsymbol{u}_{p,N_p}, h^{th}_{p,N_p}), \tag{2.39}$$

Because of the indiscernible properties of the droplets, indexes can be freely exchanged and because of the assumption of point particles, the NDF can be expressed as a sum of product of Dirac delta function. As a consequence, such NDF takes the expression:

$$f = \sum_{i=1}^{N_p} \delta\left(\boldsymbol{x} - \boldsymbol{x}_{p,i}(t)\right) \delta\left(S - S_{p,i}(t)\right) \delta\left(\boldsymbol{c} - \boldsymbol{u}_{p,1}(t)\right) \delta\left(h_p^{th} - h_{p,1}^{th}(t)\right), \tag{2.40}$$

where the size S, velocity $\boldsymbol{c}$ and thermal enthalpy h_p^{th} are the variable of the phase space.

Under that formalism, it can be observed that the NDF (2.40) follows the Liouville equation stating $\frac{\mathrm{d}f}{\mathrm{d}t} = 0$ (Müller-Kirsten 2013) since the distribution function is constant along any trajectory in phase space. Defining $\boldsymbol{u}_{p,i}$, $R_{s,i}$, $\boldsymbol{F}_i$ and H_i as the rate of change of position, size, velocity and enthalpy, this leads to:

$$\partial_t f + \sum_{i=1}^{N} \mathrm{div}_{\boldsymbol{x}_i}\left(\boldsymbol{u}_{p,i} f\right) + \sum_{i=1}^{N} \partial_S\left(R_{s,i} f\right) + \sum_{i=1}^{N} \mathrm{div}_{\boldsymbol{u}_{p,i}}\left(\boldsymbol{F}_i f\right) + \sum_{i=1}^{N} \partial_{\left(h_{p,i}^{th}\right)} H_i f = 0, \tag{2.41}$$

where the rate of changes, $\boldsymbol{u}_{p,i}$, $R_{s,i}$, $\boldsymbol{F}_i$ and H_i include all the effects applying on an isolated droplet (see Section 2.2.1) but also group effects such as collisions in $\boldsymbol{F}_i$ or coalescence in $R_{s,i}$ (see Section 2.2.2) despite these terms become singular for such discrete events.

This Liouville equation (2.41) does not rely on any averaging procedure. Aside the assumption of indiscernibility, the model is exact.

2.3.2.2 The Williams-Boltzmann equation

To reach the level of the Boltzmann equation, an ensemble averaging is conducted. We thus define again a NDF from the (2.40) as follow

$$f(\boldsymbol{x}, t, S, \boldsymbol{c}, h_p^{th}) = \lim_{N_s \to \infty} \frac{1}{N_s} \sum_{i=1}^{N_s} \delta\left(\boldsymbol{x} - \boldsymbol{x}_{p,i}(t)\right) \delta\left(S - S_{p,i}(t)\right) \delta\left(\boldsymbol{c} - \boldsymbol{u}_{p,i}(t)\right) \delta\left(h_p^{th} - h_{p,i}^{th}(t)\right), \tag{2.42}$$

where N_s is the number of droplet samples used in the realizations of the ensemble averaging.

Thanks to that statistical convergence, it is now possible to define local quantities. In particular, the Probability Density Function (PDF) (2.42) is scaled by the number density to define the

NDF, in other words such that its integral over the phase space is equal to the number density:

$$n(x,t) = \int_{\mathbb{R}} \int_{\mathbb{R}^3} \int_{\mathbb{R}^+} f(\boldsymbol{x}, t, S, \boldsymbol{c}, h_p^{th}) \mathrm{d}S \mathrm{d}\boldsymbol{c} \mathrm{d}h_p^{th}, \tag{2.43}$$

As for the Liouville equation, it is assumed that the particles or droplets interact with the carrier fluid and with each other only by the models described Section 2.2. Putting the terms describing the collisions and break-ups on the right hand side, the limit for an infinite number of realizations of the Liouville equation (2.41) leads to the Williams-Boltzmann equation (Williams 1958), driving the dynamic of the NDF (2.42):

$$\underbrace{\partial_t f + \mathrm{div}_{\boldsymbol{x}}\left(\boldsymbol{c} f\right)}_{\text{free transport}} + \underbrace{\partial_S\left(R_s f\right)}_{\text{evaporation}} + \underbrace{\mathrm{div}_{\boldsymbol{c}}\left(\boldsymbol{F} f\right)}_{\text{drag force}} + \underbrace{\partial_{h_p^{th}}\left(H f\right)}_{\text{thermal transfert}} = \underbrace{\mathfrak{C}_{coal}}_{\text{collision}} + \underbrace{\mathfrak{B}}_{\text{break-up}}, \tag{2.44}$$

As observed in (Pottier 2007), put aside coalescence and break-up, the equation of Boltzmann type (2.44) is equivalent to the equation of Liouville type (2.41) for one particle. The difference lies in the form given to the NDF and in the interpretation of it. The Boltzmann equation (2.44) is rarely solved directly. However, it is a description at the mesoscopic scale of the problem and is a reference to be approximated.

2.3.3 Lagrangian modeling

The approaches presented Section 2.3.1 close directly the problem at a macroscopic level. Such way to model the flow necessarily requires subsequent assumptions on its form in order to close the systems, due to the the spatial averaging procedure. Taking advantage of the properties of disperse flows and point particle characteristics, other methodologies can be investigated.

We thus make here the distinction between Euler-Euler models, where the two phases are represented in an Eulerian framework, and Euler-Lagrange models, where particle or droplet behaviors are tracked in the domain while the carrier fluid remain in the usual framework. That last class of approach is briefly reviewed here.

2.3.3.1 Discrete Particle Simulation

A Discrete particle Simulation (DPS) (also said Lagrangian DPS) is the simulation of a disperse flow where each agglomerate of matter, represented as a point particle, is tracked. Each can evolve in the physical domain according to the carrier phase properties at its position. Each droplet i among the N_p observed is driven by the system of Ordinary Differential Equations

(ODEs) that follows:

$$\partial_t \boldsymbol{x}_{p,i} = \boldsymbol{u}_{p,i}; \qquad \partial_t S_{p,i} = R_{s,i}; \qquad \partial_t \boldsymbol{u}_{p,i} = \boldsymbol{F}_i; \qquad \partial_t h^{th}_{p,i} = H_i, \tag{2.45}$$

where $\boldsymbol{x}_{p,i}$ is the position of the particle i of velocity $\boldsymbol{u}_{p,i}$, size $S_{p,i}$ and thermal enthalpy $h^{th}_{p,i}$ on which mass, momentum and heat transfer, $R_{s,i}$, $\boldsymbol{F}_i$ and H_i, are applied.

Firstly introduced in (Riley and Patterson 1974), the approach has been extended to evaporating droplet (Mashayek et al. 1997) and turbulent combustion (Reveillon and Vervisch 2005) and collisions. Formally, if the droplets are considered indiscernible, this approach is equivalent to the direct resolution of the Liouville equation (2.41). Since this method focused on tracking every particle, the approach is clearly deterministic and can be referred as point-particle DNS (Pai and Subramaniam 2012). However, such character raises several problems including boundary and initial conditions that have to be set representative enough to be coherent with the modeled configuration. Additionally, in industrial configurations, the use of DPS is far from be always possible due to the computational cost inherent to the tracking of each particle in an industrial system.

2.3.3.2 Stochastic Lagrangian

In order to limit the numerical cost of a DPS, the idea is to limit the number of particles considered by tracking samples representing a group of particles or realizations. Such approach, referred as Stochastic Parcel (SP) simulation, consists in approximating the NDF (2.40) by weighting a reduced set of tracked samples that are called *parcel*. Mathematically, this leads to:

$$f \approx \sum_{i=1}^{I} \omega_i \delta\left(\boldsymbol{x} - \boldsymbol{x}_{p,i}\right) \delta\left(S - S_{p,i}\right) \delta\left(\boldsymbol{u}_p - \boldsymbol{u}_{p,1}\right) \delta\left(h^{th}_p - h^{th}_{p,1}\right), \tag{2.46}$$

where ω_i is the statistical weight attributed to the parcel i and I is the number of parcel.

Under that formalism, it can be observed that the NDF follows the Liouville equation (2.41) where the number of particles N_p has been replaced by the number of parcels I. From a more probabilistic vision of the problem, such resolution is an approximation of the Boltzmann kinetic equation (Subramaniam 2001) (see equation (2.44)) Due to (Bird 1970) for molecular gas dynamic, the Direct Monte-Carlo Simulation (DMCS) approach aims at approximating the Boltzmann equation through sampling. It can be proved that the proposed algorithm converges to the solution of the Boltzmann equation (Wagner 1992) but at the price of a large number of statistical particles. In practice, the main difference between the SP and the DMCS approaches lies in the convergence criteria, since these methods do not aim at approximating the same description of the flow and the algorithm determining the particle collisions. That last feature is not necessarily considered for SP simulation but is at the core of DMCS method. Considering two-phase flows, we refer in the following to both methods under the name of stochastic Lagrangian simulation.

2.3.3.3 Specificities of Euler-Lagrange modeling and simulation

Intrinsically, Lagrangian models have the advantage to be able to treat PTC since each droplet follows its own trajectory and the behavior of the ensemble, that is modeled in the Eulerian framework, is directly deduced from the sample distribution in the Lagrangian framework. Such feature can however be achieved only with a sufficient number of parcels in the same neighborhood in order to properly and accurately represent the flow, especially in case of coalescence (Laurent, Massot, and Villedieu 2004; Fox, Laurent, and Massot 2008). In some cases, for DMCS, the number of samples necessary for convergence can exceed the number of particles of an actual DPS.

Another specificity of the Euler-Lagrange modeling implies the two-way coupling. If the action of the carrier fluid, in the Eulerian framework, on a stochastic sample can be computed straightforwardly, the determination of the backward effect is not. Indeed the contribution of the point particle on the carrier fluid is pointwise and thus singular. Optimally, the influence of the Lagrangian parcels shall be integrated over an area of influence and along the particle path. Such feature shall thus be treated carefully (Capecelatro and Desjardins 2013; Capecelatro, Desjardins, and Fox 2016; Zamansky et al. 2014) in order to ensure convergence through a Eulerian grid refinement.

Aside two-way coupling that is a difficulty in itself, Lagrangian numerical methods are generally highly robust. These properties are very desirable for simulation but, using domain decomposition, these approaches hardly scale on a large number of processors compared to Eulerian based methods. Such problematic is inherent to the Lagrangian method since the scaling is limited, first, by the unbalance arithmetic load on the processor due to the particle sample positions and, second, by the memory exchange overhead caused by particles moving from a processor to another.

2.3.4 Eulerian statistical modeling

The existence of a statistical modeling of the disperse flow is not linked to the Euler-Lagrange framework. Far from it, several methods aiming at solving a statistical filtering of the disperse phase in an Eulerian framework can be distinguished.

2.3.4.1 A moment hierarchy

Instead of multiplying the number of samples to converge, it is proposed that such process has been already fulfilled and that the NDF that follows is itself the variable of the problem and not only the solution aimed. Additionally, due to the difficulty to directly solve the NDF as a variable, it is preferred to integrate the NDF over the phase space and to work with the moments of f defined as:

$$\mathcal{M}_k^{(l)[m]} = \iiint_{\mathcal{D}_f} \left(\otimes^k \boldsymbol{c}\right) S^l (h_p^{th})^m f \mathrm{d}\boldsymbol{c}\mathrm{d}S\mathrm{d}h_p^{th}, \tag{2.47}$$

where $\mathcal{D}_f$ is the domain of definition of f in the phase space and the operator $\otimes^k$ represents the k^{th}-power of the tensorial product such as:

$$\otimes^0 \boldsymbol{c} = 1, \qquad \otimes^1 \boldsymbol{c} = \boldsymbol{c}, \qquad \otimes^2 \boldsymbol{c} = \boldsymbol{c} \otimes \boldsymbol{c}, \qquad \otimes^3 \boldsymbol{c} = \boldsymbol{c} \otimes \boldsymbol{c} \otimes \boldsymbol{c}, \qquad \text{and so on.} \tag{2.48}$$

By definition, the following standard values can be specified:

1. number density: $n(x,t) = \mathcal{M}_0^{(0)[0]}$,
2. average velocity: $\boldsymbol{u}_p(x,t) = \mathcal{M}_1^{(0)[0]}/\mathcal{M}_0^{(0)[0]}$,
3. covariant matrix or velocity dispersion: $\boldsymbol{\Sigma}(x,t) = \left(\mathcal{M}_0^{(0)[0]}\mathcal{M}_2^{(0)[0]} - \mathcal{M}_1^{(0)[0]} \otimes \mathcal{M}_1^{(0)[0]}\right)/\left(\mathcal{M}_0^{(0)[0]}\right)^2$,
4. average size: $\overline{S}(x,t) = \mathcal{M}_0^{(1)[0]}/\mathcal{M}_0^{(0)[0]}$,
5. average enthalpy: $\overline{h_{p,th}}(x,t) = \mathcal{M}_0^{(0)[1]}/\mathcal{M}_0^{(0)[0]}$.

The Eulerian methods of the category defined here propose to solve equations describing the evolution of the moments of f. From this approach, two main problems arise and require closures. First, taking only into account the free transport in (2.44) and integrating it over the moment space, one obtains:

$$\partial_t f + \mathrm{div}_{\boldsymbol{x}}\,(cf) = 0 \Rightarrow \partial_t \mathcal{M}_k^{(l)[m]} + \mathbf{div}_{\boldsymbol{x}}\left(\mathcal{M}_{k+1}^{(l)[m]}\right) = 0, \tag{2.49}$$

for $k, l, m \in \mathbb{N}^3$.

The main issue of such process is that any equation describing the time evolution of $\mathcal{M}_k^{(l)[m]}$ requires the expression of $\mathcal{M}_{k+1}^{(l)[m]}$. Therefore, a closure on the velocity is needed in order to obtain a finite set of equations to solve. Secondly, due to the non-linearity of the evolution rates R_s, $\boldsymbol{F}$ and H of the Williams-Boltzmann equation (2.44), additional closure informations are needed on the size, velocity and temperature distribution.

Definition 2.1. Let $\mathcal{M}_K^{(L)[M]}$ a truncated sequence of moments $\mathcal{M}_k^{(l)[m]}$ with $k \leq K$, $l \leq L$ and $m \leq M$ defined by (2.47). Then the moment space $G_K^{(L)[M]}$ is defined by:

$$G_K^{(L)[M]} = \left\{ \mathcal{M}_k^{(l)[m]} \middle| f(\boldsymbol{x}, t, S, \boldsymbol{c}, h_p^{th}) \geq 0 \right\} \tag{2.50}$$

where $f(\boldsymbol{x}, t, S, \boldsymbol{c}, h_p^{th})$ is thus a positive measure.

For the sake of the consistency with the Eulerian statistical modeling of the disperse flow, the moments constitute the observable of the problem and therefore have to belong to the moment space. As a consequence, the preservation of the solution in moment space is a key point in both model derivation and numerical scheme design.

2.3.4.2 Algebraic closure

Algebraic Closure-Based Moment Method (ACBMM) class of closing methods aims at expressing the missing quantities through physical/mathematical assumptions. The considerations raised are mostly inspired from turbulence and LES modeling. Starting from the Mesoscopic Eulerian Formalism (MEF) considerations (Fevrier, Simonin, and Squires 2005), the key is to express Random-Uncorrelated-Motion (RUM) tensor $\boldsymbol{R}_p$, that is consistent with the velocity dispersion, and defined such that

$$\boldsymbol{\Sigma} \equiv \boldsymbol{R}_p = \boldsymbol{R}_p^\star + \frac{2\delta\Theta_p}{N_{dim}}\mathbb{I}, \tag{2.51}$$

where $\boldsymbol{R}_p^\star$ is the deviatoric part of $\boldsymbol{R}_p$, $\delta\Theta_p$ is the RUM Kinetic Energy (RUE) and N_{dim} is the number of physical dimensions.

This last term is obtained thanks to an equation on the kinetic energy deduced from the second order moment tensor $\mathcal{M}_2$. Taking into account, as conservation laws, mass momentum and *scalar* energy (thus the zeroth, first order moment tensor and the trace of the second one), several closures can be envisioned:

- **VISCO**: $\boldsymbol{R}_p^\star = -2\tau_{\boldsymbol{u}}\frac{\delta\Theta_p}{N_{dim}}\boldsymbol{S}^\star$ (Simonin, Fevrier, and Lavieville 2002; Kaufmann et al. 2008),
- **2-Φ-EASM** : $\boldsymbol{R}_p^\star = 2\delta\Theta_p\left[G_1\boldsymbol{S}^\star + G_2\left(\boldsymbol{S}^\star\boldsymbol{\Omega} + \boldsymbol{\Omega}\boldsymbol{S}^\star\right) + G_3\left(\boldsymbol{S}^\star\boldsymbol{S}^\star - \frac{\mathrm{tr}(\boldsymbol{S}^\star\boldsymbol{S}^\star)}{N_{dim}}\mathbb{I}\right)\right]$, with $G_1 = -\frac{\sqrt{2\mathrm{tr}(\boldsymbol{S})+2\mathrm{tr}(\boldsymbol{\Omega})}}{2\mathrm{tr}(\boldsymbol{S})}$, $G_2 = \frac{-1}{2\mathrm{tr}(\boldsymbol{S})}$ and $G_3 = \frac{1}{\mathrm{tr}(\boldsymbol{S})}$ (Masi and Simonin 2012).

where $\boldsymbol{S} = \frac{1}{2}\left(\mathbf{grad}\left(\boldsymbol{u}_p\right) + \mathbf{grad}\left(\boldsymbol{u}_p\right)^T\right)$ is the strain tensor, $\boldsymbol{S}^\star = \boldsymbol{S} - \frac{\mathrm{tr}(\boldsymbol{S})}{N_{dim}}\mathbb{I}$ its deviatoric part and $\boldsymbol{\Omega} = \frac{1}{2}\left(\mathbf{grad}\left(\boldsymbol{u}_p\right) - \mathbf{grad}\left(\boldsymbol{u}_p\right)^T\right)$ the rotational.

While the VISCO closure is based on the local equilibrium assumption, similar to the one used for the EEMs, the 2-Φ-EASM relies on a hypothesis of self-similarity. Other choices are possible and a detailed hierarchy of closure for $\boldsymbol{R}_p^\star$ is given in (Masi 2010) to close the problem considering that velocity dispersion is mostly generated by turbulence. This class of models has been successfully applied on academic and industrial configurations, including for SRMs (Simoes 2006).

In case of pure turbulence driven flows, other ACBMM closures are possible. Resolving the equations of the velocity moment of zeroth, first and second order tensors, it is aimed in (Zaichik, Simonin, and Alipchenkov 2009) to close the problem assuming that the subgrid transport is driven by the carrier phase fluctuations. Based on the assumption that the fourth-order cumulant moments are null and that time evolution and convection of velocity dispersion can be neglected compared to its dissipation and non-convective transport, the closing term $\sigma_{ijk} =$

$\frac{1}{\mathcal{M}_0^{(0)[0]}} \int (c_i - u_{p,i})(c_j - u_{p,j})(c_k - u_{p,k}) f \mathrm{d}\boldsymbol{c}$ takes the expression:

$$\sigma_{ijk} = -\frac{1}{3}\left(D^r_{p,in}\frac{\partial \sigma_{jk}}{\partial x_n} + D^r_{p,jn}\frac{\partial \sigma_{ik}}{\partial x_n} + D^r_{p,kn}\frac{\partial \sigma_{ij}}{\partial x_n}\right), \qquad D^r_{p,ij} = \tau_{\boldsymbol{u}}\left(\sigma_{ij} + g^r_u \tau^r_{ij}\right), \tag{2.52}$$

where σ_{ij} are the components of the velocity dispersion $\boldsymbol{\Sigma}$, and τ^r_{ij} are the component of the subgrid diffusion tensor of the carrier phase and g^r_u is the response coefficient of the particles.

Extension of the models for thermal temperature dispersion are given in (Masi 2010) and evaporating spray in (Masi, Simonin, and Bédat 2011) but are not detailed here.

2.3.4.3 Assumed shape NDF

Another strategy consists in considering a finite set of moments for which we can associate in a one-to-one correspondence a unique kinetic velocity distribution detaining a sufficient number of parameters equal to the given set of moments.

2.3.4.3.1 NDF decomposition The NDF is a multidimensional distribution not only spread over the physical space but also in the phase space that we aim here at describing through a limited set of its moments (2.47). Velocity, size and temperature are correlated in terms of dynamic since along the flow, they depend on each other. To do so, it is possible to take into account coupled moments as proposed in (Vié, Laurent, and Massot 2013) for size and velocity, with the so-called Coupled Size Velocity Moments (CSVM) method.

In general however, it is assumed that no coupled moments, i.e. in the sens that no mixed combination of velocity, size or enthalpy, are involved in the conservation laws. In other words, the NDF is assumed to be the product of PDFs dedicated to each phase space or a sum of such product. Therefore, it can be assumed that the NDF takes the following form:

$$f = \sum_{i=1}^{N_{dist}} n_i(t,\boldsymbol{x}) f_{\boldsymbol{c}}(t,\boldsymbol{x},S,\boldsymbol{c}) f_S(t,\boldsymbol{x},S) f_{h_p^{th}}(t,\boldsymbol{x},S,h_p^{th}) \tag{2.53}$$

where N_{dist} is the number of distribution summed.

In general, we simply assume $f_{h_p^{th}}$ under the form of a Dirac delta function conditioned by size, such that a unique droplet temperature is considered for each distribution. For the other PDFs, several strategies are possible in order to take into account size and velocity polydispersion effects.

2.3.4.3.2 Velocity dispersion, the KBMM class The most simple closure is obtained by simply considering that at each spatial point, all the droplets have the same velocity. Such

assumption leads to the so-called monokinetic (MK) closure that takes the form:

$$^{MK} f_{\boldsymbol{c}}(t, \boldsymbol{x}, \boldsymbol{c}) = n(t, \boldsymbol{x}) \delta(\boldsymbol{u}(t, \boldsymbol{x}) - \boldsymbol{c}), \tag{2.54}$$

Since taking only into account the first order moments is equivalent to an average procedure, such basic form of the velocity is equivalent to the two-fluid average model described in Section 2.3.1.1. The limit of this closure relies in the necessary null local velocity dispersion. As a consequence, models based on the MK closure prevent any PTC to occur creating instead a δ-shock, that is a Dirac delta function in density coupled to velocity discontinuity (Bouchut 1994; Chaisemartin 2009).

Assumed shape NDF methods have been widely inspired from the kinetic theory of gases and thus developed for cases where the velocity distribution is more complex than (2.54). For the modeling of droplets of large inertia, it is essential to be able to take into account PTC. To do so, polykinetic velocity distributions that take into account local velocity dispersion have to be considered. We can observe three categories of closures in that case:

- $f_{\boldsymbol{c}}$ is an unique continuous distribution, as for the IG and AG closures (Vié, Doisneau, and Massot 2015; Sabat 2016),

- $f_{\boldsymbol{c}}$ is a composition of continuous distributions as for the Extended Quadrature Method Of Moments (EQMOM) class (Yuan, Laurent, and Fox 2012; Chalons et al. 2017),

- Quadrature-Based Moment Methods (QBMM) class: $f_{\boldsymbol{c}}$ is a composition of discrete velocities, through quadratures as for QBMM (McGraw 1997; Chalons, Kah, and Massot 2012), the Direct Quadrature Method Of Moments (DQMOM) (Fox 2008a) and Conditional Quadrature Method Of Moments (CQMOM) methods (Yuan and Fox 2011).

Not every closure can lead to models with well posed mathematical properties. To work properly, two additional important features have to be taken into account.

- Set of moments: in multidimensional framework, especially using methods based on quadratures, a selection of the moments to be solved have to be proceeded. As observed in (Fox 2008b), an optimal set exists and provides the best condition number to the problem to be inserted,

- Hyperbolicity of the moments equations: the resulting system of equation shall provide physically coherent properties, as a bounded information propagation velocity and the causality of the Cauchy problem (Godunov 1961; Godunov 1999a; Peshkov and Romenski 2016).

- Mathematical entropy inequality: the distribution shall be consistent with the second principle of thermodynamic and thus fulfill an entropy equality. While solving each moments up to the order 2, an AG distribution (Vié, Doisneau, and Massot 2015) is sufficient and gives explicitly a compatible solution. For higher moment closure, mathematical difficulties arise (Groth and McDonald 2009) and Entropy maximization procedures can be considered (McDonald and Torrilhon 2013) .

Each closure has its own abilities, advantages and drawbacks. The Chapter 3 is dedicated to the development related to these methods according to the particle dynamics, stressing the specificities of particle-laden flows. A link is proposed between the kinetic theory of gases and the modeling of two-phase disperse flows.

2.3.4.3.3 Size polydispersion In the case of non-evaporating flows, without coalescence nor break-up, the size of the particles can be simply considered as a fixed parameter. For evaporating flows however, moments in size need to be added to the system of equations to solve. To do so, most of the models rely, additionally to the moments in velocity and enthalpy, on a mass conservation equation (size moment of order 3/2), impacted by evaporation processes, supplementary to the zeroth order moment that is the conservation of the number, not modified by such phenomena. Retaining only these two equations, such approach leads to:

$$\left\{\begin{array}{lll} \partial_t n & +\mathbf{div}_{\boldsymbol{x}}\left(n\boldsymbol{u}_p\right) & = 0, \\ \partial_t \rho_p & +\mathbf{div}_{\boldsymbol{x}}\left(\rho_p\boldsymbol{u}_p\right) & = \dot{m}_p, \end{array}\right. \tag{2.55}$$

where n is the number density and ρ_p the mass density.

Assuming a monodisperse flow, the droplet diameter can thus be deduced dynamically through the formula $d_p = \sqrt[3]{\frac{6\rho_p}{\mathring{M}_p \pi n}}$. This so-called mono-class method is able to treat evaporation but not size polydispersion. The most direct way to do so, is thus to use several *classes* detaining their own governing equations (zeroth, velocity and enthalpy moments) corresponding to distinct diameter and behaving independently one to another. This multi-class has however a limited ability in the treatment of size polydispersion and related phenomena.

Introducing a hierarchy of moments, as for (2.49), methods in size for treatment of the size polydispersion have been proposed. Integrating the Williams-Boltzmann Equation (WBE) (2.44), only taking into account free transport and evaporation effects, the equation driving the dynamic of genuine size moment is:

$$\partial_t f + \mathrm{div}_{\boldsymbol{x}}\left(cf\right) + \partial_S\left(R_s f\right) = 0 \Rightarrow \partial_t \mathcal{M}_0^{(l)[0]} + \mathbf{div}_{\boldsymbol{x}}\left(\mathcal{M}_1^{(l)[0]}\right) = \boldsymbol{S}_{evap}, \tag{2.56}$$

where the evaporation source term $\boldsymbol{S}_{evap}$, is a function of the considered moments and the carrier gas,

Since the NDF is here considered under the form (2.53), (2.56) can be simplified in:

$$\partial_t \mathcal{M}_0^{(l)[0]} + \mathbf{div}_{\boldsymbol{x}}\left(\mathcal{M}_0^{(l)[0]}\boldsymbol{u}_p\right) = \boldsymbol{S}_{evap}, \tag{2.57}$$

Unlike for the velocity distribution, no closure is required for the transport of size moments, but it is necessary to accurately treat the source term. That $\boldsymbol{S}_{evap}$ provided the evaporation that is a transport in the size phase space. Aside some exceptions and the work conducted during this thesis (see Chapter 4), approaches are mostly based on the MK assumption in velocity. Several possibilities exit to close the integration of the source terms:

Pivot method : evaluation of the source terms through point-wise estimation (Kumar and Ramkrishna 1996a, 1996b; Kumar et al. 2006), mostly used for droplet and particle aggregation and aerosols,

Method Of Moments with Interpolative Closure (MOMIC) : expression of the source terms thanks to integer and fractional moments. The last ones are obtained through interpolations (Frenklach and Harris 1987; Frenklach 2002) and the methods dedicated to non-inertial droplets,

Quadrature Method Of Moments (QMOM) : use of quadrature in the phase space (McGraw 1997). Since the problem is one dimensional in size, no specific algorithms as for the velocity quadratures are required. Quadrature in the four-dimensional space (3-physical and the size phase) are possible through DQMOM (Fox, Laurent, and Massot 2008) with an accurate resolution of the collision terms but cannot describe evaporation,

Eulerian Multi-Size Moment (EMSM) : reconstruction of the NDF on the basis of an entropy maximization on an exponential of a high order polynomial (Kah et al. 2012; Essadki et al. 2016; Massot et al. 2010), providing high accuracy for evaporating cases.

Aside the DQMOM, the methods presented above are unable to treat hetero-PTC because of the underlying assumption that all the droplets have the same kinematic behavior (same average, and eventually dispersion, velocity) independently from their size. Under the formalism of (2.53), it is possible to remedy to that problem using different governing equations for large and small droplets. To do so, the sectional approach, initially proposed in (Tambour 1980), suggests to discretize the size phase space in *sections*. In each of these sections, the distribution is assumed to be uniform, which leads to a first order convergence in term of size distribution accuracy. Unlike for multi-class methods, such discretization enables the possibility of size moment flux between sections and is able to treat coalescence and break-up. Thanks to such features, the evaporation can be efficiently resolved compared other methods (Fox, Laurent, and Massot 2008).

Initially formalized in (Laurent and Massot 2001) establishing a clear link with the WBE, the Multi-Fluid (MF) framework is based on the sectional approach, where uniform reconstructions are called One Size Moment (OSM) methods. Its advantage however is to allow several size moments in each section, and thus to increase the convergence order of the methods. Typically exponential or affine reconstructions (Laurent, Sibra, and Doisneau 2016) (called Two Size Moment (TSM) methods) are used, but the whole EMSM hierarchy can be considered for such purpose as well. Additionally, this class of method can be combined with velocity polydispersion. Combining the AG closure in velocity with the TSM methods in size, one can obtain the AG-TSM model (Boileau et al. 2016) as proposed Chapter 4.

Another analog approach, MUltiple SIze Group (MUSIG) (Krepper et al. 2008), consists in piecewise constant size distribution in each section, thus subdividing them. This avoids the consideration of a too large number of equations, each droplet of a large section has the same velocity and temperature but mass is scattered in the subdivisions. Such approach has however as drawback that the convergence in size remains at order one according to the number of subdivisions. All the size distributions described in this section are illustrated on Figure 2.8.

The Chapter 4 presents the development conducted during the thesis for the treatment of

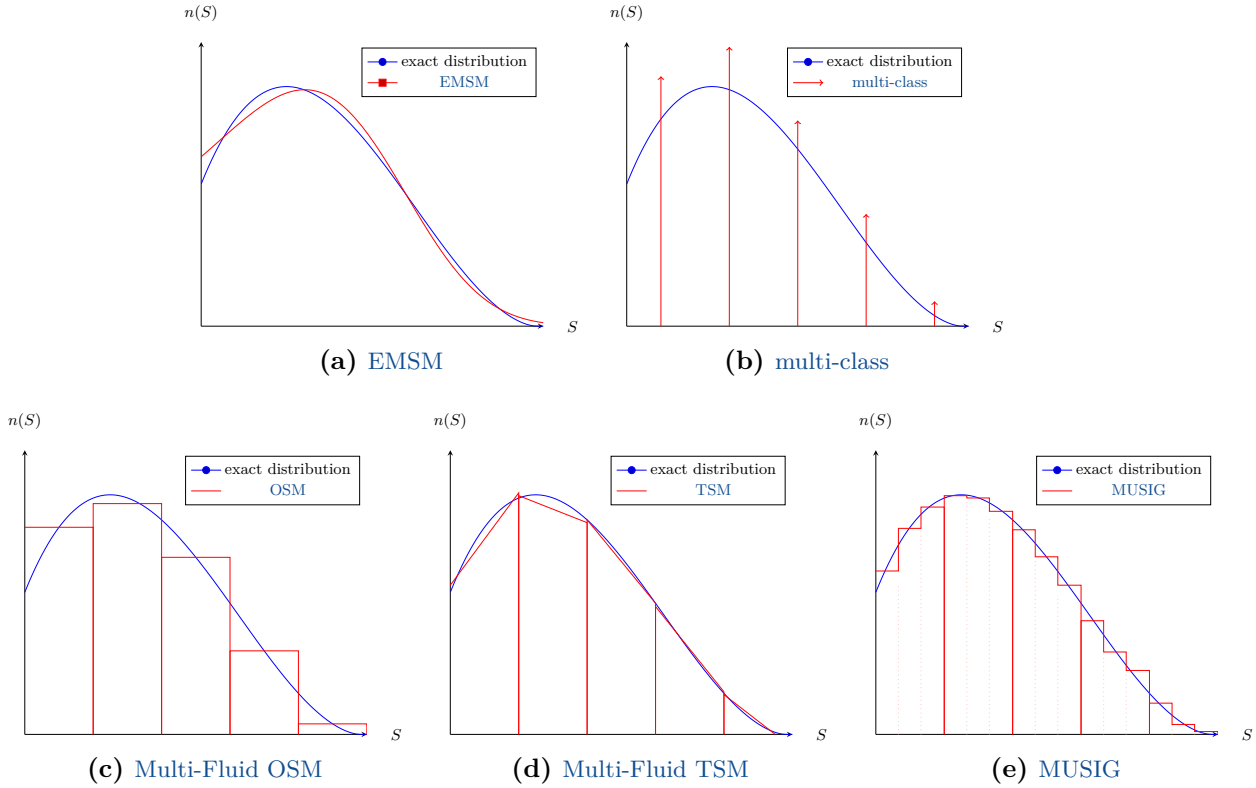

(a) EMSM **(b)** multi-class

(c) Multi-Fluid OSM **(d)** Multi-Fluid TSM **(e)** MUSIG

Figure 2.8: *Model representations of size polydispersion*

size polydispersion, based on the affine reconstruction of (Laurent, Sibra, and Doisneau 2016). Additionally, a model is proposed to treat simultaneously size and velocity dispersions.

2.3.5 Relations between modeling methods

Establishing this link is of utmost importance for spray injection where small and large scale phenomena are aimed at being described simultaneously. Doing so observing the disperse phase alone, as proposed in this chapter, it is possible to characterize the effect and consequence of each assumption made in the modeling process and therefore to establishing the ability of the derived model. A review of all the models, closures and methods is proposed on Figure 2.9 where they are organized according to the general assumptions used for their derivation.

An important feature of this work is to build this link while preserving important features that are the entropy inequality and the hyperbolicity of the governing equations. Such properties are crucial for the development of numerical methods as discuss Part II, as observed in (Vié et al. 2012) where Kinetic-Based Moment Methods (KBMM) and ACBMM are compared. Also, thanks to these coarse graining processes it is possible, in the context of SRMs as presented here, to establish a clear link between the description of the aluminum oxide spray and the model of KBMM class developed in this manuscript:

1. To model the moderately dense spray observed in the SRMs, assumption of point particles is made. As a consequence, solutions of Discrete particle Simulation (DPS) is considered

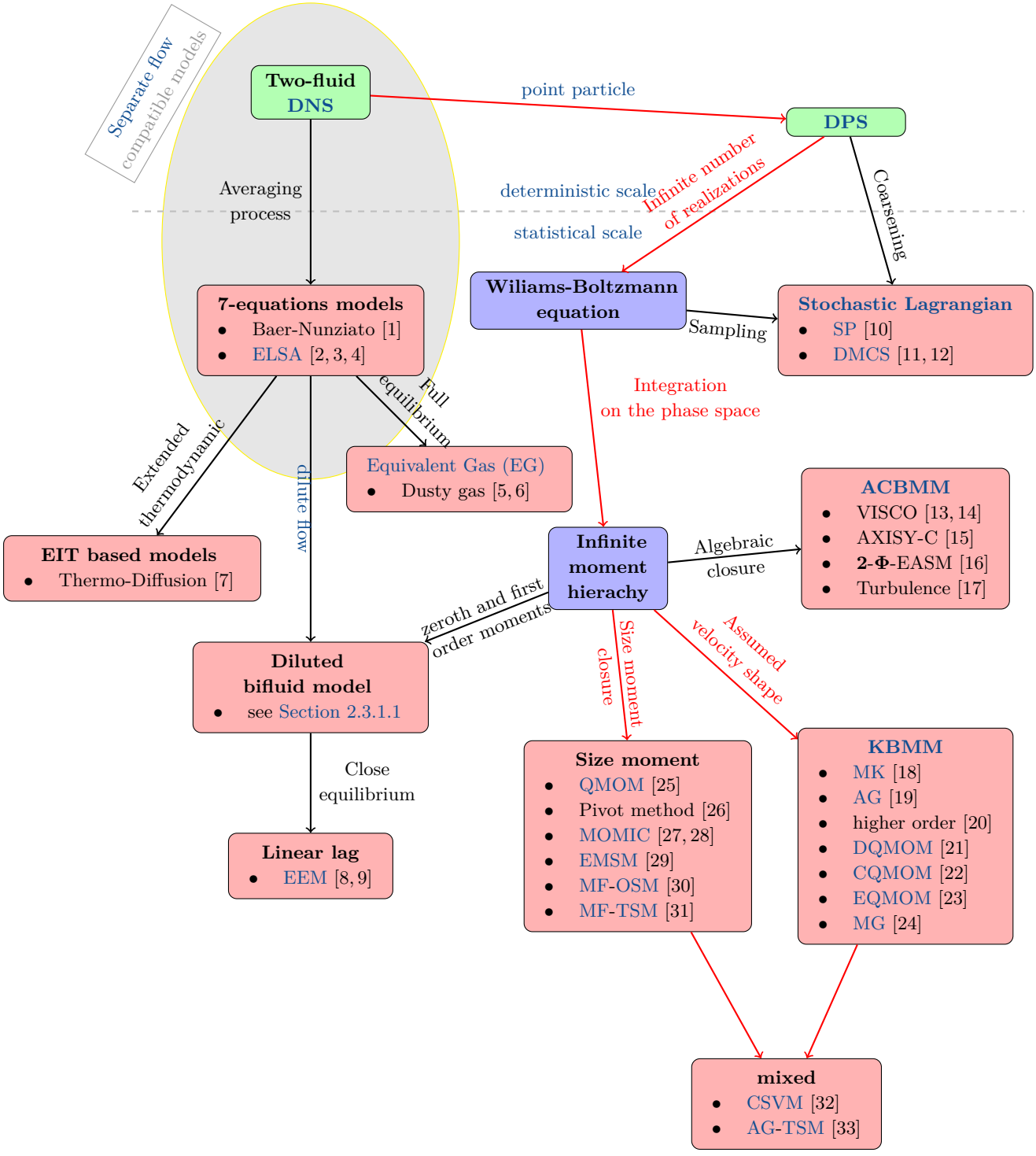

Figure 2.9: *Disperse phase model chart, green boxes: microscopic levels, blue boxes: mesoscopic levels, red boxes: macroscopic levels, red arrows: approach developed in the manuscript, (see references Table 2.1)*

as the model reference,

2. The problem is approximated in a statistical way assuming an infinite number of realizations and the existence of a Number Density Function (NDF) representing the ensemble averaging of DPS results. This level can be approximated through stochastic Lagrangian simulations,

3. The NDF of the disperse phase and its dynamic are approximated by moments of (2.42),

4. The problem is closed by a Kinetic-Based Moment Methods (KBMM) procedure for the velocity and either a multi-class or a MF approach for the size. This approximates the NDF through a finite number of its moments and its dynamic through the resolution of the WBE (2.44). More precisely, efforts have been concentrated on the AG and the affine TSM closures. The choice in this manuscript not to use EMSM methods is the higher numerical efficiency and precision of the TSM for coalescence (Laurent, Sibra, and Doisneau 2016). Such work is however only envisioned as a future perspective.

The reasons concerning the choice of this class of modeling are the following:

- They can be designed such that they possess a well defined mathematical structure (see Chapter 3),

- An efficient formalism for size polydispersion exists, based on this class (see Chapter 4),

- It is possible to design accurate robust and efficient dedicated numerical methods for these models (see Chapter 5 and Chapter 6),

The approach proposed here is not unique and shall not be considered as absolute. Moreover, this does not prevent the models from *reconciliation*, in other words the derivation of the same model through distinct processes according to different assumptions. Inside the rich variety of described models, it appears that the same governing equations can arise from distinct paths or theories. Such reconciliation can be observed for example, in the case of monodisperse flows, between the KBMM class of model using the MK and the diluted two-fluid model (2.33) or for the SP approach and the DMCS. The development conducted in the following chapters focuses on the expression of the derivation of the AG closure that is assumed to be sufficiently realistic for the targeted application. When possible, the results are generalized for all the KBMM class of governing equations.

Table 2.1: *References of Figure 2.9*

Block	Reference number	Reference
7-equations models	[1]	Baer and Nunziato 1986
	[2]	Vallet and Borghi 1999
	[3]	Lebas et al. 2005
	[4]	Lebas et al. 2009
EG	[5]	Saffman 1962
	[6]	Marble 1970
EIT based models	[7]	Lebon, Lhuillier, and Palumbo 2007
Linear lag	[8]	Ferry and Balachandar 2001

	[9]	Ferry and Balachandar 2002
Stochastic Lagrangian	[10]	O'Rourke 1981
	[11]	Vallet and Borghi 1999
	[12]	Lebas et al. 2005
ACBMM	[13]	Simonin, Fevrier, and Lavieville 2002
	[14]	Kaufmann et al. 2008
	[15]	Masi 2010
	[16]	Masi and Simonin 2012
	[17]	Zaichik, Simonin, and Alipchenkov 2009
KBMM	[18]	Laurent and Massot 2001
	[19]	Vié, Doisneau, and Massot 2015
	[20]	Levermore and Morokoff 1998
	[21]	Fox 2008a
	[22]	Yuan and Fox 2011
	[23]	Yuan, Laurent, and Fox 2012
	[24]	Chalons et al. 2017
Size moments	[25]	McGraw 1997
	[26]	Kumar et al. 2006
	[27]	Frenklach and Harris 1987
	[28]	Frenklach 2002
	[29]	Kah et al. 2012
	[30]	Laurent and Massot 2001
	[31]	Laurent, Sibra, and Doisneau 2016
mixed	[32]	Vié, Laurent, and Massot 2013
	[33]	Boileau et al. 2016

Chapter 3

Kinetic closure for particle laden flows

> There is, for example, the physicist who introduced me to one of my favorite "laws", which he described as the "Murphy's law or fourth law of thermodynamics" (actually there were only three the last I heard) which states: "If anything can go wrong, it will.".
>
> Anne Roe, The making of a scientist.

As explained in Chapter 2, managing of velocity dispersion is the key feature to cope with PTC. As proposed Section 2.3.4.3.2, the approach chosen in this manuscript is based on the KBMM procedure that leads to similar derivations in both gas dynamics and two-phase disperse flows. While working on a simplified form of the WBE (2.44), a hierarchy of models is established and the corresponding transport equations are derived. Letting the subject of size polydispersion and thermal energy for Chapter 4, properties of these equations, governing the kinematic of the particle laden flow, are discussed.

This chapter therefore organized as follow. Section 3.1 is dedicated to the proper derivation of the models based on the KBMM procedure. Distinction is made between the development conducted for the carrier phase on the one hand and for the disperse phase on the other hand. The derivation is focused on the resolution of moment up to the second order and on single distribution velocity closure ($N_{dist} = 1$ in the general form (2.53)), which does not include QBMM and EQMOM class of methods. Models relying on moments higher than the order 2 are not considered in this work because of theoretical difficulties associated (Junk 1998; Junk and Unterreiter 2002; Groth and McDonald 2009). Section 3.2 is focused on the properties of the AG closure, highlighting the specificities of this system of equations. Finally, in Section 3.3, the governing equations is expressed in an axisymmetric coordinate system and include specific closures associated to the velocity dispersion tensor. This last feature is important for SRMs because of the geometry of these engines.

3.1 KBMM derivation

3.1.1 A simplified Williams-Boltzmann Equation

For the sake of simplicity, we focus in this chapter on a simplified WBE that, compared to (2.44), only takes into account the particle velocity $\boldsymbol{c}$ in the phase space. For two-phase flows, this leads to the consideration of a spray monodisperse in size and temperature. Assuming the existence of an external force that can depend on $\boldsymbol{c}$, the kinetic equation for $f(t, \boldsymbol{x}, \boldsymbol{c})$ reads, (Williams 1958; Laurent and Massot 2001):

$$\underbrace{\partial_t f + \partial_{\boldsymbol{x}} \cdot (\boldsymbol{c} f)}_{\text{Free transport}} + \underbrace{\partial_{\boldsymbol{c}} \cdot (\boldsymbol{F} f)}_{\text{External force}} = \frac{1}{Kn} \mathfrak{C}(f, f), \tag{3.1}$$

where $\boldsymbol{F}$ is the external force field, Kn the Knudsen number and $\mathfrak{C}(f, f)$ the collision operator.

Such as given above, equation (3.1) can either describe the carrier or the carried phase. However, these two phases do not obey to the same regime according to the Knusden number Kn, which is small for the gas ($\approx 10^{-5}$) and close to infinity for the disperse phase. As a consequence, the physics of the carrier phase is driven by the collision operator quickly relaxing the molecular distribution of the gas toward equilibrium, whereas carried disperse phases and more precisely in the case of dilute flows are mostly driven by the viscous effects caused by the carrier fluid. For the disperse phase, this is justified by the fact that the mean free path is considered as infinitely large ($Kn \approx +\infty$), so that the influence of the collision term is negligible. On the other hand, when considering the gaseous phase, the Knudsen number can be taken as null in a first approximation ($Kn \approx 0$), which imply that the relaxation of the distribution f toward the thermodynamical equilibrium $\mathfrak{C}(f_{eq}, f_{eq}) \approx 0$ is infinitely fast. For more details about the collision operator in the context of the kinetic theory of gases, we refer to (Chapman and Cowling 1970; Pottier 2007; Levermore 1996; Giovangigli and Massot 1998) among others.

3.1.2 The infinite moment hierarchy

3.1.2.1 Moment properties

Following the KBMM strategy, the transport equation (3.1) is not solved directly but through its moments. For the simplified WBE (3.1), this moment definition (2.47) boils down to:

$$\mathcal{M}_k = \int_{\mathbb{R}^d} \left(\otimes^k \boldsymbol{c}\right) \; f(t, \boldsymbol{x}, \boldsymbol{c}) d\boldsymbol{c}, \tag{3.2}$$

Because of the symmetry of the tensorial product of $\boldsymbol{c}$ by itself, moments with matching indexes, as $(\mathcal{M}_2)_{12}$ and $(\mathcal{M}_2)_{21}$, are equals. Therefore, if d denotes the dimension of the physical space, the dimension of the k^{th}-order moments is $\binom{k+d-1}{k}$.

Additionally, these moments have to be the integral of a non-negative real NDF and thus belong to the moment space. For one dimensional cases on a closed interval, one can refer to (Dette and Studden 1997) for the determination of such moment space. However, for multidimensional cases, much less results are available (Nicolis and Nicolis 1998; Fialkow and Petrovic 2005; Kleiber and Stoyanov 2013).

3.1.2.2 Moment integration

By considering the velocity moments of the kinetic equation (3.1) for the disperse phase, where collisions are neglected, one can obtain the governing equations for the tensorial moments. While the integration of the free transport terms is trivial, the same procedure for the drag force requires more development. We thus focus on a unique component of velocity moment and integrate the drag term over the phase space.

$$\left(\int_{\mathbb{R}^d}\left(\otimes^k \boldsymbol{c}\right)\ \frac{\partial \boldsymbol{F} f}{\partial \boldsymbol{c}}\mathrm{d}\boldsymbol{c}\right)_{i_1,\ldots,i_k} = \int_{\mathbb{R}^d}\prod_{q=1}^{k} c_{i_q}\sum_{j=1}^{d}\frac{\partial F_j f}{\partial c_j}\mathrm{d}\boldsymbol{c} \tag{3.3}$$

Before proceeding to an integration by part, it has to be remarked that to obtain moments of finite values, f has to fulfill:

$$\forall i \in [\![1;d]\!], \forall n \in \mathbb{N}, \qquad \lim_{c_i\to\pm\infty} c_i^n f(t,\boldsymbol{x},\boldsymbol{c}) = 0 \tag{3.4}$$

The condition (3.4) is obviously fulfilled by quadratures and Gaussian distributions. Then using an integration by part on the right hand side of (3.3), one can obtain:

$$\sum_{j=1}^{d}\left[\prod_{q=1}^{k} c_{i_q} F_j f(t,\boldsymbol{x},\boldsymbol{c})\right]_{c_j=-\infty}^{c_j=+\infty} = \sum_{j=1}^{d}\left[\int_{\mathbb{R}^d}\left(\partial_{c_j}(\prod_{q=1}^{k} c_{i_q})\right) F_j f\mathrm{d}\boldsymbol{c}\right] + \int_{\mathbb{R}^d}\prod_{q=1}^{k} c_{i_q}\sum_{j=1}^{d}\partial_{c_j}(F_j f)\mathrm{d}\boldsymbol{c} = 0 \tag{3.5}$$

Thus

$$\begin{aligned}\left(\int_{\mathbb{R}^d}\left(\otimes^k \boldsymbol{c}\right)\ \frac{\partial \boldsymbol{F} f}{\partial \boldsymbol{c}}\mathrm{d}\boldsymbol{c}\right)_{i_1,\ldots,i_k} &= -\sum_{j=1}^{d}\int_{\mathbb{R}^d}\frac{\partial\left(\prod_{q=1}^{k} c_{i_q}\right)}{\partial c_j}F_j f\mathrm{d}\boldsymbol{c}\\ &= -\int_{\mathbb{R}^d}\sum_{p=1}^{k}\left(\prod_{q\neq p} c_{i_q}\right)\left(F_{i_p} f\right)\mathrm{d}\boldsymbol{c}\\ &= -\int_{\mathbb{R}^d}\frac{1}{(k-1)!}\sum_{\sigma\in S(k)}\left(\left(\otimes^{k-1}\boldsymbol{c}\right)\otimes \boldsymbol{F} f\right)_{\sigma(i_1,\ldots,i_k)}\mathrm{d}\boldsymbol{c}\end{aligned} \tag{3.6}$$

where $S(k)$ stands for all the permutations of k elements.

We introduce the symbol $\vee$ as the symmetric outer product (Levermore 1996):

Definition 3.1 (Symmetric outer product)**.** Let $\mathbb{B}$ and $\mathbb{D}$, two tensors of orders p and q, with $p+q=n$, then, their symmetric outer product is

$$(\mathbb{B}\vee\mathbb{D})_{(i_1,\ldots,i_n)} = \frac{1}{n!}\sum_{\sigma\in S(n)}(\mathbb{B}\otimes\mathbb{D})_{\sigma(i_1,\ldots,i_n)}\,, \tag{3.7}$$

Which let the relation (3.6) be simplified to:

$$\int_{\mathbb{R}^d}\left(\otimes^k \boldsymbol{c}\right)\ \frac{\partial \boldsymbol{F} f}{\partial \boldsymbol{c}}\mathrm{d}\boldsymbol{c} = -k\int_{\mathbb{R}^d}\left(\otimes^{k-1}\boldsymbol{c}\right)\vee \boldsymbol{F} f\mathrm{d}\boldsymbol{c} \tag{3.8}$$

Since it has been assumed that $\boldsymbol{F}$ is a function of $\boldsymbol{c}$, its shape has to be assumed in order to integrate (3.8). We thus assume $\boldsymbol{F}$ under the form of a Stokes law depending only of the local gas average velocity:

$$k\int_{\mathbb{R}^d}\left(\left(\otimes^{k-1}\boldsymbol{c}\right)\vee \boldsymbol{F}^{\mathrm{St}} f\right)_{i_1,\ldots,i_k}\mathrm{d}\boldsymbol{c} = \frac{k\left(\mathcal{M}_{k-1}\vee \boldsymbol{u}_g - \mathcal{M}_k\right)}{\tau_{\boldsymbol{u}}} \tag{3.9}$$

For other drag models (see Section 2.2.1.1), a new expression may be needed and non-integer moment eventually be used. To overcome that difficulty in this manuscript, it is supposed that (3.9) using $\tau_{\boldsymbol{u}}$ as a function of the average velocity only. Keeping the expression of the drag as given in (3.9) is consistent with a one point quadrature of the problem and thus a fair approximation for the cases targeted. Therefore, each moment of the NDF (3.2) obeys to the partial differential equation that follow:

$$\partial_t \mathcal{M}_k + \partial_{\boldsymbol{x}}\cdot\mathcal{M}_{k+1} = \frac{k\left(\mathcal{M}_{k-1}\vee \boldsymbol{u}_g - \mathcal{M}_k\right)}{\tau_{\boldsymbol{u}}} \tag{3.10}$$

As already discussed Section 2.3.4.3.2, governing equations based on (3.10) require a closure in order to express $\mathcal{M}_{k+1}$ from the moments of order lower than k.

3.1.3 Closures

Depending on the conditions of the particle flow, several options can be envisioned. We develop governing equations for a usual set of distributions.

3.1.3.1 The MK closure

In order to cope with the zeroth and first order moments only, it can be assumed that all the particles at a given point have the same velocity $\boldsymbol{u}(t,\boldsymbol{x})$ (see the NDF (2.54)), or that no crossing can occur. In this context, the second order centered moment:

$$\mathbb{P} = \int_{\mathbb{R}^d} \otimes^2 (\boldsymbol{c}-\boldsymbol{u})\, f d\boldsymbol{c}$$

is taken to be null, and the so-called Pressureless Gas Dynamic (PGD) or MK closure leads to:

$$^{MK}\mathcal{M}_0 = \rho, \qquad ^{MK}\mathcal{M}_1 = \rho\boldsymbol{u}, \qquad ^{MK}\mathcal{M}_2 = \rho\boldsymbol{u}\otimes\boldsymbol{u}. \tag{3.11}$$

where ρ denotes the particle density, which is in this chapter equivalent to the number density described Chapter 2.

Put under a system of equations, this leads to:

$$\left\{\begin{array}{lll} \partial_t\rho & +\mathrm{div}_{\boldsymbol{x}}(\rho\boldsymbol{u}) & = 0, \\ \partial_t\rho\boldsymbol{u} & +\mathbf{div}_{\boldsymbol{x}}(\rho\boldsymbol{u}\otimes\boldsymbol{u}) & = \frac{\rho(\boldsymbol{u}_g-\boldsymbol{u})}{\tau_{\boldsymbol{u}}}. \end{array}\right. \tag{3.12}$$

This model is exact for low inertia particles for which $\mathbb{P}=\mathbb{O}$ since no PTC occurs. Also, the left hand side of this system degenerates to the Burgers equation for the velocity field when no singularity occurs (Bouchut 1994; Chaisemartin 2009):

$$\partial_t\boldsymbol{u} + \boldsymbol{u}\mathrm{div}_{\boldsymbol{x}}(\boldsymbol{u}) = \frac{(\boldsymbol{u}_g-\boldsymbol{u})}{\tau_{\boldsymbol{u}}}. \tag{3.13}$$

In other situations where trajectories should cross, the MK closure produces the so called δ-shock singularity: a velocity discontinuity linked to a Dirac delta function in density (Jabin 2002; Chaisemartin 2009). This behavior is caused by the weak hyperbolicity of the PGD system of equations.

Using that closure, the only requirement for realizability is the positivity of the density. However, in practice, such condition can be difficult to be fulfill in a simulation because of the non-linearity of this system of equations. In fact, δ-shocks can be in contact with vacuum area and refinement procedures increase the density magnitude in the vicinity of δ-shocks. Such properties are challenging for numerical methods as explained in Chapter 6.

Additionally, for particles free from drag effects, the velocity $\boldsymbol{u}$ fulfills a maximum principle (Bouchut 1994). In other words, for a given domain Ω:

$$\forall \mathrm{t}{>}0,\ \boldsymbol{x} \in \Omega,\ i \in [\![1;d]\!] \qquad \min_{\boldsymbol{x}\in\Omega}\left(u_i(\boldsymbol{x},0)\right) \leq u_i(\boldsymbol{x},t) \leq \max_{\boldsymbol{x}\in\Omega}\left(u_i(\boldsymbol{x},0)\right) \tag{3.14}$$

3.1.3.2 The AG closure

To avoid the appearance of δ-shocks, it is possible to close the system (3.10) at second order, which enable to consider local velocity dispersion and thus small scale crossings (or statistical PTC). Treating large scale PTC would lead to the necessity of using a set of composition of velocity distribution and the QBMMs or EQMOM which come along.

In order to genuinely fulfill an entropy inequality, the velocity distribution is chosen to be a multivariate Gaussian form:

$${}^{AG}f(t,\boldsymbol{x},\boldsymbol{c}) = n(t,\boldsymbol{x})\frac{det(\boldsymbol{\Sigma})^{-1/2}}{(2\pi)^{d/2}}\exp\left(-\frac{1}{2}(\boldsymbol{u}-\boldsymbol{c})^T\boldsymbol{\Sigma}^{-1}(\boldsymbol{u}-\boldsymbol{c})\right). \tag{3.15}$$

where d is the number of dimension considered.

Proposed in (Levermore and Morokoff 1998; Groth and McDonald 2009; Vié, Doisneau, and Massot 2015), this form has the advantage, using moments up to the second order, to provide explicitly the solution maximizing the entropy (McDonald and Torrilhon 2013). Similarly to the MK case, the choice of a velocity distribution shape allows to close the system, this time at second order. Indeed, in this case one can express the moments up to order three as:

$$\begin{cases} {}^{AG}\mathcal{M}_0 = \rho, & {}^{AG}\mathcal{M}_2 = \rho\left(\boldsymbol{u}\otimes\boldsymbol{u}+\boldsymbol{\Sigma}\right) = 2\rho\mathbb{E}, \\ {}^{AG}\mathcal{M}_1 = \rho\boldsymbol{u}, & {}^{AG}\mathcal{M}_3 = \rho\left(\boldsymbol{u}\otimes\boldsymbol{u}+3\boldsymbol{\Sigma}\right)\vee\boldsymbol{u} = 2\rho\mathbb{H}\vee\boldsymbol{u}, \end{cases} \tag{3.16}$$

where $\mathbb{E}$ and $\mathbb{H} = \mathbb{E}+\mathbb{P}/\rho$ are respectively defined as the *total energy* and *total enthalpy* matrices. It is obvious that the primitive variables ρ, $\boldsymbol{u}$ and $\boldsymbol{\Sigma}$ can be reconstructed from the knowledge of ${}^{AG}\mathcal{M}_0$, ${}^{AG}\mathcal{M}_1$ and ${}^{AG}\mathcal{M}_2$, and hence the system is closed at order 2.

In order to deal with $\rho\mathbb{E}$ rather than $\mathcal{M}_2$, the equations of the moments of second order are generally multiplied by $\frac{1}{2}$. Obviously, this does not change the properties of the system nor the

genericity of (3.10). Therefore the AG system of equations yields:

$$\begin{cases} \partial_t \rho & +\mathbf{div}_{\boldsymbol{x}}\left(\rho \boldsymbol{u}\right) & = 0, \\ \partial_t \rho \boldsymbol{u} & +\mathbf{div}_{\boldsymbol{x}}\left(\rho\left(\boldsymbol{u}\otimes\boldsymbol{u}+\boldsymbol{\Sigma}\right)\right) & = \rho\frac{\boldsymbol{u}_g-\boldsymbol{u}}{\tau_{\boldsymbol{u}}}, \\ \partial_t \rho \mathbb{E} & +\mathbf{div}_{\boldsymbol{x}}\left(\rho\mathbb{H}\vee\boldsymbol{u}\right) & = \rho\dfrac{\boldsymbol{u}_g\vee\boldsymbol{u}-2\mathbb{E}}{\tau_{\boldsymbol{u}}}. \end{cases} \tag{3.17}$$

Inspired from rarefied gas dynamics, this approach has been proposed for two-phase flows in (Vié, Doisneau, and Massot 2015) where it is referred as the minimal model able to take into account PTC while being *well-posed*. The system of equations deduced from the AG closure fulfills an entropy inequality and, unlike the PGD, is strictly hyperbolic, preventing from δ-shock formations. We refer to (Berthon 2006a) for more details on the mathematical structure of this system of equations.

An important feature of this closure is its anisotropic character that can conserve a singular crossing direction. Additionally, the equations of PGD are the asymptotic limit of the AG system when the pressure $\mathbb{P} = \rho\Sigma$ tends to the null tensor $\mathbb{O}$. Since the velocity dispersion $\boldsymbol{\Sigma}$ models statistical PTC, the two systems give exactly the same final solution when no PTC occurs. They can be said to be physically equivalent in the low inertia regime. Nevertheless, in this specific regime, the AG model is uselessly more expensive than PGD in practice.

Remark 3.1. *The enthalpy matrix $\mathbb{H}$ is related to the kinematic behavior of the particles as a group and is not to be mistaken with the enthalpy of the particle related to its heat capacity. The ensemble representing the particle kinematic has its own thermodynamics, which is independent from the usual thermal properties of the particle material.*

Despite this enthalpy corresponds to the usual one for gases, an additional enthalpy $h_{p,th}$ corresponding to the thermodynamics of an isolated particle can be taken into account. The dynamics of this last enthalpy is not deduced from the KBMM procedure but directly introduced in the kinetic equation (2.44), as already presented Chapter 2 and detailed Chapter 4.

In the case of particle laden flows, the use of the AG closure is justified from the point of view of the information theory. This AG closure is the most probable velocity distribution under the constraint that moment up to the order 2 and only these are solved. This follows the maximization of Shannon entropy (Holway 1966) which is also the minimum of microscopic entropy (Andries et al. 2000). By reference to rarefied gas dynamic, the original paper (Vié, Doisneau, and Massot 2015) suggests the existence of *notional collision operator* relaxing the particle distribution toward a multivariate Gaussian form while generating entropy. Due to the assumption of large Knudsen, no effective collisional process can justify such behavior or hydrodynamic limit, explaining its *notional* character. From another point of view, one can suppose the action of a projection operator (Öttinger 1998), projecting at each infinitesimal time step the unknown NDF over a multivariate Gaussian form from the knowledge of its moments up to the order 2, fulfilling entropy constraints.

For rarefied gas flows, the collision operator plays a significant role acting on the equation of energy. Taking the model proposed in (Levermore and Morokoff 1998), one can replace the drag source term of (3.17) by a relaxation term derived from a Bhatnagar-Gross-Krook (BGK)

approach (Bhatnagar, Gross, and Krook 1954) such that:

$$\left\{\begin{array}{lll} \partial_t \rho & +\mathrm{div}_{\boldsymbol{x}}\left(\rho \boldsymbol{u}\right) & = 0, \\ \partial_t \rho \boldsymbol{u} & +\mathbf{div}_{\boldsymbol{x}}\left(\rho\left(\boldsymbol{u}\otimes\boldsymbol{u}+\boldsymbol{\Sigma}\right)\right) & = 0, \\ \partial_t \rho \mathbb{E} & +\mathbf{div}_{\boldsymbol{x}}\left(\rho \mathbb{H}\vee\boldsymbol{u}\right) & = \lambda\rho^2\left(\theta\mathbb{I}-\boldsymbol{\Sigma}\right). \end{array}\right. \tag{3.18}$$

where $\theta = r_g T_g = \frac{1}{3}\mathrm{tr}\left(\boldsymbol{\Sigma}\right)$ and the term λ can be deduced from the gas viscosity such that:

$$\lambda = \frac{\theta}{\mu_g(T_g)} \tag{3.19}$$

The convective terms deduced from the AG closure, the left hand side of (3.17) and (3.18) can be found in other applications such that microscale flows (McDonald and Groth 2005), plasma dynamics (Graille, Magin, and Massot 2009) or magnetic reconnection (Johnson 2011) without being exhaustive. These subjects are clearly out of the scope of this work but the development conducted regarding this system of equations can be applied straightforwardly to these application fields.

Remark 3.2. *At second order, the any NDF form ensuring the nullity of the third order centered moment would have been sufficient to close* (3.10)*. However, as explained Section 2.3.4.3.2, it is also wished to obtain the hyperbolicity and an entropy inequality which motivate the multivariate Gaussian closure* (3.15)*.*

3.1.3.3 The Euler equation

From the observation of (3.18), the collision process relax the AG distribution toward an Isotropic Gaussian (IG) one where it can be observed that:

$$\boldsymbol{\Sigma} = \theta\mathbb{I} \quad \Leftrightarrow \quad \mathbb{P} = P\mathbb{I}. \tag{3.20}$$

Such state is reached in the limit of a very small Knudsen number. The prevalence of the inter-particle collisions keeps the system everywhere at the Maxwellian equilibrium, due to a infinitely fast relaxation process. The kernel of the collision term can be shown to be written as (3.15), with an isotropic velocity dispersion, so that (3.20) stands true everywhere leading to the distribution (3.21):

$${}^{IG}f(t,\boldsymbol{x},\boldsymbol{c}) = n(t,\boldsymbol{x})\frac{\sigma^{-1/2}}{(2\pi)^{d/2}}\exp\left(-\frac{1}{2\sigma}(\boldsymbol{u}-\boldsymbol{c})\cdot(\boldsymbol{u}-\boldsymbol{c})\right), \tag{3.21}$$

By definition, at this equilibrium, the collision operator $\mathfrak{C}$ is null and the system is closed such that the AG closure moments (3.16) boils down to the Euler equations. The detailed link

between the anisotropic Gaussian closure for rarefied gas and the Euler equations can be found in both (Levermore and Morokoff 1998) and (Öttinger and Struchtrup 2007). Such transition is simplified here for the sake of legibility. From the AG system, the isotropic pressure hypothesis allows to consider only the trace of the total energy equation. The total energy $E = \mathrm{tr}\,(\mathbb{E})$, which is now a scalar, provides the following EOS:

$$\rho E = \frac{1}{2}\rho \boldsymbol{u}\cdot\boldsymbol{u} + \frac{d}{2}P \quad \Leftrightarrow \quad P = (\gamma-1)\left(\rho E - \frac{1}{2}\rho \boldsymbol{u}\cdot\boldsymbol{u}\right), \tag{3.22}$$

where we introduce the heat capacity γ ratio defined as $\gamma = \frac{2+d}{d}$, where d is the number of degrees of freedom, typically $d = 3$ for a monoatomic gas, but we keep the ability to choose $\gamma \in]1,3[$ for the description of larger category of perfect gases. Taking the trace of the energy conservation equation in the AG system (3.18), it boils down to the Euler equation:

$$\left\{\begin{array}{lll} \partial_t \rho & +\mathrm{div}_{\boldsymbol{x}}\,(\rho\boldsymbol{u}) & = 0, \\ \partial_t \rho\boldsymbol{u} & +\mathbf{div}_{\boldsymbol{x}}\,(\rho\boldsymbol{u}\otimes\boldsymbol{u} + P\mathbb{I}) & = 0, \\ \partial_t \rho E & +\mathbf{div}_{\boldsymbol{x}}\,(\rho h\boldsymbol{u}) & = 0. \end{array}\right. \tag{3.23}$$

where $h = E + P/\rho$ is the total enthalpy, consistent with the one of a fluid particle in a perfect gas, as already said in remark 3.1.

In the case of two-phase disperse flow as stated until here, no relaxation process can justify the use of the Euler equation. Moreover, quick deviation of particle flow dynamic compared to Lagrangian references have already been observed in (Vié et al. 2012; Sabat 2016) using that closures. However the drag acceleration plays the role of a dissipation phenomenon and can be shown, in the presence of Brownian motion or subgrid turbulent agitation, to lead to Maxwell-Boltzmann equilibrium distribution in the limit of a zero Stokes number (Zaichik, Alipchenkov, and Sinaiski 2008).

Remark 3.3. *Using the AG closure in one-dimension only ($d = 1$), one can deduce from it the system (3.23) in one dimension with $\gamma = 3$.*

3.1.3.4 The Navier-Stokes equation

In the context of the two-phase flows to be modeled, the Euler equation is not sufficient to represent the carrier phase. For the sake of consistency of the physical model, especially regarding particle drag, boundary layers or also turbulent effects, it is necessary to add a viscous stress tensor $\boldsymbol{T}_{NS}$ in order to upgrade the Euler equations to the Navier-Stokes equations. Therefore, the governing equations of the carrier phase as studied in this manuscript yields:

$$\left\{\begin{array}{lll} \partial_t \rho & +\mathrm{div}_{\boldsymbol{x}}\,(\rho\cdot\boldsymbol{u}_g) & = 0, \\ \partial_t\,(\rho\boldsymbol{u}_g) & +\mathbf{div}_{\boldsymbol{x}}\,(\rho\boldsymbol{u}\otimes\boldsymbol{u}_g + P\mathbb{I}) & = \mathbf{div}_{\boldsymbol{x}}\,(\boldsymbol{T}_{NS})\,, \\ \partial_t\,(\rho E) & +\mathrm{div}\,(\rho h\boldsymbol{u}_g) & = \mathrm{div}\,(\boldsymbol{T}_{NS}\cdot\boldsymbol{u}_g)\,\boldsymbol{x}. \end{array}\right. \tag{3.24}$$

Using the Stokes hypothesis and assuming a Newtonian fluid, the stress tensor takes the form:

$$\boldsymbol{T}_{NS} = \mu_g \left[\left(\mathbf{grad}\left(\boldsymbol{u}_g\right) + \mathbf{grad}\left(\boldsymbol{u}_g\right)^T \right) - \frac{2}{3}\mathrm{div}\left(\boldsymbol{u}_g\right)\mathbb{I} \right], \tag{3.25}$$

where μ_g is the dynamical viscosity, assumed to be constant hereafter.

This form can also be obtained thanks to a Chapman-Enskog procedure as it can be found in (Cercignani 1988; Chapman and Cowling 1970). It is obtained from the assumption of a small deviation of NDF from its Maxwellian equilibrium (3.21), letting appear velocity derivatives in the stress tensor. Because of such last viscous terms, (3.24) is no more hyperbolic as (3.17), (3.18) and (3.23) but a composition of a hyperbolic part, consistent with the Euler equation, and a parabolic one driven by viscous stress tensor $\boldsymbol{T}_{NS}$.

Remark 3.4. *The underlying developments can be applied in the context of the AG, leading to the Grad closure hierarchy (Grad 1949). Since, as observed in (Groth and McDonald 2009), this closure can break hyperbolicity not far away from the equilibrium condition, such an option is not retained in this work. As a consequence, we prefer to consider Multi-Gaussian (MG) closure (Chalons et al. 2017) as potential extensions of the presented work to higher order closures.*

3.1.4 General form of the studied system

A hierarchy of models has thus be defined, which is totally embraced by AG closure with viscous terms. Therefore we will now mostly consider the AG system: all the results may be extended to the Euler or the MK equations by respectively considering the trace of the energy tensor equation or by setting $\mathbb{P} = \mathbb{O}$ everywhere. System (3.10) can be rewritten in a compact form:

$$\partial_t \boldsymbol{W} + \mathbf{div}_{\boldsymbol{x}}\left(\boldsymbol{\mathcal{F}}(\boldsymbol{W})\right) = \boldsymbol{\mathcal{S}}(\boldsymbol{W}), \tag{3.26}$$

where, for the carried phase, the conservative vector $\boldsymbol{W}$, the flux function $\boldsymbol{\mathcal{F}}$ and the source term vector $\boldsymbol{\mathcal{S}}$ read:

$$\boldsymbol{W} = \left(\rho, \rho\boldsymbol{u}, \rho\mathbb{E}\right)^t, \quad \boldsymbol{\mathcal{F}}(\boldsymbol{W}) = \left(\rho\boldsymbol{u}, 2\rho\mathbb{E}, \rho\mathbb{H}\vee\boldsymbol{u}\right)^t, \quad \boldsymbol{\mathcal{S}}(\boldsymbol{W}) = \left(0, \rho\frac{\boldsymbol{u}_g - \boldsymbol{u}}{\tau_{\boldsymbol{u}}}, \rho\frac{\boldsymbol{u}_g\vee\boldsymbol{u} - 2\mathbb{E}}{\tau_{\boldsymbol{u}}}\right)^t, \tag{3.27}$$

where the conserved quantities have been defined in 3.16.

For the carrier phase, the conservative equation, containing no backward effect of the droplets flow in the source term vector at this level, takes the form:

$$\begin{cases} \boldsymbol{W} = \left(\rho_g, \rho_g\boldsymbol{u}_g, \rho_g E\right)^t, \\ \boldsymbol{\mathcal{F}}(\boldsymbol{W}) = \left(\rho_g\boldsymbol{u}_g, \rho_g\boldsymbol{u}_g\otimes\boldsymbol{u}_g + P\mathbb{I}, \rho H\boldsymbol{u}_g\right)^t, \\ \boldsymbol{\mathcal{S}}(\boldsymbol{W}) = \left(0, \overrightarrow{\mathbf{0}}, 0\right)^t. \end{cases} \tag{3.28}$$

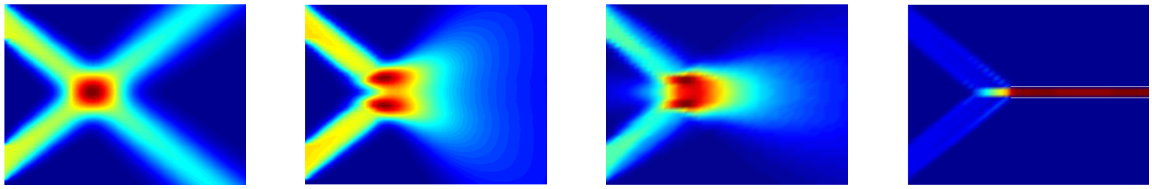

(a) QBMM **(b)** AG **(c)** IG **(d)** MK

Figure 3.1: *KBMM closure behavior for large scale crossings (Doisneau 2013)*

Such approach is consistent with one-way coupling and is extended to two-way coupling in Chapter 4 without loss in the genericity of the results given in this chapter.

3.2 Model properties

In this section the properties and validity domain of the small moment hierarchy of closure proposed Section 3.1 is discussed for the interest of particle laden flows. After describing the physical property of the models, a small review of the mathematical properties of the system of equations is proposed.

3.2.1 Physical properties

3.2.1.1 Crossings

The elements of this small hierarchy proposed here-above can be discriminated according to their ability to treat PTC. Since the local velocity dispersion given by the monokinetic closure is necessary null, the models based on this assumption prevents any PTC to occurs creating instead a δ-shock. Using a QBMM closure of any kind (Chalons, Kah, and Massot 2012), large scale PTC (see Figure 3.1) can be solve for a finite number of local velocities, that depends on the specific QBMM closure. However, δ-shocks cannot be strictly prevented using this class of methods (Chalons, Kah, and Massot 2012). On the contrary, PTC can be taken into account and δ-shocks avoided using the IG or the AG closures due to the presence of a velocity dispersion term under a scalar or tensorial form in their constitutive NDF. Such closures do not manage to solve large scale PTC but rather statistical PTC (see Figure 3.2) that are representative of a chaotic, lowly organized, velocity distribution as in turbulent field (Sabat 2016; Boileau et al. 2017).

The exact resolution of a deterministic crossing such as in Figure 3.1 is possible using a model of QBMM class with 2 velocities. However, if the number of quadrature used is lower than the number of crossing jet, the obtained solution does not manage to solve the problem deterministically.

Concerning the aimed application, it is expected to improve the resolution of statistical crossing area, such as in the vortexes that can be observed Figure 3.3, by switching from the MK to the

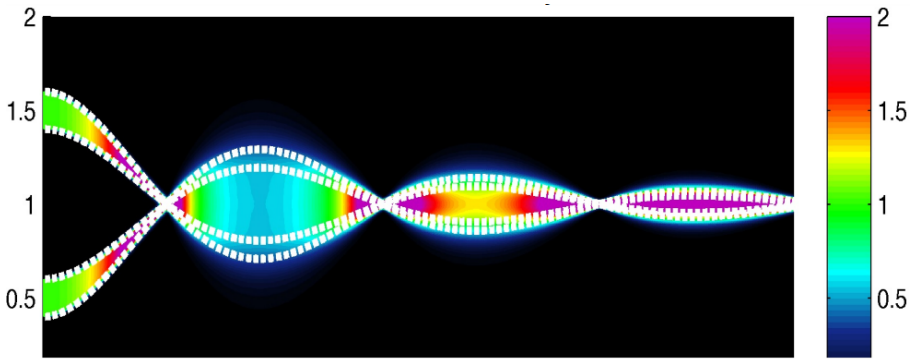

Figure 3.2: *AG closure behavior for a double crossing jet test case (Doisneau 2013), AG density field (color contour) compared to Lagrangian paths (dotted lines)*

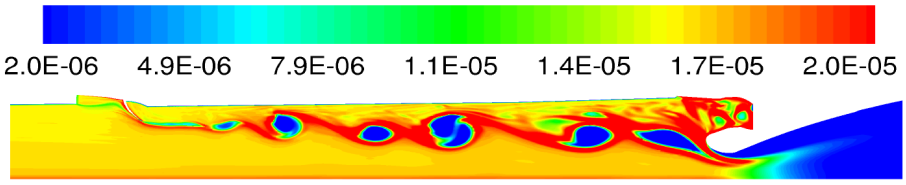

Figure 3.3: *volume fraction of moderately inertial particle in a P230 SRM simulation using the MK closure (Sibra 2015)*

AG closure. Also large scale crossings that usually appear on the symmetry axis are aimed at being treated through the AG closure. However, it is not expected to reproduce deterministic crossings as in Figure 3.1 but to avoid the formation of δ-shocks.

3.2.1.2 Turbulence

For two-phase disperse flows, it has been additionally observed (Vié et al. 2012; Sabat 2016; Sabat et al. 2018) that, in frozen HIT cases, the use of the IG quickly leads to the loss of the disperse flow dynamic unlike for the AG closure. While the results are logically identical for particles under the critical Stokes, quick divergence between the closures are observed for Stokes numbers above the critical one as it can be observed on the segregation. In the same conditions of fozen HIT presented in Figure 2.5 (see Section 2.1.2.5), the dynamics of the MK closure and of the AG closure can be observed Figure 3.4 and Figure 3.5 respectively. Differences can be observed between these closures for Stokes larger than one, when PTC occur, and can be quantified by looking at the segregation.

Additionally, it has been observed in (Sabat et al. 2014) that the use of an IG closure does not enable the correct treatment of the HIT cases when PTC occur. The preservation of the crossing direction, and consequently anisotropy of the velocity dispersion, thus appears to be a critical feature while dealing with PTC.

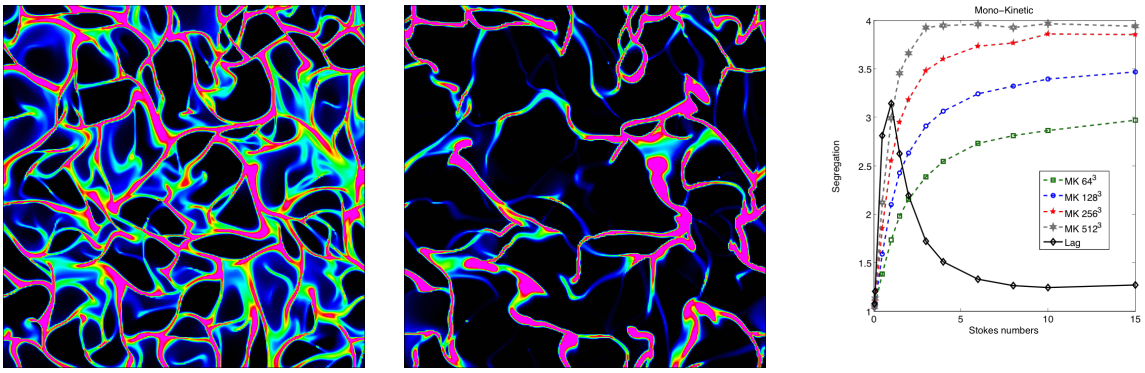

(a) St = 0.8Stc **(b)** St = 4.2Stc **(c)** segregation

Figure 3.4: *Frozen HIT simulations using MK model (Sabat 2016)*

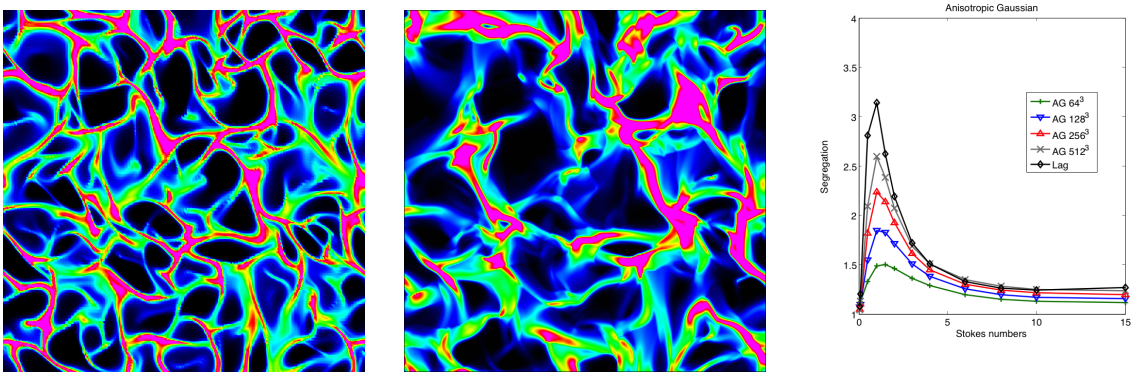

(a) St = 0.8Stc **(b)** St = 4.2Stc **(c)** segregation

Figure 3.5: *Frozen HIT simulations using AG model*

3.2.2 Mathematical properties

We give here additional details on the structure of the system of equations that this work is focused on, which means the equations of Pressureless Gas Dynamic (3.12), the 10-moment Anisotropic Gaussian system (3.17) and the Euler equation (3.23). Additionally, we here only take into account the convective terms -i.e. the left hand side- of these systems. The properties presented can thus be straightforwardly extended to the AG system for rarefied gases (3.18) and the Navier-Stokes equation (3.24).

3.2.2.1 Realizability condition

Definition 3.2. realizability is a condition fulfilled when the set of moment studied belongs to the moment space (see Definition 2.1) and thus are the moment of a physically plausible, positive semi-definite, phase space distribution function.

The sufficient realizability for PGD is the positivity of the density, the zeroth order moment is positive. In the case of AG system, the velocity dispersion matrix has also to be positive semi-definite to fulfill realizability conditions, which correspond to the positivity of the internal energy for the Euler equation. Thus, the realizability conditions for the systems studied yield:

$$G^{\mathrm{MK}} = \left\{ \boldsymbol{W} = \begin{pmatrix} \rho \\ \rho \boldsymbol{u} \end{pmatrix} \middle| \rho > 0 \right\} \tag{3.29}$$

$$G^{\mathrm{Euler}} = \left\{ \boldsymbol{W} = \begin{pmatrix} \rho \\ \rho \boldsymbol{u} \\ \rho E \end{pmatrix} \middle| \rho > 0,\, e = E - \frac{1}{2}\boldsymbol{u}\cdot\boldsymbol{u} > 0 \right\} \tag{3.30}$$

$$G^{\mathrm{AG}} = \left\{ \boldsymbol{W} = \begin{pmatrix} \rho \\ \rho \boldsymbol{u} \\ \rho \mathbb{E} \end{pmatrix} \middle| \rho \geq 0,\ \sigma_{ii} > 0\, \forall i,\ \sigma_{ij}^2 < \sigma_{ii}\sigma_{jj}\, \forall i \neq j \right\} \tag{3.31}$$

Since the moment space is a convex space (Dette and Studden 1997; Gautschi 2004), thus by definition, any convex combination of realizable moment leads to a realizable state. More generally, it can be remarked that in the usual framework of gas dynamics, the set of admissible states is an open convex set (Giovangigli and Massot 1998). This property is especially useful for the design of realizable numerical schemes (see Chapter 6)

3.2.2.2 Jacobian matrix decomposition

Starting from the generic form (3.26), we express here the hyperbolic system of interest under a quasi-linear form in a two-dimensional Cartesian framework:

$$\partial_t \boldsymbol{W} + \boldsymbol{A}_x(\boldsymbol{W})\partial_x \boldsymbol{W} + \boldsymbol{A}_y(\boldsymbol{W})\partial_y \boldsymbol{W} = 0 \tag{3.32}$$

where $\boldsymbol{A}_x$ and $\boldsymbol{A}_y$ are the Jacobian matrices of the system in the x and y directions.

3.2.2.2.1 AG system Aiming at unstructured meshes, the Jacobian matrix is given for an arbitrary direction $\overrightarrow{\boldsymbol{n}}$ such that $\boldsymbol{A}_{\overrightarrow{\boldsymbol{n}}}(\boldsymbol{W}) = n_x\boldsymbol{A}_x(\boldsymbol{W}) + n_y\boldsymbol{A}_y(\boldsymbol{W})$. For the AG system, this Jacobian matrix is always diagonalizable and leads to the following 6 eigenvalues:

$$\lambda_i^{\text{AG}} = \boldsymbol{u}\cdot\overrightarrow{\boldsymbol{n}} \pm \sqrt{3}c_{nn}, \quad \boldsymbol{u}\cdot\overrightarrow{\boldsymbol{n}} \pm c_{nn}, \quad \boldsymbol{u}\cdot\overrightarrow{\boldsymbol{n}}, \tag{3.33}$$

where the eigenvalue $\boldsymbol{u}\cdot\overrightarrow{\boldsymbol{n}}$ is always double in two dimensions and we rely on the notation:

$$c_{nn} = \sqrt{\overrightarrow{\boldsymbol{n}}^T\boldsymbol{\Sigma}\overrightarrow{\boldsymbol{n}}} = \sqrt{\sigma_{xx}n_x^2 + 2\sigma_{xy}n_xn_y + \sigma_{yy}n_y^2}, \tag{3.34}$$

The signal velocities $\boldsymbol{u}\cdot\overrightarrow{\boldsymbol{n}} \pm c_{nn}$ and $\boldsymbol{u}\cdot\overrightarrow{\boldsymbol{n}}$ are associated to linearly degenerated fields whereas the signals $\boldsymbol{u}\cdot\overrightarrow{\boldsymbol{n}} \pm \sqrt{3}c_{nn}$ are genuinely non-linear. In that context, organizing the eigenvalues in increasing order, one can express the matrix of eigenvectors under a tensorial form:

$$\boldsymbol{R}_{\text{AG}} = (\boldsymbol{r}_1, \boldsymbol{r}_2, \boldsymbol{r}_3, \boldsymbol{r}_4, \boldsymbol{r}_5, \boldsymbol{r}_6) \tag{3.35}$$

where the eigenvectors are:

$$\begin{aligned}
\boldsymbol{r}_{6^+/1^-} &= \left(1 \;,\; \boldsymbol{u} \pm \frac{\sqrt{3}\boldsymbol{\sigma}_n}{c_{nn}} \;,\; \frac{1}{2}\otimes^2\left(\boldsymbol{u} \pm \frac{\sqrt{3}\boldsymbol{\sigma}_n}{c_{nn}}\right) + \frac{c_{nn}^2\boldsymbol{\Sigma} - \otimes^2\boldsymbol{\sigma}_n}{2c_{nn}^2} \right)^t \\
\boldsymbol{r}_{5^+/2^-} &= \left(0 \;,\; \overrightarrow{\boldsymbol{t}} \;,\; \left(\boldsymbol{u} \pm \frac{\boldsymbol{\sigma}_n}{c_{nn}}\right) \vee \overrightarrow{\boldsymbol{t}} \right)^t \\
\boldsymbol{r}_3 &= \left(1 \;,\; \boldsymbol{u} \;,\; \frac{\boldsymbol{u}\otimes\boldsymbol{u}}{2} \right)^t \\
\boldsymbol{r}_4 &= \left(0 \;,\; \overrightarrow{\boldsymbol{0}} \;,\; \overrightarrow{\boldsymbol{t}}\otimes\overrightarrow{\boldsymbol{t}} \right)^t
\end{aligned} \tag{3.36}$$

with $\boldsymbol{\sigma}_n = \boldsymbol{\Sigma}\overrightarrow{\boldsymbol{n}}$ and $\overrightarrow{\boldsymbol{t}}$ the tangent vector such that $(\overrightarrow{\boldsymbol{n}}, \overrightarrow{\boldsymbol{t}})$ is an orthonormal basis $\overrightarrow{\boldsymbol{t}} = (-n_y, n_x)^T$.

Additionally, we define the left eigenvector matrix $\boldsymbol{L} = \boldsymbol{R}^{-1}$ as:

$$\boldsymbol{L}_{\mathrm{AG}} = (\boldsymbol{l}_1, \boldsymbol{l}_2, \boldsymbol{l}_3, \boldsymbol{l}_4, \boldsymbol{l}_5, \boldsymbol{l}_6)^T \tag{3.37}$$

$$\begin{array}{rcl}
\boldsymbol{l}_{6^+/1^-} & = \dfrac{1}{3c_{nn}^2}\Bigg(& \dfrac{u_n}{2}\left(u_n \mp \sqrt{3}c_{nn}\right) \quad , \quad -\left(u_n \mp \dfrac{\sqrt{3}}{2}c_{nn}\right)\overrightarrow{\boldsymbol{n}} \quad , \quad \overrightarrow{\boldsymbol{n}} \otimes \overrightarrow{\boldsymbol{n}} \quad \Bigg) \\
\boldsymbol{l}_{5^+/2^-} & = \dfrac{1}{2c_{nn}^3}\Bigg(& (\boldsymbol{\sigma}_n \cdot \boldsymbol{u}^\perp)(c_{nn} \mp u_n) \quad , \quad \begin{array}{c}(c_{nn} \mp u_n)\boldsymbol{\sigma}_n^\perp \\ \pm(\boldsymbol{\sigma}_n \cdot \boldsymbol{u}^\perp)\ \overrightarrow{\boldsymbol{n}}\end{array} \quad , \quad \pm 2\boldsymbol{\sigma}_n^\perp \vee \overrightarrow{\boldsymbol{n}} \quad \Bigg) \\
\boldsymbol{l}_3 & = \dfrac{1}{3c_{nn}^2}\Bigg(& 3c_{nn} - u_n^2 \quad , \quad 2u_n\ \overrightarrow{\boldsymbol{n}} \quad , \quad -2(\overrightarrow{\boldsymbol{n}} \otimes \overrightarrow{\boldsymbol{n}}) \quad \Bigg) \\
\boldsymbol{l}_4 & = \dfrac{1}{3c_{nn}^4}\Bigg(& \dfrac{1}{2}\begin{pmatrix} 3(\boldsymbol{\sigma}_n \cdot \boldsymbol{u}^\perp)^2 \\ -u_n^2\,|\boldsymbol{\Sigma}| \end{pmatrix} \quad , \quad \begin{array}{c}(u_n\ |\boldsymbol{\Sigma}|)\ \overrightarrow{\boldsymbol{n}} \\ +3\left(\boldsymbol{\sigma}_n \cdot \boldsymbol{u}^\perp\right)\boldsymbol{\sigma}_n^\perp\end{array} \quad , \quad \begin{array}{c}3 \otimes^2 \boldsymbol{\sigma}_n^\perp \\ -|\boldsymbol{\Sigma}|\ \overrightarrow{\boldsymbol{n}} \otimes \overrightarrow{\boldsymbol{n}}\end{array} \quad \Bigg)
\end{array} \tag{3.38}$$

where $u_n = \boldsymbol{u} \cdot \overrightarrow{\boldsymbol{n}}$ is the normal velocity.

Thanks to this formalism, it is possible to express the quasi-linear form of the problem in a one-dimensional form according to the direction $\overrightarrow{\boldsymbol{n}}$ and decompose it such that:

$$\partial_t \boldsymbol{W} + \boldsymbol{R}(\boldsymbol{W})\Lambda(\boldsymbol{W})\boldsymbol{L}(\boldsymbol{W})\partial_{\boldsymbol{x}\,\cdot\,\overrightarrow{\boldsymbol{n}}}\boldsymbol{W} = 0 \tag{3.39}$$

where $\Lambda(\boldsymbol{W}) = \boldsymbol{diag}\left(\lambda_1^{\mathrm{AG}}, \ldots, \lambda_6^{\mathrm{AG}}\right)$ and $\partial_{\boldsymbol{x}\,\cdot\,\overrightarrow{\boldsymbol{n}}}$ is the partial derivative in the $\boldsymbol{x} \cdot \overrightarrow{\boldsymbol{n}}$ direction.

For three dimensional cases, the eigen values and their associated nature remain identical. But while $\boldsymbol{u} \cdot \overrightarrow{\boldsymbol{n}} \pm \sqrt{3}c_{nn}$ remain singles, $\boldsymbol{u} \cdot \overrightarrow{\boldsymbol{n}} \pm \sqrt{3}c_{nn}$ become double and the eigenvalue $\boldsymbol{u} \cdot \overrightarrow{\boldsymbol{n}}$ is associated to 5 linearly degenerated fields. We refer to (Brown 1996) for the expression of the Jacobian matrices $\boldsymbol{A}_x$ and $\boldsymbol{A}_y$ in three dimensions for the AG equations.

3.2.2.2.2 Euler equation In the case of the Euler equations, such decomposition is standard and leads to the eigenvalues:

$$\lambda_i^{\mathrm{Euler}} = \boldsymbol{u} \cdot \overrightarrow{\boldsymbol{n}} \pm a_g, \quad \boldsymbol{u} \cdot \overrightarrow{\boldsymbol{n}}, \tag{3.40}$$

where $a_g = \sqrt{\gamma \frac{P}{\rho_g}}$ is the acoustic wave velocity.

We refer to (Rohde 2001) for the expression of $\boldsymbol{R}$ and $\boldsymbol{L}$ in an arbitrary direction.

3.2.2.2.3 MK system The case of PGD has also been investigated by several authors (Bouchut 1994; Brenier and Grenier 1998; Bouchut and James 1999; Sheng and Zhang 1999; Chaisemartin 2009; Chalons, Kah, and Massot 2012) For this system of equations, the Jacobian

matrix is a Jordan block causing the weak hyperbolic character of the system, observable through δ-shocks and vacuum appearance. In this case, only one eigenvalue can be observed and yields:

$$\lambda_i^{\mathrm{MK}} = \boldsymbol{u} \cdot \overrightarrow{\boldsymbol{n}}. \tag{3.41}$$

Unlike for the AG and Euler systems of equations, the eigenvectors $\boldsymbol{u} \cdot \overrightarrow{\boldsymbol{n}}$ are not linearly degenerated but equals. As a consequence, the right eigenvector matrix $\boldsymbol{R}_{\mathrm{MK}}$ is not invertible and thus the Jacobian cannot be diagonalized.

3.2.2.3 Entropy

The system of conservation laws presented Section 3.1 have to be supplemented by some entropy conditions (in the mathematical sense) which states (see (Lax 1971; Godlewski and Raviart 1996; Toro 2009) among others for further details) that there exists for any convex function $\mathcal{F}$ of a scalar s depending on $\boldsymbol{W}$ such that:

$$\partial_t \left(\rho \mathcal{F}(s)\right) + \mathrm{div}_{\boldsymbol{x}} \left(\rho u \mathcal{F}(s)\right) \leq 0, \qquad s = s(\boldsymbol{W}). \tag{3.42}$$

where u is the average velocity and the problem is analyzed in the x direction only.

For the Euler equations, it is well known that the scalar value $s_{\mathrm{Euler}} = \frac{P}{\rho^\gamma}$. Analyzed in (Bouchut 1994; Chalons, Kah, and Massot 2012) in the case of PGD and mostly relying on the maximum principle fulfilled by this system of equations, one can find $s_{\mathrm{MK}} = u^2$. As a consequence, the kinetic energy is not conserved and can only decrease in the case of the PGD which is a direct consequence of the MK closure.

The AG system possesses a Lax entropy pair (Berthon 2006a; Levermore and Morokoff 1998) that yields:

$$\begin{cases} s_{\mathrm{AG}} &= \frac{\sigma_{ii}}{\rho^2} \quad \forall i, \\ \widetilde{s}_{\mathrm{AG}} &= \frac{|\boldsymbol{\Sigma}|}{\rho^2}. \end{cases} \tag{3.43}$$

Remark 3.5. *While the* mathematical *entropy as presented here is diminishing, the* physical *entropy is increasing.*

3.3 Expression in the axisymmetric framework

Because of the geometry of revolution usually encountered in SRM, there is a practical interest in deriving the models for axisymmetric framework. This sections proposed such derivation in three parts. First, in Section 3.3.1 the systems of equations are derived in the cyclindrical coordinates. Then, adapted axisymmetric closures are proposed Section 3.3.2. Finally, Section

3.3.2.4 focuses on the expression of the solution on the symmetry axis.

3.3.1 Derivation in the cylindrical coordinates

After detailing the general strategy based on tensorial algebra (Kay 1988; Michal 1947) to obtain the governing equations in any coordinates system, this procedure is specifically applied to cylindrical coordinates. The final result is also valid for all models of the KBMM class.[1]

3.3.1.1 Overall strategy

Let $\mathbb{E}_d$ be the d-dimensional Euclidean space used so far. In this ground coordinate system, every point is located by d real numbers $(x_1, x_2, ..., x_d)$, called *coordinates*. A new coordinate system S_f is given by a $\mathcal{C}^1$-diffeomorphism $\boldsymbol{r}$, mapping $\mathbb{E}_d$ one-to-one onto itself, such that one can write:

$$\boldsymbol{r} = \boldsymbol{r}(x_1, x_2, ..., x_d) \qquad \Leftrightarrow \qquad x_{\boldsymbol{i}} = x_{\boldsymbol{i}}(\boldsymbol{r}). \tag{3.44}$$

In that new coordinate system, we define the *natural* and *physical* bases, $\widehat{\boldsymbol{e}}_i$ and $\widetilde{\boldsymbol{e}}_i$, as well as the change-of-basis matrix $\boldsymbol{A}$, as:

$$\widehat{\boldsymbol{e}}_i = \frac{\partial \boldsymbol{r}}{\partial x_i}, \qquad \widetilde{\boldsymbol{e}}_i = \frac{\widehat{\boldsymbol{e}}_i}{\|\widehat{\boldsymbol{e}}_i\|}, \qquad \boldsymbol{A} = \boldsymbol{diag}\left(\frac{1}{\|\widehat{\boldsymbol{e}}_1\|}, \dots, \frac{1}{\|\widehat{\boldsymbol{e}}_d\|}\right). \tag{3.45}$$

The components of a tensor $\mathbb{T}$ of order p in the natural basis and in the physical basis will be respectively denoted $(\mathbb{T})_{\widehat{i_1,..,i_p}}$ and $(\mathbb{T})_{\widetilde{i_1,..,i_p}}$. The gradient of such a tensor is a tensor of order $p+1$, which expression in the natural basis reads:

$$(\mathbf{grad}\,(\mathbb{T}))_{\widehat{i_1...i_p l}} = \frac{\partial\,(\mathbb{T})_{\widehat{i_1...i_p}}}{\partial x_l} - \sum_{m=1}^{d}\left[(\mathbb{T})_{\widehat{m...i_p}}\,\Gamma^m_{i_1 l} + \dots + (\mathbb{T})_{\widehat{i_1...m}}\,\Gamma^m_{i_p l}\right], \tag{3.46}$$

where d is the dimension of the euclidean space, $l = 1, \dots, d$ is the component of the gradient we are looking at and $\Gamma^k_{ij} = \Gamma^k_{ji}$ are the Christoffel coefficients defined by $\frac{\partial \widehat{\boldsymbol{e}}_i}{\partial x_j} = \Gamma^k_{ij}\widehat{\boldsymbol{e}}_k$.

Assuming that the tensor is symmetric, the formula (3.46) can be slightly simplified:

$$(\mathbf{grad}\,(\mathbb{T}))_{\widehat{i_1..i_p l}} = \frac{\partial\,(\mathbb{T})_{\widehat{i_1...i_p}}}{\partial x_l} - \sum_{k=1}^{p}\sum_{m=1}^{d}(\mathbb{T})_{\widehat{m\,\underline{\mathbf{i}}_{\{j\neq k\}}}}\,\Gamma^m_{i_k l} \tag{3.47}$$

where $\underline{\mathbf{i}}_{\{j\neq k\}}$ is the set of i_j indexes with $j \in [\![1, p]\!] \setminus \{k\}$.

[1] Although such approach is not proposed here, we observed that the same conclusions can be obtained starting from a three-dimensional finite volume of vanishing thickness, such as in (Goudjo and Desideri 1989) for the Euler equation. This approach however appears to be heavy when the system of equations becomes large.

From this definition of the gradient, the divergence tensor, of order $p-1$, can be deduced by the expression:

$$\mathbf{div}\left(\mathbb{T}\right) = \mathbf{grad}\left(\mathbb{T}\right) : \boldsymbol{G}, \tag{3.48}$$

where $(G)_{ij} = \boldsymbol{e}_i \cdot \boldsymbol{e}_j$ is the metric tensor (here expressed for an arbitrary basis) and : is the double contracted product.

If the natural basis is orthogonal, then in the physical basis $(G)_{\widetilde{ij}} = \delta_{ij}$ and (3.48) can be transformed in:

$$\left(\mathbf{div}\left(\mathbb{T}\right)\right)_{\widetilde{i_1,..,i_{p-1}}} = \left(\mathbf{grad}\left(\mathbb{T}\right)\right)_{\widetilde{i_1,..,i_{p-1},i_p,l}} : \mathbb{I}_d = \sum_{k=1}^{d} \left(\mathbf{grad}\left(\mathbb{T}\right)\right)_{\widetilde{i_1,..,i_{p-1},k,k}}. \tag{3.49}$$

For the sake of legibility, mixed-variant component tensors are avoided in this contribution. Also, only the change of basis between the natural and physical bases are needed is this paper. The steps to obtain the developed form of the governing equations are thus the following:

1. Obtain the gradient of the tensor in the natural basis thanks to equation (3.46),
2. Convert this gradient in the physical basis,
3. Deduce the divergence thanks to equation (3.48).

Since only symmetric tensors and orthogonal bases are involved in the following development, simplified equations (3.47) and (3.49) are sufficient. In this context, only the terms of indices $i_1..i_{p-1}kk$ of $\mathbf{grad}\left(\mathbb{T}\right)$ are needed to compute the divergence of any tensor $\mathbb{T}$. This greatly reduces the number of terms to be expanded.

3.3.1.2 Cartesian coordinates

The development of the equations in Cartesian coordinates are straightforward and corresponds to the system of equations in the initial euclidean space. The system for the AG closure is given here for the reminder:

$$\begin{cases} \mathbf{div}\left(\mathcal{M}_1\right) & = \displaystyle\sum_{k=1}^{d} \frac{\partial \rho u_k}{\partial x_k}, \\ \left(\mathbf{div}\left(\mathcal{M}_2\right)\right)_{\widetilde{i}} & = \displaystyle\sum_{k=1}^{d} \frac{\partial \rho u_i u_k + P_{ik}}{\partial x_k}, \\ \left(\mathbf{div}\left(\frac{1}{2}\mathcal{M}_3\right)\right)_{\widetilde{ij}} & = \displaystyle\sum_{k=1}^{d} \frac{\partial \frac{\rho}{3}\left[u_k h_{ij} + u_i h_{jk} + u_j h_{ik}\right]}{\partial x_k}, \end{cases} \tag{3.50}$$

where the h_{ij} scalars are the components of the enthalpy matrix $\mathbb{H}$, see equation (3.16).

3.3.1.3 Cylindrical coordinates

Let us define the position vector in the cylindrical coordinate system: $\boldsymbol{r}(r,\theta,z) = r(\cos(\theta)\boldsymbol{x}_1 + \sin(\theta)\boldsymbol{x}_2) + z\boldsymbol{x}_3$. Thus, by (3.45), the natural basis writes:

$$\widehat{\boldsymbol{e}}_r = \cos(\theta)\boldsymbol{x}_1 + \sin(\theta)\boldsymbol{x}_2, \qquad \widehat{\boldsymbol{e}}_\theta = r(-\sin(\theta)\boldsymbol{x}_1 + \cos(\theta)\boldsymbol{x}_2), \qquad \widehat{\boldsymbol{e}}_z = \boldsymbol{x}_3. \tag{3.51}$$

It is obviously orthogonal and the corresponding orthonormal physical basis is:

$$\widetilde{\boldsymbol{e}}_r = \widehat{\boldsymbol{e}}_r, \qquad \widetilde{\boldsymbol{e}}_\theta = \frac{\widehat{\boldsymbol{e}}_\theta}{r}, \qquad \widetilde{\boldsymbol{e}}_z = \widehat{\boldsymbol{e}}_z, \tag{3.52}$$

and the change-of-basis matrix takes the form $\boldsymbol{A}_{cyl} = \boldsymbol{diag}(1, \frac{1}{r}, 1)$.

Definition 3.3. Let $\mathbf{card}_j(\underline{\mathbf{i}})$ be the number of times index j appears in the set of indices $\underline{\mathbf{i}} = \{i_1, ..., i_p\}$.

Then, the conversion from physical to natural basis, simply reads:

$$(\mathbb{T})_{\widehat{\underline{\mathbf{i}}}} = r^{\tilde{n}_\theta} (\mathbb{T})_{\widetilde{\underline{\mathbf{i}}}}, \qquad \tilde{n}_\theta = \mathbf{card}_\theta(\underline{\mathbf{i}}) \tag{3.53}$$

Also, simple calculus leads to the only non-null Christoffel coefficients:

$$\Gamma^\theta_{r\theta} = \Gamma^\theta_{\theta r} = \frac{1}{r} \qquad \Gamma^r_{\theta\theta} = -r. \tag{3.54}$$

This information is enough to obtain the divergence in the cylindrical coordinates. Now, the derivation is generically conducted for the divergence of $\mathcal{M}_p$, which is of order $p-1$ and indexed by $\underline{\mathbf{i}} = i_1 \dots i_{p-1}$. Thanks to the nullity of all the Christoffel coefficients related to z ($\Gamma^j_{zi}, \forall i, j$), indices $\underline{\mathbf{i}}zz$ of the gradient of $\mathcal{M}_p$ come easily. For the indices $\underline{\mathbf{i}}rr$ the contribution of the Christoffel coefficient and change of basis cancel each other and lead to the same trivial form:

$$(\mathbf{grad}(\mathcal{M}_p))_{\widetilde{\underline{\mathbf{i}}zz}} = \frac{\partial(\mathcal{M}_p)_{\widetilde{\underline{\mathbf{i}}z}}}{\partial z}, \quad \text{and} \quad (\mathbf{grad}(\mathcal{M}_p))_{\widetilde{\underline{\mathbf{i}}rr}} = \frac{\partial(\mathcal{M}_p)_{\widetilde{\underline{\mathbf{i}}r}}}{\partial r}. \tag{3.55}$$

For the $\underline{\mathbf{i}}\theta\theta$ components, the contributions of the Christoffel coefficient and change of basis remain:

$$(\mathbf{grad}(\mathcal{M}_p))_{\widetilde{\underline{\mathbf{i}}\theta\theta}} = \frac{1}{r}\left[\frac{\partial(\mathcal{M}_p)_{\widetilde{\underline{\mathbf{i}}\theta}}}{\partial\theta} - \mathbf{card}_r(\underline{\mathbf{i}})(\mathcal{M}_p)_{\widetilde{\underline{\mathbf{i}}_{(r-1,\theta+1)}\theta}} + \mathbf{card}_\theta(\underline{\mathbf{i}})(\mathcal{M}_p)_{\widetilde{\underline{\mathbf{i}}_{(\theta-1,r+1)}\theta}} - (\mathcal{M}_p)_{\widetilde{\underline{\mathbf{i}}r}}\right]. \tag{3.56}$$

The calculus leading to these results are given in Appendix C.1.

Remark 3.6. *If $p = 1$ and consequently $\underline{\boldsymbol{i}} = \emptyset$, the empty set of indices, then*

$$\boldsymbol{card}_j(\underline{\boldsymbol{i}}) = 0 \quad \forall j = r, \theta, z.$$

.

Since the coordinate system is orthogonal, relation (3.49) can be used to get the divergence of

$\mathcal{M}_p$:

$$\begin{aligned}\left(\mathbf{div}\left(\mathcal{M}_p\right)\right)_{\widetilde{\underline{\mathbf{i}}}} = \quad & \frac{\partial\left(\mathcal{M}_p\right)_{\widetilde{\underline{\mathbf{i}}\underline{r}}}}{\partial r} + \frac{1}{r}\frac{\partial\left(\mathcal{M}_p\right)_{\widetilde{\underline{\mathbf{i}}\underline{\theta}}}}{\partial\theta} + \frac{\partial\left(\mathcal{M}_p\right)_{\widetilde{\underline{\mathbf{i}}\underline{z}}}}{\partial z} \\ & \underbrace{-\frac{1}{r}\left[\mathbf{card}_r\left(\underline{\mathbf{i}}\right)\left(\mathcal{M}_p\right)_{\widetilde{\underline{\mathbf{i}}_{(r-1,\theta+1)}\theta}} - \mathbf{card}_\theta\left(\underline{\mathbf{i}}\right)\left(\mathcal{M}_p\right)_{\widetilde{\underline{\mathbf{i}}r}} + \left(\mathcal{M}_p\right)_{\widetilde{\underline{\mathbf{i}}r}}\right]}_{\text{Geometrical correction}}.\end{aligned} \tag{3.57}$$

Since the last term on the right hand side, later denoted by $\widehat{\boldsymbol{\mathcal{S}}}^{axi}$, is scaled by the geometrical parameter r, it is called the *geometrical correction*. Yet, multiplying (3.57) by r allows to rearrange the terms and remove this dependency. It is hence more convenient to study the time evolution of $r\mathcal{M}_p$ instead of $\mathcal{M}_p$:

$$r\left(\mathbf{div}\left(\mathcal{M}_p\right)\right)_{\widetilde{\underline{\mathbf{i}}}} = \frac{\partial\left(r\mathcal{M}_p\right)_{\widetilde{\underline{\mathbf{i}}r}}}{\partial r} + \frac{\partial\left(\mathcal{M}_p\right)_{\widetilde{\underline{\mathbf{i}}\underline{\theta}}}}{\partial\theta} + \frac{\partial\left(r\mathcal{M}_p\right)_{\widetilde{\underline{\mathbf{i}}\underline{z}}}}{\partial z} \underbrace{-\left[\mathbf{card}_r\left(\underline{\mathbf{i}}\right)\left(\mathcal{M}_p\right)_{\widetilde{\underline{\mathbf{i}}_{(r-1,\theta+1)}\theta}} - \mathbf{card}_\theta\left(\underline{\mathbf{i}}\right)\left(\mathcal{M}_p\right)_{\widetilde{\underline{\mathbf{i}}r}}\right]}_{\text{Axisymmetrical source terms}}. \tag{3.58}$$

Now, the last term is scale independent and later called the *axisymmetrical source term* and denoted $\boldsymbol{\mathcal{S}}^{axi}$.

When considering $\mathcal{M}_1$ and $\mathcal{M}_2$, one obtains the classical formula for the divergence in cylindrical coordinates. Nonetheless, relations (3.57) and (3.58) also allow to get the divergence of the moment $\mathcal{M}_3$, necessary to close the AG equations and for a generalization to higher order tensors, if needed by the closure. Finally, the spatial derivatives of the AG system of equations in cylindrical coordinates write:

$$\begin{cases} r\left(\operatorname{div}\left(\mathcal{M}_1\right)\right) = \frac{\partial r\rho u_r}{\partial r} + \frac{\partial \rho u_\theta}{\partial\theta} + \frac{\partial r\rho u_z}{\partial z}, \\ r\left(\mathbf{div}\left(\mathcal{M}_2\right)\right)_{\widetilde{i}} = \frac{\partial r\rho(u_i u_r+\sigma_{ir})}{\partial r} + \frac{\partial\rho(u_i u_\theta+\sigma_{i\theta})}{\partial\theta} + \frac{\partial r\rho(u_i u_z+\sigma_{iz})}{\partial z} - \left(\boldsymbol{\mathcal{S}}_1^{axi}\right)_i, \\ \frac{r}{2}\left(\mathbf{div}\left(\mathcal{M}_3\right)\right)_{\widetilde{ij}} = \frac{\partial\frac{r\rho}{3}[u_r h_{ij}+u_i h_{jr}+u_j h_{ir}]}{\partial r} + \frac{\partial\frac{\rho}{3}\left[u_\theta h_{ij}+u_i h_{j\theta}+u_j h_{i\theta}\right]}{\partial\theta} + \frac{\partial\frac{r\rho}{3}[u_z h_{ij}+u_i h_{jz}+u_j h_{iz}]}{\partial z} - \left(\boldsymbol{\mathcal{S}}_2^{axi}\right)_{ij} \end{cases} \tag{3.59}$$

where $\boldsymbol{\mathcal{S}}_1^{axi}$ and $\boldsymbol{\mathcal{S}}_2^{axi}$ are symmetric tensors of order 1 and 2, belonging to the vector of tensors $\boldsymbol{\mathcal{S}}^{axi} = \left(0, \boldsymbol{\mathcal{S}}_1^{axi}, \boldsymbol{\mathcal{S}}_2^{axi}\right)$. Their components take the expression:

$$\left(\boldsymbol{\mathcal{S}}_1^{axi}\right)_r = \rho u_\theta u_\theta + P_{\theta\theta}, \quad \left(\boldsymbol{\mathcal{S}}_1^{axi}\right)_\theta = -\rho u_r u_\theta - P_{r\theta}, \quad \left(\boldsymbol{\mathcal{S}}_1^{axi}\right)_z = 0, \tag{3.60}$$

$$\begin{aligned} \left(\boldsymbol{\mathcal{S}}_2^{axi}\right)_{rr} &= \tfrac{2\rho}{3}\left[2u_\theta h_{r\theta} + u_r h_{\theta\theta}\right], & \left(\boldsymbol{\mathcal{S}}_2^{axi}\right)_{r\theta} &= \rho u_\theta h_{\theta\theta} - \tfrac{\rho}{3}\left[2u_r h_{r\theta} + u_\theta h_{rr}\right], \\ \left(\boldsymbol{\mathcal{S}}_2^{axi}\right)_{\theta\theta} &= -\tfrac{2\rho}{3}\left[2u_\theta h_{r\theta} + u_r h_{\theta\theta}\right], & \left(\boldsymbol{\mathcal{S}}_2^{axi}\right)_{\theta z} &= -\tfrac{\rho}{3}\left[u_\theta h_{rz} + u_r h_{z\theta} + u_z h_{r\theta}\right], \\ \left(\boldsymbol{\mathcal{S}}_2^{axi}\right)_{zz} &= 0, & \left(\boldsymbol{\mathcal{S}}_2^{axi}\right)_{zr} &= \tfrac{\rho}{3}\left[2u_\theta h_{z\theta} + u_z h_{\theta\theta}\right]. \end{aligned} \tag{3.61}$$

3.3.1.4 Case of the viscous tensor

In the case of the carrier phase, the stress tensor also needs to be expressed in the cylindrical coordinates, as well as its divergence. Such procedure is just a combination of developments already presented. Thus, in the cylindrical framework, thanks to generic relations (3.55) (3.56) and (3.57), the viscous stress (3.25) takes the form:

$$\begin{array}{ll}(\boldsymbol{T}_{NS})_{\widetilde{ij}} & = \mu\left[\left(\frac{1}{r^{\delta_{j\theta}}}\frac{\partial u_{g,i}}{\partial x_j}+\frac{1}{r^{\delta_{i\theta}}}\frac{\partial u_{g,j}}{\partial x_i}+\frac{1}{r}\left[\delta_{i\theta}\delta_{j\theta}2u_{g,r}-(\delta_{ir}\delta_{j\theta}+\delta_{i\theta}\delta_{jr})u_{g,\theta}\right]\right)\right] \\ & -\delta_{ij}\frac{2\mu}{3}\left(\frac{\partial u_{g,r}}{\partial r}+\frac{1}{r}\frac{\partial u_{g,\theta}}{\partial\theta}+\frac{\partial u_{g,z}}{\partial z}+\frac{u_{g,r}}{r}\right).\end{array} \tag{3.62}$$

Since $\boldsymbol{T}_{NS}$ is a second order symmetric tensor, the same formula (3.58) can be used. For the same axisymmetrical assumptions, its derivation leads to:

$$r\left(\mathbf{div}\left(\boldsymbol{T}_{NS}\right)\right)_{\widetilde{i}}=\frac{\partial r\left(\boldsymbol{T}_{NS}\right)_{\widetilde{ir}}}{\partial r}+\frac{\partial\left(\boldsymbol{T}_{NS}\right)_{\widetilde{i\theta}}}{\partial\theta}+\frac{\partial r\left(\boldsymbol{T}_{NS}\right)_{\widetilde{iz}}}{\partial z}+\boldsymbol{\mathcal{S}}\lceil_i^{axi}, \tag{3.63}$$

where $\boldsymbol{\mathcal{S}}\lceil^{axi}$ is the axisymmetrical source term related to the viscosity, whose components are:

$$\begin{array}{lll}\boldsymbol{\mathcal{S}}\lceil_r^{axi} & = -\left(\boldsymbol{T}_{NS}\right)_{\widetilde{\theta\theta}} & = -\mu\left[2\frac{1}{r}\frac{\partial u_{g,\theta}}{\partial\theta}+\frac{2u_{g,r}}{r}-\frac{2}{3}\left(\frac{\partial u_{g,r}}{\partial r}+\frac{1}{r}\frac{\partial u_{g,\theta}}{\partial\theta}+\frac{\partial u_{g,z}}{\partial z}+\frac{u_{g,r}}{r}\right)\right], \\ \boldsymbol{\mathcal{S}}\lceil_\theta^{axi} & = \left(\boldsymbol{T}_{NS}\right)_{\widetilde{r\theta}} & = \mu\left[\frac{\partial u_{g,\theta}}{\partial r}+\frac{1}{r}\frac{\partial u_{g,r}}{\partial\theta}-\frac{2u_{g,\theta}}{r}\right], \\ \boldsymbol{\mathcal{S}}\lceil_z^{axi} & = 0. & \end{array} \tag{3.64}$$

Unlike the previous $\boldsymbol{\mathcal{S}}^{axi}$ source terms originating from convection, $\boldsymbol{\mathcal{S}}\lceil^{axi}$ includes both the radial position r and spatial derivatives. The numerical method applied to $\boldsymbol{\mathcal{S}}\lceil^{axi}$ thus differs from $\boldsymbol{\mathcal{S}}^{axi}$. Despite such properties, we keep the denomination *axisymmetrical source term*.

3.3.2 Axisymmetric closing hypothesis

The presented developments consist in successive assumptions, which allow to reduce the spatial dimensions of the problem from three to two and to reduce the number of equations. Starting from the left hand side of (3.26), and thus without taking into account the standard source terms for now, the divergence operator is explicitly given in the axisymmetrical framework. This considerably reduces the computation resources needed for the resolution of axisymmetrical problems (see Part III).

3.3.2.1 Disperse phase governing equation

3.3.2.1.1 Homogeneous azimuthal flow First, the field is assumed to be homogeneous in the azimuthal θ direction, so that its θ derivatives cancel and equations (3.59) simplify in:

$$\left\{\begin{array}{lll} \frac{\partial r\mathcal{M}_0}{\partial t} & +\frac{\partial r\rho u_r}{\partial r} & +\frac{\partial r\rho u_z}{\partial z} = 0, \\ \frac{\partial r(\mathcal{M}_1)_{\widetilde{i}}}{\partial t} & +\frac{\partial r\rho(u_i u_r+\sigma_{ir})}{\partial r} & +\frac{\partial r\rho(u_i u_z+\sigma_{iz})}{\partial z} = \left(\boldsymbol{\mathcal{S}}_1^{axi}\right)_i, \\ \frac{\partial r\left(\frac{1}{2}\mathcal{M}_2\right)_{\widetilde{ij}}}{\partial t} & +\frac{\partial \frac{r\rho}{3}[u_r h_{ij}+u_i h_{jr}+u_j h_{ir}]}{\partial r} & +\frac{\partial \frac{r\rho}{3}[u_z h_{ij}+u_i h_{jz}+u_j h_{iz}]}{\partial z} = \left(\boldsymbol{\mathcal{S}}_2^{axi}\right)_{ij}, \end{array}\right. \tag{3.65}$$

where indices i and j belong to $\{r,\theta,z\}$.

As remarked in (Clain, Rochette, and Touzani 2010), this procedure does not reduce the number of equations but only the dimensions of the problem. This consequently diminishes the cost of the discretization. Since the azimuthal component are still solved, homogeneous swirling effects can be taken into account by system (3.65).

3.3.2.1.2 Azimuthal velocity symmetry Additional assumptions can be stated in order to reduce the number of solved equations.

The first one assumes the symmetry of the velocity distribution with respect to the θ coordinate. If ${}^{AG}f_{\theta sym}(t,\boldsymbol{x},\boldsymbol{c})$ is symmetric in c_θ, then

$$\int_{c_\theta=-\infty}^{+\infty} c_\theta \left[{}^{AG}f_{\theta sym}(t,\boldsymbol{x},\boldsymbol{c})\right] dc_\theta = 0 \quad \Rightarrow \quad u_\theta = 0, \tag{3.66}$$

but also

$$(\mathcal{M}_2)_{\widetilde{i\theta}} = \int_{c_i=-\infty}^{+\infty} c_i \int_{c_\theta=-\infty}^{+\infty} c_\theta \left[{}^{AG}f_{\theta sym}(t,\boldsymbol{x},\boldsymbol{c})\right] dc_\theta dc_i = 0 \quad \Rightarrow \quad P_{i\theta} = 0, \quad i \in \{r,z\}. \tag{3.67}$$

As a consequence:

$$h_{\theta\theta} = \frac{3}{2}\sigma_{\theta\theta}, \quad h_{r\theta} = 0, \quad \text{and} \quad h_{z\theta} = 0. \tag{3.68}$$

Therefore, the momentum equation on θ and the energy equations on $r\theta$ and $z\theta$ become trivial and can be suppressed. The resulting system of equations thus becomes:

$$\left\{\begin{array}{lll} \frac{\partial r\mathcal{M}_0}{\partial t} & +\frac{\partial r\rho u_r}{\partial r} & +\frac{\partial r\rho u_z}{\partial z} = 0, \\ \frac{\partial r(\mathcal{M}_1)_{\widetilde{i}}}{\partial t} & +\frac{\partial r\rho(u_i u_r+\sigma_{ir})}{\partial r} & +\frac{\partial r\rho(u_i u_z+\sigma_{iz})}{\partial z} = \left(\boldsymbol{\mathcal{S}}_{sym,1}^{axi}\right)_i, \\ \frac{\partial r\left(\frac{1}{2}\mathcal{M}_2\right)_{\widetilde{ij}}}{\partial t} & +\frac{\partial \frac{r\rho}{3}[u_r h_{ij}+u_i h_{jr}+u_j h_{ir}]}{\partial r} & +\frac{\partial \frac{r\rho}{3}[u_z h_{ij}+u_i h_{jz}+u_j h_{iz}]}{\partial z} = \left(\boldsymbol{\mathcal{S}}_{sym,2}^{axi}\right)_{ij}, \\ \frac{\partial\left(\frac{1}{2}r\mathcal{M}_2\right)_{\widetilde{\theta\theta}}}{\partial t} & +\frac{\partial r u_r \frac{1}{2}P_{\theta\theta}}{\partial r} & +\frac{\partial r u_z \frac{1}{2}P_{\theta\theta}}{\partial z} = \left(\boldsymbol{\mathcal{S}}_{sym,2}^{axi}\right)_{\theta\theta}, \end{array}\right. \tag{3.69}$$

where i and j belong to $\{r,z\}$ and:

$$\left(\boldsymbol{\mathcal{S}}_{sym,1}^{axi}\right)_r = P_{\theta\theta}, \quad \left(\boldsymbol{\mathcal{S}}_{sym,1}^{axi}\right)_z = 0, \tag{3.70}$$

$$\begin{aligned} \left(\boldsymbol{\mathcal{S}}^{axi}_{sym,2}\right)_{rr} &= u_r P_{\theta\theta}, & \left(\boldsymbol{\mathcal{S}}^{axi}_{sym,2}\right)_{\theta\theta} &= -u_r P_{\theta\theta}, \\ \left(\boldsymbol{\mathcal{S}}^{axi}_{sym,2}\right)_{zz} &= 0, & \left(\boldsymbol{\mathcal{S}}^{axi}_{sym,2}\right)_{rz} &= \tfrac{1}{2} u_z P_{\theta\theta}. \end{aligned} \tag{3.71}$$

This hypothesis keeps the possibility of a velocity dispersion along the θ coordinate. In gas dynamics, since the collision operator distributes the velocity in every direction, a positive $P_{\theta\theta}$ is required. For particle laden flows, effects of turbulence or Brownian motion can also motivate such closure. Moreover, as discussed in Chapter 7, such closure needs to be considered when looking at the specificity of the PTC on the symmetry axis.

3.3.2.1.3 Azimuthal velocity degeneracy Since the collision operator in the disperse phase is generally neglected, the velocity dispersion $\sigma_{\theta\theta}$ naturally tends to 0 away from the symmetry axis because of the drag. Thus, if no phenomenon excites the azimuthal velocity dispersion, it can be neglected since it cannot be generated by the PTC in the radial and axial directions. As a consequence, we have the additional assumption that $P_{\theta\theta} = 0$. Therefore, the equation of $(\mathcal{M}_2)_{\widetilde{\theta\theta}}$ can be suppressed and every source term in (3.70) and (3.71) are null. In this case, system (3.65) reduces to:

$$\begin{cases} \dfrac{\partial r \mathcal{M}_0}{\partial t} + \dfrac{\partial r \rho u_r}{\partial r} + \dfrac{\partial r \rho u_z}{\partial z} = 0, \\ \dfrac{\partial r \left(\mathcal{M}_1\right)_{\widetilde{i}}}{\partial t} + \dfrac{\partial r \rho \left(u_i u_r + \sigma_{ir}\right)}{\partial r} + \dfrac{\partial r \rho \left(u_i u_z + \sigma_{iz}\right)}{\partial z} = 0, \\ \dfrac{\partial r \left(\frac{1}{2}\mathcal{M}_2\right)_{\widetilde{ij}}}{\partial t} + \dfrac{\partial \frac{r\rho}{3} \left[u_r h_{ij} + u_i h_{jr} + u_j h_{ir}\right]}{\partial r} + \dfrac{\partial \frac{r\rho}{3} \left[u_z h_{ij} + u_i h_{jz} + u_j h_{iz}\right]}{\partial z} = 0, \end{cases} \tag{3.72}$$

where i and j belong to $\{r, z\}$.

Remark 3.7. *Because of the three types of closure possible for the AG system of equations in the axisymmetric framework, the following notations will be used in that case:*

- *AG genuinely refers to the system (3.65) where the less restrictive hypothesis for axisymmetry is used,*
- *AX refers to the system (3.69),*
- *degenerated Anisotropic Gaussian (AGd) refers to the system (3.72),*

3.3.2.1.4 Case of the Pressureless Gas Dynamics Under the monokinetic assumption, $P_{ij} = \sigma_{ij} = 0,\ \forall (i,j)$ and the system can be easily derived from (3.65). Since, without additional

assumption, swirling effects are taken into account, this leads to:

$$\left\{\begin{array}{llll} \frac{\partial r\rho}{\partial t} & +\frac{\partial r\rho u_r}{\partial r} & +\frac{\partial r\rho u_z}{\partial z} & = 0, \\ \frac{\partial r\rho u_r}{\partial t} & +\frac{\partial r\rho u_r u_r}{\partial r} & +\frac{\partial r\rho u_r u_z}{\partial z} & = \rho u_\theta u_\theta, \\ \frac{\partial r\rho u_\theta}{\partial t} & +\frac{\partial r\rho u_\theta u_r}{\partial r} & +\frac{\partial r\rho u_\theta u_z}{\partial z} & = -\rho u_\theta u_r, \\ \frac{\partial r\rho u_z}{\partial t} & +\frac{\partial r\rho u_z u_r}{\partial r} & +\frac{\partial r\rho u_z u_z}{\partial z} & = 0. \end{array}\right. \tag{3.73}$$

In the case of non-swirling flows, both azimuthal velocity degeneracy and azimuthal velocity symmetry hypotheses lead to the same result which is $u_\theta = 0$. Therefore, all source terms are canceled and the PGD equations for non-swirling cases yield:

$$\left\{\begin{array}{llll} \frac{\partial r\rho}{\partial t} & +\frac{\partial r\rho u_r}{\partial r} & +\frac{\partial r\rho u_z}{\partial z} & = 0, \\ \frac{\partial r\rho u_r}{\partial t} & +\frac{\partial r\rho u_r u_r}{\partial r} & +\frac{\partial r\rho u_r u_z}{\partial z} & = 0, \\ \frac{\partial r\rho u_z}{\partial t} & +\frac{\partial r\rho u_z u_r}{\partial r} & +\frac{\partial r\rho u_z u_z}{\partial z} & = 0. \end{array}\right. \tag{3.74}$$

This result is consistent with the numerical study already conducted in (Chaisemartin et al. 2007).

3.3.2.2 Case of the carrier phase equations

Starting from the development already conducted, the equations modeling the carrier phase are obtained from the AG closure for the convective part and from the results of Section 3.3.1.4 for the viscous part. A homogeneous azimuthal flow (or swirl in the case of fluids) is first considered, and next reduced a non-swirling case.

3.3.2.2.1 Swirling flow Starting from (3.65), we consider an isotropic pressure tensor $\mathbb{P} = P\mathbb{I}$. The mass and momentum conservation equations read:

$$\left\{\begin{array}{lllll} \frac{\partial r\rho}{\partial t} & + & \frac{\partial r\rho u_{g,r}}{\partial r} & + & \frac{\partial r\rho u_{g,z}}{\partial z} = 0, \\ \frac{\partial r\rho u_i}{\partial t} & + & \frac{\partial r\left[\rho u_{g,r}u_{g,i} + (\boldsymbol{P}_{NS})_{\widetilde{ir}}\right]}{\partial r} & + & \frac{\partial r\left[\rho u_{g,z}u_{g,i} + (\boldsymbol{P}_{NS})_{\widetilde{iz}}\right]}{\partial z} = \left(\boldsymbol{\mathcal{S}}^{axi}_{sym,1}\right)_i + \boldsymbol{\mathcal{S}}\lceil^{axi}_i. \end{array}\right. \tag{3.75}$$

for $i \in \{r, z, \theta\}$, where $(\boldsymbol{P}_{NS})_{\widetilde{ij}} = \delta_{ij} P - (\boldsymbol{T}_{NS})_{\widetilde{ij}}$ and the axisymmetrical source terms take the values:

$$\begin{array}{ll} \left(\boldsymbol{\mathcal{S}}^{axi}_{sym,1}\right)_r = \rho u^2_{g,\theta} + P, & \boldsymbol{\mathcal{S}}\lceil^{axi}_{r} = -\mu\left[\frac{2u_{g,r}}{r} - \frac{2}{3}\left(\frac{\partial u_{g,r}}{\partial r} + \frac{\partial u_{g,z}}{\partial z} + \frac{u_{g,r}}{r}\right)\right], \\ \left(\boldsymbol{\mathcal{S}}^{axi}_{sym,1}\right)_z = 0, & \boldsymbol{\mathcal{S}}\lceil^{axi}_{z} = 0, \\ \left(\boldsymbol{\mathcal{S}}^{axi}_{sym,1}\right)_\theta = -\rho u_{g,r} u_{g,\theta}, & \boldsymbol{\mathcal{S}}\lceil^{axi}_{\theta} = \mu\left[\frac{\partial u_{g,\theta}}{\partial r} - \frac{2u_{g,\theta}}{r}\right]. \end{array} \tag{3.76}$$

Since $(\boldsymbol{T}_{NS})_{\widetilde{\theta\theta}}$ is not needed, the stress tensor (3.62) can be reduced to:

$$(\boldsymbol{T}_{NS})_{\widetilde{ij}} = \frac{\mu}{r^{\mathbf{card}_\theta(ij)}}\left[\left(\frac{\partial u_{g,i}}{\partial x_j} + \frac{\partial u_{g,j}}{\partial x_i} + \delta_{ij,r\theta}\frac{2u_{g,\theta}}{r}\right) - \delta_{ij}\frac{2}{3}\left(\frac{\partial u_{g,r}}{\partial r} + \frac{\partial u_{g,z}}{\partial z} + \frac{u_{g,r}}{r}\right)\right], \tag{3.77}$$

where the term $\delta_{ij,r\theta} = (1-\delta_{ij})(1-\delta_{iz})(1-\delta_{zj})$ is equal to 1 only for $ij = r\theta$ and $ij = \theta r$.

3.3.2.2.2 Energy equation Concerning the energy equation, one can observe that the diagonal source terms from the convective contribution $\left(\boldsymbol{\mathcal{S}}^{axi}_2\right)_{rr}$ and $\left(\boldsymbol{\mathcal{S}}^{axi}_2\right)_{\theta\theta}$ given in (3.61) cancel each other when the trace of the energy matrix is considered. Therefore, the trace of the source term $\left(\boldsymbol{\mathcal{S}}^{axi}_2\right)_{ii}$ vanishes and the equation on the scalar energy is:

$$\frac{\partial r\rho E}{\partial t} + \frac{\partial r\rho h u_r - \sum_i (\boldsymbol{T}_{NS})_{\widetilde{ri}}\, u_i}{\partial r} + \frac{\partial r\rho h u_z - \sum_i (\boldsymbol{T}_{NS})_{\widetilde{zi}}\, u_i}{\partial z} = 0. \tag{3.78}$$

Since the same conclusion applies to $\boldsymbol{T}_{NS}$, no source term comes from the viscosity in the energy equation.

3.3.2.2.3 Transported scalar without diffusion For various reasons, the equation of a scalar Y transported by the mean velocity field can be added to the governing equations. This can be used for chemistry (necessary for combustion) or size moments for instance and interacts with the system of equations through source terms. If no diffusion is considered, such an equation takes the tensorial form:

$$\frac{\partial \rho Y}{\partial t} + \mathrm{div}\,(\rho Y \boldsymbol{u}) = S_Y(\boldsymbol{W}) \tag{3.79}$$

where $S_Y(\boldsymbol{W})$ is the production rate of ρY.

In axisymmetrical framework, due to the scalar character of Y, there is no source term associated to axisymmetry and the conservative equation can be written:

$$\frac{\partial r\rho Y}{\partial t} + \frac{\partial\,(r\rho Y u_{g,r})}{\partial r} + \frac{\partial\,(r\rho Y u_{g,z})}{\partial z} = r S_Y(\boldsymbol{W}) \tag{3.80}$$

3.3.2.2.4 Non-swirling flow In the context of the carrier phase, the azimuthal velocity degeneracy assumption cannot be applied since it is equivalent to neglecting the pressure. However, when considering an azimuthal velocity symmetry, *i.e.* $u_\theta = 0$, the swirl is canceled. Starting from (3.75), the momentum equation on θ is suppressed and both the source terms and the stress tensor are simplified as:

$$\begin{array}{ll} \left(\boldsymbol{\mathcal{S}}^{axi}_{sym,1}\right)_r = P, & \boldsymbol{\mathcal{S}}\lceil^{axi}_r = -\mu\left[\frac{2u_{g,r}}{r} - \frac{2}{3}\left(\frac{\partial u_{g,r}}{\partial r} + \frac{\partial u_{g,z}}{\partial z} + \frac{u_{g,r}}{r}\right)\right], \\ \left(\boldsymbol{\mathcal{S}}^{axi}_{sym,1}\right)_z = 0, & \boldsymbol{\mathcal{S}}\lceil^{axi}_z = 0, \end{array} \tag{3.81}$$

$$(\boldsymbol{T}_{NS})_{\widetilde{ij}} = \mu\left[\left(\frac{\partial u_{g,i}}{\partial x_j} + \frac{\partial u_{g,j}}{\partial x_i}\right) - \delta_{ij}\frac{2}{3}\left(\frac{\partial u_{g,r}}{\partial r} + \frac{\partial u_{g,z}}{\partial z} + \frac{u_{g,r}}{r}\right)\right]. \tag{3.82}$$

The complexity of the source terms are thus greatly reduced but the contribution of the pressure still remains. Regarding (3.71), one can observe that this pressure is the result of the $P_{\theta\theta}$ component only. Therefore, the complete suppression of the axisymmetrical source term can only be reached if the velocity distribution of the underlying particles exists in the (r, z) plane only and not along the θ coordinate.

Remark 3.8. *It is now clear that swirling and non-swirling assumptions may not be the only options to reduce the dimensions and the number of equations of a higher order moment closure. These hypotheses are sufficient for the AG model and its sub-systems, but we suggest that other hypotheses may be possible to reduce higher order closures, as in the Levermore hierarchy (Levermore 1996).*

The systems of equations built in this section are all given in Appendix B under their expanded form.

3.3.2.3 Uniform steady state

We here aim at establishing the subspace of realizable states $\boldsymbol{W}_a$ that remains steady if the field is uniform and equal to $\boldsymbol{W}_a$. The analysis only considers the systems where the flux is a composition of symmetric tensors, which is the case of the systems of equations introduced in this paper. For any steady uniform state, the expression of the divergence (3.57) leads to:

$$\mathbf{card}_r\left(\underline{\mathbf{i}}\right)\left(\mathcal{M}_p\right)_{\underset{\sim}{\underline{\mathbf{i}}_{(r-1,\theta+1)}}\theta} = \left(\mathbf{card}_\theta\left(\underline{\mathbf{i}}\right) - 1\right)\left(\mathcal{M}_p\right)_{\widetilde{\underline{\mathbf{i}}r}}. \tag{3.83}$$

In the case of the axisymmetric AG closure (3.65), where no additional assumption is used this

leads to:

$$u_r = 0, \quad u_\theta = 0, \quad \sigma_{rr} = \sigma_{\theta\theta}, \quad \sigma_{ri} = 0, \tag{3.84}$$

where $i \in \{z, \theta\}$.

As a consequence, to ensure the steady state, no swirling nor radial velocity are allowed for every presented closure. Moreover, a steady and uniform velocity dispersion exists only if the radial velocity dispersion is equal to the aximuthal one. Such condition is automatically fulfilled by the Euler equation since the pressure is isotropic. However, in the case of the azimuthal velocity degeneracy closure (3.72), the presence of a radial velocity dispersion does not allow the steadiness of a uniform state since $\sigma_{\theta\theta}$ in forced to nullity.

3.3.2.4 This axi-isotropic subspace

Definition 3.4. On the axis, a realizable state $\boldsymbol{W}_{cyl}$ described in the euclidean space is said to be axi-isotropic according to the vector $\overrightarrow{\boldsymbol{n}}_a$ if and only if it is invariant by any rotation transformation around $\overrightarrow{\boldsymbol{n}}_a$. Therefore:

$$\boldsymbol{W}_{cyl} = \boldsymbol{\mathcal{R}}(\boldsymbol{W}_{cyl}, \theta, \overrightarrow{\boldsymbol{n}}_a), \quad \forall \theta \in [0, 2\pi[\,, \tag{3.85}$$

where $\boldsymbol{\mathcal{R}}(\boldsymbol{W}, \theta, \overrightarrow{\boldsymbol{n}})$ is the transformation of the conservative vector $\boldsymbol{W}$ by rotation around the axis of vector $\overrightarrow{\boldsymbol{n}}$ with an angle θ.

We denote $G_{axi}(\overrightarrow{\boldsymbol{n}}_a)$ the subspace of the realizable states G to which belongs $\boldsymbol{W}_{cyl}$.

For the reminder, let $\mathbb{T}$ be an arbitrary tensor of order n, this transformation yields:

$$(\mathbb{T})_{i_1 i_2 \dots i_n} = R^{-1}_{i_1 p_1} R^{-1}_{i_2 p_2} \dots R^{-1}_{i_n p_n} (\mathbb{T})_{p_1 p_2 \dots p_n}\,, \tag{3.86}$$

where $R^{-1} = R^T$ is the inverse of the rotation matrix R.

Applied to the AG system of equations, $\overrightarrow{\boldsymbol{n}}_a = \overrightarrow{\boldsymbol{n}}_3$ the subspace $G_{axi}(\overrightarrow{\boldsymbol{n}}_z)$ describing such state has to fulfill the conditions:

$$(\rho, u_3, e_{33}, \sigma_0) \in \mathbb{R}^4, \qquad u_1 = u_2 = 0, \qquad e_{12} = e_{23} = e_{13} = 0, \qquad e_{11} = e_{22} = \frac{1}{2}\sigma_0, \tag{3.87}$$

where σ_0 is the velocity dispersion in the tangential direction of the axis of symmetry.

It has been chosen to express the final system in a physical basis. Therefore, for each position in this new orthogonal basis, there exists a transformation leading to the Euclidean space $\mathbb{E}_d$ used for the closure of the model that is consistent with a rotation. Then, according to the transformation provided by (3.51) in the physical basis (3.52), the axi-isotropic subspace $G_{axi}(\overrightarrow{\boldsymbol{n}}_z)$ (3.87) is rewritten:

$$(\rho, u_z, e_{zz}, \sigma_0) \in \mathbb{R}^4, \qquad u_r = u_\theta = 0, \qquad e_{rz} = e_{r\theta} = e_{z\theta} = 0, \qquad e_{rr} = e_{\theta\theta} = \frac{1}{2}\sigma_0. \tag{3.88}$$

3.3.2.5 Continuous solution in axisymmetry

Theorem 3.1. Let Ω the two dimension axi-symmetric domain containing both the symmetry axis and the interior of the studied domain, then, for all z, we have $\lim_{\boldsymbol{x}\to(0,z)^T} \boldsymbol{W} \in G_{axi}(\overrightarrow{\boldsymbol{n}}_z)$ if $\boldsymbol{W}(\boldsymbol{x})$ is C^0 solution on Ω.

Proof. If $\boldsymbol{W}(\boldsymbol{x})$ is C^0, then by definition: $\forall \boldsymbol{x}$, $\exists \tilde{\boldsymbol{x}}$, $\forall \epsilon > 0$, $\quad \|\boldsymbol{W}(\tilde{\boldsymbol{x}}) - \boldsymbol{W}(\boldsymbol{x})\| < \epsilon$. Let $\boldsymbol{x} = (0, z)^T$ be a position on the symmetry axis and thus $\boldsymbol{W}_z = \boldsymbol{W}(\boldsymbol{x}) \in G_{axi}(\overrightarrow{\boldsymbol{n}}_z)$, then it comes that for any path, $\lim\limits_{\tilde{\boldsymbol{x}}\to\boldsymbol{x}} \boldsymbol{W}(\tilde{\boldsymbol{x}}) = \boldsymbol{W}_z$ which end the proof. □

The consequence of theorem 3.1 is crucial for the choice of the axisymmetric formulation of the AG system. Whereas for every closures of the PGD or Euler equation we obviously have $G_{axi}(\overrightarrow{\boldsymbol{n}}_z) \subset G$, such property is not fulfilled for all the closure of the AG system. According to the expression of the $G_{axi}(\overrightarrow{\boldsymbol{n}}_z)$ (3.88) the existence of a velocity dispersion in the radial direction is necessarily associated to the existence of an equal velocity dispersion in the azimuthal direction. Since that last $\sigma_{\theta\theta}$ is null for the AGd system, while σ_{rr} can be positive, we have:

$$G_{axi}(\overrightarrow{\boldsymbol{n}}_z) \subset G^{AG}, \qquad G_{axi}(\overrightarrow{\boldsymbol{n}}_z) \subset G^{AX}, \qquad G_{axi}(\overrightarrow{\boldsymbol{n}}_z) \not\subset G^{AGd} \tag{3.89}$$

Therefore, using the AGd system, the solution on the symmetry axis is necessarily singular except if $\sigma_{rr} = 0$ in the vicinity of the axis. In that last case, no PTC can be modeled across the symmetry axis.

Chapter 4

Modeling polydisperse particle-laden flows

仏神は貴し仏神を たのまず

新免武蔵, 獨行道

Respect Buddha and the gods without counting on their help.

SHIMMEN Musashi, Dokkôdô (The Way of Walking Alone).

In this chapter, a new modeling of the disperse flow is proposed to combine velocity and size polydispersions. The derivation is based in this Chapter on a simplified form of the kinetic equation (2.44) where the coalescence and break-up terms have been neglected. That kinetic equation takes the following form:

$$\underbrace{\partial_t f + \mathrm{div}_{\boldsymbol{x}}\left(\cdot c f\right)}_{\text{free transport}} + \underbrace{\partial_S\left(R_s f\right)}_{\text{evaporation}} + \underbrace{\mathrm{div}_{\boldsymbol{u}_p}\left(\cdot \boldsymbol{F} f\right)}_{\text{drag force}} + \underbrace{\partial_{h_p^{th}}\left(H f\right)}_{\text{thermal transfert}} = 0. \tag{4.1}$$

Section 4.1 introduces an approach based on the multifluid framework in order to extend the AG system of equations to size polydispersion. The affine TSM method originally developed for the MK closure in (Laurent, Sibra, and Doisneau 2016; Sibra et al. 2017) is here extended to velocity dispersion. In Section 4.2, this model is coupled to the carrier phase, letting appear the complete governing equations aimed at being solved in the following chapters.

4.1 Modeling size polydispersion

4.1.1 Multi-fluid framework

It is here proposed to adapt the developments previously conducted on polykinetic closures to cases with size polydispersion. To do so, we base our approach on the multi-fluid framework originally developed in (Laurent and Massot 2001; Laurent, Sibra, and Doisneau 2016). The closure presented here has been firstly proposed in (Boileau et al. 2016).

4.1.1.1 The semi-kinetic level

Conservation equations of n, $n\boldsymbol{u}$, $n\mathbb{E}$ and $n\overline{h}_{p,th}$ can be obtained integrating the moments in velocity and in enthalpy of kinetic equation (4.1). For this first step, the integration over the size phase space is not conducted, this feature will be treated in a specific way on a further step. A NDF conditioned by size is thus defined taking into account a unique temperature, or equivalently enthalpy, and an AG velocity distribution for each size S.

$$\begin{aligned} f(t,\boldsymbol{x},S,\boldsymbol{c},h_{p,th}) = n(t,\boldsymbol{x},S)\delta(h_{p,th}-\overline{h}_{p,th}(t,\boldsymbol{x},S))\frac{det(\boldsymbol{\Sigma}(t,\boldsymbol{x},S))^{-1/2}}{(2\pi)^{d/2}}\times \\ \exp\left(-\frac{1}{2}(\boldsymbol{u}(t,\boldsymbol{x},S)-\boldsymbol{c})^T\boldsymbol{\Sigma}^{-1}(t,\boldsymbol{x},S)(\boldsymbol{u}(t,\boldsymbol{x},S)-\boldsymbol{c})\right) \end{aligned} \tag{4.2}$$

Integrating the kinetic equation (4.1) on the velocity and temperature phase spaces as well as assuming the distribution (4.2), one can obtain:

$$\left\{\begin{array}{llll} \partial_t n & +\mathrm{div}_{\boldsymbol{x}}\left(n\boldsymbol{u}\right) & = -\partial_S(R_s n), & \\ \partial_t(n\boldsymbol{u}) & +\mathbf{div}_{\boldsymbol{x}}\left(n(\boldsymbol{u}\otimes\boldsymbol{u}+\boldsymbol{\Sigma})\right) & = -\partial_S(R_s n\boldsymbol{u}) & +\frac{n}{\tau_p^u(S)}(\boldsymbol{u}_g-\boldsymbol{u}), \\ \partial_t(n\mathbb{E}) & +\mathbf{div}_{\boldsymbol{x}}\left(n(\mathbb{E}+\boldsymbol{\Sigma})\vee\boldsymbol{u}\right) & = -\partial_S(R_s n\mathbb{E}) & +\frac{n}{\tau_p^u(S)}(\boldsymbol{u}_g\vee\boldsymbol{u}-2\mathbb{E}), \\ \partial_t(n\overline{h}_{p,th}) & +\mathrm{div}_{\boldsymbol{x}}\left(n\boldsymbol{u}\overline{h}_{p,th}\right) & = -\partial_S(R_s n\overline{h}_{p,th}) & +\frac{nC_{p,l}}{\tau_p^T(S)}(T_g-T_p), \end{array}\right. \tag{4.3}$$

Such level of description, called the semi-kinetic level, do not rely on any assumption on the size distribution and related hypothesis but is also not integrated on all the phase space. We refer to (Laurent and Massot 2001) for the same procedure based on the MK assumption.

4.1.1.2 The sectional approach

As discussed Section 2.1.2.2, the dynamic of particles is clearly influenced by their size such that small particles follow the gas, acting as tracers, while large particles follow ballistic trajectories and are barely influenced by the gas surrounding them. We therefore consider the discretization $0 = S^{(0)} < \cdots < S^{(N_S)} = S_{\max}$ of the size interval $[0, S_{\max}[$, such that the particles belonging

to different sections are governed by distinct systems of equations. It is generally chosen to consider the droplet surface as the size parameter since the rate of change of this variable through evaporation is close to be constant. Such approach is considered hereafter since it provides the highest accuracy for mass exchanges.

To design the governing equations studied in this paper, we chose to conserve the following size-velocity moments of the NDF in each section k corresponding to $[S^{(k-1)}, S^{(k)}[$. Skipping the $(t, \boldsymbol{x})$ dependence in the notations, the conservative variables yield:

$$\begin{pmatrix} n^{(k)} \\ m^{(k)} \end{pmatrix} = \int_{S^{(k-1)}}^{S^{(k)}} \begin{pmatrix} 1 \\ \frac{\check{M}_l}{6\sqrt{\pi}} S^{3/2} \end{pmatrix} n(S)\mathrm{d}S, \tag{4.4}$$

where $\check{M}_l$ is the material density of the droplets, assumed to be constant in this work,

$$m^{(k)}\boldsymbol{u}^{(k)} = \int_{S^{(k-1)}}^{S^{(k)}} \frac{\check{M}_l}{6\sqrt{\pi}} S^{3/2} n(S)\boldsymbol{u}(S)\mathrm{d}S, \tag{4.5}$$

$$m^{(k)}\mathbb{E}^{(k)} = \int_{S^{(k-1)}}^{S^{(k)}} \frac{\check{M}_l}{6\sqrt{\pi}} S^{3/2} n(S)\mathbb{E}(S)\mathrm{d}S. \tag{4.6}$$

$$m^{(k)}h_{th}^{(k)} = \int_{S^{(k-1)}}^{S^{(k)}} \frac{\check{M}_l}{6\sqrt{\pi}} S^{3/2} n(S)\overline{h}_{p,th}(S)\mathrm{d}S. \tag{4.7}$$

Moreover, $\boldsymbol{\Sigma}^{(k)}$ is also defined by: $\mathbb{E}^{(k)} = \frac{1}{2}\left(\boldsymbol{u}^{(k)} \otimes \boldsymbol{u}^{(k)} + \boldsymbol{\Sigma}^{(k)}\right)$. These definitions of primitive variables according to the section differs from the size conditioned variable of equations (4.3) from two perspectives. Firstly because they are no more conditioned by size but averaged in the size section and secondly, for the enthalpy and velocity variables, because the use of their moment coupled with the size moment of order 3/2 provides genuine conservation laws on mass, momentum and energy. These moments have equivalent conservation laws in the model of the carrier phase and thus allows a strict conservation of these quantities through the coupling. The only exception to that affirmation is the kinetic energy, that is a tensor for the disperse phase due to the AG closure and thus can be only coupled to the Navier-Stokes equation through its trace.

The conservation laws aim therefore at involving the zeroth order moment $n^{(k)}$ and the 3/2 order moment in size $m^{(k)}$, leading to a representation of the size distribution through two moments inside each sections (leading to the so-called Two Size Moment (TSM) models). To complete the system of equations, we add two moments related to velocity, through $\boldsymbol{u}^{(k)}$ and $\boldsymbol{\Sigma}^{(k)}$ representing 5 equations in $2D$ and 9 equations in $3D$ and one scalar moment in temperature through $h_{th}^{(k)}$. The model thus possesses 8 equations per section in two dimensions and 12 in three dimensions. However, the moment integration of the kinetic equation does not provide sufficient information to close this system and we shall rely on the following hypothesis:

[HV] In each section, the velocity distribution does not depend on the size of the particles,

[HT] In each section, the temperature (and therefore the enthalpy) does not depend on the size of the particles,

[HS] In each section, the shape of the distribution of n as a function of S is presumed and only depends on the section boundaries and the size moments belonging to that same section.

By removing the coupled size-velocity and size-temperature dependencies thanks to [HS](Laurent and Massot 2001), assumptions [HV] and [HT] provide the ability of closing the governing system of equations using the conservative variables (4.4), (4.5), (4.6) and (4.7). Not developed in this work, we remind the reader that [HV] were overridden in the monokinetic case by taking into account coupled moments as in (Vié, Laurent, and Massot 2013) or without additional moments in (Laurent, Sibra, and Doisneau 2016; Sibra et al. 2017). For the assumptions here considered, one can deduce a system of governing equations for the disperse phase that takes the form for $k \in \{1, ..., N_S\}$:

$$\left\{\begin{array}{lll}
\partial_t n^{(k)} & +\mathrm{div}_{\boldsymbol{x}}\left(n^{(k)}\boldsymbol{u}^{(k)}\right) & = \mathcal{N}^{(k+\frac{1}{2})} - \mathcal{N}^{(k-\frac{1}{2})}, \\
\partial_t m^{(k)} & +\mathrm{div}_{\boldsymbol{x}}\left(m^{(k)}\boldsymbol{u}^{(k)}\right) & = \mathcal{F}^{(k+\frac{1}{2})} - \mathcal{F}^{(k-\frac{1}{2})} - \mathcal{M}^{(k)}, \\
\partial_t (m^{(k)}\boldsymbol{u}^{(k)}) & +\mathbf{div}_{\boldsymbol{x}}\left(m^{(k)}(\boldsymbol{u}^{(k)} \otimes \boldsymbol{u}^{(k)} + \boldsymbol{\Sigma}^{(k)})\right) & = \frac{m^{(k)}}{\tau_k^u}(\boldsymbol{u}_g - \boldsymbol{u}^{(k)}) - \mathcal{M}^{(k)}\boldsymbol{u}^{(k)} \\
 & & +\mathcal{F}^{(k+\frac{1}{2})}\boldsymbol{u}^{(k+1)} - \mathcal{F}^{(k-\frac{1}{2})}\boldsymbol{u}^{(k)}, \\
\partial_t (m^{(k)}\mathbb{E}^{(k)}) & +\mathbf{div}_{\boldsymbol{x}}\left(m^{(k)}(\mathbb{E}^{(k)} + \boldsymbol{\Sigma}^{(k)}) \vee \boldsymbol{u}^{(k)}\right) & = \frac{m^{(k)}}{\tau_k^u}(\boldsymbol{u}_g \vee \boldsymbol{u}^{(k)} - 2\mathbb{E}^{(k)}) - \mathcal{M}^{(k)}\mathbb{E}^{(k)} \\
 & & +\mathcal{F}^{(k+\frac{1}{2})}\mathbb{E}^{(k+1)} - \mathcal{F}^{(k-\frac{1}{2})}\mathbb{E}^{(k)}, \\
\partial_t (m^{(k)}h_{th}^{(k)}) & +\mathrm{div}_{\boldsymbol{x}}\left(m^{(k)}h_{th}^{(k)}\boldsymbol{u}^{(k)}\right) \cdot & = C_{p,l}\frac{m^{(k)}}{\tau_k^T}(T_g - T^{(k)}) - \mathcal{M}^{(k)}h_{th}^{(k)} \\
 & & +\mathcal{F}^{(k+\frac{1}{2})}h_{th}^{(k+1)} - \mathcal{F}^{(k-\frac{1}{2})}h_{th}^{(k)}.
\end{array}\right. \tag{4.8}$$

where N_S is the number of sections, $T^{(k)}$ is the particle temperature related to $h_{th}^{(k)}$ and with $\tau_k^u = \tau_p^u(S_k^{moy})$, $\tau_k^T = \tau_p^T(S_k^{moy})$ the averaged relaxation times. Moreover, the average particle surface S_k^{moy}, the particle number and mass fluxes between adjacent sections $\mathcal{N}^{(k-\frac{1}{2})}$ and $\mathcal{F}^{(k-\frac{1}{2})}$ and the mass exchange with the gas $\mathcal{M}^{(k)}$ are defined by:

$$S_k^{moy} = \frac{\int_{S^{(k-1)}}^{S^{(k)}} S^{3/2}\kappa^{(k)}(S)\mathrm{d}S}{\int_{S^{(k-1)}}^{S^{(k)}} S^{1/2}\kappa^{(k)}(S)\mathrm{d}S}, \qquad \mathcal{N}^{(k-\frac{1}{2})} = -R_s\kappa^{(k)}(S^{(k-1)}), \tag{4.9}$$

$$\mathcal{F}^{(k-\frac{1}{2})} = -R_s\frac{S^{3/2}}{6\sqrt{\pi}}\kappa^{(k)}(S^{(k-1)}), \qquad \mathcal{M}^{(k)} = -\int_{S^{(k-1)}}^{S^{(k)}} \frac{S^{1/2}}{4\sqrt{\pi}}R_s\kappa^{(k)}(S)\mathrm{d}S. \tag{4.10}$$

All these terms need the expression of $\kappa^{(k)}(S)$ which represents the reconstruction of n in the section from the moment transported by (4.8). More specifically, we consider the form of the

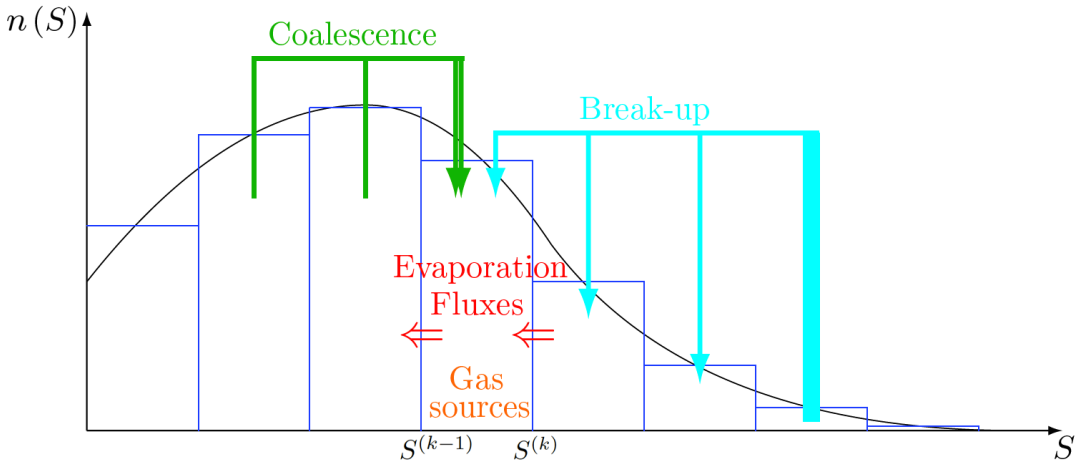

Figure 4.1: *Modeled phenomena in sectional approach (Doisneau 2013)*

size distribution as:

$$f_S(t,\boldsymbol{x},S)=\sum_{k=1}^{N_S}\kappa^{(k)}(S)\mathbb{1}_{(S^{(k-1)},S^{(k)})}(S),\qquad \mathbb{1}_{(S^{(k-1)},S^{(k)})}(S)=\begin{cases}1, & \text{if } S\in\left[S^{(k-1)},S^{(k)}\right],\\ 0, & otherwise.\end{cases} \tag{4.11}$$

According to [HS], the distribution $\kappa^{(k)}(S)$ is a function of the zeroth order moment and the considered size moments only. This closes the problem but does not solve the integration of these source terms which is the subject of Chapter 5.

4.1.2 The One Size Moment method

The MF approach originally relies on piecewise constant distribution. Therefore, the size distribution function takes the form:

$$f_S(t,\boldsymbol{x},S)=\sum_{k=1}^{N_S}\alpha^{(k)}\mathbb{1}_{(S^{(k-1)},S^{(k)})}(S). \tag{4.12}$$

For each section, only a single size variable is needed to deduce the parameter $\alpha^{(k)}$. As a consequence, only one moment relating to the size is needed and the closure is called One Size Moment (OSM). Starting for the system (4.8), the equation of the number density is simply dropped and $\alpha^{(k)}$ deduced from the mass conservation law and the definition of $m^{(k)}$ (4.4).

Additionally to evaporation, it is possible, based on such approach, to model coalescence and break-up as illustrated Figure 4.1. We refer to (Doisneau et al. 2013) and the references within

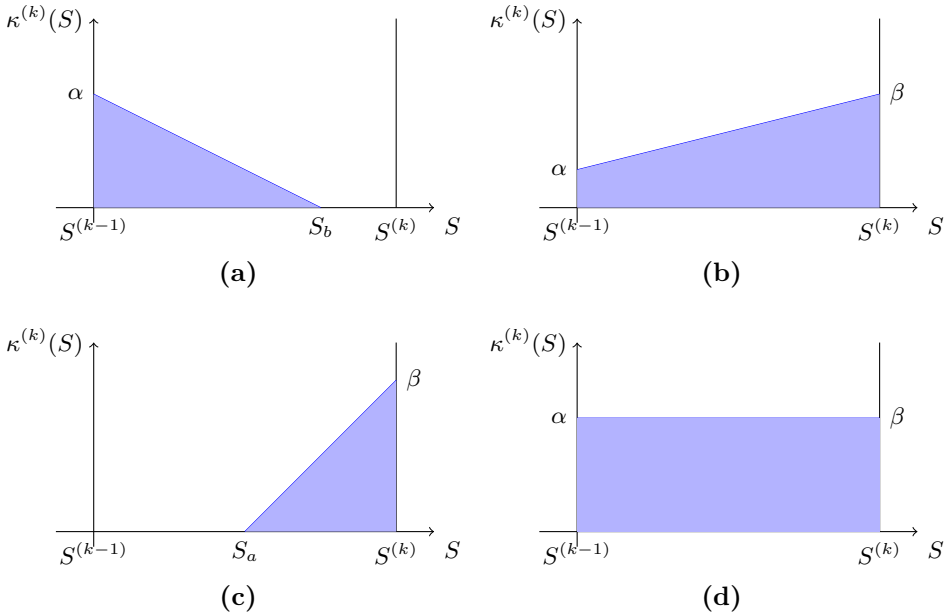

Figure 4.2: *The three types of affine reconstructions (a), (b) and (c) together with a OSM reconstruction (d)*

for more details on this subject.

4.1.3 The affine Two Size Moment method

Based on the work of (Laurent, Sibra, and Doisneau 2016), it is proposed to reconstruct the surface distribution inside the section with an affine function such that:

$$f_S(t,\boldsymbol{x},S) = \sum_{k=1}^{N_S} \left[\alpha_k \frac{S_{b,k}-S}{S_{b,k}-S_{a,k}} + \beta_k \frac{S-S_{a,k}}{S_{b,k}-S_{a,k}} \right] \mathbb{1}_{(S_{a,k},S_{b,k})}(S), \tag{4.13}$$

which allow three cases (a), (b) and (c) as represented Figure 4.2.

In such context, we define the following quantities, constant in a section with fixed boundaries:

$$\begin{cases} \Delta S_k &= S^{(k)} - S^{(k-1)}, \\ S_{5/2}^{(k)} &= \frac{2}{5}\left(\left(S^{(k)}\right)^{5/2} - \left(S^{(k-1)}\right)^{5/2} \right) \\ S_{7/2}^{(k)} &= \frac{2}{7}\left(\left(S^{(k)}\right)^{7/2} - \left(S^{(k-1)}\right)^{7/2} \right) \\ \overline{S}_a^{(k)} &= S^{(k)} S_{5/2}^{(k)} - S_{7/2}^{(k)}, \\ \overline{S}_b^{(k)} &= S_{7/2}^{(k)} - S^{(k-1)} S_{5/2}^{(k)}. \end{cases} \tag{4.14}$$

The key issue, is to obtain the effective reconstruction bounds of the affine distribution $S_{a,k}$

and $S_{b,k}$ as well as the values α_k and β_k of the distribution function (4.13). It is assumed that $n^{(k-1)}$ and $m^{(k)}$ fulfill realizability conditions, which, from a practical perspective, stipulates that the d_{30} diameter of the shall belong to the section:

$$\frac{\check{M}_l}{6\sqrt{\pi}}\left(S^{(k-1)}\right)^{3/2} n^{(k-1)} < m^{(k)} < \frac{\check{M}_l}{6\sqrt{\pi}}\left(S^{(k)}\right)^{3/2} n^{(k)} \qquad \text{or } (n^{(k)}, m^{(k)}) = (0,0). \tag{4.15}$$

Then, depending on the realizable value of $m^{(k)}/n^{(k)}$, one obtains the following values for the parameters:

(a) For $\frac{6\sqrt{\pi}}{\check{M}_l}\frac{m^{(k)}}{n^{(k)}} < \frac{2\overline{S}_a^{(k)}}{(\Delta S_k)^2}$ we have:

$$\begin{cases} S_{a,k} = S^{(k-1)}, & \alpha_k = \frac{2n^{(k)}}{S_{b,k}-S^{(k-1)}}, \\ \Phi^{(k)}(S_{b,k}, \frac{m^{(k)}}{n^{(k)}}, S^{(k-1)}) = 0, & \beta_k = 0. \end{cases} \tag{4.16}$$

(b) For $\frac{2\overline{S}_a^{(k)}}{(\Delta S_k)^2} \leq \frac{6\sqrt{\pi}}{\check{M}_l}\frac{m^{(k)}}{n^{(k)}} \leq \frac{2\overline{S}_b^{(k)}}{(\Delta S_k)^2}$ we have:

$$\begin{cases} S_{a,k} = S^{(k-1)}, & \alpha_k = \frac{n^{(k)}\overline{S}_b^{(k)}/\Delta S_k - 3m^{(k)}\sqrt{\pi}\Delta S_k/\check{M}_l}{\frac{1}{2}\left(\overline{S}_b^{(k)} - \overline{S}_a^{(k)}\right)}, \\ S_{b,k} = S^{(k)}, & \beta_k = \frac{-n^{(k)}\overline{S}_a^{(k)}/\Delta S_k + 3m^{(k)}\sqrt{\pi}\Delta S_k/\check{M}_l}{\frac{1}{2}\left(\overline{S}_b^{(k)} - \overline{S}_a^{(k)}\right)}. \end{cases} \tag{4.17}$$

(c) For $\frac{6\sqrt{\pi}}{\check{M}_l}\frac{m^{(k)}}{n^{(k)}} > \frac{2\overline{S}_b^{(k)}}{(\Delta S_k)^2}$ we have:

$$\begin{cases} \Phi^{(k)}(S_{a,k}, \frac{m^{(k)}}{n^{(k)}}, S^{(k)}) = 0, & \alpha_k = 0, \\ S_{b,k} = S^{(k)}, & \beta_k = \frac{2n^{(k)}}{S^{(k)}-S_{a,k}}. \end{cases} \tag{4.18}$$

(d) For an OSM degeneracy:

$$\begin{cases} S_{a,k} = S^{(k-1)}, & \alpha_k = \frac{6m^{(k)}\sqrt{\pi}}{\check{M}_l S_{5/2}^{(k)}}, \\ S_{b,k} = S^{(k)}, & \beta_k = \alpha_k. \end{cases} \tag{4.19}$$

The term $\Phi^{(k)}(X, \frac{m^{(k)}}{n^{(k)}}, \widetilde{S}) = 0$, as expressed here above, indicates that in the case a) and c), the unknown effective bound of the affine reconstruction is the root, according to X of the polynomial $\Phi^{(k)}$. This function can be derived from (4.4) according to the distribution given

under the form (4.13) and leads to:

$$\begin{aligned}\Phi^{(k)}(X,\frac{m^{(k)}}{n^{(k)}},\widetilde{S}) = 2X^5 + 4\sqrt{\widetilde{S}}X^4 + 6\widetilde{S}X^3 + \left(8\left(\widetilde{S}\right)^{3/2} - \frac{6\sqrt{\pi}}{\check{M}_l}\frac{35m^{(k)}}{4n^{(k)}}\right)X^2 \\ + \left(10\left(\widetilde{S}\right)^{3/2} - \frac{6\sqrt{\pi}}{\check{M}_l}\frac{35m^{(k)}}{4n^{(k)}}\right)\sqrt{\widetilde{S}}X + \left(8\left(\widetilde{S}\right)^{3/2} - \frac{6\sqrt{\pi}}{\check{M}_l}\frac{35m^{(k)}}{4n^{(k)}}\right)\widetilde{S}\end{aligned} \tag{4.20}$$

The root of this polynomial has been proved to be unique (Laurent, Sibra, and Doisneau 2016) but, in practice, the value of this root can only be obtained by a converging procedure, typically a Muller method (Muller 1956) in this work. This affine reconstruction has been compared in the original publication to the exponential reconstruction that does not rely on such approximations but on expensive numerical function. Conclusion of that comparison states that the affine reconstruction in surface was the most relevant in terms of numerical efficiency and accuracy.

It can also be proposed to reconstruct an affine function in volume as in (Laurent, Sibra, and Doisneau 2016) or according to the radius parameter as in (Nguyen et al. 2016) for soot simulation. The procedures to determine the coefficient of such affine functions do not rely on an approximation procedure neither on expensive numerical functions. However, the choice of these size reconstruction variable is not optimal for the modeling of evaporation process. Therefore, such possibilities are not tested in this manuscript.

4.1.4 The multi-class method

From another perspective, independent from the MF approach, one can assume the particle flows as a composition of discrete size. This consideration leads to the NDF that follows:

$$f = \sum_{i=1}^{N_c} n_i \delta(S - S_i)\delta(h_{p,th} - (\overline{h}_{p,th})_i)\frac{det(\mathbf{\Sigma}_i)^{-1/2}}{(2\pi)^{d/2}}\exp\left(-\frac{1}{2}(\boldsymbol{u}_i - \boldsymbol{c})^T\mathbf{\Sigma}_i^{-1}(\boldsymbol{u}_i - \boldsymbol{c})\right) \tag{4.21}$$

where N_c is the number of discrete sizes, called *classes*, considered.

This size sampling (Laurent and Massot 2001; Dupays 1996) also refer as the multi-class method (Murrone and Villedieu 2011) is a straightforward extension of monodisperse flow to size polydispersion but detains several major drawbacks compared to the MF approach. Since the considered classes are independents, they can only interact with each other through the gas. Therefore, it is hardly possible to consider coalescence or break-up since resulting droplets would likely possess a size that does not match any class. This however does no prevent the model from taking into account evaporation or combustion effect, but each class exchanges mass and associated momentum and energy with the carrier phase alone.

Therefore, considering the same moments as for the TSM system of equations and using the

same notation in this new context, the multi-class disperse phase governing equations yields:

$$\begin{cases} \partial_t n^{(k)} & +\partial_{\boldsymbol{x}} \cdot (n^{(k)} \boldsymbol{u}^{(k)}) & = 0, \\ \partial_t m^{(k)} & +\partial_{\boldsymbol{x}} \cdot (m^{(k)} \boldsymbol{u}^{(k)}) & = -\dot{m}_p, \\ \partial_t (m^{(k)} \boldsymbol{u}^{(k)}) & +\partial_{\boldsymbol{x}} \cdot (m^{(k)} (\boldsymbol{u}^{(k)} \otimes \boldsymbol{u}^{(k)} + \boldsymbol{\Sigma}^{(k)})) & = \frac{m^{(k)}}{\tau_k^u} (\boldsymbol{u}_g - \boldsymbol{u}^{(k)}) - \dot{m}_p^{(k)} \boldsymbol{u}^{(k)}, \\ \partial_t (m^{(k)} \mathbb{E}^{(k)}) & +\partial_{\boldsymbol{x}} \cdot (m^{(k)} (\mathbb{E}^{(k)} + \boldsymbol{\Sigma}^{(k)}) \vee \boldsymbol{u}^{(k)}) & = \frac{m^{(k)}}{\tau_k^u} (\boldsymbol{u}_g \vee \boldsymbol{u}^{(k)} - 2\mathbb{E}^{(k)}) - \dot{m}_p^{(k)} \mathbb{E}^{(k+1)}, \\ \partial_t (m^{(k)} h_{th}^{(k)}) & +\partial_{\boldsymbol{x}} \cdot (m^{(k)} h_{th}^{(k)} \boldsymbol{u}^{(k)}) & = C_{p,l} \frac{m^{(k)}}{\tau_k^T} (T_g - T^{(k)}) - \dot{m}_p^{(k)} h_{th}^{(k)}. \end{cases}$$

$$k \in [1, N_c] \tag{4.22}$$

Since the droplets have an identical diameter, that variable can be deduced from $m^{(k)}$ and $n^{(k)}$ for a droplet class by evaluation the d_{30} diameter, thus:

$$d_p^{(k)} = \sqrt[3]{\frac{6m^{(k)}}{\pi n^{(k)} \breve{M}_l}} \tag{4.23}$$

One can observe that the droplet number is conserved through evaporation which is not the case for MF methods where a flux of droplets from a section to another can occur. As a consequence, the droplets belonging to a class simultaneously disappear as their size reaches 0 unlike for the MF methods.

4.2 Coupled system of equations

As expressed until here, the carrier phase is not influenced by the disperse phase and is thus independent. These one-way coupling formulation needs to be extended to two-way coupling for the sake of SRM simulations.

4.2.1 Coupling the gas and droplets

In the case of the MK closure, the coupling is straightforward since thanks to the global conservation of mass, momentum and energy. In addition, put aside their complete disappearance, the droplet number is conserved through the evaporation process and therefore this quantity is not impacted by two-way coupling effects. Such an approach however finds its limits for the AG system of equations since the energy tensor of the disperse phase find no equivalent in the Navier-Stokes equations. Therefore, an additional assumption is stated:

[HG] The reciprocal effect of the droplet velocity dispersion only affects the gas through its energy equation, more precisely, only the trace of the energy matrix tensor is taken into

account.

Therefore, only the kinetic energy stored in $\boldsymbol{\Sigma}^{(k)}$, its trace, is coupled with the energy equation of the gas. This relies on the underlying assumption that small scale flow disturbances caused by the particle trails immediately relax to a homogeneous flow thanks to viscosity. Moreover since no velocity dispersion is considered in the gas at the fluid level, the droplet velocity dispersion cannot increase through two-way coupling effects.

For a proper closure, a genuine statistical treatment of the carrier phase would be needed. Therefore the WBE shall be derived again taking into account the possibility of the carrier phase unsteadiness, eventually through kinetic description of the gas at the *fluid* level as in (Chen et al. 2004).

4.2.2 Systems of governing equations

Taking into account the assumption [HG] and a treatment of size polydispersion through a multi-class approach, this leads to the governing equations:

$$
\left\{
\begin{array}{lll}
\partial_t \rho_g & +\partial_{\boldsymbol{x}} \cdot (\rho \cdot \boldsymbol{u}_g) & = \sum_{k=1}^{N_c} \dot{m}_p^{(k)} \\
\partial_t (\rho_g \boldsymbol{u}_g) & +\partial_{\boldsymbol{x}} \cdot (\rho_g \boldsymbol{u}_g \otimes \boldsymbol{u}_g + P\mathbb{I} - \boldsymbol{T}_{NS}) & = -\sum_{k=1}^{N_c} \frac{m^{(k)}}{\tau_k^u}(\boldsymbol{u}_g - \boldsymbol{u}^{(k)}) + \sum_{k=1}^{N_c} \dot{m}_p^{(k)} \boldsymbol{u}^{(k)} \\
\partial_t (\rho_g E) & +\partial_{\boldsymbol{x}} \cdot (\rho h \boldsymbol{u}_g - \boldsymbol{T}_{NS} \cdot \boldsymbol{u}_g) & = -\sum_{k=1}^{N_c} \frac{m^{(k)}}{\tau_k^u} \mathrm{tr}\left(\boldsymbol{u}_g \vee \boldsymbol{u}^{(k)} - 2\mathbb{E}^{(k)}\right) \\
 & & - \sum_{k=1}^{N_c} C_{p,l} \frac{m^{(k)}}{\tau_k^T}(T_g - T^{(k)}) + \sum_{k=1}^{N_c} \dot{m}_p^{(k)} \mathrm{tr}\left(\mathbb{E}^{(k)}\right)
\end{array}
\right.
$$

$$
\left.
\begin{array}{lll}
\partial_t n^{(k)} & +\partial_{\boldsymbol{x}} \cdot (n^{(k)} \boldsymbol{u}^{(k)}) & = 0, \\
\partial_t m^{(k)} & +\partial_{\boldsymbol{x}} \cdot (m^{(k)} \boldsymbol{u}^{(k)}) & = -\dot{m}_p^{(k)}, \\
\partial_t (m^{(k)} \boldsymbol{u}^{(k)}) & +\partial_{\boldsymbol{x}} \cdot (m^{(k)} (\boldsymbol{u}^{(k)} \otimes \boldsymbol{u}^{(k)} + \boldsymbol{\Sigma}^{(k)})) & = \frac{m^{(k)}}{\tau_k^u}(\boldsymbol{u}_g - \boldsymbol{u}^{(k)}) \\
 & & \quad -\dot{m}_p^{(k)} \boldsymbol{u}^{(k)}, \\
\partial_t (m^{(k)} \mathbb{E}^{(k)}) & +\partial_{\boldsymbol{x}} \cdot (m^{(k)} (\mathbb{E}^{(k)} + \boldsymbol{\Sigma}^{(k)}) \vee \boldsymbol{u}^{(k)}) & = \frac{m^{(k)}}{\tau_k^u}(\boldsymbol{u}_g \vee \boldsymbol{u}^{(k)} - 2\mathbb{E}^{(k)}) \\
 & & \quad -\dot{m}_p^{(k)} \mathbb{E}^{(k)}, \\
\partial_t (m^{(k)} h_{th}^{(k)}) & +\partial_{\boldsymbol{x}} \cdot (m^{(k)} h_{th}^{(k)} \boldsymbol{u}^{(k)}) & = C_{p,l} \frac{m^{(k)}}{\tau_k^T}(T_g - T^{(k)}) \\
 & & \quad -\dot{m}_p^{(k)} h_{th}^{(k)},
\end{array}
\right\} \forall k \in [1, N_c]
$$

(4.24)

Using the assumption [HG] on the AG closure considering this time a TSM treatment of size polydispersion, the complete set of governing equations yields:

$$
\left\{
\begin{array}{lll}
\partial_t \rho_g & +\partial_{\boldsymbol{x}} \cdot (\rho \cdot \boldsymbol{u}_g) & = +\sum_{k=1}^{N_S} \mathcal{M}^{(k)} \\
\partial_t (\rho_g \boldsymbol{u}_g) & +\partial_{\boldsymbol{x}} \cdot (\rho_g \boldsymbol{u}_g \otimes \boldsymbol{u}_g + P\mathbb{I} - \boldsymbol{T}_{NS}) & = -\sum_{k=1}^{N_S} \frac{m^{(k)}}{\tau_k^u}(\boldsymbol{u}_g - \boldsymbol{u}^{(k)}) + \sum_{k=1}^{N_S} \mathcal{M}^{(k)} \boldsymbol{u}^{(k)} \\
\partial_t (\rho_g E) & +\partial_{\boldsymbol{x}} \cdot (\rho h \boldsymbol{u}_g - \boldsymbol{T}_{NS} \cdot \boldsymbol{u}_g) & = -\sum_{k=1}^{N_S} \frac{m^{(k)}}{\tau_k^u} \mathrm{tr}\left(\boldsymbol{u}_g \vee \boldsymbol{u}^{(k)} - 2\mathbb{E}^{(k)}\right) \\
 & & \quad -\sum_{k=1}^{N_S} C_{p,l} \frac{m^{(k)}}{\tau_k^T}(T_g - T^{(k)}) + \sum_{k=1}^{N_S} \mathcal{M}^{(k)} \mathrm{tr}\left(\mathbb{E}^{(k)}\right) + \sum_{k=1}^{N_S} \mathcal{M}^{(k)} h_{th}^{(k)} \\
 & & \\
\partial_t n^{(k)} & +\partial_{\boldsymbol{x}} \cdot (n^{(k)} \boldsymbol{u}^{(k)}) & = \mathcal{N}^{(k+\frac{1}{2})} - \mathcal{N}^{(k-\frac{1}{2})}, \\
\partial_t m^{(k)} & +\partial_{\boldsymbol{x}} \cdot (m^{(k)} \boldsymbol{u}^{(k)}) & = \mathcal{F}^{(k+\frac{1}{2})} - \mathcal{F}^{(k-\frac{1}{2})} - \mathcal{M}^{(k)}, \\
\partial_t (m^{(k)} \boldsymbol{u}^{(k)}) & +\partial_{\boldsymbol{x}} \cdot (m^{(k)} (\boldsymbol{u}^{(k)} \otimes \boldsymbol{u}^{(k)} + \boldsymbol{\Sigma}^{(k)})) & = \frac{m^{(k)}}{\tau_k^u}(\boldsymbol{u}_g - \boldsymbol{u}^{(k)}) + \mathcal{F}^{(k+\frac{1}{2})} \boldsymbol{u}^{(k+1)} - \mathcal{F}^{(k-\frac{1}{2})} \boldsymbol{u}^{(k)} - \mathcal{M}^{(k)} \boldsymbol{u}^{(k)}, \\
\partial_t (m^{(k)} \mathbb{E}^{(k)}) & +\partial_{\boldsymbol{x}} \cdot (m^{(k)} (\mathbb{E}^{(k)} + \boldsymbol{\Sigma}^{(k)}) \vee \boldsymbol{u}^{(k)}) & = \frac{m^{(k)}}{\tau_k^u}(\boldsymbol{u}_g \vee \boldsymbol{u}^{(k)} - 2\mathbb{E}^{(k)}) + \mathcal{F}^{(k+\frac{1}{2})} \mathbb{E}^{(k+1)} - \mathcal{F}^{(k-\frac{1}{2})} \mathbb{E}^{(k)} - \mathcal{M}^{(k)} \mathbb{E}^{(k)}, \\
\partial_t (m^{(k)} h_{th}^{(k)}) & +\partial_{\boldsymbol{x}} \cdot (m^{(k)} h_{th}^{(k)} \boldsymbol{u}^{(k)}) & = C_{p,l} \frac{m^{(k)}}{\tau_k^T}(T_g - T^{(k)}) + \mathcal{F}^{(k+\frac{1}{2})} h_{th}^{(k+1)} - \mathcal{F}^{(k-\frac{1}{2})} h_{th}^{(k)} - \mathcal{M}^{(k)} h_{th}^{(k)},
\end{array}
\right. \quad \forall k \in [1, N_S]
\tag{4.25}
$$

The resolution of these systems and their subsequent forms, using the MK closure, one-way coupling form or monodisperse flow formulation, is the subject of the next part of this manuscript.

Part II

Numerical methods for Eulerian polydisperse spray

Chapter 5

Numerical methods for coupled systems of equations

子曰："三年，不至于谷，不易得也。"

孔子, 論語

The master said:'It is not easy to find someone who is able to study for even the space of three years without the inducement of an official salary.'

Confucius, Analects of Confucius

Since the governing equations have been derived, a numerical strategy has to be designed to solve such system. Therefore the objective of this chapter is two-fold: first, to present an high level strategy to resolve the systems of equations considered and second, to introduce the time integration method used and designed in this work. Aside standard time-integration that can be used either to integrate an ODE or semi-discrete form of a Partial Differential Equation (PDE), a numerical method is proposed to integrate simultaneously drag, heat transfer and evaporation in the case of the AG-TSM system (4.25). This different approach is motivated by the need to cope with the non-linearities encountered for that operator and the difficulties to maintain the realizability.

The chapter is thus divided as follow: Section 5.1 presents the operator splitting technique used in this work. Then Section 5.2 details the methods used for the time integration of the operators. Finally, in the context of the AG-TSM model (4.25), Section 5.3 proposes a dedicated scheme for the resolution of the source terms and the transport in the phase space.

5.1 Operator splitting

5.1.1 System decomposition

The systems of interest, represented the two-phase disperse flow as in Section 4.2, can be divided in three distinct parts:

- The transport of the gas in the physical space, associated with the operator $\boldsymbol{\mathcal{T}}_g$,
- The transport of the droplets in the physical space, associated with the operator $\boldsymbol{\mathcal{T}}_k$ for each class or section k,
- The source terms coupling the phases and solving the transport in the phase space, associated with the operator $\boldsymbol{\mathcal{S}}_{gp}$.

Each *operator* corresponds to a part of the complete system of equations and each of these subsystems can be solved independently from the others. The transport operators have already been defined in Chapter 3. For the gas, we rely on the Navier-Stokes equation (3.24) to describe the viscous carrier fluid. In the case of the disperse phase, several choices are possible depending on the closure considered and we focus more particularly on the MK (3.12) and AG (3.17) closures, valid for each section. For the sake of stability, as discussed in details in Section 6.2.3, the axisymmetrical source terms (see Section 3.3) are considered as belonging to the transport operators.

Put aside the source terms of $\boldsymbol{\mathcal{S}}_{gp}$ coupling the phases, considering N_S classes or sections, these $N_S + 1$ systems of equations, and thus operators, are completely independent one to another. These systems of equations involve spatial derivation that do not appear in $\boldsymbol{\mathcal{S}}_{gp}$. While the carrier phase equations, solved by $\boldsymbol{\mathcal{T}}_g$ have a hyperbolic/parabolic character, the equations of the disperse phase are hyperbolic or weakly hyperbolic and thus are not submitted to the same singularities in the configurations studied. As a consequence, it is proposed in this manuscript to rely on this particularity to apply different numerical methods to each of these. Additionally, we define the global transport operator $\boldsymbol{\mathcal{T}} = \boldsymbol{\mathcal{T}}_g + \sum_k \boldsymbol{\mathcal{T}}_k$ solving all the operators $\boldsymbol{\mathcal{T}}_g$ and $\boldsymbol{\mathcal{T}}_k$ in an arbitrary order or in parallel, using eventually distinct methods.

The coupling source terms have not been described alone until here but coupled with the transport operators in Chapter 4 building the global system of equations. We consider in $\boldsymbol{\mathcal{S}}_{gp}$ all the terms related to the evolution of the system in the phase space. In the great majority of cases, as for the multi-class approach (4.24) for instance, it simply consists in the computation of the time evolution according to the right hand side of the system only. Considering (4.24)

for example, this leads to the following ODE:

$$\left\{\begin{array}{lll}
\mathrm{d}_t\rho_g & = \sum_{k=1}^{N_c}\dot{m}_p^{(k)} & \\
\mathrm{d}_t\rho_g\boldsymbol{u}_g & = -\sum_{k=1}^{N_c}\frac{m^{(k)}}{\tau_k^u}(\boldsymbol{u}_g-\boldsymbol{u}^{(k)})+\sum_{k=1}^{N_c}\dot{m}_p^{(k)}\boldsymbol{u}^{(k)} & \\
\mathrm{d}_t\rho_g E & = -\sum_{k=1}^{N_c}\frac{m^{(k)}}{\tau_k^u}\mathrm{tr}\left(\boldsymbol{u}_g\vee\boldsymbol{u}^{(k)}-2\mathbb{E}^{(k)}\right) & \\
 & \quad -\sum_{k=1}^{N_c}C_{p,l}\frac{m^{(k)}}{\tau_k^T}(T_g-T^{(k)})+\sum_{k=1}^{N_c}\dot{m}_p^{(k)}\mathrm{tr}\left(\mathbb{E}^{(k)}\right) & \\
\left.\begin{array}{lll}
\mathrm{d}_t n^{(k)} & = & 0,\\
\mathrm{d}_t m^{(k)} & = & -\dot{m}_p^{(k)},\\
\mathrm{d}_t m^{(k)}\boldsymbol{u}^{(k)} & = & \frac{m^{(k)}}{\tau_k^u}(\boldsymbol{u}_g-\boldsymbol{u}^{(k)})-\dot{m}_p^{(k)}\boldsymbol{u}^{(k)},\\
\mathrm{d}_t m^{(k)}\mathbb{E}^{(k)} & = & \frac{m^{(k)}}{\tau_k^u}(\boldsymbol{u}_g\vee\boldsymbol{u}^{(k)}-2\mathbb{E}^{(k)})-\dot{m}_p^{(k)}\mathbb{E}^{(k)},\\
\mathrm{d}_t m^{(k)}h_{th}^{(k)} & = & C_{p,l}\frac{m^{(k)}}{\tau_k^T}(T_g-T^{(k)})-\dot{m}_p^{(k)}h_{th}^{(k)},
\end{array}\right\}\forall k\in[1,N_c]
\end{array}\right. \tag{5.1}$$

In the context of the multi-fluid discretization of the size phase space, a transport of the distribution in this phase component can be observed through the terms $\mathcal{N}^{(k-\frac{1}{2})}$ and $\mathcal{F}^{(k-\frac{1}{2})}$ associated with the particle number and mass fluxes between adjacent sections. Nonetheless, assuming an upwinding of the transport of these terms, an ODE can be deduced. In practice, this solution do not offer an a sufficient robustness and we refer however to Section 5.3 for an alternative method ensuring realizability.

5.1.2 Operator splitting

To solve through distinct methods the different components of the system of equations, we propose to use a time operator splitting. Developed in the sixties (Marchuk 1968; Strang 1968; Yanenko 1971; Marchuk 1990) with the main objective of reducing computational resources, these methods became popular thanks to their flexibility. Then, each of the operators presented above, sub-systems of the governing equations, can be solved separately in order to rely on the most relevant numerical method for them (Doisneau et al. 2014; Descombes, Duarte, and Massot 2016). The stability of splitting schemes is fulfilled as long as the stability of the methods solving the subsystem is ensured. In this context, adequate methods can be chosen in order to deal with stiff source terms and fast transient phenomena without influencing other operators (see (Verwer et al. 1996; Verwer et al. 1999; Ropp and Shadid 2009; Duarte et al. 2012) for instance). However, the separate time evolution of each subproblem during a global time step leads to the so-called *splitting error* and such methods need to be used with caution in order to converge toward the valid dynamics.

We denote $\boldsymbol{\mathcal{R}}(\Delta t)\boldsymbol{W}^n$ the transformation of the solution $\boldsymbol{W}^n$ by the operator $\boldsymbol{\mathcal{R}}$ over a time step Δt. To proceed to the combination of several operators, two main operator splitting schemes are proposed in the literature: the first order Lie scheme (Trotter 1959) and the second order Strang scheme (Strang 1963). Despite the theoretical feasibility of higher order schemes of this kind, they are usually not suitable for PDEs and more particularly stiff PDEs (Hundsdorfer and Verwer 2003) as studied in this manuscript.

The Lie scheme couples two operators realizing a time step by executing an operator after another. Coupling the global system thus leads either to:

$$\boldsymbol{W}^{n+1} = \boldsymbol{\mathcal{T}}(\Delta t)\boldsymbol{\mathcal{S}}_{gp}(\Delta t)\boldsymbol{W}^{n} \tag{5.2}$$

or to:

$$\boldsymbol{W}^{n+1} = \boldsymbol{\mathcal{S}}_{gp}(\Delta t)\boldsymbol{\mathcal{T}}(\Delta t)\boldsymbol{W}^{n} \tag{5.3}$$

where the second version (5.3) is to be privileged if $\boldsymbol{\mathcal{S}}_{gp}$ is the stiffest operator since it is used in the final step (Descombes and Massot 2004).

In order to achieve a second order, the Strang scheme proceeds to three successive operations, where one of the operator is called twice on half a time step, which leads to:

$$\boldsymbol{W}^{n+1} = \boldsymbol{\mathcal{T}}(\frac{\Delta t}{2})\boldsymbol{\mathcal{S}}_{gp}(\Delta t)\boldsymbol{\mathcal{T}}(\frac{\Delta t}{2})\boldsymbol{W}^{n} \tag{5.4}$$

or to its symmetric form:

$$\boldsymbol{W}^{n+1} = \boldsymbol{\mathcal{S}}_{gp}(\frac{\Delta t}{2})\boldsymbol{\mathcal{T}}(\Delta t)\boldsymbol{\mathcal{S}}_{gp}(\frac{\Delta t}{2})\boldsymbol{W}^{n} \tag{5.5}$$

where, once again, the second version (5.5) is more accurate when $\boldsymbol{\mathcal{S}}_{gp}$ is stiffer than $\boldsymbol{\mathcal{T}}$ (Descombes and Massot 2004).

Starting for the time step n, (5.5) leads successively to:

1. Integrate the source terms during half a time step only,
2. Solve to the transport of the gas and droplets in each section during a full time step,
3. Finish the procedure by solving the source terms during half a time-step.

Other kind of splitting dedicated to a specific problem can be used. For example, it is possible to reduce the number of call of the $\boldsymbol{\mathcal{T}}_k$ operator by splitting them from the phenomena related to acoustics $\boldsymbol{\mathcal{T}}_g$ and $\boldsymbol{\mathcal{S}}_{gp}$ (Doisneau et al. 2014). Such procedure is efficient inside the SRM combustion chamber, at low Mach, where the maximal time step for stability of the $\boldsymbol{\mathcal{T}}_k$ operators is much larger than for $\boldsymbol{\mathcal{T}}_g$ due to the carrier phase acoustic velocity. Thus, in these conditions, for one use of the $\boldsymbol{\mathcal{T}}_k$ operator, $\boldsymbol{\mathcal{T}}_g$ can be called several times. However, in the nozzle in supersonic regime and therefore for complete motor simulations where these time steps are of the same magnitude, such approach lacks of interest. Also, using adaptive schemes and relying on a fine analysis of the involved equations, the error caused by the splitting and the subsequent operators can be mastered (Descombes, Duarte, and Massot 2016). We refer to (Duarte 2011) for more details on the subject of splitting and adaptive methods.

5.2 General time integration

In this section, a brief review of the time integration methods used in this work is proposed and more specifically focused on robust methods of order up to three. The classes introduced are well fitted for the resolution of ODE, local in the physical and size phase space, and of semi-discrete equation in the context of the transport in the physical space. However, for the transport in the size phase space, that is notably associated to evaporation in the sectional approach, other dedicated class of methods as proposed in Section 5.3 shall be considered.

5.2.1 Generic form for time integration

To integrate the problem of interest, we put here the equations solved by an operator under the form:

$$\mathrm{d}_t \boldsymbol{W} = \boldsymbol{\mathcal{L}}(\boldsymbol{W}) \tag{5.6}$$

The function $\boldsymbol{\mathcal{L}}(\boldsymbol{W})$ can represent two distinct classes of operations:

1. $\boldsymbol{\mathcal{L}}(\boldsymbol{W})$ is the source terms of the problem. Thus (5.6) typically corresponds to (5.1) and more generally to the right hand side of the system studied in this manuscript. $\boldsymbol{W}$ can be either local or global in the spatial domain studied.

2. The $\boldsymbol{\mathcal{L}}$ operator refers to an approximation of the integration of the system of equations in the physical space associated to the transport operator. Since this integration has not been conducted in time, (5.6) corresponds to the so-called *semi-discretized* form (see Chapter 6 and equation (6.42)). This method also called *method of lines* allows the use of this general expression for the time integration procedure presented hereafter (Hundsdorfer and Verwer 2003). Due to the spatial integration, $\boldsymbol{W}$ refers to the solution on the entire domain.

The most basic time integration is the explicit Euler forward method. Based on a time step Δt, this scheme takes the form:

$$\boldsymbol{W}^{n+1} = \boldsymbol{W}^n + \Delta t \boldsymbol{\mathcal{L}}(\boldsymbol{W}^n) \tag{5.7}$$

This Euler forward scheme remains first order accurate but constitutes a fundamental building block for the explicit time integration procedure presented hereafter. In the case of hyperbolic system of equations, the stability of the Euler forward scheme is associated to a limit time step τ_{max} required for stability. This characteristic firstly studied in (Courant, Friedrichs, and Lewy 1928) for PDEs also applies for ODEs (Hairer and Wanner 1996b).

5.2.2 The SSPRK schemes

We focus here on a specific class of explicit multi-stage Runge-Kutta (RK) time integration fulfilling Stong Stability Preserving (SSP) conditions (Gottlieb, Shu, and Tadmor 2001), originally named Total Variation Diminishing (TVD) by reference to the resolution of hyperbolic transport equations (Shu and Osher 1988). This condition states that if the Euler forward scheme (5.7) is stable under Courant–Friedrichs–Lewy (CFL) condition, the SSPRK method is also stable under a non-null fraction of the associated limit time step τ_{max}. More precisely, we define the SSP conditions as:

Definition 5.1. Let the Euler forward method (5.7) be stable for all $\Delta t < \tau_{max}$, then a methods is said to be SSP if there exists $c > 0$, such that for all $\Delta t < c\tau_{max}$, the integration method is stable as well.

Additionally, we denote the RK methods fulfilling SSP condition, SSPRK schemes. It was proven in (Shu and Osher 1988, 1989) that up to fourth order, there exists an optimal SSPRK integrator, meaning being both that:

- The number of stage is equal to the order of accuracy,
- The time step stability constraint is optimal, $c = 1$.

From these constraints, the optimal SSPRK of second and third order yield:

- Optimal SSPRK2 method:

$$\begin{cases} \boldsymbol{W}^{(1)} = \boldsymbol{W}^n + \Delta t \boldsymbol{\mathcal{L}}(\boldsymbol{W}^n) \\ \boldsymbol{W}^{n+1} = \frac{1}{2}\boldsymbol{W}^n + \frac{1}{2}\left(\boldsymbol{W}^{(1)} + \Delta t \boldsymbol{\mathcal{L}}(\boldsymbol{W}^{(1)})\right) \end{cases} \tag{5.8}$$

- Optimal SSPRK3 method:

$$\begin{cases} \boldsymbol{W}^{(1)} = \boldsymbol{W}^n + \Delta t \boldsymbol{\mathcal{L}}(\boldsymbol{W}^n) \\ \boldsymbol{W}^{(2)} = \frac{3}{4}\boldsymbol{W}^n + \frac{1}{4}\left(\boldsymbol{W}^{(1)} + \Delta t \boldsymbol{\mathcal{L}}(\boldsymbol{W}^{(1)})\right) \\ \boldsymbol{W}^{n+1} = \frac{1}{3}\boldsymbol{W}^n + \frac{2}{3}\left(\boldsymbol{W}^{(2)} + \Delta t \boldsymbol{\mathcal{L}}(\boldsymbol{W}^{(2)})\right) \end{cases} \tag{5.9}$$

One can observe that in (5.8) and (5.9), one can express $\boldsymbol{W}^{n+1}$ as a convex combination of successive Euler forward time integrations (5.7). To go to fourth order and above while respecting the SSP conditions with non-linear operator $\boldsymbol{\mathcal{L}}$ and being optimal, the introduction of at least a negative time step is necessary (Shu and Osher 1988). If the $\boldsymbol{\mathcal{L}}$ operator represents the resolution method of a hyperbolic system of equations, the associated step is equivalent to a downwind scheme and consequently, the method become unstable. This feature can however be overcome by the trick proposed in (Shu and Osher 1988) for instance. Also, it is still possible to reach the fourth order accuracy by relying on the five stage procedure (Spiteri and Ruuth 2002; Kraaijevanger 1991). We refer to (Gottlieb, Ketcheson, and Shu 2011) for more details of such SSPRK methods.

Since we do not aim at such high order convergence rate in this manuscript, the multi-stage

methods (5.8) and (5.9) will be considered sufficiently robust and accurate for most of the operators used through this work according to the experience acquired in (Dupays 1996; Doisneau 2013; Sibra 2015). These SSPRK versions are described in (Gottlieb 2005) together with non-optimal RK methods and arbitrary high order RK schemes that are SSP under the assumption of the linearity of the studied system of equations.

5.2.3 Other kind of time integration

Complementary to the class of schemes presented above, we denote the existence of complementary time integration methods not developed in this manuscript. As explain through the text, these solutions have not been retained for various reasons in view of the applications considered. Among them, the following classes of time integration methods are briefly described:

- **The multi-step methods:** Originally published by F. Bashforth in (Bashforth 1883) based on a proposition of J.C. Adams, this class of methods uses the information of the solution at previous time steps to increase the order of accuracy. The solution obtained is a non-convex combination of the Euler forward and solutions at the former time steps. Therefore, this cannot be proven SSP and are not adapted to operator splitting strategies.

- **The implicit RK methods:** The RK procedures can be expressed under an implicit form ensuring the unconditional stability of the method. Such methods however require a converging procedure and are therefore much more costly than explicit RK methods.

- **The adaptive methods:** Through an error estimate procedure, the time step or the order of accuracy the method is dynamically determined to ensure the stability of the integration procedure. Among others, this is the case of the $RK5(4)$ family of adaptive time step method based on RK procedures (Dormand and Prince 1980) and of the ROCK4 method proposed in (Abdulle 2002) that use a dynamic accuracy order. This class of method is well adapted to the resolution of stiff source terms and quick transient processes as flame front (Duarte et al. 2012) for instance. Implementation of such methods can however lead to arithmetical unbalancing on parallel computers and are not fitted for the time integration of transport operators.

- **The parareal methods:** It consists in a decomposition of the time step into sub-time steps such that each of these can be solved concurrently. Forcing the continuity of the solution over the wished time step, the integration method can be parallelized in time (Nievergelt 1964; Lions, Maday, and Turinici 2001; Gander and Vandewalle 2007). Their main advantage is their capacity to be implemented for parallel computation but the scalability of the method alone is rather limited and shall thus be used as an over layer of standard parallelization methods as domain decomposition. Therefore, methods of this class can find interest at solving large problems using a great number of computation unit, where the parallelization through other procedures finds its limits.

We refer to (Butcher 2016; Hairer, Nørsett, and Wanner 1993b; Hairer and Wanner 1996b) among others for a broader view of ODE numerical integration methods.

5.3 A dedicated Quadrature Kinetic Scheme

Complementary to the time integration methods presented above, it is here proposed to design a robust and accurate dedicated numerical scheme able to solve the source terms operator of the AG-TSM model (4.25). While preserving realizability, the evolution of the conservative variables due simultaneously to drag, heat transfer and evaporation is complex and the specific computation of these terms can be difficult to proceed due to non-linearities. In order to avoid such issues, as originally proposed in (Laurent, Sibra, and Doisneau 2016; Sibra et al. 2017) for the MK closure, a realizable scheme is adapted to the considered system.

5.3.1 Original concept

The original idea of the Quadrature Kinetic Scheme (QKS) (Laurent, Sibra, and Doisneau 2016) consists in approximating the evolution of the moments at a local point, due to evaporation, drag and heat transfer, by using a finite number of quadrature points. When considered, the coalescence and break-up terms are solved separately, using the splitting method (Doisneau et al. 2013; Laurent, Sibra, and Doisneau 2016). This kind of schemes was developed originally for moment methods, for evaporation (Massot et al. 2010), coupled to drag (Vié, Laurent, and Massot 2013) and was adapted to the TSM method (Laurent, Sibra, and Doisneau 2016). Its reinterpretation in (Laurent, Sibra, and Doisneau 2016) gave it its name: moments at time $n+1$ are given as an approximation by a size quadrature of the moments obtained by a kinetic scheme, thus using the analytical solution of the kinetic equation on the time step, starting from the reconstruction at time n. But it can be seen, like in (Vié, Laurent, and Massot 2013), as the evolution during the time step of well chosen quadrature points and their corresponding velocity. However, unlike for QMOM size distribution, where the quadrature directly describes the size polydispersion, these quadratures approximate parts of the affine TSM reconstruction which remains the closure. The quadrature points are thus deduced from the affine reconstruction and aim at approximating mass, momentum and heat transfer terms.

To sum up the procedure, it consists in determining the affine size reconstruction from the moments, then in deducing sets of quadrature weights and abscissa from parts of it before finally computing the evolution of the velocity moment corresponding to each quadrature point. The moments belonging to the conservation equations (4.25) are then computed again from the quadratures. All the steps are sum up in the Figure 5.1 and illustrated Figure 5.2.

The procedure proposed mostly differs from (Laurent, Sibra, and Doisneau 2016) since the original publication did not take into account velocity dispersion. The link between the kinetic and macroscopic model is conserved and ensures the realizability (Chaisemartin 2009; Sibra et al. 2017; Bouchut, Jin, and Li 2003). However, instead of using additional quadrature on the velocity phase space, we rely on analytic solutions to the velocity dispersion evolution corresponding to each quadrature point established from the size phase space. Such new method, already presented in (Boileau et al. 2016), is detailed in Section 5.3.3 and the extension for two-way coupling case is presented Section 5.3.4. Validated Section 9.3, this new features enable the possibilities of applied SRM simulations as proposed Chapter 11.

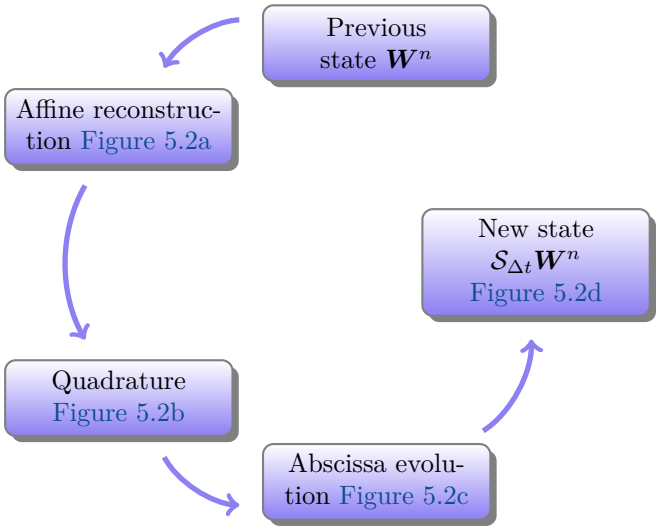

Figure 5.1: *QKS procedure applied to two size moment methods*

5.3.2 Quadrature

5.3.2.1 Section splitting

In a first step, each section is divided in two sub-sections (see Figure 5.2a) according to section of arrival of the droplets at the end of the time step Δt. While the droplets of the first sub-section change of size (through evaporation $R_s < 0$ or condensation $R_s > 0$) such that there are transported from a section to another, the droplets of the second sub-section remain in their original section despite the size evolution. Indeed, for a constant size change rate $R_s^{(k)} < 0$ in the section k, after the time step Δt, the droplets of size in $(S^{(k-1)} - R_s^{(k)}\Delta t, S^{(k)})$ stay in section k and the droplets of size in $(S^{(k-1)}, S^{(k-1)} - R_s^{(k)}\Delta t)$ go from the section k to the section $k-1$ $\forall k \geq 2$ and disappear in the carrier phase for the first section $k = 1$. For condensation $R_s^{(k)} > 0$, similar droplet exchanges between sections can be observed. Since for affine reconstruction, effective boundaries of distribution of the solution in the section are $S_{a,k}$ and $S_{b,k}$. Thus for a constant $R_s^{(k)}$ the size $S_{int}^{(k)}$, the section split abscissa is:

$$S_{int}^{(k)} = \begin{cases} \max\left(S_{a,k}, S^{(k-1)} - R_s^{(k)}\Delta t\right) & R_s^{(k)} \leq 0 \\ \min\left(S_{b,k}, S^{(k)} - R_s^{(k)}\Delta t\right) & R_s^{(k)} > 0 \end{cases} \tag{5.10}$$

In the case of an empty sub-section, if $R_s^{(k)} = 0$ or $S_{int}^{(k)} \notin]S_{a,k}, S_{b,k}[$, weights of quadrature corresponding to that sub-section are equal to 0. Therefore values associated to these quadratures can be set arbitrarily since the concerned quadrature have no effect while computing the moment inside the section at the end of the time-step.

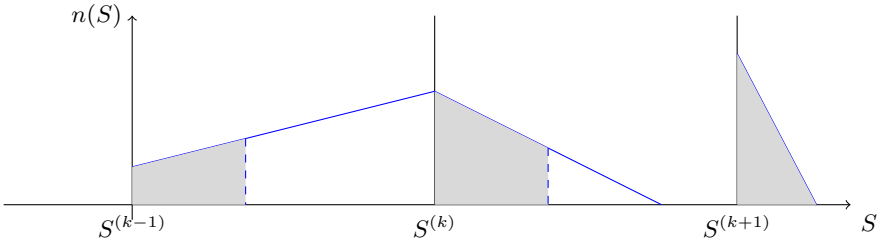

(a) Section splitting

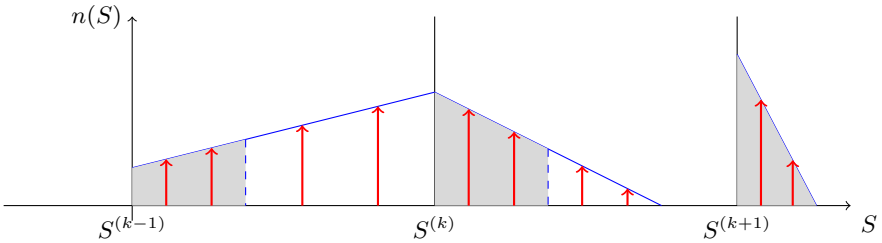

(b) Quadrature sampling

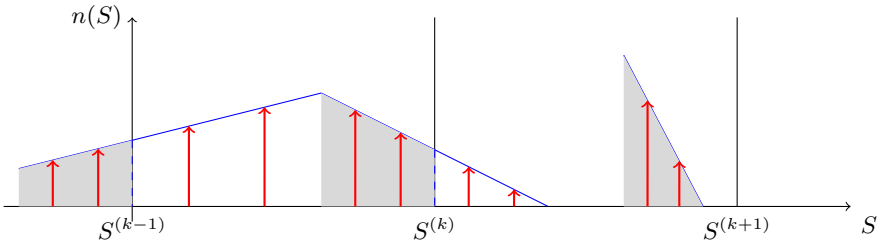

(c) Quadrature evolution

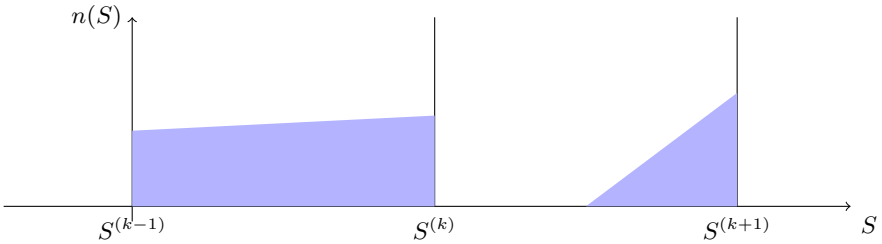

(d) Projection

Figure 5.2: *Quadrature sampling for affine TSM problems*

5.3.2.2 Quadrature approximation

We now describe the methodology to sample the sub-sections with quadratures nodes (see Figure 5.2b). In order to still conserve the moments of order 0 and 3/2, we use a two point quadrature on the moments of order 0,1/2,1,3/2. Since only the moments of order 0 and 3/2 are known, we use the knowledge of the $\kappa^{(k)}$ size distribution in that section to deduce the missing moments. Thus for each sub-sections, we define the quadrature weights and abscissa as the solution of:

- For the left sub-section:

$$\int_{S_{a,k}}^{S_{int}^{(k)}} S^{j/2}\kappa^{(k)}(S)\mathrm{d}S = \sum_{i=1}^{2} \tilde{n}^{(i,1,k)} \left(S^{(i,1,k)}\right)^{j/2} \qquad \forall j \in \{0,1,2,3\} \tag{5.11}$$

- For the right sub-section:

$$\int_{S_{int}^{(k)}}^{S_{b,k}} S^{j/2}\kappa^{(k)}(S)\mathrm{d}S = \sum_{i=1}^{2} \tilde{n}^{(i,2,k)} \left(S^{(i,2,k)}\right)^{j/2} \qquad \forall j \in \{0,1,2,3\} \tag{5.12}$$

where $\tilde{n}^{(i,j,k)}$ is the weight (consistent with a number density) and $S^{(i,j,k)}$ the size associated to the quadrature i of subsection j of section k. Using the change of variable $R = \sqrt{S}$, analytic results to that problem can be found in (McGraw 1997; Desjardins, Fox, and Villedieu 2008).

Together with the TSM reconstruction, the choice of a two node quadrature aims at obtaining a second order of accuracy in size discretization. It is also possible to use only one point quadrature thanks to the moments of order 0 and 3/2 in order to reduce the computational cost of the method but at the price of a first order accuracy (Sibra et al. 2017; Laurent, Sibra, and Doisneau 2016).

5.3.2.3 Associated value reconstruction

For the sake of simplicity, we propose to assume a constant in size distribution of the velocity, velocity dispersion and temperature, as for the hypothesis [HV] and [HT] of Section 4.1.1.2. Therefore, for each quadrature q belonging to a section k, we have:

$$\boldsymbol{u}^{(q)} = \boldsymbol{u}^{(k)}, \qquad \boldsymbol{\Sigma}^{(q)} = \boldsymbol{\Sigma}^{(k)}, \qquad h_{th}^{(q)} = h_{th}^{(k+1)}, \tag{5.13}$$

where each quadrature is indexed by (q) instead of (i,j,k) for the sake of legibility.

This choice, despite being the simplest leads to a first order convergence for the mean velocity and velocity dispersion. The solution, as originally proposed in (Laurent, Sibra, and Doisneau 2016) for the MK closure, is to introduce a velocity reconstruction in the size phase space and thus associate different velocities to the quadratures belonging to the same section. In the case of the AG closure, such reconstruction has also to be conducted on the velocity dispersion

matrix.

In that conditions, ensuring both realizability and conservation leads to the necessity of slope limitation. Typically, a velocity slope inside a section leads to the generation of a residual velocity dispersion $\widetilde{\boldsymbol{\Sigma}}$ such that $m^{(k)}\widetilde{\boldsymbol{\Sigma}} = \sum_{q\in k} m^{(q)}\boldsymbol{u}^{(q)}\otimes\boldsymbol{u}^{(q)} - m^{(k)}\boldsymbol{u}^{(k)}\otimes\boldsymbol{u}^{(k)}$. Therefore, it is necessary to limit the velocity slope in order to conserve the kinetic energy in the section $m^{(k)}\mathbb{E}^{(k)} = \sum_{q\in k} m^{(q)}\mathbb{E}^{(q)}$ and maintain a positive velocity dispersion for each quadrature $\boldsymbol{\Sigma}^{(q)}$. Work is in progress on that subject to improve the QKS method for the AG closure.

5.3.3 Quadrature points evolution

5.3.3.1 Governing equations of the quadrature points

In the original philosophy of the method, the problem is solved directly at the kinetic level. However for the sake of simplicity, we do not base the derivation of the scheme on such approach in the present contribution. We base the derivation on the fact that, under the effect of drag, the Gaussian form of the velocity distribution is conserved even at the kinetic level. It is therefore possible to obtain the same results than starting from another point of view.

We thus remark that, once the quadratures are established, the piecewise affine approximation of the solution is approximated through a set of discrete size at which conservative quantities are associated. As a consequence, the problem is at this point consistent with a multi-class description of the problem. Therefore, we simply adapt the system (5.1), in one-way coupling conditions, using quadratures

$$\left\{\begin{array}{lcll} \mathrm{d}_t n^{(q)} & = & 0, & \\ \mathrm{d}_t m^{(q)} & = & \dot{m}_p^{(q)}, & \\ \mathrm{d}_t m^{(q)}\boldsymbol{u}^{(q)} & = & \frac{m^{(q)}}{\tau_{\boldsymbol{u}}^{(q)}}(\boldsymbol{u}_g - \boldsymbol{u}^{(q)}) + \dot{m}_p^{(q)}\boldsymbol{u}^{(q)}, & \\ \mathrm{d}_t m^{(q)}\mathbb{E}^{(q)} & = & \frac{m^{(q)}}{\tau_{\boldsymbol{u}}^{(q)}}(\boldsymbol{u}_g \vee \boldsymbol{u}^{(q)} - 2\mathbb{E}^{(q)}) + \dot{m}_p^{(q)}\mathbb{E}^{(q)}, & \\ \mathrm{d}_t m^{(q)} h_{th}^{(q)} & = & C_{p,l}\frac{m^{(q)}}{\tau_T^{(q)}}(T_g - T^{(q)}) + \dot{m}_p^{(q)} h_{th}^{(q)}, & \end{array}\right. \qquad \forall q \in [1, N_q] \tag{5.14}$$

where $N_q = 4N_s$ is the number of quadratures generated.

Due to the assumption of Stokes regime and a constant evaporation rate $R_s^{(q)}$ for each quadrature point, the system (5.14) admits an analytic solution. We thus rewrite the (5.14) to obtain the evolution laws of $n^{(q)}$,$S^{(q)}$,$\boldsymbol{u}^{(q)}$,$T^{(q)}$ and $\boldsymbol{\Sigma}^{(q)} = 2\mathbb{E}^{(q)} - \boldsymbol{u}^{(q)}\otimes\boldsymbol{u}^{(q)}$. Remarking that $\mathrm{d}_t m^{(q)}\alpha = m^{(q)}\mathrm{d}_t\alpha + \alpha\dot{m}_p^{(q)} \quad \forall\alpha \in \left\{\boldsymbol{u}^{(q)}, h_{th}^{(q)}, \mathbb{E}^{(q)}\right\}$ to simplified (5.14) in a first step, then introducing the evolution law of $\boldsymbol{u}^{(q)}$ in the one of $\mathbb{E}^{(q)}$ to obtain the governing equation of $\boldsymbol{\Sigma}^{(q)}$ and using

the definition of $\dot{m}_p^{(q)}$ (2.14), we conclude:

$$\begin{cases} \mathrm{d}_t n^{(q)} &= 0, \\ \mathrm{d}_t m^{(q)} &= \dfrac{\rho_l}{4\sqrt{\pi}} R_s \left(S^{(q)}\right)^{1/2}, \\ \mathrm{d}_t \boldsymbol{u}^{(q)} &= \dfrac{\boldsymbol{u}_g - \boldsymbol{u}^{(q)}}{\mathcal{A}_{drag} S^{(q)}}, \\ \mathrm{d}_t \boldsymbol{\Sigma}^{(q)} &= \dfrac{-2\boldsymbol{\Sigma}^{(q)}}{\mathcal{A}_{drag} S^{(q)}}, \\ \mathrm{d}_t T^{(q)} &= \dfrac{T_g - T^{(q)}}{\mathcal{A}_{heat} S^{(q)}}, \end{cases} \qquad \forall q \in [1, N_q] \tag{5.15}$$

where we have $\tau_T^{(q)} = \mathcal{A}_{heat} S^{(q)}$ and $\tau_{\boldsymbol{u}}^{(q)} = \mathcal{A}_{drag} S^{(q)}$, which for a Stokes law (2.9) (2.11) leads to:

$$\mathcal{A}_{drag} = \frac{\rho_l}{18\pi\mu_g}, \qquad \mathcal{A}_{heat} = \mathcal{A}_{drag} \frac{3C_{p,l}}{2C_{p,g}} P_r. \tag{5.16}$$

5.3.3.2 Time evolution

Since one can remark in (5.16) that $\mathcal{A}_{drag}$ and $\mathcal{A}_{heat}$ are independent of the surface term S it is possible to solve (5.15) from the knowledge of $S^{(q)}(t)$ alone. Let $S^{(q)}(0) = S_0^{(q)}$, we directly have $S^{(q)}(t) = S_0^{(q)} + R_s\, t$ because of the constant rate $R_s^{(q)}$. Then, one can thus integrate (5.15) and obtain:

$$\begin{cases} \begin{cases} n^{(q)}(t) &= n_0^{(q)}, \\ m^{(q)}(t) &= m_0^{(q)} \left[\max\left(1 + \frac{R_s\, t}{S_0^{(q)}}\right)\right]^{3/2}, \\ \boldsymbol{u}^{(q)}(t) &= \boldsymbol{u}_g + (\boldsymbol{u}_0^{(q)} - \boldsymbol{u}_g)\left(1 + \frac{R_s\, t}{S_0^{(q)}}\right)^{\frac{-1}{\mathcal{A}_{drag} R_s^{(q)}}}, \qquad \text{if } R_s^{(q)} \in \mathbb{R}^*, \\ \boldsymbol{\Sigma}^{(q)}(t) &= \boldsymbol{\Sigma}^{(q)}{}_0 \left(1 + \frac{R_s\, t}{S^0}\right)^{\frac{-2}{\mathcal{A}_{drag} R_s^{(q)}}}, \\ T^{(q)}(t) &= T_g + (T_0^{(q)} - T_g)\left(1 + \frac{R_s\, t}{S_0^{(q)}}\right)^{\frac{-1}{\mathcal{A}_{heat} R_s^{(q)}}}, \end{cases} \\ \begin{cases} n^{(q)}(t) &= n_0^{(q)}, \\ m^{(q)}(t) &= m_0^{(q)}, \\ \boldsymbol{u}^{(q)}(t) &= \boldsymbol{u}_g + (\boldsymbol{u}_0^{(q)} - \boldsymbol{u}_g) \exp\left(\frac{-t}{\mathcal{A}_{drag} S_0^{(q)}}\right), \qquad \text{if } R_s^{(q)} = 0. \\ \boldsymbol{\Sigma}^{(q)}(t) &= \boldsymbol{\Sigma}^{(q)}{}_0 \exp\left(\frac{-2t}{\mathcal{A}_{drag} S_0^{(q)}}\right), \\ T^{(q)}(t) &= T_g + (T_0^{(q)} - T_g) \exp\left(\frac{-t}{\mathcal{A}_{heat} S_0^{(q)}}\right), \end{cases} \end{cases} \tag{5.17}$$

Such evolution is illustrated Figure 5.2c. We shall remark that, in case of evaporation, the

quadrature of the first subsection of the first section leads to negative density. It is however not necessary to compute the time evolution of these quadratures since they completely disappear in the gas. Therefore, the effects of these quadratures are only visible by computing again the moments.

5.3.3.3 Update of the solution

During that last step, we deduce the solution in a section k from the sum of the quadratures belonging to this section k at time $t^n+\Delta t$ (see Figure 5.2d). Let's denote $\boldsymbol{W}_{(i,j,k)}(t)$ the vector of conservative quantities deduced from the evolution of a quadrature during a time step according to (5.17) and $\boldsymbol{W}_k^n$ the vector of conservative quantities belonging to the section k at the time step n. Then, in the case of evaporation, the QKS leads to the update:

$$\boldsymbol{W}_k^{n+1} = \underbrace{\sum_{i=1}^{2} \boldsymbol{W}_{(i,2,k)}(\Delta t)}_{\substack{\text{Quadratures remaining} \\ \text{in section } k}} + \underbrace{\sum_{i=1}^{2} \boldsymbol{W}_{(i,1,k+1)}(\Delta t)}_{\substack{\text{Quadratures moving} \\ \text{to section } k}} \tag{5.18}$$

and for condensation:

$$\boldsymbol{W}_k^{n+1} = \underbrace{\sum_{i=1}^{2} \boldsymbol{W}_{(i,1,k)}(\Delta t)}_{\substack{\text{Quadratures remaining} \\ \text{in section } k}} + \underbrace{\sum_{i=1}^{2} \boldsymbol{W}_{(i,2,k-1)}(\Delta t)}_{\substack{\text{Quadratures moving} \\ \text{to section } k}} \tag{5.19}$$

Definition 5.2. A realizable scheme is a numerical method ensuring the conservation of the realizability conditions through a time step.

Proposition 5.1. Under CFL conditions, $R_s^{(k)} \frac{\Delta t}{\Delta S_k} \leq 1$ for any $k \in [1, N_S]$, the QKS is realizable.

Proof. Let a quadrature at t=0, $\boldsymbol{W}_{(i,j,k)}(0)$, considering the procedure described, we obviously have $S^{(k-1)} < S_0^{(i,j,k)} < S^{(k)}$ and the remaining values (velocities and temperature) are attributed to $\boldsymbol{W}_{(i,j,k)}(0)$ such that remaining realizability conditions are fulfilled. Indeed, the evolution of the quadratures (5.17) ensures that:

- $\|\boldsymbol{u}^{(q)}(t) - \boldsymbol{u}_g\| \leq \|\boldsymbol{u}^{(q)}(0) - \boldsymbol{u}_g\| \qquad \forall t > 0,$
- $\|T^{(q)}(t) - T_g\| \leq \|T^{(q)}(0) - T_g\| \qquad \forall t > 0,$
- $\sigma_{ii}^{(q)}(0) \leq \sigma_{ii}^{(q)}(t) \qquad \forall t > 0,,$
- $\frac{\sigma_{ij}^2}{\sigma_{ii}\sigma_{jj}} = cst.$

and thus realizability constraints are fulfilled by these variables.

Considering the droplet size moments, we can observed that the choice of summation (5.18) and (5.19) provides that:

$$\begin{cases} S^{(k-1)} < S_0^{(i,j,k)} + R_s\,\Delta t < S^{(k)}, & \text{for quadratures remaining in section } k, \\ S^{(k-1)} < S_0^{(i,j,k')} + R_s\,\Delta t < S^{(k)}, & \text{for quadratures moving to section } k \text{ from section } k', \end{cases} \tag{5.20}$$

As a consequence, each quadrature $\boldsymbol{W}_{(i,j,k)}(\Delta t)$ at $t = \Delta t$ belong to the moment space corresponding to the section of arrival. Thus, since either (5.18) and (5.19) are sums of realizable states, thank to the convexity of the moment space, $\boldsymbol{W}_k^{n+1}$ is realizable such as the scheme. □

The realizability of the method is a great advantage for numerical simulations where small characteristic relaxation time can appear, and evaporation can lead to the occurrence of empty sections. One can remark that this case is straightforwardly taken into account by the method through the kinetic evolution of the quadrature. As a consequence, the spray can completely evaporate and its dynamics resolved without any spurious effect while conserving a high level of accuracy (see Section 9.3). In addition, the explicit character of the methods is an advantage in terms of computational efficiency compared to implicit methods.

5.3.4 Two-way coupling

In the case of two-phase flow with an effective two-way coupling and non constant evaporation rate such as in Solid Rocket Motors, the quadrature evolution proposed in Section 5.3.3 needs either to be derived again or adapted. It is thus proposed to use this simplified procedure as the building block of more complex models. Additionally, in the case of complex drag, heat transfer and evaporation laws such as for combustion cases, the following modifications of the assumption are thus considered:

1. The coefficients $\mathcal{A}_{drag}$ and $\mathcal{A}_{heat}$ can be corrected, by a Ranz-Marshall law for instance, and thus can depend on size,

2. For each quadrature R_s, $\mathcal{A}_{drag}$ and $\mathcal{A}_{heat}$ are considered constant during their evolution on a time step and deduced for the condition of the quadratures at the beginning of the time step, thus according to $S_0^{(i,j,k)}$.

Using these new assumptions, the evolution of the quadratures already presented can be used as an approximation of the solution on a given time step. These however only describe the evolution of the disperse phase. Therefore, applying the global mass, momentum and energy conservation on the gas-droplet mixture and relying on the hypothesis [HG], the reciprocal effect

of the coupling on the gas can be deduced:

$$\begin{cases} \rho_g^{n+1} & = \rho_g^n + \sum_{q=1}^{N_q} m_0^{(q)} - \sum_{q=q_{min}}^{N_q} m^{(q)}(\Delta t) \\ (\rho_g \boldsymbol{u}_g)^{n+1} & = (\rho_g \boldsymbol{u}_g)^n + \sum_{q=1}^{N_q} m_0^{(q)} \boldsymbol{u}_0^{(q)} - \sum_{q=1}^{N_q} m^{(q)}(\Delta t) \boldsymbol{u}^{(q)}(\Delta t) \\ (\rho_g E)^{n+1} & = (\rho_g E)^n + \sum_{q=1}^{N_q} m_0^{(q)} \left[h_{th,0}^{(q)} + \mathrm{tr}\left(\mathbb{E}_0^{(q)}\right)\right] - \sum_{q=1}^{N_q} m^{(q)}(\Delta t) \left[h_{th}^{(q)}(\Delta t) + \mathrm{tr}\left(\mathbb{E}^{(q)}(\Delta t)\right)\right] \end{cases} \tag{5.21}$$

Finally, in order to take into account non-linearity of both the two-way coupling and physical laws contained in R_s, $\mathcal{A}_{drag}$ and $\mathcal{A}_{heat}$, the procedure is embedded in a SSPRK3 time integration method (5.9) as for the $\boldsymbol{\mathcal{L}}$ operator. Since each new state of a quadrature provides a realizable state and the Runge-Kutta procedure can be expressed as a convex combination of these, the method proposed is realizable and therefore highly robust.

Chapter 6

Numerical schemes for transport operators

> There are at least two ways to combat stiffness. One is to design a better computer, the other, to design a better algorithm.
>
> R. Lomax, Aiken, 1985

This chapter is dedicated to the numerical methods designed and tested throughout this work to solve the transport operators for both the carrier and the disperse phases. The governing equations of these operators are essentially hyperbolic and parabolic. As a consequence, even considering the weak hyperbolicity of the MK closure, similar numerical methods can theoretically be used for the various systems considered. In practice however, due to non-linearities and the studied flow regimes, strong singularities can be observed. Therefore, according to the studied system of equations, a dedicated design of the numerical methods is needed to ensure the quality of the solution. The parabolic terms associated to the viscous contributions of the Navier-Stokes equations is treated separately.

The large size of this chapter are explained by the elements and developments presented in it and that constitutes the core of the work conducted during the thesis. Across this review of the numerical schemes, contributions are proposed and detailed. By order of apparition, these new developments are the following:

- A general formulation of Finite Volume schemes for hyperbolic conservation laws is established and a solution to compute exactly and explicitly the geometrical terms involved is proposed in Section 6.2.4,
- The HLL flux is derived in Section 6.3.3.3 in an original way to take into account the axisymmetric character of the geometry,
- For the governing equations targeted, a robust second order accurate MUSCL multislope strategy, valid in multi-dimensional frameworks including the 2D axi-symmetrical one and

for general unstructured meshes, is proposed in Section 6.4.2,

- In Section 6.4.2.2, an original limiter for the MUSCL multislope method is derived making use of the local geometry to improve its accuracy,

- Under specific conditions, fulfilled by this last class of numerical methods, a proof of realizability is proposed in Section 6.4.3 in the context of high order Finite Volume schemes.

Numbers of others subjects are discussed. These have been either considered, used without specific development or envisioned for future work. All these features are presented for a point of view specific to this work that aims at solving very non-linear problem with a high level of accuracy while ensuring an unfailing robustness in the context of general unstructured meshes.

The chapter is thus organized as follow: Section 6.1 proposes a brief overview of the different categories of numerical methods dedicated to the resolution of PDEs. Focusing on the description of these schemes for hyperbolic problems and the issues concerning the simulations of disperse flows, key notions and properties are introduced. Section 6.2 is dedicated to the formulation of the Finite Volume (FV) framework in a multidimensional context. This development is proposed for several classes of meshes and various dimensions including a 2D-axisymmetric framework. Additionally, an accurate methodology to compute the geometric terms is proposed. Section 6.3 details the expression of the numerical fluxes, key components of the schemes for the resolution of hyperbolic systems of conservation laws. Then Section 6.4 presents a MUSCL scheme dedicated to each studied system and dimensional frameworks. This development is conducted such that the scheme ensures the realizability of the solution. Finally, Section 6.5 briefly details the method used to solve the viscous terms appearing in the model of the carrier phase. This chapter does not treat the question of the boundary conditions and related issues that is the subject of the next chapter.

6.1 Transport operator generalities

To solve the equations of the transport operator, it is first needed to discretize the physical space. After briefly detailing the major classes of existing schemes, basic properties of numerical methods are discussed.

6.1.1 Classes of methods

Before entering in the details of the construction of a numerical scheme, we here propose to specify the framework on which the solution is represented and that obviously strongly influences the construction of a numerical method. Among the classes of methods, one can observe three major categories (Ferziger and Peric 2012): the Finite Difference (FD) methods, Finite Volume (FV) methods and Finite Element Method (FEM) to which we add the Discontinuous Galerkin (DG) methods (Cockburn, Karniadakis, and Shu 2000) and that is actually a subclass of FEM. Such review is far from being exhaustive and we refer to the various monographs cited along the discussion for more details on this subject.

6.1.1.1 Finite Difference (FD) methods

These methods are the oldest known and are believed to have been used for the first time by Euler in the XVIIIth century (Ferziger and Peric 2012). This is also the easiest class of methods to implement. As a starting point, we consider the conservation equations under its differential form. Considering one-dimensional hyperbolic systems of conservation laws, the studied differential equations can be put under the form:

$$\partial_t \boldsymbol{W} + \partial_x \boldsymbol{f}(\boldsymbol{W}) = 0 \tag{6.1}$$

Mapping the physical space with a grid, the solution is represented point-wise at each node i. Thus, $\boldsymbol{W}_i^n$ approximates the exact solution $\boldsymbol{W}(x,t)$ at a node i of position x_i and at the time step n of time t^n and is defined as:

$$\boldsymbol{W}_i^n \simeq \boldsymbol{W}(x_i, t^n) \tag{6.2}$$

Then, the key aspect of the FD method is to approximate the spatial derivatives with finite difference approximations (LeVeque 2007). Classical space difference approximations for regular space discretization can be found in (Richardson 1954; Jordán 1965; Smith 1985) among others and in (Fornberg 1988) for non-uniform grid. For the sake of brevity, we here only retain central, forward and backward finite differences that approximate a k^{th} derivative on a uniform grid as:

$$\begin{aligned}
&[\partial_x \boldsymbol{f}(\boldsymbol{W})]_i^n \simeq \tilde{\delta}_i^k [\boldsymbol{f}(\boldsymbol{W})]^n \\
&= \begin{cases}
\delta_i^k[\boldsymbol{f}(\boldsymbol{W})]^n &= \frac{1}{\Delta x^k} \sum_{j=0}^k C_k^j (-1)^j \boldsymbol{f}\left(\boldsymbol{W}_{i+(k/2-j)}^n\right) \quad \text{(Central difference)} \\
\Delta_i^k[\boldsymbol{f}(\boldsymbol{W})]^n &= \frac{1}{\Delta x^k} \sum_{j=0}^k C_k^j (-1)^j \boldsymbol{f}\left(\boldsymbol{W}_{i+j}^n\right) \quad \text{(Forward difference)} \\
\nabla_i^k[\boldsymbol{f}(\boldsymbol{W})]^n &= \frac{1}{\Delta x^k} \sum_{j=0}^k C_k^j (-1)^j \boldsymbol{f}\left(\boldsymbol{W}_{i-j}^n\right) \quad \text{(Backward difference)}
\end{cases}
\end{aligned} \tag{6.3}$$

where $[\bullet]_i^n$ indicate the exact solution of a continuous field at a position i and time step n, Δx is the distance between two nodes and $C_n^p = \frac{n!}{p!(n-p)!}$.

For unsteady problems, aspects related to the time derivative have also to be treated. To do so, two time stepping procedures, inspired from the ODE literature (Hairer, Nørsett, and Wanner 1993a; Hairer and Wanner 1996a), are generally considered:

- **Taylor expansion**: With the objective of avoiding intermediate steps, a Taylor expansion of $\partial_t \boldsymbol{W}_i^n$ is derived and high order time derivatives are expressed as spatial differences thanks to (6.1) (see Section 6.3.1.1.1 for an example of it). Using a truncation at first order, one can find the Euler forward method.

- **Multi-stage strategy**: Starting from this Euler forward form, the method is embedded in an RK procedure (see Section 5.2.2) or intermediate approximations are used (see Section 6.3.1.4 for an example).

On Cartesian grid, this class of method is very simple to integrate, effective and can be easily

extended to high order. However, several drawbacks are known:

- The conservation of the scheme is not necessarily ensured, especially for non-uniform grid,
- Their formulations are generally restricted to simple geometry,
- Spurious oscillations are observed on the great majority of the scheme of order 2 or higher, as soon as the regularity of the solution is not ensured.

A selection of FD methods is detailed Section 6.3.1.

6.1.1.2 Finite Volume (FV) methods

From another point of view, FV methods propose to solve the problem under its integrated form taking advantage of the property of conservation of the governing equations aimed at being solved (Godlewski and Raviart 1996; Fornberg 1988). For one dimensional configuration, it is thus needed to specify the positions $x_{i+1/2}$ at the interface of cells i and $i+1$. Then starting from (6.1) and integrating on the cell then using the Green formula, one can obtain:

$$\partial_t \int_{x_{i-1/2}}^{x_{i+1/2}} \boldsymbol{W} \mathrm{d}x + \int_{x_{i-1/2}}^{x_{i+1/2}} \partial_x \boldsymbol{f}\left(\boldsymbol{W}\right) \mathrm{d}x = 0$$
$$\Leftrightarrow \mathrm{d}_t \boldsymbol{W}_i + \frac{1}{\Delta x_i}\left[\boldsymbol{f}\left(\left[\boldsymbol{W}\right]_{x_{i+1/2}}\right) - \boldsymbol{f}\left(\left[\boldsymbol{W}\right]_{x_{i-1/2}}\right)\right] = 0 \quad (6.4)$$

where we define the average $\boldsymbol{W}_i$ of the quantities belonging to the cell such that:

$$\boldsymbol{W}_i = \frac{1}{\Delta x_i}\int_{x_{i-1/2}}^{x_{i+1/2}} \boldsymbol{W}(x,t)\mathrm{d}x \quad (6.5)$$

Starting from this integrated form (6.4) and using an Euler forward time integration, one can obtain the general form of FV methods:

$$\boldsymbol{W}_i^{n+1} = \boldsymbol{W}_i^n - \frac{\Delta t}{\Delta x_i}\left[\mathfrak{F}_{i+1/2} - \mathfrak{F}_{i-1/2}\right] \quad (6.6)$$

where $\mathfrak{F}_{i+1/2}$ is the numerical flux between cells i and $i+1$ at position $x_{i+1/2}$ and $\boldsymbol{W}_i^n = \frac{1}{\Delta x_i}\int_{x_{i-1/2}}^{x_{i+1/2}} \boldsymbol{W}(x,t^n)\mathrm{d}x$ are the variables of the problem.

A great advantage of this kind of formulation is that it can be easily generalized to multidimensional framework. To do so, we consider computational domain Ω tessellated in a finite number of non-self-intersecting polygons C_i such that $C_i \subset \Omega$, $C_i \cap C_j = \emptyset$ and $\sum_i C_i = \Omega$. In

multidimensional Cartesian coordinates, (6.6) can be generalized in:

$$\boldsymbol{W}_i^{n+1} = \boldsymbol{W}_i^n - \frac{\Delta t}{|C_i|} \sum_{j \in \mathcal{V}_i} |S_{ij}| \, \mathfrak{F}_{ij} \tag{6.7}$$

where $\mathcal{V}_i$ is the set of cells sharing an edge with the cell i, $|C_i|$ is the size of the cell i (length in 1D, surface in 2D and volume in 3D) and $|S_{ij}|$ the size of the interface between cells i and j (without dimension in 1D ($|S_{ij}| = 1$), length in 2D and surface in 3D cases).

In the case of axisymmetry, the integrals (6.4) and (6.5) are changed because of the radial position parameter and the source terms, influencing the relation (6.7). We refer to Section 6.2 for more details on this integration procedure for multidimensional frameworks, especially in the 2D axisymmetric case.

FV schemes are thus genuinely defined by the expression of the numerical flux $\mathfrak{F}_{ij}$ between two cells that make them conservative. Also, conservative FD schemes can be expressed as under the form (6.6) and thus be compared to FV methods or defined again and generalized in this context (see Section 6.3.1.5 for instance). Additionally to the conservation property, FV schemes have several advantages compared to FD methods:

- Their formulation can be generalized to complex geometry and any kind of mesh,
- It is possible to provide oscillation free and realizable methods through this framework.

The main disadvantage of this class of methods lies in its extension to order of convergence higher than 2, especially for multidimensional framework.

6.1.1.3 Finite Element Methods (FEMs)

The FEMs are similar to the FV methods in the sense that they are defined through the weak formulation of the problem. The main difference lies in the representation of the solution that is weighted by a function in the case of FEM. As a consequence, the solution is approximated under the following form:

$$\boldsymbol{W}(\boldsymbol{x}, t) \simeq \boldsymbol{W}_h(\boldsymbol{x}, t) = \sum_{j=1}^{N_{dof}} \boldsymbol{W}^j(t) \phi^j(\boldsymbol{x}) \tag{6.8}$$

where ϕ^j are the weight functions, $\boldsymbol{W}^j$ are the solution represented at each node, N_{dof} is the number of degrees of freedom of the problem, the number of unknown (and eventually nodes)

considered and, by definition, $\boldsymbol{W}_h(\boldsymbol{x},t)$ verifies:

$$\int_\Omega \left[\partial_t \boldsymbol{W}_h + \mathbf{div}_{\boldsymbol{x}}\left(\boldsymbol{\mathcal{F}}(\boldsymbol{W}_h)\right)\right]\phi^i(\boldsymbol{x})\mathrm{d}\boldsymbol{x} = 0 \quad \forall i \in [\![1, N_{dof}]\!] \tag{6.9}$$

Then, the discretized system of equations to be solved is obtained by combining (6.8) and (6.9) and by proceeding to an integration by part. This leads to:

$$\sum_{j=1}^{N_{dof}} \int_\Omega \left(\phi^j(\boldsymbol{x})\phi^i(\boldsymbol{x})\right)\mathrm{d}\boldsymbol{x}\mathrm{d}_t\boldsymbol{W}^j(t) - \int_\Omega \left[\boldsymbol{\mathcal{F}}(\boldsymbol{W}_h(t,\boldsymbol{x}))\cdot\nabla_{\boldsymbol{x}}\phi^i(\boldsymbol{x})\right]\mathrm{d}\boldsymbol{x} + \underbrace{\int_{\partial\Omega}\phi^i(\boldsymbol{s})\boldsymbol{\mathcal{F}}(\boldsymbol{W}_h(t,\boldsymbol{s}))\mathrm{d}\boldsymbol{s}}_{\text{Boundary conditions}} = 0 \quad \forall i \in [\![1, N_{dof}]\!] \tag{6.10}$$

Letting the boundary conditions apart for now and considering we hold for the system of equation $\boldsymbol{\mathcal{F}}(\boldsymbol{W}_h(t,\boldsymbol{x})) = \sum_{j=1}^{N_{dof}} \boldsymbol{\mathcal{F}}(\boldsymbol{W}^j(t))\phi^j(\boldsymbol{x})$ (otherwise quadratures shall be used), the problem can be reduced under the form:

$$(\mathcal{M}_e)_{ij}\,\mathrm{d}_t\boldsymbol{W}^j(t) - (\mathcal{C}_e)^t_{ij}\cdot\boldsymbol{\mathcal{F}}(\boldsymbol{W}^j(t)) = 0 \tag{6.11}$$

where mass matrix $\mathcal{M}_e$ and convection matrix $\mathcal{C}_e$ are defined as

$$(\mathcal{M}_e)_{ij} = \int_\Omega \left(\phi^j(\boldsymbol{x})\phi^i(\boldsymbol{x})\right)\mathrm{d}\boldsymbol{x} \qquad (\mathcal{C}_e)_{ij} = \int_\Omega \left(\phi^j(\boldsymbol{x})\nabla_{\boldsymbol{x}}\phi^i(\boldsymbol{x})\right)\mathrm{d}\boldsymbol{x} \tag{6.12}$$

Usually, the weight functions ϕ^j are linear elements between nodes forcing the continuity but higher order elements can also be considered. Then, providing a correct time integration scheme, the FEM consists in solving the linear problem (6.11).

In practice, for convection dominating flows, several issues on stability can arise and specific stabilization methods or formulation of the problem are necessary. Among them, one can remark the Taylor-Galerkin class of schemes (Donea 1984; Colin and Rudgyard 2000) that can be interpreted as a proper extension of FD schemes in multidimensional frameworks. The formulation of these methods relies on a Taylor expansion in time of the governing equation (see an example in Section 6.3.1.1.1) and an expression of the gradients and Laplacians thanks to the Finite Element (FE) description of the problem. Such methods are not investigated in this work and we refer to (Donea and Huerta 2003) for more details on this subject.

6.1.1.4 Discontinuous Galerkin (DG) methods

Part of the FEM, DG methods can be seen as a combination of the FV and FE methods (Raviart and Thomas 1977; Hesthaven and Warburton 2007). To do so, it is aimed at representing a continuous high order solution inside each elements covering a cell and considering the existence of discontinuities between these cells. Such form can be derived from the previous formulation using well chosen weight functions, but this genuine consideration of discontinuities induces the need of a numerical flux $\mathfrak{F}_{ij}$ that can be taken from FV methods. Then, considering N_{dof} degree of freedom in each element k, we define again the form of the solution as:

$$\boldsymbol{W}(\boldsymbol{x},t) \simeq \boldsymbol{W}_h(\boldsymbol{x},t) = \sum_{k=1}^{N_e} \mathbb{1}_k(\boldsymbol{x}) \sum_{j=1}^{N_{dof}} \boldsymbol{W}_k^j(t)\phi_k^j(\boldsymbol{x}), \qquad \mathbb{1}_k(\boldsymbol{x}) = \begin{cases} 1, & \text{if } \boldsymbol{x} \in C_k \\ 0, & \text{otherwise} \end{cases} \tag{6.13}$$

where N_e is the number of considered elements.

Proceeding as above, on can obtain a problem under the form:

$$(\mathcal{M}_e)_{ijk}\, \mathrm{d}_t \boldsymbol{W}_k^j(t) - (\mathcal{C}_e)_{ijk}^t \cdot \boldsymbol{\mathcal{F}}(\boldsymbol{W}_k^j(t)) + \underbrace{\int_{\partial C_k} \phi_k^i(\boldsymbol{s}) \mathfrak{F}(\boldsymbol{W}_{h,k}^{in}(t,\boldsymbol{s}), \boldsymbol{W}_{h,k}^{out}(t,\boldsymbol{s}))\mathrm{d}\boldsymbol{s}}_{\text{inter-element exchanges}} = 0 \tag{6.14}$$

where $\boldsymbol{W}_{h,k}^{in}(t,\boldsymbol{s})$ and $\boldsymbol{W}_{h,k}^{out}(t,\boldsymbol{s})$ are the values obtained at the boundary of the element from the knowledge from respectively the inside and the outside of the element k.

Here, since a problem is inverted in each element, we introduce a numerical flux between each elements (or cells) which is a feature distinct from the boundary conditions. Depending on the form of weight function $\phi_k^j(\boldsymbol{x})$ chosen, the method can be said to be *modal* ($\phi_k^j(\boldsymbol{x})$ is an orthogonal basis) or *nodal* ($\phi_k^j(\boldsymbol{x})$ are Lagrange polynomials and $\boldsymbol{W}_k^j(t)$ are associated to quadratures) Also, since considering a uniform weight function $\phi_k^j(\boldsymbol{x}) = \mathbb{1}_k(\boldsymbol{x})$, one can derive again an FV method, it is possible to interpret DG methods as an high order extension of FV.

Despite effort have been provide to enhance the robustness of the DG methods (Zhang and Shu 2010a; Zhang, Xia, and Shu 2012) to a satisfactory level, even for two-phase flows (Sabat et al. 2014), such option did not have been investigated because of the architecture of the CFD code used for this work (see Chapter 8). We refer to (Cockburn, Karniadakis, and Shu 2000) for more details on the origins and developments of the DG methods.

6.1.1.5 Other classes of methods

The classes of methods described until here rely on the existence of a fixed mesh (or grid). This usual assumption is not mandatory and several extension of these schemes or numerical methods based on completely different approaches exist. Among them, we remark particularly the following ones:

- **Arbitrary Lagrangian-Eulerian (ALE):** FV methods adapted to a moving meshes

(Benson 1992; Hirt, Amsden, and Cook 1974), typically fitted for moving geometries, as in automotive engines (Emre et al. 2015; Kah et al. 2015). In addition, Lagrange-remap methods rely on a mesh moving at material velocity, splitting acoustic and convection terms (Duboc et al. 2010; Bernard-Champmartin and De Vuyst 2014; Chalons and Girardin 2016),

- **Adaptive meshes:** Based on the pioneer work of (Berger and Oliger 1984), Adaptive Mesh Refinement (AMR) consists in successive local refinements of coarse grid in order to limit the dissipation of the method. Refinement, through patch (patch based AMR) or octree (cell based AMR) typically, is generally conducted through the detection of high gradients in the solution. Also, *multiresolution* methods, as introduced by (Harten 1994) and in many point similar to cell based AMR, project fine grid solution on a coarser overlaping grid in order to evaluate the need of adaptive refinement of the mesh and provide an error control.

- **Semi-lagrangian methods:** To take advantage of the properties of a Lagrangian modeling (see Section 2.3.3) and associated numerical methods (Falcone and Ferretti 1998; Xiu and Karniadakis 2001), the Eulerian FV solution is sampled in well chosen representative Lagrangian sample (or quadratures). These are transported inside the grid thanks to a Lagrangian methods and the solution is projected on the Eulerian FV description of the problem for the resolution of the source term coupling operator. Despite a high robustness, such formulation remain today first order accurate for our applications (Doisneau, Arienti, and Oefelein 2017b; Doisneau, Arienti, and Oefelein 2017a). Higher order formulations exists (Cottet et al. 2014) but face realizability issues.

- **Meshfree methods:** It is possible to design methods without the need of a mesh. They however rely on particle or point-wise descriptions of the solution to which can be associated interpolations. We refer to (Liu and Gu 2005) for more details on that field.

6.1.2 Properties of numerical methods for transport equations

In Chapter 5 some properties of the numerical methods were already presented form a general perspective, including the definition of the realizability of a method. Such definitions are here completed in the context of numerical schemes for the transport operators in a multidimensional physical space and additional specificities are given in the context of FV schemes. Discussion is oriented on the abilities of the four main classes of methods described until here. After defining a way to compare solutions one to another, stability and accuracy of numerical methods are defined with a focus on the consequence of these definitions on the numerical flux.

6.1.2.1 Norm of a solution

Definition 6.1 (FV projection operator)**.** Let $\boldsymbol{W}(\boldsymbol{x},t)$ be a solution, we define $\mathscr{H}_i$ the operator projecting the solution on the cell C_i of a mesh such that:

$$\mathscr{H}_i(\boldsymbol{W}(\boldsymbol{x},t)) = \frac{1}{|C_i|}\int_{C_i} \boldsymbol{W}(\boldsymbol{x},t)\mathrm{d}\boldsymbol{x} \tag{6.15}$$

Thanks to that operator $\mathscr{H}_i$, it is possible to compare an exact solution to an approximate one $\boldsymbol{W}_h(\boldsymbol{x},t)$. For FEM and DG frameworks, these approximations are defined by (6.8) and (6.13). Also, for FV and FD methods, we consider:

$$\boldsymbol{W}_h(\boldsymbol{x},t^n) = \sum_i \boldsymbol{W}_i^n \mathbb{1}_k(\boldsymbol{x}) \tag{6.16}$$

Which is an exact definition in FV framework but an adapted one for FD methods since the problem is approximated point-wise. As a consequence, we get:

$$\begin{cases} \mathscr{H}_i(\boldsymbol{W}_h(\boldsymbol{x},t^n)) = \boldsymbol{W}_i^n, & \text{for FD and FV} \\ \mathscr{H}_i(\boldsymbol{W}_h(\boldsymbol{x},t^n)) = \sum_{j=1}^{N_{dof}} \boldsymbol{W}_i^j(t) \frac{\int_{C_i} \phi_i^j(\boldsymbol{x})\mathrm{d}\boldsymbol{x}}{|C_i|}, & \text{for DG} \end{cases} \tag{6.17}$$

For general FEM methods, $\mathscr{H}_i(\boldsymbol{W}_h(\boldsymbol{x},t^n))$ depends on the form of the chosen elements. For the sake of legibility, we also use the notation $\mathscr{H}(\boldsymbol{W}(\boldsymbol{x},t^n))$ to define the solution projected on a finite volume mesh and also for FV schemes we get $\mathscr{H}(\boldsymbol{W}_h(\boldsymbol{x},t^n)) \equiv \boldsymbol{W}^n$. This formalism is necessary while comparing FD, FV and FEM methods and their properties since they are based on nonequivalent representations of the solution.

Definition 6.2 (FV norm)**.** Let $\|\bullet\|_L$ be a norm of a vector space, then the norm of a solution $\mathscr{H}(\boldsymbol{W}(\boldsymbol{x},t))$ in a FV domain Ω is defined as:

$$\|\mathscr{H}(\boldsymbol{W}(\boldsymbol{x},t))\|_L = \sum_{C_i \subset \Omega} \|\mathscr{H}_i(\boldsymbol{W}(\boldsymbol{x},t))\|_L |C_i| \tag{6.18}$$

6.1.2.2 Method consistency, stability and convergence

Definition 6.3 (Local truncation error)**.** We define the *local truncation error* as the error to an exact solution $\boldsymbol{W}(\boldsymbol{x},t^{n+1})$ produced by an scheme, described by operator $\boldsymbol{\mathcal{T}}$, starting from $\boldsymbol{W}^n$ (expressed either in the FD, FV orFEM framework) such that $\mathscr{H}(\boldsymbol{W}^n) = \mathscr{H}(\boldsymbol{W}(\boldsymbol{x},t^n))$ as:

$$\epsilon^n = \frac{1}{\Delta t}\left[\mathscr{H}\left(\boldsymbol{W}(\boldsymbol{x},t^{n+1})\right) - \mathscr{H}\left(\boldsymbol{\mathcal{T}}(\Delta t)\boldsymbol{W}^n\right)\right] \tag{6.19}$$

Definition 6.4 (Consistent scheme)**.** A scheme is *consistent* for a norm L if:

$$\forall n;\, t^n < T, \quad \lim_{\Delta t \to 0} \|\epsilon^n\|_L \to 0 \tag{6.20}$$

Definition 6.5 (Global error)**.** The *global error* is defined as the net difference of approximation $\boldsymbol{W}_h$ to an exact solution $\boldsymbol{W}$ on a given mesh, such that:

$$E_i^n = \mathscr{H}_i(\boldsymbol{W}_h(\boldsymbol{x},t^n)) - \mathscr{H}_i(\boldsymbol{W}(\boldsymbol{x},t^n)) \tag{6.21}$$

Obviously, the objective of a numerical scheme is to reduce this *global error* to the minimum. It is expected from a scheme to tend toward an exact solution as the time step diminishes

together with the cell size that can be associated to a grid length h representative of the mesh discretization.

Definition 6.6 (Convergence)**.** Let a time step Δt and a grid length h be linearly proportional (typically through a CFL condition), then the method is convergent if:

$$\lim_{\substack{\Delta t \to 0 \\ h \to 0}} \|E^n\| = 0 \tag{6.22}$$

Additionally the method accuracy is assessed remarking that:

Definition 6.7 (Order of convergence)**.** In conditions of convergence, there exists C and α reals such that:

$$\|E^n\| \sim Ch^\alpha \tag{6.23}$$

where α is the order of accuracy of the method.

As a complement to stability and accuracy, we wish to conserve the monotonicity of the solution that shall be fulfilled if the system of equations satisfies a maximum principle at the PDE level. This especially applies to linear advection, the Burgers equation (3.13) and the velocity field of the PGD (3.12).

Property 6.1 (Monotonicity)**.** If the dynamics of the scalar field w in Ω is monotone, then:

1. No new spatial local extrema in Ω shall be created,
2. Local minimum are non-decreasing and local maximum are non-increasing.

Property 6.2 (Monotone scheme)**.** According to (LeVeque 1992), a scheme under the form

$$w_i^{n+1} = H(w_{i-k_l+1}^n, \dots, w_{i+k_r+1}^n) \tag{6.24}$$

where k_l and k_r are non-negative integers, is said monotone if:

$$\frac{\partial H}{\partial w_j^n} \geq 0 \qquad \forall j. \tag{6.25}$$

To evaluate the ability of a scheme to fulfill this property, Harten (Harten 1983) proposed the following measure:

Definition 6.8 (Total variation)**.** Let w be a scalar function on Ω, then the total variation of w is:

$$TV(w) = \sup \left\{ \int_\Omega \|w \mathrm{div}_{\boldsymbol{x}}(\varphi)\| \mathrm{d}\boldsymbol{x};\ \varphi \in C_0^1(\Omega),\ \|\varphi\|_\infty \leq 1 \right\} \tag{6.26}$$

For a one-dimensional case with uniform discretization, where $w^n = (w_i^n)_{i\in\mathbb{Z}}$ approximate :

$$TV(w^n) = \sum_{i\in\mathbb{Z}} |w_{i+1}^n - w_i^n| \tag{6.27}$$

As a consequence, if the field v fulfills Property 6.1, then the total variation is non-increasing.

Thus, it is wished that the scheme respects this same characteristic.

Definition 6.9 (Total Variation Diminishing (TVD) scheme)**.** Let a scheme approximating $w(t^n, \boldsymbol{x})$ with a sequence $w^n = (w_i^n)_{i\in\mathbb{Z}}$ defined on Ω. Then, this scheme is TVD if the total variation of w^n is a time decreasing function such that:

$$TV\left(w^{n+1}\right) \leq TV\left(w^n\right) \tag{6.28}$$

For multidimensional problems however, it appears that this formulation of the regularity is not optimal and one can refer to (Jameson 1995a) for an applied example. Therefore, another definition can be proposed to assess the ability of a scheme to ensure the regularity of a solution.

Definition 6.10 (Local Extrema Diminishing (LED) scheme)**.** A scheme is Local Extrema Diminishing (LED) if for a scalar w in Ω if:

$$\exists c_{ij}^n \geq 0, \quad w_i^{n+1} - w_i^n = \sum_{j\in\mathcal{V}_i} c_{ij}^n \left(w_j^n - w_i^n\right), \qquad c_{ij}^n \geq 0 \tag{6.29}$$

We generalize this definition to systems of conservation laws with

$$\exists c_{ij}^n \geq 0, \quad \boldsymbol{W}_i^{n+1} - \boldsymbol{W}_i^n = \sum_{j\in\mathcal{V}_i} c_{ij}^n \left(\boldsymbol{W}_j^n - \boldsymbol{W}_i^n\right), \qquad c_{ij}^n \geq 0 \tag{6.30}$$

Proposition 6.1. A LED scheme is a monotone scheme.

Also, one can deduce from Definition 6.10 that any maximum is decreasing and any minimum is increasing. We also define the complementary condition that follow:

Definition 6.11 (convexity condition)**.** A LED scheme fulfills the convexity condition, if:

$$\forall i, \qquad \sum_{j\in\mathcal{V}_i} c_{ij}^n \leq 1 \tag{6.31}$$

Proposition 6.2. If $\boldsymbol{W}$ belongs to a convex space, then a LED scheme fulfilling convexity condition is realizable.

Proof. Merging (6.30) and (6.31), one find $\boldsymbol{W}_i^{n+1}$ as a convex combination of states $\boldsymbol{W}_i^n$ and $\boldsymbol{W}_j^n$, $\forall j \in \mathcal{V}_i$. Therefore, since $\boldsymbol{W}$ belong to a convex space, $\boldsymbol{W}_i^{n+1}$ is realizable. □

Finally, according to the governing conservation laws, we add as a constraint that the quantities stored in the conservative vector $\boldsymbol{W}_i^n$ are globally conserved across the computational domain.

Definition 6.12 (Conservative scheme)**.** A scheme is *conservative* if it conserves the total among of the conserved quantities belonging to $\boldsymbol{W}$ on the domain Ω. More precisely, if a FV scheme is conservative, one can write:

$$\sum_i |C_i|\, \boldsymbol{W}_i^{n+1} = \sum_i |C_i|\, \boldsymbol{W}_i^n + \boldsymbol{W}_{\partial\Omega}^n \tag{6.32}$$

where $\boldsymbol{W}_{\partial\Omega}^n$ is the among of conserved quantity exchanged with the outside of the domain between the time steps n and $n+1$.

6.1.2.3 Numerical flux property

Definition 6.13 (Conservative numerical flux)**.** A numerical flux $\mathfrak{F}_{ij}$ from the cell i to the cell j is conservative if $\mathfrak{F}_{ij} = \mathfrak{F}_{ji}$.

In general, the numerical flux depends on two states $\boldsymbol{W}_{ij}$ and $\boldsymbol{W}_{ji}$ representing the solution on each side of a discontinuity, associated to the cell interface, and a normal vector $\overrightarrow{\boldsymbol{n}}_{ij}$ indicating the direction of the discontinuity. In such a case, we state that the numerical flux is conservative if:

$$\mathfrak{F}\left(\boldsymbol{W}_{ij}, \boldsymbol{W}_{ji}, \overrightarrow{\boldsymbol{n}}_{ij}\right) = \mathfrak{F}\left(\boldsymbol{W}_{ij}, \boldsymbol{W}_{ji}, -\overrightarrow{\boldsymbol{n}}_{ij}\right) \tag{6.33}$$

As observed by (LeVeque 2002), one can expect from such flux to provide the effective flux $\boldsymbol{\mathcal{F}}$ if the solution is uniform

Definition 6.14 (Basic numerical flux consistency)**.** A numerical flux $\mathfrak{F}$ is said to be consistent if for a uniform state $\overline{\boldsymbol{W}}$, the flux fulfills:

$$\mathfrak{F}\left(\overline{\boldsymbol{W}}, \overline{\boldsymbol{W}}, \overrightarrow{\boldsymbol{n}}_{ij}\right) = \boldsymbol{\mathcal{F}}\left(\overline{\boldsymbol{W}}\right) \cdot \overrightarrow{\boldsymbol{n}}_{ij} \tag{6.34}$$

Additionally, as observed in (LeVeque 2002), one can expect some continuity from the numerical flux function such that $\mathfrak{F}\left(\boldsymbol{W}_{ij}, \boldsymbol{W}_{ji}, \overrightarrow{\boldsymbol{n}}_{ij}\right) \to \boldsymbol{\mathcal{F}}\left(\overline{\boldsymbol{W}}\right) \cdot \overrightarrow{\boldsymbol{n}}_{ij}$ as $\boldsymbol{W}_{ij}, \boldsymbol{W}_{ji} \to \overline{\boldsymbol{W}}$. Thus one can impose a Lipschitz continuity on $\mathfrak{F}$.

Definition 6.15 (Numerical flux consistency)**.** A numerical flux $\mathfrak{F}_{ij}$ is consistent if:

$$\exists L > 0, \quad \text{such that} \quad \|\mathfrak{F}\left(\boldsymbol{W}_{ij}, \boldsymbol{W}_{ji}, \overrightarrow{\boldsymbol{n}}_{ij}\right) - \boldsymbol{\mathcal{F}}\left(\overline{\boldsymbol{W}}\right) \cdot \overrightarrow{\boldsymbol{n}}_{ij}\| \leq L \max\left(\|\boldsymbol{W}_{ij} - \overline{\boldsymbol{W}}\|, \|\boldsymbol{W}_{ji} - \overline{\boldsymbol{W}}\|\right) \tag{6.35}$$

It can be observed that Definition 6.14 is a requirement for Definition 6.15 since, imposing $\boldsymbol{W}_{ij} = \boldsymbol{W}_{ji} = \overline{\boldsymbol{W}}$ in (6.35), one obtains:

$$\|\mathfrak{F}\left(\overline{\boldsymbol{W}}, \overline{\boldsymbol{W}}, \overrightarrow{\boldsymbol{n}}_{ij}\right) - \boldsymbol{\mathcal{F}}\left(\overline{\boldsymbol{W}}\right) \cdot \overrightarrow{\boldsymbol{n}}_{ij}\| = 0 \tag{6.36}$$

which automatically leads to (6.34).

6.2 Multidimensional Finite Volume framework

A wide variety of mesh can be used for the resolution of the governing equations and we review here the standard FV formulation according to them. Starting from structured two-dimensional meshes, the complexity of the mesh is increased toward unstructured formulations and the axisymmetric framework. Additionally the detailed procedure to obtain the geometrical parameters is provided based on the computer graphics literature.

6.2.1 Finite volume mesh description

Before designing the numerical schemes, we first define the meshes on which these numerical methods rely. From a non-exhaustive point of view, we observe the following class of meshes:

- Structured mesh: mesh relying on a regular connectivity between cell that is implicit such that information can be stored in memory through multidimensional arrays,
- Block structured mesh: mesh composed of a set of structured meshes connected with each others,
- Cell-based AMR and *multiresolution*: the cells are organized in a tree data structure in which each internal node has can be subdivided to contain a set of smaller cells through a refinement process,
- Unstructured mesh: mesh relying on an irregular connectivity between cells that has to be explicitly described,
- Hybrid mesh: mesh composed of a set of structured meshes and unstructured meshes connected with each others.

In two dimensions, some specific cases can be observed and we focus among them on the following ones:

- Structured meshes:
  - Cartesian meshes: meshes composed of congruent quadrangles with faces normal to the coordinate directions. The cells can be either square ($\Delta x = \Delta y = cst$, see Figure 6.1a), of the same rectangular shape ($\Delta x \neq \Delta y$),
  - Rectilinear grid: meshes composed of quadrangles with faces normal to the coordinate directions with edge size can vary along the domain,
  - Structured deformed meshes: meshes composed of quadrangles organized such that they can be referenced through indexes (i, j), The shape of the cells is not imposed rectangular such that it can follow curved geometry (see Figure 6.1c),
- Cell-based AMR meshes and/or *multiresolution*:
  - Quad-tree meshes: tree structures composed of quadrangles able to possess four quadrangles children, and so recursively (see Figure 6.1d),
- Unstructured meshes:
  - Triangular meshes: meshes composed of two dimensional simplexes (see Figure 6.1b).
  - Hybrid meshes: meshes composed of distinct triangular and structured deformed domains bounded together.

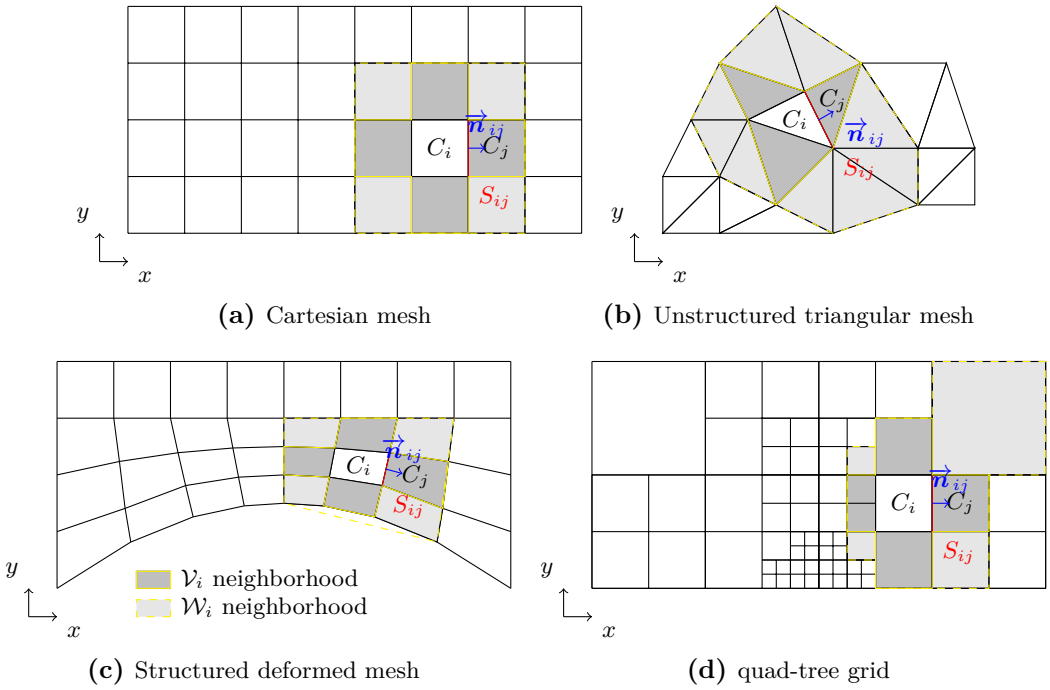

(a) Cartesian mesh **(b)** Unstructured triangular mesh

(c) Structured deformed mesh **(d)** quad-tree grid

Figure 6.1: *Example of structured and unstructured meshes*

  - General unstructured meshes: meshes composed of arbitrary polygon (see Figure 6.2).

For three dimensional cases, these structures find equivalent forms:

- Structured meshes:
  - Cartesian meshes: meshes composed of congruent rectangular cuboids,
  - Structured deformed meshes: meshes composed of organized cuboids that can be referenced through indexes (i, j, k). We add as a constraint that the vertexes composing a face belong to the same plane such the faces of the cuboid remain planar,
- Cell-based AMR meshes and/or *multiresolution*:
  - Octree meshes: tree structures composed of cuboids able to recursively possess eight children,
  - Tetrahedral AMR: tree structures composed of tetrahedrons (Cohen, Kaber, and Postel 2003; Duarte 2011; Drui 2017)
- Unstructured meshes:
  - Tetrahedral meshes: meshes composed of three dimensional simplexes,
  - Hybrid meshes: meshes composed of distinct tetrahedral and structured deformed

domains bounded together,

– General unstructured meshes: meshes composed of arbitrary polyhedral. Unlike for the two dimensional cases, where each cell is delimited by one dimensional linear element, in the three dimensional case, the faces are not necessarily formed of simplexes. In such case, one can either subdivide these faces through triangulation (see (Boissonnat 1984) for example) or dedicated procedures out of the scope of this thesis can be investigated.

In the work presented here, we focus the effort on the development of methods for two and three dimensional general unstructured meshes. It can be observed that every other meshes can be formulated as a specific case of this class of mesh.

We however notice some specificities:
Definition 6.16 (Non-conformal meshes)**.** A mesh is said to be non-conform if there exists at least one cell with a face shared with two or more other cells.

According to Definition 6.16, cell-based AMR meshes are a specific case of non-conformal meshes. In this conditions, to fit in a a conformal general unstructured mesh, the surfaces connected to several neighbors or subdivided such that each subdivision of the surface involved is connected to a unique neighbor.
Definition 6.17 (Convex cell)**.** Let C_i be a cell described by N vertexes P_{ij} of position vector $\boldsymbol{P}_{ij}$. C_i is convex if any position $\boldsymbol{M}$ expressed as a convex combination of the $\boldsymbol{P}_{ij}$ belong to C_i.

The use of general unstructured meshes, especially when cells are not delimited by triangles, may lead to the possible occurrence of non-convex cells. This situation can be problematic for higher order reconstructions, when the barycenter of a cell does not belong to its interior for instance. However, experiments show that for meshes with cells that are not too distorted compared to a convex ones, the Monotonic Upwind Scheme for Conservation Laws (MUSCL) scheme proposed in Section 6.4 remains able to provide accurate results with a high level of robustness.

6.2.2 Multidimensional Cartesian framework

6.2.2.1 FV in general unstructured mesh context

We start for a system of equations taken from the general form (3.26) and expressed in Cartesian coordinates:

$$\frac{\partial \boldsymbol{W}}{\partial t} + \nabla \cdot (\boldsymbol{\mathcal{F}}(\boldsymbol{W})) = \boldsymbol{\mathcal{S}}(\boldsymbol{W}), \tag{6.37}$$

where the nabla operator $\nabla \cdot ()$ taken for an arbitrary vector $\boldsymbol{u}$ the expression:

$$\begin{aligned} \nabla \cdot (\boldsymbol{u}) &= \frac{\partial \boldsymbol{u}}{\partial x} + \frac{\partial \boldsymbol{u}}{\partial y}, && \text{in 2D,} \\ \nabla \cdot (\boldsymbol{u}) &= \frac{\partial \boldsymbol{u}}{\partial x} + \frac{\partial \boldsymbol{u}}{\partial y} + \frac{\partial \boldsymbol{u}}{\partial z}, && \text{in 3D.} \end{aligned} \tag{6.38}$$

Remark 6.1. *The distinction is here made between the nabla operator $\nabla\cdot(\bullet)$ and the spatial divergence operator $\boldsymbol{div_x}(\bullet)$. As observed in (Garrigues 2016) for example, while the two formulations are equivalent in Cartesian coordinates due to null Christoffel coefficients, the result differs for a general system of coordinates. An example of the sort has been already presented for axisymmetric cases in Section 3.3, which explains why finite volume formulation for axisymmetric framework is specifically treated in Section 6.2.3*

Let Ω be the computational domain in the (O,x,y) frame of reference for two dimensional cases and (O,x,y,z) for three dimensional configuration. The set Ω is tessellated in a finite number of non-self-intersecting convex polyhedron $C_i\subset\Omega$. For each cell C_i, $\mathcal{V}_i$ denotes the set of cells C_j sharing with C_i an edge S_{ij} and $\mathcal{W}_i$ the set of cells C_j sharing at least a vertex with C_i, as presented in 2D in Figure 6.1. Thus integrating (6.37) spatially over a cell i and using the Green formula, one obtains:

$$\partial_t\int_{C_i}\boldsymbol{W}\mathrm{d}\boldsymbol{x}+\int_{C_i}\nabla\cdot(\boldsymbol{\mathcal{F}}(\boldsymbol{W}))\,\mathrm{d}\boldsymbol{x}=\int_{C_i}\boldsymbol{\mathcal{S}}(\boldsymbol{W})\mathrm{d}\boldsymbol{x}\Leftrightarrow$$
$$\partial_t\int_{C_i}\boldsymbol{W}\mathrm{d}\boldsymbol{x}+\sum_{j\in\mathcal{V}_i}\int_{S_{ij}}\boldsymbol{\mathcal{F}}(\boldsymbol{W})\overrightarrow{\boldsymbol{n}}_{ij}\mathrm{d}\boldsymbol{s}=\int_{C_i}\boldsymbol{\mathcal{S}}(\boldsymbol{W})\mathrm{d}\boldsymbol{x},\quad(6.39)$$

where $\boldsymbol{s}$ is a surface element, $\overrightarrow{\boldsymbol{n}}_{ij}$ the outward oriented normal vector to the surface S_{ij} between cells i and j.

Then, we define the following quantities that are aimed at being approximated by the scheme:

$$\begin{cases}\boldsymbol{W}_i^n &= \frac{1}{\Delta t|C_i|}\int_{t^n}^{t^{n+1}}\int_{C_i}\boldsymbol{W}(\boldsymbol{x},t^n)\mathrm{d}\boldsymbol{x}\mathrm{d}t,\\ \boldsymbol{\mathfrak{F}}_{ij}^n &= \frac{1}{|S_{ij}|}\int_{S_{ij}}\boldsymbol{\mathcal{F}}(\boldsymbol{W}(\boldsymbol{x},t^n))\overrightarrow{\boldsymbol{n}}_{ij}\mathrm{d}\boldsymbol{s}\\ \boldsymbol{\mathcal{S}}_i^n &= \frac{1}{\Delta t|C_i|}\int_{t^n}^{t^{n+1}}\int_{C_i}\boldsymbol{\mathcal{S}}(\boldsymbol{W}(\boldsymbol{x},t^n))\mathrm{d}\boldsymbol{x}\mathrm{d}t\end{cases}\quad(6.40)$$

where the geometrical operators yield:

$$\begin{cases}|C_i| &= \int_{C_i}1\mathrm{d}x\mathrm{d}y,\\ |S_{ij}| &= \int_{S_{ij}}1\mathrm{d}x\mathrm{d}y,\end{cases}\text{ in 2D,}\qquad\begin{cases}|C_i| &= \int_{C_i}1\mathrm{d}x\mathrm{d}y\mathrm{d}z,\\ |S_{ij}| &= \int_{S_{ij}}1\mathrm{d}x\mathrm{d}y\mathrm{d}z,\end{cases}\text{ in 3D.}\quad(6.41)$$

A method to compute these geometrical parameters on arbitrary polygon or polyhedron is proposed in Section 6.2.4.

As a consequence, the spatial integration leads to the *semi-discretized* form:

$$\mathrm{d}_t\boldsymbol{W}_i^n=-\frac{1}{|C_i|}\sum_{j\in\mathcal{V}_i}|S_{ij}|\,\boldsymbol{\mathfrak{F}}_{ij}^n+\mathrm{d}_t\left(\int_{C_i}\boldsymbol{\mathcal{S}}(\boldsymbol{W}(\boldsymbol{x}_i,t^n))\mathrm{d}\boldsymbol{x}\right).\quad(6.42)$$

Put aside the source terms that can be solved independently through an operator splitting, (6.42) constitutes the $\boldsymbol{\mathcal{L}}$ operator of Section 5.2.1. For the sake of legibility, we rely on an Euler forward time integration (5.7) in the development and demonstration that follows. This first order time stepping operation leads to:

$$\boldsymbol{W}_i^{n+1} = \boldsymbol{W}_i^n - \frac{\Delta t}{|C_i|} \sum_{j \in \mathcal{V}_i} |S_{ij}| \, \mathfrak{F}_{ij}^n + \Delta t \boldsymbol{\mathcal{S}}_i^n. \tag{6.43}$$

If higher order time convergences are needed, we rely on the SSPRK methods described Section 5.2.2.

6.2.2.2 FV in structured mesh context

In the case of 2D structured meshes, each cell can be identified by the indexes (i, j) and only four neighbors. Thus, starting from (6.43), we get:

$$\begin{aligned} \boldsymbol{W}_{i,j}^{n+1} = \boldsymbol{W}_{i,j}^n - \frac{\Delta t}{|C_{i,j}|} \Big[\Big| S_{i,j+1/2} \Big| \, \mathfrak{F}_{i,j-1/2}^n - \Big| S_{i,j-1/2} \Big| \, \mathfrak{F}_{i,j+1/2}^n \\ + \Big| S_{i+1/2,j} \Big| \, \mathfrak{F}_{i-1/2,j}^n - \Big| S_{i-1/2,j} \Big| \, \mathfrak{F}_{i-1/2,j}^n \Big] + \Delta t \boldsymbol{\mathcal{S}}_i^n. \end{aligned} \tag{6.44}$$

Additionally, for Cartesian meshes, the geometrical terms can be simplified thanks to the parameters Δx and Δy such that:

$$\boldsymbol{W}_{i,j}^{n+1} = \boldsymbol{W}_{i,j}^n \underbrace{- \frac{\Delta t}{\Delta x} \left[\mathfrak{F}_{i+1/2,j}^n - \mathfrak{F}_{i-1/2,j}^n \right]}_{\text{convection in x}} \underbrace{- \frac{\Delta t}{\Delta y} \left[\mathfrak{F}_{i,j+1/2}^n - \mathfrak{F}_{i,j-1/2}^n \right]}_{\text{convection in y}} + \Delta t \boldsymbol{\mathcal{S}}_i^n. \tag{6.45}$$

The extension of the structured FV formulation presented here in three dimensions is straightforward. In that last formulation (6.45), one can remark that the derivation of fully multi-dimensional finite volume methods is not needed. Actually, it is possible to rely on an operator splitting according to the directions of the convection to solve (6.45). Then applying a one dimensional transport scheme in each direction and relying on a so-called *dimensional splitting* (Toro 2009; LeVeque 2002; Hirsch 1990), multi-dimensional simulations can be conducted. Such approach is not investigated in this work due to the inherent restriction of the Cartesian meshes geometry.

6.2.3 2D structured axisymmetric framework

This section focuses on a finite volume approach to solve for axisymmetric disperse flows. For their convective and source parts, we recall the governing equations in the axisymmetric framework that either take the generic form:

$$\frac{\partial \boldsymbol{W}}{\partial t} + \frac{\partial \boldsymbol{F}_r}{\partial r} + \frac{\partial \boldsymbol{F}_z}{\partial z} = \widehat{\boldsymbol{\mathcal{S}}}^{axi}(r) + \boldsymbol{\mathcal{S}}, \tag{6.46}$$

if one starts from relation (3.57), or:

$$\frac{\partial r\boldsymbol{W}}{\partial t} + \frac{\partial r\boldsymbol{F}_r}{\partial r} + \frac{\partial r\boldsymbol{F}_z}{\partial z} = \boldsymbol{\mathcal{S}}^{axi} + r\boldsymbol{\mathcal{S}}, \tag{6.47}$$

if one chooses to start from the scale invariant relation (3.58).

As one can see, both generic forms include geometric terms that need specific treatments in the scope of a fully second order numerical discretization. However, as in (Baraille 1991), we now choose system (6.47) instead of (6.46). This is justified first by the dependency of $\widehat{\boldsymbol{\mathcal{S}}}^{axi}$ on the geometrical parameter r. This may be an issue in the development of high order transport scheme. Also, as explained is the previous part, depending on the system of equations to solve, the term $\boldsymbol{\mathcal{S}}^{axi}$ may vanish and this specificity can be an opportunity to reduce the computational cost and avoid the non-trivial integration of this specific source term.

Adding the viscous contribution in order to be able to model the carrier phase, the general governing equation (6.47) takes the form:

$$\frac{\partial r\boldsymbol{W}}{\partial t} + \frac{\partial r(\boldsymbol{F}_r - \boldsymbol{T}_r)}{\partial r} + \frac{\partial r(\boldsymbol{F}_z - \boldsymbol{T}_z)}{\partial z} = \boldsymbol{\mathcal{S}}^{axi} + \boldsymbol{\mathcal{S}}\lceil^{axi}(r) + r\boldsymbol{\mathcal{S}}, \tag{6.48}$$

where $\boldsymbol{T}_r$ and $\boldsymbol{T}_z$ are the viscous fluxes in the r and z directions and the viscous axisymmetric source terms $\boldsymbol{\mathcal{S}}\lceil^{axi}(r)$ can be taken from (3.64) or its derived forms.

The numerical resolution of these viscous contributions is detailed in Section 6.5.

We here let Ω be the computational domain in the (O, r, z) frame of reference to which a symmetry axis is added. Also, we consider the constraint that the polygons composing Ω stand only on one side of the symmetry axis (O, z), as presented Figure 6.2.

Then, by integrating (6.47) over the cell C_i and using the Green formula, one obtains:

$$\frac{\mathrm{d}}{\mathrm{d}t}\int_{C_i} \boldsymbol{W}(r,z,t) r\mathrm{d}r\mathrm{d}z + \int_{\partial C_i} \left(\boldsymbol{F}_r(\boldsymbol{W})n_{i,r} + \boldsymbol{F}_z(\boldsymbol{W})n_{i,z}\right) r\mathrm{d}s = \int_{C_i} \boldsymbol{\mathcal{S}}^{axi}(\boldsymbol{W})\mathrm{d}r\mathrm{d}z + \int_{C_i} \boldsymbol{\mathcal{S}}(\boldsymbol{W}) r\mathrm{d}r\mathrm{d}z, \tag{6.49}$$

where ∂C_i is the boundary of C_i with $\boldsymbol{n}_i = (n_{i,r}, n_{i,z})^T$ its outward unit normal vector and $\mathrm{d}s$ an infinitesimal element of such interface.

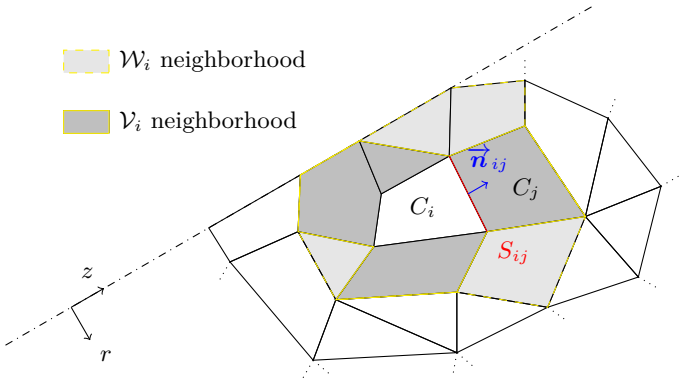

Figure 6.2: *Arbitrary unstructured mesh in an axisymmetric configuration*

Next, integrating equation (6.49) over the time interval $[t^n, t^{n+1}]$ leads to:

$$\int_{C_i} \boldsymbol{W}(r,z,t^{n+1}) r\mathrm{d}r\mathrm{d}z = \int_{C_i} \boldsymbol{W}(r,z,t^n) r\mathrm{d}r\mathrm{d}z - \int_{t^n}^{t^{n+1}} \int_{\partial C_i} \left(\boldsymbol{F}_r(\boldsymbol{W}) n_{i,r} + \boldsymbol{F}_z(\boldsymbol{W}) n_{i,z}\right) r\mathrm{d}s\mathrm{d}t + \int_{t^n}^{t^{n+1}} \int_{C_i} \boldsymbol{\mathcal{S}}^{axi}(\boldsymbol{W}) \mathrm{d}r\mathrm{d}z\mathrm{d}t + \int_{t^n}^{t^{n+1}} \int_{C_i} \boldsymbol{\mathcal{S}}(\boldsymbol{W}) r\mathrm{d}r\mathrm{d}z\mathrm{d}t. \quad (6.50)$$

We here define again the FV quantities to adapt them to the axisymmetric framework:

$$\begin{aligned} \boldsymbol{W}_i^n &= \frac{1}{|C_i|_r} \int_{C_i} \boldsymbol{W}(r,z,t^n) r\mathrm{d}r\mathrm{d}z, & F_{ij}^n &= \frac{1}{\Delta t\, |S_{ij}|_r} \int_{t^n}^{t^{n+1}} \int_{S_{ij}} \left(\boldsymbol{\mathcal{F}}(\boldsymbol{W}) \cdot \vec{\boldsymbol{n}}_{ij}\right) r\mathrm{d}s\mathrm{d}t, \\ \boldsymbol{\mathcal{S}}_i^n &= \frac{1}{\Delta t\, |C_i|_r} \int_{t^n}^{t^{n+1}} \int_{C_i} \boldsymbol{\mathcal{S}}(\boldsymbol{W}) r\mathrm{d}r\mathrm{d}z\mathrm{d}t, & \boldsymbol{\mathcal{S}}_i^{axi,n} &= \frac{1}{\Delta t\, |C_i|} \int_{t^n}^{t^{n+1}} \int_{C_i} \boldsymbol{\mathcal{S}}^{axi}(\boldsymbol{W}) \mathrm{d}r\mathrm{d}z\mathrm{d}t, \end{aligned} \quad (6.51)$$

where the scalings in space and time are:

$$\Delta t = t^{n+1} - t^n, \quad |C_i| = \int_{C_i} \mathrm{d}r\mathrm{d}z, \quad |C_i|_r = \int_{C_i} r\mathrm{d}r\mathrm{d}z \quad \text{and} \quad |S_{ij}|_r = \int_{S_{ij}} r\mathrm{d}s. \quad (6.52)$$

The determination of these values is the subject of Section 6.2.4.

With these notations, equation (6.50) simply writes:

$$|C_i|_r\, \boldsymbol{W}_i^{n+1} = |C_i|_r\, \boldsymbol{W}_i^n - \Delta t \sum_{j \in \mathcal{V}_i} |S_{ij}|_r\, F_{ij}^n + \Delta t\, |C_i|\, \boldsymbol{\mathcal{S}}_i^{axi,n} + \Delta t\, |C_i|_r\, \boldsymbol{\mathcal{S}}_i^n. \quad (6.53)$$

As a consequence, in comparison to 2D planar cases, a specific source term is added and the geometrical terms definition are modified.

Proposition 6.3. For any numerical flux fulfilling basic consistency condition (see Definition 6.14), (6.53) exactly preserves the steadiness of any steady uniform solution of systems of the class described section 3.3.2.3.

Proof. Let a uniform steady state $\boldsymbol{W}_u$ be composed by the moments $\mathcal{M}_p^u$. Obviously in such condition for a uniform field, the standard source terms disappears for the sake of steadiness

and the first order scheme (6.53) is rewritten into:

$$\boldsymbol{W}_i^{n+1} = \boldsymbol{W}_u - \Delta t \sum_{j \in \nu_i} \frac{|S_{ij}|_{1,0}}{|C_i|_{1,0}} \boldsymbol{\mathcal{F}}(\boldsymbol{W}_u) \cdot \boldsymbol{n}_{ij} + \Delta t \frac{|C_i|_{0,0}}{|C_i|_{1,0}} \boldsymbol{\mathcal{S}}^{axi}(\boldsymbol{W}_u). \tag{6.54}$$

Using the definition of $|S_{ij}|_{1,0}$ and the green formula, we obtain:

$$\sum_{j \in \nu_i} |S_{ij}|_{1,0} \boldsymbol{\mathcal{F}}(\boldsymbol{W}_u) \cdot \boldsymbol{n}_{ij} = \sum_{j \in \nu_i} \int_{S_{ij}} r \boldsymbol{\mathcal{F}}(\boldsymbol{W}_u) \cdot \boldsymbol{n}_{ij} \mathrm{d}s = \int_{C_i} \nabla \cdot (r \boldsymbol{\mathcal{F}}(\boldsymbol{W}_u)) \, \mathrm{d}r\mathrm{d}z. \tag{6.55}$$

where we use the Nabla operator $\nabla \cdot (\boldsymbol{\mathcal{F}}) = \frac{\partial \boldsymbol{F}_r}{\partial r} + \frac{\partial \boldsymbol{F}_z}{\partial z}$.

Since the state $\boldsymbol{W}_u$ is considered uniform in the cell, we get $\nabla \cdot (r \boldsymbol{\mathcal{F}}(\boldsymbol{W}_u)) = \boldsymbol{F}_r(\boldsymbol{W}_u)$ and thus:

$$\sum_{j \in \nu_i} |S_{ij}|_{1,0} \boldsymbol{\mathcal{F}}(\boldsymbol{W}_u) \cdot \boldsymbol{n}_{ij} = \int_{C_i} \boldsymbol{F}_r(\boldsymbol{W}_u) \mathrm{d}r\mathrm{d}z = |C_i|_{0,0} \boldsymbol{F}_r(\boldsymbol{W}_u) \tag{6.56}$$

Then, introducing (6.56) in (6.54), one can obtain:

$$\boldsymbol{W}_i^{n+1} = \boldsymbol{W}_u + \Delta t \frac{|C_i|_{0,0}}{|C_i|_{1,0}} \left[\boldsymbol{\mathcal{S}}^{axi}(\boldsymbol{W}_u) - \boldsymbol{F}_r(\boldsymbol{W}_u) \right] \tag{6.57}$$

Since, by definition, the steady state requirement (3.83) impose a specific form of $\boldsymbol{W}_u$, we have the additional relation:

$$\mathbf{card}_\theta \left(\underline{\mathbf{i}}\right) \left(\mathcal{M}_p^u\right)_{\underset{\sim}{\underline{\mathbf{i}}r}} - \mathbf{card}_r \left(\underline{\mathbf{i}}\right) \left(\mathcal{M}_p^u\right)_{\underset{\sim}{\underline{\mathbf{i}}_{(r-1,\theta+1)}\theta}} = \left(\mathcal{M}_p^u\right)_{\underset{\sim}{\underline{\mathbf{i}}r}} \equiv \boldsymbol{\mathcal{S}}^{axi}(\boldsymbol{W}_u) = \boldsymbol{F}_r(\boldsymbol{W}_u). \tag{6.58}$$

Introducing (6.58) in (6.57), it can be immediately observed that the steady state $\boldsymbol{W}_u$ is preserved by the scheme. □

6.2.4 Geometric terms computation

6.2.4.1 Two dimensional geometry terms computation

Assuming that the mesh is fixed, the geometrical parameters (6.52) can be computed once at the beginning of the simulation. In the two dimensional frame (O, r, z), these parameters can

be seen as moments of the polygons and of their border line segments, which are defined as:

$$|C_i|_{n,m} = \int_{C_i} r^n z^m \mathrm{d}r\mathrm{d}z, \qquad |S_{ij}|_{n,m} = \int_{S_{ij}} r^n z^m \mathrm{d}s. \tag{6.59}$$

Let us notice that $|C_i| = |C_i|_{0,0}$, $|C_i|_r = |C_i|_{1,0}$, $|S_{ij}| = |S_{ij}|_{0,0}$ and $|S_{ij}|_r = |S_{ij}|_{1,0}$. Then, such generic integrals have explicit solutions on arbitrary polygons, as detailed in (Singer 1993): if C_i is defined by N_i sorted points $P_j = (r_j, z_j)^T_{j\in[\![1,N_i]\!]}$, then $|C_i|_{n,m}$ is given by the formula

$$|C_i|_{n,m} = \sum_{j=0}^{n_i-1} \alpha_j \sum_{p=0}^{n}\sum_{q=0}^{m} C_{p,q}(n,m) r_j^p r_{j+1}^{n-p} z_j^q z_{j+1}^{m-q}, \tag{6.60}$$

where the convention $P_0 = P_n$ is retained for the sake of legibility and:

$$\alpha_j = \frac{z_{j+1}r_j - z_j r_{j+1}}{2}, \qquad C_{p,q}(n,m) = 2\frac{n!m!(p+q)!(n+m-p-q)!}{(n-p)!(m-q)!p!q!(n+m+2)!}. \tag{6.61}$$

This form can be extended to the integral over a line segment bounded by end-points $A = (r_A, z_A)^T$ and $B = (r_B, z_B)^T$:

$$|S_{ij}|_{n,m} = \sqrt{(r_A - r_B)^2 + (z_A - z_B)^2} \sum_{p=0}^{n}\sum_{q=0}^{m} \frac{n+m+2}{2} C_{p,q}(n,m) r_A^p r_B^{n-p} z_A^q z_B^{m-q}. \tag{6.62}$$

The sign of the result depends on the way the points of the polygonal broken-line have been sorted. Hence, we may end up with negative surfaces, for example. The original paper assumes that the polygonal border is always described counterclockwise, to avoid such an issue. However, this is not necessarily the case in general unstructured meshes. A solution to avoid this issue consists in multiplying the moment $|C_i|_{n,m}$ by the sign of the zeroth order moment $|C_i|_{0,0}$, which is positive unless the numbering of the nodes of the polygon is clockwise. This renders the result independent of the numbering.

6.2.4.2 Three dimensional geometry terms computation

In three dimension, the objective is here to obtain the volume of a cell, the surface of its faces and the barycenter of both of them. It is proposed to rely on the same formalism in order to obtain $|S_{ij}|_{k_1,k_2,k_3}$ and $|C_i|_{k_1,k_2,k_3}$ defined as:

$$|C_i|_{k_1,k_2,k_3} = \int_{C_i} x^{k_1} y^{k_2} z^{k_3} \mathrm{d}y\mathrm{d}y\mathrm{d}z, \qquad |S_{ij}|_{k_1,k_2,k_3} = \int_{S_{ij}} x^{k_1} y^{k_2} z^{k_3} \mathrm{d}s. \tag{6.63}$$

We assume here that the polyhedron C_i of interest can be decomposed in a finite number of tetrahedrons $T_{ij}^{(3)}$ defined by the origin and the three points defining S_{ij} that is assumed to be

a triangle. Then one directly obtain:

$$\int_{C_i} x^{k_1} y^{k_2} z^{k_3} \mathrm{d}y\mathrm{d}y\mathrm{d}z = \sum_{j \in \mathcal{V}_i} \int_{T_{ij}^{(3)}} x^{k_1} y^{k_2} z^{k_3} \mathrm{d}y\mathrm{d}y\mathrm{d}z \tag{6.64}$$

Remark 6.2. *If a surface S_{ij} is not a triangle, we assume that it can be decomposed through a triangulation procedure such that:*

$$|S_{ij}|_{k_1,k_2,k_3} = \sum_{l=1}^{N_{ij}^{(T)}} \left|T_{ijl}^{(2)}\right|_{k_1,k_2,k_3} \tag{6.65}$$

$N_{ij}^{(T)}$ is the number of triangle $T_{ijl}^{(2)}$ in which S_{ij} is decomposed.

We refer to (Nielson 1994) and the reference within for a description of such triangulation procedures.

For three dimensional polyhedrons one can rely on an iterative determination of the moments as in (Li 1993). In such context, it is possible to obtain the $\left|T_{ij}^{(3)}\right|_{k_1,k_2,k_3}$ either through an iterative procedure (Li 1993) or through an explicit formula (Tuzikov, Sheynin, and Vasiliev 2003) described here-after.

Let $T_{ij}^{(3)} = T_{ij}^{(3)}(\boldsymbol{a}, \boldsymbol{b}, \boldsymbol{c})$ be the tetrahedron defined by the origin and the points of three dimensional coordinates $\boldsymbol{a}$, $\boldsymbol{b}$ and $\boldsymbol{c}$. In the context of the decomposition of the polyhedron into tetrahedrons, $\boldsymbol{a}$, $\boldsymbol{b}$ and $\boldsymbol{c}$ are organized counter-clockwise according to the outward normal vector of S_{ij}. Let $A = (a_{m,n}) = [\boldsymbol{a}, \boldsymbol{b}, \boldsymbol{c}]$ be the matrix composed of these coordinates and $\mathscr{K}$ the set of $(k_{m,n})$ 3×3 matrix with $0 \leq k_{m,n} \leq k_m$ and $\sum_{n=1}^{3} k_{m,n} = k_m$. Then, the moment $\left|T_{ijl}^{(2)}\right|_{k_1,k_2,k_3}$ of order $k = k_1 + k_2 + k_3$ gets the expression:

$$\left|T_{ij}^{(3)}\right|_{k_1,k_2,k_3} = \det(A) \frac{k_1! k_2! k_3!}{(k+3)!} \sum_{(k_{m,n}) \in \mathscr{K}} \frac{\prod_{n=1}^{3} \left(\left(\sum_{m=1}^{3} k_{m,n}\right)!\right)}{\prod_{n,m=1}^{3} (k_{m,n}!)} \prod_{n,m=1}^{3} a_{m,n}^{k_{m,n}}. \tag{6.66}$$

With a similar formula, one can get the surface moment $|S_{ij}|_{k_1,k_2,k_3}$ using the relation:

$$|S_{ij}|_{k_1,k_2,k_3} = 2\,|S_{ij}|_{0,0,0} \frac{k_1! k_2! k_3!}{(k+2)!} \sum_{(k_{m,n}) \in \mathscr{K}} \frac{\prod_{n=1}^{3} \left(\left(\sum_{m=1}^{3} k_{m,n}\right)!\right)}{\prod_{n,m=1}^{3} (k_{m,n}!)} \prod_{n,m=1}^{3} a_{m,n}^{k_{m,n}}. \tag{6.67}$$

where $|S_{ij}|_{0,0,0}$ is the surface of the triangle defined by coordinates $\boldsymbol{a}$, $\boldsymbol{b}$ and $\boldsymbol{c}$, that, for the

reminder, yields:

$$|S_{ij}|_{0,0,0} = \frac{1}{2}\|(\boldsymbol{b}-\boldsymbol{a})\times(\boldsymbol{c}-\boldsymbol{a})\|_2. \tag{6.68}$$

Remark 6.3. *Such an approach has been extended to higher dimensional polyhedra (Sheynin and Tuzikov 2001). The loop giving the moments is then conducted on the $N_i - 1$ simplices of dimension $d-1$ composing a closed shell at the border of the d-dimensional polyhedra.*

6.3 Numerical flux determination

In order to complete the schemes, it is necessary to define accurately the numerical fluxes associated to the chosen FV frameworks. First in Section 6.3.1, we describe relevant conservative numerical flux derived from FD framework. Depending on the interpretation from which they are derived, some of these schemes can find a dedicated FV formulation. Then numerical flux genuinely developed in the FV context are presented Section 6.3.2. While these are generally defined in one-dimensional context, extensions are proposed for multi-dimensional framework in Section 6.3.3.

6.3.1 Finite Difference base numerical flux

Since finite difference methods are mostly designed in a simplify context, in terms of geometry and systems of equations, we define the linear advection equation in one-dimensional context as:

$$\partial_t w + \partial_x f(w) = 0, \qquad f(w) = aw \tag{6.69}$$

where a is a real constant, considered positive here-after for the sake of legibility and $w(x,t)$ is a transported scalar.

Using a uniform grid, it is possible to develop high order schemes for (6.69), in the FD framework. The difficulties encountered to extend this category of methods to multidimensional framework, and to non-linear systems of equations explain the reasons of the efforts conducted in the context of FV methods and FEM. However, this simplified context let appear fundamental behavior of numerical schemes for hyperbolic conservation. Also many tools were developed in the context of FD schemes and were extended for FV later, which explains the relevance of describing the FD schemes from such a perspective.

6.3.1.1 A hierarchy of finite difference schemes for linear advection

6.3.1.1.1 Arbitrary high order scheme According to (Del Pino and Jourdren 2006) it is possible to built an arbitrary high order centered scheme for one-dimensional linear advection (6.69). The initial idea behind the proposed hierarchy of methods is to conduct a Taylor expansion of this equation around $[w]_i^n = w(x_i, t_n)$. To do so, classical Taylor expansions are written separately in time and space to express respectively the value of $[w]_i^{n+1}$ starting from $[w]_i^n$ for the first one $[w]_i^n$ starting from $[w]_{i-1}^n$ for the second one. One can then deduce from these equations an estimate of the derivatives $\partial_x w$ and $\partial_t w$ such that:

$$\partial_x w = \frac{[w]_i^n - [w]_{i-1}^n}{\Delta x} - \sum_{k=2}^{N} \frac{(-\Delta x)^{k-1}}{k!} \partial_x^k w + O(\Delta x^{N+1}) \tag{6.70}$$

$$\partial_t w = \frac{[w]_i^{n+1} - [w]_i^n}{\Delta t} - \sum_{k=2}^{N} \frac{(-\Delta t)^{k-1}}{k!} \partial_t^k w + O(\Delta t^{N+1}) \tag{6.71}$$

Where Δt is the time step and Δx the length of the cells of the regular space discretization. To express $\partial_x w$, $[w]_i^n$ and $[w]_{i-1}^n$ have been chosen to ensure the upwind discretization.

The governing equation (6.69) can be injected in that last relation (6.71) in order to obtain a time derivation only depending on space derivative. To do so, as presented in (Del Pino and Jourdren 2006), a Cauchy-Kowalewski procedure is applied to (6.69), which results in the following expression of every k^{th} time derivatives of w from its space differentiation results in:

$$\partial_t^k w = (-a)^k \partial_x^k w, \qquad k \in \mathbb{N}^* \tag{6.72}$$

This let (6.71) be rewritten as:

$$\partial_t w = \frac{[w]_i^{n+1} - [w]_i^n}{\Delta t} + a \sum_{k=2}^{N} \frac{(\nu \Delta x)^{k-1}}{k!} \partial_x^k w + O(\Delta t^{N+1}) \tag{6.73}$$

where $\nu = a\frac{\Delta t}{\Delta x}$ is the CFL number. Starting from (6.70) and (6.73), one can express (6.69) as a sum of these two expansions.

$$\begin{aligned} \partial_t w + a\partial_x w = & \frac{[w]_i^{n+1} - [w]_i^n}{\Delta t} + a\frac{[w]_i^n - [w]_{i-1}^n}{\Delta x} \\ & + a \sum_{k=2}^{N} \frac{(\nu \Delta x)^{k-1}}{k!} \partial_x^k w - a \sum_{k=2}^{N} \frac{(-\Delta x)^{k-1}}{k!} \partial_x^k w \\ & + O(\Delta t^{N+1}) + O(\Delta x^{N+1}) = 0 \end{aligned} \tag{6.74}$$

Then merging both components depending on $\partial_x^k w$, one can finally obtain:

$$\begin{aligned}[w]_i^{n+1} = [w]_i^n &- a\Delta t \frac{[w]_i^n - [w]_{i-1}^n}{\Delta x} \\ &+ a\Delta t \sum_{k=2}^{N} \frac{(\nu^{k-1} - (-1)^{k+1})(\Delta x)^{k-1}}{k!} \partial_x^k w \\ &+ O(\Delta t^{N+1}) + O(\Delta x^{N+1})\end{aligned} \tag{6.75}$$

The equation (6.75) will now be the foundation of the family of schemes that follows. To do so, the truncation errors in time and space $O(\Delta t^{N+1})$ and $O(\Delta x^{N+1})$ are neglected, the exact solution $[w]_i^n$ are replaced by the approximated solutions w_i^n at the same time t_n and position x_i and finally, the space derivatives $\partial_x^k w$ are approximated by $\tilde{\delta}_i^k[w^n]$ around the same time and position. The exact way the approximation of this difference is conducted is not yet assigned.

$$w_i^{n+1} = w_i^n - \frac{\Delta t}{\Delta x} \underbrace{[a w_i^n - a u_{i-1}^n]}_{\text{First order flux}} + \frac{\Delta t}{\Delta x} \sum_{k=2}^{N} \underbrace{\frac{a(\nu^{k-1} - (-1)^{k+1})(-\Delta x)^k}{k!} \tilde{\delta}_i^k[w^n]}_{\text{Correction of order } k} \tag{6.76}$$

This lets the value of u_i^{n+1} at the time step $n+1$ be the function of the solution at the time step n and conclude the time step procedure of that family of schemes that now only depends on the closure of $\tilde{\delta}_i^k[w^n]$.

According to (Del Pino and Jourdren 2006), and using a well chosen form of $\tilde{\delta}_i^k[w^n]$ based on the finite difference expressions (6.3), one can obtain a scheme under the following conservative form:

$$w_i^{n+1} = w_i^n - \frac{\Delta t}{\Delta x}(F_{i+1/2}^N - F_{i-1/2}^N) \tag{6.77}$$

where N is the order of accuracy of the numerical flux and:

$$\begin{cases} F_{i+1/2}^1 = & a w_i^n \\ F_{i+1/2}^N = & F_{i+1/2}^{N-1} + \frac{a}{N!} \left(\prod_{j=-m, j\neq 0}^{M} (\nu + j) \right) \left(\sum_{k=0}^{N-1} (-1)^{k+N} C_{N-1}^k w_{i+M-k}^n \right) \end{cases} \tag{6.78}$$

6.3.1.1.2 First order scheme Equation (6.78) describes a hierarchy that has the quality of being of arbitrary high order but does not represent all the possibilities of FD methods. Focusing on first order FD schemes, and a stencil restricted to the direct neighbors, on can find

the three following FD schemes:

$$\begin{cases} w_i^{n+1} &= w_i^n - \frac{a\Delta t}{\Delta x}\left(w_i^n - w_{i-1}^n\right), & \text{(upwind)} \\ w_i^{n+1} &= w_i^n - \frac{a\Delta t}{2\Delta x}\left(w_{i+1}^n - w_{i-1}^n\right), & \text{(centered)} \\ w_i^{n+1} &= w_i^n - \frac{a\Delta t}{\Delta x}\left(w_{i+1}^n - w_i^n\right), & \text{(downwind)} \end{cases} \tag{6.79}$$

Among the first order schemes proposed in (6.79), only the upwind scheme converges under a CFL condition, the others are known to be unconditionally unstable. One can quickly conclude from its expression that this upwind scheme fulfills LED conditions and therefore is TVD. The idea of selecting the form of the scheme such that an upwind form is always chosen is called *upwinding*. Such principle is generally used to ensure the stability of schemes and explains why, at first order ($N = 1$), the hierarchy (6.78) degenerates to the first order upwind scheme.

6.3.1.1.3 Second order scheme Closed at second order, FD schemes can lead to the Lax-Wendroff scheme (Lax and Wendroff 1960) using centered differences:

$$\underbrace{w_i^{n+1} = w_i^n - \nu(w_i^n - w_{i-1}^n)}_{\text{first order scheme}} \underbrace{-\Delta_-\left\{\frac{1}{2}(1-\nu)\nu(w_{i+1}^n - w_i^n)\right\}}_{\text{anti-diffusive term}} \tag{6.80}$$

where $\nu = \frac{a\Delta t}{\Delta x}$ and $\Delta_-\{\bullet\} = \{\bullet\}_i - \{\bullet\}_{i-1}$ is the difference operator between the states at points i and $i-1$.

or to the Beam–Warming (Warming and Beam 1976) using upwind differences:

$$\underbrace{w_i^{n+1} = w_i^n - \nu(w_i^n - w_{i-1}^n)}_{\text{first order scheme}} \underbrace{-\Delta_-\left\{\frac{1}{2}(1-\nu)\nu(w_i^n - w_{i-1}^n)\right\}}_{\text{anti-diffusive term}} \tag{6.81}$$

It is to be observed than both (6.80) and (6.81) are expressed as an extension of the first order upwind scheme (6.79). Both are stable but because of their anti-diffusive part, these schemes are no more TVD.

6.3.1.2 The Lax-Friedrichs scheme

For one dimensional non-linear hyperbolic conservation laws (6.1) in general, it is not always possible to rely on an upwinding to ensure the stability. However, searching for the fulfillment of the TVD property, one can remark that it is possible to stabilize the method by updating the average value of the neighbor cells $i-1$ and $i+1$ instead of the cell i itself. This idea originally

proposed in (Lax 1954) is consistent with adding diffusion in the equation to solve. Since the deduced flux is conservative, this following formalism is used:

$$\boldsymbol{W}_i^{n+1} = \boldsymbol{W}_i^n - \frac{\Delta t}{\Delta x}\left[\mathfrak{F}_{i+1/2} - \mathfrak{F}_{i-1/2}\right] \tag{6.82}$$

where for the Lax-Friedrich scheme, the expression of the numerical flux $\mathfrak{F}_{i+1/2}^{LF}$ yields:

$$\mathfrak{F}_{i+1/2}^{LF} = \frac{1}{2}\left(\boldsymbol{f}_i + \boldsymbol{f}_{i+1}\right) + \frac{\Delta x}{2\Delta t}\left(\boldsymbol{W}_{i+1}^n - \boldsymbol{W}_i^n\right) \tag{6.83}$$

where $\boldsymbol{f}_i = \boldsymbol{f}(\boldsymbol{W}_i^n)$

Despite this scheme holds many appreciable properties for stability, its large dissipation causes a poor accuracy. It is thus needed to aim at diminishing this dissipation with numerical methods of order of accuracy higher than 1.

6.3.1.3 One step Lax-Wendroff scheme

While searching for higher order FD schemes for (6.1) it is not possible to efficiently rely on a Cauchy-Kowalewski procedure (6.72) since it leads to the necessity of using the Jacobian of the flux $\boldsymbol{A}(\boldsymbol{W}) = \frac{\partial \boldsymbol{f}(\boldsymbol{W})}{\partial \boldsymbol{W}}$. Commented by Hirsch (Hirsch 1990), these schemes have the main inconvenient of requiring the evaluation of the Jacobian matrix, which can be a tedious operation in practice. Restricting the use of this mathematical object to the strict minimal, one can obtain the one-step Lax-Wendroff scheme (Lax and Wendroff 1960):

$$\begin{aligned}\mathfrak{F}_{i+1/2}^{LW} &= \frac{\boldsymbol{f}_{i+1}+\boldsymbol{f}_i}{2} - \frac{\Delta t}{2\Delta x}\boldsymbol{A}_{i+1/2}\left(\boldsymbol{f}_{i+1} - \boldsymbol{f}_i\right)\right) \\ &= \boldsymbol{f}_i - \frac{1}{2}\left(1 - \frac{\Delta t}{\Delta x}\boldsymbol{A}_{i+1/2}\right)\left(\boldsymbol{f}_{i+1} - \boldsymbol{f}_i\right)\end{aligned} \tag{6.84}$$

While one can clearly observe no direction is privileged in the first expression, it is possible to find the linear scalar form from (6.80) in the second expression. An additional difficulty of this scheme relies in the determination of $\boldsymbol{W}_{i+1/2}$ to compute $\boldsymbol{A}_{i+1/2}$ since it is an unknown. While a Roe average (see Section 6.3.2.2.2) is to be privileged, an arithmetic average of $\boldsymbol{W}_i$ and $\boldsymbol{W}_{i+1}$ is generally a simpler option.

6.3.1.4 S_β^α class of schemes

To overcome these issues, the schemes of two-step Lax-Wendroff class use a predictor-corrector procedure of order 2 in space and time. A generalization has been defined by Lerat and Peyret through the S_β^α class of schemes (Lerat and Peyret 1975), (Peyret 1979), (Lerat 1981). It is to

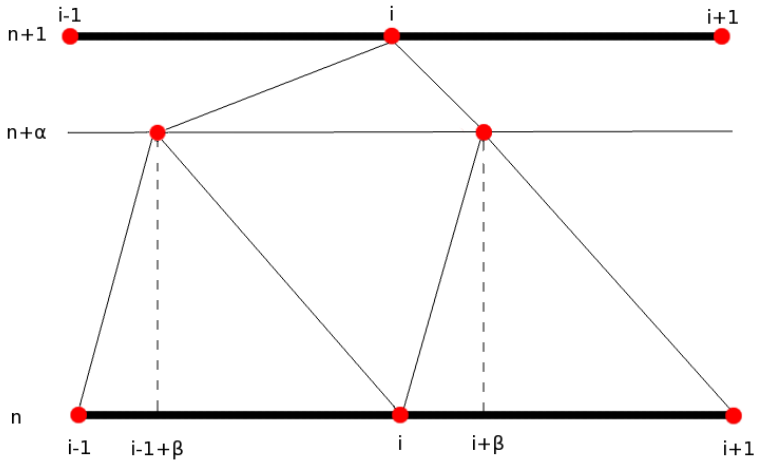

Figure 6.3: *Stencil of a S^{α}_{β} scheme in a finite difference framework*

be observed that, for linear advection (6.69), any scheme of this class boils down to the form (6.80).

The terms α and β correspond to the position of predictor point calculated as showed Figure 6.3. These parameters virtually establish a solution on a new grid at the predictor step. From this formalism, the Richtmyer schemes $S^{1/2}_{1/2}$ (Lax and Wendroff 1960) establishes this solution at the cell interfaces at half a time-step through a Lax-Friedrich scheme (6.82) before computing the flux from that specific grid. Also the MacCormack (MacCormack 1969) defined by S^{1}_{0} or in its reversed form S^{1}_{1} establishes predicted solution on the studied mesh directly that allows efficient implementations (Dupays 1996). Put under a conservative form, the numerical flux of the S^{α}_{β} class of schemes takes the expression:

$$\widetilde{\boldsymbol{W}_i^{n+1}} = \boldsymbol{W}_i^n + \beta\left(\boldsymbol{W}_{i+1}^n - \boldsymbol{W}_i^n\right) - \alpha\frac{\Delta t}{\Delta x}\left(f(\boldsymbol{W}_{i+1}^n) - f(\boldsymbol{W}_i^n)\right) \tag{6.85}$$

$$\mathfrak{F}_{i+1/2}^{S^{\alpha}_{\beta}} = \frac{1}{2\alpha}\left((\alpha-\beta)\boldsymbol{f}(\boldsymbol{W}_{i+1}^n) + (\alpha+\beta-1)\boldsymbol{f}(\boldsymbol{W}_i^n) + \boldsymbol{f}(\widetilde{\boldsymbol{W}_i^{n+1}})\right) \tag{6.86}$$

where $\widetilde{\boldsymbol{W}^{n+1}}$ is the solution at the predictor step.

According to Lerat and Peyret, the manipulation of α and β influences the dissipation and the dispersion of the method. For the Burgers equation (3.13), it is possible to investigate the modified equation (Warming and Hyett 1974) solved by this class of schemes letting appear the

third order derivative actually resolved by the method:

$$\partial_t w + w\partial_x w = (\Delta x)^2 \left[E_1 \partial_{xxx} w + E_2 \partial_{xx} w \partial_x w + E_3 (\partial_x w)^3\right] \tag{6.87}$$

where the expressions of E_1, E_2 and E_3 depend on the $\nu = \frac{w\Delta x}{\Delta t}$, α, β and w :

$$\begin{cases} E_1 = \frac{w}{6}(\nu^2 - 1) \\ E_2 = \frac{1}{2}((3-\alpha)\nu^2 + (2\beta - 1)\nu + \frac{\beta(\beta-1)}{\alpha} - 1) \\ E_3 = \frac{\Delta x}{4\Delta t}(2(2-\alpha)\nu + 2\beta - 1) \end{cases} \tag{6.88}$$

The study presented in (Lerat and Peyret 1975) shows that the values $\alpha = 1 + \sqrt{\frac{5}{2}}$ and $\beta = \frac{1}{2}$ gives a maximal dissipation around shock waves and a minimal antidissipative terms for the expansion waves. Such a choice reduces at most E_2 and E_3 but has no influence on E_1 that is dominant at low CFL ($\nu << 1$). As a consequence, the third order error produced by the scheme, that can lead to spurious oscillation, cannot be prevented by the manipulation of α and β. Those constants are kept for systems of equations even if the analysis of the modified equation is tedious and has not been extended toward these cases.

The equations given above are valid for one dimensional regular space discretization. In this case, there is an equivalence between the expression of the S^{α}_{β} class of schemes for finite difference and finite volume context thanks essentially to the conservative property of the scheme. However, depending on the interpretation of the used method, the expressions of the schemes for multidimensional cases of deformed or unstructured mesh can diverge.

6.3.1.5 The MacCormack scheme

Due to its specific interpretation, the MacCormack schemes (MacCormack 1969) can be easily and efficiently extended for multidimensional FV structured meshes. Thanks to that, these schemes have been widely spread (see (Davis 1984b; Causon 1989; Vincent, Caltagirone, and Bonneton 2001) among others) and used by the ONERA in the 90's (Lupoglazoff and Vuillot 1992a, 1994; Vuillot and Lupoglazoff 1996; Dupays 1996; Lupoglazoff et al. 2000) for transport equations of both gas and particles in SRMs context. Intrinsically linked to a structured grid, the indexes of position i and j are introduced in its formulation:

$$\begin{cases} \widetilde{\boldsymbol{W}_{i,j}^{n+1}} = \boldsymbol{W}_{i,j}^{n} - \frac{\Delta t}{|C_{i,j}|} \sum_{k \in \mathcal{V}_{i,j}} |S_k| \, \boldsymbol{\mathcal{F}}\left(\boldsymbol{W}^{n}_{k\pm_x\pm_y}\right) \cdot \vec{\boldsymbol{n}}_{k\pm_x\pm_y} \\ \boldsymbol{W}_{i,j}^{n+1} = \frac{1}{2}\left[\boldsymbol{W}_{i,j}^{n} + \widetilde{\boldsymbol{W}_{i,j}^{n+1}}\right] - \frac{\Delta t}{2|C_{i,j}|} \sum_{k \in \mathcal{V}_{i,j}} |S_k| \, \boldsymbol{\mathcal{F}}\left(\widetilde{\boldsymbol{W}^{n+1}_{k\mp_x\mp_y}}\right) \cdot \vec{\boldsymbol{n}}_{k\mp_x\mp_y} \end{cases} \tag{6.89}$$

with:

$$\sum_{k\in\mathcal{V}_{i,j}} |S_k|\,\boldsymbol{\mathcal{F}}\left(\boldsymbol{W}^n_{k\pm_x\pm_y}\right)\cdot\overrightarrow{\boldsymbol{n}}_{k\pm_x\pm_y} =$$
$$\left|S_{i+1/2,j}\right|\boldsymbol{\mathcal{F}}\left(\boldsymbol{W}^n_{i+1/2\pm_x 1/2,j}\right)\cdot\overrightarrow{\boldsymbol{n}}_{i+1/2,j} - \left|S_{i-1/2,j}\right|\boldsymbol{\mathcal{F}}\left(\boldsymbol{W}^n_{i-1/2\pm_x 1/2,j}\right)\cdot\overrightarrow{\boldsymbol{n}}_{i-1/2,j}$$
$$+\left|S_{i,j+1/2}\right|\boldsymbol{\mathcal{F}}\left(\boldsymbol{W}^n_{i,j+1/2\pm_y 1/2}\right)\cdot\overrightarrow{\boldsymbol{n}}_{i,j+1/2} - \left|S_{i,j-1/2}\right|\boldsymbol{\mathcal{F}}\left(\boldsymbol{W}^n_{i,j-1/2\pm_y 1/2}\right)\cdot\overrightarrow{\boldsymbol{n}}_{i,j-1/2} \tag{6.90}$$

where $\pm_i$ is the side chosen for flux prediction according to the i direction of the mesh.

Because of the globally known flow orientation, it is usually chosen to use a predictor upstream oriented, in other words, toward the grain for the horizontal faces and toward the head-end for the vertical faces. As a consequence, depending on the orientation of the used MacCormack scheme, spurious oscillations can have different magnitude on the same problem.

6.3.1.6 Artificial viscosity

In order to limit, and sometime to completely cancel, spurious oscillations, it is proposed to artificially add dissipation in the scheme. Unlike for the Lax-Friedrich scheme (6.83) where, the dissipation is sufficient to provide the LED property in any situation, the Artificial Viscosity (AV) described here aims at adding dissipation close to large gradients only where spurious oscillations are likely to appear. Originally designed to improve the Lax-Wendroff class of schemes, this kind of procedure can be applied to other types of numerical methods.

Following the general description provided in (Jameson 1995a) and used among this work, it consists in adding new terms including viscosity of 2^{nd} and 4^{th} order to the system. It aims at adding dissipation of 2^{nd} order close to discontinuities to force the scheme to act as a 1^{st} order accurate scheme near these singularities. Fourth order artificial viscosity smears the solution when oscillations (also called wiggles) appear. The two main drawbacks of the AV are first that the physics of the problem is changed and second that free variables remain and are problem-dependent.

A general expression of the AV can take the following form:

$$\boldsymbol{W}^{n+1} = \overline{\boldsymbol{W}}^{n+1} + D_2(\boldsymbol{W}^n) + D_4(\boldsymbol{W}^n) \tag{6.91}$$

where $\overline{\boldsymbol{W}}^{n+1}$ is the solution given by the original scheme, $D_2(\boldsymbol{W}^n)$ is the artificial viscosity adjustments of order 2 and $D_4(\boldsymbol{W}^n)$ the one of order 4, that, for one dimensionnal problems

and conservation property, take the form (Jameson, Schmidt, and Turkel 1981):

$$\begin{cases} D_2(\boldsymbol{W}_i^n) = d_{2;i+\frac{1}{2}}(\boldsymbol{W}^n) - d_{2;i-\frac{1}{2}}(\boldsymbol{W}^n) \\ D_4(\boldsymbol{W}_i^n) = d_{4;i+\frac{1}{2}}(\boldsymbol{W}^n) - d_{4;i-\frac{1}{2}}(\boldsymbol{W}^n) \end{cases} \tag{6.92}$$

where

$$\begin{cases} d_{2;i+\frac{1}{2}}(\boldsymbol{W}^n) = \varepsilon^{(2)}(\boldsymbol{W}_{i+1}^n - \boldsymbol{W}_i^n) \\ d_{4;i+\frac{1}{2}}(\boldsymbol{W}^n) = \varepsilon^{(4)}(\boldsymbol{W}_{i+2}^n - 3\boldsymbol{W}_{i+1}^n + 3\boldsymbol{W}_i^n - \boldsymbol{W}_{i-1}^n) \end{cases} \tag{6.93}$$

These last expressions have then been improved by Jameson and Baker in (Jameson and Baker, July 1983) using scaling factors on each faces of a cell. Such scaling factors represent the information fluxes through the faces.

$$\begin{cases} d_{2;i+\frac{1}{2}}(\boldsymbol{W}^n) = \varepsilon^{(2)}\nu_{i+1/2}\left(\boldsymbol{W}_{i+1}^n - \boldsymbol{W}_i^n\right) \\ d_{4;i+\frac{1}{2}}(\boldsymbol{W}^n) = \varepsilon^{(4)}\nu_{i+1/2}\left(\boldsymbol{W}_{i+2}^n - 3\boldsymbol{W}_{i+1}^n + 3\boldsymbol{W}_i^n - \boldsymbol{W}_{i-1}^n\right) \end{cases} \tag{6.94}$$

where $\nu_{i+1/2}$ is the CFL associated to the flux of the face $i + 1/2$.

We refer to (Jameson 1995a) for an extension of (6.93) and (6.94) for multidimensional cases and unstructured mesh. In a general FV framework, ν_{ij} can be expressed as:

$$\nu_{ij} = \max_{k \in N_w} \left(\|\lambda_k(\boldsymbol{W}_i^n)\|, \|\lambda_k(\boldsymbol{W}_j^n)\| \right) \frac{2\Delta t \, |S_{ij}|}{|C_i| + |C_j|} \tag{6.95}$$

where $\lambda_k(\boldsymbol{W})$ is the k^{th} characteristic velocity.

In both expression of $d_{2;i+\frac{1}{2}}(\boldsymbol{W}^n)$ and $d_{4;i+\frac{1}{2}}(\boldsymbol{W}^n)$, the artificial viscosity variables $\varepsilon^{(2)}$ and $\varepsilon^{(4)}$ get the form:

$$\begin{cases} \varepsilon_{i+\frac{1}{2}}^{(2)} = \tilde{\mu}_2 \max(\check{\Delta}_i, \check{\Delta}_{i+1}) \\ \varepsilon_{i+\frac{1}{2}}^{(4)} = \max(0, \tilde{\mu}_4 \varepsilon_{i+\frac{1}{2}}^{(2)}) \end{cases} \tag{6.96}$$

Where $\tilde{\mu}_2$ and $\tilde{\mu}_4$ are constant which are respectively typically equal to $\frac{1}{4}$ and $\frac{1}{256}$ (Jameson, Schmidt, and Turkel 1981) but still have to be adjusted depending on the flow. Moreover this expression shows the sensor $\check{\Delta}$ which aims at detecting discontinuity. The original sensor

proposed in (Jameson, Schmidt, and Turkel 1981) for Euler equations is based on pressure.

$$\check{\Delta}_{Jam} = \frac{\|P_{i+1} - 2P_i + P_{i-1}\|}{\|P_{i+1}\| + \|2P_i\| + \|P_{i-1}\|} \tag{6.97}$$

Swanson and Turkel (Swanson and Turkel 1991) improved the sensor to make it closer to the TVD properties but added a new parameter χ in the problem, leading to:

$$\check{\Delta}_{Swan} = \frac{\|P_{i+1} - 2P_i + P_{i-1}\|}{(1-\chi)\left(\|P_{i+1} - P_i\| + \|P_i - P_{i-1}\|\right) + \chi\left(\|P_{i+1}\| + \|2P_i\| + \|P_{i-1}\|\right)} \tag{6.98}$$

Finally, these last sensors were slightly changed by ONERA in order to take into account the absolute velocity and pressure at the same time, then adding a new variable α. For PGD Dupays (Dupays 1996) modified the sensor of Swanson and Turkel in order to take into account the density instead of the pressure and used the same methodology as Lupoglazoff and Vuillot (Lupoglazoff and Vuillot 1991) to introduce a term depending on the absolute velocity. Extending the equations (6.97) and (6.98) to arbitrary scalar values φ_1 and φ_2, those can be written:

$$\check{\Delta} = \alpha\check{\Delta}\varphi_1 + (1-\alpha)\check{\Delta}\varphi_2 \tag{6.99}$$

Even if the AV is generally needed in order to correctly fulfill a simulation where singularities occur, this procedure has a non-negligible cost. An audit of performance made on SIERRA by Dupays (Dupays 1996) showed that for the disperse phase the AV procedure alone costs 25% more CPU time than the original MacCormack procedure itself and thus can more than double the CPU time of a simulation. Moreover, the adjustment of four problem dependent variables can require a non negligible human time to be set.

6.3.1.7 Flux limiter

6.3.1.7.1 Second order TVD scheme for linear advection The flux limiter technology has been developed in the 80's and 90's to overcome the main drawbacks of the artificial viscosity which are the case dependency and the sensor design. This development find common origins in the works of Van leer (van Leer 1974), Roe (Roe 1981), Harten (Harten 1983) and finally Sweby (Sweby 1984) who defined the notion of second order accurate TVD flux limiter. The general objective of the flux limiter is to adapt second order FD based scheme in order to provide TVD property starting from a detailed analysis of the behavior of these schemes on the linear

advection equation (6.69). We thus define a scheme under the following form:

$$w_i^{n+1} = w_i^n - \nu(w_i^n - w_{i-1}^n) - \Delta_- \left\{ \varphi_i \frac{1}{2}(1-\nu)\nu(w_{i+1}^n - w_i^n) \right\} \tag{6.100}$$

where φ_i is the limiter associated to the cell i.

In view of (6.80) but also (6.81), it appears that the objective of the limiter is to limit the anti-diffusion. It shall be remarked that for $\varphi_i = \varphi_{\text{LW}} = 1$, (6.100) is equivalent to the Lax-Wendroff scheme (6.80) and for $\varphi_i = \varphi_{\text{BW}} = r_i = \frac{w_i^n - w_{i-1}^n}{w_{i+1}^n - w_i^n}$, where the r_i is the slope ratio, it corresponds to the Beam-Warming scheme (6.81). Then by searching the conditions on φ_i such that the update w_i^{n+1} is necessarily a convex combination of w_{i-1}^n, w_{i-1}^n and w_{i-1}^n, it is possible to put (6.100) under the form (6.30) and to deduce the conditions to provide the LED property. This gives:

$$w_i^{n+1} - w_i^n = \nu \left(1 - \frac{\varphi_{i-1}}{2}(1-\nu) + \frac{\varphi_i}{2r_i}(1-\nu) \right) (w_{i-1}^n - w_i^n) \tag{6.101}$$

To set sufficient conditions on φ_i such that it can be determined locally, it is supposed that $\varphi_i \geq 0$. Then, one can easily deduce the following sufficient TVD conditions, allowing a CFL dependence or under CFL-free conditions, assuming $0 \leq \nu \leq 1$:

$$\begin{cases} 0 \leq \varphi_i^{CFL} \leq \frac{2}{1-\nu}, \\ 0 \leq \frac{\varphi_i^{CFL}}{r_i} \leq \frac{2}{\nu}, \end{cases} \qquad \begin{cases} 0 \leq \varphi_i \leq 2, \\ 0 \leq \frac{\varphi_i}{r_i} \leq 2. \end{cases} \tag{6.102}$$

To complete such constraints, it is also wished that the scheme remains globally second order. Such a property can be obtained through the so-called *Sweby zone* that defines, depending on the slope ratio, the domain where (6.100) is both TVD in the sense of (6.102) and second-order. This *Sweby zone* area is represented in Figure 6.4. If it is wished to use the flux limiter to correct the Lax-Wendroff scheme only when it is required to fulfill TVD condition, then, it shall take the form (Sweby 1984):

$$\varphi_{\text{TVD-LW}}(r) = \max(0, \min(2r, 1)) \tag{6.103}$$

Also, to clearly separate the dissipation induced by the limiter from the original Lax-Wendroff scheme aimed at being used, one can rewrite (6.100) as :

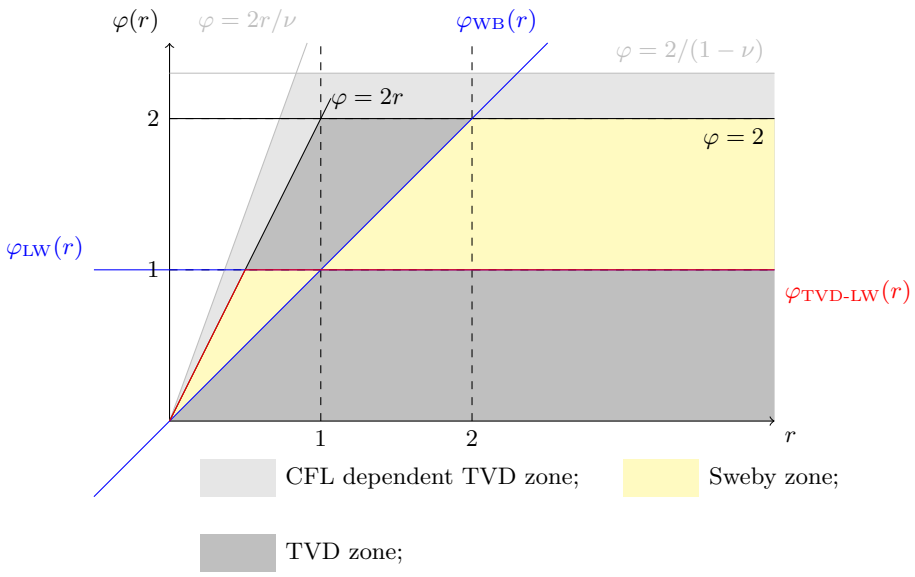

Figure 6.4: *Sweby zone and remarkable flux limiters*

$$\underbrace{w_i^{n+1} = w_i^n - \nu(w_i^n - w_{i-1}^n) - \Delta_- \left\{ \varphi_i \frac{1}{2}(1-\nu)\nu(w_{i+1}^n - w_i^n) \right\}}_{\text{Lax-Wendroff scheme}} + \underbrace{\Delta_- \left\{ (1-\varphi_i) \frac{1}{2}(1-\nu)\nu(w_{i+1}^n - w_i^n) \right\}}_{\text{Artificial disspation}} \quad (6.104)$$

Starting from the form (6.104), it is possible to attempt to design an artificial dissipation able to ensure TVD property.

6.3.1.7.2 Extension to non-linear systems of equations Applied in a more general context, for non-linear systems of equations, the use of such a method is however not straightforward. As explained in Section 6.3.1.1.1 and Section 6.3.1.4, the Lax-Wendroff scheme for non-linear systems of equations can take several forms. Moreover, such non-TVD schemes are usually implemented in programs and can give excellent results for smooth cases without the need of adjustment. A standard formulation of the TVD method has then been given by Davis (Davis 1984b) soon after the work of Sweby (Sweby 1984), summed up here-above, in order to express the TVD adjustment as an additional step to a scheme of Lax-Wendroff class. The procedure leads to an additional term that is homogeneous to a diffusion and explains why the original paper (Davis 1984b) named *artificial viscosity* that additional TVD step.

This last step takes the following form:

$$\boldsymbol{W}_i^{n+1} = \overline{\boldsymbol{W}}_i^{n+1} + \left[\overline{G}^+(r_i^+) + \overline{G}^-(r_{i-1}^-) \right] (\boldsymbol{W}_{i+1}^n - \boldsymbol{W}_i^n) - \left[\overline{G}^+(r_{i-1}^+) + \overline{G}^-(r_i^-) \right] (\boldsymbol{W}_i^n - \boldsymbol{W}_{i-1}^n) \quad (6.105)$$

where $\overline{\boldsymbol{W}}_i^{n+1}$ is the solution obtained by an uncorrected scheme of Lax-Wendroff class and $\overline{G}^{\pm}$ such as $r^{\pm}$ are given by:

$$\begin{cases} r_i^+ = \frac{<\boldsymbol{W}_i^n - \boldsymbol{W}_{i-1}^n, \boldsymbol{W}_{i+1}^n - \boldsymbol{W}_i^n>}{<\boldsymbol{W}_{i+1}^n - \boldsymbol{W}_i^n, \boldsymbol{W}_{i+1}^n - \boldsymbol{W}_i^n>} & r_i^- = \frac{<\boldsymbol{W}_i^n - \boldsymbol{W}_{i-1}^n, \boldsymbol{W}_{i+1}^n - \boldsymbol{W}_i^n>}{<\boldsymbol{W}_i^n - \boldsymbol{W}_{i-1}^n, \boldsymbol{W}_i^n - \boldsymbol{W}_{i-1}^n>} \\ \overline{G}^{\pm}(r_i^{\pm}) = \frac{1}{2} C(\nu_i) \left[1 - \varphi(r_i^{\pm}) \right] & C(\nu_i) = \begin{cases} \nu_i(1-\nu_i), & \nu_i \leqslant 0.5 \\ 0.25, & \nu_i > 0.5 \end{cases} \\ \varphi(r_i^{\pm}) = \max(0, \min(2r_i^{\pm}, 1)) & \nu_i = \max(|\lambda_i|) \frac{\Delta t}{\Delta x} \end{cases} \quad (6.106)$$

where this operator $< \bullet, \bullet >$ is the inner product.

Typically, the $\overline{\boldsymbol{W}}_i^{n+1}$ is obtained by a MacCormack scheme (Davis 1984b; Causon 1989; Yee 1987; Vincent, Caltagirone, and Bonneton 2001) (see Section 6.3.1.5) because of its numerical efficiency and ability for supersonic flows. Also, it is possible to improve the limiter by taking into account simultaneously the slope ratio from both sides of the interfaces (Roe 1984).

The main drawback of such a correction lies in the definition given to the slope ratio. Since a

vector of conservative quantities is taken into account while the limiter is a scalar function, the inner product of (6.106) is arbitrarily chosen. However because of this choice, the presence of a discontinuity on any field leads to a maximal level of dissipation on every quantities. This explains why (Causon 1989) proposed to add an artificial compression terms to correct this issue.

A second strategy consists in diagonalizing the Jacobian matrix in order to apply the limiter on a linearized conservative form. Expressed for the first time by Yee (Yee 1987) for implicit/explicit schemes in the context of steady configurations, it has been formulated for explicit methods in (Vincent, Caltagirone, and Bonneton 2001) based on the work of Jameson (Jameson 1995b) and results in a less diffusive formulation. Starting from the description of (Vincent, Caltagirone, and Bonneton 2001), we describe the TVD step under the following form:

$$\boldsymbol{W}_i^{n+1} = \overline{\boldsymbol{W}_i^{n+1}} - \frac{\Delta x}{\Delta t}\left(\boldsymbol{R}_{i+1/2}\boldsymbol{\varphi}_{i+1/2} - \boldsymbol{R}_{i-1/2}\boldsymbol{\varphi}_{i-1/2}\right) \tag{6.107}$$

where $\boldsymbol{R}$ is the right Eigenmatrix (see Section 3.2.2.2) and limiter vector that can be expressed through each of its component k as:

$$\varphi_{i+1/2}^k = \frac{1}{2}\left[\|\lambda_{i+1/2}^k\| - \frac{\Delta x}{\Delta t}(\lambda_{i+1/2}^k)^2\right](\alpha_{i+1/2}^k - Q_{i+1/2}^k) \tag{6.108}$$

where $\lambda_{i+1/2}^k$ is the local characteristic velocity of the kth component, $\boldsymbol{\alpha}_{i+1/2} = \boldsymbol{L}_{i+1/2}(\boldsymbol{W}_{i+1} - \boldsymbol{W}_i)$ the variation expressed in the characteristic space, also called *wave strength*, and $Q_{i+1/2}^k$ the flux limiter of the corresponding component.

Inspired by the work of (Roe 1984), the authors proposed to use a minmod limiter such as $Q_{i+1/2}^k = \text{minmod}(\alpha_{i-1/2}^k, \alpha_{i+1/2}^k, \alpha_{i+3/2}^k)$ which is described as giving sufficiently good results while ensuring robustness.

However, the implementation requires an initial analysis of the used system of equations and is then not generically applicable to every hyperbolic systems. Moreover, for PGD, such method cannot be directly used since the Jacobian matrix is not diagonalizable.

Finally, a last solution to design a TVD scheme for non-linear system of equations is to express it in the following way:

$$\begin{cases} \boldsymbol{W}_i^{n+1} = \boldsymbol{W}_i^n - \frac{\Delta t}{\Delta x}(\mathfrak{F}_{i+1/2}^{TVD} - \mathfrak{F}_{i-1/2}^{TVD}) \\ \mathfrak{F}_{i+1/2}^{TVD} = \mathfrak{F}_{i+1/2}^{H} - (1-\varphi_{i+1/2})(\mathfrak{F}_{i+1/2}^{H} - \mathfrak{F}_{i+1/2}^{L}) \end{cases} \tag{6.109}$$

where $\mathfrak{F}_{i+1/2}^{TVD}$ is the TVD flux, $\mathfrak{F}_{i+1/2}^{H}$ is a high order flux and $\mathfrak{F}_{i+1/2}^{L}$ a low order flux.

To be consistent with the other TVD schemes presented until here, $\mathfrak{F}_{i+1/2}^{H}$ shall be a flux of Lax-Wendroff class and $\mathfrak{F}_{i+1/2}^{L}$ a Roe flux (see Section 6.3.2.2.2). However, other choices are

possible. That last approach has been widely investigated in the context of FEM (Boris and Book 1997; Löhner et al. 1987; Kuzmin 2009)

The procedures described here have the common objective to *add* an artificial dissipation in an independent step. Such way to express the problem leads to difficulties and to formulation of the dissipative almost dedicated to each system of equations to obtain satisfactory results. Put aside the constraints of FD scheme concerning the meshes, this need of an *external* dissipation is the major drawback of FD methods and mostly fails at dealing with truly non-linear system of equations, singularities and realizability issues.

6.3.2 Finite volume based numerical flux

Unlike the FD approaches, the FV framework genuinely defines fluxes at discontinuities. The absence of knowledge of the solution at the cell interface is not an issue and is at the origin of a wide category of numerical schemes.

6.3.2.1 The Godunov approach

6.3.2.1.1 The concept The original idea proposed by Godunov (Godunov 1959) is to introduce the resolution of a small physical problem inside the numerical scheme (Godunov 1999b). To do so, between each interface, a Riemann problem is solved and the flux is deduced from the resolution of this singularity. Let a one-dimensional discontinuity be defined at an interface of position $x = 0$, then the initial condition of a Riemann problem yields:

$$\begin{cases} \boldsymbol{W}(x) = \boldsymbol{W}_l, & \text{if } x < 0, \\ \boldsymbol{W}(x) = \boldsymbol{W}_r, & \text{if } x > 0, \end{cases} \tag{6.110}$$

where $\boldsymbol{W}_l$ and $\boldsymbol{W}_r$ are the constant states on the left and the right side of the interface.

Most systems of equations, including the whole set of models studied in this work, are self-similar according to the characteristic field. As a consequence, the solution in the (x, t) plan is a function of the characteristic x/t only. Such problem thus has a unique solution that can be $\boldsymbol{\omega}_{RP}(\boldsymbol{W}_l, \boldsymbol{W}_r, \frac{x}{t})$.

At first order, the solution inside a cell is assumed to be uniform, as represented in Figure 6.5. Therefore, since the flux at each side of the cell is constant and known thanks to the Riemann solver, the Godunov scheme yields:

$$\begin{cases} \boldsymbol{W}_i^{n+1} = \boldsymbol{W}_i^n - \frac{\Delta t}{\Delta x}\left(\boldsymbol{f}\left(\boldsymbol{W}_{i+1/2}^*\right) - \boldsymbol{f}\left(\boldsymbol{W}_{i-1/2}^*\right)\right), \\ \boldsymbol{W}_{i+1/2}^* = \boldsymbol{\omega}_{RP}(\boldsymbol{W}_i^n, \boldsymbol{W}_{i+1}^n, \frac{x}{t} = 0). \end{cases} \tag{6.111}$$

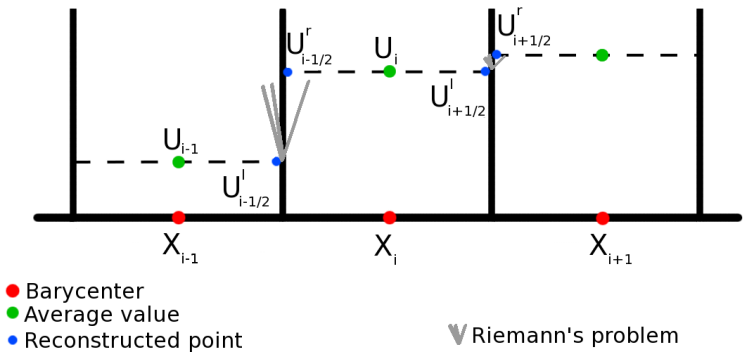

Figure 6.5: *First order reconstruction of the Godunov class of schemes*

The discontinuities can be genuinely treated since such situation is considered at each interface and this formulation of the problem ensures the respect of the positivity of the solution. It is a proper extension of the first order upwind scheme (6.79), designed for the linear advection (6.69), that is able to treat the complete non-linear eigen structure of the system of equations. In this section, only one-dimensional Riemann solvers are discussed. Extensions and specificities related to multidimensional frameworks are given Section 6.3.3.

6.3.2.1.2 Typical exact solvers In some cases, the exact Riemann solver associated to the system of equations is available and can be easily derived:

6.3.2.1.2.1 Linear advection In this highly simplified case, the Riemann solver corresponds to the detection of the simple upwinding direction:

$$\boldsymbol{\omega}_{RP}^{lin}(w_l, w_r, \frac{x}{t}) = \begin{cases} w(x) = w_l, & \text{if } \frac{x}{t} < a, \\ w(x) = w_r, & \text{if } \frac{x}{t} > a, \end{cases} \tag{6.112}$$

6.3.2.1.2.2 Burgers equation In the case of the Burgers equation (3.13), either an isolated shock ($u_l > u_r$) or a rarefaction wave ($u_l \leq u_r$) can appear in the Riemann problem (see Figure 6.6) and thus these two cases have to be treated. This exact Riemann solver has been treated as an example in (LeVeque 1992; Massot and Larat 2014) and yields:

$$\boldsymbol{\omega}_{RP}^{\text{Burgers}}(u_l, u_r, \frac{x}{t}) = \begin{cases} \begin{cases} u_l & \text{for } x < V_s t, \\ u_r & \text{for } x > V_s t, \quad \text{if } u_l > u_r, \\ \sigma & \text{for } x = V_s t, \end{cases} \\ \begin{cases} u_l & \text{for } x \leq u_l t, \\ \frac{x}{t} & \text{for } u_l t < x < u_r t, \quad \text{if } u_l \leq u_r, \\ u_r & \text{for } x \geq u_r t, \end{cases} \end{cases} \tag{6.113}$$

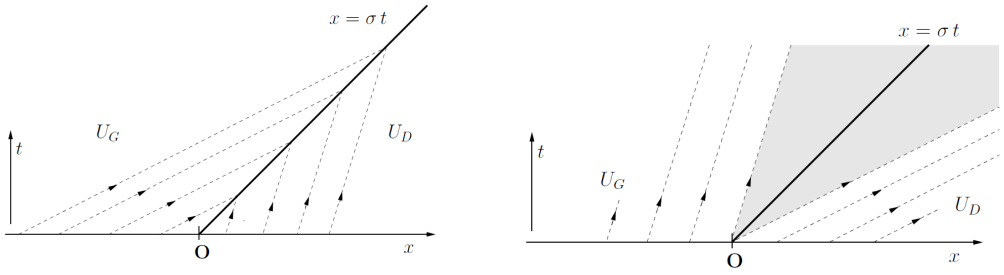

(a) shock case **(b)** rarefaction case

Figure 6.6: *Solution of the Riemann problem on Burgers equation*

where $V_s = \frac{u_l+u_r}{2}$ is the shock velocity.

6.3.2.1.2.3 Pressureless Gas Dynamic Since this system is weakly hyperbolic, there is, as for the Burgers equation, only one possible shock wave. However no rarefaction wave is created since vacuum appears instead and no velocity can thus be described. The solution presented here is the same as introduced in (Bouchut, Jin, and Li 2003):

$$\boldsymbol{\omega}_{RP}^{\mathrm{PGD}}(\boldsymbol{W}_l, \boldsymbol{W}_r, \frac{x}{t}) = \begin{cases} \begin{cases} \boldsymbol{W}_l & \text{for } x < V_s t, \\ [m(t), m(t)V_s]^t & \text{for } x = V_s t, \quad \text{if } u_l > u_r, \\ \boldsymbol{W}_r & \text{for } x > V_s t, \end{cases} \\ \begin{cases} \boldsymbol{W}_l & \text{for } x < u_l t, \\ [0,0]^t & \text{for } u_l t \geq x \leq u_r t, \quad \text{if } u_l \leq u_r, \\ \boldsymbol{W}_r & \text{for } x > u_r t, \end{cases} \end{cases} \tag{6.114}$$

where the δ-shock mass $m(t)$ and velocity V_s are defined by:

$$\begin{cases} m(t) &= \sqrt{\rho_l \rho_r}(u_l - u_r)t, \\ V_s &= \frac{\sqrt{\rho_l}u_l + \sqrt{\rho_r}u_r}{\sqrt{\rho_l}+\sqrt{\rho_r}}. \end{cases} \tag{6.115}$$

Two specific cases can arise at an interface from the exact solution, the vacuum and the stationary δ-shock. In both cases however, no flux is deduced through the interface since the density is null in the case of vacuum and the velocity is null (or equal to the interface velocity) in the case of the δ-shock. Therefore, thanks to the FV formulation of the problem, such singularities are not an issue since the flux is known.

6.3.2.1.2.4 Euler equation Due to the three equations involved in the problem, three discontinuities can occur. The solution is usually represented with an expansion fan and a shock wave surrounding a contact discontinuity. More generally, it is possible to obtain two shocks or two expansion waves but a contact discontinuity remains between both of them. The only case where the contact discontinuity disappears occurs when vacuum is generated.

Aside from the vacuum case, the solution needs the determination of the pressure around the contact discontinuity. This term has no explicit solution and has then to be approximated through an iterative procedure of convergence. One of the most efficient exact Riemann solver for Euler equation can be found in (Gottlieb and Groth 1988).

6.3.2.2 Approximate Riemann solvers

In practice, due to the non-linearities, an exact Riemann solver has a prohibitive cost, as it usually relies on a iterative solver. Thus, a realizability preserving and entropy consistent approximate Riemann solver is generally preferred to reduce the computational cost. Some relevant approximate Riemann solvers are introduced here and we refer to (Toro 2009) for a broader view of this field. The approximate Riemann solvers do not necessarily rely on the estimation of the solution of the Riemann problem $\boldsymbol{W}^*_{i+1/2}$ as in (6.111) but directly approximate the flux such that:

$$\boldsymbol{W}_i^{n+1} = \boldsymbol{W}_i^n - \frac{\Delta t}{\Delta x}\left(\mathfrak{F}\left(\boldsymbol{W}_i^n, \boldsymbol{W}_{i+1}^n\right) - \mathfrak{F}\left(\boldsymbol{W}_{i-1}^n, \boldsymbol{W}_i^n\right)\right), \tag{6.116}$$

6.3.2.2.1 Rusanov flux Presented in (Rusanov 1961), it has been designed in order to add a sufficient level of dissipation to ensure the stability of the flux starting from a centered estimation. As a consequence, the flux takes the expression:

$$\mathfrak{F}^{\text{Rusanov}}\left(\boldsymbol{W}_l, \boldsymbol{W}_r\right) = \frac{1}{2}\left(\boldsymbol{f}(\boldsymbol{W}_l) + \boldsymbol{f}(\boldsymbol{W}_r)\right) - \frac{\|\lambda_{max}(\boldsymbol{W}_l, \boldsymbol{W}_r)\|}{2}\left(\boldsymbol{W}_r - \boldsymbol{W}_l\right), \tag{6.117}$$

where $\|\lambda_{max}\|$ is the norm of the maximal propagation wave speed estimated from $\boldsymbol{W}_l$ and $\boldsymbol{W}_r$

The flux is also referred as the *Local Lax-Friedrichs* flux since one can observe that it has the same form as the Lax-Friedrichs flux where the grid dependent term $\frac{\Delta x}{\Delta t}$ has been replaced by the norm of the signal velocity $\|\lambda_{max}\|$.

6.3.2.2.2 Roe flux An important class of approximate Riemann solvers has been introduced by Roe (Roe 1981; Roe and Pike 1985).

6.3.2.2.2.1 Upwind flux Put in a nutshell, it consists in approximating the Jacobian matrix of the system with a constant coefficient matrix in the neighbor of the interface of interest. From the linear transport of the information in the characteristic field, one can deduce a flux.

$$\mathfrak{F}^{\text{Roe}}\left(\boldsymbol{W}_l, \boldsymbol{W}_r\right) = \frac{1}{2}\left(\boldsymbol{f}(\boldsymbol{W}_l) + \boldsymbol{f}(\boldsymbol{W}_r)\right) - \frac{1}{2}\overline{\boldsymbol{R}}\left|\overline{\boldsymbol{\Lambda}}\right|\overline{\boldsymbol{L}}\left(\boldsymbol{W}_r - \boldsymbol{W}_l\right), \tag{6.118}$$

where the index $*$ indicate the evaluation of the matrix through the Roe average, $\left|\overline{\boldsymbol{\Lambda}}\right| = \boldsymbol{diag}\left(\|\overline{\lambda}_1\|, \ldots, \|\overline{\lambda}_N\|\right)$ is diagonal matrix of the normalized characteristics and N is the number of equations in the system.

This implicitly leads to correcting a centered flux by approximating the *upwinding* according in the characteristic fields, which would be the case if the system were linear. This explains why the Roe flux can appear in the derivation of FD base flux as in (Daru and Tenaud 2004). The difficulty relies in the determination of the eigenmatrix $\overline{\boldsymbol{A}}$ and its decomposition at the interface since the solution is unknown at this position.

6.3.2.2.2.2 Roe average The value $\overline{\boldsymbol{W}}$ used to compute $\overline{\boldsymbol{A}}$ could have been interpreted as a arithmetic average between $\boldsymbol{W}_l$ and $\boldsymbol{W}_r$, which is the easiest choice from a practical perspective. However, it would be purely arbitrary since the value at the cell interface is unknown. One of the most famous method to approximate $\overline{\boldsymbol{A}}$ is proposed by Roe in (Roe 1981) alongside its scheme. The idea is to find the matrix $\boldsymbol{A}_*(\boldsymbol{W}_l, \boldsymbol{W}_r)$ that fulfills the following properties:

1. $\overline{\boldsymbol{A}}$ constitutes a linear mapping from the vector space $\boldsymbol{W}$ to the vector space $\boldsymbol{f}$,
2. $\overline{\boldsymbol{A}}(\boldsymbol{W}, \boldsymbol{W}) = \boldsymbol{A}(\boldsymbol{W})$,
3. $\overline{\boldsymbol{A}_*}(\boldsymbol{W}_l, \boldsymbol{W}_r) \cdot (\boldsymbol{W}_l - \boldsymbol{W}_r) = (\boldsymbol{f}_l - \boldsymbol{f}_r)$ for any $\boldsymbol{W}_l$, $\boldsymbol{W}_r$,
4. The eigenvectors of $\overline{\boldsymbol{A}}$ are linearly independent.

One can then define the Roe's average vector $\overline{\boldsymbol{W}}$ of $\boldsymbol{W}_l$ and $\boldsymbol{W}_r$ such that $\overline{\boldsymbol{A}}(\boldsymbol{W}_l, \boldsymbol{W}_r) = \boldsymbol{A}(\overline{\boldsymbol{W}})$. Considering the development of one-step Lax-Wendroff and high order FD based schemes for non-linear systems of equations, such as (6.84), this is more coherent to describe the Jacobian matrix $\boldsymbol{A}$ from the Roe's average than from the arithmetic one, since such need naturally appears in the Cauchy-Kowalewski procedure. For the reminder, Roe's averages of some non-linear equations are sum up here:

- **Burgers equation:** $\overline{u} = \frac{u_l + u_r}{2}$ that is equivalent to the arithmetic average,
- **PGD equations:** $\overline{u} = \frac{\sqrt{\rho_l}u_l + \sqrt{\rho_r}u_r}{\sqrt{\rho_l} + \sqrt{\rho_r}}$,
- **Euler equation:** $\overline{u} = \frac{\sqrt{\rho_l}u_l + \sqrt{\rho_r}u_r}{\sqrt{\rho_l} + \sqrt{\rho_r}}$, $\overline{h} = \frac{\sqrt{\rho_l}h_l + \sqrt{\rho_r}h_r}{\sqrt{\rho_l} + \sqrt{\rho_r}}$
- **10 Moments closure:** $\overline{u_i} = \frac{\sqrt{\rho_l}u_{i,l} + \sqrt{\rho_r}u_{i,r}}{\sqrt{\rho_l} + \sqrt{\rho_r}}$, $\overline{h_{ij}} = \frac{\sqrt{\rho_l}h_{ij,l} + \sqrt{\rho_r}h_{ij,r}}{\sqrt{\rho_l} + \sqrt{\rho_r}}$.

A common problem encountered for the PGD, Euler and 10 Moments closure equations is that the density does not appear in the Jacobian. As explain in (Brown 1996), it is generally assumed for the density that the following relation is true:

$$\Delta(\rho u) = \overline{\rho}\Delta(u) + \overline{u}\Delta(\rho). \tag{6.119}$$

For the systems cited, this leads to:

$$\overline{\rho} = \sqrt{\rho_l \rho_r}. \tag{6.120}$$

These results can be found in (Hirsch 1990) for Euler and Burgers equations and in (Brown 1996) for the 10 Moment closure. It shall also be remarked that despite a Roe's average exists for Pressureless Gas Dynamic, no Roe flux can be determined because of the weak-hyperbolicity of this system. Also, as observed in (Einfeldt et al. 1991), the Roe average is not necessarily a realizable state, especially near vacuum.

6.3.2.2.2.3 Entropy fix A known drawback of the Roe flux, namely the *entropy glitch*, is a discontinuity appearing in an expansion then the velocity reaches at sonic point. Such shock is not physical and is caused by the anti-dissipative effect of the changing of sign of non linear degeneration characteristics. As consequence an *entropy fix* needs to be used (Harten and Hyman 1983) and we refer to the dedicated section of (Toro 2009) for more details on this subject.

6.3.2.2.3 HLL class of solvers From a completely different perspective, it is possible to establish a flux starting from the conservation property of the system of equations. Called from the initials of the authors that designed it (Harten, Lax, and Van Leer 1983), the Harten, Lax, van Leer (HLL) scheme assumes the existence of a uniform state $\boldsymbol{W}_{HLL}$ in the area disturbed by the discontinuity bounded by the signal velocities λ_l and λ_r. Thus, we look for a flux for an approximated solution of the Riemann problem under the form:

$$\boldsymbol{W}(x,t) \approx \begin{cases} \boldsymbol{W}_l, & \forall \frac{x}{t} \leq \lambda_l, \\ \boldsymbol{W}_{HLL} & \forall \lambda_l \leq \frac{x}{t} \leq \lambda_r, \\ \boldsymbol{W}_r & \forall \lambda_r \leq \frac{x}{t}, \end{cases} \tag{6.121}$$

Imposing conservation of $\boldsymbol{W}$ across the disturbed area, one can find:

$$\boldsymbol{W}_{HLL} = \frac{\lambda_r \boldsymbol{W}_r - \lambda_l \boldsymbol{W}_l + \boldsymbol{f}_l - \boldsymbol{f}_r}{\lambda_r - \lambda_l}, \tag{6.122}$$

The numerical flux is not defined as the flux of this state ($\mathfrak{F}^{HLL}(\boldsymbol{W}_l, \boldsymbol{W}_r) \neq \boldsymbol{f}(\boldsymbol{W}_{HLL})$) but is deduced from conservation laws. Thanks to the autosimilarity of the problem, the flux at the interface is constant. It is thus possible to evaluate it by determining the flux necessary to update $\boldsymbol{W}_l$ and $\boldsymbol{W}_r$ to $\boldsymbol{W}_{HLL}$ in the intermediate area. Then, thanks to conservation relations,

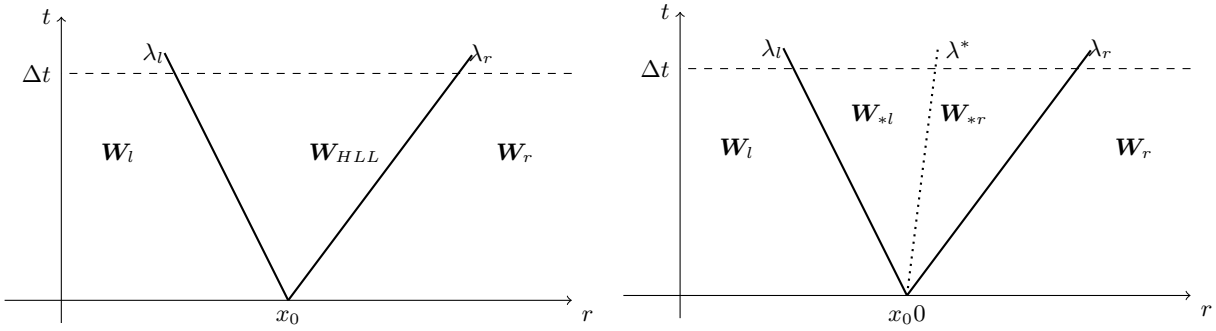

(a) HLL **(b)** HLLC

Figure 6.7: *HLL and HLLC approximation of the Riemann problem*

on can obtain:

$$\mathfrak{F}^{HLL}(\boldsymbol{W}_l, \boldsymbol{W}_r) = \frac{\lambda_r \boldsymbol{f}(\boldsymbol{W}_l) - \lambda_l \boldsymbol{f}(\boldsymbol{W}_r) + \lambda_r \lambda_l (\boldsymbol{W}_r - \boldsymbol{W}_l)}{\lambda_r - \lambda_l}. \tag{6.123}$$

We refer to Section 6.3.3.3 for a proper and general derivation of this scheme. In any case, the expression of the flux completely depends on the value given to λ_l and λ_r. To ensure the realizability of $\boldsymbol{W}_{HLL}$ on which the update is based, λ_l and λ_r shall embrace all the characteristics velocities. Starting from the approximation that these values are deduced from the left and right states, one can obtain:

$$\begin{cases} \lambda_r &= \max\left(0, \lambda_{max}\right), \\ \lambda_l &= \min\left(0, \lambda_{min}\right), \end{cases} \qquad \begin{aligned} \lambda_{max} &= \max\left(\lambda^+(\boldsymbol{W}_l), \lambda^+(\boldsymbol{W}_r)\right), \\ \lambda_{min} &= \min\left(\lambda^-(\boldsymbol{W}_l), \lambda^-(\boldsymbol{W}_r)\right), \end{aligned} \tag{6.124}$$

where λ^- and λ^+ are the smallest and highest physical signal velocities taken from a given state.

An improvement of Einfeldt (Einfeldt 1988; Einfeldt et al. 1991) (but also Davis (Davis 1988)) proposes to introduce the Roe average, when realizable, in the signal velocity determination (6.124) defining thus the Harten, Lax, van Leer-Einfeldt (HLLE) flux. Such a modification increases the robustness and sometime prevents from spurious oscillations, especially near large shocks.

Remark 6.4. *Setting $\lambda_r = -\lambda_l = \|\lambda_{max}\|$, one can deduce from (6.123) the Rusanov flux (6.117). Moreover, we designate* Rusanov state *the HLL state (6.122) associated to that specific definition of the signal velocities, this leads to:*

$$\boldsymbol{W}^{Rusanov} = \frac{1}{2}\left[\boldsymbol{W}_r + \boldsymbol{W}_l\right] + \frac{\boldsymbol{f}_l - \boldsymbol{f}_r}{2\|\lambda_{max}\|}, \tag{6.125}$$

6.3.2.2.4 HLLC class of solvers One of the main drawbacks of the HLL scheme lies in its diffusion. This phenomenon has an important impact on the resolution of the intermediate waves such has the contact discontinuity. The idea behind the HLL-Contact (HLLC) scheme (Toro, Spruce, and Speares 1994) is to consider the presence of two states separated by a discontinuity inside the disturbed area, as shown Figure 6.7. Therefore the solution of the Riemann problem and the associated flux are approximated by:

$$\boldsymbol{W}(x,t) \approx \begin{cases} \boldsymbol{W}_l, & \forall \frac{x}{t} \leq \lambda_l, \\ \boldsymbol{W}_{*l} & \forall \lambda_l \leq \frac{x}{t} \leq \lambda^*, \\ \boldsymbol{W}_{*r} & \forall \lambda^* \leq \frac{x}{t} \leq \lambda_r, \\ \boldsymbol{W}_r & \forall \lambda_r \leq \frac{x}{t}, \end{cases} \qquad \mathfrak{F}^{\text{HLLC}} = \begin{cases} \boldsymbol{f}_l, & \forall 0 \leq \lambda_l, \\ \boldsymbol{f}_{*l} & \forall \lambda_l \leq 0 \leq \lambda^*, \\ \boldsymbol{f}_{*r} & \forall \lambda^* \leq 0 \leq \lambda_r, \\ \boldsymbol{f}_r & \forall \lambda_r \leq 0. \end{cases} \tag{6.126}$$

Then, using the conversation property on the characteristic field, one can obtain the three equations that follows:

$$\begin{cases} \boldsymbol{f}_{*l} &= \boldsymbol{f}_l + \lambda_l \left(\boldsymbol{W}_{*l} - \boldsymbol{W}_l \right), \\ \boldsymbol{f}_{*r} &= \boldsymbol{f}_{*r} + \lambda^* \left(\boldsymbol{W}_{*r} - \boldsymbol{W}_{*l} \right), \\ \boldsymbol{f}_{*r} &= \boldsymbol{f}_r + \lambda_r \left(\boldsymbol{W}_{*r} - \boldsymbol{W}_r \right), \end{cases} \tag{6.127}$$

where $\boldsymbol{W}_{*l}$,$\boldsymbol{W}_{*r}$,$\boldsymbol{f}_{*l}$ and $\boldsymbol{f}_{*r}$ are unknowns.

The key issue in schemes of this class is to set additional conditions based on the physical properties of the model in order to close these three equations system with four unknown variables and deduce the numerical flux. Such development has original been conducted for the Euler equation and the problem is closed from the properties associated to the contact discontinuity, which imposes that the velocities and pressures of $\boldsymbol{W}_{*l}$ and $\boldsymbol{W}_{*r}$ are equal. Once again, after stating that λ^* is equal to the convection velocity in the disturbed region, the problem is completely driven by λ_l and λ_r that have to be chosen carefully (Batten et al. 1997; Toro 2009). Thus we use the same estimations than for the HLLE to take into account the most constraining waves established from the left and right states $\boldsymbol{W}_l$ and $\boldsymbol{W}_r$ as well as their Roe average.

This method greatly improves the resolution of the contact discontinuity compare to a HLL solver and it also solves accurately the transported scalar that are overly diffused by the HLL scheme. It is however possible to obtain similar results without relying on a scheme that have to be specifically derived for each model.

6.3.2.2.5 HLLEM solver The HLLE-Modified (HLLEM) scheme (Einfeldt 1988; Einfeldt et al. 1991), aims at reducing the dissipation caused by the HLL scheme by taking into account the intermediate waves. Originally designed as an alternative to the HLLC schemes, the theory on which relies the HLLEM is much more generalizable. It aims at reducing the dissipation of the HLL scheme by a linear decomposition of the flux in the disturbed area through a development associated to the Roe flux. Starting from the formulation given in (Dumbser and Balsara 2016), the numerical flux of this solver yields:

$$\mathfrak{F}^{HLLEM}(\boldsymbol{W}_l,\boldsymbol{W}_r)=\underbrace{\frac{\lambda_r\boldsymbol{f}(\boldsymbol{W}_l)-\lambda_l\boldsymbol{f}(\boldsymbol{W}_r)+\lambda_r\lambda_l(\boldsymbol{W}_r-\boldsymbol{W}_l)}{\lambda_r-\lambda_l}}_{\text{HLL flux}} - \underbrace{\varphi\frac{\lambda_r\lambda_l}{\lambda_r-\lambda_l}\overline{\boldsymbol{R}}\,\overline{\delta}\overline{\boldsymbol{L}}\,(\boldsymbol{W}_r-\boldsymbol{W}_l)}_{\text{anti-dissipative correction}}. \quad (6.128)$$

where the correction parameter φ is set to 1 and the diagonal matrix $\overline{\delta}$ takes the expression:

$$\overline{\delta}=\mathbb{I}-\frac{\overline{\Lambda}^-}{\lambda_l}-\frac{\overline{\Lambda}^+}{\lambda_r},\qquad \overline{\Lambda}^{\pm}=\frac{1}{2}\left(\overline{\Lambda}\pm\left|\overline{\Lambda}\right|\right), \quad (6.129)$$

From another perspective, one can see the HLLEM as a correction of the Roe flux (Einfeldt et al. 1991), stabilized thanks to an HLL procedure that plays the role of the entropy fix. Also, imposing $\lambda_l=-\lambda_r$ in (6.128), one can find the expression of the Roe flux (6.118).

6.3.2.2.6 HLLE+ solver Proposed in (Park and Kwon 2003) for the Euler equations, the HLLE+ consists in expressing φ as a function of the flow velocity in order to add a dissipation close to the sonic point and diminish carbuncles. The original paper gives the expression:

$$\varphi=\frac{a}{\|u\|+a},\qquad \|u\|=\|\frac{\lambda_r+\lambda_l}{2}\|, \quad (6.130)$$

where a is the acoustic velocity at the interface, originally taken from the Roe average between $\boldsymbol{W}_l$ and $\boldsymbol{W}_r$.

One of the drawbacks of the Roe and HLLEM schemes is that they rely on a Roe average, which is not always realizable. In such condition, we get $\overline{a}^2<0$ for the Euler equation and similarly $\overline{c}^2_{nn}<0$ for the AG system. Therefore, to degenerate to a HLLE flux when the problem cannot be linearized we take:

$$a=\begin{cases}\sqrt{\max\left(0,\overline{a}^2\right)} & \text{For the Euler equation,}\\ \sqrt{\max\left(0,\overline{c}^2_{nn}\right)} & \text{For the AG system.}\end{cases} \quad (6.131)$$

6.3.2.2.7 Kinetic solver Knowing the underlying kinetic velocity distribution $f_{eq}(\boldsymbol{c},\boldsymbol{W})$ of a state $\boldsymbol{W}$, it is possible to establish the flux of matter, momentum and energy across the interface. The so-called Kinetic Flux Vector Splitting (KFVS) (Mandal and Deshpande 1994) consists in establishing the flux from the sum of particles crossing the interface from one side or the other and neglecting collision terms. Then the numerical flux is transform in the following

way:

$$\mathfrak{F}\left(\boldsymbol{W}_l, \boldsymbol{W}_r, \overrightarrow{\boldsymbol{n}}_{ij}\right) = \mathfrak{G}^+\left(\boldsymbol{W}_l\right) + \mathfrak{G}^-\left(\boldsymbol{W}_r\right), \tag{6.132}$$

where the terms $\mathfrak{G}^{\pm}$ are defined by the following integral:

$$\mathfrak{G}^+ = \int_{\boldsymbol{c}\in\mathbb{R}^d} \max\left(0, \boldsymbol{c}\cdot\overrightarrow{\boldsymbol{n}}_{ij}\right)\boldsymbol{C} f_{eq} \mathrm{d}\boldsymbol{c}, \qquad \mathfrak{G}^- = \int_{\boldsymbol{c}\in\mathbb{R}^d} \min\left(0, \boldsymbol{c}\cdot\overrightarrow{\boldsymbol{n}}_{ij}\right)\boldsymbol{C} f_{eq} \mathrm{d}\boldsymbol{c}, \tag{6.133}$$

where $\boldsymbol{c}$ is the kinetic velocity of the particle associated to the NDF f_{eq}, d the number of dimension considered and $\boldsymbol{C}$ is the moment function vector that depends on the closure such that:

$$\boldsymbol{C} = \begin{cases} \left[1, \boldsymbol{c}\right]^t, & \text{for the MK closure,} \\ \left[1, \boldsymbol{c}, \frac{1}{2}\boldsymbol{c}\cdot\boldsymbol{c}\right]^t, & \text{for the Euler equation,} \\ \left[1, \boldsymbol{c}, \frac{1}{2}\boldsymbol{c}\otimes\boldsymbol{c}\right]^t, & \text{for the AG closure,} \end{cases} \tag{6.134}$$

Such class of numerical fluxes is however known to be highly dissipative, especially for the contact discontinuity in the case of the Euler equations. The failure of this method come from the absence of the collision terms in (6.133) that has the consequence to smear the solution (Ohwada 2002), but improvements are possible (Jaisankar and Rao 2007).

In the case of PGD, where such corrections are useless, this solution is an interesting option and provides accurate results (Bouchut, Jin, and Li 2003). More generally in two-phase flows, where the collision terms are neglected, the option can be attractive but remains unable to solve contact discontinuities appearing from the AG closure.

6.3.2.3 MUSCL schemes

6.3.2.3.1 High order TVD schemes Using exact or approximate Riemann solvers, the schemes based on the Godunov approach, (6.116) and illustrated in Figure 6.5, are only first order accurate. The reason is not to seek in the Riemann solver but on the first order reconstruction, which states that the solution inside a cell i is uniform and equal to the stored value $\boldsymbol{W}_i^n$. A solution to overcome this issue is to allow others values to be reconstructed at the boundaries of the cells and then to use a Riemann solver. Put under a mathematical form, this supposes that the high-order schemes we want are based on the form:

$$\boldsymbol{W}_i^{n+1} = \boldsymbol{W}_i^n - \frac{\Delta t}{\Delta x}\left(\mathfrak{F}\left(\boldsymbol{W}_{i+1/2}^L, \boldsymbol{W}_{i+1/2}^R\right) - \mathfrak{F}\left(\boldsymbol{W}_{i-1/2}^L, \boldsymbol{W}_{i-1/2}^R\right)\right) \tag{6.135}$$

where $\boldsymbol{W}_{i+1/2}^{L}$ and $\boldsymbol{W}_{i+1/2}^{R}$ are the reconstructions of the solution at the left and right side of the interface $i+1/2$.

However, and despite this extended formulation, there are limits that schemes cannot overtake.
Theorem 6.1 (Godunov's theorem)**.** There are no monotone, linear schemes for (6.69) of second or higher order of accuracy.

From that theorem, Godunov was convinced that only the first order schemes could conserve the monotonicity and did not provide further effort to design high order schemes. However, authors were very active in the 70's and 80's to increase the order of accuracy of numerical method while preserving the monotonicity of the solution. This is the starting point of the series of papers *"towards the ultimate conservative difference scheme"* of Van Leer (Van Leer 1973; van Leer 1974; Van Leer 1977; Leer 1977, 1979) and the subject of the fundamental contribution of Harten (Harten 1983) among others. The stated objective of these papers was to overcome this *first order wall* and end-up with the conception of the MUSCL schemes.

In this contribution, it is a key issue to fulfill monotony and LED properties that are key conditions to ensure the robustness and realizability of the method. As a consequence and following the Godunov's theorem, we are not interested in the design of schemes of order higher than two. The main issues of the methods designed in this work is to provide sufficient robustness to overcome all the singularities expected from the Eulerian modeling of two phase flows. In such context, the procedures ensuring the robustness, Artificial Viscosity or limiters, are the effective limits establishing the order of accuracy. Efforts are thus concentrated in providing the less restrictive and most accurate procedures guaranteeing the validity of the numerical results.

6.3.2.3.2 The MUSCL reconstruction The MUSCL approach aims at reconstructing the solution inside the cell assuming the existence of a slope or, equivalently, that the solution exists under an affine form. For a one-dimensional uniform mesh, this leads to a reconstructed values at the interface following the form:

$$\begin{cases} \boldsymbol{W}_{i+1/2}^{L} = \boldsymbol{W}_i + p_i^{+}\frac{\Delta x}{2} \\ \boldsymbol{W}_{i+1/2}^{R} = \boldsymbol{W}_{i+1} - p_{i+1}^{-}\frac{\Delta x}{2} \end{cases} \tag{6.136}$$

To ensure the monotony, slopes p_i^{+} and p_i^{-} are *limited*. It consists, here based on a slope estimated centered by default, in adjusting the slope thanks to a limiter φ. Conventionally, this limiter is associated to a cell i and function of a slope ratio r established from the direct neighbors. We thus rewrite (6.136) under the form:

$$\begin{cases} \boldsymbol{W}_{i+1/2}^{L} = \boldsymbol{W}_i + \frac{1}{2}\varphi(r_i^{L})(\boldsymbol{W}_{i+1} - \boldsymbol{W}_i) \\ \boldsymbol{W}_{i+1/2}^{R} = \boldsymbol{W}_{i+1} + \frac{1}{2}\varphi(r_{i+1}^{R})(\boldsymbol{W}_i - \boldsymbol{W}_{i+1}) \end{cases} \quad \text{where} \quad \begin{cases} r_i^{L} = \frac{\boldsymbol{W}_i - \boldsymbol{W}_{i-1}}{\boldsymbol{W}_{i+1} - \boldsymbol{W}_i} \\ r_{i+1}^{R} = \frac{\boldsymbol{W}_{i+2} - \boldsymbol{W}_{i+1}}{\boldsymbol{W}_{i+1} - \boldsymbol{W}_i} \end{cases} \tag{6.137}$$

Put under that form, the role of the limiter can have several interpretations:

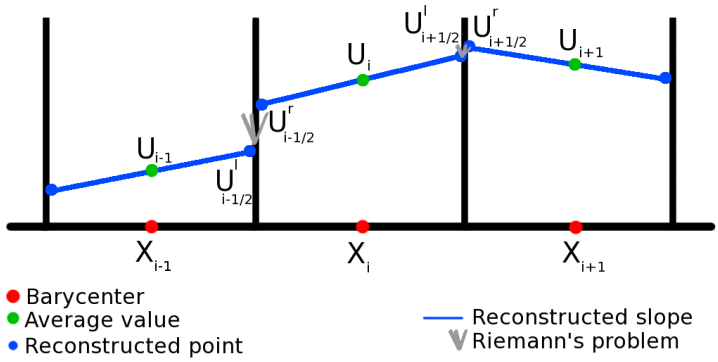

Figure 6.8: *second order reconstruction of the MUSCL 'monoslope' class of schemes*

- Starting from an estimated slope, the limiter provides sufficient dissipation to ensure the stability of the scheme. Despite being the starting point of the term *limiter*, by analogy with flux limiters (see Section 6.3.1.7), that description does not fit the role given to the slope limiter in the MUSCL context.

- It is a predictor-corrector procedure where the centered slope is the predicted slope and the limiter φ acts as the corrector.

- It is a convenient change of variable between the slope established across the interface (forward slope) and another determined upwind to the reconstruction (backward slope), to the slope ratio and the forward slope.

We base our analysis on this last point of view. The concept of forward and backward slope are used by reference to the *multislope* approach described in Section 6.4 that allows, in multi-dimensional framework, several slopes to be used inside the same cell. This explains the unusual formulation of $\boldsymbol{W}^R_{i+1/2}$ given in (6.137). Assuming a unique slope in the cell, as illustrated in Figure 6.8, one can get:

$$\begin{cases} \boldsymbol{W}^L_{i+1/2} = \boldsymbol{W}_i + \frac{1}{2}\varphi(r_i)(\boldsymbol{W}_{i+1} - \boldsymbol{W}_i) \\ \boldsymbol{W}^R_{i-1/2} = \boldsymbol{W}_i - \frac{1}{2}\varphi(r_i)(\boldsymbol{W}_{i+1} - \boldsymbol{W}_i) \end{cases} \tag{6.138}$$

That second *monoslope* formulation is completely compatible with (6.137). Assuming that the solution reconstructed by (6.138) shall be identical looking at the problem from left to right or from right to left. We define the symmetry condition for a limiter:

$$\frac{\varphi(r)}{r} = \varphi\left(\frac{1}{r}\right) \tag{6.139}$$

One can thus remark that, if the limiter fulfills the symmetry conditions, reconstructions (6.137) and (6.138) are equivalent.

Once the reconstruction provided, most of the approaches extrapolate $\boldsymbol{W}_{i+1/2}^{L}$ and $\boldsymbol{W}_{i+1/2}^{R}$ and define piecewise constant data on each side of the boundary (see (Berthon 2005) for example). Thanks to that last hypothesis, the numerical flux remains established from one of the Riemann solver described in Section 6.3.2.1.2 or Section 6.3.2.2 and the update is obtained thanks to the FV framework, which is associated to (6.135) for one-dimensional case. Since that reconstruction is mostly determined by the limiter, its expression is detailed.

6.3.2.3.3 TVD slope limiter constraint We set here the constraint on the limiter such that the scheme is TVD. In the case of one-dimensional linear advection (6.69), the update only depends on the values $\boldsymbol{W}_{i+1/2}^{L}$ due to the flux determination that is necessarily upwind and therefore, once again, results given are identical between (6.137) and (6.138). The update depending on the slope limiter takes a form very similar to the one obtained in the FD context for flux limiter (see Section 6.3.1.7) and yields:

$$w_i^{n+1} = w_i^n - \nu(w_i^n - w_{i-1}^n) - \Delta_- \left\{ \varphi_i \frac{1}{2} \nu (w_{i+1}^n - w_i^n) \right\} \tag{6.140}$$

Thanks to the same development, one can obtain a similar CFL dependent TVD sufficient conditions and the identical CFL-free TVD limits:

$$\begin{cases} 0 \leq \varphi_i^{CFL} \leq 2, \\ 0 \leq \frac{\varphi_i^{CFL}}{r_i} \leq \frac{2}{\nu}, \end{cases} \qquad \begin{cases} 0 \leq \varphi_i \leq 2, \\ 0 \leq \frac{\varphi_i}{r_i} \leq 2. \end{cases} \tag{6.141}$$

Also, to be of second order the reconstructed slope shall be a convex combination of the upwind ($\varphi = r$) and centered slopes ($\varphi = 1$). As a consequence, we shall have $\varphi(1) = 1$ and thus any affine solution can be exactly reconstructed if the limiter fulfills second order condition.

6.3.2.3.4 Slope limiter Under the given constraints, a large choice of limiters fulfilling TVD conditions is possible. We here propose a set of remarkable limiters:

Superbee : $\varphi(r) = \max(0, \min(2r, 1), \min(r, 2))$,

Minmod : $\varphi(r) = \max(0, \min(r, 1))$,

Van Leer : $\varphi(r) = \max(0, \min(\frac{r+|r|}{1+|r|}, 2))$,

Koren : $\varphi(r)) = \max(0, \min(2r, \min(\frac{1}{3}r + \frac{2}{3}, 2)))$,

Quadratic : $\varphi(r)) = \max(0, \min(2r, \min(\frac{3+r}{4}, 2)))$

Among them, the Superbee and Minmod have a specific role. Superbee is the less restrictive

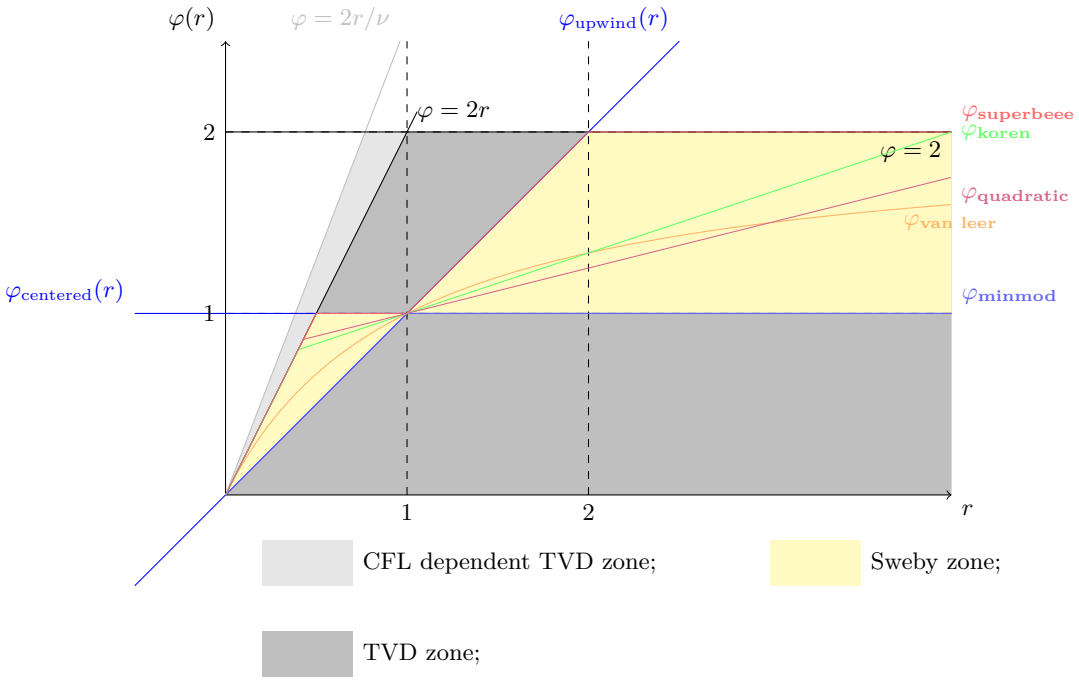

Figure 6.9: *Slope limiters representation and Sweby zone*

limiter existing inside the Sweby region and fits its upper bound. The use of this limiter on the MUSCL scheme however leads to an anti-dissipative behavior and is known to create artificial shocks from smooth solution. At the opposite Minmod is the most restrictive limiter and fit the lower bound of the Sweby zone. Despite fulfilling all the stability requirements, this limiter is the most dissipative and can in practice significantly reduce the order of convergence. This reduction of the order of accuracy is mostly observable at extremas where $r < 0$ and therefore all the MUSCL schemes with limiters fulfilling the conditions (6.141) degenerate at first order in the vicinity of these locations. The more the limiter is dissipative, the more this phenomenon is important.

Additional limiters less dissipative than the Minmod and less problematic than the Superbee can be designed. One of the most famous, developed by Van Leer (van Leer 1974) under the name *harmonic*, has been designed in order to respect the monotonicity of the scheme.

The *quadratic* limiter, obtained from the assumption of parabolic interpolation between w_{i-1}, w_i and w_{i+1} in order to represent $w_{i+1/2}$. More generally, this corresponds to a Quadratic Upwind Interpolation (QUICK) approach where the TVD requirements (6.141) have been enforced. Finally, the Koren limiter describe in (Koren 1993) was design to reduce at most the third order error on the linear advection equation while belonging to the Sweby zone. Unlike the previous limiters, the Koren and *quadratic* limiters do not fulfill the symmetry condition (6.139). All these limiters are represented in Figure 6.9.

For more details on the limiters, we refer to (Waterson and Deconinck 2007) who sum up the development conducted over the years on that subject and propose an unified approach to classify most of them. Also, the limiters defined here above are valid for a one-dimensional uniform mesh. We refer to (Berzins and Ware 1995), (Holstad 2001) and Section 6.4.2.2 for some extensions to non-uniform meshes.

Remark 6.5. *Usual formulations of the limiter are based on a upwind prediction of the slope and not a centered one as proposed in this contribution through equation* (6.137)*. This explains differences between the formulation given in the original papers and the ones in this manuscript since they have been adapted for the need of the presented work.*

6.3.2.3.5 Reconstruction variables In the case of system of equations, only the conservative variables are updated and thus need to be stored. However, proceeding to the reconstruction based on the conservative variables, more precisely on each component of $\boldsymbol{W}$, is not the only choice, and most of the time not the most efficient (Berthon 2005). Starting from the solution at a given time step t^n and for each cell C_i, the conservative variables $\boldsymbol{W}_i^n$ can be converted to the reconstruction variables $\boldsymbol{V}_i^n$.

Property 6.3. A set of reconstruction variables has to fulfill three properties:

1. There exists a bijective function $\boldsymbol{f}_{reco}$ such that $\boldsymbol{V}_i^n = \boldsymbol{f}_{reco}(\boldsymbol{W}_i^n)$ for all $\boldsymbol{W}_i^n$ belonging to the interior of the realizable domain (see Section 3.2.2.1),

2. For all $\boldsymbol{W}_i^n$ belonging to the boundary of the realizable domain, such as for null density, undetermined values, such as velocity for vacuum case, shall not influence the reconstruction,

3. For any convex combination of realizable reconstruction variables, the conservation variable of the reconstructed state are realizable.

For robustness issues due to the non-linearities, more elaborated variables can be used instead of the conservation ones (see (Berthon 2005)). For the set of studied equations, these are:

- ρ and $\boldsymbol{u}$ for the MK closure,
- ρ, $\boldsymbol{u}$ and P for the Euler equations,
- ρ, $\boldsymbol{u}$, σ_{ii} and $\frac{\sigma_{ij}}{\sqrt{\sigma_{ii}\sigma_{jj}}}$ for $i \neq j$ for the AG closure.

These choices, detailed in (Dupif et al. 2016), ensure the realizability of the corresponding schemes and the close behavior between the MK and the AG closure, when no PTC occurs. This same procedure is conserved such that, close to vacuum, the particle velocity relax to the gas velocity and the velocity dispersion vanishes.

6.3.2.3.6 Summing up the MUSCL procedure For the sake of clarity, the step by step MUSCL procedure is summed up here:

1. Conversion of the conservative variables into primitive reconstruction variables,

2. Reconstruction procedure according to affine slopes and adequate limiters,

3. Computation of the flux at each cell interfaces thanks to a Riemann solver,

4. Flux summation on the cells, according to (6.43).

That procedure provides a second order accurate scheme in space but only first order in time. Therefore, to maintain the same order of accuracy in space and time, a SSPRK method of order 2, as described in Section 5.2.2, is chosen.

Also, it shall be remarked that the limit CFL number for stability is reduced in the case of the MUSCL schemes compared to the first order Godunov one. Several others (Berthon 2006b; Toro 2009; Clain and Clauzon 2010) observed that, in one dimension $\nu_{lim} < \frac{1}{4}$.

Remark 6.6. *In several dimension, this limit is related to the number of faces and the relation yields (Clain and Clauzon 2010; Le Touze, Murrone, and Guillard 2015):*

$$\nu_{lim} < \frac{1}{2\alpha}, \qquad \alpha = \max_{i\in\Omega}\left(\#\mathcal{V}_i\right) \tag{6.142}$$

where $\#\mathcal{V}_i$ is the number of elements in the set of neighbors $\mathcal{V}_i$.

However, that formula is based on the assumption that the contribution to the flux from every faces is identical and, in practice, imposing $\nu_{lim} < \frac{1}{2}$ is sufficient most of the time. This is mostly due to the compensation between the fluxes. Such compensation can be observed by deriving the sufficient TVD conditions (6.141) from (6.140). The effective stability constraint is:

$$0 \leq 1 - \frac{\varphi_{i-1}}{2} + \frac{\varphi_i}{2r_i} \leq \frac{1}{\nu} \tag{6.143}$$

One can see that, in that case of smooth solution, $\varphi_{i-1} \simeq \varphi_i$ and $r_i \simeq 1$, which leads to a compensation of the terms. This is however not true in any cases and evaluating such compensation is a difficult task that requires all the cells to communicate with each other.

6.3.2.4 Higher order class of schemes

Seeking for higher order schemes, reconstruction of increasingly high order of accuracy can be aimed. However, to respect the LED properties, limitation procedures restrain the order of convergence of the numerical methods. Since these LED corrections appears to be the effective limits for the order of accuracy, less restrictive constraints can be proposed.

Definition 6.18 (ELED)**.** A scheme is Essentially Local Extrema Diminishing (ELED) if, in the limit of the refinement ($\forall i \in \Omega\ |C_i| \to 0$), this same scheme is LED.

Among the high order schemes based on (6.135), we remark the following ones:

- Piecewise Parabolic Method (PPM) class (Colella and Woodward 1984): from the same principle as the MUSCL schemes, the solution is reconstructed under a parabolic form in the vicinity of each interface,

- Essentially Non-Oscillatory (ENO) class (Harten et al. 1987; Shu and Osher 1988, 1989): a set of stencils in the vicinity of a cell is selected to provide different possibilities of reconstruction. Among them, the *smoothest* one is chosen. This class of scheme fulfills

ELED properties,

- Weighted Essentially Non-Oscillatory (WENO) class (Liu, Osher, and Chan 1994; Jiang and Shu 1996): use of a convex combination of all ENO candidates, increasing the order of accuracy. A smoothness indicator is used to degenerate to a ENO scheme when a discontinuity is detected to provide the ELED property.

- Centered Essentially Non-Oscillatory (CENO) class: $k-$exact polynomial reconstruction, with enforcement of monotony,

- Gradient exchange class (Haider et al. 2014): $k-$exact polynomial reconstruction, unlike the CENO, a recursive information exchange between direct neighbors based on high order derivative is used for the reconstruction. A linear limitation procedure, similar to (Zhang and Shu 2010b) in the DG context, is used,

- Multi-dimensional Optimal Order Detection (MOOD) class (Clain, Diot, and Loubère 2011): An high order polynomial is reconstructed inside the cell without limitation and a posteriori limited to fulfill realizability conditions inside the cell.

Many of these schemes enforce the conservation in the reconstruction procedure. In other words the solution is reconstructed all over the cell such that the integral of this reconstruction corresponds to the average stored value. We state in this contribution that such process is not necessary since the conservation is already provided by the FV framework and the numerical flux. This is an important feature of the *multislope* reconstruction presented for general unstructured mesh in Section 6.4.

6.3.3 Multi-dimensional Riemann solver

In multi-dimensional frameworks, the direction of the discontinuity needs to be explicitly defined. Therefore, the Riemann solver has to be adapted in consequence. After a general description of the standard Riemann solvers based on the HLLEM, we focus on specificities directly related to the multi-dimensional context.

Before entering in the details, we generalized the semi-discretized form of the schemes of Godunov class with reconstruction (6.135) to general multidimensional frameworks based on (6.42):

$$\mathrm{d}_t \boldsymbol{W}_i^n = -\frac{1}{|C_i|} \sum_{j \in \mathcal{V}_i} |S_{ij}| \, \mathfrak{F}(\boldsymbol{W}_{ij}, \boldsymbol{W}_{ji}, \overrightarrow{\boldsymbol{n}}_{ij}). \tag{6.144}$$

where $\boldsymbol{W}_{ij}$ and $\boldsymbol{W}_{ji}$ are the reconstructed values at each side of S_{ij}.

6.3.3.1 Generic HLLEM scheme

The numerical flux for the multi-dimensional case is straightforwardly obtained thanks to the projection of the multidimensional flux $\boldsymbol{\mathcal{F}}$ on the direction normal to the surface and through

the rotation of the system of equations for the Jacobian matrix.

$$\mathfrak{F}^{HLLEM}(\boldsymbol{W}_{ij},\boldsymbol{W}_{ji},\overrightarrow{\boldsymbol{n}}_{ij}) = \underbrace{\frac{\lambda_r\boldsymbol{\mathcal{F}}(\boldsymbol{W}_{ij})-\lambda_l\boldsymbol{\mathcal{F}}(\boldsymbol{W}_{ji})+\lambda_r\lambda_l(\boldsymbol{W}_{ji}-\boldsymbol{W}_{ij})}{\lambda_r-\lambda_l}}_{\text{HLL flux}} - \underbrace{\varphi\frac{\lambda_r\lambda_l}{\lambda_r-\lambda_l}\overline{\boldsymbol{R}}(\overrightarrow{\boldsymbol{n}}_{ij})\overline{\delta\boldsymbol{L}}(\overrightarrow{\boldsymbol{n}}_{ij})\left(\boldsymbol{W}_{ji}-\boldsymbol{W}_{ij}\right)}_{\text{anti-dissipative correction}}. \quad (6.145)$$

where $\varphi\in[0,1]$ is a constant added to control the anti-dissipation, the Jacobian matrix and its decomposition terms depends on the direction of interest (see Section 3.2.2.2) and the diagonal matrix $\overline{\delta}$ takes the expression:

$$\overline{\delta\boldsymbol{L}}(\overrightarrow{\boldsymbol{n}}_{ij}) = \mathbb{I} - \frac{\overline{\Lambda}^{-}(\overrightarrow{\boldsymbol{n}}_{ij})}{\lambda_l} - \frac{\overline{\Lambda}^{+}(\overrightarrow{\boldsymbol{n}}_{ij})}{\lambda_r}, \qquad \overline{\Lambda}^{\pm} = \frac{1}{2}\left(\overline{\Lambda}(\overrightarrow{\boldsymbol{n}}_{ij}) \pm \left|\overline{\Lambda}(\overrightarrow{\boldsymbol{n}}_{ij})\right|\right) \quad (6.146)$$

Also, we take into account the following the Roe average to determine the signal velocities λ_r and λ_l:

$$\begin{cases} \lambda_r &= \max\left(0,\lambda_{max}\right), \\ \lambda_l &= \min\left(0,\lambda_{min}\right), \end{cases} \qquad \begin{aligned} \lambda_{max} &= \max\left(\lambda^+(\boldsymbol{W}_{ij},\overrightarrow{\boldsymbol{n}}_{ij}),\lambda^+(\boldsymbol{W}_{ji},\overrightarrow{\boldsymbol{n}}_{ij}),\lambda^+(\overline{\boldsymbol{W}},\overrightarrow{\boldsymbol{n}}_{ij})\right), \\ \lambda_{min} &= \min\left(\lambda^-(\boldsymbol{W}_{ij},\overrightarrow{\boldsymbol{n}}_{ij}),\lambda^-(\boldsymbol{W}_{ji},\overrightarrow{\boldsymbol{n}}_{ij}),\lambda^-(\overline{\boldsymbol{W}},\overrightarrow{\boldsymbol{n}}_{ij})\right), \end{aligned} \quad (6.147)$$

Playing on the expression of the signal velocities and φ, most of the Riemann solvers described in Section 6.3.2.2 can be found through the relation (6.145):

HLLEM flux : $\varphi=1$ and the signal velocities are determined thanks to (6.147),

HLLE+ flux ((Park and Kwon 2003) for Euler equation): the signal velocities determined thanks to (6.147) and $\varphi=\frac{\overline{a}}{\|u\|+\overline{a}}$ where $\|u\|=\|\frac{\lambda_r+\lambda_l}{2}\|$ and $\overline{a}$ is the acoustic velocity at the Roe state,

HLLE flux : $\varphi=0$ and the signal velocities are determined thanks to (6.147),

Rusanov flux : $\varphi=0$ and $\lambda_r=-\lambda_l=\|\lambda_{max}\|$,

Roe flux : $\varphi=1$ and $\lambda_r=-\lambda_l=\|\lambda_{max}\|$,

The expression of the HLLC flux cannot be derived from (6.145) but easily deduced from the one-dimensional form (see Section 6.3.2.2.4) or taken from (Toro 2009).

6.3.3.2 Multidimensional corrections

The Riemann problem is purely one-dimensional, but in the multi-dimensional context, issues can appear because of this restrictive approach.

6.3.3.2.1 Low-Mach corrections Its has been remarked, for the Euler equations, that at low Mach number, where the fluid is close to be incompressible (Lions and Masmoudi 1998; Dellacherie 2010), the dissipation induced by schemes of Godunov class can create unexpected results. Such effect is especially important for Cartesian meshes and we refer to (Guillard and Murrone 2004; Park, Lee, and Kwon 2006; Dellacherie 2010; Drui 2017) for some examples. This behavior is caused by a truncation error in the velocity fields that is $\mathcal{O}(\frac{\Delta x}{M})$ where M is the Mach number.

As summarize in (Drui 2017), several solutions can be envisioned:

Incompressible equations : Use weakly compressible models that extends incompressible model to density variation (Munz et al. 2003; Pianet et al. 2010). Such solution does not however fit all Mach problems,

Preconditioning : Artificially change the compressibility of the fluid system at low-Mach regime. Thanks to a preconditioning matrix, the equations are solved at the time scaled of the convection. This method has been originally proposed in (Turkel 1987, 1993) and further developed in (Guillard and Murrone 2004). For the HLLE+ flux, a correction is proposed in (Park, Lee, and Kwon 2006).

Modification of the state laws : Artificially modify the EOS in order to reduce the acoustic wave velocity (Chanteperdrix, Villedieu, and Vila 2002). This solution is not always physically relevant.

Modified flux : Cancellation of the artificial pressure error, based on an analysis of the consistency errors of an approximate Riemann solver (Chalons and Girardin 2016). Such approach is fitted for flux of HLLC class (Drui 2017).

Staggered grids : Considering that velocity and pressure are discretized at different locations thanks to a staggered grids (fitted for the resolution of incompressible flows (Hirsch 1990)), the specific, centered, discretization of the pressure cancel the $\mathcal{O}(\frac{\Delta x}{M})$ error (Woodward and Colella 1984; Bernard-Champmartin and De Vuyst 2014). These methods however require AV for stabilization.

Triangular grids : For some systems of equations, a minor impact on the solution is observed at low-Mach number using triangular cells (Dellacherie 2010; Drui 2017). More generally, the effect is lowered on unstructured mesh but does not vanish.

We refer to (Guillard and Nkonga 2017) for more details on the subject of low-Mach limit corrections.

6.3.3.2.2 Rotationally biased Riemann solvers The normal direction to the faces of the meshes is generally not the direction of the discontinuity. Therefore as it was originally proposed in (Davis 1984a) and improved in (Nishikawa and Kitamura 2008), it can be aimed at detecting the effective direction of the shock and solve a Riemann problem according to that new direction.

We here take the formulation given by (Nishikawa and Kitamura 2008). First, the velocity vector is used to approximate the direction normal to a shock or parallel to a shear layer if one of them exists. This leads to the following definition of the direction normal to the expected shock $\boldsymbol{n}_1$:

$$\boldsymbol{n}_1 = \begin{cases} \frac{\boldsymbol{u}_{ji}-\boldsymbol{u}_{ij}}{\|\boldsymbol{u}_{ji}-\boldsymbol{u}_{ij}\|_2}, & \text{if } \|\boldsymbol{u}_{ji}-\boldsymbol{u}_{ij}\|_2 > \epsilon \\ \overrightarrow{\boldsymbol{n}}_{ij}, & \text{otherwise} \end{cases} \tag{6.148}$$

where $\boldsymbol{u}_{ij}$ is the velocity vector of the reconstructed state ij and ϵ, taken small, avoids the division by zero at stagnation points.

Then we define the tangential vector $\boldsymbol{n}_2$ such that $\boldsymbol{n}_1 \cdot \boldsymbol{n}_2 = 0$, $(\boldsymbol{n}_1 \times \boldsymbol{n}_2) \cdot \overrightarrow{\boldsymbol{n}}_{ij} = 0$ and $\|\boldsymbol{n}_2\|_2 = 1$. As a consequence, solving two Riemann problems, in the $\boldsymbol{n}_1$ and $\boldsymbol{n}_2$ direction, then projecting the flux on the $\overrightarrow{\boldsymbol{n}}_{ij}$ direction, on can get a rotationally biased Riemann solver:

$$\mathfrak{F}^{R-1-2}(\boldsymbol{W}_{ij}, \boldsymbol{W}_{ji}, \overrightarrow{\boldsymbol{n}}_{ij}) = (\boldsymbol{n}_1 \cdot \overrightarrow{\boldsymbol{n}}_{ij})\, \mathfrak{F}^1(\boldsymbol{W}_{ij}, \boldsymbol{W}_{ji}, \boldsymbol{n}_1) + (\boldsymbol{n}_2 \cdot \overrightarrow{\boldsymbol{n}}_{ij})\, \mathfrak{F}^2(\boldsymbol{W}_{ij}, \boldsymbol{W}_{ji}, \boldsymbol{n}_2) \tag{6.149}$$

where $\mathfrak{F}^1$ and $\mathfrak{F}^2$ are the standard Riemann solver used in the directions normal and tangential to the shock.

There is an interest in using the same numerical flux in both directions $\boldsymbol{n}_1$ and $\boldsymbol{n}_2$. However, it is proposed in (Nishikawa and Kitamura 2008) to rely on a robust solver, such as a HLLE, in the $\boldsymbol{n}_1$ direction normal to the shock and on a less dissipative one, as a Roe or HLLEM, in the $\boldsymbol{n}_2$ direction.

6.3.3.3 Dedicated HLL Riemann solver for axisymmetric configurations

In the case of axisymmetric configuration, the average procedure leading to the HLL flux is modified. Such derivation is not usually conducted since most authors simply adapt from one dimensional solvers and the result would not differ from the derivation proposed here in a Cartesian framework. As proposed in (Dupif et al. 2018a), we here take into account the intrinsic geometry, specific to the axisymmetric framework, to build a new approximate Riemann solver.

6.3.3.3.1 A geometry dependent Riemann solver In order to take into account the specific geometry, we hereby write again the conservation laws leading to the HLL Riemann solver in the context of an axisymmetric conservation law. Such an approach differs from classical axisymmetric scheme that rely on the same Riemann solver as developed for Cartesian frameworks. Starting from the same approach based on conservation laws, a time step dependent *virtual geometry* is defined in the vicinity of an interface.

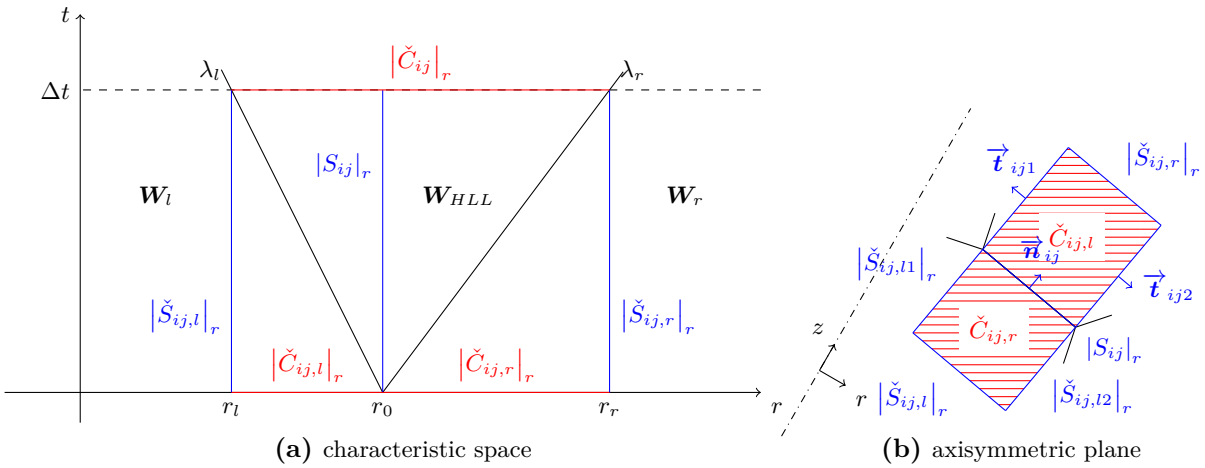

(a) characteristic space **(b)** axisymmetric plane

Figure 6.10: *Virtual control volumes*

The *virtual volumes* are the extrusions of $|S_{ij}|_r$ in the normal direction $\overrightarrow{\boldsymbol{n}}$ of the surface establishing a volume where the solution is disturbed during the time step because of the discontinuity at the interface. In the positive side the extrusion containing the perturbation caused by the signal velocity λ_r during the time step Δt which defines the virtual volume $\left|\check{C}_{ij,r}\right|_r$. Same definition applies in the negative side using the signal velocity λ_l to define $\left|\check{C}_{ij,l}\right|_r$. Their union $\left|\check{C}_{ij}\right|_r$ is bounded by the *virtual surfaces* $\left|\check{S}_{ij,l}\right|_r$ and $\left|\check{S}_{ij,r}\right|_r$ as represented in Figure 6.10a. In addition, as drawn 6.10b, it is needed to take into account *virtual surfaces* $\left|\check{S}_{ij,l1}\right|_r$, $\left|\check{S}_{ij,l2}\right|_r$, $\left|\check{S}_{ij,r1}\right|_r$ and $\left|\check{S}_{ij,r2}\right|_r$ to border $\left|\check{C}_{ij}\right|_r$ in the the axisymmetric plane. In Cartesian coordinates the fluxes associated to these faces cancel each other but not in the current case since, in general, $\left|\check{S}_{ij,l1}\right|_r \neq \left|\check{S}_{ij,l2}\right|_r$ and $\left|\check{S}_{ij,r1}\right|_r \neq \left|\check{S}_{ij,r2}\right|_r$.

Since the update is fully driven by the numerical flux $\boldsymbol{\mathcal{F}}_{HLL}$, only the external influence on $\left|\check{S}_{ij,l1}\right|_r$ and $\left|\check{S}_{ij,r1}\right|_r$ of outward oriented normal vector $\overrightarrow{\boldsymbol{t}}_{ij1}$ and $\left|\check{S}_{ij,l2}\right|_r$, $\left|\check{S}_{ij,r2}\right|_r$ of normal $\overrightarrow{\boldsymbol{t}}_{ij2}$ is to be taken into account. Therefore, assuming a uniform state $\boldsymbol{W}_{HLL}$ inside the fastest and slowest signal velocity $\lambda_r \geq 0$ and $\lambda_l \leq 0$, the conservation laws (6.47), to which source terms has not be taken into account, leads to the $\boldsymbol{W}_{HLL}$ value that follows:

$$\begin{aligned}\left|\check{C}_{ij}\right|_r \boldsymbol{W}_{HLL} = \left|\check{C}_{ij,l}\right|_r \boldsymbol{W}_l + \left|\check{C}_{ij,r}\right|_r \boldsymbol{W}_r + \Delta t \left(\left|\check{S}_{ij,l}\right|_r \boldsymbol{\mathcal{F}}(\boldsymbol{W}_l)\cdot\overrightarrow{\boldsymbol{n}}_{ij} - \left|\check{S}_{ij,r}\right|_r \boldsymbol{\mathcal{F}}(\boldsymbol{W}_r)\cdot\overrightarrow{\boldsymbol{n}}_{ij}\right)\\ - \Delta t \left(\left|\check{S}_{ij,l1}\right|_r \boldsymbol{\mathcal{F}}(\boldsymbol{W}_l)\cdot\overrightarrow{\boldsymbol{t}}_{ij1} + \left|\check{S}_{ij,l2}\right|_r \boldsymbol{\mathcal{F}}(\boldsymbol{W}_l)\cdot\overrightarrow{\boldsymbol{t}}_{ij2}\right)\\ - \Delta t \left(\left|\check{S}_{ij,r1}\right|_r \boldsymbol{\mathcal{F}}(\boldsymbol{W}_r)\cdot\overrightarrow{\boldsymbol{t}}_{ij1} + \left|\check{S}_{ij,r2}\right|_r \boldsymbol{\mathcal{F}}(\boldsymbol{W}_r)\cdot\overrightarrow{\boldsymbol{t}}_{ij2}\right). \quad (6.150)\end{aligned}$$

Using the equation (6.56) for an uniform field, the following relations on the *virtual volumes* $\left|\check{C}_{ij,l}\right|_r$ and $\left|\check{C}_{ij,r}\right|_r$ can be obtained:

$$\begin{aligned}&\left|\check{C}_{ij,l}\right|_0 \boldsymbol{F}_r(\boldsymbol{W}_l) = \\ &\left|\check{S}_{ij,l1}\right|_r \boldsymbol{\mathcal{F}}(\boldsymbol{W}_l)\cdot\overrightarrow{\boldsymbol{t}}_{ij1} + \left|\check{S}_{ij,l2}\right|_r \boldsymbol{\mathcal{F}}(\boldsymbol{W}_l)\cdot\overrightarrow{\boldsymbol{t}}_{ij2} + \left|\check{S}_{ij,l}\right|_r \boldsymbol{\mathcal{F}}(\boldsymbol{W}_l)\cdot\overrightarrow{\boldsymbol{n}}_{ij} - |S_{ij}|_r \boldsymbol{\mathcal{F}}(\boldsymbol{W}_l)\cdot\overrightarrow{\boldsymbol{n}}_{ij},\end{aligned} \tag{6.151}$$

$$\begin{aligned}&\left|\check{C}_{ij,r}\right|_0 \boldsymbol{F}_r(\boldsymbol{W}_r) = \\ &\left|\check{S}_{ij,r1}\right|_r \boldsymbol{\mathcal{F}}(\boldsymbol{W}_r)\cdot\overrightarrow{\boldsymbol{t}}_{ij1} + \left|\check{S}_{ij,r2}\right|_r \boldsymbol{\mathcal{F}}(\boldsymbol{W}_r)\cdot\overrightarrow{\boldsymbol{t}}_{ij2} - \left|\check{S}_{ij,r}\right|_r \boldsymbol{\mathcal{F}}(\boldsymbol{W}_r)\cdot\overrightarrow{\boldsymbol{n}}_{ij} + |S_{ij}|_r \boldsymbol{\mathcal{F}}(\boldsymbol{W}_r)\cdot\overrightarrow{\boldsymbol{n}}_{ij}.\end{aligned} \tag{6.152}$$

Introducing (6.151) and (6.152) in (6.150) one can deduce:

$$\begin{aligned}\left|\check{C}_{ij}\right|_r \boldsymbol{W}_{HLL} = \left|\check{C}_{ij,l}\right|_r \boldsymbol{W}_l + \left|\check{C}_{ij,r}\right|_r \boldsymbol{W}_r + \Delta t\,|S_{ij}|_r \left(\boldsymbol{\mathcal{F}}(\boldsymbol{W}_l)\cdot\overrightarrow{\boldsymbol{n}}_{ij} - \boldsymbol{\mathcal{F}}(\boldsymbol{W}_r)\cdot\overrightarrow{\boldsymbol{n}}_{ij}\right) \\ - \Delta t\left(\left|\check{C}_{ij,l}\right|_0 \boldsymbol{F}_r(\boldsymbol{W}_l) + \left|\check{C}_{ij,r}\right|_0 \boldsymbol{F}_r(\boldsymbol{W}_l)\right).\end{aligned} \tag{6.153}$$

Now, using the same derivation, the HLL flux $\boldsymbol{\mathcal{F}}_{HLL}$ can be obtained by integrating either on the left or the right virtual volume:

$$\begin{cases}\left|\check{C}_{ij,l}\right|_r \boldsymbol{W}_{HLL} = \left|\check{C}_{ij,l}\right|_r \boldsymbol{W}_l + \Delta t\,|S_{ij}|_r \left(\boldsymbol{\mathcal{F}}(\boldsymbol{W}_l)\cdot\overrightarrow{\boldsymbol{n}}_{ij} - \boldsymbol{\mathcal{F}}_{HLL}\right) - \Delta t\left|\check{C}_{ij,l}\right|_0 \boldsymbol{F}_r(\boldsymbol{W}_l), \\ \left|\check{C}_{ij,r}\right|_r \boldsymbol{W}_{HLL} = \left|\check{C}_{ij,r}\right|_r \boldsymbol{W}_r + \Delta t\,|S_{ij}|_r \left(\boldsymbol{\mathcal{F}}_{HLL} - \boldsymbol{\mathcal{F}}(\boldsymbol{W}_r)\cdot\overrightarrow{\boldsymbol{n}}_{ij}\right) - \Delta t\left|\check{C}_{ij,r}\right|_0 \boldsymbol{F}_r(\boldsymbol{W}_r).\end{cases} \tag{6.154}$$

As reminded in (Toro 2009), $\boldsymbol{\mathcal{F}}_{HLL} \neq \boldsymbol{\mathcal{F}}(\boldsymbol{W}_{HLL})$ since the flux is chosen to provide the wished update and not by an approximate solution at the interface. Merging (6.153) with either equations of (6.154), one obtains:

$$\begin{aligned}\Delta t\left|\check{C}_{ij}\right|_r |S_{ij}|_r \boldsymbol{\mathcal{F}}_{HLL} = \left|\check{C}_{ij,l}\right|_r \left|\check{C}_{ij,r}\right|_r \boldsymbol{W}_l + \left(\left|\check{C}_{ij,r}\right|_r - \left|\check{C}_{ij}\right|_r\right)\left|\check{C}_{ij,r}\right|_r \boldsymbol{W}_r \\ + \Delta t\left|\check{C}_{ij,r}\right|_r |S_{ij}|_r \boldsymbol{\mathcal{F}}(\boldsymbol{W}_l)\cdot\overrightarrow{\boldsymbol{n}}_{ij} + \Delta t\left(\left|\check{C}_{ij}\right|_r - \left|\check{C}_{ij,r}\right|_r\right)|S_{ij}|_r \boldsymbol{\mathcal{F}}(\boldsymbol{W}_r)\cdot\overrightarrow{\boldsymbol{n}}_{ij} \\ - \left(\left|\check{C}_{ij,r}\right|_0 - \left|\check{C}_{ij}\right|_0\right)\left|\check{C}_{ij,r}\right|_r \boldsymbol{F}_r(\boldsymbol{W}_l) + \left|\check{C}_{ij,l}\right|_0 \left|\check{C}_{ij,r}\right|_r \boldsymbol{F}_r(\boldsymbol{W}_r).\end{aligned} \tag{6.155}$$

Since by definition we have $\left|\check{C}_{ij}\right|_r = \left|\check{C}_{ij,l}\right|_r + \left|\check{C}_{ij,r}\right|_r$ and $\left|\check{C}_{ij}\right|_0 = \left|\check{C}_{ij,l}\right|_0 + \left|\check{C}_{ij,r}\right|_0$, (6.155) simplifies in:

$$\begin{aligned}\Delta t \left|\check{C}_{ij}\right|_r |S_{ij}|_r \boldsymbol{\mathcal{F}}_{HLL} = \left|\check{C}_{ij,l}\right|_r \left|\check{C}_{ij,r}\right|_r (\boldsymbol{W}_l - \boldsymbol{W}_r) \\ + \Delta t\, |S_{ij}|_r \left(\left|\check{C}_{ij,r}\right|_r \boldsymbol{\mathcal{F}}(\boldsymbol{W}_l)\cdot\overrightarrow{\boldsymbol{n}}_{ij} + \left|\check{C}_{ij,l}\right|_r \boldsymbol{\mathcal{F}}(\boldsymbol{W}_r)\cdot\overrightarrow{\boldsymbol{n}}_{ij}\right) \\ - \Delta t \left|\check{C}_{ij,l}\right|_0 \left|\check{C}_{ij,r}\right|_0 (\boldsymbol{F}_r(\boldsymbol{W}_l) - \boldsymbol{F}_r(\boldsymbol{W}_r))\end{aligned} \tag{6.156}$$

Now, we derive the explicit expression of the *virtual geometry* for an interface S_{ij} defined by the vertices $\boldsymbol{r}_1 = (r_1, z_1)$ and $\boldsymbol{r}_2 = (r_2, z_2)$ and its normal vector $\overrightarrow{\boldsymbol{n}}$, oriented from the left to the right state. The displacement of these by the left and right signal leads to the virtual vertices $\boldsymbol{r}_i^l = \boldsymbol{r}_i + S_l\overrightarrow{\boldsymbol{n}}$ and $\boldsymbol{r}_i^r = \boldsymbol{r}_i + S_r\overrightarrow{\boldsymbol{n}}$ for $i \in \{1,2\}$. Defining $\check{C}_{ij,r}$ by its vertexes $\{\boldsymbol{r}_1, \boldsymbol{r}_2, \boldsymbol{r}_2^r, \boldsymbol{r}_1^r\}$ and $\check{C}_{ij,l}$ by the vertexes $\left\{\boldsymbol{r}_1, \boldsymbol{r}_1^l, \boldsymbol{r}_2^l, \boldsymbol{r}_2\right\}$ and thanks to the developments of Section 6.2.4 (see also the explicit expressions Appendix C.2), the expression of the virtual volumes comes directly:

$$\begin{aligned}\left|\check{C}_{ij,l}\right|_0 &= -|S_{ij}|_0\,\lambda_l\Delta t, & \left|\check{C}_{ij,l}\right|_r &= \left|\check{C}_{ij,l}\right|_0 \left(r_m + \tfrac{\lambda_l\Delta t\, n_r}{2}\right). \\ \left|\check{C}_{ij,r}\right|_0 &= |S_{ij}|_0\,\lambda_r\Delta t, & \left|\check{C}_{ij,r}\right|_r &= \left|\check{C}_{ij,r}\right|_0 \left(r_m + \tfrac{\lambda_r\Delta t\, n_r}{2}\right). \\ \left|\check{C}_{ij}\right|_0 &= |S_{ij}|_0\,(\lambda_r - \lambda_l)\,\Delta t, & \left|\check{C}_{ij}\right|_r &= \left|\check{C}_{ij}\right|_0 \left[r_m + (\lambda_r + \lambda_l)\,\tfrac{\Delta t\, n_r}{2}\right].\end{aligned} \tag{6.157}$$

where $r_m = |S_{ij}|_r / |S_{ij}|_0 = (r_1 + r_2)/2$.

Introducing these expressions in (6.156) and simplifying by Δt and $|S_{ij}|_0$, both assumed to be strictly positive, the expression of the flux boils down to:

$$\begin{aligned}(\lambda_r - \lambda_l)\left[1 + (\lambda_r + \lambda_l)\,\frac{\Delta t\, n_r}{2r_m}\right]\boldsymbol{\mathcal{F}}_{HLL} = \\ - \lambda_l\lambda_r \left(1 + \frac{\lambda_l\Delta t\, n_r}{2r_m}\right)\left(1 + \frac{\lambda_r\Delta t\, n_r}{2r_m}\right)(\boldsymbol{W}_l - \boldsymbol{W}_r) \\ + \left(\lambda_r \left(1 + \frac{\lambda_r\Delta t\, n_r}{2r_m}\right)\boldsymbol{\mathcal{F}}(\boldsymbol{W}_l)\cdot\overrightarrow{\boldsymbol{n}}_{ij} - \lambda_l \left(1 + \frac{\lambda_l\Delta t\, n_r}{2r_m}\right)\boldsymbol{\mathcal{F}}(\boldsymbol{W}_r)\cdot\overrightarrow{\boldsymbol{n}}_{ij}\right) \\ + \frac{\lambda_l\lambda_r}{r_m}\,(\boldsymbol{F}_r(\boldsymbol{W}_l) - \boldsymbol{F}_r(\boldsymbol{W}_r))\end{aligned} \tag{6.158}$$

This expression assume $r_m > 0$ and thus a surface detached from the axis of symmetry.

Equation (6.158) reveals that in axisymmetric cases, the computation of the HLL flux is adjusted according to the wave propagation in the radial direction and to the r weight for $\boldsymbol{W}$. Such a phenomenon is the direct consequence of the averaging procedure leading to the HLL state, that takes into account the weighting of the conservative vector by the distance to the axis r. Away from the axis, or for normal vector oriented in the axial direction, where $\frac{S_l\Delta t\, n_r}{r_m} \approx \frac{S_r\Delta t\, n_r}{r_m} \approx 0$, one recovers the usual expression of the HLL flux:

$$\mathfrak{F}^{HLL}(\boldsymbol{W}_l, \boldsymbol{W}_r, \overrightarrow{\boldsymbol{n}}) = \frac{\lambda_r\boldsymbol{\mathcal{F}}(\boldsymbol{W}_l)\cdot\overrightarrow{\boldsymbol{n}} - \lambda_l\boldsymbol{\mathcal{F}}(\boldsymbol{W}_r)\cdot\overrightarrow{\boldsymbol{n}} + \lambda_r\lambda_l(\boldsymbol{W}_r - \boldsymbol{W}_l)}{\lambda_r - \lambda_l}. \tag{6.159}$$

However, close to the axis without reaching it, the flux is influenced by the geometric effects and yields:

$$\mathfrak{F}^{HLLA}(\boldsymbol{W}_l,\boldsymbol{W}_r,r_m,\overrightarrow{\boldsymbol{n}}) = \frac{\lambda_r\,(1+\alpha_r)\,\boldsymbol{\mathcal{F}}(\boldsymbol{W}_l)\cdot\overrightarrow{\boldsymbol{n}}_{ij} - \lambda_l\,(1+\alpha_l)\,\boldsymbol{\mathcal{F}}(\boldsymbol{W}_r)\cdot\overrightarrow{\boldsymbol{n}}_{ij}}{(\lambda_r-\lambda_l)\,[1+\alpha_l+\alpha_r]} + \frac{\lambda_l\lambda_r\,(1+\alpha_l)\,(1+\alpha_r)\,(\boldsymbol{W}_r-\boldsymbol{W}_l)}{(\lambda_r-\lambda_l)\,[1+\alpha_l+\alpha_r]} + \frac{\lambda_l\lambda_r}{r_m}\left(\boldsymbol{F}_r(\boldsymbol{W}_l)-\boldsymbol{F}_r(\boldsymbol{W}_r)\right), \quad (6.160)$$

where $\alpha_l = \frac{S_l\Delta t\,n_r}{2r_m}$, $\alpha_r = \frac{S_r\Delta t\,n_r}{2r_m}$ and the A superscript indicates the consideration of the framework topology. Such deviation from the usual formulation is dominant on the symmetry axis and is the subject of Section 7.4.

Remark 6.7. *The approach remains fully consistent with the classical HLL solvers. Transforming the conservation laws (6.150) and (6.154) by substituting the 2D axisymmetric geometry by 2D are equivalently 3D Cartesian, the following conservations laws are obtained:*

$$\begin{cases} \left|\check{C}_{ij}\right|_0 \boldsymbol{W}_{HLL} &= \left|\check{C}_{ij,l}\right|_0 \boldsymbol{W}_l + \left|\check{C}_{ij,r}\right|_0 \boldsymbol{W}_r + \Delta t\left(\left|\check{S}_{ij,l}\right|_r \boldsymbol{\mathcal{F}}(\boldsymbol{W}_l)\cdot\overrightarrow{\boldsymbol{n}}_{ij} - \left|\check{S}_{ij,r}\right|_0 \boldsymbol{\mathcal{F}}(\boldsymbol{W}_r)\cdot\overrightarrow{\boldsymbol{n}}_{ij}\right) \\ \left|\check{C}_{ij,l}\right|_0 \boldsymbol{W}_{HLL} &= \left|\check{C}_{ij,l}\right|_0 \boldsymbol{W}_l + \Delta t\left(\left|\check{S}_{ij,l}\right|_0 \boldsymbol{\mathcal{F}}(\boldsymbol{W}_l)\cdot\overrightarrow{\boldsymbol{n}}_{ij} - |S_{ij}|_0\,\boldsymbol{\mathcal{F}}_{HLL}\right), \\ \left|\check{C}_{ij,r}\right|_0 \boldsymbol{W}_{HLL} &= \left|\check{C}_{ij,r}\right|_0 \boldsymbol{W}_r + \Delta t\left(|S_{ij}|_0\,\boldsymbol{\mathcal{F}}_{HLL} - \left|\check{S}_{ij,r}\right|_0 \boldsymbol{\mathcal{F}}(\boldsymbol{W}_r)\cdot\overrightarrow{\boldsymbol{n}}_{ij}\right). \end{cases} \quad (6.161)$$

In this context one can derive the geometrical relation $\left|\check{S}_{ij,l}\right|_r = \left|\check{S}_{ij,r}\right|_r \equiv |S_{ij}|_0$, $\left|\check{C}_{ij,l}\right|_0 = -|S_{ij}|_0\,\lambda_l\Delta t$ *and* $\left|\check{C}_{ij,r}\right|_r = |S_{ij}|_0\,\lambda_r\Delta t$. *Introducing these equalities in (6.161), the reader can straightforwardly deduces the standard HLL flux (6.159).*

6.3.3.3.2 Flux consistency

Theorem 6.2. The flux (6.160) fulfills basic the consistency condition (see Definition 6.14).

Proof. It is possible to prove the consistency of the corrected flux (6.156). Stating $\boldsymbol{W}_l = \boldsymbol{W}_r = \boldsymbol{W}_a$, (6.156) can be rewritten and boils down to:

$$\Delta t\left|\check{C}_{ij}\right|_r |S_{ij}|_r\,\boldsymbol{\mathcal{F}}_{HLL} = \Delta t\,|S_{ij}|_r\left(\left|\check{C}_{ij,r}\right|_r + \left|\check{C}_{ij,l}\right|_r\right)\boldsymbol{\mathcal{F}}(\boldsymbol{W}_a)\cdot\overrightarrow{\boldsymbol{n}}_{ij} \quad (6.162)$$

Since by definition, $\left|\check{C}_{ij}\right|_r = \left|\check{C}_{ij,r}\right|_r + \left|\check{C}_{ij,l}\right|_r$, therefore $\mathfrak{F}^{HLLA}(\boldsymbol{W}_a,\boldsymbol{W}_a,r_m,\overrightarrow{\boldsymbol{n}}) = \boldsymbol{\mathcal{F}}(\boldsymbol{W}_a)\cdot\overrightarrow{\boldsymbol{n}}$ and the flux is consistent. □

6.4 Realizable MUSCL multislopes schemes

We now propose to describe the MUSCL multislope scheme that has been adapted and improved for the need of the presented work. After a quick overview of the numerical methods generalizing

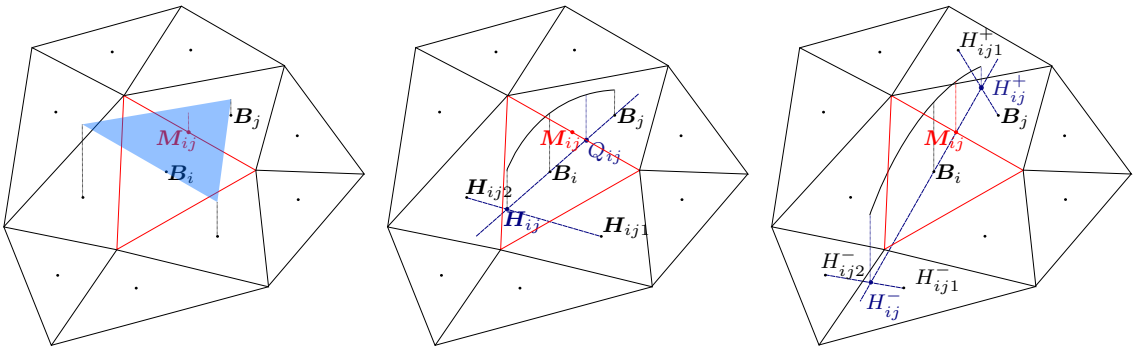

(a) monoslope **(b)** original multislope (Buffard and Clain 2010) **(c)** general multislope (Le Touze, Murrone, and Guillard 2015)

Figure 6.11: *Geometric interpretations of the MUSCL scheme on a 2D unstructured mesh*

the MUSCL methods in multidimensional framework in Section 6.4.1, the MUSCL version used in this work is detailed in Section 6.4.2 together with development conducted on this subject during the thesis. Finally, Section 6.4.3 demonstrates the realizability of the proposed method.

6.4.1 Review of the MUSCL schemes

Although an intensive development for one-dimensional configurations, the extension of MUSCL methods to multidimensional unstructured meshes is not straightforward. As discussed in (Buffard and Clain 2010) for cell-centered FV methods, one can choose to interpret the one dimensional *slope* as a gradient over the cell (the monoslope method, see Figure 6.11a) or as a linear reconstruction in the vicinity of its interfaces (the multislope approach, see Figures 6.11b and 6.11c) projecting the solution on a one dimensional axis. This second interpretation provides robust and efficient methods fulfilling the LED property but loses the concept of the in-cell reconstruction and needs an adequate interpretation. There is no contradiction with the general form (6.144) which only requires accurate approximations of the solution at the cells interfaces. The restriction applied on the time step together with the limiter applied on the reconstruction provides the stability and the robustness of the method.

In this contribution, linear reconstruction through a general multislope approach is considered. As related in (Buffard and Clain 2010) and (Clauzon 2008), the original multislope method is restricted to smooth triangular meshes and the second order of accuracy is not completely reached. This is mainly due to the fact that the reconstructed point is not placed at the barycenters $\boldsymbol{M}_{ij}$ of the interfaces, but on the points Q_{ij}, positioned at the intersection between the cell interface and the axis defined by the barycenters $\boldsymbol{B}_i$ and $\boldsymbol{B}_j$ (see Figure 6.11b). A correction of this issue is proposed in (Clauzon 2008), but at the price of the loss of the LED property, which is a key point in two phase flow simulations. Starting from these conclusions, Le Touze (Le Touze 2015; Le Touze, Murrone, and Guillard 2015) extended that work to general unstructured meshes, introducing two innovating concepts. First, for each reconstruction on the side C_i of the edge S_{ij}, their barycenters, respectively $\boldsymbol{B}_i$ and $\boldsymbol{M}_{ij}$, build the axis on which the projection points are aligned. The choice of these points leads to a second order of accuracy in smooth areas and an efficient resolution of the singularities. Second, all neighbors sharing at least one vertex $\mathcal{W}_i$, and not only neighbors belonging to $\mathcal{V}_i$ only sharing one edge, is used for

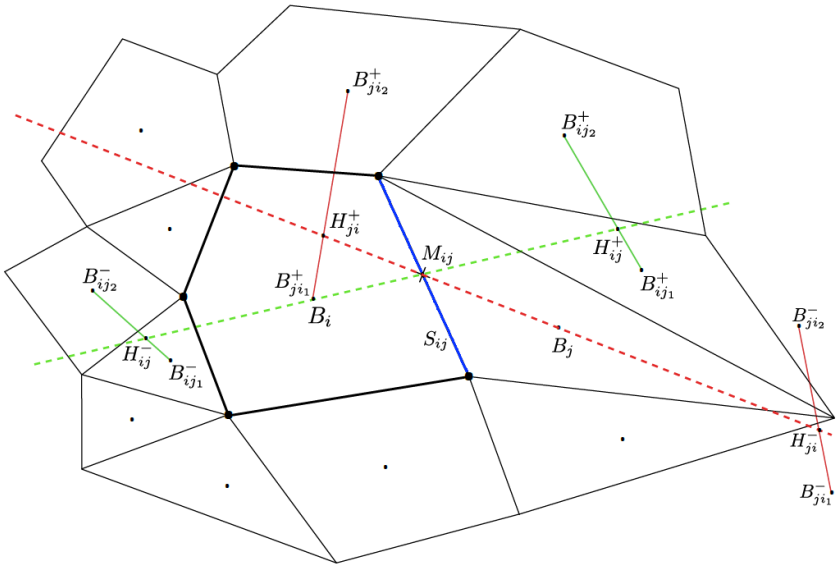

Figure 6.12: *Backward and forward value reconstruction for multislope method on a 2D unstructured mesh (Le Touze, Murrone, and Guillard 2015)*

the reconstruction (see Figure 6.1), which allows more freedom of the possible geometries.

6.4.2 Multislope reconstruction procedure

6.4.2.1 Reconstruction axis

In order to explain the procedure, we present here the two dimensional reconstruction at a surface S_{ij}, boundary of the cells C_i and C_j, with their barycenters respectively noted $\boldsymbol{B}_i$ and $\boldsymbol{B}_j$. The objective is to evaluate the reconstructed value $\boldsymbol{V}_{ij}$, or more exactly each of its components, at the barycenter $\boldsymbol{M}_{ij}$ of S_{ij} from the side C_i of the face. The procedure consists in estimating the value at a point $\boldsymbol{H}^-_{ij}$, positioned at the intersection of the axis $(\boldsymbol{B}_i\boldsymbol{M}_{ij})$ and the line $(\boldsymbol{B}^-_{ij1}\boldsymbol{B}^-_{ij2})$, defined by the barycenters of the best backward neighbors C^-_{ij1} and C^-_{ij2}. Thus, the best specific neighbor is defined by:

$$C^-_{ij1} = \left\{ C^-_{ij} \middle| \cos\left(\boldsymbol{B}^-_{ij}\boldsymbol{B}_i, \boldsymbol{B}_i\boldsymbol{M}_{ij}\right) = \max_{k\in\mathcal{V}_i} \cos\left(\boldsymbol{B}_k\boldsymbol{B}_i, \boldsymbol{B}_i\boldsymbol{M}_{ij}\right) \right\}. \tag{6.163}$$

And the second neighbor is obtained from the same evaluation with the restriction that C^-_{ij2} shall be on the other side of the reconstruction axis:

$$C^-_{ij2} = \left\{ C^-_{ij} \middle| \cos\left(\boldsymbol{B}^-_{ij}\boldsymbol{B}_i, \boldsymbol{B}_i\boldsymbol{M}_{ij}\right) = \max_{k\in\widetilde{\mathcal{V}}_i} \cos\left(\boldsymbol{B}_k\boldsymbol{B}_i, \boldsymbol{B}_i\boldsymbol{M}_{ij}\right) \right\}, \tag{6.164}$$

with

$$\widetilde{\mathcal{V}}_i = \left\{ k \middle| k \in \mathcal{V}_i, C_k \neq C_{ij1}^-, \sin\left(\boldsymbol{B}_{ij}^- \boldsymbol{B}_i, \boldsymbol{B}_i \boldsymbol{M}_{ij}\right) \sin\left(\boldsymbol{B}_k \boldsymbol{B}_i, \boldsymbol{B}_i \boldsymbol{M}_{ij}\right) \leq 0 \right\}. \tag{6.165}$$

As a consequence, $\boldsymbol{B}_{ij1}^-$ and $\boldsymbol{B}_{ij2}^-$ are the closest barycenters to the reconstruction axis previously defined and established on both sides of the reconstruction axis and on the C_i side of S_{ij}. In a symmetric way, one can evaluate C_{ij1}^+ and C_{ij2}^+, best forward neighbors the closest to the same reconstruction axis but established on the C_j side of S_{ij} as represented Figure 6.12. The same procedure is applied on the other side of S_{ij} to obtained C_{ji1}^-, C_{ji2}^-, C_{ji1}^+ and C_{ji2}^+, used to evaluate $\boldsymbol{V}_{ji}$. Since the evaluation of $\boldsymbol{V}_{ij}$ and $\boldsymbol{V}_{ji}$ are conducted independently, only the reconstruction of $\boldsymbol{V}_{ij}$ is treated.

To be able to reconstruct exactly a solution with a uniform gradient, the value evaluated at $\boldsymbol{H}_{ij}^\pm$ is obtained from a convex combination of the value associated to the cells $C_{ij1}^\pm$ and $C_{ij2}^\pm$ such that:

$$\boldsymbol{V}_{ij}^\pm = \beta_{ij1}^\pm \boldsymbol{V}_{ij1}^\pm + \beta_{ij2}^\pm \boldsymbol{V}_{ij2}^\pm, \tag{6.166}$$

where:

$$\beta_{ij1}^\pm = \frac{\|\boldsymbol{B}_{ij2}^\pm \boldsymbol{H}_{ij}^\pm\|_2}{\|\boldsymbol{B}_{ij1}^\pm \boldsymbol{B}_{ij2}^\pm\|_2}, \qquad \beta_{ij2}^\pm = \frac{\|\boldsymbol{B}_{ij1}^\pm \boldsymbol{H}_{ij}^\pm\|_2}{\|\boldsymbol{B}_{ij1}^\pm \boldsymbol{B}_{ij2}^\pm\|_2}, \qquad \beta_{ij1}^\pm + \beta_{ij2}^\pm = 1. \tag{6.167}$$

Since the $\boldsymbol{V}_{ij}^-$,$\boldsymbol{V}_i$,$\boldsymbol{V}_{ij}^+$ and the aimed reconstruction $\boldsymbol{V}_{ij}$ are on the same axis, the evaluation of $\boldsymbol{V}_{ij}$ is reduced to a one-dimensional problem.

Remark 6.8. *For three dimensional reconstructions, it is aimed at reconstructing a triangular surface intersected the axis $\boldsymbol{B}_i\boldsymbol{M}_{ij}$. It is thus necessary to select three neighbors able to provide a forward and backward reconstruction through a convex combination such that:*

$$\boldsymbol{V}_{ij}^\pm = \beta_{ij1}^\pm \boldsymbol{V}_{ij1}^\pm + \beta_{ij2}^\pm \boldsymbol{V}_{ij2}^\pm + \beta_{ij3}^\pm \boldsymbol{V}_{ij3}^\pm. \tag{6.168}$$

where:

$$\forall k \in \{1,2,3\}, \qquad \beta_{ijk}^\pm \geq 0, \qquad \beta_{ij1}^\pm + \beta_{ij2}^\pm + \beta_{ij2}^\pm = 1. \tag{6.169}$$

We refer to the original paper (Le Touze, Murrone, and Guillard 2015) for the detailed procedure to obtain the $C_{ijk}^\pm$ and $\beta_{ijk}^\pm$. The developments that follow are dedicated to the one-dimensional

problem posed on the reconstruction axis, that is identical in two and three dimensional cases.

6.4.2.2 Slope limiter

Similarly to MUSCL methods used on a multidimensional mesh, no ultimate solution exists for slope limiters. But thanks to the multislope method, the points used for the reconstruction are aligned. From these projections, the problem can be reduced to a one dimensional slope limitation case where the inter-cell distance is no more constant. Using the notation of (Le Touze, Murrone, and Guillard 2015), the slope is evaluated based on a forward reconstruction, that is a multi-dimensional extension of (6.137):

$$\boldsymbol{V}_{ij} = \boldsymbol{V}_i + p_{ij}^{+}\varphi(r_{ij}, G_{ij})\|\boldsymbol{B}_i\boldsymbol{M}_{ij}\|_2 \tag{6.170}$$

where $\varphi(r_{ij}, G_{ij})$ is the limiter function that depends on the slope ratio r_{ij} and G_{ij} a set of geometrical parameter depending on the neighborhood of the reconstruction, and $p_{ij}^{\pm}$ are the forward and backward scalar slopes that get the expression:

$$p_{ij}^{+} = \frac{\boldsymbol{V}_{ij}^{+} - \boldsymbol{V}_i}{\|\boldsymbol{B}_i\boldsymbol{H}_{ij}^{+}\|_2} \qquad p_{ij}^{-} = \frac{\boldsymbol{V}_i - \boldsymbol{V}_{ij}^{-}}{\|\boldsymbol{B}_i\boldsymbol{H}_{ij}^{-}\|_2} \qquad r_{ij} = p_{ij}^{-}/p_{ij}^{+} \tag{6.171}$$

As explained in (Berger, Aftosmis, and Murman 2005), the irregular distribution of the cells changes the LED[1] properties. Then the LED domain, to which the slope limiter should belong, is no more constant and changes depending on the local distribution of the point around the reconstruction. The LED boundaries, as shown in (Le Touze, Murrone, and Guillard 2015), slightly change and depend on local reconstruction parameters. The new LED boundaries of the LED zone are then given by:

$$\begin{cases} 0 \leq \varphi^{CFL}(r_{ij}, G_{ij}) \leq \min(\eta_{ij}^{+}, \frac{\eta_{ij}^{-} r_{ij}}{2\nu_{ij}^{+}}) \\ 0 \leq \varphi(r_{ij}, G_{ij}) \leq \min(\eta_{ij}^{+}, \eta_{ij}^{-} r_{ij}) \end{cases} \tag{6.172}$$

where $\nu_{ij}^{+} = \lambda_{max}\Delta t\,|S_{ij}|\,/\,|C_i|$ is the CFL associated to the reconstruction and the geometric parameters yields:

$$\eta_{ij}^{+} = \frac{\|\boldsymbol{B}_i\boldsymbol{H}_{ij}^{+}\|_2}{\|\boldsymbol{B}_i\boldsymbol{M}_{ij}\|_2} \qquad \eta_{ij}^{-} = \frac{\|\boldsymbol{B}_i\boldsymbol{H}_{ij}^{-}\|_2}{\|\boldsymbol{B}_i\boldsymbol{M}_{ij}\|_2} \tag{6.173}$$

[1] Since the aimed problem is now multi-dimensional, TVD and LED properties are no more equivalent. Considering the demonstration provided by (Le Touze, Murrone, and Guillard 2015), only the term LED is adapted to the reconstruction.

Remark 6.9. *For a one dimensional uniform mesh,* $\|\boldsymbol{B}_i\boldsymbol{H}_{ij}^+\|_2 = \Delta x$ *and* $\|\boldsymbol{B}_i\boldsymbol{M}_{ij}\|_2 = \frac{\Delta x}{2}$. *Therefore* $\eta_{ij}^+ = \eta_{ij}^- = 2$ *and the classical one-dimensional TVD limiter constraint is obtained:* $0 \leq \varphi_{ij} \leq \min(2, 2r_{ij})$.

And thanks to definition (6.173), it is possible to conveniently rewrite (6.170) as:

$$\boldsymbol{V}_{ij} = \boldsymbol{V}_i + \frac{\boldsymbol{V}_{ij}^+ - \boldsymbol{V}_i}{\eta_{ij}^+}\varphi_{ij}(r_{ij}, \eta_{ij}^+, \eta_{ij}^-), \tag{6.174}$$

By extending the previously presented limiters considering the new LED conditions, new expressions are obtained. A solution consists simply to rewrite the limiters by taking into account the new LED constraints (6.172):

Superbee $\varphi(r_{ij}, G_{ij}) = \max(0, \min(\eta_{ij}^- r_{ij}, 1), \min(r_{ij}, \eta_{ij}^+))$

Koren $\varphi(r_{ij}, G_{ij}) = \max(0, \min(\eta_{ij}^- r_{ij}, \min(\frac{1}{3} + \frac{2}{3}r_{ij}, \eta_{ij}^+)))$

Van Leer (1974) $\varphi(r_{ij}, G_{ij}) = \max(0, \min(\eta_{ij}^- r_{ij}, \frac{r_{ij}+|r_{ij}|}{1+|r_{ij}|}, \eta_{ij}^+))$

Minmod $\varphi(r_{ij}, G_{ij}) = \max(0, \min(r_{ij}, 1))$

Even if the name of the extensions are the same, no unique solution exists in order to extend regular limiters to limiters used on multislope reconstruction. We propose thus to derive again the *quadratic* limiter. Since an interpolation is aimed, we set a one dimensional reconstruction under the form $\boldsymbol{V}(x) = ax^2 + bx + c$ fulfilling the constraints:

$$\boldsymbol{V}(x_i) = \boldsymbol{V}_i, \qquad \boldsymbol{V}(x_{ij-}) = \boldsymbol{V}_{ij}^-, \qquad \boldsymbol{V}(x_{ij+}) = \boldsymbol{V}_{ij}^+, \tag{6.175}$$

where x_i, x_{ij-} and x_{ij+} are position of $\boldsymbol{B}_i$, $\boldsymbol{H}_{ij}^-$ and $\boldsymbol{H}_{ij}^+$ along the reconstruction axis.

For the sake of simplicity, positions of where the reconstruction are done are scaled such that:

$$x_i = 0, \qquad x_{ij-} = -\|\boldsymbol{B}_i\boldsymbol{H}_{ij}^-\|_2, \qquad x_{ij+} = \|\boldsymbol{B}_i\boldsymbol{H}_{ij}^+\|_2, \qquad x_{ij} = \|\boldsymbol{B}_i\boldsymbol{M}_{ij}\|_2 \tag{6.176}$$

where x_{ij} is the position of the barycenter of the surface where the reconstruction shall occur.

Then, the parameters of $\boldsymbol{V}(x)$ are obtained through the system:

$$\begin{cases} \boldsymbol{V}_i & = c \\ \boldsymbol{V}_{ij}^- - \boldsymbol{V}_i & = ax_{ij-}^2 + bx_{ij-} \\ \boldsymbol{V}_{ij}^+ - \boldsymbol{V}_i & = ax_{ij+}^2 + bx_{ij+} \end{cases} \tag{6.177}$$

a and b can be deduced from (6.177), thus one obtains:

$$\begin{cases} a &= \frac{x_{ij+}\left(\boldsymbol{V}_{ij}^{-}-\boldsymbol{V}_i\right)-x_{ij-}\left(\boldsymbol{V}_{ij}^{+}-\boldsymbol{V}_i\right)}{x_{ij+}x_{ij-}\left(x_{ij-}-x_{ij+}\right)} \\ b &= \frac{-x_{ij+}^2\left(\boldsymbol{V}_{ij}^{-}-\boldsymbol{V}_i\right)-x_{ij-}^2\left(\boldsymbol{V}_{ij}^{+}-\boldsymbol{V}_i\right)}{x_{ij+}x_{ij-}\left(x_{ij-}-x_{ij+}\right)} \end{cases} \tag{6.178}$$

Then the reconstruction is obtained through the relation:

$$\boldsymbol{V}_{ij} = \boldsymbol{V}(x_{ij}) = \boldsymbol{V}_i + ax_{ij}^2 + bx_{ij} \tag{6.179}$$

Remarking that by definition $\eta_{ij}^{-} = -x_{ij-}/x_{ij}$ and $\eta_{ij}^{+} = x_{ij+}/x_{ij}$, we get the basic form of the multislope QUICK limiter by merging (6.178) into (6.179):

$$\begin{aligned} \boldsymbol{V}_{ij} &= \boldsymbol{V}_i + \frac{\eta_{ij}^{+}\left(\eta_{ij}^{+}-1\right)\left(\boldsymbol{V}_{ij}^{-}-\boldsymbol{V}_i\right)+\eta_{ij}^{-}\left(1+\eta_{ij}^{-}\right)\left(\boldsymbol{V}_{ij}^{+}-\boldsymbol{V}_i\right)}{\eta_{ij}^{-}\eta_{ij}^{+}\left(\eta_{ij}^{-}+\eta_{ij}^{+}\right)} \\ &= \boldsymbol{V}_i + \underbrace{\frac{\left(\eta_{ij}^{+}-1\right)r_{ij}+\left(1+\eta_{ij}^{-}\right)}{\eta_{ij}^{-}+\eta_{ij}^{+}}}_{\text{multislope QUICK limiter}}\frac{\left(\boldsymbol{V}_{ij}^{+}-\boldsymbol{V}_i\right)}{\eta_{ij}^{+}} \end{aligned} \tag{6.180}$$

Associating this new formulation of the QUICK limiter to the LED constraints (6.172), we get an original limiter that depends on the local geometry:

Quadratic :

$$\varphi(r_{ij},G_{ij}) = \max\left(0,\min\left(\eta_{ij}^{-}r_{ij},\min\left(\frac{\left(\eta_{ij}^{+}-1\right)r_{ij}+\left(1+\eta_{ij}^{-}\right)}{\eta_{ij}^{-}+\eta_{ij}^{+}},\eta_{ij}^{+}\right)\right)\right) \tag{6.181}$$

Compared to the others limiters, not only the LED limits are modified but also its reconstruction inside the Sweby zone is adapted according to the local geometry, as shown Figure 6.13. We suggest that each limiter should be derived again to fit the multislope framework.

Remark 6.10. *The notion of symmetry can also be defined in the context of multislope reconstruction. Supposing that the same slope shall be reconstructed based on the centered slope* (6.174) *or the more classical upwind based formulation, one can obtain:*

$$\varphi\left(\frac{1}{r_{ij}},G_{ij}\right) = \frac{\varphi(r_{ij},G_{ij})}{r_{ij}} \tag{6.182}$$

We however claim here that such a constraint is useless in the context of the multislope approach. Since the local slope projected is only associated to unique reconstruction $\boldsymbol{V}_{ij}$*, the non-symmetric*

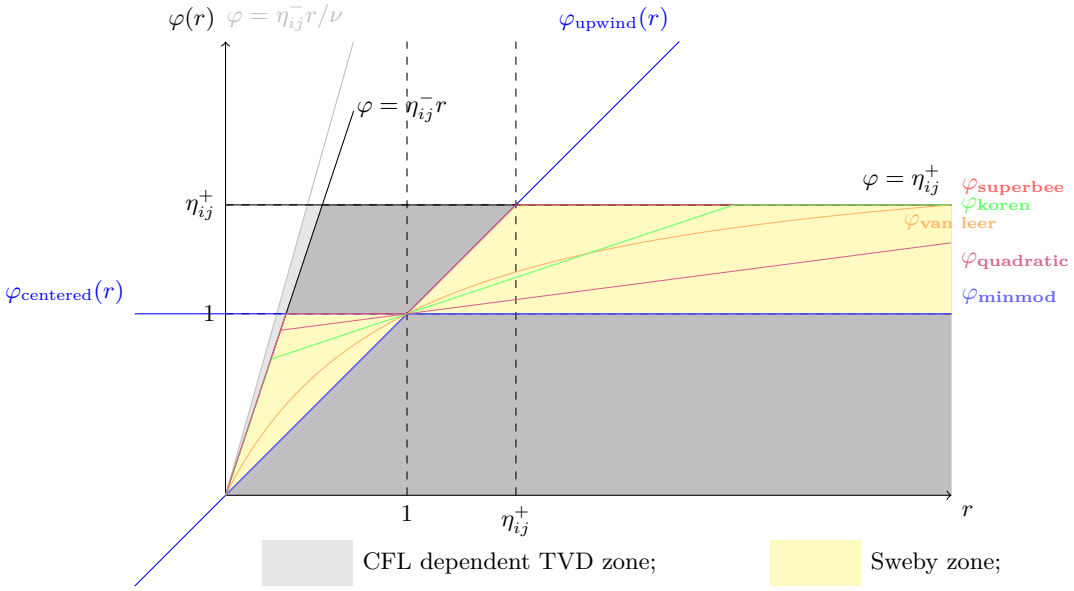

(a) $\eta_{ij}^- = 3$, $\eta_{ij}^+ = 1.6$

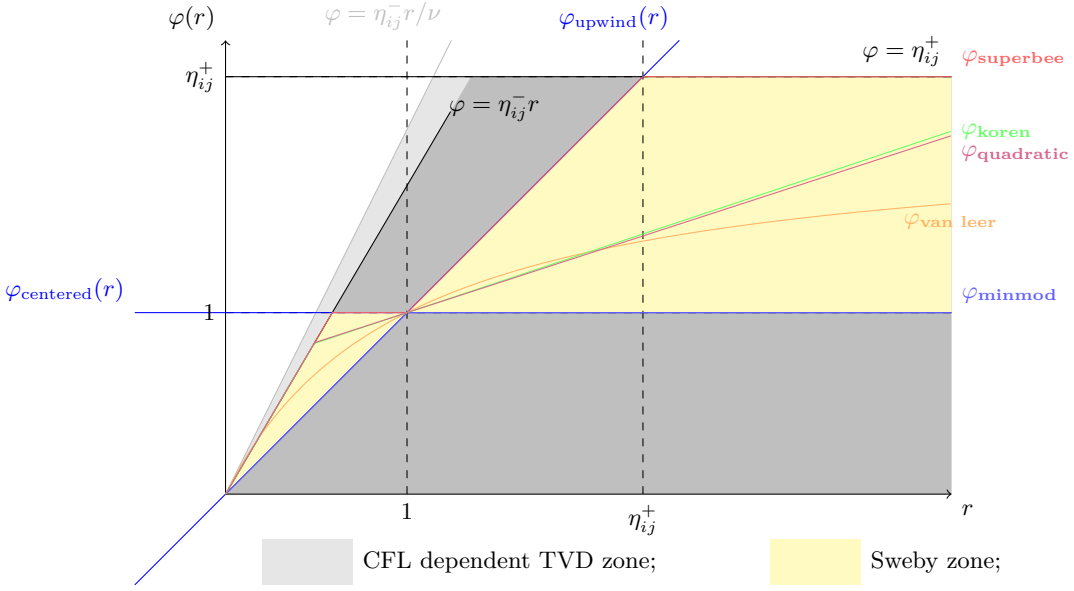

(b) $\eta_{ij}^- = 1.7$, $\eta_{ij}^+ = 2.3$

Figure 6.13: *Slope limiter representation and Sweby zone in the multislope context for two sets of local geometric parameters* η_{ij}^- *and* η_{ij}^+

character does not impact the frame independence of the reconstruction. Also one can remark that the LED constraint itself (6.172) does not fulfill symmetry conditions.

Remark 6.11. *It shall be observed that the presented limiters does not prevent from saw-tooth effect as for the original multislope method (Clauzon 2008). Since on each side of the face S_{ij} of interest, forward reconstructions $\boldsymbol{H}_{ij}^{+}$ and $\boldsymbol{H}_{ji}^{+}$ do not match $\boldsymbol{B}_j$ and $\boldsymbol{B}_i$, and thus the local monotony cannot be ensured, using only $\boldsymbol{V}_i$, $\boldsymbol{V}_{ij}^{-}$ and $\boldsymbol{V}_{ij}^{+}$ without being first order.*

6.4.2.3 Adaptation to axisymmetrical framework

When designing the scheme for axisymmetric framework, the reconstruction variable $r\boldsymbol{W}$ is studied whereas the property of the system of equations are known on $\boldsymbol{W}$. The distribution of $\boldsymbol{W}$ over the cell is thus weighted by r, which induces a displacement of the barycenters $\boldsymbol{B}_i$ at which $\boldsymbol{W}$ is represented at a second order of accuracy. The position of these barycenters are obtained thanks to the relations:

$$\boldsymbol{B}_i = \frac{\int_{C_i} r^{i_{axi}} \boldsymbol{x} dxdz}{\int_{C_i} r^{i_{axi}} dxdz}, \qquad \boldsymbol{M}_{ij} = \frac{\int_{S_{ij}} r^{i_{axi}} \boldsymbol{x} dxdz}{\int_{S_{ij}} r^{i_{axi}} dxdz}, \tag{6.183}$$

which by definition, for the considered tessellation yields:

$$\boldsymbol{B}_i = \frac{1}{|C_i|_{i_{axi},0}} \begin{pmatrix} |C_i|_{i_{axi}+1,0} \\ |C_i|_{i_{axi},1} \end{pmatrix}, \qquad \boldsymbol{M}_{ij} = \frac{1}{|S_{ij}|_{i_{axi},0}} \begin{pmatrix} |S_{ij}|_{i_{axi}+1,0}, \\ |S_{ij}|_{i_{axi},1} \end{pmatrix}, \tag{6.184}$$

with $\boldsymbol{x} = [r, z]^T$, $i_{axi} = 0$ for 2D planar framework and $i_{axi} = 1$ for 2D axisymmetrical framework.

This is the only modification needed to adapt the reconstruction method described in (Le Touze, Murrone, and Guillard 2015) to the axisymmetrical context. The remaining axisymmetric source term integration can be conducted independently.

6.4.3 Realizable schemes for general unstructured mesh

The multislope method (Le Touze, Murrone, and Guillard 2015) thus provides the existence of a finite time step ensuring such a convex combination and therefore ensuring the stability of the procedure. However, in the case of the AG model in the vicinity of particle free areas, it has been observed that the intrinsic dissipation of a Riemann solver of the HLL class (6.159), and the associated raise of entropy production, increase the propagation velocity leading to an abrupt reduction of the stability time step. Therefore, even though this time step necessarily exists, it rapidly tends toward zero. As proposed in (Vié, Doisneau, and Massot 2015), a limitation on the entropy variable is applied to prevent such cases.

This section aims at demonstrate the robustness of the proposed numerical strategy. Unlike for the references cited above, the demonstration is provided both for unstructured mesh and

non-linear hyperbolic equations. More specifically, the following assumptions are required for the validity of the demonstration:

- The system of equations is hyperbolic and can be put under the form $\partial_t \boldsymbol{W} + \mathbf{div}_x\left(\boldsymbol{f}\left(\boldsymbol{W}\right)\right) = 0$,
- The set of admissible states is convex,
- The computational domain is discretized in a finite volumes framework, Ω is tasselated in a set of non-self-intersecting polyhedron $C_i \subset \Omega$.

6.4.3.1 First order scheme: realizability for unstructured mesh

To begin, at first order, we define the notion of realizable flux which ensure, for Godunov schemes, that in the vicinity of the discontinuities created by the method, the update is realizable. We rely on the *virtual geometry* formalism for this definition, explicitly establishing the notion of *vicinity* for the sake of the theorems that follows. The definition is thus inspired from the derivation of the HLL scheme in axisymmetry.

Definition 6.19 (Realizable flux)**.** A numerical flux $\mathfrak{F}_{ij}$ is realizable, if there exists a realizable state $\check{\boldsymbol{W}}_l$ called *virtual state* associated to virtual surfaces and volumes such that:

$$\Delta t \left|S_{ij}\right| \mathfrak{F}_{ij} = \left|\check{C}_{ij,l}\right| \left(\boldsymbol{W}_l - \check{\boldsymbol{W}}_l\right) + \Delta t \left|\check{S}_{ij,l}\right| \boldsymbol{\mathcal{F}}(\boldsymbol{W}_l) \cdot \overrightarrow{\boldsymbol{n}}. \tag{6.185}$$

and reciprocally, for the other side of the discontinuity, there exists $\check{\boldsymbol{W}}_r$ such that:

$$\Delta t \left|S_{ij}\right| \mathfrak{F}_{ij} = \left|\check{C}_{ij,r}\right| \left(\check{\boldsymbol{W}}_r - \boldsymbol{W}_r\right) + \Delta t \left|\check{S}_{ij,r}\right| \boldsymbol{\mathcal{F}}(\boldsymbol{W}_r) \cdot \overrightarrow{\boldsymbol{n}}. \tag{6.186}$$

Corollary 6.1. Because of the conservation property of the flux, we get the following relation between $\check{\boldsymbol{W}}_l$ and $\check{\boldsymbol{W}}_r$:

$$\left|\check{C}_{ij,l}\right| \left(\boldsymbol{W}_l - \check{\boldsymbol{W}}_l\right) + \Delta t \left|\check{S}_{ij,l}\right| \boldsymbol{\mathcal{F}}(\boldsymbol{W}_l) \cdot \overrightarrow{\boldsymbol{n}} = \left|\check{C}_{ij,r}\right| \left(\check{\boldsymbol{W}}_r - \boldsymbol{W}_r\right) + \Delta t \left|\check{S}_{ij,r}\right| \boldsymbol{\mathcal{F}}(\boldsymbol{W}_r) \cdot \overrightarrow{\boldsymbol{n}} \tag{6.187}$$

Remark 6.12. *Rewriting* (6.187)*, one can identify the definition of the HLL state* (6.150) *and deduce the relation:*

$$\left|\check{C}_{ij,l}\right| \check{\boldsymbol{W}}_l + \left|\check{C}_{ij,r}\right| \check{\boldsymbol{W}}_r = \left(\left|\check{C}_{ij,l}\right| + \left|\check{C}_{ij,r}\right|\right) \boldsymbol{W}_{HLL} \tag{6.188}$$

Proposition 6.4. For $\boldsymbol{W}$ belonging to a convex realizable space G, an exact Riemann solver provide a realizable flux.

Proof. Let $\boldsymbol{\omega}_{RP}(\boldsymbol{W}_l, \boldsymbol{W}_r, \frac{x}{t})$ be the exact solution of a Riemann problem and $\mathfrak{F}_{ij} = \boldsymbol{\mathcal{F}}\left(\boldsymbol{\omega}_{RP}(\boldsymbol{W}_l, \boldsymbol{W}_r, 0)\right)$ the flux of the exact Riemann solver. Then, due to the hyperbolic character of the considered system of equations, there exists λ_l and λ_r such that $\boldsymbol{W}_l = \boldsymbol{\omega}_{RP}(\boldsymbol{W}_l, \boldsymbol{W}_r, \lambda_l)$ and $\boldsymbol{W}_r = \boldsymbol{\omega}_{RP}(\boldsymbol{W}_l, \boldsymbol{W}_r, \lambda_r)$. Therefore, integrating the problem on the characteristic plane, one

gets:

$$\int_{\lambda_l \Delta t}^{0} \left|\check{S}_{ij}(\boldsymbol{x})\right| \boldsymbol{\omega}_{RP}(\boldsymbol{W}_l, \boldsymbol{W}_r, \boldsymbol{x}) \mathrm{d}\boldsymbol{x} = \left|\check{C}_{ij,l}\right| \boldsymbol{W}_l + \Delta t \left(\left|\check{S}_{ij,l}\right| \boldsymbol{\mathcal{F}}(\boldsymbol{W}_l) \cdot \overrightarrow{\boldsymbol{n}} - |S_{ij}| \boldsymbol{\mathcal{F}}\left(\boldsymbol{\omega}_{RP}(\boldsymbol{W}_l, \boldsymbol{W}_r, 0)\right) \right), \tag{6.189}$$

Stating the expression of the virtual volume as $\left|\check{C}_{ij,l}\right| = \int_{\lambda_l \Delta t}^{0} \left|\check{S}_{ij}(\boldsymbol{x})\right| \mathrm{d}\boldsymbol{x} = -\lambda_l \Delta t \left|\check{S}_{ij,l}\right|$, one can define the left virtual state:

$$\check{\boldsymbol{W}}_l = \frac{1}{\left|\check{C}_{ij,l}\right|} \int_{\lambda_l \Delta t}^{0} \left|\check{S}_{ij}(\boldsymbol{x})\right| \boldsymbol{\omega}_{RP}(\boldsymbol{W}_l, \boldsymbol{W}_r, \boldsymbol{x}) \mathrm{d}\boldsymbol{x}. \tag{6.190}$$

Since the $\left|\check{S}_{ij}(\boldsymbol{x})\right|$ is positive, (6.190) is a weighted integral of realizable states $\boldsymbol{\omega}_{RP}(\boldsymbol{W}_l, \boldsymbol{W}_r, \boldsymbol{x})$ and because of the convexity of G, $\check{\boldsymbol{W}}_l$ is realizable. Identically, we can define:

$$\check{\boldsymbol{W}}_r = \frac{1}{\left|\check{C}_{ij,r}\right|} \int_{0}^{\lambda_r \Delta t} \left|\check{S}_{ij}(\boldsymbol{x})\right| \boldsymbol{\omega}_{RP}(\boldsymbol{W}_l, \boldsymbol{W}_r, \boldsymbol{x}) \mathrm{d}\boldsymbol{x}. \tag{6.191}$$

that is realizable and which end the proof. □

Proposition 6.5. Let $\tilde{\boldsymbol{W}}$ be defined by:

$$\tilde{\boldsymbol{W}} = \boldsymbol{W} + \frac{\boldsymbol{\mathcal{F}}(\boldsymbol{W}) \cdot \overrightarrow{\boldsymbol{n}}_{ij}}{\lambda} \tag{6.192}$$

For any hyperbolic system of equations and $\boldsymbol{W}$ belonging to a convex realizable space, there exists $\hat{\lambda} > 0$ such that for all $\lambda \geq \hat{\lambda}_l$ $\tilde{\boldsymbol{W}}$ is realizable

Proof. Assuming a Riemann problem where the right state is vacuum, then from (6.187) we can obtain:

$$\left|\check{C}_{ij,r}\right| \check{\boldsymbol{W}}_r = \left|\check{C}_{ij,l}\right| \left(\boldsymbol{W}_l - \check{\boldsymbol{W}}_l\right) + \Delta t \left|\check{S}_{ij,l}\right| \boldsymbol{\mathcal{F}}(\boldsymbol{W}_l) \cdot \overrightarrow{\boldsymbol{n}} \tag{6.193}$$

Substituting (6.188), this lead to:

$$\left|\check{C}_{ij}\right| \boldsymbol{W}_{HLL} = \left|\check{C}_{ij,l}\right| \boldsymbol{W}_l + \Delta t \left|\check{S}_{ij,l}\right| \boldsymbol{\mathcal{F}}(\boldsymbol{W}_l) \cdot \overrightarrow{\boldsymbol{n}} \tag{6.194}$$

For any α real, one has $\alpha \boldsymbol{\mathcal{F}}(\boldsymbol{W}_l) = \boldsymbol{\mathcal{F}}(\alpha \boldsymbol{W}_l)$. Thus defining $\alpha = \left|\check{C}_{ij,l}\right| / \left|\check{C}_{ij}\right| = -\lambda_l \Delta t \left|\check{S}_{ij,l}\right| / \left|\check{C}_{ij}\right|$ and $\boldsymbol{W}_a = \alpha \boldsymbol{W}_l$, it can be deduced:

$$\boldsymbol{W}_{HLL} = \frac{\left|\check{C}_{ij,l}\right|}{\left|\check{C}_{ij}\right|} \boldsymbol{W}_l + \frac{\Delta t \left|\check{S}_{ij,l}\right|}{\left|\check{C}_{ij}\right|} \boldsymbol{\mathcal{F}}(\boldsymbol{W}_l) \cdot \overrightarrow{\boldsymbol{n}} = \boldsymbol{W}_a + \frac{\boldsymbol{\mathcal{F}}(\boldsymbol{W}_a) \cdot \overrightarrow{\boldsymbol{n}}}{-\lambda_l} \tag{6.195}$$

We also remark that, by definition in the given context:

$$\boldsymbol{W}_{HLL} = \frac{1}{\left|\check{C}_{ij}\right|}\int_{\lambda_l}^{\lambda_r}\left|\check{S}_{ij}(\boldsymbol{x})\right|\boldsymbol{\omega}_{RP}(\boldsymbol{W}_l, \overrightarrow{\mathbf{0}}, \boldsymbol{x}/t)\mathrm{d}\boldsymbol{x}, \tag{6.196}$$

Thus for $\lambda_l \leq 0$ sufficiently small and $\lambda_r \geq 0$ sufficiently large to contain the expansion in vacuum, $\boldsymbol{W}_{HLL}$ is realizable. As a consequence setting $\lambda > -\lambda_l$, $\tilde{\boldsymbol{W}}$ of (6.192) is realizable. □

Remark 6.13. *Using well defined velocities, the HLL scheme is realizable for the set of equations considered in this manuscript. More precisely, the HLL state on which this flux relies is realizable (see (Vié, Doisneau, and Massot 2015) for the AG closure).*

Theorem 6.3. For any realizable numerical flux $\mathfrak{F}$, the finite volume methods (6.144) at the first order, with an Euler forward time integration, is realizable under CFL condition.

Proof. Starting from the standard expression of the scheme (6.144) at first order and substituting the numerical flux thanks to (6.185), one gets:

$$\boldsymbol{W}_i^{n+1} = \boldsymbol{W}_i^n - \sum_{j\in\nu_i}\frac{\left|\check{C}_{ij,l}\right|}{|C_i|}\left[\boldsymbol{W}_i^n - \check{\boldsymbol{W}}_{ij,l} + \frac{\Delta t\left|\check{S}_{ij,l}\right|}{\left|\check{C}_{ij,l}\right|}\boldsymbol{\mathcal{F}}(\boldsymbol{W}_i^n)\cdot\overrightarrow{\boldsymbol{n}}_{ij}\right] \tag{6.197}$$

Since in Cartesian referential, $\sum_{j\in\nu_i}\left|\check{S}_{ij,l}\right|\overrightarrow{\boldsymbol{n}}_{ij} = 0$ and $\left|\check{C}_{ij,l}\right| = -\lambda_{ij,l}\Delta t\left|\check{S}_{ij,l}\right| \geq 0$, (6.197) reduces to:

$$\boldsymbol{W}_i^{n+1} = \boldsymbol{W}_i^n - \sum_{j\in\nu_i}\frac{-\lambda_{ij,l}\Delta t\left|\check{S}_{ij,l}\right|}{|C_i|}\left[\boldsymbol{W}_i^n - \check{\boldsymbol{W}}_{ij,l}\right] \tag{6.198}$$

Then under CFL constraint $\sum_{j\in\nu_i}\frac{-\lambda_{ij,l}\Delta t\left|\check{S}_{ij,l}\right|}{|C_i|} \leq 1$, according to (6.201), $\boldsymbol{W}_i^{n+1}$ is a convex combination of realizable states. □

Remark 6.14 (low Mach CFL constraint)**.** *Let $\lambda_l = -c$, be the isotropic acoustic velocity, that is an approximation of the Low-Mach regimes. Under the analogy of on-dimensional schemes where the CFL $\nu = \frac{c\Delta t}{\Delta x}$ is associated to the length Δx consistent with the size of the cell, one can define equivalent length $(\Delta x)_{eq} = \sum_{j\in\nu_i}\frac{\left|\check{S}_{ij,l}\right|}{|C_i|}$ in multidimensional coordinates.*

6.4.3.2 Multislope MUSCL realizability for unstructured mesh

Proposition 6.6 (realizable reconstruction)**.** Let $\boldsymbol{W}^n$ be a realizable solution. Then, for reconstruction variables fulfilling Property 6.3 (see Section 6.3.2.3) and for a limiter respecting the constraint (6.172), the value $\boldsymbol{W}_{ij}$ reconstructed by the MUSCL method is realizable.

Proof. Merging (6.166) in (6.174) one obtain:

$$\boldsymbol{V}_{ij} = \boldsymbol{V}_i + \frac{\varphi_{ij}(r_{ij}, \eta_{ij}^+, \eta_{ij}^-)}{\eta_{ij}^+} \sum_{k=1}^{N_{dim}} \beta_{ijk}^+ \left(\boldsymbol{V}_{ijk}^+ - \boldsymbol{V}_i \right), \tag{6.199}$$

Since to fulfill the LED constraints (6.172), we get $0 \leq \varphi_{ij} \leq \eta_{ij}^+$ and it clearly appears that $\boldsymbol{V}_{ij}$ is a convex combination of $\boldsymbol{V}_i$ and $\boldsymbol{V}_{ijk}^+$ for $k \in [1, N_{dim}]$ since by definition $0 \geq \beta_{ijk}^+ \leq 1$.

Since the reconstruction variables fulfill Property 6.3, such convex combination leads to a realizable state. □

Theorem 6.4. For any realizable numerical flux $\mathfrak{F}$ and realizable reconstructions, the finite volume methods (6.144) is realizable under CFL condition.

Proof. As for the first order case, we begin from an adapted form of (6.144):

$$\boldsymbol{W}_i^{n+1} = \boldsymbol{W}_i^n - \sum_{j \in \nu_i} \frac{\left|\check{C}_{ij,l}\right|}{|C_i|} \left[\boldsymbol{W}_{ij} - \check{\boldsymbol{W}}_{ij,l} + \frac{\Delta t \left|\check{S}_{ij,l}\right|}{\left|\check{C}_{ij,l}\right|} \boldsymbol{\mathcal{F}}(\boldsymbol{W}_{ij}) \cdot \vec{\boldsymbol{n}}_{ij} \right] \tag{6.200}$$

Introducing wisely the $\boldsymbol{W}_i^n$ in the sum, (6.200) can be rewritten:

$$\begin{aligned} \boldsymbol{W}_i^{n+1} = \boldsymbol{W}_i^n &- \sum_{j \in \nu_i} \frac{-\lambda_{ij,l} \Delta t \left|S_{ij}\right|}{|C_i|} \left[\boldsymbol{W}_i^n - \check{\boldsymbol{W}}_{ij,l} \right] \\ &- \sum_{j \in \nu_i} \frac{-\lambda_{ij,l} \Delta t \left|S_{ij}\right|}{|C_i|} \left[\boldsymbol{W}_{ij} - \boldsymbol{W}_i^n + \frac{\Delta t \left|S_{ij}\right|}{\left|\check{C}_{ij,l}\right|} \boldsymbol{\mathcal{F}}(\boldsymbol{W}_{ij}) \cdot \vec{\boldsymbol{n}}_{ij} \right] \end{aligned} \tag{6.201}$$

We now assume the existence of $\boldsymbol{W}_{ij}^*$ such that $\boldsymbol{W}_i^n$ is the virtual state for a realizable flux between $\boldsymbol{W}_{ij}^*$ and $\boldsymbol{W}_{ij}$. To do so, we choose a Rusanov flux. Since by the relation between the Rusanov flux and the HLL flux leads, in the context of virtual volumes for Cartesian coordinates, to $\left|\check{C}_{ij,l}\right| = \left|\check{C}_{ij,r}\right|$, one obtains thanks to the relation (6.187):

$$\begin{aligned} \boldsymbol{W}_i^{n+1} = \boldsymbol{W}_i^n &- \sum_{j \in \nu_i} \frac{-\lambda_{ij,l} \Delta t \left|S_{ij}\right|}{|C_i|} \left[\boldsymbol{W}_i^n - \check{\boldsymbol{W}}_{ij,l} \right] \\ &- \sum_{j \in \nu_i} \frac{-\lambda_{ij,l} \Delta t \left|S_{ij}\right|}{|C_i|} \left[\boldsymbol{W}_i^n - \boldsymbol{W}_{ij}^* + \frac{\Delta t \left|S_{ij}\right|}{\left|\check{C}_{ij,l}\right|} \boldsymbol{\mathcal{F}}(\boldsymbol{W}_{ij}^*) \cdot \vec{\boldsymbol{n}}_{ij} \right] \end{aligned} \tag{6.202}$$

Let $\tilde{\boldsymbol{W}}_{ij}^*$ such that:

$$\tilde{\boldsymbol{W}}_{ij}^* = \boldsymbol{W}_{ij}^* - \frac{\boldsymbol{\mathcal{F}}(\boldsymbol{W}_{ij}^*) \cdot \vec{\boldsymbol{n}}_{ij}}{\tilde{\lambda}_{ij,l}} \tag{6.203}$$

As shown in Proposition 6.5, for any realizable state $\boldsymbol{W}_{ij}^*$, there exists $\tilde{\lambda}_{ij,l}$ sufficiently small to

ensure the realizability of $\tilde{\boldsymbol{W}}_{ij}^{*}$ in (6.203). Then, introducing (6.203) in (6.202) one obtain:

$$\boldsymbol{W}_i^{n+1} = \boldsymbol{W}_i^n - \sum_{j\in\nu_i} \frac{-\lambda_{ij,l}\Delta t\,|S_{ij}|}{|C_i|}\left[\boldsymbol{W}_i^n - \check{\boldsymbol{W}}_{ij,l}\right] - \sum_{j\in\nu_i} \frac{-\lambda_{ij,l}\Delta t\,|S_{ij}|}{|C_i|}\left[\boldsymbol{W}_i^n - \tilde{\boldsymbol{W}}_{ij}^{*}\right] \tag{6.204}$$

Thus under the CFL constraint $\sum_{j\in\nu_i} \frac{-\lambda_{ij,l}\Delta t|S_{ij}|}{|C_i|} \leq \frac{1}{2}$, $\boldsymbol{W}_i^{n+1}$ is a convex combination of realizable state and thus is realizable. □

Remark 6.15. *It is not always possible or wished to determine explicitly the less restrictive value of $\tilde{\lambda}_{ij,l}$ ensuring the realizability. Thus to provide additional robustness to the FV scheme at high order using the an HLLE numerical flux, one can enforce the definition of the signal velocities (6.147) such that:*

$$\begin{cases} \lambda_{max} &= \max\left(\lambda^+(\boldsymbol{W}_j, \overrightarrow{\boldsymbol{n}}_{ij}), \lambda^+(\boldsymbol{W}_{ij}, \overrightarrow{\boldsymbol{n}}_{ij}), \lambda^+(\boldsymbol{W}_{ji}, \overrightarrow{\boldsymbol{n}}_{ij}), \lambda^+(\overline{\boldsymbol{W}}_{ij,ji}, \overrightarrow{\boldsymbol{n}}_{ij})\right), \\ \lambda_{min} &= \min\left(\lambda^-(\boldsymbol{W}_i, \overrightarrow{\boldsymbol{n}}_{ij}), \lambda^-(\boldsymbol{W}_{ij}, \overrightarrow{\boldsymbol{n}}_{ij}), \lambda^-(\boldsymbol{W}_{jj}, \overrightarrow{\boldsymbol{n}}_{ij}), \lambda^-(\overline{\boldsymbol{W}}_{ij,ji}, \overrightarrow{\boldsymbol{n}}_{ij})\right), \end{cases} \tag{6.205}$$

and

$$\lambda_r = \max(0, \lambda_{max}), \qquad \lambda_l = \min(0, \lambda_{min}). \tag{6.206}$$

Remark 6.16. *According to Theorem 6.4 and Proposition 6.6, the multislope MUSCL method is realizable using limiters fulfilling LED constraints (6.172), reconstruction variables with Property 6.3 and a realizable numerical flux.*

As a consequence, it is possible to design, as proposed through the work presented here, fully realizable methods for PGD, the Euler equations and the AG closure. Such property is proved in this manuscript true for these non-linear hyperbolic systems of conservation laws, in multidimensional cases using general unstructured meshes. Moreover, the conclusions can be applied to any systems with variables belonging to a convex space. Therefore, even in complex configurations, all singularities can be treated without leading to non-realizable states ensuring the robustness of the proposed strategy.

However, realizability does not ensure the LED property in the case of non-linear system. Such feature can be provided only if the system of equations possesses a maximum principle on a variable.

Remark 6.17. *Theorem 6.4 ensures that there exists a time step associated to a set of $\lambda_{ij,l}$ values such that the update is realizable. However, it does not ensure that this time step tends to zero after several iteration. Such case has been observed in (Vié, Doisneau, and Massot 2015) with the AG system, near vacuum, the entropy and thus acoustic velocity can abruptly increase and thus $\lambda_{ij,l}$ can tend to $-\infty$. Therefore, in such situation, imposing a fixed CFL, the simulation may stop since we can obtain $\sum_{n=0}^{+\infty}(\Delta t)_n < t_{lim}$ where $t_{lim} \in \mathbb{R}^{+*}$*

6.5 Viscous contribution

Due to the parabolic character of the viscous contribution, the integration of these terms is conducted separately in this work. Unlike for hyperbolic equations, the *upwinding* does not ensure the stability of such kind of systems and distinct numerical methods need to be used. Centered schemes are the most adapted for the resolution of this term (Hirsch 2007). After a brief introduction of the solution proposed for the resolution of these terms, an extension for axisymmetric framework is proposed.

In the SRM context, it appears that the viscous contribution is marginal compared to the convection and two-phase flow effects. Also no numerical issues has been detected during this work concerning these terms.

6.5.1 A centered scheme

6.5.1.1 One dimensional case

In one dimensional case, we introduce the linear diffusion equation:

$$\partial_t w + \mu \partial_{xx} w = 0 \tag{6.207}$$

where μ is constant.

A simple and sufficient second order scheme can be obtained through FD methodology. Expressing the second order derivative from the direct neighbors, the semi-discrete form thus yields:

$$\mathrm{d}_t w_i = -\frac{\mu}{(\Delta x)^2}\left[w_{i+1} - 2w_i + w_{i-1}\right]. \tag{6.208}$$

Or put in a conservative way:

$$\begin{aligned} \mathrm{d}_t w_i &= -\tfrac{1}{\Delta x}\left[\boldsymbol{f}^d_{i+1/2} - \boldsymbol{f}^d_{i-1/2}\right], \\ \boldsymbol{f}^d_{i+1/2} &= \mu \tfrac{w_{i+1}-w_i}{\Delta x}. \end{aligned} \tag{6.209}$$

where $\boldsymbol{f}^d_{i+1/2}$ is the diffusion flux.

Looking at (6.209), one can interpret that scheme from another perspective. It consists in an approximation of the gradient throughout the cell interface that is used to compute the diffusion flux. That last interpretation can be generalized to the FV framework.

6.5.1.2 Two-dimensional structured grid

For the conception of numerical methods in the multidimensional framework, we base our approach on that last perspective closer to the governing equations since the first step corresponds to the evaluation of the stress tensor and the second to the flux.

$$\boldsymbol{W}_i^{n+1} = \boldsymbol{W}_i^n + \sum_{j \in \nu_i} \frac{|S_{ij}|}{|C_i|} \mathfrak{D}(\widehat{\boldsymbol{W}_{ij}^n}, \widehat{\nabla \boldsymbol{W}_{ij}^n}) \cdot \boldsymbol{n}_{ij} \tag{6.210}$$

To do so, we proceed in the following steps:

1. Evaluation of the gradient centered on a cell $\nabla \boldsymbol{W}_i^n$,
2. Interpolation of the gradient at a cell interface $\widehat{\nabla \boldsymbol{W}_{ij}^n}$,
3. Deduction of the diffusion flux $\mathfrak{D}(\widehat{\boldsymbol{W}_{ij}^n}, \widehat{\nabla \boldsymbol{W}_{ij}^n}) \cdot \boldsymbol{n}_{ij}$

For the Navier-Stokes equation, it is needed to estimate $\nabla u_{g,x}$, $\nabla u_{g,y}$ and ∇T_g. In the context of two dimensional structured grids, we propose the following approximations, for a scalar field α,

$$\begin{cases} \frac{\partial \alpha_{i,j}}{\partial x} \simeq \nabla_x \alpha_{i,j} = \dfrac{\Delta_{EW}(\alpha_{i,j})\Delta_{NS}(\bar{y}_{i,j}) - \Delta_{NS}(\alpha_{i,j})\Delta_{EW}(\bar{y}_{i,j})}{\Delta_{EW}(\bar{x}_{i,j})\Delta_{NS}(\bar{y}_{i,j}) - \Delta_{NS}(\bar{x}_{i,j})\Delta_{EW}(\bar{y}_{i,j})}, \\ \frac{\partial \alpha_{i,j}}{\partial y} \simeq \nabla_y \alpha_{i,j} = \dfrac{\Delta_{EW}(\alpha_{i,j})\Delta_{NS}(\bar{x}_{i,j}) - \Delta_{NS}(\alpha_{i,j})\Delta_{EW}(\bar{x}_{i,j})}{\Delta_{EW}(\bar{y}_{i,j})\Delta_{NS}(\bar{x}_{i,j}) - \Delta_{NS}(\bar{y}_{i,j})\Delta_{EW}(\bar{x}_{i,j})}. \end{cases} \tag{6.211}$$

where $\bar{x}_{i,j}$, $\bar{y}_{i,j}$ are the coordinate of the barycenter $\boldsymbol{B}_{i,j}$ defined by (6.184) for the cell (i,j) such that $\boldsymbol{B}_{i,j} = [\bar{x}_{i,j}, \bar{y}_{i,j}]$ and the difference operators Δ_{NS} and Δ_{EW} for a arbitrary scalar field a are:

$$\Delta_{EW}(a_{i,j}) = a_{i+1,j} - a_{i-1,j}, \qquad \Delta_{NS}(a_{i,j}) = a_{i,j+1} - a_{i,j-1}. \tag{6.212}$$

These formula are adapted to structured curvilinear meshes with low distortion. Then, we approximate the derivatives at the interface through:

$$\begin{cases} \widehat{\nabla_x \alpha_{i+1/2,j}} = \frac{1}{2}\left[\nabla_x \alpha_{i,j} + \nabla_x \alpha_{i+1,j}\right] \\ \widehat{\nabla_y \alpha_{i+1/2,j}} = \frac{1}{2}\left[\nabla_y \alpha_{i,j} + \nabla_y \alpha_{i+1,j}\right] \end{cases} \tag{6.213}$$

These determinations of the derivatives are sufficient to express the stress tensor at a cell

interface and thus to solve the viscous terms for the targeted applications.

6.5.1.3 General unstructured mesh

In order to extend the approach presented above to unstructured meshes, one should rather rely on FEM class of methods. The description of these methods is not detailed in this manuscript and we refer to (Reddy and Gartling 2010), (Thomée 1984) and (Hirsch 2007) for more informations on the numerical methods dedicated to the parabolic equation.

6.5.2 Axisymmetric contribution for the Navier-Stokes equations

In the axisymmetric framework, axisymmetric sources terms associated to the viscous fluxes $\boldsymbol{\mathcal{S}}\lceil^{axi,n}$ appears and need informations of the local velocity gradients and the radial position. Additional, fluxes also need these informations at the cell interface need both the derivatives. Starting from (6.43), we add the finite difference viscous contribution as follows:

$$\boldsymbol{W}_i^{n+1} = \boldsymbol{W}_i^n - \sum_{j\in\nu_i} \frac{|S_{ij}|_{i_{axi},0}}{|C_i|_{i_{axi},0}} \left[\mathfrak{F}(\boldsymbol{W}_{ij}^n, \boldsymbol{W}_{ji}^n, \boldsymbol{n}_{ij}) - \mathfrak{D}(\widehat{\boldsymbol{W}_{ij}^n}, \widehat{\nabla \boldsymbol{W}_{ij}^n}) \cdot \boldsymbol{n}_{ij}\right] + i_{axi} \frac{|C_i|_{0,0}}{|C_i|_{1,0}} \left[\boldsymbol{\mathcal{S}}_i^{axi,n} + \boldsymbol{\mathcal{S}}\lceil_i^{axi,n}\right] + \boldsymbol{\mathcal{S}}(\boldsymbol{W}_i^n), \quad (6.214)$$

where the values $\widehat{\boldsymbol{W}_{ij}^n}$ and $\widehat{\nabla \boldsymbol{W}_{ij}^n}$ used to compute the viscous terms, are computed separately from $\boldsymbol{W}_{ij}^n$ and $\boldsymbol{W}_{ji}^n$ that are used for the convection terms, $\mathfrak{D}$ is the viscous stress vector (3.63) of tensors and $\boldsymbol{\mathcal{S}}\lceil^{axi,n}$ is the viscous source term vector (3.64) that are defined by:

$$\begin{aligned} \mathfrak{D} &= [0, \boldsymbol{T}_{NS}, \boldsymbol{T}_{NS} \cdot \boldsymbol{u}_g]^T, \\ \boldsymbol{\mathcal{S}}\lceil^{axi,n} &= \left[0, \boldsymbol{\mathcal{S}}\lceil^{axi}(\widehat{\boldsymbol{W}_{ij}^n}, \widehat{\nabla \boldsymbol{W}_{ij}^n}), 0\right]^T. \end{aligned} \quad (6.215)$$

While it is proposed to evaluate $\widehat{\nabla \boldsymbol{W}_{ij}^n}$ thanks to (6.213) once again and $\widehat{\boldsymbol{W}_{ij}^n}$ is obtained in the same way:

$$\widehat{\alpha_{ij}} = \frac{1}{2}\left[\alpha_i + \alpha_j\right] \quad (6.216)$$

Remark 6.18. *It shall be noticed that the $\widehat{\boldsymbol{W}_{ij}^n}$ does not generally match the reconstructed values obtained thanks to a MUSCL reconstruction. Such difference motivates the use of the notation $\widehat{\boldsymbol{W}_{ij}^n}$ to express this interpolated value.*

Because of the presence of the $\frac{u_{g,r}}{r}$ terms in $\boldsymbol{T}_{NS}$ and $\boldsymbol{\mathcal{S}}\lceil^{axi}$, finite volume methods fail at properly integrating the viscous tensor over a cell since $\int_{C_i} \frac{1}{r} = +\infty$ for a cell located at the symmetry axis. In practice however, not considering vacuum occurrences, we obviously have

$\lim_{r\to 0} u_{g,r} = 0$ for the carrier phase to conserve mass and ensure a finite viscous contribution. Therefore velocity derivative are obtained through finite difference at cell barycenters such that $\boldsymbol{\mathcal{S}}\lceil^{axi}$ can be computed and a null flux is imposed on the symmetry axis. For the contribution of $\mathfrak{D}$, $u_{g,r}$ and the velocity derivatives are interpolated at face barycenters from the adjacent cell barycenters. Finally, $\boldsymbol{T}_{NS}$ (as for $\boldsymbol{T}_{NS}\cdot\boldsymbol{u}$ in the energy equation) and $\boldsymbol{\mathcal{S}}\lceil^{axi}$ are respectively integrated in time with $\mathfrak{F}$ and $\boldsymbol{\mathcal{S}}^{axi,n}$ in the transport operator.

Obviously, we once again refer to the FEM literature for a better approximations of the derivatives and interpolations. The numerical procedure described here remains however sufficiently robust and accurate for our field of application. This thus concludes the description of the numerical methods in the interior of the computational domain.

Chapter 7

Boundary conditions

> Les conflits deviennent asymétriques non pas parce que l'on entre dans un rapport du faible face au fort mais parce que l'on entre dans une confrontation de la singularité contre le modèle.
>
> Philippe Baumard, Le vide stratégique, 2012

> Conflicts become asymetrical not because one get in a relation where the weak is facing the strong but because one get into a confrontation of the singularity against the model.
>
> Philippe Baumard, Le vide stratégique, 2012

Until here, the description of the numerical schemes at the boundary of the domain has been deliberately avoided for the sake of simplicity. Despite relevant contribution (Osher and Chakravarthy 1983; Hirsch 1990; Poinsot and Lele 1992; Lupoglazoff and Vuillot 1999; Ferziger and Peric 2012), this subject does not seem to have been ever treated in its totality in the literature and no dedicated monograph exists on this subject, to the knowledge of the author. Moreover, while the design of scheme and treatment of boundary conditions is often intuitive, they are rarely explained rigorously. Without the ambition to fill this gap and in the context of FV schemes, this chapter aims at providing a theoretical basis of this subject and is focused on the boundary conditions used in this contribution.

The chapter is organized as follow. After a brief review in Section 7.1 of the basis on which boundary conditions for hyperbolic PDE rely, two methodologies adapted to the numerical schemes in the FV context are proposed in Section 7.2. Then, usual boundary conditions appearing in the internal flows of SRMs are presented in Section 7.3 before concluding in Section 7.4, in the context of axisymmetry, on a specific treatment of the symmetry axis that is introduced in this work.

7.1 Boundary condition fundamentals

7.1.1 Various type of boundary conditions

In fluid mechanics, boundary conditions are divided into two main categories. Applied to scalar conservation laws, they are the followings:

Dirichlet: The solution at the boundary is imposed such that $w(\boldsymbol{x}, t) = w_{BC}$ for all $\boldsymbol{x} \in \partial\Omega$ where w_{BC} is a constant,

Von Neumann: The derivative of the solution at the boundary is imposed such that $\partial_{\boldsymbol{x}} w(\boldsymbol{x}, t) = \alpha_{BC}$ for all $\boldsymbol{x} \in \partial\Omega$ where α_{BC} is a constant,

These BC can be either strongly or weakly imposed. In the context of FEMs, the boundary conditions are either essential boundary conditions, which are included in the function spaces, or natural boundary conditions, which are written in the variational formulation of the PDEs (Ferziger and Peric 2012) Such approach, originally designed for elliptic problem cannot be straightforwardly applied in the context of hyperbolic systems of conservation laws due to the ingoing and outgoing characteristics (Donea and Huerta 2003). For hyperbolic PDE however and more specifically the FD and FV frameworks (Hirsch 1990; Godlewski and Raviart 1996), it is necessary to reconstruct the solution at the boundary of the domain or outside, in its vicinity (see Section 7.2). This can be only achieve considering the propagation of the information in the flow to remain consistent with the governing equations.

7.1.2 Information propagation

In the context of hyperbolic systems of equations, because of the information flow, we propose to rewrite the problem and impose an *upwinding* to ensure the stability of the procedure. Neglecting the effect of the source terms in this section for the sake of simplicity, it is proposed to linearize the system, such that:

$$\partial_t \boldsymbol{W} + \boldsymbol{A}_0 \partial_{\overrightarrow{\boldsymbol{n}}} \boldsymbol{W} = 0 \Leftrightarrow \partial_t \hat{\boldsymbol{W}} + \boldsymbol{\Lambda}_0 \partial_{\overrightarrow{\boldsymbol{n}}} \hat{\boldsymbol{W}} = 0 \tag{7.1}$$

where $\hat{\boldsymbol{W}} = \boldsymbol{R}^{-1}\boldsymbol{W} \in \mathbb{R}^d$ are the linearized variables, $\boldsymbol{A}_0 = \boldsymbol{R}(\boldsymbol{W}_0)\boldsymbol{\Lambda}(\boldsymbol{W}_0)\boldsymbol{R}^{-1}(\boldsymbol{W}_0)$ the Jacobian of the flux, $\boldsymbol{\Lambda}$ its Eigenvalue matrix (see Section 3.2.2.2) and $\partial_{\overrightarrow{\boldsymbol{n}}}$ is the derivative in the normal direction of the boundary of interest.

We can decompose that vector in terms of incoming/outgoing variables, such that $\hat{\boldsymbol{W}} = \left(\hat{\boldsymbol{W}}_I, \hat{\boldsymbol{W}}_{II}\right) \in \mathbb{R}^p \times \mathbb{R}^{d-p}$ where $p \in [0, d]$ is the number of variable imposed from the outside of the system. As a consequence, to be consistent with the information traveling through a boundary, it is needed to impose $\hat{\boldsymbol{W}}_I$ corresponding to p waves coming into the domain and establish $\hat{\boldsymbol{W}}_{II}$ the $d-p$ wave going out of the domain. In practice however, this is not convenient to impose the characteristic variables $\hat{\boldsymbol{W}}$ and it is generally useful to be able to impose *physical* or *measurable* quantities at a boundary, such as density, velocity and pressure among others.

Under that circumstances, as proposed in (Hirsch 1990; Godlewski and Raviart 1996), one can replace $\hat{\boldsymbol{W}}$ by a set of *primitive* variable $\hat{\boldsymbol{V}} = \left(\hat{\boldsymbol{V}}_I, \hat{\boldsymbol{V}}_{II}\right) \in \mathbb{R}^p \times \mathbb{R}^{d-p}$ and aim at imposing $\hat{\boldsymbol{V}}_I$ to describe the boundary condition. However, not every variables can be chosen to design a valid boundary condition. To check such validity, the transformation from $\hat{\boldsymbol{V}}$ to $\hat{\boldsymbol{W}}$ is written as follow:

$$\begin{pmatrix} \hat{\boldsymbol{W}}_I \\ \hat{\boldsymbol{W}}_{II} \end{pmatrix} = \begin{pmatrix} \boldsymbol{a}_I & \boldsymbol{a}_{II} \\ \boldsymbol{b}_I & \boldsymbol{b}_{II} \end{pmatrix} \begin{pmatrix} \hat{\boldsymbol{V}}_I \\ \hat{\boldsymbol{V}}_{II} \end{pmatrix} \tag{7.2}$$

where $\boldsymbol{b}_I$ and $\boldsymbol{a}_{II}$ are rectangular matrices while $\boldsymbol{a}_I$ and $\boldsymbol{b}_{II}$ are square matrices and can be of null size for supersonic conditions, in which case, (7.2) is reduced to either $\hat{\boldsymbol{W}}_I = \boldsymbol{a}_I \hat{\boldsymbol{V}}_I$ or $\hat{\boldsymbol{W}}_{II} = \boldsymbol{b}_{II} \hat{\boldsymbol{V}}_{II}$.

Since $\hat{\boldsymbol{W}}_{II}$ and $\hat{\boldsymbol{V}}_{II}$ are known from the inside of the computational domain, it is possible to deduce from (7.2) the relation:

$$\hat{\boldsymbol{W}}_I = \boldsymbol{a}_{II}\boldsymbol{b}_{II}^{-1}\hat{\boldsymbol{V}}_{II} + \left(\boldsymbol{a}_I - \boldsymbol{a}_{II}\boldsymbol{b}_{II}^{-1}\boldsymbol{b}_I\right)\hat{\boldsymbol{V}}_I \tag{7.3}$$

In case of null size $\boldsymbol{b}_{II}$ matrix, as for instance for supersonic inlet, one directly has $\hat{\boldsymbol{W}}_I = \boldsymbol{a}_I \hat{\boldsymbol{W}}_I$. Otherwise however, it is necessary to have $\boldsymbol{b}_{II}$ invertible to ensure the consistency of the incoming information. In that last case not any variables can be imposed. As an example, in case of subsonic inlet for one-dimensional Euler equation, it has been observed in (Oliger and Sundström 1978) that one can prescribe the pairs (ρ, u) and (ρ, P) but not (u, P).

As a conclusion, even if one does not work in the characteristic field, it is necessary to *strongly* impose p variables corresponding to the p waves entering in the domain through this boundary. The $d - p$ terms composing $\hat{\boldsymbol{V}}_{II}$ are also of importance but are deduced from the conditions inside the computational domain. As a consequence and in a general manner, the components of $\hat{\boldsymbol{V}}_I$ are imposed and their determination is associated with Dirichlet conditions while $\hat{\boldsymbol{V}}_{II}$ deduced, typically from null gradient or extrapolation (uniform gradient), and thus associated with von Neumann boundary conditions.

7.2 Standard flux computation

The numerical treatment associated with a boundary condition directly depends on the used framework and we focus here on the case of FV methods. To evaluate the flux at a boundary edge, two options are possible: evaluate the state at the boundary as proposed Section 7.2.1 or relying on a Riemann solver as discussed Section 7.2.2.

7.2.1 Direct flux deduction

Starting from the general FV scheme formulation (6.7), we first separate the flux through surfaces strictly inside the domain and at its boundary such that:

$$\boldsymbol{W}_i^{n+1} = \boldsymbol{W}_i^n - \frac{\Delta t}{|C_i|} \sum_{j \in \mathcal{V}_i} |S_{ij}| \, \mathfrak{F}_{ij} - \frac{\Delta t}{|C_i|} \sum_{j \in \breve{\mathcal{V}}_i} \left| \breve{S}_{ij} \right| \breve{\mathfrak{F}}_{ij} \tag{7.4}$$

where the superscript $\breve{\bullet}$ distinguishes the values associated with the boundaries of the computational domain.

The first solution consists in deducing value $\breve{\boldsymbol{W}}_{ij}$ at $\breve{\boldsymbol{M}}_{ij}$ the barycenter of the boundary of the computational domain (see Figure 7.1a) by *strongly* imposed the values from Dirichlet or von Neumann condition. Therefore, if such value is known and assumed to be constant during a time step then one can directly deduce the numerical flux as:

$$\breve{\mathfrak{F}}_{ij} = \boldsymbol{\mathcal{F}} \left(\breve{\boldsymbol{W}}_{ij} \right) \cdot \overrightarrow{\boldsymbol{n}}_{ij} \tag{7.5}$$

It is thus possible, by manipulating $\breve{\boldsymbol{W}}_{ij}$, to strictly impose quantities such as mass flux, which is a clear advantage while designing wall and injection boundary conditions.

Remark 7.1. *The global order of accuracy is limited to* 2 *because of the subsequent assumption of a linear (planar) edge at the boundary and the use of a single quadrature on that surface. Since it is not aimed at going above that order of accuracy, we do not enter in these details and refer to (Costa et al. 2018) for a proposition to overcome this limit. The developments that follows can be extended for such cases by interchanging* $\boldsymbol{W}_i$ *with the reconstructed variable at the boundary* $\boldsymbol{W}_{ij}$*.*

7.2.2 Riemann problem at the boundary

Another solution to set up boundary conditions in FV schemes and more specifically for methods of Godunov class, is to rely on the Riemann solver. To do so, a cell, referred as *ghost-cell*, is virtually created on the other side of the boundary as represented Figure 7.1b. Once again, considering the conditions imposed at the limits of the computational domain, a value $\breve{\boldsymbol{W}}_{ji}$ is associated with that ghost cell. Thus at first order, considering a Riemann solver $\mathfrak{F}^{BC}$, the flux is *weakly* determined at the boundary and becomes:

$$\breve{\mathfrak{F}}_{ij} = \mathfrak{F}^{BC} \left(\boldsymbol{W}_i, \breve{\boldsymbol{W}}_{ji}, \overrightarrow{\boldsymbol{n}}_{ij} \right) \cdot \overrightarrow{\boldsymbol{n}}_{ij} \tag{7.6}$$

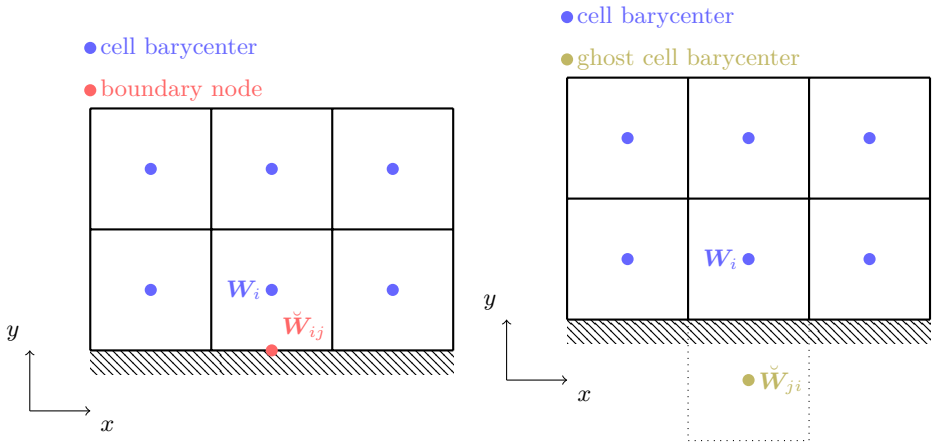

(a) Direct flux **(b)** Ghost cell

Figure 7.1: *Two methodologies*

That last formulation has the advantage to be able to take into account all the waves associated with the problem. As a consequence, even if more variables than needed are associated with $\breve{\boldsymbol{W}}_{ji}$, a flux can be deduced without having a overdetermined problem. This is the case of pressure imposed outlet, where the Riemann problem automatically detects the subsonic/supersonic transition without conditional procedure or detection of the fluid regime. Such kind of methodology is thus well fitted for fluid boundaries. Moreover, it is easily possible to define symmetry conditions thanks to that formalism.

Remark 7.2. *In the context of the multislope MUSCL method, in order to avoid first order degeneracy close to boundaries, we propose to take into account* $\breve{\boldsymbol{W}}_{ij}$ *at* $\breve{\boldsymbol{M}}_{ij}$ *for reconstruction purposes. This supposes that such state can be deduced from the boundary conditions such as for direct flux deduction method (see Section 7.2.1). This is not always the case since only the resulting flux, through a Riemann solver for example, is required. However, in the case where a ghost cell is considered or the solution is explicitly reconstructed at the border, these can be considered for the purposes of the multislope MUSCL reconstruction to avoid first order degeneracy near the border of the domain (Le Touze, Murrone, and Guillard 2015). In this contribution, only reconstructions at the boundary nodes* $\breve{\boldsymbol{M}}_{ij}$ *are considered. Therefore, even when ghost cells are used, values reconstructed at the interface* $\breve{\boldsymbol{W}}_{ij}$ *are also provided.*

7.3 Standard boundary conditions

Taking into consideration the previous formalism to model boundary conditions and to integrate them in the numerical methods, we here review usual boundary conditions for both phases. After an introduction using symmetry conditions, specific boundary conditions for walls and fluid boundaries are described. While such transformation is trivial for scalars and vectors in the literature, it is unusual for tensors of order 2 and above, as encountered in the AG closure, to be submitted to such transformation.

7.3.1 Symmetry

The symmetry is one of the most basic boundary conditions and is the main building block of other ones. We thus focus on establishing the symmetry of a state before describing the boundary condition itself.

7.3.1.1 Symmetric state of a vector

To begin, we here propose to derive the symmetric state $\boldsymbol{u}_s$ of a vector $\boldsymbol{u}$ according to a surface of normal $\overrightarrow{\boldsymbol{n}}$. The procedure is conducted in three steps. We firstly express $\boldsymbol{u}$ in the referential of the surface, where the first component corresponds to the normal $\overrightarrow{\boldsymbol{n}} = [n_1, n_2, n_3]^t$, thanks to a rotation. Then, after changing the sign of this first component, this symmetric vector is rotated back to the initial basis. Put under a tensorial form, this gives:

$$\boldsymbol{u}_s = \boldsymbol{T}_s \boldsymbol{u}, \qquad \boldsymbol{T}_s = \boldsymbol{R}_s^{-1} \boldsymbol{A}_s \boldsymbol{R}_s \tag{7.7}$$

where the matrix $\boldsymbol{T}_s$ is the symmetric transformation and, in three dimension, we have $\boldsymbol{A}_s = \boldsymbol{diag}\,(-1, 1, 1)$ and $\boldsymbol{R}_s$ is obtained by the Rodrigues' rotation formula such that:

$$\boldsymbol{R}_s = \mathbb{I} + \sin(\theta)\boldsymbol{K} + (1 - \cos(\theta))\boldsymbol{K}^2, \qquad \boldsymbol{K} = \begin{pmatrix} 0 & -k_3 & k_2 \\ k_3 & 0 & -k_1 \\ -k_2 & k_1 & 0 \end{pmatrix} \tag{7.8}$$

where $\boldsymbol{K}$ is the cross product matrix of $\boldsymbol{k} = [k_1, k_2, k_3]^t$ unit vector of the axis around which the rotation occurs and θ is the angle of rotation.

Because of the aimed change of basis, the terms $\boldsymbol{k}$ and $\cos(\theta)$, remaining to close the rotation, can be obtained by the relations:

$$\boldsymbol{k} = \frac{\boldsymbol{x}_1 \times \overrightarrow{\boldsymbol{n}}}{\|\boldsymbol{x}_1 \times \overrightarrow{\boldsymbol{n}}\|_2}, \qquad \cos(\theta) = \frac{\overrightarrow{\boldsymbol{n}} \cdot \boldsymbol{x}_1}{\|\overrightarrow{\boldsymbol{n}}\|_2 \cdot \|\boldsymbol{x}_1\|_2} \tag{7.9}$$

where $\boldsymbol{x}_1 = [1, 0, 0]^t$ and, in the case $\|\overrightarrow{\boldsymbol{n}} \times \boldsymbol{x}_1\|_2 = 0$, one automatically get $\boldsymbol{R}_s = \mathbb{I}$.

In two dimensions, where we necessarily have $\boldsymbol{k} = [0, 0, 1]^t$, one can deduce:

$$\boldsymbol{R}_s = \begin{pmatrix} n_1 & -n_2 \\ n_2 & n_1 \end{pmatrix}, \qquad \boldsymbol{A}_s = \begin{pmatrix} -1 & 0 \\ 0 & 1 \end{pmatrix}, \qquad \boldsymbol{T}_s = \begin{pmatrix} n_2^2 - n_1^2 & 2n_1 n_2 \\ 2n_1 n_2 & n_2^2 - n_1^2 \end{pmatrix}. \tag{7.10}$$

7.3.1.2 Symmetric state of a tensor

Starting from the symmetric transformation matrix $\boldsymbol{T}_s$, it is possible to extend the transformation of a vector to high order tensor thanks to tensor algebra (Garrigues 2016; Michal 1947). For the symmetric $\boldsymbol{S}_s$ of a tensor of second order $\boldsymbol{S}$, one can find the usual relation:

$$\boldsymbol{S}_s = \boldsymbol{T}_s \boldsymbol{S} \boldsymbol{T}_s \tag{7.11}$$

Such formula is actually a specific case of a more general relation valid for tensors of an arbitrary high order p (Garrigues 2016). For a tensor tensor $\mathbb{T}$, using the Einstein convention, it yields:

$$\left(\mathbb{T}_s\right)_{i_1 i_2 \ldots i_p} = \left(\boldsymbol{T}_s\right)_{i_1 j_1} \left(\boldsymbol{T}_s\right)_{i_2 j_2} \ldots \left(\boldsymbol{T}_s\right)_{i_p j_p} \left(\mathbb{T}\right)_{j_1 j_2 \ldots j_p} \tag{7.12}$$

In a general manner, the symmetric $\boldsymbol{W}_s$ of a vector of tensors $\boldsymbol{W}$ according to a normal $\overrightarrow{\boldsymbol{n}}$ is denoted $\boldsymbol{W}_s = \boldsymbol{sym}\left(\boldsymbol{W}, \overrightarrow{\boldsymbol{n}}\right)$.

7.3.1.3 Symmetry boundary conditions

In the context of a flux at boundaries computed thanks to a ghost cell, one directly obtain:

$$\breve{\boldsymbol{W}}_{ji} = \boldsymbol{sym}\left(\boldsymbol{W}_i, \overrightarrow{\boldsymbol{n}}_{ij}\right) \tag{7.13}$$

Also, to express the state at the interface, we propose an arithmetic averaging of $\boldsymbol{W}_i$ and $\breve{\boldsymbol{W}}_{ji}$, which ensures the symmetry of the state at the interface. Put under a mathematical form, this leads to:

$$\breve{\boldsymbol{W}}_{ij} = \frac{1}{2}\left[\boldsymbol{W}_i + \boldsymbol{sym}\left(\boldsymbol{W}_i, \overrightarrow{\boldsymbol{n}}_{ij}\right)\right] \Rightarrow \breve{\boldsymbol{W}}_{ij} = \boldsymbol{sym}\left(\breve{\boldsymbol{W}}_{ij}, \overrightarrow{\boldsymbol{n}}_{ij}\right) \tag{7.14}$$

Remark 7.3. *We remind the reader that even using the ghost cell, the expression of the value at the interface remains useful for the multislope reconstruction. In such a context, both values $\breve{\boldsymbol{W}}_{ji}$ and $\breve{\boldsymbol{W}}_{ij}$ are needed for the simulation.*

Remark 7.4. *For each scalar value, one obtain $\breve{w}_{ji} = \boldsymbol{sym}\left(w_i, \overrightarrow{\boldsymbol{n}}_{ij}\right) = w_i$, which is equivalent to a null gradient on the considered variables.*

7.3.2 Wall boundary conditions

The walls are a particular kind of boundary conditions that are associated with a null normal velocity and thus that do not allow material flux. Using symmetry conditions as proposed here above, one can also obtain a null material flux because of the orientation of the convection velocity at the interface. We thus define the tangential velocity $\breve{\boldsymbol{u}}_{ij}^t$ at the interface from a velocity $\boldsymbol{u}_i$ from the equation (7.14) as:

$$\breve{\boldsymbol{u}}_{ij}^t = \frac{1}{2}\left[\boldsymbol{u}_i + \boldsymbol{sym}\left(\boldsymbol{u}_i, \overrightarrow{\boldsymbol{n}}_{ij}\right)\right] = \boldsymbol{u}_i - \left(\boldsymbol{u}_i \cdot \overrightarrow{\boldsymbol{n}}_{ij}\right)\overrightarrow{\boldsymbol{n}}_{ij} \tag{7.15}$$

Also, in the system of equations to be solved, several waves are generally associated with the normal velocity that is necessarily null and the information corresponding to these waves remains at the interface. The reconstructed values can thus be either determined from a Dirichlet or von Neumann boundary condition. While the null normal velocity remain the value imposed by the outside of the domain, the values from the inside remain to be stated.

7.3.2.1 Walls for Pressureless Gas Dynamic

In the case of PGD, a null normal velocity is imposed and, as a consequence, of a null flux is deduced. Considering a null gradient on the density and other transported scalars, this boundary condition is strictly equivalent to a symmetry.

7.3.2.2 Slip walls for the AG closure

For the treatment of the AG closure, two assumptions are considered here:

- The droplets can bounce on the wall (elastic collision), in which case a velocity dispersion *can* be generated in the vicinity of the wall,
- The droplets stick at the wall (non-elastic collisions), in which case *no* velocity dispersion *can* appear in the vicinity of the wall,

The first option can be obtained considering a symmetry and thus leads to:

$$\left\{\begin{array}{ll} \breve{\boldsymbol{V}}_{ji} & = \left[\rho_i, \boldsymbol{sym}\left(\boldsymbol{u}_i, \overrightarrow{\boldsymbol{n}}_{ij}\right), \boldsymbol{sym}\left(\mathbb{E}_i, \overrightarrow{\boldsymbol{n}}_{ij}\right)\right]^t \\ \breve{\boldsymbol{V}}_{ij} & = \left[\rho_i, \breve{\boldsymbol{u}}_{ij}^t, \frac{1}{2}\left[\mathbb{E}_i + \boldsymbol{sym}\left(\mathbb{E}_i, \overrightarrow{\boldsymbol{n}}_{ij}\right)\right]\right]^t \end{array}\right. \tag{7.16}$$

In this context, the term $\frac{1}{2}\left[\mathbb{E}_i + \boldsymbol{sym}\left(\mathbb{E}_i, \overrightarrow{\boldsymbol{n}}_{ij}\right)\right]$ produces a transfer of macroscopic kinetic energy $\frac{1}{2}\boldsymbol{u}\otimes\boldsymbol{u}$ to microscopic kinetic energy $\frac{1}{2}\boldsymbol{\Sigma}$. To avoid such transfer and be coherent with the second assumption, we propose to consider a symmetrization of $\boldsymbol{\Sigma}$ instead of $\mathbb{E}$ and thus a

boundary condition defined by:

$$\begin{cases} \breve{\boldsymbol{V}}_{ji} &= \left[\rho_i, \boldsymbol{sym}\left(\boldsymbol{u}_i, \overrightarrow{\boldsymbol{n}}_{ij}\right), \boldsymbol{sym}\left(\boldsymbol{\Sigma}_i, \overrightarrow{\boldsymbol{n}}_{ij}\right)\right]^t \\ \breve{\boldsymbol{V}}_{ij} &= \left[\rho_i, \breve{\boldsymbol{u}}_{ij}^t, \frac{1}{2}\left[\boldsymbol{\Sigma}_i + \boldsymbol{sym}\left(\boldsymbol{\Sigma}_i, \overrightarrow{\boldsymbol{n}}_{ij}\right)\right]\right]^t \end{cases} \tag{7.17}$$

The difference between (7.16) and (7.17) can only be observed by computing the flux thanks to $\breve{\boldsymbol{V}}_{ij}$ through (7.5). Since $\breve{\boldsymbol{V}}_{ji}$ in (7.16) and (7.17) lead to the same conservative vector $\breve{\boldsymbol{W}}_{ji}$, the use of a Riemann solver through (7.6) would lead to the same result. One can investigate another solutions for wall boundary conditions for the AG, but, considering the aimed applications and the modeling of disperse flow, we believe that these are sufficient for the work presented.

7.3.2.3 Walls for the carrier phase equations

In the case of the equations of the carrier phase for wall conditions, Section 7.1.2 a value needs to be imposed from the inside of the domain. Usually, a null gradient in pressure is privileged to determine it and this is what we propose here. Such assumption can however be replaced be other more accurate estimation of the pressure at the boundary (Hirsch 1990).

7.3.2.3.1 Slip wall for Euler equations In the case of slip wall, the value associated with the ghost cell is determined by symmetry (7.13). However considering the null gradient in pressure, (7.14) cannot be used since it would lead to a constant total energy $\rho_g E = \frac{1}{2}\rho_g \boldsymbol{u}_g \cdot \boldsymbol{u}_g + (\gamma - 1)P$ and thus an increase of the pressure at the interface since $\|\breve{\boldsymbol{u}}_{g,ij}^t\|_2 \leq \|\boldsymbol{u}_{g,ij}\|_2$. Therefore, determining the state at the interface through *primitive* variables, we obtain:

$$\breve{\boldsymbol{V}}_{ij} = \left[\rho, \breve{\boldsymbol{u}_{g,ij}}^t, P_i\right]^t \tag{7.18}$$

Also, it shall be remarked that since there is no material flux through convection, the density ρ only has to be set real and positive if $\breve{\boldsymbol{V}}_{ij}$ is used to compute the convective flux through (7.5).

7.3.2.3.2 No-slip wall for Navier-Stokes equations Because of the viscosity of the fluid, the velocity at the interface have to be null. Therefore, in the ghost cell, the velocity shall be the opposite of the one inside the bordering cell. As a consequence, this gives:

$$\begin{cases} \breve{\boldsymbol{V}}_{ji} &= [\rho_i, -\boldsymbol{u}_{g,i}, P_i]^t \\ \breve{\boldsymbol{V}}_{ij} &= \left[\rho, \overrightarrow{\boldsymbol{0}}, P_i\right]^t \end{cases} \tag{7.19}$$

Looking at the convective terms, the effects of this additional assumption is only marginal compared to slip wall and is only visible using the ghost cell through (7.6). However, since viscosity has to be considered in the treatment of Navier-Stokes equation, this new hypothesis impacts the stress tensor at the boundary since gradients are evaluated between $\boldsymbol{W}_i$ and $\breve{\boldsymbol{W}}_{ij}$.

7.3.2.3.3 Adiabatic and isothermal walls Taking into account heat transfers inside the fluid, a temperature or thermal flux shall be considered at the interface. To do so, it is proposed to attribute a temperature at the wall either by imposing $T_{g,wall}$ at the interface (isothermal wall) or a null gradient (adiabatic wall). This can be achieved by imposing the density ρ of (7.18) or (7.19) such that:

$$\begin{cases} \rho = \frac{P_i}{r_g T_{g,wall}} & \text{for isothermal walls} \\ \rho = \frac{P_i}{r_g T_{g,i}} & \text{for adiabatic walls} \end{cases} \tag{7.20}$$

This modification only impacts the diffusive flux and, as already discussed, the convective flux is not modified by this transformation.

7.3.3 Fluid boundaries

Unlike walls, the fluid boundary conditions allows material flux across the limits of the computational domain. These can be divided in two categories, the supersonic conditions, where all the characteristics come inside or flow outside the domain, and subsonic conditions where both incoming and outgoing characteristics shall be considered.

7.3.3.1 Supersonic inlet/outlet

In the case of supersonic inlet, every values shall be imposed at the boundary, ensuring a supersonic incoming state $\boldsymbol{W}_{\text{inlet}}$ such that $\breve{\boldsymbol{W}}_{ji} = \breve{\boldsymbol{W}}_{ij} = \boldsymbol{W}_{\text{inlet}}$. To deduce $\boldsymbol{W}_{\text{inlet}}$, the mass flow rate, velocity and pressures are generally imposed at the boundary in the case of the Euler equations.

In the case of supersonic outlet, one can simply assume a null gradient, which leads to $\breve{\boldsymbol{W}}_{ji} = \breve{\boldsymbol{W}}_{ij} = \boldsymbol{W}_i$. Extrapolation from the interior of the domain (constant gradient) can be also considered, but the realizability of the boundary values $\breve{\boldsymbol{W}}_{ji}$ and $\breve{\boldsymbol{W}}_{ij}$ have to be ensured.

Remark 7.5. *In the case of PGD, the inlet and outlet are necessarily supersonic.*

7.3.3.2 Subsonic inlet/outlet

For subsonic boundaries, in- and outgoing informations has to be considered as well as the possibility of a material flow through the surface. We thus divide this class of boundaries into

Table 7.1: *Boundary state $\breve{\boldsymbol{W}}_{ij}$ for the Euler equation for free boundaries depending on the regime where $u_n = \boldsymbol{u}_{g,i} \cdot \overrightarrow{\boldsymbol{n}}_{ij}$ is the normal velocity and c is the acoustic velocity*

Regime	$\boldsymbol{u}_g$	T_g	P
$c < u_n$	$\boldsymbol{u}_{g,inj}$	$T_{g,inj}$	P_{inj}
$0 < u_n < c$	$\boldsymbol{u}_{g,i}$	$T_{g,inj}$	P_{inj}
$-c < u_n < 0$	$\boldsymbol{u}_{g,i}$	$T_{g,i}$	P_{inj}
$u_n < -c$	$\boldsymbol{u}_{g,i}$	$T_{g,i}$	P_i

two, the injections, where this material flow is strongly imposed, and free boundaries, where this mass flow rate is let undetermined.

7.3.3.2.1 Injection boundary In the case of injection for the Euler equations, there are two incoming and one outgoing characteristics. Determining this last one thanks to a null pressure gradient, the density is deduced through the temperature of injection, typically obtained from the grain combustion properties and the equation of state in the case of SRM simulation. The remaining characteristic, associated with the velocity, is directly deduced from the mass flow rate (homogeneous to momentum) and usually oriented normal to the injection surface. Such considerations lead to:

$$\breve{\boldsymbol{V}}_{ij} = \breve{\boldsymbol{V}}_{ji} = \left[T_{g,inj}, \dot{m}_{inj} \overrightarrow{\boldsymbol{n}}_{ij}, P_i\right]^t \tag{7.21}$$

Since at subsonic speed, the mass flux can be influenced by the Riemann solver, direct computation of the flux through (7.5) is to be privileged in that case. Also, complex injection laws related to solid propulsion can be considered (see Section 1.1.3.2 and (Lupoglazoff and Vuillot 1999) for example) without loss of genericity.

In the case of the disperse phase, it is useful to define the flux through the particle to gas mass ratio κ and assume a dynamical and thermal equilibrium with the gas at the injection, which leads to:

$$\breve{\boldsymbol{W}}_{ij} = \breve{\boldsymbol{W}}_{ji} = \left[\rho_l, \kappa\, \dot{m}_{inj}, \rho_l C_{p,l} T_{g,i}\right]^t, \qquad \rho_l = \frac{\kappa\, \dot{m}_{inj}}{\boldsymbol{u}_g \cdot \overrightarrow{\boldsymbol{n}}_{ij}} \tag{7.22}$$

Otherwise, since the mass flow rate, velocity and temperature have to be imposed and thus such injection condition is equivalent to a supersonic inlet. For the AG equations, the velocity dispersion is always assumed null at the injection in this work and the same assumptions are retained. In the future, it should be possible to evaluate the velocity dispersion from experiment and integrate this information in the boundary condition.

7.3.3.2.2 Free boundaries We refer as free boundaries, inlets and outlets where the material flow is not imposed. Typically, for the Euler equations, this can be achieved by imposing a constant pressure at the boundary and/or a null velocity gradient. However, such hypothesis is only valid for subsonic outlet cases. Directly computing the flux through (7.5), one thus need to take into account all the flow regimes as proposed Table 7.1.

Using a Riemann solver however, thanks to the formalism (7.6) with $\breve{\boldsymbol{V}}_{ji} = [\boldsymbol{u}_{g,i}, T_{g,inj}, P_{inj}]^t$,

it is possible to deal with all the regimes, put aside the supersonic inlet condition which would require to impose the inlet velocity. Thanks to this methodology, computing the flux at the boundary, the differences between flow regimes are intrinsically detected from the Riemann solver ensuring the transition between subsonic and supersonic outflow. Such methods to treat the boundaries are especially useful at initialization to treat the transition between an initial flow at rest toward a chocked nozzle just by applying a sufficiently low pressure at the exit. Other kinds of free boundary conditions can be investigated as non-reflecting boundary condition (see (Poinsot and Lele 1992)) for example but are not investigated further in this contribution.

Using the AG closure at an outlet, the same process is used relying on a null velocity dispersion in the ghost cell. The reconstruction at the boundary is obtained through a standard null gradient on all variables $\breve{\boldsymbol{W}}_{ij} = \boldsymbol{W}_i$, but has an impact on the multislope reconstruction only.

7.4 Axis of symmetry

Compared to classical planar configurations, the treatment of the boundary conditions does not differ fundamentally in axisymmetry cases. The numerical flux is only applied on the axisymmetric surface instead of the planar one. However, as explained in this section, such an approach is unable to fully render the expected physics on the symmetry axis.

Unlike any other boundary conditions, the cells bordering the symmetry axis are interacting with themselves through this boundary. Since $|S_{ij}|_r = 0$ on the symmetry axis, the contribution of this edge of the cell should be considered as null for any real numerical flux. However such an approach prevents from the resolution of the self-interacting process through the axis, which would assumes a singular value of the flux $\breve{\mathfrak{F}}_{ij}$ at the boundary of the domain.

The procedure designed aim at evaluating a control volume around the symmetry axis, where the solution is modified according to the boundary condition. Such formalism bypass the need of the surface $|S_{ij}|_r$, that is null at the symmetry, to compute the net flux from the symmetry axis. From another perspective, this corresponds to the application of the HLL scheme, dedicated for axisymmetric configuration as in Section 6.3.3.3, using the the *virtual volume formalism* on the symmetry condition where the HLL state is modified to be compatible with the isotropic subset (3.88).

Thus, starting from the standard expression of the scheme (6.144) in the axisymmetric framework and substituting the flux by the HLL expression taken from the integrand (6.154), the scheme can be rewritten as:

$$\begin{aligned}\boldsymbol{W}_i^{n+1} = \boldsymbol{W}_i^n + \frac{|C_i|_0}{|C_i|_r}\boldsymbol{\mathcal{S}}_i^{axi,n} \\ - \sum_{j\in\nu_i} \frac{\left|\check{C}_{ij,l}\right|_r}{|C_i|_r}\left[\boldsymbol{W}_{ij,l} - \boldsymbol{W}_{ij,HLL} + \Delta t \frac{\left|\check{S}_{ij}\right|_r}{\left|\check{C}_{ij,l}\right|_r}\boldsymbol{\mathcal{F}}(\boldsymbol{W}_{ij,l})\cdot\vec{\boldsymbol{n}}_{ij} - \Delta t \frac{\left|\check{C}_{ij,l}\right|_0}{\left|\check{C}_{ij,l}\right|_r}\boldsymbol{F}_r(\boldsymbol{W}_{ij,l})\right],\end{aligned} \tag{7.23}$$

where the scheme behavior is now driven by the expression of the HLL states $\boldsymbol{W}_{ij,HLL}$ and the virtual geometry.

If the HLL state is taken everywhere from (6.150), the scheme (7.23) is strictly equivalent to (6.42) with the flux (6.160). On the symmetry axis, the conservation law (6.150) providing $\boldsymbol{W}_{HLL}$, has a null right signal velocity to provide a coherent definition at the virtual volume on which is based the relation (6.150), since the solution is not defined for negative r coordinates. In such context, using $\left|\check{C}_{ij}\right|_r = \left|\check{C}_{ij,l}\right|_r = \left|\check{S}_{ij}\right|_0 \frac{(\lambda_l \Delta t)^2}{2}$, $\left|\check{C}_{ij,r}\right|_r = \left|\check{C}_{ij,r}\right|_0 = 0$, $\left|\check{C}_{ij,l}\right|_0 = \left|\check{C}_{ij}\right|_0 = -\left|S_{ij}\right|_0 \lambda_l \Delta t$ and $\left|\check{S}_{ij,r}\right|_r = 0$, (6.150) leads to:

$$\boldsymbol{W}_{HLL} = \boldsymbol{W}_l + 2\frac{\boldsymbol{F}_r(\boldsymbol{W}_l)}{\lambda_l} \tag{7.24}$$

It shall be observed at this point that, according to the Theorem 3.1, the $\boldsymbol{W}_{HLL}$ state has to be compatible with the isotropic subset of states admissible on the symmetry axis. Respecting both conservation (7.24) and compatibility theorem 3.1 lead to an overdetermined system of equations defining $\boldsymbol{W}_{HLL}$.

Taking into account the interaction of the cell with itself through the axis of symmetry, it can be observed that all the conservation laws in the axisymmetric framework do not have to be strictly respected. As a matter of fact, moments with a odd number of r component, such as the r momentum, are naturally null in the Euclidean space if the axisymmtric plan is integrated between 0 and 2π in the θ direction. Any transformation of these components thus respect the conservation laws according to the Euclidean space.

Focusing on the AG closure, $\boldsymbol{W}_{HLL}$ is defined by the parameters $(\rho, u_z, e_{zz}, \sigma_0) \in \mathbb{R}^4$, since it belongs to the isotropic subset (3.88). Density ρ, axial momentum ρu_z and axial energy ρe_{zz} are simply obtained through (7.24) since they are conserved quantities in the Euclidean space. In the case of σ_0, we aim at conserving the kinetic energy in the radial direction and thus the quantity $(\boldsymbol{W}_l)_{rr} + (\boldsymbol{W}_l)_{\theta\theta}$. Introducing this new constraint, (7.24) leads to:

$$(\boldsymbol{W}_{HLL})_{rr} = (\boldsymbol{W}_{HLL})_{\theta\theta} = \frac{1}{2}\left[(\boldsymbol{W}_l)_{rr} + (\boldsymbol{W}_l)_{\theta\theta}\right] - \frac{1}{2S_l}\left[(\boldsymbol{F}_r(\boldsymbol{W}_l))_{rr} + (\boldsymbol{F}_r(\boldsymbol{W}_l))_{\theta\theta}\right] \tag{7.25}$$

The remaining components of the conservative vector are set null by consistency with the isotropic subset (3.88).

Remark 7.6. *One can remark that for any $\boldsymbol{W}_l$ belonging to the isotropic subset, the contribution to the update of the transformation at the symmetry axis following (7.23) is null. Therefore, since for a uniform steady state is consistent with the isotropic subset, the Proposition 6.3 remain valid.*

Remark 7.7. *Even if every θ component of $\boldsymbol{W}$ can be initially null, the procedure presented is able to generate an azimuthal pressure $P_{\theta\theta}$. Therefore this process, generating an azimuthal velocity dispersion is not compatible with the azimuthal velocity degeneracy assumption leading*

to the system (3.72).

Part III

Eulerian simulation of polydisperse spray

Chapter 8

CFD code description

> A computer lets you make more mistakes faster than any invention in human history — with the possible exceptions of handguns and tequila.
>
> Mitch Ratliffe, Technology Review, April, 1992

In this chapter, it is proposed to present the CFD codes used for the needs of this work. These tools integrate the numerical strategies designed through the developments of that thesis. For the test cases evaluating the schemes in the context of solid rocket propulsion, we rely on two distinct CFD codes, CEDRE and SIERRA. While the first is a semi-industrial CFD code with many abilities, but also many constraints for the programming, the second is a more flexible in-house code used for the new developments. Moreover, in that process, SIERRA is a benchmark for new strategies and help for the CEDRE development.

Therefore, this chapter is split into two parts. First, Section 8.1 presents the CEDRE code of ONERA which is the ultimate goal of this work and has influenced the theoretical development conducted in that work. Today, elements developed in this thesis has been implemented in an experimental way and work is continuing to complete these features. Second, Section 8.2 discusses on the integration of the new schemes and models in the in-house code SIERRA, that is used for the developments of the new features introduced during the thesis and that possesses a more flexible architecture. The old structure of this code has been completely rewritten for the need of the presented developments.

8.1 CEDRE

8.1.1 A brief history

Standing for the french Calcul d'Ecoulements (Diphasiques) (Réactifs) pour l'Energétique, the CEDRE code (Refloch et al. 2011) is a multi-physics platform designed for CFD computations on general unstructured meshes that intends to solve both advance research problems and treat industrial applications in the fields of energetics. The applications targeted by the software are mostly related to propulsion that is the main problematic in the scope of the Multi-Physics for Energetics Department (DMPE) at ONERA and includes jet engines, ramjets, jet noise, atmospheric pollutants, but also LRE and SRMs for missiles and launchers, as for this thesis. Therefore, computation abilities shall cover fields of aerodynamics, combustion, conduction/convection and radiative heat transfer, water ingestion, icing and aeroacoustics. Therefore, CEDRE is able to solve multicomponent gaseous flow, two-phase flows but also integrate model and methods for thin liquid layer, heat conduction in solid and radiative heat transfer. It is not unusual to encounter singularity and stiff phenomena as shocks, flame front, phase transition layer, very low density area and strong coupling of several of these phenomena, which justify robust numerics.

Until the begin of the last decade, there existed at ONERA several CFD codes dedicated to each applications and each detained its own set of numerical methods and specific features. It has thus been decided in 2001 to combine the efforts of the different teams to create a common adaptive CFD platform to a wide variety of applications targeted for energetics. Today, CEDRE still have its own development team and gather the work of many PhD student (see (Haider 2009; Doisneau 2013; Sibra 2015; Le Touze 2015; Binauld 2018) among others) with the objective to continually improve the models, numerical methods and High Performance Computing (HPC) abilities of the software.

The differences between such CFD code for energetics and usual codes designed for aerodynamics applications rely in the numerical methods and the variety of models encountered. For that second problematic, the accurate resolution of the Navier-Stokes equations is to be privileged, often knowing that singularities are unlikely to appear. Therefore, such class of code generally detain very high order schemes and accurate RANS and LES models. For the CFD codes designed for energetics however, the order of accuracy is mostly limited by the singularities produced by the models and shall avoid spurious effects from the numerics. As a consequence, the CEDRE software detains the characteristics wished by its applications and that are the followings:

- **Robustness**, to be able to cope with the stiffness of the system of equations related to energetic applications,
- **Accuracy**, to provide reliable results even on coarse discretization,
- **Versatility**, to treat the large diversity of problematic associated with propulsion,
- **Efficiency**, to solve large cases as encountered in the industry.

8.1.2 Code organization and abilities

8.1.2.1 Solvers organization

To cope with all these models, the code is divided into solvers that are all dedicated to the resolution of a physics and that detain the adequate numerical methods to solve the problem, able to be coupled one to another. The solvers are the followings:

CHARME : Multi-species Navier-Stokes solver, including turbulent and combustion models,

SPIREE : Eulerian multi-fluid solver for disperse phases,

SPARTE : Lagrangian solver for disperse phases,

ACACIA : Solver managing conduction thermal transfer in solids,

ASTRE : Radiative heat transfer solver based on Monte-Carlo methods,

REA : Radiative heat transfer solver based on the discrete ordinate method,

FILM : Thin liquid layer solver based on Shallow-water equations,

PEUL : Stochastic Lagrangian solver for turbulent combustion and complex chemistry.

For the applications aimed and numerical strategy retained, we focus our attention on the CHARME and SPIREE solvers that share together, despite being implemented independently, Eulerian methods.

8.1.2.2 CHARME

With the objective to solve the flow inside combustion chambers, air intakes of turbine engines, scramjets and rockets among others, the solver have to be able to take into account a wide range of compressible effects including shocks and dilatations caused by combustion. In addition to these classical features contained in the Navier-Stokes equation, CHARME possesses advanced thermodynamics models to take into account the variation of the fluid properties such as viscosity, thermal capacities and consider real gas Equation Of State in addition to the reactive flow modeling inherent to the applications aimed. Also, to complete that fine description of the physic, specific modeling for combustion and turbulence (including RANS,LES and Zonal-Detached-Eddy simulation (ZDES)) have been implemented.

As a consequence, the numerical methods introduced in CEDRE have first to be designed to cope with singularities and the stiffness of the model. Moreover, for the needs of aeroacoustic simulation such as for jet noise, the accuracy of the scheme is a key issue. Therefore, since the early days of the code, CHARME is based on MUSCL schemes and today aims at high order FV schemes (Haider 2009; Haider et al. 2014). Among the numerical methods contained in CHARME, we sum up here those used in this work:

- Monoslope and multislope MUSCL methods,
- High order FV methods,
- Implicit and explicit high order RK time integrations,
- HLL class of solvers including an HLLC solver with low-Mach corrections,

It is out of the scope of this work to present the wide variety of models available in the solver. The numerical tools associated with these models are initially designed in a general context and only applied here for the needs of solid propulsion. Such ability of gathering works transversally from different origins inside the same software is one of the main strength of the CEDRE code. Despite the tools designed in this manuscript are not specifically created for such model complexity, their extensions to such composition have been anticipated and some of the developments of the thesis have been already implemented with the help of C. Le Touze.

8.1.2.3 SPIREE

The proximity of the system of equations describing the carrier phase and the disperse phase modeled in the Eulerian framework, as presented in Chapter 3, explains the close relationship between the solvers. The numerical methods of the SPIREE solver are originally based on the schemes used in CHARME. However, experience has shown that the original formulation of the monoslope MUSCL scheme (Haider, Croisille, and Courbet 2009) was not robust enough to solve disperse phase equations. This motivated the development of the multislope MUSCL as conducted in (Le Touze 2015). Therefore, the numerical methods of SPIREE are based on the following characteristic.

- Multislope MUSCL methods (Le Touze, Murrone, and Guillard 2015),
- Lie and Strang operator splitting (Doisneau et al. 2014),
- Explicit high order RK time integration and first order implicit time integration,
- Detailed particle/droplet thermodynamics,

Aside that increased need for robustness, the main difference between CHARME and SPIREE lies in the multi-fluid and multi-class formalisms that necessitates several systems of equations to be solved in parallel. Therefore, based on the MK closure several sections or classes can be taken into account as well as phenomena such as evaporation, coalescence and break-up. For several years, this solver has benefited from the work of (Doisneau 2013; Sibra 2015; Le Touze 2015).

Thanks to the recent work from C. Le Touze, the solver has been generalized to be able to take into account new transport models. Based of the work presented here, the solver has thus been extended to new system of equations including the AG system but remains work in progress. As a consequence, the choice of source terms and boundary conditions remains and specific axisymmetric closure are concerned.

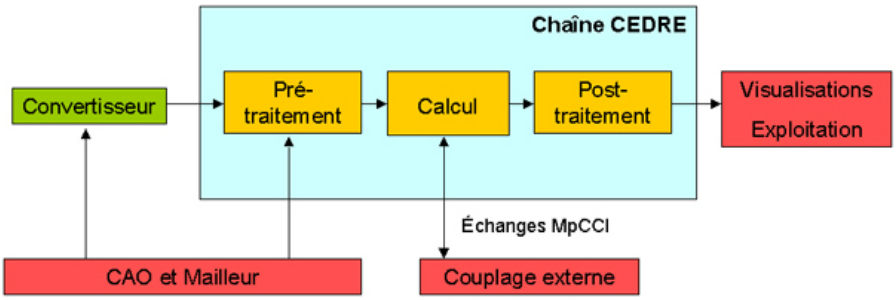

Figure 8.1: *High level structure of the CEDRE platform*

8.1.2.4 Software structure

Aside the solvers that are the core of the code, the CEDRE platform possesses complementary pre- and post-processing abilities thanks to its supplementary programs. Three distinct modules can be noticed:

EPICEA Graphical interface for the simulation set up, including the determination of the physical models, numerical methods and coupling strategy,

EPINETTE Preprocessing module for the conversion and specific treatment of the geometry. It notably includes a small meshing utility and a mesh refinement tool,

EXPLORE Post-processing module for the conversion of the output data to commercial software format.

Finally, it has to be remarked that CEDRE is able to couple with other software using the CWIPI library. Taking into account these elements, the high level software structure takes the form proposed in Figure 8.1. Since Computer-Aided Design (CAD), meshing and data visualization are essentially built thanks to external tools, the CEDRE platform possesses conversion modules. Such specificities and adaptabilities bring the code closer to an industrial platform while keeping the core of the program close to research.

8.1.3 Code efficiency

Aiming for industrial cases, the CEDRE code needs to be able to operate on powerful computers. Since these are today highly parallel, CEDRE thanks to a distributed memory parallelization strategy, based on the Message Passing Interface (MPI) libraries. As presented Figure 8.2, the software can scale above 10 000 CPU cores without significant loss of performances and thus use at most the supercomputers.

Thanks to such performance, it is today possible to reach the resolution of relatively small structures with simulations using more than a billion cells (Fabignon et al. 2016) in the context of solid propulsion (see Figure 8.3). This open the possibilities of a fine analysis of turbulent processes.

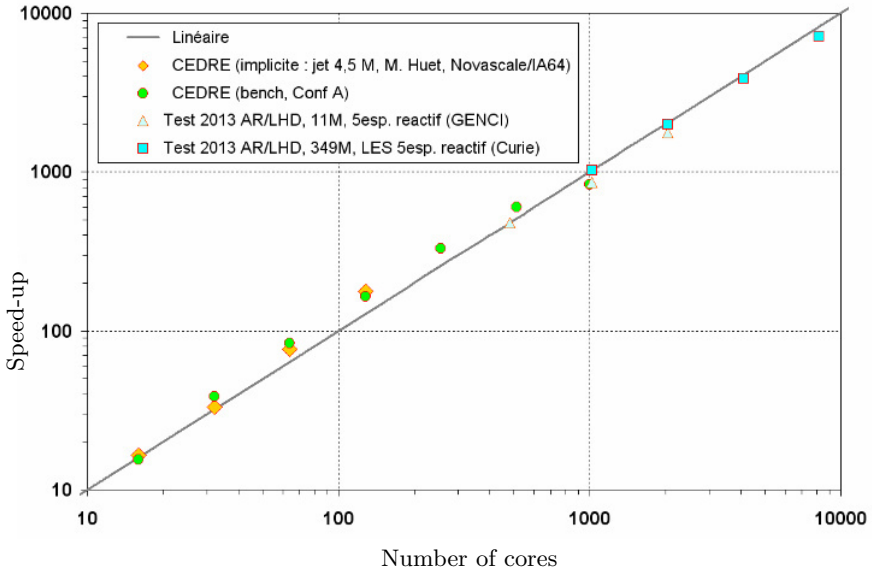

Figure 8.2: *Speed-up of the CEDRE software (Vuillot and Refloch 2014)*

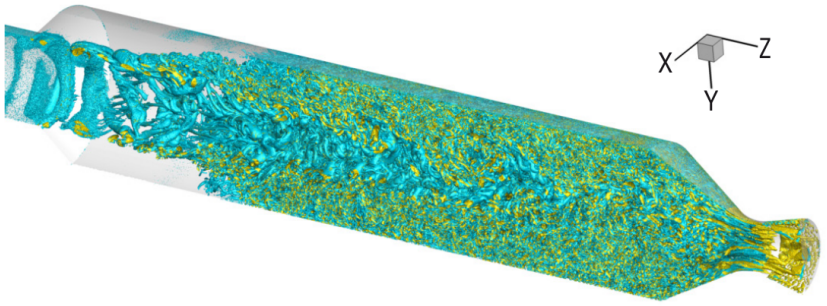

Figure 8.3: *Isosurfaces of Q criterion snapshot of the C1xb using one billion cells (Fabignon et al. 2016)*

8.2 SIERRA

Introducing a new system of equations in a CFD code can be a tedious operation in industrial softwares that requires deep changes if the code has not been design to take into account various systems of equation. As a consequence, instead of aiming directly at an integration of the developments conducted during the thesis in CEDRE, it has been chosen to first integrate the developments in an intermediary in-house CFD code, named SIERRA. Thanks to that strategy, the integration of the AG in CEDRE could have been catalyzed while it is possible to use SIERRA to validate these developments.

8.2.1 A brief history

Standing for the french Simulation Instationnaire d'Ecoulements et Régimes Réputés Acoustiques, SIERRA is a research code designed and used during the 90's for the problematics of internal flows of SRM. With roots that can be tracked down until the mid-80's, SIERRA has been originally designed to solve compressible flows thanks to a MacCormack scheme (MacCormack 1969) on 2D structured deformed grid with planar or axisymmetric referential. Until the mid-90's, the work on the code has been essentially oriented to increase the quality ofthe compressible solver. Therefore, in parallel, the MacCormack scheme and the fluid models have been improved over the time. From a initial FD formulation, the implementation of the MacCormack scheme has been changed for a FV formulation to take properly into account structured deformed mesh and Artificial Viscosity (AV) has been added to damp spurious effects. Additionally, the original Euler solver has been extended to solve the Navier-Stokes equations and include a Smagorinsky (Smagorinsky 1963) LES model. Finally, to conduct simulations on complex SRM and more specifically for the ones with thermal protections as the P230, the code has been extended to take into account block structured meshes (see Section 6.2.1), which are a composition of structured meshes binded one to another.

Under that form, research teams of ONERA studied many steady and unsteady SRM cases (Lupoglazoff and Vuillot 1992a, 1993, 1996, 1998, 1999; Vuillot 1995; Vuillot et al. 1997). Low numerical dissipation and high arithmetical efficiency were the two main qualities of the code.

During the work of Dupays (Dupays 1996), the code has been extended to two-phase flow thanks to the introduction of a disperse flows new dedicated solver based on MacCormack scheme with specific AV and coupled to the gaseous solver thanks to operator splittings. The equations solved for the disperse phase were based on a MK closure associated with a multi-class size polydispersion. Thanks to that new solver, it has been possible to investigate new unsteady SRM cases.

SIERRA was used for the last time at the beginning of the 2000's before the emergence of CEDRE. At that time, the code reached some limits because of its old program architecture based on FORTRAN 77 standard and output hardware dependent files requiring tedious human intervention for post-treatment, while commercial softwares for that purpose were appearing. As a consequence, the code was put aside in favor of more advanced and all purpose in-house softwares that were the ancestors of CEDRE.

8.2.2 SIERRA evolution

The work conducted in SIERRA aimed at two main objectives: implement new systems of equations based on the AG closures and integrate the new Godunov classes of methods investigated through the thesis. However, the consequences of such changes in this code need to be observed from another point of view based on the code structure itself.

The FORTRAN 77 code was written in a single 16 000 line file. It has been first chosen to update the old fixed FORTRAN norm of the code (FORTRAN 77 and before) to free FORTRAN (FORTRAN 90 and later). Thanks to that change of norm, it has been possible to organize the code in several modules, separated in different files and introduce a CMake script for the ease of compilation. During these deep modifications, it has been possible to improve the arithmetical precision but also introduce dynamic memory allocation avoiding specific compilation for each simulation case. Associated to new internal data structures, some object oriented features of the FORTRAN 2003 norm have been included. These actions, summed up in Table 8.1, also take into account the modifications of the input and output files that were under a dedicated formatted form. The new file structures, based on the HDF5 library on the one hand and Tecplot formatted files on the other hand, allow the visualization and analysis of the output data thanks to commercial and free softwares. Because of the new features introduced and the comments added, the size of the new code exceed 67 000 lines.

The original code was fully organized around the MacCormack scheme and its predictor/corrector procedure. The gas solver used that scheme with AV and was fully optimize in the context of the Navier-Stokes equation. For the disperse phase however, since the disperse phase solver implemented by Dupays (Dupays 1996) was based on another code provided by IUSTI (Daniel et al. 1993, 1994), there is a second MacCormack scheme strictly separated from the first one. The time of that integration, the software has been specifically adapted to modify the least the Navier-Stokes solver by coupling this new part through either a Lie or a Strang splitting. However, the solver associated with the transport of gas, to the transport of droplets and to the sources terms were not completely independent. It has been chosen in the new architecture to create the possibility to call all these operators independently thanks to knew features associated with free FORTRAN. Such as, the operator splitting methods becomes simply integrated in an overlay above calling the operators successively and new solvers could have been implemented based on the object oriented formalism available from the FORTRAN 2003 norm.

8.2.3 New model and numerical methods

Once the new code well structured, it has been possible to implement the new numerical methods. For the disperse phase solver, the main difficulties were to implement the scheme in a sufficiently generic manner to take into account new system of equations including the two-dimensional AG closure (homogeneous with the AGd system in axisymmetry) and the AX closure specifically for the axisymmetric cases. These new evolutions has been conducted maintaining all the previous abilities of the code. However, the block structured formalism, while still operative for the MacCormack scheme, has not been extended to the MUSCL multislope scheme.

Aside the numerical scheme, boundary conditions were adapted to the MacCormack scheme

Table 8.1: *SIERRA code structure modifications*

Ability	Old architecture	New architecture
FORTRAN norm	• FORTRAN 77	• Free-FORTRAN • FORTRAN 2003 and 2008 norm features
Compilation	• MakeFile	• CMake scripts
Real precision	• Single	• Double
Memory allocation	• Large fixed size arrays	• Dynamic allocation
Parameter input	• Dedicated formated file	• Dedicated formated file
Mesh input	• Dedicated formated file	• Dedicated formated file, • HDF5 format file,
Fields input	• Dedicated formated file	• Dedicated formated file, • Tecplot formated files, • HDF5 format file,
Sensor output	• Dedicated formated file	• Tecplot formated files
Fields output	• Dedicated formated file	• Tecplot formated files, • HDF5-XDMF format file,

and only took into account boundary conditions as the direct flux from a reconstructed state (see Section 7.2.1). Rewriting the procedures thanks to an object-oriented approach, it has been possible to take into account Riemann solver and thus fit the complete FV formalism described in Chapter 7.

In addition to the modification associated with the code structure, the computation of the geometric variables has been changed to fit the polygon moment formalism described in Section 6.2.4. While the edge and cell surfaces were correctly computed, the positions of the barycenters were only approximated. Originally, such approximation only influenced the computation of the viscous terms since the MacCormack scheme only requires the edge length and the cell surfaces. However, implementing the MUSCL multislope methods, the correct position of the barycenters are essential to provide a second order accuracy. Such modification provided a small improvement of the accuracy and allow the methods to be implemented exactly as in the theory. Added to all the previous features, detailed in Table 8.2, this has lead to a large extension and improvement of the code.

8.2.4 Memory shared parallel implementation

The original code contained outdated vectorization directives dedicated to Cray computer. It has been chosen to drop these directives for a memory shared parallelism strategy based on the OpenMP API. Such methods are not opposed to distributed memory parallelism, using MPI as in CEDRE for example, and can be combined with it. The advantage of this approach, compared to distributed memory parallelism, is to be able to deal with arithmetical unbalancing.

Typically, when vacuum area arise, it is not necessary to compute source terms and fluxes such that computations can be skipped. Therefore, assigning the computation associated with a group of cell to a processor, these can be executed more or less faster depending on the presence of droplets. Using to OpenMP, this can be achieve either using dynamic schedule or task based parallelism and limit the occurrences of processes waiting for the others to end.

This strategy does not however allow to scale above one computation node. The speed-up obtained on SIERRA, using two different clusters and the C1xb case with the AX-TSM model, is presented Figure 8.4. The first computer on which the tests are conducted is *fusion*, the cluster of ENS Paris-Saclay and CentraleSupélec on which each NUMA node composed of 2 Intel Xeon Haswell CPU (E5-2670 v3 at 2.30 GHz) containing 12 computation cores each. The second, *sator*, the cluster of ONERA, is composed of NUMA nodes detaining 2 Intel Intel Xeon Broadwell CPU (E5-2680v4 at 2.40 GHz) with 14 computation cores each. The tests concluded that SIERRA is able to fairly scale with an efficiency of 60% approximately on a whole nodes. Further analysis show that the maximum speed-up mostly depend on the size of the case studied (which here possess only 80 thousands cells) and is essentially caused by memory latency.

As a consequence, the new code SIERRA offers the ability to test many configurations in terms of methods and applications while being able to treat relatively large problems. More than testing academic cases it is proposed in the following chapter to test its efficiency and robustness on applied configurations. In addition, features not yet implemented in CEDRE but already integrated to SIERRA are tested and assessed, which gives an insight of the future abilities of CEDRE for large scale computations.

Table 8.2: *SIERRA numerical method modifications*

Ability	Old architecture	New architecture
Geometry computation	• Exact length and surface, • Approximated barycenters position.	• Exact through polygon moments (see Section 6.2.4).
Carrier phase solvers	• MacCormack scheme with AV.	• MacCormack scheme with AV, • First order Godunov, • MUSCL multislope.
Carried phase solvers	• MacCormack scheme with AV,	• MacCormack scheme with AV, • First order Godunov, • MUSCL multislope.
Source terms solvers	• Explicit SSPRK methods, • Implicit RK method for inert droplets.	• Explicit SSPRK methods, • QKS method for AGTSM.
Splitting	• Gas alone, • Lie and Strang splitting.	• Gas or disperse phase alone, • Lie and Strang splitting.
Boundary conditions	• Flux from reconstructed state	• Flux from reconstructed state, • Flux using Riemann problems, • Specific axisymmetric Boundary condition.

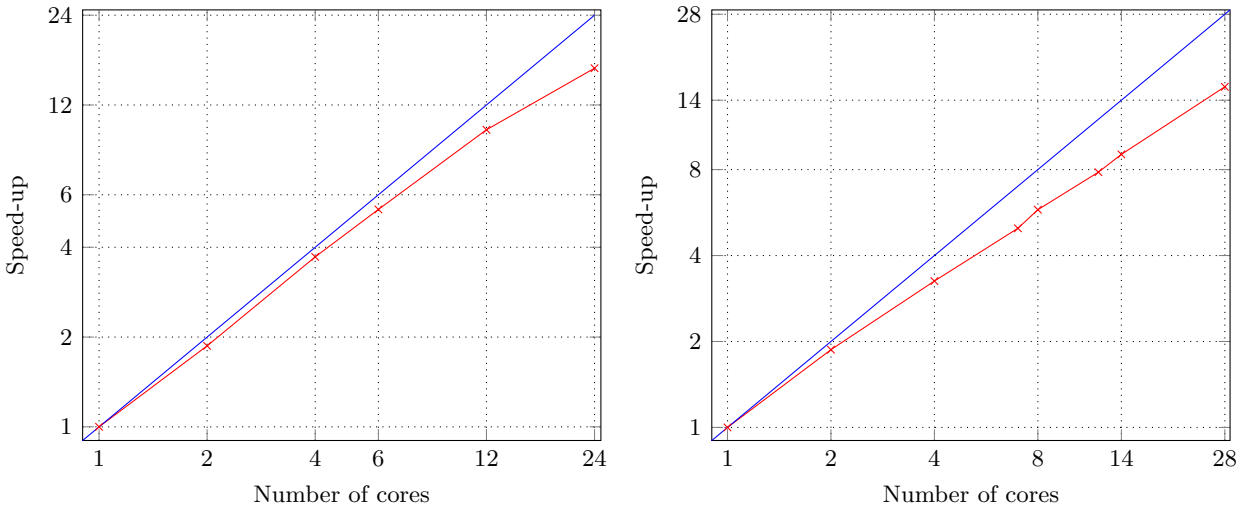

(a) *fusion* **(b)** *sator*

Figure 8.4: *Strong scaling of SIERRA (—×—) compared to ideal scaling (——)*

Chapter 9

Code verification

> Mais, comme un homme qui marche seul et dans les ténèbres, je me résolus d'aller si lentement, et d'user de tant de circonspection en toutes choses que si je n'avançais que fort peu, je me garderais bien, au moins, de tomber.
>
> René Descartes, Discours de la méthode, 1637

> But, as a man walking alone in the darkness, I decided to go so slowly, and use so much circumspection in every things that if I move not much forward, I was preventing myself, at least, to fall.
>
> René Descartes, Discourse on the Method, 1637

This Chapter is the first of a serie of three dedicated to numerical results. We focus on the distinct parts of the implementation in SIERRA related to both disperse and carrier phases. As a consequence, the numerical methods designed in Part II are tested for each operator separately. Tests involving only the transport of the gas, the transport of the particles or the source terms are conducted. This chapter focuses on *code verification*, in other words, the ability of the code and the methods integrated inside to reproduce analytic (or at least expected) solutions. Stability as well as accuracy of the schemes are evaluated. Such work proves the quality of the main tools in which the new features introduced in that work have been implemented. It also provides a basis for the verification of the numerical strategy proposed and its implementation in CEDRE.

The chapter is thus organized as follow: first, in Section 9.1, the implementation of the Euler equations is tested in both planar and axisymmetric frameworks starting from a shock tube test case. Then, in the context of the AG closure, Section 9.2 explores the specific management of the symmetry axis in axisymmetric framework as proposed in Section 7.4. Finally the accuracy

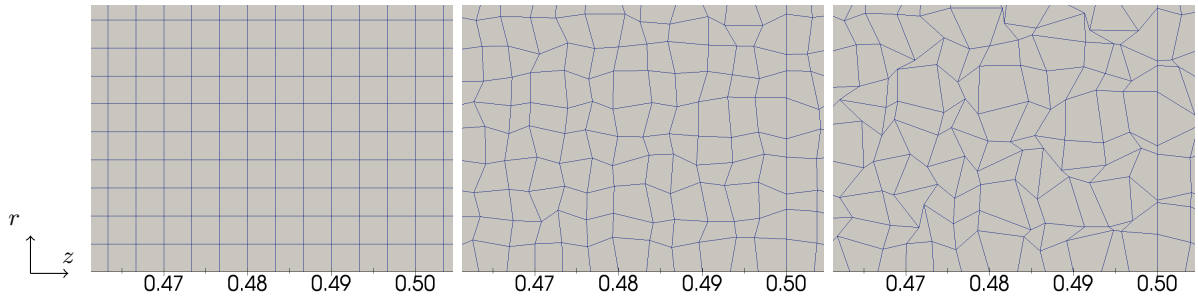

(a) Cartesian **(b)** Moderately distorted **(c)** Higly distorted

Figure 9.1: *Comparison of the distortion through a zoom on the meshes used for the Sod tube test case*

of the QKS implementation is studied in Section 9.3.

9.1 Sod shock tube

9.1.1 Case description

As a classical test case, the Sod tube (Sod 1978) is chosen to demonstrate the reliability of the numerical methods and the quality of the implementation for the Euler equations. Imposing an initial discontinuity, normal to the axial direction, the physical problem is one-dimensional and, as long as no swirl is considered, the physical solution is identical in both axisymmetrical and planar frameworks. In order to assess the strategy, three meshes, as presented Figure 9.1, are chosen: a regular cartesian mesh, a moderately distorted mesh and a highly distorted mesh, which all use 30 cells in the radial directions and 300 cells in the axial directions representing a $100cm \times 10cm$ rectangular slice of a volume. In axisymmetrical framework, the bottom side of the domain corresponds to the axis of symmetry.

Both the Cartesian and the moderately distorted meshes are composed of convex cells. However, that property is not respected by every cells of the highly distorted mesh despite they still fulfill the geometrical requirement needed by the MUSCL multislope method (Le Touze, Murrone, and Guillard 2015) to avoid first order reconstruction degeneracy. Such a mesh, with highly distorted cells, remains studied to assess the robustness of the methods.

The discontinuity is represented in the middle of the described area, at position $0.5m$. In order to solve exactly the same physical problem for each studied grid, cell interface distortions along the physical discontinuity are canceled to strictly represent the discontinuity as it can be observed in the Figure 9.1. The conditions chosen on both side of the discontinuity are given in Table 9.1.

Finally, the choice of slip walls for boundary conditions avoids any disturbance from bottom and top side of the domain to minimize spurious effects from these geometrical limits. The same choice of boundary conditions is used for the left and right side of the domain but, since the problem is stopped at $t = 750\mu s$, before the physical disturbances reach these boundaries, their influence is thus minimized.

Table 9.1: *Conditions for the Sod shock tube*

(a) Initial states

Variable	Right side state	Left side state
Density	$1kg/m^3$	$0.125kg/m^3$
Pressure	$1bar$	$0.1bar$
Velocity	$0m/s$	$0m/s$

(b) Thermodynamic properties

Variable	Value
γ	1.4
r	$287J/kg/K$

Table 9.2: *Numerical method parameters*

(a) MacCormack

Predictor sides	Top and left
AV type	Jameson and Baker[1]
Sensor	Jameson[2] based on pressure
$\tilde{\mu}_2$	0.5
$\tilde{\mu}_4$	0.03

(b) MUSCL

limiter	minmod
Riemann solver	HLLE
Reconstruction variables	ρ,$\boldsymbol{u}$, P

[1] Jameson and Baker, July 1983
[2] Jameson, Schmidt, and Turkel 1981

9.1.2 Code configuration

The tests are conducted using SIERRA in order to compare both the MacCormack scheme with artificial viscosity and the MUSCL multislope scheme for such conditions. For both methods, the parameters are given in Table 9.2. In the context of the MacCormack scheme, in addition to the choice of the predictor side, several parameters have to be manually set to ensure a sufficient level of AV and avoid divergence. While choosing the AV parameters can be a tedious task, the MUSCL scheme only needs the specification of the reconstruction variables, the limiter and the Riemann solver to be completed. Additionally, as discussed in Remark 6.16, when choosing a LED limiter and a realizable Riemann solver, the scheme ensures realizability.

Also, in the context of the Euler equations, neither the axisymmetric Riemann solver (6.160) nor the specific boundary condition at the symmetry axis (see Section 7.4) are used. Instead, a standard Riemann solver as proposed in Cartesian framework is directly applied in the standard formulation (6.53) and no flux is computed on the axis because of the null surface $|S_{ij}|_r$ associated to it. This corresponds to the classical way to treat the axisymmetry in CFD codes (Clain, Rochette, and Touzani 2010; Guardone and Vigevano 2007).

A CFL condition close to 0.45 for stability reasons which represent 0.9 time the stability constraint of the MUSCL scheme. This represents 375 iterations with a $2\mu s$ time step for the cartesian mesh, 750 iterations with a $1\mu s$ time step for the moderately distorted mesh and 3750 iterations with a $0.2\mu s$ time step for the highly distorted mesh. Such a time evolution is kept for both planar and axisymmetrical frameworks.

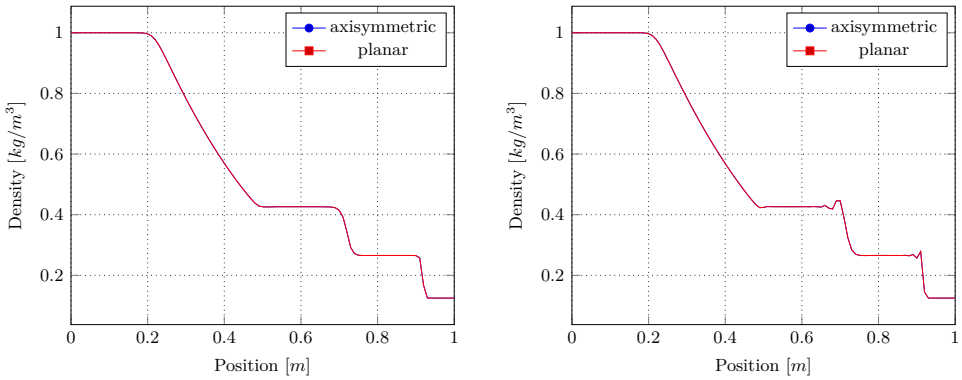

(a) MUSCL **(b)** MacCormack

Figure 9.2: *Density field in the axial direction depending on the scheme for the planar cartesian mesh*

9.1.3 Shock resolution

A classical analysis of the Sod tube in one-dimension consists in plotting the density field in the axial axis as in Figure 9.2 for the Cartesian mesh in 2D planar framework. We observe the LED character of the MUSCL scheme, that does not oscillate, compared to the MacCormack method, which produces wiggles near the discontinuity.

We focus our attention of the leading shock in the multi-dimensional context and more specifically to the disturbance caused by the mesh and the referential. During the simulation time, the leading shock created by the initial discontinuity that propagates through the domain until approximately the position $z = 0.92$. In every cases, Figure 9.3 shows that the shock is resolved in a small number of cells row as expected for a scheme of MUSCL class. For the MacCormack scheme however, while the same quick transition can be seen, disturbances behind the shock can also be observed. Also, this observations remain valid independently on the chosen mesh and referential. The results are slightly more diffused using distorted meshes but this remains fairly acceptable considering the distortion level.

The difference between both the planar and axisymmetrical frameworks cannot be seen through color in Figure 9.3 and Figure 9.4. The same observation can be conducted by plotting the pressure close to the symmetry axis as in Figure 9.5 and Figure 9.6, using linear interpolations because of the various meshes. A closer analysis on the pressures presented on Figure 9.5, for the MUSCL scheme, shows that the relative difference is at the level of the numerical precision for the cartesian mesh, bellow 0.12% for the moderately distorted mesh and bellow 0.49% for the most distorted one. The variations are much more sensitive to the mesh than to the framework for that case. Such difference, despite its small relative magnitude, is much higher for the MacCormack scheme. It can be suggested that the formulation of the AV, not specifically adapted for the axisymmetric framework as the physical viscous stress tensor (see Section 3.3.2.2), is the cause of this difference. Weighted by the surface, themselves weighted by the distance to the symmetry axis, this artificial diffusion is biased and generate a visible difference with the simulation in the Cartesian geometry. Since this radial effect can be significant, we thus focus on the disturbance in the radial direction.

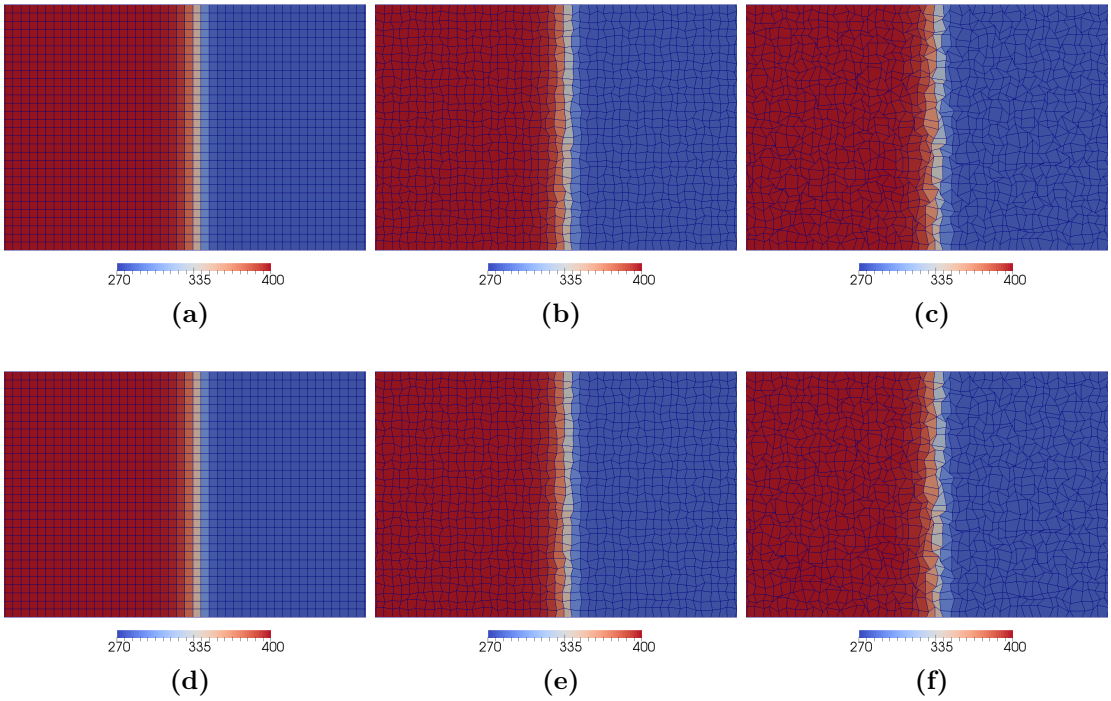

Figure 9.3: *Temperature field across the leading shock depending on the mesh for the MUSCL scheme (from left to right: Cartesian 9.3d 9.3a, moderately distorted 9.3e 9.3b and highly distorted 9.3f 9.3c) and the framework (top: planar 9.3a 9.3b 9.3c, bottom: axisymmetrical 9.3d 9.3e 9.3f)*

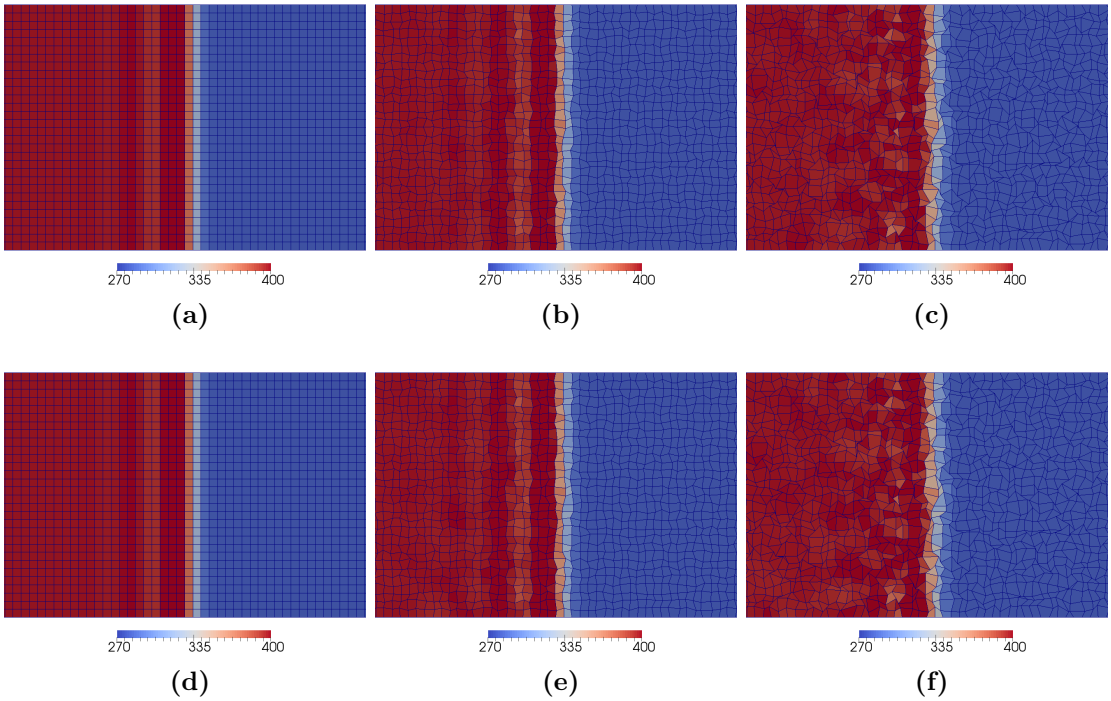

Figure 9.4: *Temperature field across the leading shock depending on the mesh for the MacCormack scheme (from left to right: Cartesian 9.4d 9.4a, moderately distorted 9.4e 9.4b and highly distorted 9.4f 9.4c) and the framework (top: planar 9.4a 9.4b 9.4c, bottom: axisymmetrical 9.4d 9.4e 9.4f)*

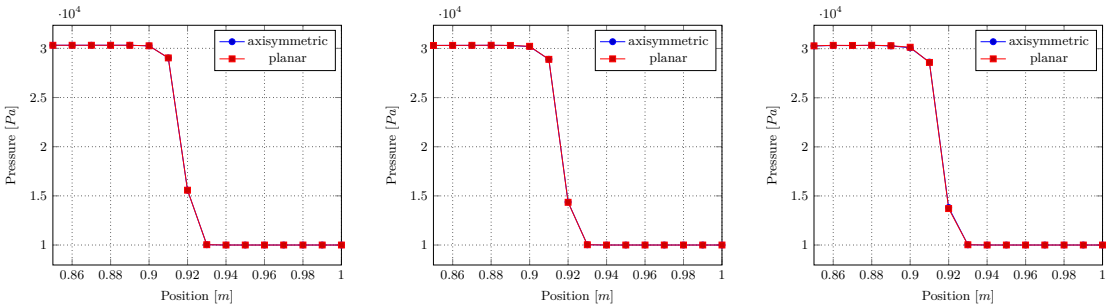

(a) Cartesian mesh **(b)** Moderately distorted mesh **(c)** Higly distorted mesh

Figure 9.5: *Pressure across the leading shock at the radial position* $r = 0.01$ *depending on the mesh and the framework for the MUSCL scheme, (planar framework: —■—, axisymmetrical framework: —●—)*

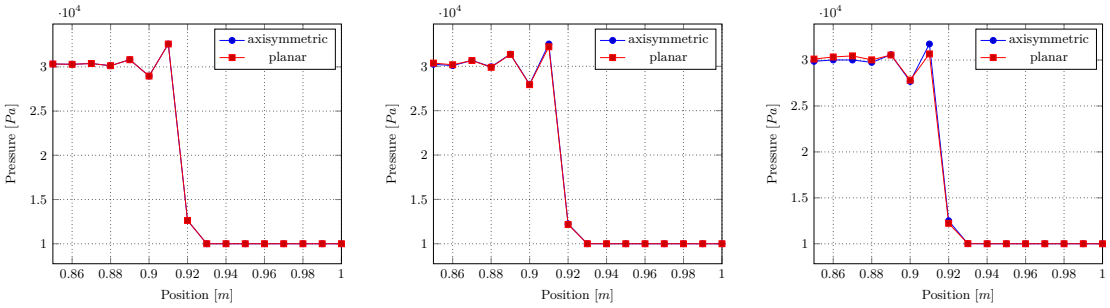

(a) Cartesian mesh **(b)** Moderately distorted mesh **(c)** Higly distorted mesh

Figure 9.6: *Pressure across the leading shock at the radial position* $r = 0.01$ *depending on the mesh and the framework for the MacCormack*

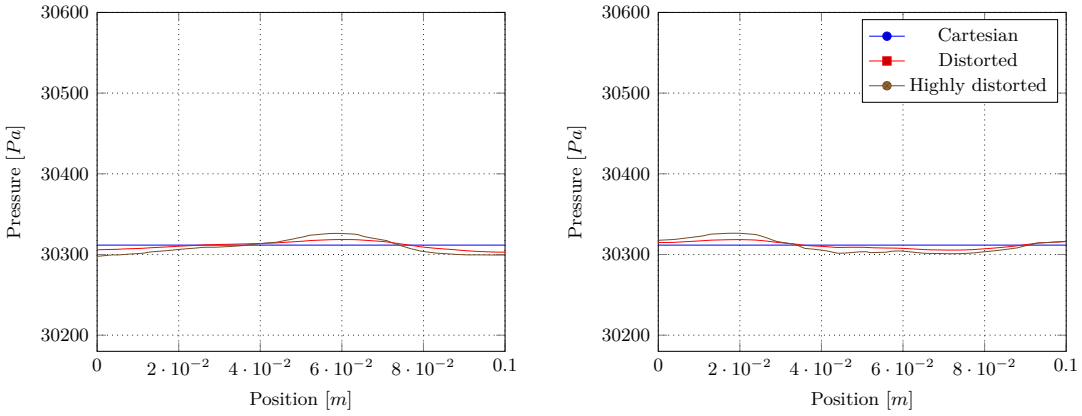

(a) Axisymmetric **(b)** Planar

Figure 9.7: *Pressure along the radial axis at position $x = 0.6$ depending on the mesh and the framework for the MUSCL scheme*

9.1.4 Radial disturbance

The objective is here to observe the impact of the framework on results along the radial direction and therefore assess the quality of the integration of the axisymmetrical source term over the cell. The results should be constant and thus once again identical between both the planar and the axisymmetrical framework. In order to fairly analyze such problem, the solution is observed in the disturbed area in the zone between the rarefaction wave and the contact discontinuity. The position $x = 0.6m$ fit such condition.

For the MUSCL scheme, the result presented in Figure 9.7 highlights the disturbance along the radial axis after both the leading shock and the contact discontinuity across the position. Using the Cartesian mesh the result is perfectly constant across the domain at the level of the numerical precision independently from the framework. Such observation is however not valid for the distorted meshes since a disparity of the pressure can be observed, higher for the highly distorted mesh. However, this variation remains lower than $30Pa$ in the worst case, which has to be compared with the $9 \cdot 10^4 Pa$ discontinuity imposed as initial condition. Since such spurious effect has approximately the same magnitude in both frameworks, the stability of the solution only depends on the mesh regularity. Furthermore, no conclusion can be established concerning the topology of these variations since they are unsteady in both referential without preferential behavior.

In the case of the MacCormack scheme, it can directly be observed that the magnitude of the disturbance is much higher than for the MUSCL scheme, reaching more than $400Pa$ for the strongly distorted mesh. Moreover, a small radial deviation from the expected results can be observed in the radial direction using the cartesian mesh. No clear explanation has been found for that phenomenon.

As a conclusion, the results are highly independent from the framework as expected for that case. This assesses that the methodology developed in this work correctly solves the physical problem. Such observation is valid even using strongly distorted grids.

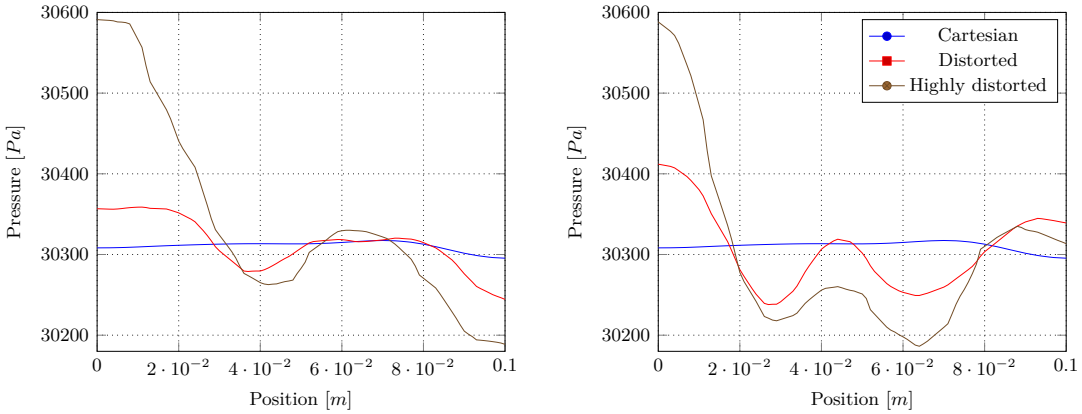

(a) Axisymmetric **(b)** Planar

Figure 9.8: *Pressure along the radial axis at position $x = 0.6$ depending on the mesh and the framework for the MacCormack scheme*

9.2 Crossing on symmetry axis

We propose here to test the new symmetry condition proposed in that work in the context of simulations in axisymmetrical framework. In order to assess the validity of this boundary condition, we focus our attention on the problematic of a concentric jet in the context of the AG closure where the velocity dispersion is generated nowhere else than on the symmetry axis. After a presentation of the expected solution based on 2D planar simulations, the correction proposed for the 2D axisymmetric simulations is discussed.

9.2.1 Description

Starting from an empty domain, the test case consists in an injection of particles in a cylindrical volume from this cylinder surface and toward the symmetry axis. Assuming the homogeneity of the flow in the cylinder axial direction, 2D planar and 2D axisymmetric cases can be compared. Modeling the flow with the AG closure and no initial velocity dispersion, that configuration creates a concentric shock and the appearance of velocity dispersion directly on the symmetry axis. No analytic solution is known for this problem. As a consequence, it is chosen to investigate such phenomenon in a 2D planar framework where this specific crossing is solved naturally inside the computational domain, which is a reference solution, and in an axisymmetrical one where this phenomenon appears at the boundary of the domain, which is the case verified. Such a situation occurs in most of the SRM simulation (see Chapter 10 and Chapter 11) since after injection, large droplets firstly cross on the symmetry axis. Therefore, this test case is the prototype of the initial crossing that appends on the axis of symmetry of an SRM.

To compare both 2D simulations, distinct computational domains are proposed as represented in Figure 9.9. The first is a circular domain in which the injection is imposed identically in each radial direction and is referred as *slice simulation*. Obviously, because of the discretization and more specifically of the form of the mesh cells, results can vary depending on the observed radial orientation. The second is a pseudo 1D problem since, in the axisymmetic plane, an homogeneity

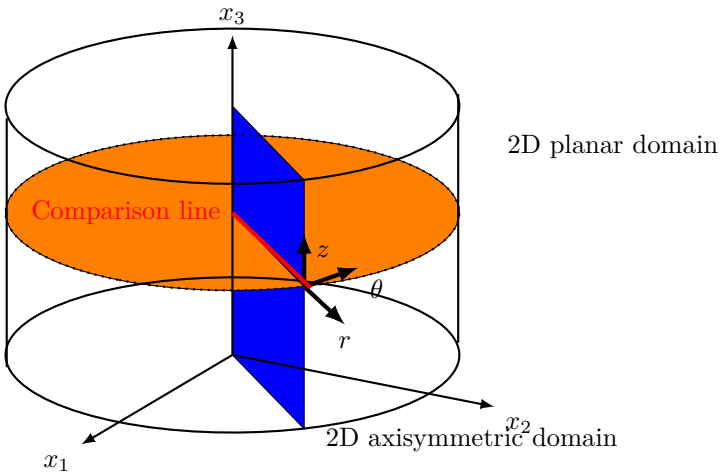

Figure 9.9: *Cylinder slice computational domain for 2D planar/axi simulation comparison*

Table 9.3: *Slice simulation parameters*

Parameter	value	unit
Radius	45	mm
Injection velocity	11.5	m/s
Mass flux	1	$kg/s/m^2$
End time	7.849	ms

in the axial direction is imposed and thus the problem reduces to a one dimensional case. Both can be compared by plotting the solution in the radial direction. For the need of comparison, we use the parameters given Table 9.3 that are inspired from the TEP motor (see Section 10.2). Also, we rely on the MUSCL multislope scheme for the numerical resolution of these cases, based on a minmod limiter and a HLLE scheme.

9.2.2 2D planar simulation

To evaluate the solution in the axisymmetric case, two meshes are designed. The first is based on structured grids, with 50×50, 100×100 and 200×200 cells, adapted to fit a circle at its borders. In this case, the cells at the center keep their regular, almost Cartesian, shape but the cells at the border of the domain are however distorted. The second mesh instead is an unstructured mesh based on triangular cells, which offers more regularity in the cell forms and distribution. That last case, relying on the CEDRE code, is used for comparison and validation of the results obtained with SIERRA. The differences between the meshes can be observed in Figure 9.10.

Since no drag source term is considered, the particles have a large inertia and are expected to cross at the center of symmetry at time $t = 3.913\,ms$. The results on various fields are presented in Figure 9.11 and Figure 9.12 at final time. One can observe that, in Figure 9.11 after the crossing, the concentric shock does not possess the expected axisymmetric property. The shape of the resulting fields is strongly dependent of the mesh structure.

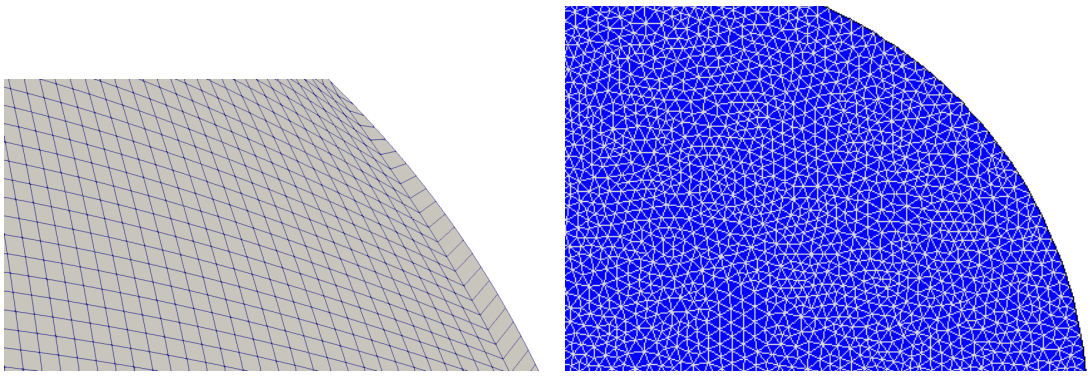

(a) Structured mesh **(b)** Triangular mesh

Figure 9.10: *Meshes investigated for cylinder radial slice simulation*

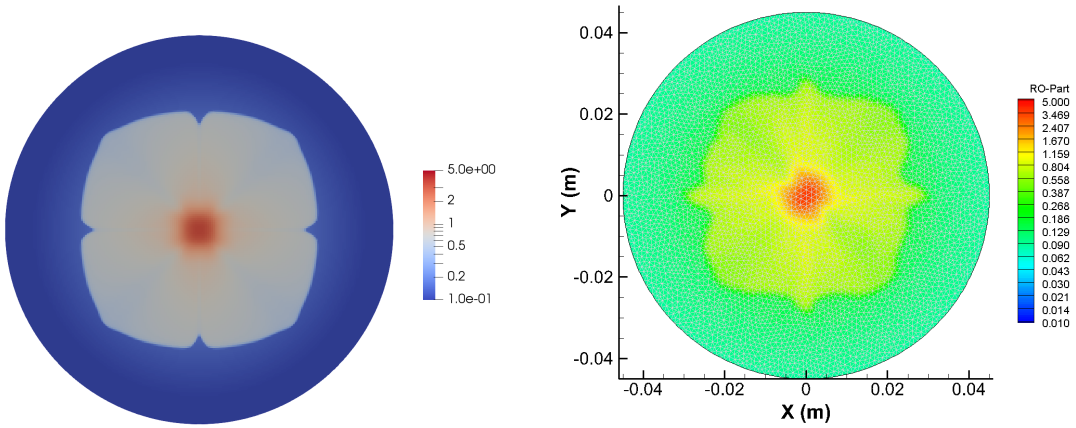

(a) Structured mesh **(b)** Triangular mesh

Figure 9.11: *Density contour solution using two distinct meshes at final time*

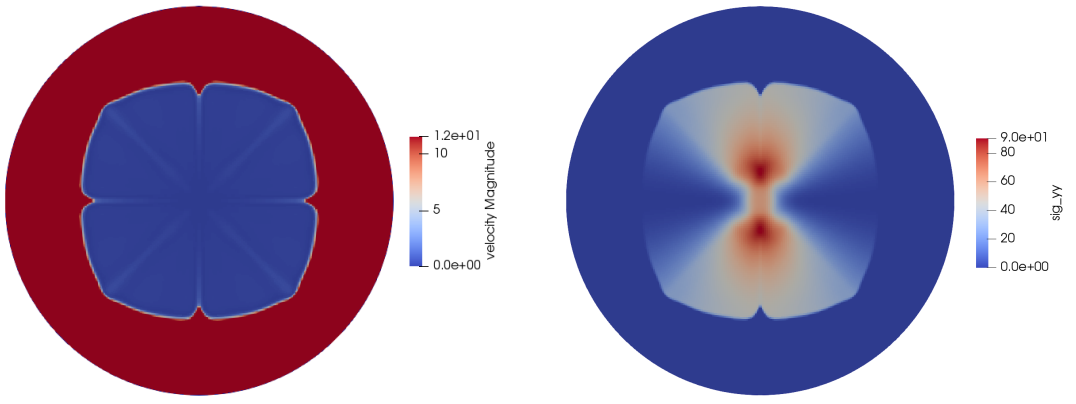

(a) Absolute velocity **(b)** σ_{yy} velocity dispersion

Figure 9.12: *Velocity and velocity dispersion contour using the structured mesh at final time*

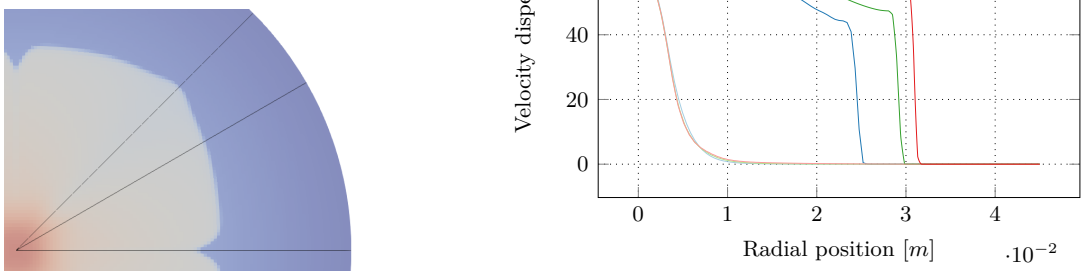

(a) Studied axis **(b)** Dispersion matrix

Figure 9.13: *Velocity dispersion matrix along different axis (using the* 200×200 *mesh)*

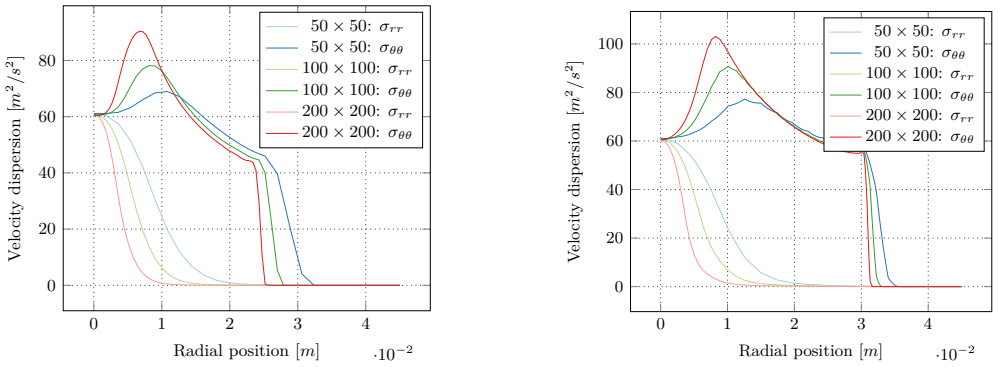

(a) Horizontal axis **(b)** 45° axis

Figure 9.14: *Velocity dispersion matrix for different grid sizes*

Another plot, in Figure 9.13, compares the final velocity dispersion along the horizontal axis and others oriented at 30 and 45 degrees. It can be observed that the $\sigma_{\theta\theta}$ field is not null and has a significant impact on the solution. More precisely, while we found $\sigma_{\theta\theta} = \sigma_{rr}$ at the symmetry axis, one can observe an exchange of energy from the azimuthal disperse kinetic energy to the radial one. These curves are almost not impacted by the radius of which the observation is conducted.

However, because of the distortion due to the mesh and the strong singularity generated on the symmetry axis, no solid conclusion can be deduced on the position of the leading shock. Only the magnitude of the velocity dispersion at the symmetry axis ($\sigma_{\theta\theta} = \sigma_{rr} = 61 m^2/s^2$) can be considered as a reliable value. Even through mesh refinement as in Figure 9.14, that value remains constant and can also be obtained from the simulation on the triangular mesh. It shall also be observed that the results tend to a singular solution of the velocity dispersion on the symmetry axis.

Finally, we focus our attention on the radial velocity. Once again, for the simulations of interest, this field varies depending on the considered radii and unlike what could be expected, the

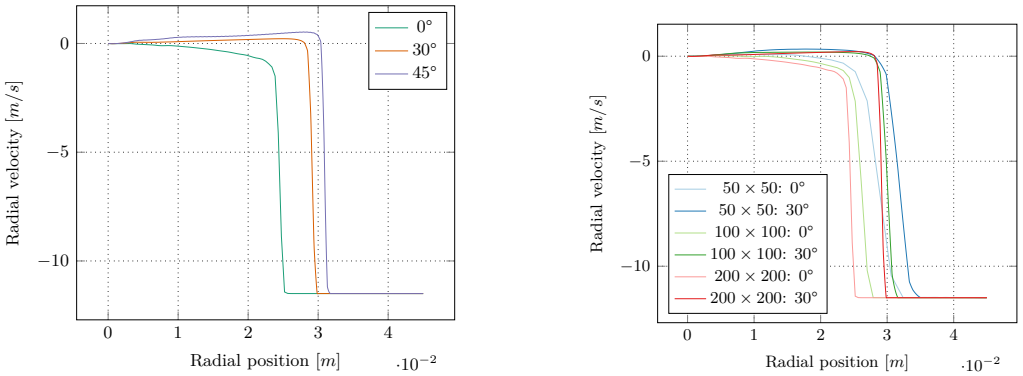

(a) Orientation dependency **(b)** Convergence

Figure 9.15: *Radial velocity for the slice simulation*

velocity is not null in the crossing area. As presented Figure 9.15a, the velocity increases almost linearly until the concentric shock in the case of angle 30° and 45°, while this field is decreasing over the vertical and horizontal axises. One can remark that this observation is dependent from the mesh size Figure 9.15b but that, because of grid refinement, this field varies more on the horizontal axis than on the 30° one. The reason of this difference in behavior is due to the specific cell interface orientation strictly perpendicular to the radial axis. As a consequence, the components of the pressure tensor perpendicular to normal direction of the shock and associated $\sigma_{\theta\theta}$ cannot contribute to the shock propagation contrarily to the other orientations.

The observed velocity increase is not a singular feature. In the case of the Euler equations, the effect has been reported in the literature of concentric shocks (see (Sachdev 2016) and the references therein) and is the subject of specific modeling in that field. In the case of the AG closure, no analytic solution or accurate semi-empirical model exists. As a consequence, we choose the 30° orientation as a reference for the sake of the comparison with the cases derived from axisymmetric closures.

9.2.3 Comparison with 2D axisymmetrical cases

We propose here a comparison in two distinct parts. First, a classical strategy is proposed to treat the axisymmetry. This numerical experiment points out the deficiency of such methods in the cases we are interested in. Secondly, the effects of the new features proposed in this work are compared with the two dimensional results analyzed above. The simulations are conducted on meshes with 50, 200 and 400 cells of uniform size in the radial direction.

9.2.3.1 Degenerated Anisotropic Gaussian (AGd) solution

In this first test, the classical HLLE Riemann solver is used and only the geometrical terms are modified. Since the surfaces are weighted by the radius, using a standard boundary condition on the axis of symmetry, the net numerical flux $|S_{ij}|_r \, \mathfrak{F}_{ij}$ is null. In these conditions, the appearance of the $\theta\theta$ component of the pressure tensor is not possible and that value remains null. As a

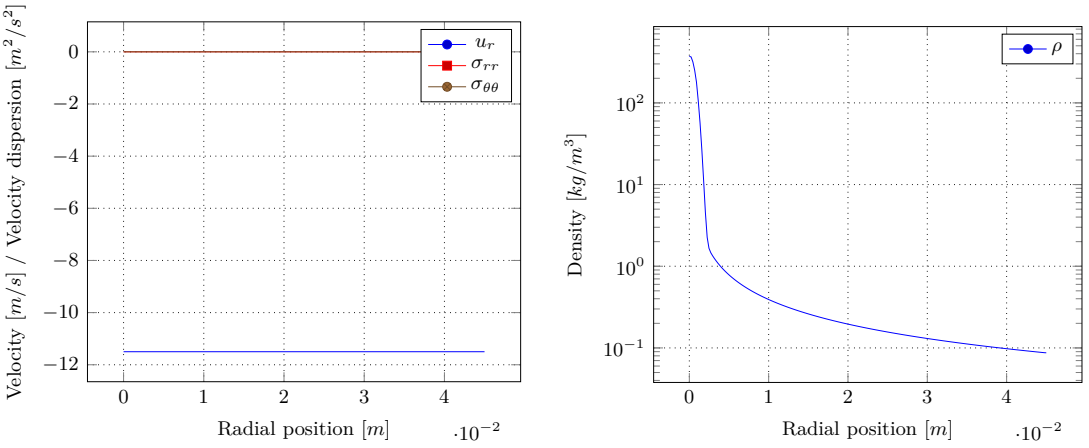

(a) Average and dispersed velocities **(b)** Density

Figure 9.16: *Radial fields for the axisymmetric case using a standard boundary condition on the* 200 *cell mesh*

consequence, the AX and AGd closures leads to an identical solution since the systems are equal for $\sigma_{\theta\theta} = 0$.

As it can be observed Figure 9.16, using that numerical strategy, the radial velocity remains constant from the injection to the symmetry axis. Whereas it is expected that the velocity dispersion drastically increases at the symmetry axis, this value remains at the level of the numerical noise. The computed solution is identical to the MK closure preventing PTC on the symmetry axis and leading to a large mass accumulation at this position.

To understand the problem, we propose to investigate the behavior of the numerical scheme in such situation and more specifically inside the cell in contact with the symmetry axis. Therefore, we write down the generic one-dimensional FV scheme (6.6) in axisymmetrical configuration. One obtains:

$$\boldsymbol{W}_i^{n+1} = \boldsymbol{W}_i^n - \frac{\Delta t}{|C_i|_r}\left[\left|S_{i+\frac{1}{2}}\right|_r \boldsymbol{F}_r(\boldsymbol{W}_{i+\frac{1}{2}}^n) - \left|S_{i-\frac{1}{2}}\right|_r \boldsymbol{F}_r(\boldsymbol{W}_{i-\frac{1}{2}}^n)\right], \tag{9.1}$$

Studying the cell N bordering the axis, it can be remarked that $\left|S_{N-\frac{1}{2}}\right|_r = 0$ since the surface is positioned on symmetry axis. Therefore the equation of evolution of $\boldsymbol{W}_N^{n+1}$ boils down to:

$$\boldsymbol{W}_N^{n+1} = \boldsymbol{W}_N^n - \frac{\Delta t\left|S_{N-\frac{1}{2}}\right|_r}{|C_N|_r}\boldsymbol{F}_r(\boldsymbol{W}_{N+\frac{1}{2}}^n), \tag{9.2}$$

Let's now assume an incoming flow without velocity dispersion $\boldsymbol{\Sigma}_{inj} = \overrightarrow{\boldsymbol{0}}$ reaches the cell N at the time step $n = 1$. The incoming flow is thus supersonic and reaches the cell N with a density

ρ_{inj} and a velocity $\boldsymbol{u}_{inj} = [-u_r, 0]^t$, where $u_r > 0$. As a consequence, until the flow inside the cell N becomes subsonic, the following sequence is respected:

$$\begin{pmatrix} \rho_N^{n+1} \\ \rho_N^{n+1}\boldsymbol{u}_N^{n+1} \\ \rho_N^{n+1}\mathbb{E}_N^{n+1} \end{pmatrix} = \begin{pmatrix} \rho_N^{n} \\ \rho_N^{n}\boldsymbol{u}_N^{n} \\ \rho_N^{n}\mathbb{E}_N^{n} \end{pmatrix} + \frac{\Delta t \left|S_{N+\frac{1}{2}}\right|_r}{|C_N|_r} \begin{pmatrix} \rho_{inj} u_r \\ \rho_{inj}\boldsymbol{u}_{inj} u_r \\ \frac{1}{2}\rho_{inj}\boldsymbol{u}_{inj} \otimes \boldsymbol{u}_{inj} u_r \end{pmatrix}, \tag{9.3}$$

Considering that at the time step $n = 0$ the cell N is empty, the evolution of the conservative value can be easily determined:

$$\begin{pmatrix} \rho_N^{n} \\ \rho_N^{n}\boldsymbol{u}_N^{n} \\ \rho_N^{n}\mathbb{E}_N^{n} \end{pmatrix} = n\frac{\Delta t u_r \left|S_{N-\frac{1}{2}}\right|_r}{|C_N|_r} \begin{pmatrix} \rho_{inj} \\ \rho_{inj}\boldsymbol{u}_{inj} \\ \frac{1}{2}\rho_{inj}\boldsymbol{u}_{inj} \otimes \boldsymbol{u}_{inj} \end{pmatrix}, \tag{9.4}$$

As a consequence, we deduce that $\boldsymbol{u}_N^n = \boldsymbol{u}_{inj}$ and $\mathbb{E}_N^n = \frac{1}{2}\boldsymbol{u}_{inj} \otimes \boldsymbol{u}_{inj}$ for all $n > 0$. Thus $\boldsymbol{\Sigma}_N^n$ is null for all time steps and the flow remains supersonic in the radial direction. Therefore, no velocity dispersion can appear inside this cell.

A decrease of the velocity magnitude is necessary to transfer kinetic energy into $\boldsymbol{\Sigma}$. However it assumes the existence of a momentum flux from the symmetry axis, that is made impossible by the null surface $|S_{ij}|_r$ and non-singular numerical flux $\mathfrak{F}_{ij}$. The correction proposed in Section 7.4, as investigated here-after, is aimed at changing this paradigm.

Remark 9.1. *In the case of the Euler equations and simulations of concentric shocks, there is always a pressure existing before the shock reaches the axis of symmetry. As a consequence, the source term, proportional to the pressure and acting on the radial momentum, forces the radial velocity to tend to zero near the axis of symmetry. Such process operates a transfer from mean field kinetic energy to internal energy and thus leads to an increase of the pressure. In the context of two-phase flows, this process enable PTC.*

9.2.3.2 Axisymmetric correction

The proposed correction aims at reproducing the numerical process generally observed on the Euler equations is described above. To do so, it is aimed at generating $\sigma_{\theta\theta}$ velocity dispersion from scratch to activate the source term vector and produce crossing in the same way as the Euler equations. It is thus necessary to rely on a non null product $|S_{ij}|_r \mathfrak{F}_{ij}$ on the axis, which also supposes a singular numerical flux $\mathfrak{F}_{ij}$, which is provides by the boundary condition designed in Section 7.4. It is first assumed in a first time that only this correction is sufficient to produce crossings on the symmetry axis. As a consequence, inside the computational domain, the standard HLLE Riemann solver is retained.

As it can be observed in Figure 9.17, thanks to that modification, that the δ-shock is avoided and velocity dispersion generated on the symmetry axis. These fields follow a dynamic very

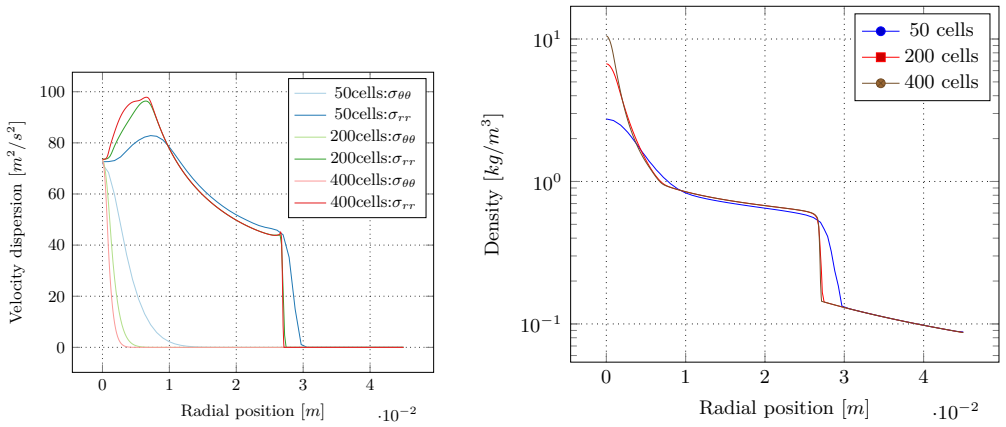

(a) Velocity dispersion **(b)** Density

Figure 9.17: *Radial fields for the axisymmetric case using a AX closure and the dedicated boundary condition on the axis*

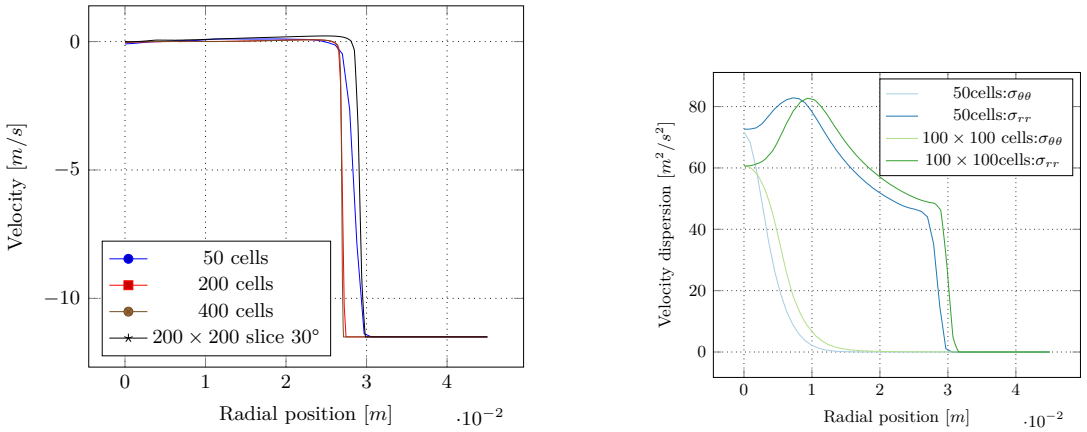

(a) Velocity **(b)** Velocity dispersion

Figure 9.18: *Radial fields comparison between the slice simulation and the axisymmetric case*

similar to the ones observed in the *slice simulations*, while having an equal value on the axis of symmetry, the $\sigma_{\theta\theta}$ field quickly decreases and the σ_{rr} magnitude increases until it reachs an upper limit and decreases as well. Also, it appears that the velocity dispersions converge towards a singular solution on the symmetry axis. However, it has not been possible to fully characterize this limit.

The shock position appears to be relatively close to the one obtained with the slice simulations and since no exact shock positions can be deduced from the slice simulations, no solid conclusion can be obtained from that parameter. The assessed issue concerning these results is mostly the magnitude of the velocity dispersions at the axis of symmetry. These do not match between axisymmetric and slices simulations even through refinement. As a cure, it is proposed to take into account the geometrical effects cause by the axisymmetry inside the Riemann solver.

Using the HLLA Riemann solver, numerical experiments show that the CFL limit is much more restrictive for that solver, especially close to the symmetry axis. Therefore we base our comparisons only on simulation with the mesh detaining 50 cells in the radial directions.

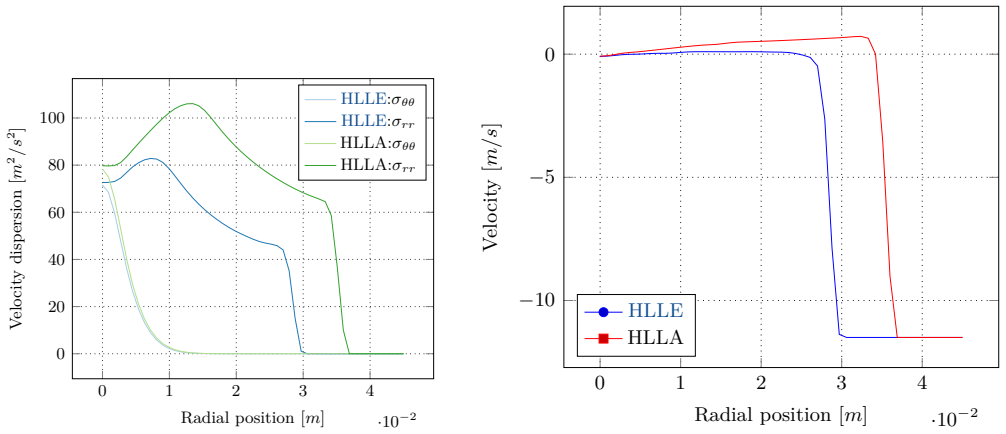

(a) Velocity dispersion **(b)** Velocity

Figure 9.19: *Radial fields comparison between use of standard and axisymmetric Riemann solvers*

The results, presented in Figure 9.19, show a greater discrepancy. While the topology of the fields remains globally the same, the shock position and the velocity dispersion magnitude differ. Work is in progress to understand that unexpected deviation.

Remark 9.2. *We suggest that the scheme, based on* (6.53)*, with source terms treated separately from the convection, cannot converges toward the exact solution because of the singularity generated on the symmetry axis. As a consequence, work is in progress to designed an Asymptotic Preserving (AP) (see (Berthon and Turpault 2011) for example in the context of HLL schemes) that should be able to conserve the expecting limit. We believe that the formalism of the* virtual geometry *on which is based the HLLA solver is fitted to extend the AP formalism proposed in (Berthon and Turpault 2011) to our problematic.*

Remark 9.3. *For the remaining chapters of the manuscript, the HLLA Riemann solver is not used because of its CFL restriction. The simulations thus rely on standard Riemann solvers and the boundary described in Section 7.4 and designed through this work. Moreover, since in the context of axisymmetry the crossing magnitude is overestimated on the axis, it is proposed to analyze the axisymmetric test cases of Section 10.2 and Chapter 11 keeping that known bias in mind.*

9.3 Source terms resolution for the QKS for AG-TSM closure

For that last verification test, the effort is focused on the resolution of the source terms in the case of polydisperse flows. We aim at showing the accuracy of the QKS method detailed in Section 5.3 according to the size phase space.

To do so, a fictive case is designed for the verification of the evaporation and drag resolution provided by the QKS scheme. A homogeneous test case is then considered, thus skipping the $\boldsymbol{x}$ dependence: a polydisperse spray is considered with an initial 2D anisotropic Gaussian velocity distribution depending on size. It experiences drag and evaporation. The gas velocity is assumed constant: $u_{g,1} = 4\,m.s^{-1}$ in the first direction and $u_{g,2} = 2\,m.s^{-1}$ in the second one. The drag force is characterized by the coefficient $1/\mathcal{A}_{drag} = 9.680385.10^{-7}\,m^2.s^{-1}$, the evaporation rate

is $R_s = -1.99.10^{-7}\, m^2.s^{-1}$ and the liquid density is $\rho_l = 634.239\, kg.m^{-3}$. Finally, the initial distribution f_0 is defined for a size S from 0 to $S_{\max} = 11310\, \mu m^2$ (corresponding to a radius equal to $30\mu m$) in such a way that for $s \in [0,1]$:

$$f_0(sS_{\max}, u) = \Phi(s) G_{\Sigma(s)}\left(u - \overline{u}(s)\right), \tag{9.5}$$

with G_Σ the centered Gaussian density function of covariance matrix Σ. The spray mean velocity is an increasing function of the surface equal to the gas velocity at $S = 0$ (non-inertial droplets):

$$\overline{\boldsymbol{u}_p}(s) - \boldsymbol{u}_g = \psi(s)\left(\overline{\boldsymbol{u}_p}(s)^0 - \boldsymbol{u}_g^0\right), \qquad \psi(s) = s(2-s), \tag{9.6}$$

with $\overline{\boldsymbol{u}_p}(s)^0 - \boldsymbol{u}_g^0 = [1,2]^t\ m.s^{-1}$. In the same way, the covariance matrix components depend on size and are zero at $S = 0$:

$$\Sigma(s) = \sigma_0 \boldsymbol{A} \psi(s), \qquad \boldsymbol{A} = \begin{pmatrix} 1 & 0 \\ 0 & 2 \end{pmatrix}, \tag{9.7}$$

with $\sigma_0 = 1\, m^2.s^{-2}$. Finally, the normalized initial size distribution is given by the following regular function (see Figure 9.20):

$$\Phi(s) = \phi_0 \left(1 + 8s\right)(1-s)^2 \exp\left(0.001\left(1 - \frac{1}{(1-s)^2}\right)\right)$$
$$\text{with} \int f(S, \boldsymbol{c}) \mathrm{d}\boldsymbol{c} = \Phi(S/S_{\max}). \tag{9.8}$$

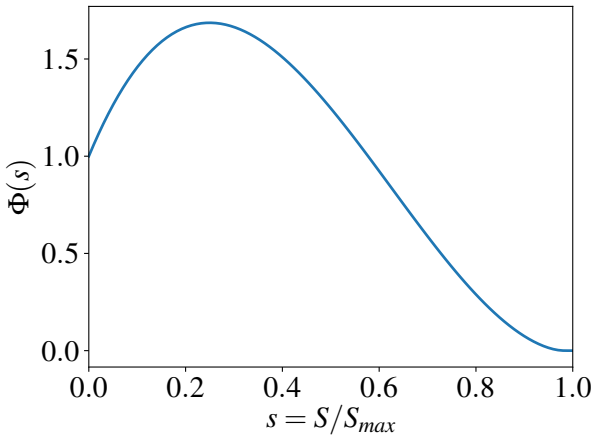

Figure 9.20: *Initial normalized size distribution* $\Phi(s)/\phi_0$.

The analytical solution of this homogeneous problem reads:

$$f(t,S,u) = \left(1 + \frac{-R_s t}{S}\right)^{\frac{2}{-\mathcal{A}_{drag} R_s}} \Phi\left(\frac{S - R_s t}{S_{\max}}\right)$$
$$G_{\Sigma\left(\frac{S-R_s t}{S_{\max}}\right)}\left(\boldsymbol{u}_g + (\boldsymbol{u}_p - \boldsymbol{u}_g)\left(1 + \frac{-R_s t}{S}\right)^{\frac{1}{-\mathcal{A}_{drag} R_s}} - \overline{\boldsymbol{u}_p}\left(\frac{S - R_s t}{S_{\max}}\right)\right),$$

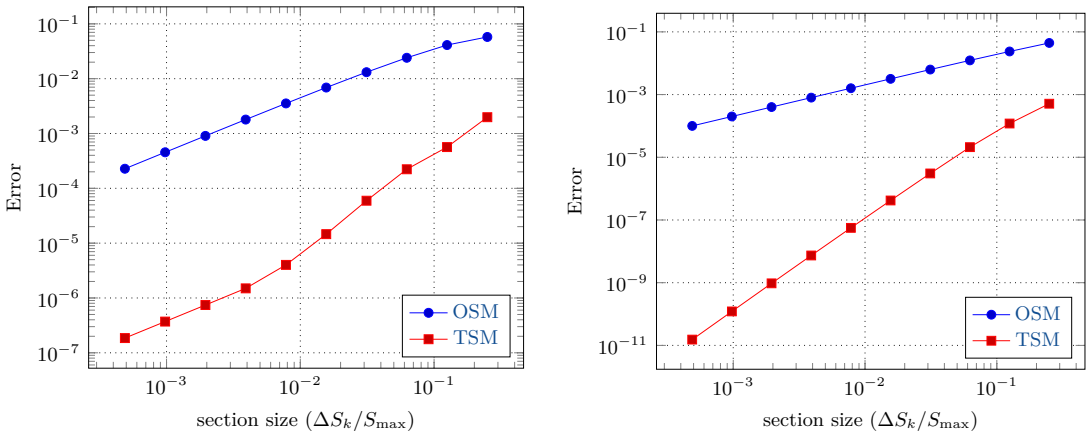

(a) Total number **(b)** Total mass

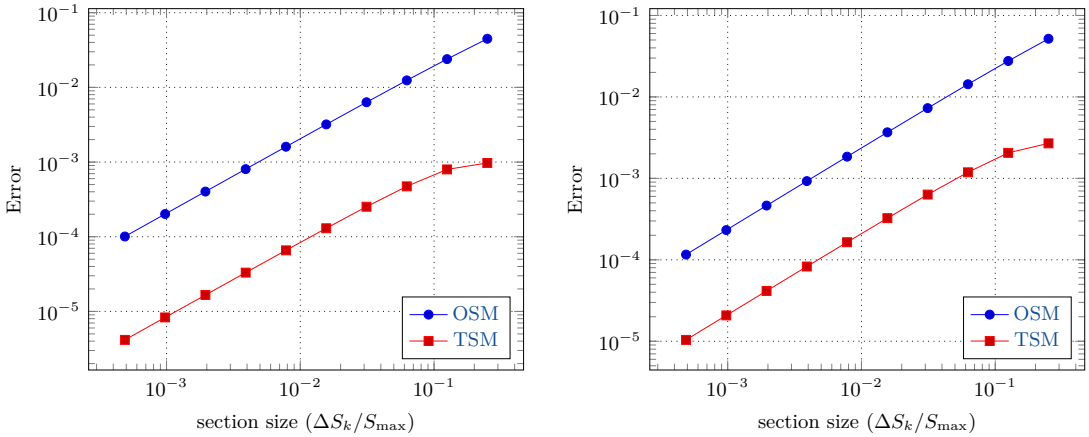

(c) Total momentum **(d)** Total energy

Figure 9.21: *Normalized maximum values of the errors on the global variables as a function of the relative section size*

which is still a Gaussian distribution in velocity, in such a way that the model can capture it. Let us remark that even if there is no correlation between the velocities in the two directions, such kind of correlation appears globally for the spray due to its size polydispersion and size-dependent velocity distributions.

Thus, the size discretization and the numerical scheme for evaporation and drag are verified in this case compatible with the Gaussian assumption for the velocity. Simulations are done with the TSM and OSM models from $t = 0$ to $t = t_{max} = 0.06\,s$. Several levels of discretizations are considered, with 4 equidistributed sections for the coarsest one to 2048 for the finest one. Additionally, the evaporation CFL like number is fixed to 0.2. The maximum values of the errors on the global variables $\sum_k (n^{(k)})^n$, $\sum_k (m^{(k)})^n$, $\sum_k (m^{(k)})^n (\boldsymbol{u}^{(k)})^n$, $\sum_k (m^{(k)})^n (\mathbb{E}^{(k)})^n$ are presented in Figure 9.21, normalized respectively by $\sum_k (n^{(k)})^0$, $\sum_k (m^{(k)})^0$, $\sum_k (m^{(k)})^0 \|\boldsymbol{u}_g\|$, $\frac{1}{2}\sum_k (m^{(k)})^0 \|\boldsymbol{u}_g\|^2$.

Figure 9.21 exhibits a convergence with a first order of accuracy for the velocity and the energy due to the constant reconstruction of the mean velocity and the variance in the section, whereas the order of accuracy is higher for moments of order zero in the velocity as for the total mass.

However, as already noted in (Laurent, Sibra, and Doisneau 2016), there is a loss of order of accuracy for the first section only visible on the total number density when more than 256 sections are used. This is due to a loss of accuracy of the quadrature in this section, which can be solved by increasing the number of quadrature points, and also considering a specific set of moments of the affine reconstruction, including negative moments, as in (Essadki et al. 2017).

Reducing the number of sections is of paramount importance when going towards real cases that require very large computing grids as the CPU time scales with the number of sections for both transport and evaporation-drag steps. Moreover, for high evaporation rate, small size sections may limit the time step for the phase space due to the CFL-like condition (see Section 5.3). In the present case, for the same level of accuracy, the TSM model is found 780 times faster than the OSM if the evaporation CFL limits the time step and 40 times faster if the transport CFL is limiting.

Chapter 10

Numerical method assessment

> Nobody's perfect, and most people drastically underestimate their distance from that state.
>
> Mahaffy's First Law of Human Nature

In this chapter, we propose to investigate fictitious test cases inspired from real applications and to study the advantages and drawbacks of a wide panel of numerical methods. For such comparisons, the effects on numerical solutions of the AG closure and of the numerical schemes designed through this work are studied. A great importance is given on the quality of the obtained solution and the artifacts that can be observed. Because of the complexity of the cases proposed in this chapter, both in terms of physics and geometry, the proposed analysis is mostly qualitative but remains highly valuable since the observed phenomenology is close to the ones of the applications.

Three test cases presented in three distinct sections are investigated. In Section 10.1, a 2D planar spray injection is tested. This study was conducted in the frame of a scientific exchange with the Sandia National Laboratory, Combustion Research Facility (CRF) at Livermore. The MUSCL multislope method is compared with a semi-Lagragian method also able to solve the governing equations of the AG closure (Doisneau, Arienti, and Oefelein 2017b). Section 10.2 is devoted to the TEP geometry, that has been designed to be the most simple SRM configuration. While proposed under a 2D planar and 2D axi-symmetrical geometry, this steady test case exhibits many singularities and proves the efficiency of realizable schemes over the use of Artificial Viscosity. Finally, in Section 10.3, it is proposed to investigate the VSA instability and the impact of both the numerical strategy and the modeling. While being 2D planar and thus not comparable with experimental studies, a high sensitivity of the pressure signals is observed.

10.1 Injection

The droplet modeling, proposed in this work for SRM applications, can also find its use in the context of automotive spray injection (Doisneau, Arienti, and Oefelein 2017a). This choice,

Table 10.1: *Initial cavity condition*

Quantity	Value	Unit	Notes
M_s	0.028965338	kg/mol	Air
$C_{p,g}$	1004	J/kg	Air at $293\,K$
μ_g	$1.71e-5$	$Pa.s$	Air at $273-323\,K$
Pr	0.713	N.A.	Air at $273-323\,K$
P_0	60	bar	Spray A
$T_{g,0}$	900	K	Spray A

Table 10.2: *Deduced parameters for the initial cavity condition*

Quantity	Value	Unit	Notes
γ	1.4	N.A.	Air
r_g	287.058	$J.kg^{-1}.K^{-1}$	Air at $293\,K$
ρ_g	23.224	$kg.m^{-3}$	Air at $273-323\,K$
a_g	601.409	$m.s^{-1}$	initial sound velocity

implemented in the code Raptor and proposed by F. Doisneau (Doisneau, Arienti, and Oefelein 2017b), relies on a numerical method that substantially differs from the MUSCL scheme proposed in this manuscript and still provides a high level of robustness. With parameters inspired from a real experimental case, this fictitious 2D injection at high Reynolds number exhibits nonlinearities due to compressible effects. The two strategies are compared.

10.1.1 Spray A case definition

The configuration describes here is a two-phase flow injection in a cavity filled with air and where physical parameters of the case are inspired from the *Spray A* configuration[1] sensibly using its operating conditions[2] (Pickett et al. 2010). Basically, the computing domain consists in a rectangular box with the injection at the west side and a constant pressure outlet on the east side. Because of the large droplet to gas mass ratio, the problem is considered to be strongly two-way coupled. As a consequence, the shear stress between the pure gaseous phase and the injected particle-laden flow causes an instability on the jet.

10.1.1.1 Cavity condition

The cavity in which the particle laden flow is injected remains at rest at the beginning of the simulation. The imposed conditions are exactly the same as for the Spray A test case. In other words, the cavity is filled with air at high pressure and temperature. Even for such conditions the air is assumed to behave as a perfect gas. The initial conditions corresponding to that case are indicated in the Table 10.1 and the injection parameters are given in the Table 10.2.

Aside the injection boundary condition described in Section 10.1.1.2, the north and south boundary conditions are slip walls. The gaseous velocity is imposed to be parallel to the wall with

[1] see http://www.sandia.gov/ecn/cvdata/targetCondition/injectorNozGeom.php
[2] see hhttp://www.sandia.gov/ecn/cvdata/targetCondition/sprayA.php

Table 10.3: *Box boundary conditions*

Boundary	condition	Notes
North	slippery wall	-
South	slippery wall	-
West	slippery wall	Not at the injection
East	free boundary	constant pressure $P = 60\,bar$

Table 10.4: *Injection boundary conditions for particles*

Quantity	Value	Unit	Notes
$\check{M}_l$	702	$kg.m^{-3}$	$C_{12}H_{26}$ at 363K
$C_{p,l}$	2315	J/kg	$C_{12}H_{26}$ at 363K
$\rho_{l,inj}$	$\rho_{g,inj}$	$kg.m^{-3}$	$\rho_{l,inj}/\rho_{g,inj} = 1$
$u_{l,inj}$	200	m/s	dynamic equilibrium
$T_{l,inj}$	900	K	thermal equilibrium
d_p	$4e-7$	m	$\tau_{\boldsymbol{u}} = 91.2\,ns$

a tangential velocity gradient (according to the normal of boundary) equal to zero. The pressure and temperature gradients are imposed to be zero which implies adiabatic walls. Same conditions are set on the west boundary except on the injection.

A constant pressure is imposed at the east boundary condition and set at the initial pressure of the chamber. Additionally, temperature and velocity gradients are set to zero. The box boundary conditions are summarized in Table 10.3.

10.1.1.2 Spray properties

The injected flow is composed of particles transported by a gaseous co-flow from the west boundary of the box. Both phases are injected in thermal and dynamical equilibrium. The disperse phase is taken to be homogeneous to a n-dodecane mixture ($C_{12}H_{26}$), as used in the Spray A, and the associated thermodynamical characteristics are retained (see Table 10.4). The injected gaseous phase is chosen to have the same thermodynamical properties as the gas in the cavity.

Several boundary conditions according to the carrier phase can be chosen as discussed Section 7.3.3.2. Since we would like to impose the injection velocity to $200\,m/s$, the subsonic character of the flow is to be considered. Therefore, by imposing the velocity and the temperature, the pressure is then chosen to be imposed by the inlet condition but extrapolated according to the flow inside the cavity. To do so, the pressure gradient is assumed constant around the boundary. These properties describing the inlet conditions are summarized in Table 10.5.

For this test case, the particle to mass ratio of the injected flow is equal to the unity. Together with a small relaxation time, one can expect strong two-way coupling effects. Approximating the acoustic relaxation time of the gas from the injection characteristics with $\tau_g = \frac{d_{inj}}{u_{g,inj}+\sqrt{\gamma r_g T_{g,inj}}}$, one can find an acoustic Stokes number of the spray St = 0.8. Therefore, none of the phases clearly drives the dynamics and because of the high interactions, the flow can be driven either

Table 10.5: *Injection boundary conditions for gas*

Quantity	Value	Unit	Notes
M_s	0.028965338	kg/mol	Air
$C_{p,g}$	1004	J/kg	Air at 293K
μ_g	$1.71e-5$	$Pa.s$	Air at 273-323K
P_r	0.713	N.A.	Air at 273-323K
$\boldsymbol{u}_{g,inj}$	200	$m.s^{-1}$	M≈ 0.3
$T_{g,inj}$	900	K	Spray A
P_{inj}	$\nabla P = cst$	$Pa.m^{-1}$	extrapolation
$d_{p,inj}$	$90e-6$	m	Spray A diameter

Table 10.6: *Box mesh properties (*1800×1000*)*

Quantity	Value	Unit	Notes
N_x	1000	cells	-
N_y	1800	cells	32 points in d_{inj}
l_{mesh}	2.8125e-6	m	$d_{inj}/32$
Δt	3	ns	Full Mach explicit, CFL≈ 0.93

by the gas or the droplets depending on the area. As a consequence, it can not be concluded, from an a priori study, if the droplets behave as ballistic objects due to the inertia of the core or as tracers like it is expected for the detached arms and packets.

10.1.2 Geometry

Because the walls and the high inlet velocity, it has been observed during first studies that the acoustic waves generated by the injection and bouncing on the borders of the domains disturb the injection core and at least help to trigger the hydrodynamic instability. To diminish the effect of this issue, it has been chosen to enlarge the computational domain. Two other solutions, could have been investigated:

1. Use non-reflecting boundary conditions to limit that effect,

2. Exponentially increase the grid size away from the injection to avoid acoustic waves reflections or to damp it away from the area of interest.

Since SIERRA does not possess non-reflecting boundary conditions, and the semi-Lagrangian implementation until now can only take into account meshes with uniform cell geometry, it has been chosen to use a large domain to delay the droplet flow distortion. Therefore, for the the sake of simplicity, Cartesian meshes with constant space discretization in both x and y directions are imposed. Moreover, for the mesh of reference, it has been chosen to introduce 32 cells in the injection limit and use a 1000 cells wide and 1800 cells high computational domain as specify in Table 10.6.

Calculations on this case is affordable on SIERRA but needs a significant time to provided results because of its OpenMP implementation that limit its scaling. Even if, thanks to the shared memory parallelism strategy of SIERRA, it has been possible to reduce the elapse time to

solution of the computation avoiding the computations in droplet-free area despite arithmetical unbalancing. The HPC abilities of SIERRA are not equivalent to the ones of Raptor. In the case of Raptor however, results could have been obtained in a reasonable time-span thanks to its MPI parallel ability. Therefore, an additional mesh, composed of a 3200×2000 and thus 64 cells in the injection diameter, has been tested on Raptor only.

Remark 10.1. *An investigation, using Raptor only, is proposed in Appendix D.1 comparing MK, IG and AG closures and several levels of discretization.*

10.1.3 SIERRA numerical setup

10.1.3.1 Scheme

The scheme used for the resolution of particles is based on the MUSCL multislope method proposed in (Le Touze, Murrone, and Guillard 2015) with the reconstruction given in Section 6.3.2.3.2, a minmod limiter and the HLLE Riemann solver proposed in Section 6.3.3.1. To maintain the same order of accuracy in space and time, a SSPRK2 time integration is used. Moreover, the code is optimized in order to avoid the computation of numerical fluxes and source terms when the density is under the threshold of $10^{-12}\, kg/m^3$.

For the gaseous phase, a MacCormack scheme, as described in Section 6.3.1.5, is used. Since the predictor-corrector formalism need the predictor orientations, the usual choice of SRMs computation are kept. In other word, the predictor is oriented towards the south for the y-axis and the west for the x-axis. Also, because of the known spurious oscillations of such a scheme, an artificial viscosity of Jameson (Jameson and Schmidt 1985) with a sensor based on the pressure completes the configuration.

10.1.3.2 Preliminary solution assessment

The results presented in Figure 10.1 are obtained at the reference times $3\,\mu s$, $5.1\,\mu s$ and $7.5\,\mu s$ using an AG closure. These have been chosen in order to avoid the disturbance of the acoustic reflection.

Until that point, the symmetry is well conserved. Both arms of the particle flow coming back toward the core of the jet but do not interact with it before $5.1\,\mu s$. At the $7.5\,\mu s$, it can be seen that the arms interact with the core but do not clearly penetrate inside it. Instead, it can be assumed that a gas pocket is concealed between the returning arms and the core. However, since this phenomenon occurs in a few cells only, one can not conclude on the physical reason of that observed gap.

Also, an unexpected small hole is created at the leading edge of the jet. A low particle density has been detected inside that hole with a density of approximately $10^{-5}\ kg/m^3$. Compared with the density inside the head of the jet that reach 200 kg/m^3, this area can be considered to be actually empty and the gradient at the front of the jet is well resolved.

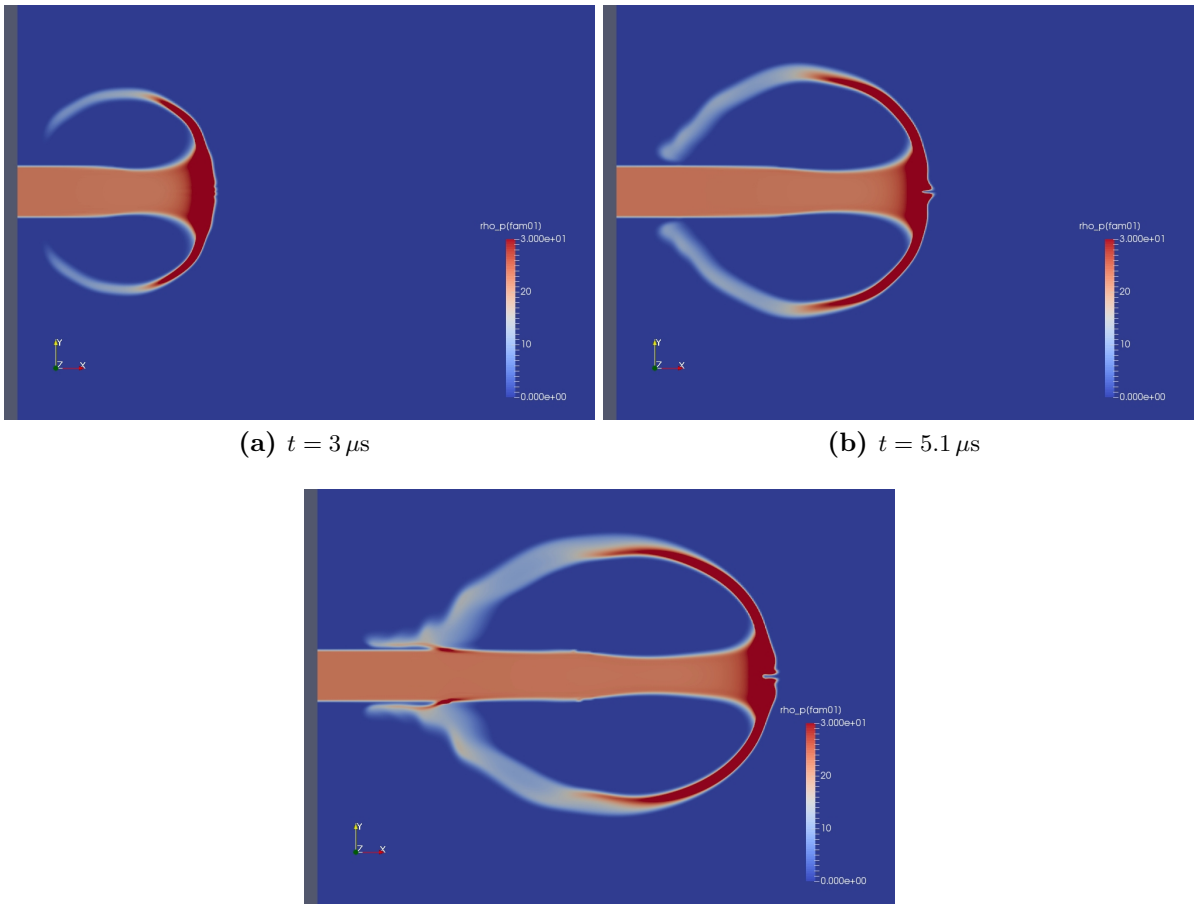

(a) $t = 3\,\mu$s **(b)** $t = 5.1\,\mu$s

(c) $t = 7.5\,\mu$s

Figure 10.1: *Density contour time evolution (contour using interpolation) using the AG equations computed with SIERRA.*

10.1.3.3 Closure dependent solution

The set of images in Figure 10.2 presents the evolution of the jet using SIERRA on the coarsest grid. The MK and AG closure has been both used in this configuration. Until $7.5\mu s$, just before the impact of the arms on the dense core, the result obtained with both closures cannot be discriminated. Almost all the phenomena observed with the AG closure are found again with the MK closure, including the hole in the jet front. Even the arms have an identical dynamics. Also, despite the high compression of the head of the jet, no PTC can be observe in this area.

The main differences occur during the impact on the arms of the dense core. Using the MK closure, one can observe δ-shock formations on the edges of the jet that are ejected from the core. These filaments protect the core by stopping the penetration of the arms and by capturing the mass of the returning arms. Such phenomenon does not appear with the AG closure since the momentum of the arms can penetrate through the core thanks to the modeled granular pressure.

The final state presented at $9.0\mu s$ shows that the instabilities generated on the core continue to evolve at the core surface with the AG closure. However, with the MK closure and because of the δ-shocks created upstream of the jet, the core of the jet is protected from the back flow of the arms and is thus less disturbed.

Another difference can be observed in the head of the jet. The two peaks bounding the hole at the head smoothly disappear at the front of the jet using the AG closure. On the contrary, they continue to exist with a high inertia using the MK closure. It can be assumed that they are created by particle trajectory crossing inside the jet. However, such conclusion is hard to validate since this phenomenon occurs in a few cells only.

10.1.4 Code comparison

The Raptor code uses a second order staggered scheme for the carrier phase and a first order semi-Lagrangian scheme for the transport of the droplets able to solve the MK, IG and AG closures. As a consequence, comparing to the second order of the MUSCL, a clear difference can be observed between the codes on the droplet density field caused by the dissipation of the semi-Lagrangian scheme. This effect can be especially observed on the arms of the jet, which are much more diffused using Raptor, and at the head that takes the form of a spade. Only mesh refinement can correct this, but as it can be observed Figure 10.3, even with the refined mesh, the level of resolution of Raptor remains below the one of SIERRA.

Aside this general conclusion, several differences can be observed and associated to numerical artifacts. The first of them is the behavior of the spray along the axis of symmetry. The semi-lagrangian method produces an unexpected mass accumulation on the axis of symmetry leading to the spade shape of the jet front. Expected for first order methods using the MK closure (Bouchut, Jin, and Li 2003), the occurrence of such phenomenon appears to be a numerical artifact using the AG closure. In contrast, the solution using SIERRA shows two spikes instead of one and no mass increase on the symmetry. Separated by a very small number of cells, it cannot be ensured that these are physical. However, no mass increase at the symmetry is observed using SIERRA unlike for Raptor.

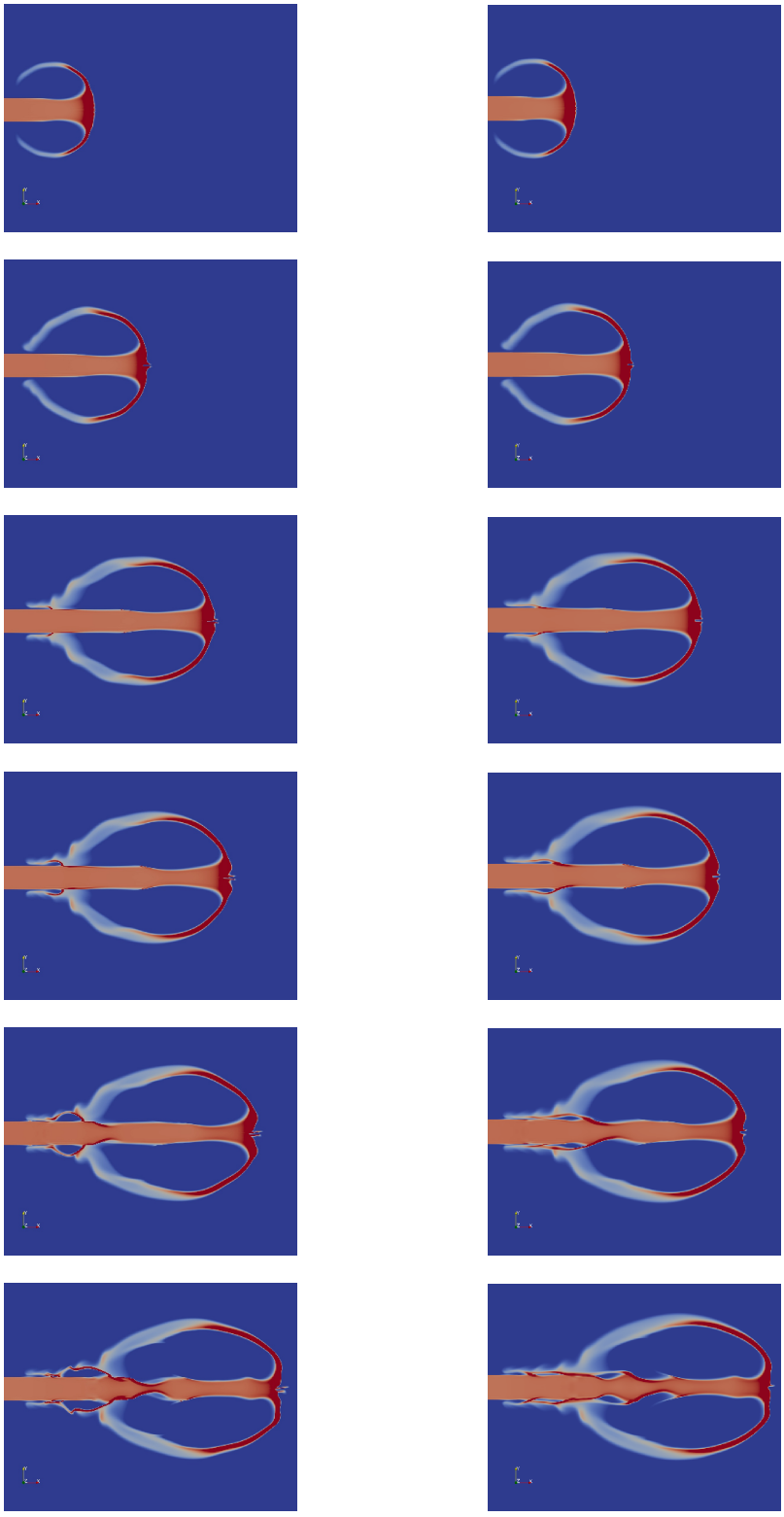

Figure 10.2: *Results with SIERRA (mesh* 1800×1000*) after* $3\,\mu s$*,* $5.1\,\mu$*,* $7.5\,\mu s$*,* $8.1\,\mu s$*,* $9.0\,\mu s$*, and* $9.9\,\mu s$ *(from top to bottom) using the MK (left) and AG (right) closures.*

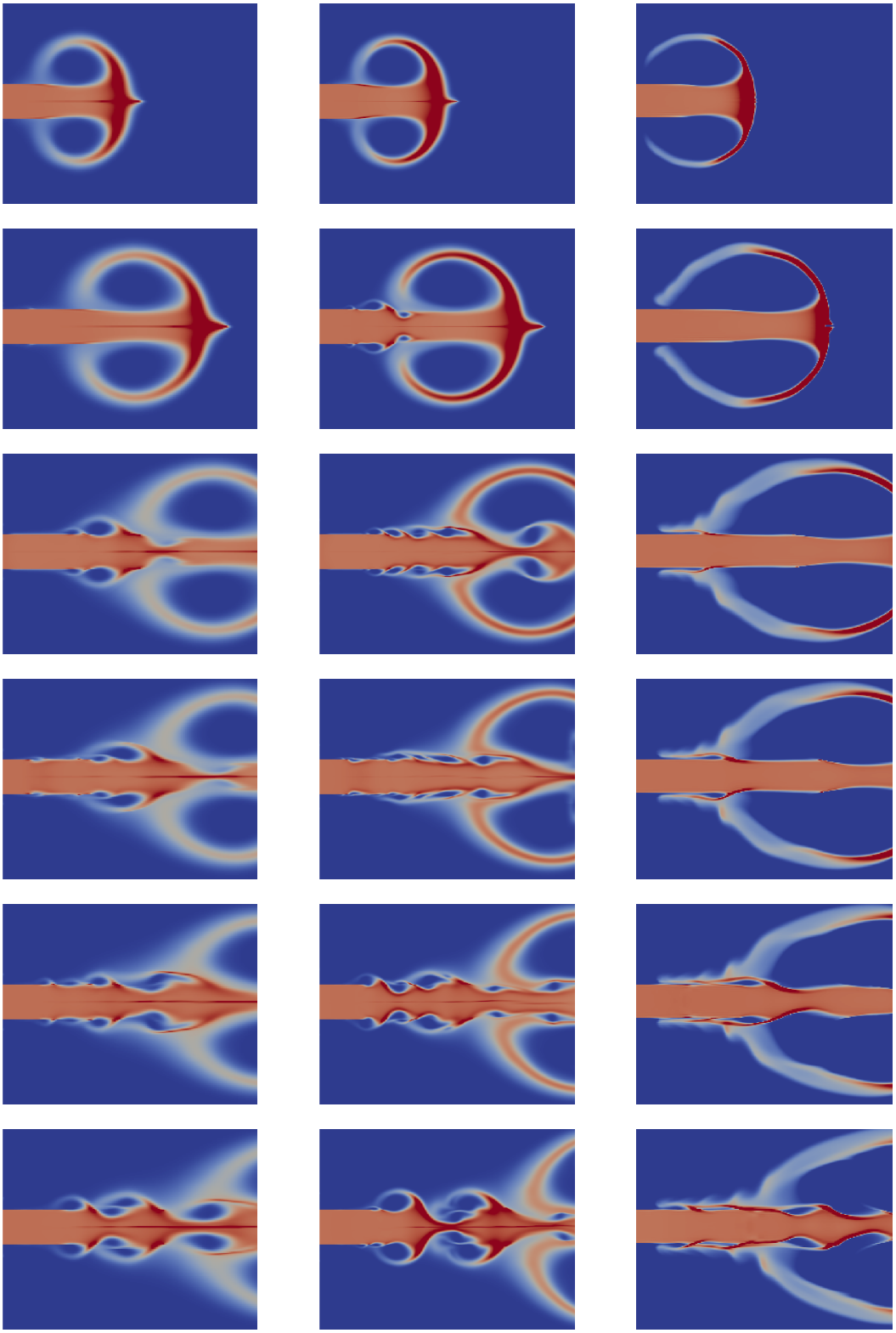

Figure 10.3: *Results with Raptor (left: standard mesh (32), center: refined mesh (64)) and SIERRA (right: standard mesh) after* $3\,\mu s$, $5.1\,\mu$, $7.5\,\mu s$, $8.1\,\mu s$, $9.0\,\mu s$, *and* $9.9\,\mu s$ *from top to bottom.*

Another aspect discriminating the codes is the connection of the arms with the core. Compared to the result obtained with SIERRA, it seems that the diffusion of the semi-Lagrangian connects the arms and the core at an early time. As a consequence, the shape of the distortion of the droplet core flow are clearly different depending on the used numerical method. Additionally, on the refined mesh, one can observe the appearance of smaller vortices, caused by the higher resolution of the gaseous flow. It has not been possible to determine the smallest scales of the problem because of the singular form of the injection. As a consequence, since no analytic or sufficiently refined solution are available, we can essentially conclude that the MUSCL scheme provide solutions of an higher accuracy with less numerical artifacts.

10.2 Steady TEP case

It is proposed now to investigate a test case fully inspired from SRMs. The geometry corresponds to a simple SRM designed with a cylindrical combustion chamber, where the flow is injected from the propellant grain through the lateral boundaries of the computation domain, and a de Laval nozzle. Originally designed for code verification (Lupoglazoff and Vuillot 1992b; Vuillot et al. 1997; Dupays 1996; Simoes 2006), this configuration offers the most basic features encountered in steady solid rocket motor. Moreover, due to the particle drift velocity, the disperse phase resolution exhibits two challenging features:

- the particle trajectory crossing through the nozzle and/or on the symmetry axis,
- the particle-free area near the nozzle wall.

These can be observed separately in 2D planar or 2D axisymmetric cases, because of the specific phenomena occurring at the symmetry axis in axisymmetric configuration. In Section 10.2.1, focusing on the MK, numerical methods are compared. Then, in Section 10.2.2, relying on the MUSCL multislope scheme, MK and AG closures are compared and the correction on the symmetry axis is assessed.

10.2.1 Planar case

10.2.1.1 Case description

The TEP configuration produces several levels of singularities representative of what will be encountered in realistic SRM simulations. Usually, the TEP geometry corresponds to a cylindrical port motor of chamber length $170\,mm$ and inner radius $45\,mm$ continued by a converging-diverging nozzle of throat radius $16.77\,mm$ for an overall motor length of $270\,mm$ (see Figure 10.4). Here, the simulations are conducted in a 2D-planar configuration with the gas and particle properties provided in Table 10.7. Presenting no difficulty for full gaseous simulations (Lupoglazoff and Vuillot 1992b), the numerical method used for solving the carrier phase flow will have, in that case, a negligible influence on the results. However, complications occur for two-phase flows (Simoes 2006; Daniel 2000) resulting, for the Lax-Wendroff class of scheme, in the need of an adaptation of the AV. The study is here focused on the resolution of the MK

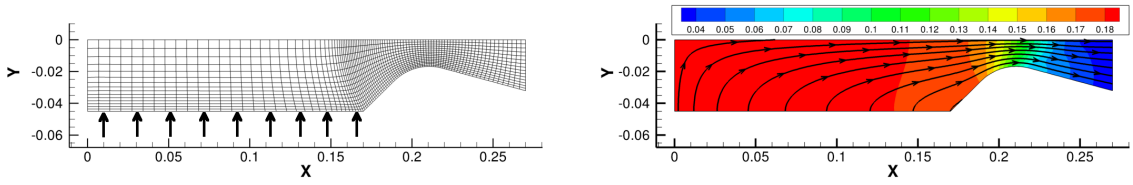

(a) Standard mesh (98×15 cells) and injection wall **(b)** Gas density and streamlines

Figure 10.4: *TEP configuration representation*

Table 10.7: *Thermodynamic and inlet properties for the TEP test case*

(a) gas

Variable	Value
Thermal capacity at constant pressure	$2437 J/kg/K$
Molar mass	$27.78 g/mol$
Dynamic viscosity	$9.06 \cdot 10^{-5} kg/m/s$
Prandtl	0.484
γ	1.14
Inlet mass flux	$9.3398 kg/m^2/s$
Inlet temperature	$3347 K$

(b) particle

Variable	Value
Thermal capacity	$1177 J/kg/K$
Material density	$1803 kg/m^3$
Inlet mass flux	$2.0502 kg/m^2/s$
Inlet temperature	$2600 K$

closure with the injection at $1\,m/s$ of $30\,\mu m$ droplet, sufficiently large to cause PTC but small enough to avoid the generation of singularities that the MacCormarck scheme could not bear. The discussion will be oriented toward the resolution of the δ-shocks and of the interface with vacuum, which turns out to be the most critical area relatively to scheme behavior; the impact of mesh refinement in the presence of such singularities will then be investigated.

10.2.1.2 Resolution of singularities and vacuum

Due to the compression of the flow in the nozzle inlet, trajectories of the particles originating from the aft-end part of the grain encounter the path of the particles coming from the head-end and flowing downstream. The physical PTC occurring even for such low inertia particles results in a mathematical δ-shock with a position that depends on the numerical method used for the resolution of the disperse phase. For instance, the first order scheme produces a δ-shock attached to the nozzle inlet wall (see Figure 10.5) while the same δ-shock is solved detached from it using higher order schemes. Moreover, because of the numerical diffusion related to the used scheme, the position and the amplitude of the shock can change, moving toward the chamber under the effect of diffusion.

The drift velocity due to the inertia of the particles naturally produces a vacuum zone in the diverging part of the nozzle. Moreover, since the δ-shock prevents any PTC, vacuum naturally appears right behind it, thus creating an especially high gradient that the numerical methods have to cope with. The MacCormack scheme is challenged in such a condition since intrinsic spurious oscillations appear and can easily lead to negative density close to vacuum. The AV then has a high impact on the resolution in such an area. However, since the first order upwind

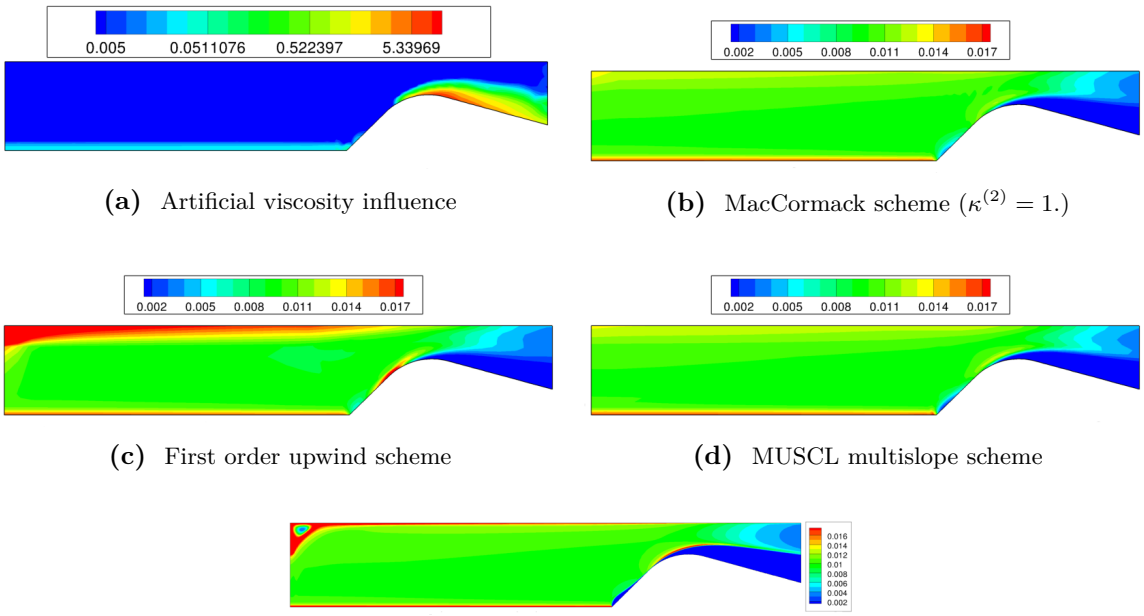

(a) Artificial viscosity influence

(b) MacCormack scheme ($\kappa^{(2)} = 1.$)

(c) First order upwind scheme

(d) MUSCL multislope scheme

(e) MUSCL multislope scheme on highly refined mesh (784×120 cells)

Figure 10.5: *Influence of the scheme on the density field resolution for TEP case*

scheme and the MUSCL scheme are intrinsically designed to avoid negative density, no numerical artifact resulting from the interface with vacuum can be observed. The width of the transition zone from vacuum to the δ-shock depends however on the level of numerical diffusion. In the presented case, the widest zone is observed for the first order Godunov scheme, the thinnest for the MUSCL scheme. For the MacCormack scheme, its width highly depends on the AV parameters.

10.2.1.3 Influence of mesh refinement on the results

If differences are expected from the approximation of a mathematical solution by several methods, successive mesh refinements should lead to a unique solution. However, singularities occurring in the TEP do not ensure the ability of the methods to provide the converged solution. Aside the more accurate resolution of the particle flow, the finer resolution of the carrier phase reveals small structures, naturally occurring and taking place at the head end on the symmetry plane and at the junction between the injection surface and the nozzle. These lower scale structures lead to physical stagnation points and therefore droplet accumulations that challenge even more the centered schemes.

Since the gradients increase with mesh refinement, the second order artificial viscosity coefficient has to be increased to prevent the simulation from diverging. The use of the minimal amount of artificial viscosity for stability leads to oscillations similar to those already observed with the standard mesh as in Figure 10.6. A high increase of the AV in order to reduce these wiggles actually leads to more intense oscillations. As a consequence, even if an optimal level of AV can be reached, the MacCormack scheme, in this standard form and using this kind of AV, does

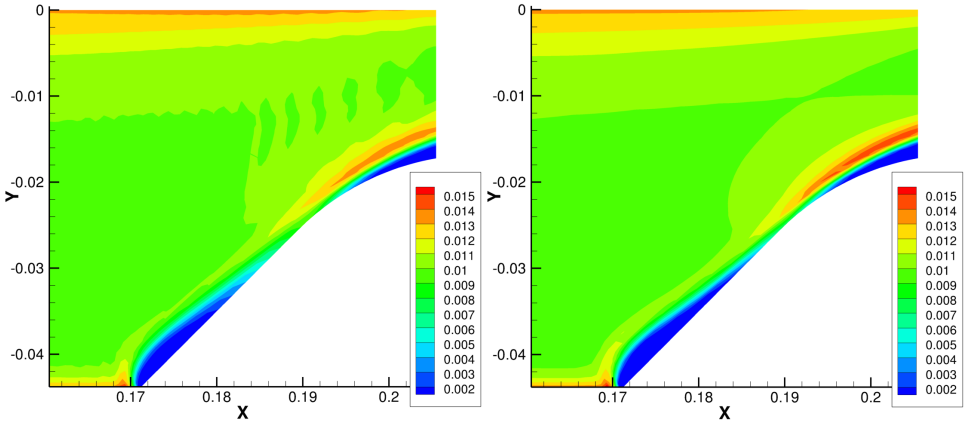

(a) MacCormack scheme **(b)** MUSCL multislope scheme

Figure 10.6: *Droplet density field in the converging part of the nozzle for TEP refined mesh (*196×30 *cells)*

not allow to get rid of the oscillating fields and requires tedious manual adjustment in order to reach a satisfactory solution.

In contrast, the upwind class of schemes does not need AV nor case dependent corrections. For the first order scheme, it can be seen that high mass accumulations occur at the head-end of the engine and near the symmetry plane. These artificial singularities are limited to the boundary cells where δ-shocks are actually created through diffusion. Using a MUSCL second-order extension, these numerical singularities disappear and effective mass accumulations due to stagnation points are revealed. Observing the transition zone to vacuum, even if refined meshes leads to a thinner transition zone with first order scheme, the use of the MUSCL scheme is much more efficient in reducing the spreading of the zone due to numerical diffusion. Comparing the accuracy of the solution obtained at comparable computational cost, the effort conducted in order to get a stable and accurate second order extension is then fully justified since the MUSCL scheme can provide more accurate results on coarser meshes than the first order method.

The design of a specific scheme is needed in order to resolve both vacuum zones and δ-shock but more importantly to obtain coherent solutions in every configurations. Consequently, applying a mesh refinement without tackling these issues can lead to unexpected phenomena and the false interpretation of numerical effects. Eventually, the proposed upwind scheme, which combines accuracy and stability, allows to conduct a proper mesh refinement study without any inference from parameters, which are difficult to control.

10.2.2 Axisymmetric case

10.2.2.1 Case description

It is now proposed to use the same geometry but in axisymmetric conditions. Also, we rely on two levels of discretization, the original 98×16 mesh with 1460 cells (Lupoglazoff and Vuillot 1992b; Vuillot et al. 1997; Dupays, Wey, and Fabignon 2001) and a refined 785×121

grid composed of 94080 cells. At the inlet, the mass fluxes of both the gas and the particles are imposed and both phases are injected at the same velocity and with no initial velocity dispersion for the particles. A supersonic condition is set at the outlet of the nozzle for both phases because of the de Laval nozzle. The remaining walls, at the head end and along the nozzle are considered adiabatic. Finally, the procedure at the symmetry described Section 7.4 is applied. Inlet conditions and thermodynamic properties of the mixture are summarized in Table 10.7.

It is aimed here at observing the differences between the MK and AG closures when droplets of $100\mu m$ diameter are injected to ensure an intensive crossing on the symmetry axis because of their inertia. More specifically, the AX closure is investigated as well as the treatment of the symmetry axis. In the case presented here, we focus on the results obtained with the MUSCL multislope scheme and the minmod limiter for both phases. For the MacCormack scheme, no sufficiently efficient sensor has been found to ensure the realizability of the AG closure both close to vacuum and near null velocity dispersion areas, which explain why this class of scheme is not presented in this section.

10.2.2.2 Case analysis

As presented Figure 10.7, for both simulations using the MK and the AX without correction (see Section 7.4), the particles accumulate on the symmetry axis in an analog way. The velocity dispersion observed in the AX simulation without correction is caused by the crossing of particles with inertia coming from the head end of the engine and the ones injected near the aft end.

No significant raise of the velocity dispersion on the symmetry axis is observed using the AX without correction. Additionally, results obtained using the AGd closure are strictly identical to the AX without correction on the axis since the $P_{\theta\theta}$ field remains uniformly null. Using the correction however, as shown Figure 10.7c, the mass accumulation is smeared on the axis. This difference is even more visible on the refined mesh (see Figure 10.8). This effect is due to the significant PTC that can occur on the symmetry axis thanks to the correction as shown Figure 10.9. Consequently, a large area inside the chamber, where PTC occur, can be observed.

The anatomy of the flow where PTC occurs can be deduced from Figure 10.9. Three PTC areas can be observed, separated by the velocity dispersion field discontinuities:

1. In the core of the chamber due to the crossings on the symmetry axis,

2. In the nozzle, starting from the throat, due to the presence of particles that already crossed the axis and in inertia from the head end but not from particles directly coming from the grain,

3. At the end of the nozzle due to the intersection of the second crossing area with the symmetry axis.

The two first areas can be distinguished from the σ_{rr} field whereas the third one is essentially visible from the σ_{zz} and the $\sigma_{\theta\theta}$ field. That third zone matches the extrema in particle density observed in the refined AX simulation, which reaches approximately $15.63 kg/m^3$. Such value is

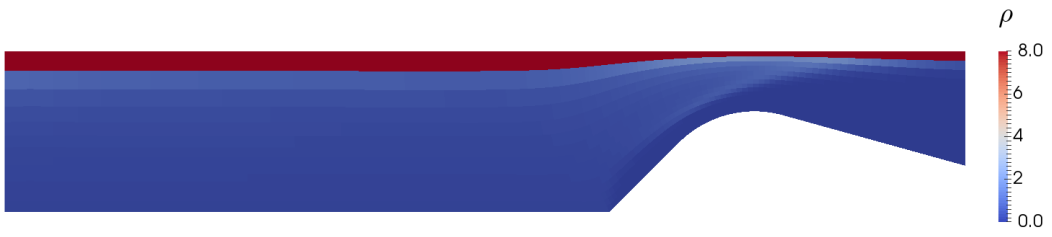

(a) MK

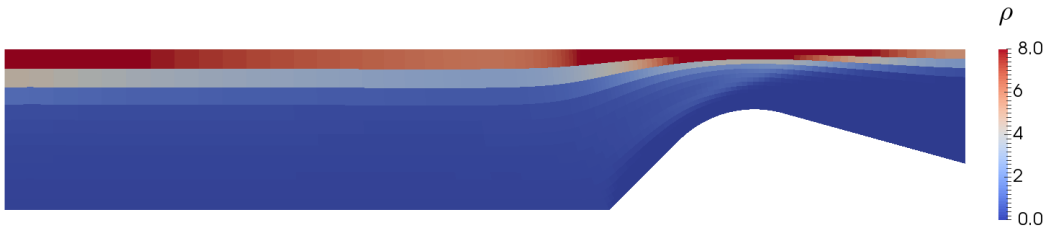

(b) AX without correction on the axis

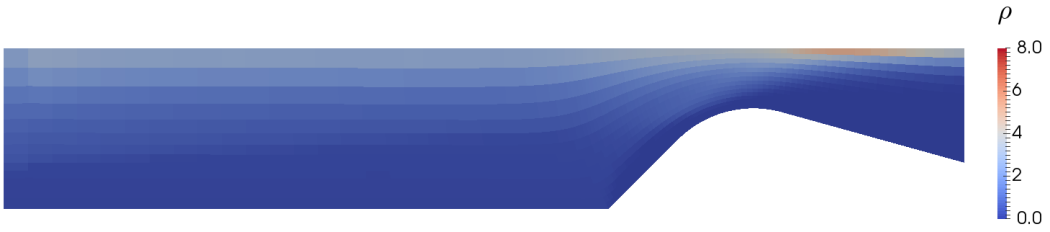

(c) AX with correction on the axis

Figure 10.7: *Particle density field in the TEP at steady state on the coarse mesh depending on the closure*

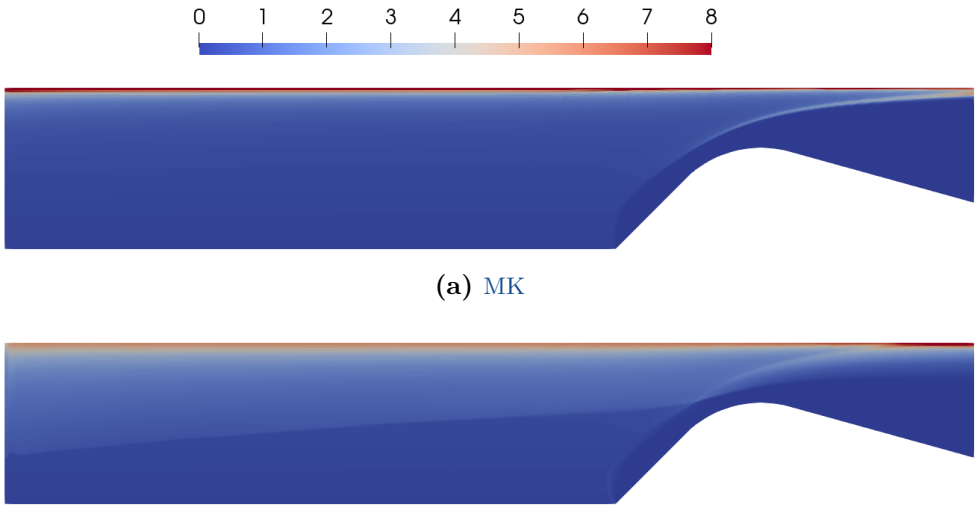

(a) MK

(b) AX

Figure 10.8: *Particle density field in the TEP at steady state on the fine mesh depending on the closure*

(a) σ_{rr}

(b) $\sigma_{\theta\theta}$

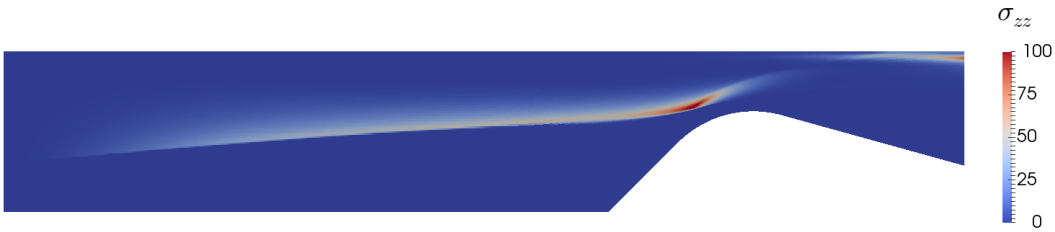

(c) σ_{zz}

Figure 10.9: *Velocity dispersion fields on the fine mesh using the AX closure without correction on the axis*

much smaller than the particle density extrema observed in refined MK simulation, which exceed $9000 kg/m^3$. Since that last value is higher than the particle material density, the assumption of negligible volume needed for the disperse phase model validity fails for the MK model.

The plot on the radial direction given on Figure 10.10 at position $z = 0.1$, shows the action of the velocity dispersion field of the AX model on the density and average velocity field. The deviation between the MK and AX models appears at the position of the shock where the magnitude of the velocity dispersion in both the radial and axial direction rises. Behind this discontinuity, the velocity diminishes until reaching zero, which prevent from the mass accumulation. Finally we observe that the magnitude of the azimuthal velocity dispersion near the symmetry axis is very close to the one of the radial velocity dispersion as originally expected. That field only participates in the dynamics near the axis, as it can be observed Figure 10.10, but is crucial for the PTC to be possible.

Remark 10.2. *It has been observed that, starting the simulation from the steady state (see Figure 10.8b) with the AX model without the correction on the symmetry axis, the deviation is small. The correction on the axis essentially generates the PTC from zero on the axis, but this*

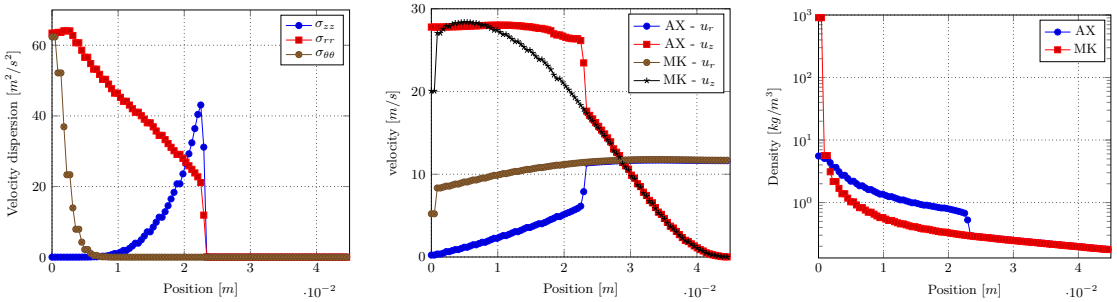

(a) Velocity dispersion **(b)** Average velocity **(c)** Density

Figure 10.10: *Disperse phase characteristic in the radial direction at position $z = 0.1$ for the AX and MK closure*

correction is not necessary to maintain PTC. Looking at the axisymmetric source terms of the model (3.69), it appears that, for an initial positive $P_{\theta\theta}$, the system close to the symmetry axis naturally goes to an equilibrium where $u_r = 0$ and $P_{\theta\theta} = P_{rr}$. The occurrence of PTC is mainly driven by the axisymmetric source terms whereas the axisymmetric correction mostly act as a trigger.

10.3 Unsteady C1

Keeping in mind the issues of the previous stationary case, this study of the C1 unsteady configuration aims at quantifying the effect of the chosen simulation set up on pressure oscillations occurring inside this fictitious SRM with low and moderate inertia particles. Thanks to well chosen sizes, it is possible to investigate the sensitivity caused by the models but also the scheme accuracy and to stress the importance of an accurate particle field resolution.

10.3.1 Description

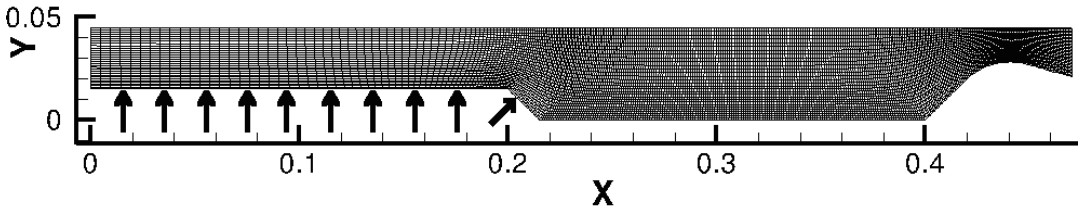

Figure 10.11: *C1 standard mesh*

The C1 test case corresponds to the internal geometry of a motor built to favor a vortex shedding phenomenon inside the chamber. To achieve this, the injection surface, the grain, is located in the first half of the chamber and is interrupted by a sharp edge. This configuration gives rise to a flow induced excitation coupled to the acoustics of the chamber, essentially locked on the second longitudinal mode of the chamber, initiated by a VSA. The test case assumes a 2D-planar geometry and thus cannot be compared with any experimental data. The configuration was originally designed for single phase flow (Lupoglazoff and Vuillot 1992a; Kourta 1999),

Table 10.8: *Gas and particle properties for the C1 test case*

Gas	Value	**Droplets**	Value
γ	1.14	ρ_p	$1766\,Kg/m^3$
$\dot{m}_g$	$21.201\,Kg/m^2/s$	$\dot{m}_p$	$8.3956\,Kg/m^2/s$
$C_{p,g}$	$2439.03\,J/Kg/K$	$C_{p,p}$	$1375\,J/Kg/K$
T_0	$3387\,K$	$T_{p,0}$	$3387\,K$
μ	$3.6 \times 10^{-4}\,Pa \cdot s$	$V_{p,inj}$	$= V_{g,inj}$
Pr	1		

then extended to the study of two-phase flow (Morfouace and Tissier 1995; Dupays 1996) with properties given in Table 10.8 and mesh provided in Figure 10.11.

Since unsteady acoustic phenomena are the main issues under investigation, a high temporal resolution is needed, which induces small time steps. A long integration time and a high number of iterations are also required in order to attempt to draw some firm conclusions on the frequency analysis of the observed periodic flows, which justifies to some extent the relatively small size of the considered meshes. According to (Morfouace and Tissier 1995) one can find a main frequency of $2650Hz$ for the gas alone and $2250Hz$ for a flow loaded with $5\mu m$ particles. Using $16\mu m$ particles (for which the acoustic Stokes number defined as the ratio of particle relaxation time to the acoustic time (Temkin and Dobbins 1966) is close to one), oscillations are observed in (Morfouace and Tissier 1995) to be totally damped, revealing the impact of the size of the disperse phase particles on the physics in such configurations.

10.3.2 Unsteady behavior with $5\mu m$ particles

10.3.2.1 Influence of the numerical strategy

For this first step, we focus on the MK closure only. For every level of refinement, a VSA instability is triggered as it can be observed Figure 10.12 on the gas vorticity field, for the coarsest mesh of this investigation. For the C1 configuration, the impact of $5\mu m$ particles has already been studied and analyzed (Morfouace and Tissier 1995; Dupays 1996). In the present study, a monochromatic signal on the head-end pressure sensor is recorded in accordance with these previous works.

For the presented investigation, several numerical strategies are retained. Using CEDRE, a full MUSCL multislope strategy is proposed for the gas, using a HLLC scheme, and the droplets, using an exact Riemann solver. Using SIERRA, several schemes are proposed for the droplet flow and a MacCormack scheme is retained for the carrier phase. While the MUSCL scheme of CEDRE relies on a hybrid limiter (Le Touze, Murrone, and Guillard 2015), SIERRA uses a Koren limiter (see Section 6.4.2.2). As a consequence, various schemes and refinement levels, as presented in Table 10.9, are assessed on this challenging configuration. The methods give coherent results but differences exist and mostly depend on the diffusion induced by the schemes on both gas and particles. Additionally, in order to reduce the computational cost, two strategies have been considered:

1. With CEDRE, an implicit time step on the gas can be used. However, in practice, it has

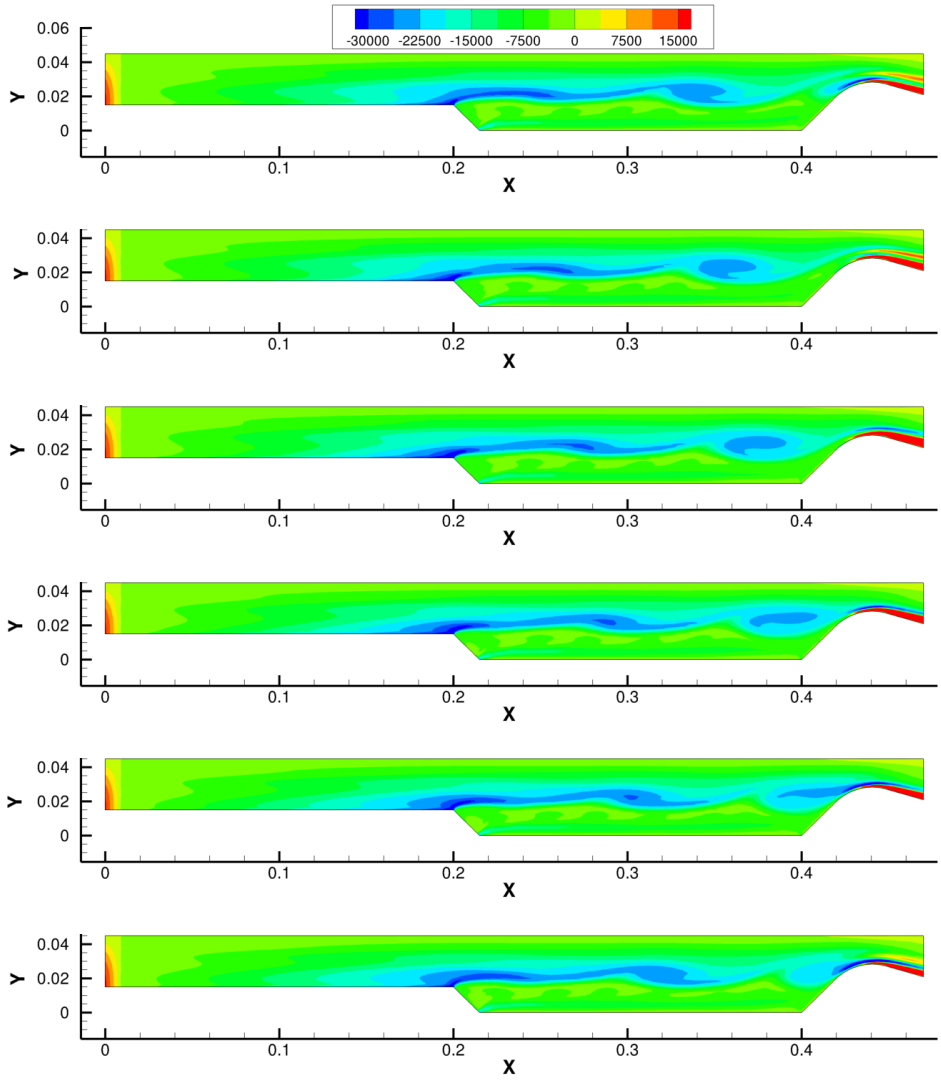

Figure 10.12: *Vorticity field evolution at established regime for* $5\mu m$ *particles using the MK closure on the standard mesh, at time* $0\,\mu s$*,* $73\,\mu s$*,* $147\,\mu s$*,* $220\,\mu s$*,* $294\,\mu s$*,* $367\,\mu s$*, from top to bottom*

Table 10.9: *Head end pressure signal for the 5μm particle configuration with the MK closure*

Scheme for: $\mathcal{T}_p$	$\mathcal{T}_g$	Main frequency	$\sqrt{2}RMS\ (mbar)$
Standard Mesh	(317×30)		
First order	MacCormack[a]	$2089 \pm 6\,Hz$	19.45
MacCormack	MacCormack[a]	$2141 \pm 6\,Hz$	33.91
Multislope	MacCormack[a]	$2153 \pm 6\,Hz$	33.63
Multislope	Multislope[b]	$2165 \pm 7\,Hz$	24.34
Multislope	Multislope[c]	$2173 \pm 7\,Hz$	19.73
Multislope	Multislope[d]	$2173 \pm 7\,Hz$	16.87
Refined Mesh	(634×60)		
First order	MacCormack[a]	$2129 \pm 6\,Hz$	25.14
MacCormack	MacCormack[a]	$2165 \pm 6\,Hz$	32.45
Multislope	MacCormack[a]	$2171 \pm 6\,Hz$	35.12
Multislope	Multislope[b]	$2165 \pm 15\,Hz$	32.72
Multislope	Multislope[c]	$2157 \pm 10\,Hz$	31.26

[a] SIERRA simulation [b] Explicit RK2 time integration using CEDRE
[c] Implicit RK1 time integration using CEDRE and twice larger time step
[d] Implicit RK1 time integration using CEDRE and three time larger time step

the effect of reducing the oscillation amplitude while the acoustic wave velocity, and thus the instability frequency remains fairly identical,

2. With SIERRA, a first order scheme for the resolution of the droplet flow can be chosen. This smears out the oscillations and introduces a shift in frequency in the same time.

As instabilities are coupled to the acoustics of the chamber, it is possible to compare the ratio of the two-phase to single-phase oscillation frequencies to the theoretical ratio of the sound propagation speed in a homogeneous two-phase medium to the one in a pure gas, as explained for instance in (Temkin and Dobbins 1966). With data provided in Table 10.9, the second ratio is 0.836, while simulations yield a first ratio of 0.83 for the more accurate simulations, using SIERRA with the MacCormack/MUSCL strategy, and about 0.81 for the first order scheme on the refined mesh. Consequently, it can be observed that the heterogeneous spatial repartition of the particles, even if better resolved by the most accurate schemes, has less influence on the speed of sound than the dispersive character of the first order scheme. Second order explicit methods for both gas and particles are necessary in order to obtain predictive results on such coarse space discretizations.

The MUSCL scheme used for the transport of particles respects the LED properties. It is thus first order at extrema which lowers the oscillation amplitude obtained in the CEDRE simulations. However, the solution quickly converges through mesh refinement to the values obtained using the MacCormack scheme for gas. Let us highlight that in the context of the MacCormack scheme used for particles, the increase of the AV for stability issues leads to an increase of the numerical diffusion and thus to a slight reduction of the oscillation amplitude through the refined mesh. Considering this behavior and the need to increase even more the AV while refining the mesh, such as in the TEP test case, the ability of this numerical strategy to produce more accurate result on such configuration is not ensured.

Table 10.10: *Head end pressure signal for the 5μm particle configuration using SIERRA and MK closure with MacCormack scheme for gas and MUSCL multislope scheme for droplets*

Closure	VSA detection	Main frequency	$\sqrt{2}RMS$ $(mbar)$	Av. Pressure (bar)
Standard mesh	(317×30)			
MK	yes	$2157 \pm 6\,Hz$	29.21	5.436
AG	yes[a]	$2144 \pm 6\,Hz$	43.48	5.469
Refined mesh	(634×60)			
MK	yes	$2164 \pm 7\,Hz$	33.77	5.448
AG	yes	$2182 \pm 7\,Hz$	34.53	5.580
Highly refined mesh	(1268×120)			
MK	yes	$2178 \pm 35\,Hz$	31.80	5.442
AG	yes	$2178 \pm 35\,Hz$	69.83	5.464

[a] Polychromatic signal

10.3.2.2 Influence of the kinetic closure

It is now proposed, using SIERRA, to evaluate the differences obtained on the pressure signal between the MK and AG closures. The numerical strategy is here the same for all the simulation and is composed of a MacCormack scheme with artificial viscosity for the carrier phase and of a MUSCL scheme with a quadratic limiter (see Section 6.4.2.2) for the particles.

While it can be clearly observed that the signal magnitude is much higher using the AG closure, no clear tendency can be deduced leading to a converged signal amplitude. Despite no clear difference can be observed between the density field of the MK and AG simulation, it appears that, thanks to the AG closure, the particles have a smaller dissipative effect on the instability. Such property can be observed both on the oscillation magnitude and on the average pressure that is also higher for the AG simulations. It can be suggested that the strict conservation of the kinetic energy of the particles through their transport by the AG contributes to that effect, however this contribution is not proved to be the main cause of this magnitude increase. Concerning instability frequency, no clear differences can be observed.

The AG simulation conducted on the coarsest grid exhibits a singular polychromatic signal as shown in Figure 10.13. By decreasing amplitude, the four main frequencies composing the signal are $2144 \pm 7H_z$, $810 \pm 7H_z$, $1334 \pm 7H_z$ and $2954 \pm 7H_z$. Using other meshes, model and numerical methods these can appear but generally at a much lower level. While the first $2144 \pm 7H_z$ and the $2954 \pm 7H_z$ frequencies correspond roughly to the second and third longitudinal mode of the chamber, the $810 \pm 7H_z$ and the $1334 \pm 7H_z$ modes are located before and after the first longitudinal mode that was originally aimed at being excited by this configuration. A detailed analysis of the normal modes of the chamber, taking into account the vortices, would be needed to understand the existence of this set of frequencies.

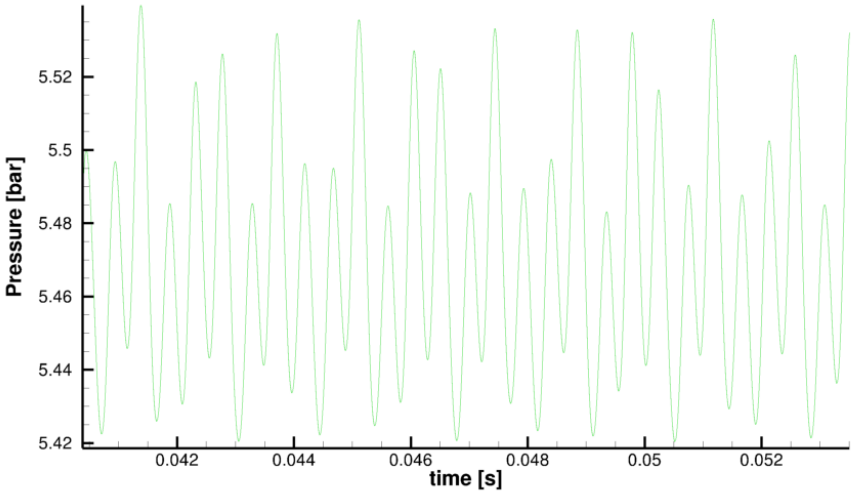

(a) Signal

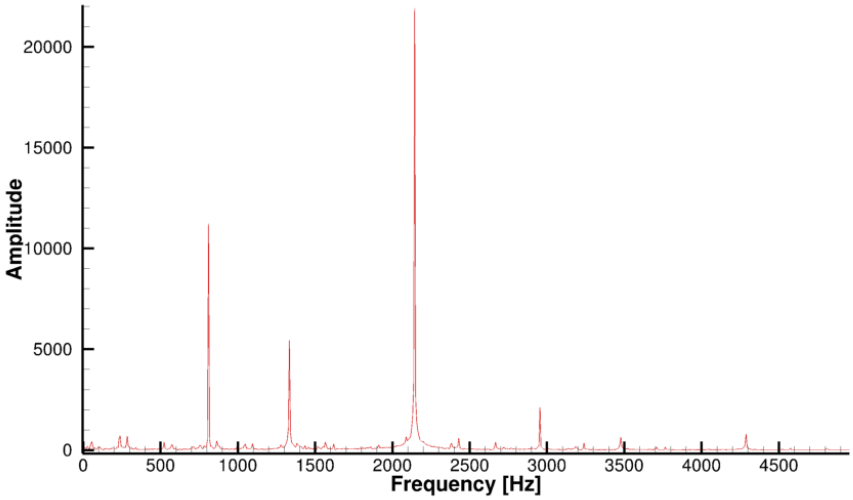

(b) FFT

Figure 10.13: *Head-end pressure signal and its FFT for* $5\,\mu m$ *particle configuration with the AG closure and the standard mesh*

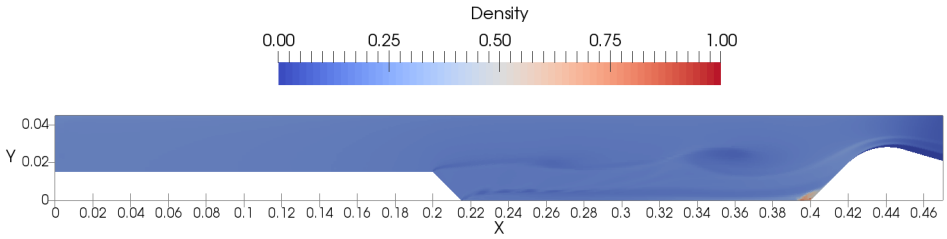

(a) $5\,\mu m$

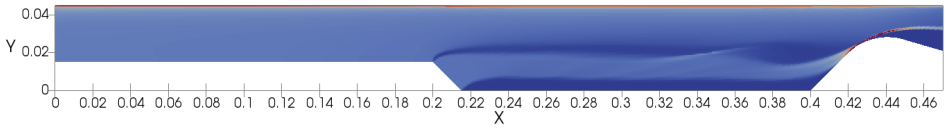

(b) $20\,\mu m$

Figure 10.14: *C1 density field obtained with SIERRA on the refined mesh using* $5\mu m$ *and* $20\mu m$ *particles with the MK closure*

10.3.3 Instability development for $20\mu m$ particles

10.3.3.1 Effect of the numerical strategy

In order to discriminate the sensitivity of the methods, simulations with $20\mu m$ particles have been conducted corresponding to a limit between a steady and an unsteady configurations, close to a bifurcation point. First, only the MK closure is studied and the same numerical methods as for Section 10.3.2.1 are retained. In Figure 10.14, it can be observed that the particles are much more scattered across the computational domain. The detection of a VSA phenomenon can be obtained using accurate schemes and/or refined mesh (see Table 10.11). Only the less diffusive scheme, with multislope method for particles and a MacCormack scheme for the carrier phase, is able to detect an instability on the standard mesh. However the observed amplitude is highly lowered compared to the results obtained through mesh refinement, which also reveals a shift of the main frequency from $2121\,Hz$ to $1463\,Hz$.

Such a mode does not match with any acoustic mode of the chamber but has already been observed in the case of $5\,\mu m$ particles using the AG. We suggest that this frequency is specifically associated to the VSA. The accurate resolution of the problem through a 1268×120 mesh using the CEDRE code confirms this tendency but it has to be highlighted that in both cases the observed signal is no more monochromatic.

10.3.3.2 Influence of the modeling

In this section, it is proposed to investigate the effect of the model on the development of this instability mode. As for the Section 10.3.3.2, SIERRA is used with the same configuration with both the MK and AG closures. Additionally, Euler-Lagrangian simulations are conducted using CEDRE and its solver SPARTE for comparison on the 634×60 and on the 1268×120 meshes. In average, the computational domain contains 4 millions of parcels for the 634×60 mesh and

Table 10.11: *Head end pressure signal for the 20μm particle configuration*

Scheme for: $\mathcal{T}_p$	$\mathcal{T}_g$	VSA detection	Main frequency	$\sqrt{2}RMS$ $(mbar)$
Standard mesh	(317×30)			
First order	MacCormack	no	-	-
MacCormack	MacCormack	no	-	-
Multislope	MacCormack	yes	$2121 \pm 16\,Hz$	0.262
Multislope	Multislope[a]	no	-	-
Refined mesh	(634×60)			
First order	MacCormack	no	-	-
MacCormack	MacCormack	no	-	-
Multislope	MacCormack	yes	$1463 \pm 13\,Hz$	17.8
Multislope	Multislope[a]	yes	$2173 \pm 13\,Hz$	6.21
Highly refined mesh	(1268×120)			
Multislope	Multislope[a]	yes	$1430 \pm 35\,Hz$	5.57

[a] Explicit RK2 time integration using CEDRE

Table 10.12: *Head end pressure signal for the 20μm particle configuration using SIERRA and MK closure with MacCormack scheme for gas and MUSCL multislope scheme for droplets*

Closure	VSA detection	Main frequency	$\sqrt{2}RMS$ $(mbar)$	Av. Pressure (bar)
Standard mesh	(317×30)			
MK	no	-	0.00	5.147
AG	yes	$2144 \pm 6\,Hz$	5.65	5.124
Refined mesh	(634×60)			
MK	yes	$2164 \pm 13\,Hz$	5.36	5.145
AG	yes	$2182 \pm 7\,Hz$	8.25	5.118
Lagrangian	yes[a]	$2128 \pm 35\,Hz$	5.31	5.165
Highly refined mesh	(1268×120)			
MK	yes	$2178 \pm 35\,Hz$	5.43	5.134
AG	yes	$2178 \pm 35\,Hz$	7.90	5.114
Lagrangian	yes[a]	$1395 \pm 70\,Hz$	5.07	5.175

[a] Polychromatic signal

12 millions for the most refined one. A snaphot of the density field obtained with each of these models is proposed in Figure 10.15.

Remark 10.3. *Despite the large number of parcels used in the Lagrangian simulation, no convergence study has been conducted and the results obtained cannot be considered as references.*

The effect of the AG on the PTC on the symmetry is not obvious. Despite velocity dispersion can be spotted in that area, the inertia of the particles is not large enough to provide a significant crossing and thus the density fields around the symmetry axis are fairly similar. The velocity dispersion is essentially located in the nozzle and in the vortices, which are larger with the AG, explaining the highest pressure signal amplitude. This lower dissipation caused by the closure leads to the appearance of VSA on the standard mesh with a significant magnitude.

Looking at the Table 10.12, it appears that the sensitivity of this case is singularly high. Using SIERRA, the simple change of limiter using the MK closure locked the frequency on the second

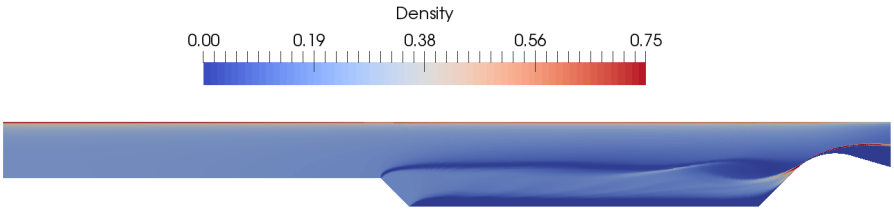

(a) MK closure

(b) AG closure

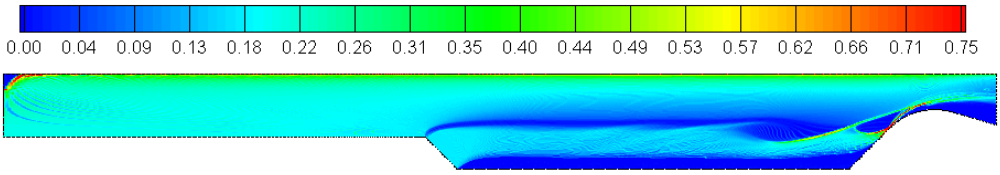

(c) Lagrangian

Figure 10.15: *C1 density field using different models*

longitudinal mode and appears to prevent from any switch of main frequency. Moreover only the frequencies of the second and third longitudinal modes appears. However, this polychromatic spectrum, involving the frequency of approximatively $1450H_z$, is not an artifact of the numerical scheme since it is clearly visible from Lagrangian simulation in Figure 10.16.

We suggest that this behavior is caused by the proximity of the configuration to a bifurcation point. In these conditions, the characteristics of the instabilities are highly dependent on the numerical methods but also on the model used for the representation of the disperse phase. The results on the frequencies, determining the nature of the instabilities, require further analysis since the magnitude of the pressure signal and the average pressure are difficult to interpret so far. We are not for now able to fully assess the obtained improvement and this work is in progress.

In order to draw firm conclusions on this case, it is essential to proceed to a much more detail analysis of the physics of this instability that is out of the scope of this work. Moreover, to ensure the reliability of the analysis, comparison with experiments appears to be necessary and cannot be conducted in a 2D planar framework beside looking for other configuration less sensitive in order to complement the obtained results. In any case however, this configuration stresses the importance of the disperse phase modeling in SRM simulation since, changing slightly the resolution of this phase only, the solved instability can be significantly affected.

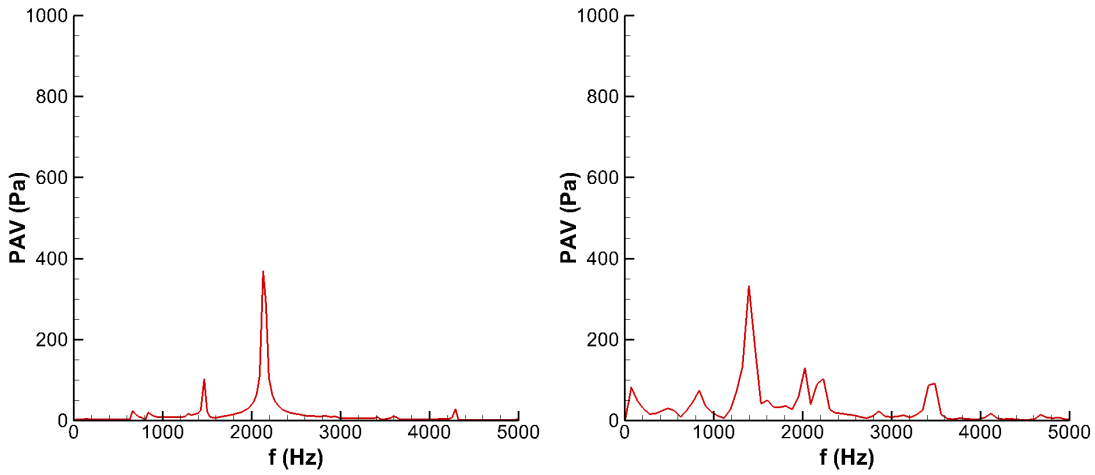

(a) 634×60 **(b)** 1268×120

Figure 10.16: *Head-end pressure FFT signal for the* $20\,\mu m$ *for Euler-Lagrange simulation with CEDRE depending on the mesh*

Chapter 11

Model validation for solid rocket motor simulations

Nobody said it was easy
It's such a shame for us to part
Nobody said it was easy
No one ever said it would be this hard
Oh, take me back to the start.

Coldplay, The scientist

This last chapter is dedicated to the investigation of an actual SRM case used for experimental studies (Dupays 1996) in order to provide a demonstration of the new simulation abilities acquired thanks to the new models and numerical methods. In a two dimensional axisymmetric geometry, it is proposed to observe the consequence of the modeling on the pressure signal measured at the head-end of the engine. Taking into account both size and velocity polydispersion, the most advanced developments provided during this work is assessed, using SIERRA only. After an introduction of the test case Section 11.1, Section 11.2 discusses of the progresses in predictability achieved thanks to this work.

11.1 C1xb test case

The C1xb has been originally designed in order to observe the VSA instability, which is the coupling between the acoustics of the chamber and vortices, caused by the occurrence of a sharp edge in the propellant grain geometry, as it can be observed on the gas vorticity field Figure 11.1. For applications, in the worst case scenario, such instability can be coupled with the natural acoustic modes of the combustion chamber and have for instance deleterious effect on the launcher components. In the case of the C1xb, it has been chosen to exacerbate this phenomenon by locating a sharp angle at the middle of the chamber to foster the coupling of hydrodynamic instabilities with the first axial acoustic mode of the cavity. The presence of particles in the internal flow, by interacting with the acoustic waves and by exchanging energy and momentum with the carrier phase, can either intensify or damp this instability or

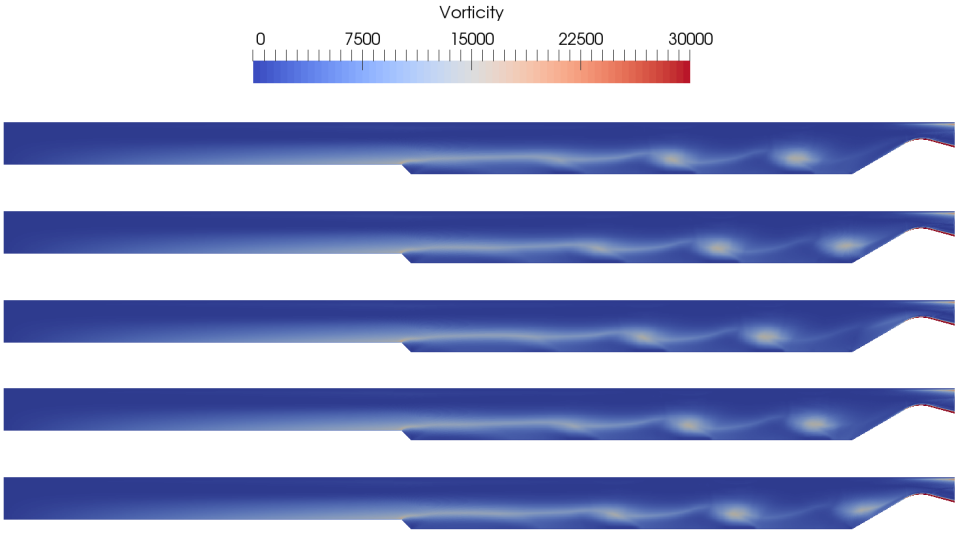

Figure 11.1: *Gas vorticity magnitude fields at established regime on the fine mesh using the AX closure at time* $0ms$*,* $0.544ms$*,* $1.088ms$*,* $1.632ms$*,* $2.176ms$*, from top to bottom*

even suppress it completely. Since the combustion of the particles can also participate to the instability, a non-reacting material has been used in order to isolate the effect of gas-particle interactions from chemical reactions.

Four models are tested in this work:

- An Equivalent Gas (EG), that is a modification of the gas thermodynamic characteristics, assuming a thermal and dynamical equilibrium between the phases (see Section 2.3.1.3),
- A monodisperse MK model where the particles are all assumed to have the same size,
- A monodisperse AG model, more specifically AX closure because of the axisymmetric character of the flow.
- An AX-TSM polydisperse simulation with 5 sections corresponding to the model presented in Section 4.2.

The original propellant has been filled with zircon particles of roughly $70\mu m$ in diameter, representing 5% of the propellant mass and a measurement of the number distribution shows a d_{10} diameter of $68.81\mu m$ and a variance of $178.9\mu m^2$. These informations can be used to build a lognormal size distribution from which the spray polydispersion is approximated. Polydisperse simulations use 5 TSM sections, that are set up based on the approximate lognormal distribution, while monodisperse simulations are conducted with a mean diameter of $70\,\mu m$. The relative mass distribution along the sections as well as the d_{30} diameter at the propellant surface for each section are given Table 11.1.

Thermodynamic properties of the propellant combustion products are given in Table 11.2. The values given in column *equivalent gas* are deduced from chemical, thermal and dynamical equilibrium of the mixture after combustion. Values given in column *gas alone* are deduced from the thermodynamical properties at equilibrium of the gaseous products. These components are

Table 11.1: *Mass ratio and d_{30} diameter for each section of the polydisperse simulations*

section	$0-55\mu m$	$55-65\mu m$	$65-75\mu m$	$75-90\mu m$	$90-120\mu m$
mass ratio	5.04%	17.0%	27.0%	33.6%	17.4%
D_{30}	$50.3\mu m$	$60.4\mu m$	$69.8\mu m$	$81.3\mu m$	$98.1\mu m$

Table 11.2: *Thermodynamic properties of the mixture*

(a) Carrier phase properties

Characteristic	equivalent gas	gas alone
γ	1.246	1.253
r	$374.97\,J/kg/K$	$394.71\,J/kg/K$
μ_g	$6.6\cdot10^{-5}\,kg/m/s$	$6.6\cdot10^{-5}\,kg/m/s$
P_r	0.458	0.472

(b) Carried phase properties

$C_{p,l}$	$821.7\,J/kg/K$
ρ_l	$3850\,kg/m^3$

then injected in the chamber using the properties provided in Table 11.3, with both phases at dynamical equilibrium.

Finally, the presented modeling does not involve turbulence and the governing equations (4.25) are solved directly without any filtering or Reynolds averaging procedure. At the chosen instant, experiments exhibit a clear dominance of the vortex shedding on the turbulence and, therefore, even without modeling of the turbulence, the numerical results can be compared with it (Kourta 1999). Moreover, in order to provide a sufficient frequency resolution, numerous iterations are necessary and thus, to maintain affordable computational cost, the mesh size remains rather coarse and the referential 2D axisymmetric. Two grids of different levels of refinement are used. The coarse one with 506×40 cells, already used in (Dupays 1996; Dupays et al. 2000), and a fine one with 1012×80 cells.

The numerical method used for this case relies on a MacCormack scheme for the gas and a MUSCL multislope method for the droplets using an HLLE Riemann solver and a minimod limiter for the disperse phase. Obviously, since the simulation is axisymmetric, the boundary condition designed in Section 7.4 is used on the symmetry (see Section 9.2 and Section 10.2.2 for further explanations). Aside the injection already described and the supersonic outlet, the remaining boundary conditions are adiabatic no-slip walls.

11.2 Model discrimination

On the coarse grid, no VSA is detected due to the intrinsic diffusion of the scheme together with the grid. However, as it is reported on the Table 11.4, the instability is triggered on the fine mesh.

Table 11.3: *Injection conditions*

Characteristic	equivalent gas	gas alone	droplets
$\dot{m}_{inj}$	$6.80757\,kg/m^2/s$	$6.467191\,kg/m^2/s$	$0.340378\,kg/m^2/s$
T_{inj}	$2064K$	$2064K$	$2064K$

Table 11.4: *Head-end pressure sensor main oscillation*

Grid	Closure	Average	Main frequency	$\sqrt{2}RMS$
507×41	EG	$11.235bar$	$676.7 \pm 5Hz$	$1.39mbar$
507×41	MK	$10.794bar$	-	-
507×41	AX	$10.796bar$	-	-
507×41	MK-TSM	$10.743bar$	$698 \pm 6Hz$	$6.40mbar$
507×41	AX-TSM	$10.746bar$	$686 \pm 13Hz$	$11.35mbar$
1013×81	EG	$11.28bar$	$667 \pm 15Hz$	$11.7mbar$
1013×81	MK	$10.790bar$	$704 \pm 15Hz$	$14.5mbar$
1013×81	AX	$10.798bar$	$704 \pm 15Hz$	$25.4mbar$
1013×81	MK-TSM	$10.752bar$	$660 \pm 30Hz$	$9.19mbar$
1013×81	AX-TSM	$10.762bar$	$643 \pm 45Hz$	$10.1mbar$
Experiment	-	$11.5 \pm 0.5bar$	$740 \pm 15Hz$	$15 \pm 2mbar$

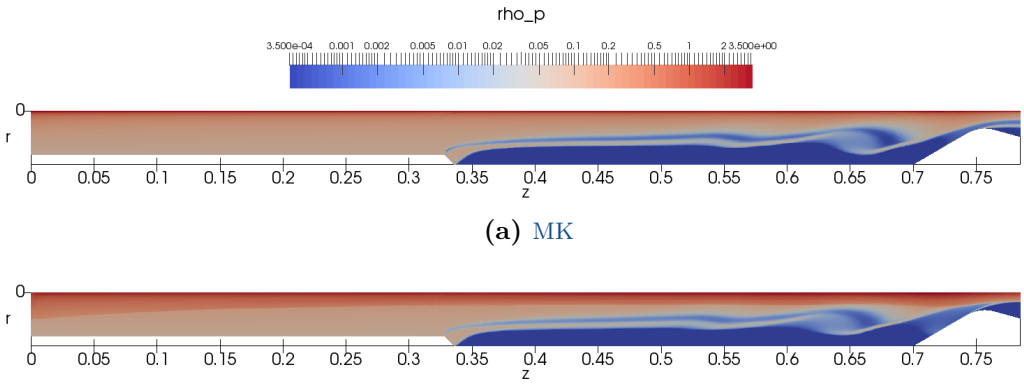

(a) MK

(b) AX

Figure 11.2: *Instantaneous density fields using the MK and AX closure on the monodisperse C1xb case*

Such capacity of the instability to be triggered however also depends on the represented droplet size distribution. It appears that using a monodisperse spray, the VSA is completely damped and relying of the EG model, the amplitude of the disturbance is rather small. However, using the TSM description of the spray polydispersion, the instability is triggered. Such phenomenon is supposed to be caused by the large variety of droplet sizes, containing the diameter range able to exacerbate the first acoustic modes of the chamber and thus stimulate the vortex shedding.

As already observed in Section 10.3, the amplitude obtained with the AG closure is much higher than with the MK closure. The explanation proposed for the C1 remains identical here. It can however be observed that the δ-shock visible in Figure 11.2 disappears with the AX closure thanks to velocity dispersion, which was not clearly visible with the C1 because of the relatively small inertia of the particles. The extrema of density observed in the C1xb MK simulation is of $1073\,kg/m^3$ whereas using the AX closure, the density does not exceed $3.8\,kg/m^3$. This is the consequence of the spatial mass distribution that is much more diffused across the computational domain using the AX closure. This results is obtained thanks to the PTC occurring on the symmetry axis with this closure as it can be seen in Figure 11.3.

On the fine mesh, the consideration of size polydispersion decreases the magnitude of the signal obtained, compared to monodisperse simulations. Such dissipation of the signal is caused by

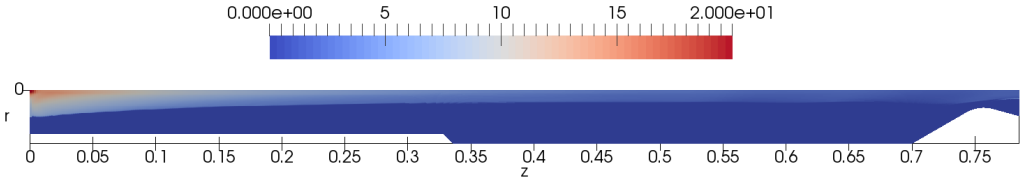

(a) σ_{rr}

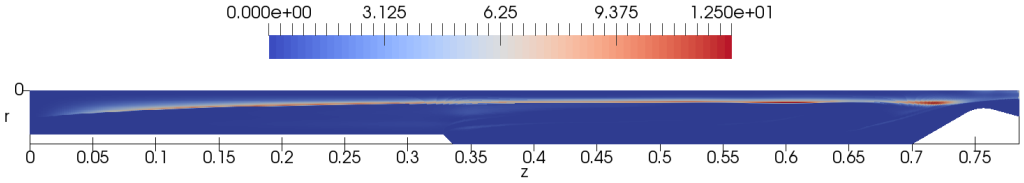

(b) σ_{zz}

Figure 11.3: *Instantaneous velocity dispersion using AX closure on the monodisperse C1xb case*

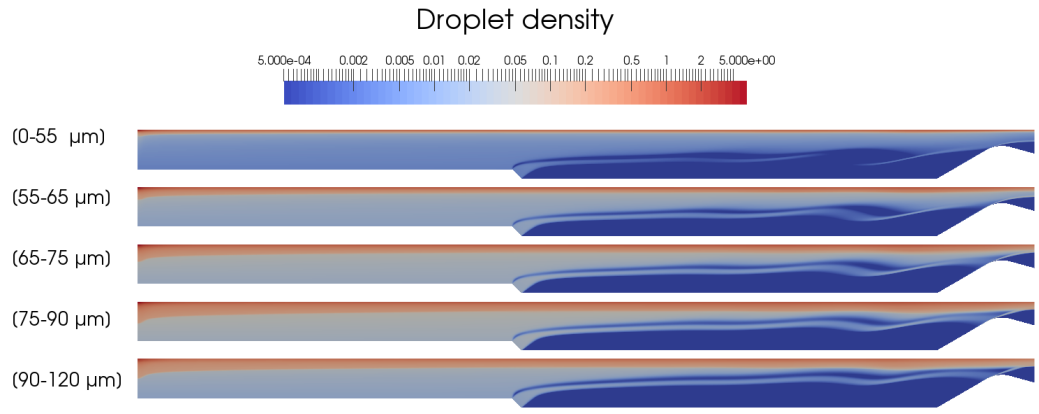

Figure 11.4: *Instantaneous droplet density fields using AX-TSM closure on the C1xb case*

the multi-fluid TSM size discretization for both kinetic closures because of the consideration of smaller droplets in the flow. Results presented Table 11.3 exhibit the effects of the closures on the pressure signal obtained. Independently and combined, size and velocity polydispersion significantly change the characteristics of the instability predicted.

The results are however difficult to compare with the experiments since a significant gap remains between the numerical results and the experimental ones. Because the frequency of the first longitudinal mode and the pressure are higher than the predicted one. It can be supposed that the temperature of combustion of the propellant, not measured but theoretically obtained, may have been underestimated or fluid characteristics wrongly determined. Nevertheless, other configurations, including industrial applications, shall be investigated in the future in order to acquire a complete knowledge of improvement obtained by the enhancement of two-phase flow models.

Remark 11.1. *Using a less dissipative limiter for the carried phase, it has been possible to trigger the instability on the* 507×41 *mesh with monodisperse closures. But, for the homogeneity of the numerical methods for all the simulations, the minmod limiter has been kept.*

Conclusion

I find my own completeness
The darkness and the weakness
The light, the fight, the quietness

Silent Poets, Asylums for the Feeling

Motivated in predicting SRMs performances with a high fidelity, the work conducted in this thesis aimed at modeling the internal two-phase flow of these engines and more specifically the dynamics of the disperse phase. Capturing hydrodynamic instabilities remains a major goal for the prediction of the behavior of these engines and the subject of numerous researches (Kuentzmann 1973; Dupays 1996; Simoes 2006; Doisneau 2013; Sibra 2015; Genot 2018; Hirschberg et al. 2018). This work specifically contributed to this area of research by the design of numerical tools for the resolution of the droplets flow. Since the engine behavior is clearly modified by two-way coupling effects, it is a key issue to model the disperse phase, for which a high sensitivity can be observed. In this context, aiming at predicting the behavior of these engines through numerical simulations, the work focused on state of the art models and numerical methods for the resolution of the disperse phase.

For this objective, it has been chosen to rely on a Euler-Euler modeling of the flow. Taking into account PTC while representing the droplet dynamics in an Eulerian framework is a challenging task, which has been proposed to be tackled thanks to the assumption of the local velocity distribution of the droplets under the form of multi-variate Gaussian form (AG). Thanks to the well posed mathematical properties of the systems of equations derived from this closure, it has been possible to design efficient and accurate numerical methods able to cope with a large panel of singularities, including shocks, δ-shocks, vacuum and zero pressure areas. Ensuring the realizability and the high order accuracy of schemes for the transport of particles in the physical space, especially in industrial configuration involving unstructured meshes, a new step in the predictive character of the numerical method for SRMs has been reached. Thus, comparing to the state of the art during the 90's, instabilities can be triggered with coarser meshes and spurious effects are almost completely removed. Such achievement is critical since, for the mesh resolution that can be reached today, the singularities become increasingly difficult to cope with, especially for δ-shocks that cause an intensive and non-physical coupling between the phases. The introduction AG closure prevents this last phenomena and, together with the designed realizable numerical methods, opens the way for two-phase flows simulation of very high resolution for SRM applications.

The developments provided during this thesis focus on the MF modeling of droplet flows with

size and velocity polydispersion and the resolution of these systems of equations. Relying on an AG closure in velocity and a affine TSM method for the size polydispersion, the internal flow of SRM is accurately described. Then, thanks to the MUSCL multislope on the one hand and to the QKS method on the other hand, polydisperse spray with droplet of low up to moderate inertia can be solved with accuracy thanks to highly robust methods. Moreover, aiming at application and industrial geometries, the presented work is fully compatible with general unstructured meshes and has been extended to the axisymmetric framework. In this last context, innovative treatment of the symmetry axis and a original derivation of the HLL Riemann solver were proposed is order to cope with PTC on the symmetry axis.

Thanks to the collaboration with C. Le Touze (Le Touze, Murrone, and Guillard 2015), the integration of the new closure is in progress in CEDRE. The effort provided in rewriting the in-house code SIERRA allowed, ahead from the integration in CEDRE, to assess numerical strategies and implementation methodologies, including an investigation of memory shared parallelization through the OpenMP API. Tests conducted in various configurations, mostly dedicated to SRM simulations, proved the ability of the strategy to be robust and accurate, providing precious comparison tools to validate future implementations. We finally summarized the contributions and the perspectives of the work conducted during this thesis:

Achievement:

- **Design of the AG-TSM model**: a closure, taking into account both the size and the velocity polydispersion, has been proposed for purpose of modeling two-phase disperse flows in SRMs. The derived systems of equations have possess well-posed mathematical properties.

- **Derivation in the axisymmetric framework**: the AG closure has been derived in a cylindrical coordinate system for the purpose of axisymmetric simulations. It appears that, unlike for the Euler equations, the assumptions are not limited to the swirling and no-swirling flow duality. More specifically, an intermediate assumption of symmetric velocity distribution has been revealed to be crucial for axisymmetric particle flow.

- **Design of dedicated and realizable numerical schemes for the transport of the droplets**: a realizable MUSCL multislope scheme has been designed for the resolution of the AG equations able to cope its non-linearities. In many configurations, singularities such as vacuum, shocks and zero pressure areas have been solved without the generation of spurious phenomena. Innovative developments have been proposed for limiters and Riemann solvers. This scheme, is proved realizable, and thus appeared through the tests to be highly robust and accurate.

- **Specific treatment of the symmetry axis**: through the tests conducted in the axisymmetric framework, it was shown that a specific treatment of this boundary was needed in the case of the AG closure for two-phase disperse flow. With the methods found in the literature, no PTC on the symmetry axis could be generated for AG. A solution has been proposed for that purpose but still requires some improvements.

- **Design of an accurate scheme for the treatment of the combined effects of drag, heat exchange and evaporation**: based on the work of (Laurent, Sibra, and Doisneau 2016; Sibra et al. 2017), the QKS has been derived for the sake of the resolu-

tion of the AG-TSM closure and proved realizable. As a consequence, combined with the designed MUSCL multislope scheme, a realizable numerical strategy able to solve industrial configurations considering size and velocity polydispersion has been provided and assessed.

- **Development of an in-house CFD code**: for the need of the integration of the new models and numerical methods ahead from the CEDRE software, the SIERRA has been rewritten. Through this development, investigations on memory shared parallelism strategies and implementation methodologies, based on object oriented programming, have been conducted.

Observations:

- **Sensitivity to the numerical methods**: one of the first observations concerns the quality of the resolution of the numerical methods. The test cases provided stress the necessity of high resolution schemes to trigger instabilities on coarse grids. Moreover, numerical spurious effects appearing near singularities and, especially with the MK closure when δ-shocks or vacuum arise, can prevent the simulations to converge toward the exact solution. The improvements, compared the state of art of the 90's, have been observed on SRM configurations.

- **Sensitivity to the closure**: studying the pressure signals in both the C1 and the C1xb test cases, it has been observed that the signal magnitude is increased using the AG closure instead of the MK. Another influence can be observed from the size polydispersion using the affine TSM model, suggesting that both size and velocity polydispersion need to be considered for predictive simulations. No clear tendency of the modifications of the pressure signal can however be deduced and, to our knowledge, this case remains dependent. The effects of the numerics and the closure, depending on the condition, can be of the same order of magnitude.

Perspectives:

- **Improvement of the QKS method**: still under development, the QKS should soon be improved thanks to the reconstruction of the average velocity of the distribution and its dispersion in the phase space for the AG-TSM. Already proposed for the MK closure (Laurent, Sibra, and Doisneau 2016), it is expected to obtain the second order accuracy in any fields thanks to the QKS.

- **Asymptotic preserving schemes for the axisymmetric source terms**: because of the major singularity potentially appearing on the axis of symmetry, the used of asymptotic preserving scheme (Berthon and Turpault 2011) shall be investigated to manage the axisymmetric source terms and preserve the consistency of the methods near this limit. These terms have been determined to drive the crossing on the axis, where they dominate the flow.

- **Determinations of I_{sp} losses**: still difficult to be achieved todays, the amelioration of the predictability of the CFD codes thanks to an improvement of models and numerical methods lets hope for reliable prediction of the I_{sp} losses in a near future.

- **Coalescence and break-up**: not studied through this work, the AG closure enables the possibility to treat the coalescence not only between different sections but also inside the same section through the MF formalism. Despite having, together with the break-up, a significant impact on the SRM behavior and performances (Doisneau et al. 2013), these have been neglected in this work for the sake of simplicity.

- **Combustion**: also neglected in this work, there is a great interest in the modeling of aluminum combustion and the resolution of ITHAC (Sibra 2015; Genot, Gallier, and Schuller 2017). For the resolution of such phenomena, the AG-TSM method and corresponding numerical schemes can be easily extended while ensuring realizability and is thus a valuable candidate.

- **Turbulence**: advanced three dimensional simulations clearly shows the presence of turbulence inside SRMs (Fabignon et al. 2016), Following the work of (Zaichik, Alipchenkov, and Sinaiski 2008; Sabat 2016; Mercier 2018), it is possible to model the spacial dispersion of the droplets thanks to the AG approach. However, the consideration of two-way coupling effects remains a complex task, which may required an adapted closure of the carrier phase for the sake of consistency.

- **Instability and performance prediction**: thanks to the introduction in CEDRE of always more realistic physical models and to the continuously improvement of the associated numerical methods, an enhancement of the reliability of the CFD simulation is to be expected. Moreover, thanks to the industrial configuration able to be carried out by CEDRE, an improvement of the knowledge of SRMs in the future thanks to simulations as well as an enhancement of their design can be foreseen.

- **Other applications**: finally we suggest that the developments provided during this work can find other fields of applications including energetic applications as automotive and aeronautic injection (Sabat 2016; Emre 2014), Liquid Rocket Engines (Cordesse 2019) or icing but also of other fields of physics as micron-scale and rarefied gas dynamics (McDonald and Groth 2005; Groth and McDonald 2009) or plasmas (Graille, Magin, and Massot 2009), where the AG closure is also considered. Such derivations of these tools, designed in the manuscript for the sake of SRM simulations, shall be achieved naturally through CEDRE for all applications related to energetics while the theoretical development conducted should find even wider usage.

Appendix A

Résumé en français

Les gouttes d'oxyde d'aluminium présentes en masse dans l'écoulement interne des moteurs-fusées à propergol solide ont tendance à influencer de façon significative l'écoulement et le fonctionnement du moteur quel que soit le régime. L'objectif de la thèse est d'améliorer les modèles diphasiques eulériens présents dans le code de calcul semi-industriel pour l'énergétique de l'ONERA, CEDRE, en y incluant la possibilité d'une dispersion locale en vitesse des particules en plus de la dispersion en taille déjà présente dans le code, tout en gardant une structure mathématique bien posée du système d'équations à résoudre. Cette nouvelle caractéristique rend le modèle capable de traiter les croisements de trajectoires anisotropes, principale difficulté des modèles eulériens classiques pour les gouttes d'inertie modérément grande.

En plus de la conception et de l'analyse détaillée d'une classe de modèles basés sur des méthodes de moments, le travail se concentre sur la résolution des systèmes d'équations obtenus en configurations industrielles. Pour cela, de nouvelles classes de schémas précis et réalisables pour le transport des particules dans l'espace physique et l'espace des phases sont développées. Ces schémas assurent la robustesse de la simulation malgré différentes singularités (dont des chocs, δ-chocs, zones de pression nulle et zones de vide...) tout en gardant une convergence d'ordre deux pour les solutions régulières. Ces développements sont conduits en deux et trois dimensions, en plus d'un référentiel bidimensionnel axisymétrique, dans le cadre de maillages non structurés.

La capacité des schémas numériques à maintenir un niveau de précision élevé tout en restant robustes dans toutes les conditions est un point clé pour les simulations industrielles de l'écoulement interne des moteurs à propergol solide. Pour illustrer cela, le code de recherche SIERRA, originellement conçu durant les année 90 pour les problématiques d'instabilités de fonctionnement en propulsion solide, a été réécrit afin de pouvoir comparer deux générations de modèles et de méthodes numériques et servir de banc d'essais avant une intégration dans CEDRE. Les résultats obtenus confirment l'efficacité de la stratégie numérique choisie ainsi que le besoin d'introduire, pour les simulations axisymétriques, une condition à la limite spécifique, développée dans le cadre de cette thèse. En particulier, les effets à la fois du modèle et de la méthode numérique dans le contexte d'une simulation de l'écoulement interne instationnaire dans les moteurs-fusées à propergol solide sont détaillés. Par cette approche, les liens entre des aspects fondamentaux de modélisation et de schémas numériques ainsi que leurs conséquences pour les applications sont mis en avant.

Le manuscrit est divisé en onze chapitres répartis dans trois parties. Ces derniers décrivent le travail effectué comme il suit :

- La Partie I s'intéresse à la modélisation de l'écoulement interne des moteurs-fusées à propergol solide, allant de la modélisation en pré-étude aux modèles les plus avancés comme ceux étudiés et dérivés au cours de la thèse,

  - Le Chapitre 1 est plus particulièrement dédié au contexte de la thèse et aux moteurs-fusées à propergol solide. Après une description du fonctionnement de ces moteurs par une approche historique et technologique, une description des enjeux dans ce domaine met en avant le besoin de prédiction de performance de ces moteurs,

  - Prenant en compte les caractéristiques de fonctionnement de tels engins, le Chapitre 2 se concentre sur la modélisation des écoulements diphasiques. Après une revue générale du problème, une classe de modèles eulériens satisfaisant de bonne propriétés mathématiques est choisie pour des investigations plus poussées,

  - Dans le Chapitre 3, grâce à une approche de type Kinetic-Based Moment Methods (KBMM), les équations de transport du gaz et des particules sont fermées grâce à différente hypothèses incluant notamment la fermeture Gaussienne Anisotrope (AG) pour prendre en compte la dispersion en vitesse de la phase dispersée. La dérivation se concentre entre autre sur les propriétés mathématiques de ces systèmes et sur la fermeture des équations dans un référentiel axisymétrique en détaillant les hypothèses associées,

  - En se basant sur une approche Multi-Fluid (MF), le Chapitre 4 propose une classe de fermeture capable de prendre en compte simultanément la dispersion en taille et en vitesse des particules. En couplant les descriptions du gaz et des particules, des modèles prenant en compte les effets de couplage réciproque (two-way coupling) sont proposés,

- La Partie II se concentre sur les méthodes numériques associées aux systèmes d'équations dérivées. Une attention particulière est portée sur la préservation de la réalisabilité des champs étudiés, même en configurations industrielles,

  - Dans le Chapitre 5, les schémas d'intégrations en temps sont décrits en se basant sur une stratégie de séparation d'opérateur. Afin de traiter les termes source associés aux sprays évaporants avec précision et robustesse, un schéma dédié de type Quadrature Kinetic Scheme (QKS) est mis en place,

  - Le Chapitre 6 se focalise quant à lui sur la résolution des équations de transport dans un référentiel eulérien. Le développement proposé se base essentiellement sur des méthodes de type volumes finis avec des apports spécifiques pour les configurations axisymétriques. Les méthodes d'ordre deux mises en place sont prouvées réalisables,

  - Le Chapitre 7 complète le précédent avec la description du traitement des bords du domaine de calcul. Au-delà des solutions standards, une méthodologie spécifique et originale pour l'axe de symétrie en condition axisymétrique est proposée.

- La Partie III illustre l'apport des développements conduits dans les précédentes à travers un ensemble de cas tests. Ils mettent en avant les particularités des schémas et des fermetures,

  – Dans un premier temps, le Chapitre 8 présente les codes de calcul utilisés. Les capacités et performances du code multi-physique pour l'énergétique CEDRE de l'ONERA et du code de recherche SIERRA sont mis en avant,

  – La qualité d'implémentation et les capacités des méthodes numériques mises en place sont vérifiées Chapitre 9. Ce dernier se base sur des cas tests standards auxquels un cas spécifique est ajouté mettant en avant les difficultés intrinsèques au traitement de l'axe de symétrie pour cette classe de modèle, particulièrement critique dans le cadre de ce travail,

  – Le Chapitre 10 met en avant les effets de la dispersion en vitesse des particules. Les configurations choisies, bien que fictives, permettent une description qualitative de l'apport de ce nouveau niveau de modélisation proposé dans la thèse,

  – Finalement, le Chapitre 11 présente un calcul de démonstration sur un moteur tiré expérimentalement. Les effets de la phase dispersée et de la polydispersion en taille et/ou en vitesse sont mis en avant.

Le travail effectué se situe dans un contexte large et pluridisciplinaire faisant intervenir notamment la modélisation d'écoulement de phase dispersée, la conception de schémas numériques pour les équations différentielles partielles hyperboliques et l'implémentation de ces apports sur un code parallèle. Plus concrètement, les apports les plus importants de la thèse se concentrent dans les points suivants :

- **Dérivation de l'AG en coordonnées axisymétrique :** Une dérivation des équations pour la fermeture gaussienne anisotrope et plus généralement pour toutes les équations basées sur des méthodes de moments a été conduite Section 3.3. Cette approche met en avant des particularités près de l'axe de symétrie qui ne sont habituellement pas observées pour les équations d'Euler,

- **Dérivation de l'AG-TSM :** Une fermeture faisant intervenir simultanément la dispersion en taille et en vitesse des particules de la phase dispersée pour les écoulements couplés two-way est proposée Section 4.2,

- **Méthode QKS pour l'AG-TSM :** Afin de résoudre efficacement le couplage entre les phases de l'écoulement, un schéma est spécifiquement conçu Section 5.3,

- **Solveur HLL dédié à l'axi :** Un solveur de Riemann est dérivé de manière originale dans un référentiel axisymétrique Section 6.3.3.3 en faisant intervenir la distance à l'axe de symétrie dans l'expression du flux,

- **Méthode MUSCL multipente pour l'AG :** Décrite Section 6.4.2, cette méthode permet de résoudre avec précision et surtout avec robustesse les équations de transport du gaz et des particules, y compris en régimes instationnaires,

- **Démonstration de réalisabilité :** Une large classe de méthodes volumes finis sur maillage non-structuré, à laquelle appartient la méthode multipente proposée, est prouvée réalisable Section 6.4.3, pour les systèmes hyperboliques non-linéaires,

- **Condition limite dédiée :** Les fortes singularités rencontrées sur l'axe de symétrie ne permettent pas l'utilisation d'une méthodologie usuelle et demandent la mise en place d'un traitement spécifique de la limite comme proposé Section 7.4,

- **Développement d'un code parallèle :** Les modèles et méthodes ont été intégrés dans le code SIERRA, parallélisé pour l'occasion en mémoire partagée comme décrit Section 8.2 et intégrant les dernières normes FORTRAN.

Comme présenté dans les derniers chapitres, l'ensemble de ces apports permet aujourd'hui la conduite de simulations d'écoulements diphasiques polydispersés en taille et en vitesse en configurations industrielles. Cela ouvre la voie à des simulations à la prédictibilité accrue pour l'étude notamment des performances et de la stabilité des moteurs-fusées à propergol solide.

Appendix B

Devellopped form of governing equations

B.1 10-moment anisotropic Gaussian closure for disperse phase flow

B.1.1 3D form in cartesian coordinates

Starting from the following notations:

$$h_{ij} = \frac{1}{2}u_i u_j + \frac{3}{2}\sigma_{ij} = 3e_{ij} - u_i u_j = \frac{\rho e_{ij} + P_{ij}}{\rho} \tag{B.1}$$

where $u_1 = u$, $u_2 = v$ and $u_3 = w$, the system stands:

$$\begin{cases}
\partial_t \rho & +\partial_x \rho u & +\partial_y \rho v & +\partial_z \rho w = 0 \\
\partial_t \rho u & +\partial_x (\rho uu + P_{11}) & +\partial_y (\rho vu + P_{12}) & +\partial_z (\rho wu + P_{13}) = 0 \\
\partial_t \rho v & +\partial_x (\rho uv + P_{12}) & +\partial_y (\rho vv + P_{22}) & +\partial_z (\rho wv + P_{23}) = 0 \\
\partial_t \rho w & +\partial_x (\rho uw + P_{13}) & +\partial_y (\rho vw + P_{23}) & +\partial_z (\rho ww + P_{33}) = 0 \\
\partial_t (\rho e_{11}) & +\partial_x [\rho u h_{11}] & +\partial_y [\frac{\rho}{3}(2uh_{12} + vh_{11})] & +\partial_z [\frac{\rho}{3}(2uh_{13} + wh_{11})] = 0 \\
\partial_t (\rho e_{12}) & +\partial_x [\frac{\rho}{3}(2uh_{12} + vh_{11})] & +\partial_y [\frac{\rho}{3}(uh_{22} + 2vh_{12})] & +\partial_z [\frac{\rho}{3}(uh_{23} + vh_{13} + wh_{12})] = 0 \\
\partial_t (\rho e_{13}) & +\partial_x [\frac{\rho}{3}(2uh_{13} + wh_{11})] & +\partial_y [\frac{\rho}{3}(uh_{23} + vh_{13} + wh_{12})] & +\partial_z [\frac{\rho}{3}(uh_{33} + 2wh_{13})] = 0 \\
\partial_t (\rho e_{22}) & +\partial_x [\frac{\rho}{3}(uh_{22} + 2vh_{12})] & +\partial_y [\rho v h_{22}] & +\partial_z [\frac{\rho}{3}(2vh_{23} + wh_{22})] = 0 \\
\partial_t (\rho e_{23}) & +\partial_x [\frac{\rho}{3}(uh_{23} + vh_{13} + wh_{12})] & +\partial_y [\frac{\rho}{3}(2vh_{23} + wh_{22})] & +\partial_z [\frac{\rho}{3}(vh_{33} + 2wh_{23})] = 0 \\
\partial_t (\rho e_{33}) & +\partial_x [\frac{\rho}{3}(uh_{33} + 2wh_{13})] & +\partial_y [\frac{\rho}{3}(vh_{33} + 2wh_{23})] & +\partial_z [\rho w h_{33}] = 0
\end{cases} \tag{B.2}$$

B.1.2 2D-planar form

$$\begin{cases} \partial_t \rho & +\partial_x \rho u & +\partial_y \rho v = 0 \\ \partial_t \rho u & +\partial_x (\rho uu + \rho\sigma_{11}) & +\partial_y (\rho uv + \rho\sigma_{12}) = 0 \\ \partial_t \rho v & +\partial_x (\rho uv + \rho\sigma_{12}) & +\partial_y (\rho vv + \rho\sigma_{22}) = 0 \\ \partial_t (\rho uu + \rho\sigma_{11}) & +\partial_x (\rho uuu + 3\rho u\sigma_{11}) & +\partial_y (\rho uuv + \rho v\sigma_{11} + 2\rho u\sigma_{12}) = 0 \\ \partial_t (\rho uv + \rho\sigma_{12}) & +\partial_x (\rho uuv + 2\rho u\sigma_{12} + \rho v\sigma_{11}) & +\partial_y (\rho uvv + 2\rho v\sigma_{12} + \rho u\sigma_{22}) = 0 \\ \partial_t (\rho vv + \rho\sigma_{22}) & +\partial_x (\rho uvv + \rho u\sigma_{22} + 2\rho v\sigma_{12}) & +\partial_y (\rho vvv + 3\rho v\sigma_{22}) = 0 \end{cases} \tag{B.3}$$

B.1.3 2D-axisymetrical form using azimuthal homogeneous flow assumption

B.1.3.1 Using geometrical correction

$$\begin{cases} \partial_t \rho & +\partial_r \rho u_r & +\partial_z \rho u_z & = -\frac{\rho u_r}{r} \\ \partial_t \rho u_r & +\partial_r (\rho u_r u_r + P_{rr}) & +\partial_z (\rho u_z u_r + P_{rz}) & = -\frac{1}{r}\left[\rho u_r u_r + P_{rr} - (\rho u_\theta u_\theta + P_{\theta\theta})\right] \\ \partial_t \rho u_\theta & +\partial_r (\rho u_r u_\theta + P_{r\theta}) & +\partial_z (\rho u_z u_\theta + P_{\theta z}) & = -\frac{2}{r}\left[\rho u_r u_\theta + P_{r\theta}\right] \\ \partial_t \rho u_z & +\partial_r (\rho u_r u_z + P_{rz}) & +\partial_z (\rho u_z u_z + P_{zz}) & = -\frac{1}{r}\left[\rho u_r u_z + P_{rz}\right] \\ \partial_t (\rho e_{rr}) & +\partial_r [\rho u_r h_{rr}] & +\partial_z [\frac{\rho}{3}(2u_r h_{rz} + u_z h_{rr})] & = -\frac{\rho}{3r}\left[3u_r h_{rr} - 2\left(u_r h_{\theta\theta} + 2u_\theta h_{r\theta}\right)\right] \\ \partial_t (\rho e_{r\theta}) & +\partial_r [\frac{\rho}{3}(2u_r h_{r\theta} + u_\theta h_{rr})] & +\partial_z [\frac{\rho}{3}(u_r h_{\theta z} + u_\theta h_{rz} + u_z h_{r\theta})] & = -\frac{\rho}{3r}\left[2\left(2u_r h_{r\theta} + u_\theta h_{rr}\right) - 3u_\theta h_{\theta\theta}\right] \\ \partial_t (\rho e_{rz}) & +\partial_r [\frac{\rho}{3}(2u_r h_{rz} + u_z h_{rr})] & +\partial_z [\frac{\rho}{3}(u_r h_{zz} + 2u_z h_{rz})] & = -\frac{\rho}{3r}\left[2u_r h_{rz} + u_z h_{rr} - (2u_\theta h_{\theta z} + u_z h_{\theta\theta})\right] \\ \partial_t (\rho e_{\theta\theta}) & +\partial_r [\frac{\rho}{3}(u_r h_{\theta\theta} + 2u_\theta h_{r\theta})] & +\partial_z [\frac{\rho}{3}(2u_\theta h_{\theta z} + u_z h_{\theta\theta})] & = -\frac{\rho}{3r}\left[u_r h_{\theta\theta} + 2u_\theta h_{r\theta}\right] \\ \partial_t (\rho e_{\theta z}) & +\partial_r [\frac{\rho}{3}(u_r h_{\theta z} + u_\theta h_{rz} + u_z h_{r\theta})] & +\partial_z [\frac{\rho}{3}(u_\theta h_{zz} + 2u_z h_{\theta z})] & = -\frac{2\rho}{3r}\left[u_r h_{\theta z} + u_\theta h_{rz} + u_z h_{r\theta}\right] \\ \partial_t (\rho e_{zz}) & +\partial_r [\frac{\rho}{3}(u_r h_{zz} + 2u_z h_{rz})] & +\partial_z [\rho u_z h_{zz}] & = -\frac{\rho}{3r}\left[u_r h_{zz} + 2u_z h_{rz}\right] \end{cases} \tag{B.4}$$

B.1.3.2 Using weighted conservation

$$
\begin{cases}
\partial_t\left(r\rho\right) & +\partial_r\left(r\rho u_r\right) & +\partial_z\left(r\rho u_z\right) & = 0 \\
\partial_t\left(r\rho u_r\right) & +\partial_r\left(r\rho u_r u_r + rP_{rr}\right) & +\partial_z\left(r\rho u_z u_r + rP_{rz}\right) & = \rho u_\theta u_\theta + P_{\theta\theta} \\
\partial_t\left(r\rho u_\theta\right) & +\partial_r\left(r\rho u_r u_\theta + rP_{r\theta}\right) & +\partial_z\left(r\rho u_z u_\theta + rP_{\theta z}\right) & = -\rho u_r u_\theta - P_{r\theta} \\
\partial_t\left(r\rho u_z\right) & +\partial_r\left(r\rho u_r u_z + rP_{rz}\right) & +\partial_z\left(r\rho u_z u_z + rP_{zz}\right) & = 0 \\
\partial_t\left(r\rho e_{rr}\right) & +\partial_r\left(r\rho u_r h_{rr}\right) & +\partial_z\left[\frac{r\rho}{3}\left(2u_r h_{rz} + u_z h_{rr}\right)\right] & = \frac{2\rho}{3}\left[u_r h_{\theta\theta} + 2u_\theta h_{r\theta}\right] \\
\partial_t\left(r\rho e_{r\theta}\right) & +\partial_r\left[\frac{r\rho}{3}\left(2u_r h_{r\theta} + u_\theta h_{rr}\right)\right] & +\partial_z\left[\frac{r\rho}{3}\left(u_r h_{\theta z} + u_\theta h_{rz} + u_z h_{r\theta}\right)\right] & = \frac{\rho}{3}\left[3u_\theta h_{\theta\theta} - 2u_r h_{r\theta} - u_\theta h_{rr}\right] \\
\partial_t\left(r\rho e_{rz}\right) & +\partial_r\left[\frac{r\rho}{3}\left(2u_r h_{rz} + u_z h_{rr}\right)\right] & +\partial_z\left[\frac{r\rho}{3}\left(u_r h_{zz} + 2u_z h_{rz}\right)\right] & = \frac{\rho}{3}\left[2u_\theta h_{\theta z} + u_z h_{\theta\theta}\right] \\
\partial_t\left(r\rho e_{\theta\theta}\right) & +\partial_r\left[\frac{r\rho}{3}\left(u_r h_{\theta\theta} + 2u_\theta h_{r\theta}\right)\right] & +\partial_z\left[\frac{r\rho}{3}\left(2u_\theta h_{\theta z} + u_z h_{\theta\theta}\right)\right] & = -\frac{2\rho}{3}\left[u_r h_{\theta\theta} + u_\theta h_{r\theta}\right] \\
\partial_t\left(r\rho e_{\theta z}\right) & +\partial_r\left[\frac{r\rho}{3}\left(u_r h_{\theta z} + u_\theta h_{rz} + u_z h_{r\theta}\right)\right] & +\partial_z\left[\frac{r\rho}{3}\left(u_\theta h_{zz} + 2u_z h_{\theta z}\right)\right] & = -\frac{\rho}{3}\left[u_r h_{\theta z} + u_\theta h_{rz} + u_z h_{r\theta}\right] \\
\partial_t\left(\rho e_{zz}\right) & +\partial_r\left[\frac{r\rho}{3}\left(u_r h_{zz} + 2u_z h_{rz}\right)\right] & +\partial_z\left[r\rho u_z h_{zz}\right] & = 0
\end{cases}
\tag{B.5}
$$

B.1.4 2D-axisymetrical form using azimuthal symmetrical velocity distribution assumption

B.1.4.1 Using geometrical correction

$$\left\{\begin{array}{llll}
\partial_t\rho & +\partial_r\rho u_r & +\partial_z\rho u_z & =-\frac{\rho u_r}{r}\\
\partial_t\rho u_r & +\partial_r(\rho u_r u_r+P_{rr}) & +\partial_z(\rho u_z u_r+P_{rz}) & =-\frac{1}{r}\left[\rho u_r u_r+P_{rr}-P_{\theta\theta}\right]\\
\partial_t\rho u_z & +\partial_r(\rho u_r u_z+P_{rz}) & +\partial_z(\rho u_z u_z+P_{zz}) & =-\frac{1}{r}\left[\rho u_r u_z+P_{rz}\right]\\
\partial_t(\rho e_{rr}) & +\partial_r[\rho u_r h_{rr}] & +\partial_z[\frac{\rho}{3}(2u_r h_{rz}+u_z h_{rr})] & =-\frac{\rho}{3r}\left[3u_r h_{rr}\right]+u_r P_{\theta\theta}\\
\partial_t(\rho e_{rz}) & +\partial_r[\frac{\rho}{3}(2u_r h_{rz}+u_z h_{rr})] & +\partial_z[\frac{\rho}{3}(u_r h_{zz}+2u_z h_{rz})] & =-\frac{\rho}{3r}\left[2u_r h_{rz}+u_z h_{rr}\right]+\frac{1}{2}u_z P_{\theta\theta}\\
\partial_t(\rho e_{zz}) & +\partial_r[\frac{\rho}{3}(u_r h_{zz}+2u_z h_{rz})] & +\partial_z[\rho u_z h_{zz}] & =-\frac{\rho}{3r}\left[u_r h_{zz}+2u_z h_{rz}\right]\\
\partial_t(\frac{1}{2}P_{\theta\theta}) & +\partial_r\left[u_r\frac{1}{2}P_{\theta\theta}\right] & +\partial_z\left[u_z\frac{1}{2}P_{\theta\theta}\right] & =-\frac{1}{2r}u_r P_{\theta\theta}
\end{array}\right. \tag{B.6}$$

B.1.4.2 Using weighted conservation

$$\left\{\begin{array}{llll}
\partial_t\left(r\rho\right) & +\partial_r\left(r\rho u_r\right) & +\partial_z\left(r\rho u_z\right) & =0\\
\partial_t\left(r\rho u_r\right) & +\partial_r\left(r\rho u_r u_r+rP_{rr}\right) & +\partial_z\left(r\rho u_z u_r+rP_{rz}\right) & =P_{\theta\theta}\\
\partial_t\left(r\rho u_\theta\right) & +\partial_r\left(r\rho u_r u_\theta+rP_{r\theta}\right) & +\partial_z\left(r\rho u_z u_\theta+rP_{\theta z}\right) & =0\\
\partial_t\left(r\rho u_z\right) & +\partial_r\left(r\rho u_r u_z+rP_{rz}\right) & +\partial_z\left(r\rho u_z u_z+rP_{zz}\right) & =0\\
\partial_t\left(r\rho e_{rr}\right) & +\partial_r\left(r\rho u_r h_{rr}\right) & +\partial_z\left[\frac{r\rho}{3}\left(2u_r h_{rz}+u_z h_{rr}\right)\right] & =u_r P_{\theta\theta}\\
\partial_t\left(r\rho e_{rz}\right) & +\partial_r\left[\frac{r\rho}{3}\left(2u_r h_{rz}+u_z h_{rr}\right)\right] & +\partial_z\left[\frac{r\rho}{3}\left(u_r h_{zz}+2u_z h_{rz}\right)\right] & =\frac{1}{2}u_z P_{\theta\theta}\\
\partial_t\left(\rho e_{zz}\right) & +\partial_r\left[\frac{r\rho}{3}\left(u_r h_{zz}+2u_z h_{rz}\right)\right] & +\partial_z\left[r\rho u_z h_{zz}\right] & =0\\
\partial_t\left(r\rho e_{\theta\theta}\right) & +\partial_r\left[\frac{r}{2}u_r P_{\theta\theta}\right] & +\partial_z\left[\frac{r}{2}u_z P_{\theta\theta}\right] & =-u_r P_{\theta\theta}
\end{array}\right. \tag{B.7}$$

B.1.5 2D-axisymetrical form using azimuthal velocity degeneracy assumption

B.1.5.1 Using geometrical correction

$$\left\{\begin{array}{llll}
\partial_t\rho & +\partial_r\rho u_r & +\partial_z\rho u_z & =-\frac{\rho u_r}{r}\\
\partial_t\rho u_r & +\partial_r(\rho u_r u_r+P_{rr}) & +\partial_z(\rho u_z u_r+P_{rz}) & =-\frac{1}{r}\left[\rho u_r u_r+P_{rr}\right]\\
\partial_t\rho u_z & +\partial_r(\rho u_r u_z+P_{rz}) & +\partial_z(\rho u_z u_z+P_{zz}) & =-\frac{1}{r}\left[\rho u_r u_z+P_{rz}\right]\\
\partial_t(\rho e_{rr}) & +\partial_r[\rho u_r h_{rr}] & +\partial_z[\frac{\rho}{3}(2u_r h_{rz}+u_z h_{rr})] & =-\frac{\rho}{3r}\left[3u_r h_{rr}\right]\\
\partial_t(\rho e_{rz}) & +\partial_r[\frac{\rho}{3}(2u_r h_{rz}+u_z h_{rr})] & +\partial_z[\frac{\rho}{3}(u_r h_{zz}+2u_z h_{rz})] & =-\frac{\rho}{3r}\left[2u_r h_{rz}+u_z h_{rr}\right]\\
\partial_t(\rho e_{zz}) & +\partial_r[\frac{\rho}{3}(u_r h_{zz}+2u_z h_{rz})] & +\partial_z[\rho u_z h_{zz}] & =-\frac{\rho}{3r}\left[u_r h_{zz}+2u_z h_{rz}\right]
\end{array}\right. \tag{B.8}$$

B.1.5.2 Using weighted conservation

$$\left\{\begin{array}{llll}
\partial_t(r\rho) & +\partial_r(r\rho u_r) & +\partial_z(r\rho u_z) & =0\\
\partial_t(r\rho u_r) & +\partial_r\left(r(\rho u_r u_r+P_{rr})\right) & +\partial_z\left(r(\rho u_z u_r+P_{rz})\right) & =0\\
\partial_t(r\rho u_z) & +\partial_r\left(r(\rho u_r u_z+P_{rz})\right) & +\partial_z\left(r(\rho u_z u_z+P_{zz})\right) & =0\\
\partial_t(r\rho e_{rr}) & +\partial_r[r\rho u_r h_{rr}] & +\partial_z[\frac{r\rho}{3}(2u_r h_{rz}+u_z h_{rr})] & =0\\
\partial_t(r\rho e_{rz}) & +\partial_r[\frac{r\rho}{3}(2u_r h_{rz}+u_z h_{rr})] & +\partial_z[\frac{r\rho}{3}(u_r h_{zz}+2u_z h_{rz})] & =0\\
\partial_t(r\rho e_{zz}) & +\partial_r[\frac{r\rho}{3}(u_r h_{zz}+2u_z h_{rz})] & +\partial_z[r\rho u_z h_{zz}] & =0
\end{array}\right. \tag{B.9}$$

B.2 Pressurelass Gas Dynamics (monokinetic closure)

B.2.1 3D form in cartesian coordinates

$$\left\{\begin{array}{llll}
\partial_t\rho & +\partial_x\rho u & +\partial_y\rho v & +\partial_z\rho w=0\\
\partial_t\rho u & +\partial_x(\rho uu) & +\partial_y(\rho vu) & +\partial_z(\rho wu)=0\\
\partial_t\rho v & +\partial_x(\rho uv) & +\partial_y(\rho vv) & +\partial_z(\rho wv)=0\\
\partial_t\rho w & +\partial_x(\rho uw) & +\partial_y(\rho vw) & +\partial_z(\rho ww)=0
\end{array}\right. \tag{B.10}$$

B.2.2 2D-planar form

$$\left\{\begin{array}{lll}
\partial_t\rho & +\partial_x\rho u & +\partial_y\rho v=0\\
\partial_t\rho u & +\partial_x(\rho uu) & +\partial_y(\rho uv)=0\\
\partial_t\rho v & +\partial_x(\rho uv) & +\partial_y(\rho vv)=0
\end{array}\right. \tag{B.11}$$

B.2.3 2D-axisymetrical form with swirling

B.2.3.1 Using geometrical correction

$$\left\{\begin{array}{llll}
\partial_t\rho & +\partial_r\rho u_r & +\partial_z\rho u_z & =-\frac{\rho u_r}{r}\\
\partial_t\rho u_r & +\partial_r(\rho u_r u_r) & +\partial_z(\rho u_z u_r) & =-\frac{\rho}{r}\left[u_r u_r-u_\theta u_\theta\right]\\
\partial_t\rho u_\theta & +\partial_r(\rho u_r u_\theta) & +\partial_z(\rho u_z u_\theta) & =-\frac{2\rho}{r}u_r u_\theta\\
\partial_t\rho u_z & +\partial_r(\rho u_r u_z) & +\partial_z(\rho u_z u_z) & =-\frac{\rho}{r}u_r u_z
\end{array}\right. \tag{B.12}$$

B.2.3.2 Using weighted conservation

$$\left\{\begin{array}{llll}
\partial_t\left(r\rho\right) & +\partial_r\left(r\rho u_r\right) & +\partial_z\left(r\rho u_z\right) & =0\\
\partial_t\left(r\rho u_r\right) & +\partial_r\left(r\rho u_r u_r\right) & +\partial_z\left(r\rho u_z u_r\right) & =\rho u_\theta u_\theta\\
\partial_t\left(r\rho u_\theta\right) & +\partial_r\left(r\rho u_r u_\theta\right) & +\partial_z\left(r\rho u_z u_\theta\right) & =-\rho u_r u_\theta\\
\partial_t\left(r\rho u_z\right) & +\partial_r\left(r\rho u_r u_z\right) & +\partial_z\left(r\rho u_z u_z\right) & =0
\end{array}\right. \tag{B.13}$$

B.2.4 2D-axisymetrical form without swirling

B.2.4.1 Using geometrical correction

$$\left\{\begin{array}{llll} \partial_t \rho & +\partial_r \rho u_r & +\partial_z \rho u_z & = -\frac{\rho u_r}{r} \\ \partial_t \rho u_r & +\partial_r (\rho u_r u_r) & +\partial_z (\rho u_z u_r) & = -\frac{1}{r}\rho u_r u_r \\ \partial_t \rho u_z & +\partial_r (\rho u_r u_z) & +\partial_z (\rho u_z u_z) & = -\frac{1}{r}\rho u_r u_z \end{array}\right. \tag{B.14}$$

B.2.4.2 Using weighted conservation

$$\left\{\begin{array}{llll} \partial_t (r\rho) & +\partial_r (r\rho u_r) & +\partial_z (r\rho u_z) & = 0 \\ \partial_t (r\rho u_r) & +\partial_r (r\rho u_r u_r) & +\partial_z (r\rho u_z u_r) & = 0 \\ \partial_t (r\rho u_\theta) & +\partial_r (r\rho u_r u_\theta) & +\partial_z (r\rho u_z u_\theta) & = 0 \\ \partial_t (r\rho u_z) & +\partial_r (r\rho u_r u_z) & +\partial_z (r\rho u_z u_z) & = 0 \end{array}\right. \tag{B.15}$$

Appendix C

Additional mathematical developments

C.1 Gradient of a symmetric tensor in cylindrical coordinate

This appendix details the calculation to obtain $(\mathbf{grad}\,(\mathcal{M}_p))_{\widetilde{\underline{\mathbf{i}}kk}}\,\forall \in \{r,\theta,z\}$. Since for $k=z$ the result is trivial, this case is skipped.

C.1.1 For $k=r$

Taking only into account the non-null Christoffel coefficients (3.54) and using (3.47)

$$(\mathbf{grad}\,(\mathcal{M}_p))_{\widehat{\underline{\mathbf{i}}rr}} = \frac{\partial\,(\mathcal{M}_p)_{\widehat{\underline{\mathbf{i}}r}}}{\partial r} - \sum_{k=1}^{p-1}\left[(\mathcal{M}_p)_{\theta\widehat{\underline{\mathbf{i}}_{(j\neq k)}r}}\,\Gamma^{\theta}_{\theta r}\delta_{(i_k=\theta)}\right] \tag{C.1}$$

where $\underline{\mathbf{i}}_{(j\neq k)}$ is the index vector of size $p-2$ composed of the component of $\underline{\mathbf{i}}$ minus the k^{th} one.

Taking into account the symmetry of the tensor and using the definition 3.3:

$$(\mathbf{grad}\,(\mathcal{M}_p))_{\widehat{\underline{\mathbf{i}}rr}} = \frac{\partial\,(\mathcal{M}_p)_{\widehat{\underline{\mathbf{i}}r}}}{\partial r} - \frac{\mathbf{card}_{\theta}\,(\underline{\mathbf{i}})}{r}\,(\mathcal{M}_p)_{\widehat{\underline{\mathbf{i}}r}} \tag{C.2}$$

Using the relation (3.53) and considering the term $\widetilde{n}_\theta = \mathbf{card}_\theta(\underline{\mathbf{i}})$ for the sake of the legibility:

$$\begin{aligned}
(\mathbf{grad}(\mathcal{M}_p))_{\underline{\widetilde{\mathbf{i}}}\widetilde{r}r} &= r^{-\widetilde{n}_\theta}\left[\frac{\partial r^{\widetilde{n}_\theta}(\mathcal{M}_p)_{\underline{\widetilde{\mathbf{i}}}\widetilde{r}}}{\partial r} - \mathbf{card}_\theta(\underline{\mathbf{i}})\, r^{\widetilde{n}_\theta-1}(\mathcal{M}_p)_{\underline{\widehat{\mathbf{i}}}\widehat{r}}\right] \\
&= \frac{\partial(\mathcal{M}_p)_{\underline{\widetilde{\mathbf{i}}}\widetilde{r}}}{\partial r} + r^{-\widetilde{n}_\theta}\frac{\partial r^{\widetilde{n}_\theta}}{\partial r}(\mathcal{M}_p)_{\underline{\widetilde{\mathbf{i}}}\widetilde{r}} - \mathbf{card}_\theta(\underline{\mathbf{i}})\, r^{-1}(\mathcal{M}_p)_{\underline{\widetilde{\mathbf{i}}}\widetilde{r}} \\
&= \frac{\partial(\mathcal{M}_p)_{\underline{\widetilde{\mathbf{i}}}\widetilde{r}}}{\partial r} + \widetilde{n}_\theta r^{-1}(\mathcal{M}_p)_{\underline{\widetilde{\mathbf{i}}}\widetilde{r}} - \mathbf{card}_\theta(\underline{\mathbf{i}})\, r^{-1}(\mathcal{M}_p)_{\underline{\widetilde{\mathbf{i}}}\widetilde{r}} \\
&= \frac{\partial(\mathcal{M}_p)_{\underline{\widetilde{\mathbf{i}}}\widetilde{r}}}{\partial r}
\end{aligned} \tag{C.3}$$

C.1.2 For $k = \theta$

Using (3.47) and the non-null Christoffel coefficients (3.54) then reducing thank to the symmetry of the tensor:

$$\begin{aligned}
(\mathbf{grad}(\mathcal{M}_p))_{\underline{\widehat{\mathbf{i}}}\widehat{\theta}\widehat{\theta}} &= \frac{\partial(\mathcal{M}_p)_{\underline{\widehat{\mathbf{i}}}\widehat{\theta}}}{\partial\theta} - \sum_{k=1}^{p-1}\left[(\mathcal{M}_p)_{\theta\widehat{\underline{\mathbf{i}}_{(j\neq k)}}\theta}\,\Gamma^\theta_{r\theta}\delta_{(i_k=r)}\right] \\
&\quad - \sum_{k=1}^{p-1}\left[(\mathcal{M}_p)_{r\widehat{\underline{\mathbf{i}}_{(j\neq k)}}\theta}\,\Gamma^r_{\theta\theta}\delta_{(i_k=\theta)}\right] - (\mathcal{M}_p)_{\underline{\widehat{\mathbf{i}}}\widehat{r}}\,\Gamma^\theta_{r\theta} \\
&= \frac{\partial(\mathcal{M}_p)_{\underline{\widehat{\mathbf{i}}}\widehat{\theta}}}{\partial\theta} - \frac{\mathbf{card}_r(\underline{\mathbf{i}})}{r}(\mathcal{M}_p)_{\widehat{\mathbf{i}_{(r-1,\theta+1)}}\theta} + r\mathbf{card}_\theta(\underline{\mathbf{i}})(\mathcal{M}_p)_{\widehat{\mathbf{i}_{(\theta-1,r+1)}}\theta} - \frac{1}{r}(\mathcal{M}_p)_{\underline{\widehat{\mathbf{i}}}\widehat{\theta}}
\end{aligned} \tag{C.4}$$

Switching to the physical basis:

$$\begin{aligned}
(\mathbf{grad}(\mathcal{M}_p))_{\underline{\widetilde{\mathbf{i}}}\widetilde{\theta}\widetilde{\theta}} &= \frac{1}{\widetilde{r^{n_\theta+2}}}\left[r^{\widetilde{n}_\theta+1}\frac{\partial(\mathcal{M}_p)_{\underline{\widetilde{\mathbf{i}}}\widetilde{\theta}}}{\partial\theta} - \frac{1}{r}r^{\widetilde{n}_\theta+2}\mathbf{card}_r(\underline{\mathbf{i}})(\mathcal{M}_p)_{\widetilde{\mathbf{i}_{(r-1,\theta+1)}}\theta}\right] \\
&\quad + \frac{1}{\widetilde{r^{n_\theta+2}}}\left[rr^{\widetilde{n}_\theta}\mathbf{card}_\theta(\underline{\mathbf{i}})(\mathcal{M}_p)_{\widetilde{\mathbf{i}_{(\theta-1,r+1)}}\theta} - \frac{1}{r}r^{\widetilde{n}_\theta}(\mathcal{M}_p)_{\underline{\widetilde{\mathbf{i}}}\widetilde{r}}\right] \\
&= \frac{1}{r}\left[\frac{\partial(\mathcal{M}_p)_{\underline{\widetilde{\mathbf{i}}}\widetilde{\theta}}}{\partial\theta} - \mathbf{card}_r(\underline{\mathbf{i}})(\mathcal{M}_p)_{\widetilde{\mathbf{i}_{(r-1,\theta+1)}}\theta} + \mathbf{card}_\theta(\underline{\mathbf{i}})(\mathcal{M}_p)_{\widetilde{\mathbf{i}_{(\theta-1,r+1)}}\theta} - (\mathcal{M}_p)_{\underline{\widetilde{\mathbf{i}}}\widetilde{r}}\right]
\end{aligned} \tag{C.5}$$

C.2 Geometrical terms

The moment of two dimensionnal polygons and segment are defined by:

$$|C_i|_{n,m} = \int_{C_i} r^n z^m dr dz, \qquad |S_{ij}|_{n,m} = \int_{S_{ij}} r^n z^m ds \tag{C.6}$$

For simple forms and low order moments, the expressions are given.

C.2.1 General polygon

For a polygon composed of N two dimensional right-handed organized.

$$|C|_{0,0} = \frac{1}{2}\sum_{i=1}^{N}\left(z_{i+1}r_i - z_i r_{i+1}\right) \tag{C.7}$$

$$|C|_{1,0} = \frac{1}{6}\sum_{i=1}^{N}\left(z_{i+1}r_i - z_i r_{i+1}\right)\left(r_i + r_{i+1}\right) \tag{C.8}$$

$$|C|_{0,1} = \frac{1}{6}\sum_{i=1}^{N}\left(z_{i+1}r_i - z_i r_{i+1}\right)\left(z_i + z_{i+1}\right) \tag{C.9}$$

$$|C|_{2,0} = \frac{1}{12}\sum_{i=1}^{N}\left(z_{i+1}r_i - z_i r_{i+1}\right)\left(r_i^2 + r_i r_{i+1} + r_{i+1}^2\right) \tag{C.10}$$

$$|C|_{1,1} = \frac{1}{24}\sum_{i=1}^{N}\left(z_{i+1}r_i - z_i r_{i+1}\right)\left(2r_i z_i + r_{i+1}z_i + r_i z_{i+1} + 2r_{i+1}z_{i+1}\right) \tag{C.11}$$

C.2.2 Triangle

$$|C|^{\Delta}_{0,0} = \frac{1}{2}\left[\left(r_1 - r_3\right)\left(z_2 - z_3\right) - \left(r_2 - r_3\right)\left(z_1 - z_3\right)\right] \tag{C.12}$$

$$|C|^{\Delta}_{1,0} = \frac{1}{3}|C|^{\Delta}_{0,0}\left(r_1 + r_2 + r_3\right) \tag{C.13}$$

$$|C|^{\Delta}_{0,1} = \frac{1}{3}|C|^{\Delta}_{0,0}\left(z_1 + z_2 + z_3\right) \tag{C.14}$$

$$|C|^{\Delta}_{2,0} = \frac{1}{6}\,|C|^{\Delta}_{0,0}\left(r_1^2 + r_2^2 + r_3^2 + r_1 r_2 + r_2 r_3 + r_3 r_1\right) \tag{C.15}$$

$$|C|^{\Delta}_{1,1} = \frac{1}{12}\,|C|^{\Delta}_{0,0}\left(2r_1 z_1 + 2r_2 z_2 + 2r_3 z_3 + r_1 z_2 + r_2 z_1 + r_2 r_3 + r_3 r_2 + r_3 r_1 + r_1 r_3\right) \tag{C.16}$$

C.2.3 Segment

$$|S|_{0,0} = \sqrt{(r_1 - r_2)^2 + (z_1 - z_2)^2} \tag{C.17}$$

$$|C|_{1,0} = \frac{1}{2}\,|S|_{0,0}\,(r_1 + r_2) \tag{C.18}$$

$$|C|_{0,1} = \frac{1}{2}\,|S|_{0,0}\,(z_1 + z_2) \tag{C.19}$$

$$|C|_{2,0} = \frac{1}{6}\,|S|_{0,0}\left(r_1^2 + r_1 r_2 + r_2^2\right) \tag{C.20}$$

$$|C|_{1,1} = \frac{1}{12}\,|S|_{0,0}\,(2r_1 z_1 + r_2 z_1 + r_1 z_2 + 2r_2 z_2) \tag{C.21}$$

Appendix D

Complementary numerical results

D.1 Spray A Raptor solution

In the same configuration of the Spray A presented and discussed in Section 10.1, complementary results from the Raptor code using the MK, IG and AG closures are proposed here.

The results with Raptor are given in Figure D.1 with the coarse mesh (32 cells per injector diameter). The choice of the model (among MK and AG) does not seem to have an influence. The solution is presumably dominated by numerical diffusion and deviation between these two closure are observable on a fine mesh (64 cells per injector diameter) Figure D.2. For both mesh however, a deviation of the solution of the IG can be observed as soon as PTC appear. Complementary to the results obtained by (Sabat 2016), such examples thus show the questionable ability of the IG closure to treat PTCs.

Figure D.3 presents the solution of the AG closure on several level of mesh refinement. With the very fine mesh (128 cells per injector diameter), we can see new structures appearing and a loss of symmetry. We can conclude that we have not been able to converge the case nor to capture the smallest scales structure of the gas.

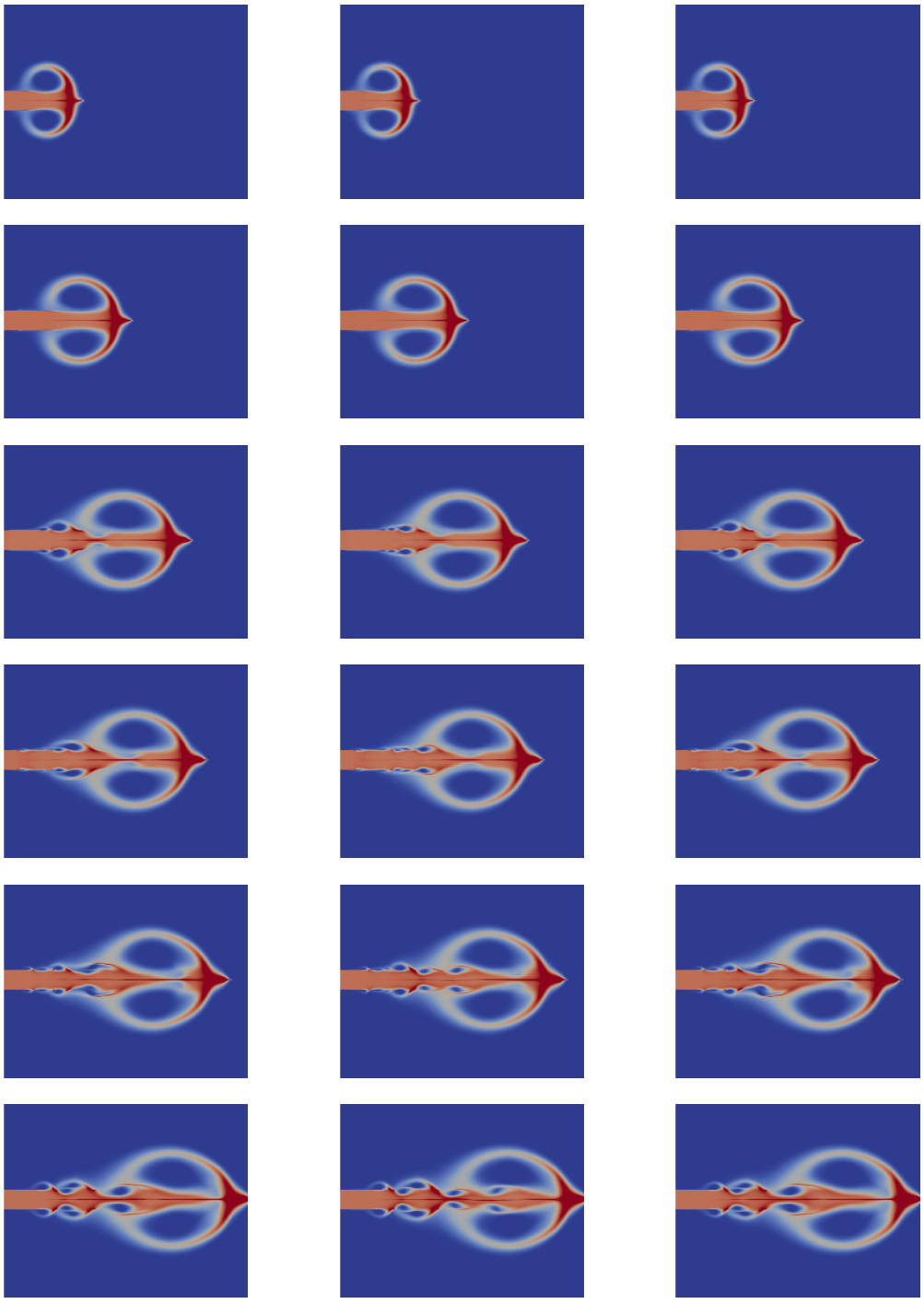

Figure D.1: *Results with Raptor (32 cells per injector diameter) and several closures (left: MK, center:IG, right:AG) after* $3\,\mu s$*,* $5.1\,\mu$*,* $7.5\,\mu s$*,* $8.1\,\mu s$*,* $9.0\,\mu s$*, and* $9.9\,\mu s$ *(from top to bottom).*

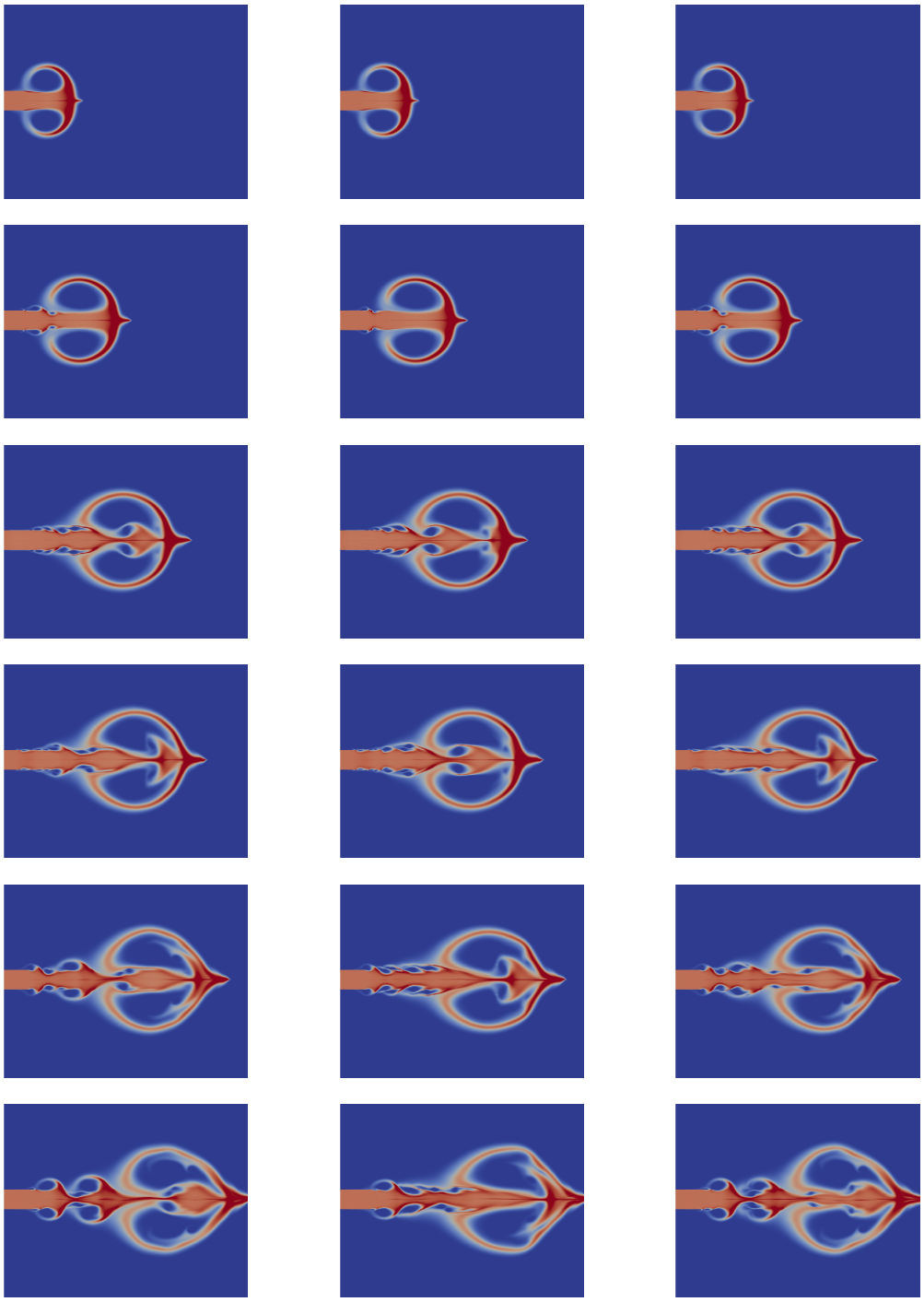

Figure D.2: *Results with Raptor (64 cells per injector diameter) and several closures (left: MK, center:IG, right:AG) after* $3\,\mu s$, $5.1\,\mu$, $7.5\,\mu s$, $8.1\,\mu s$, $9.0\,\mu s$, *and* $9.9\,\mu s$ *(from top to bottom).*

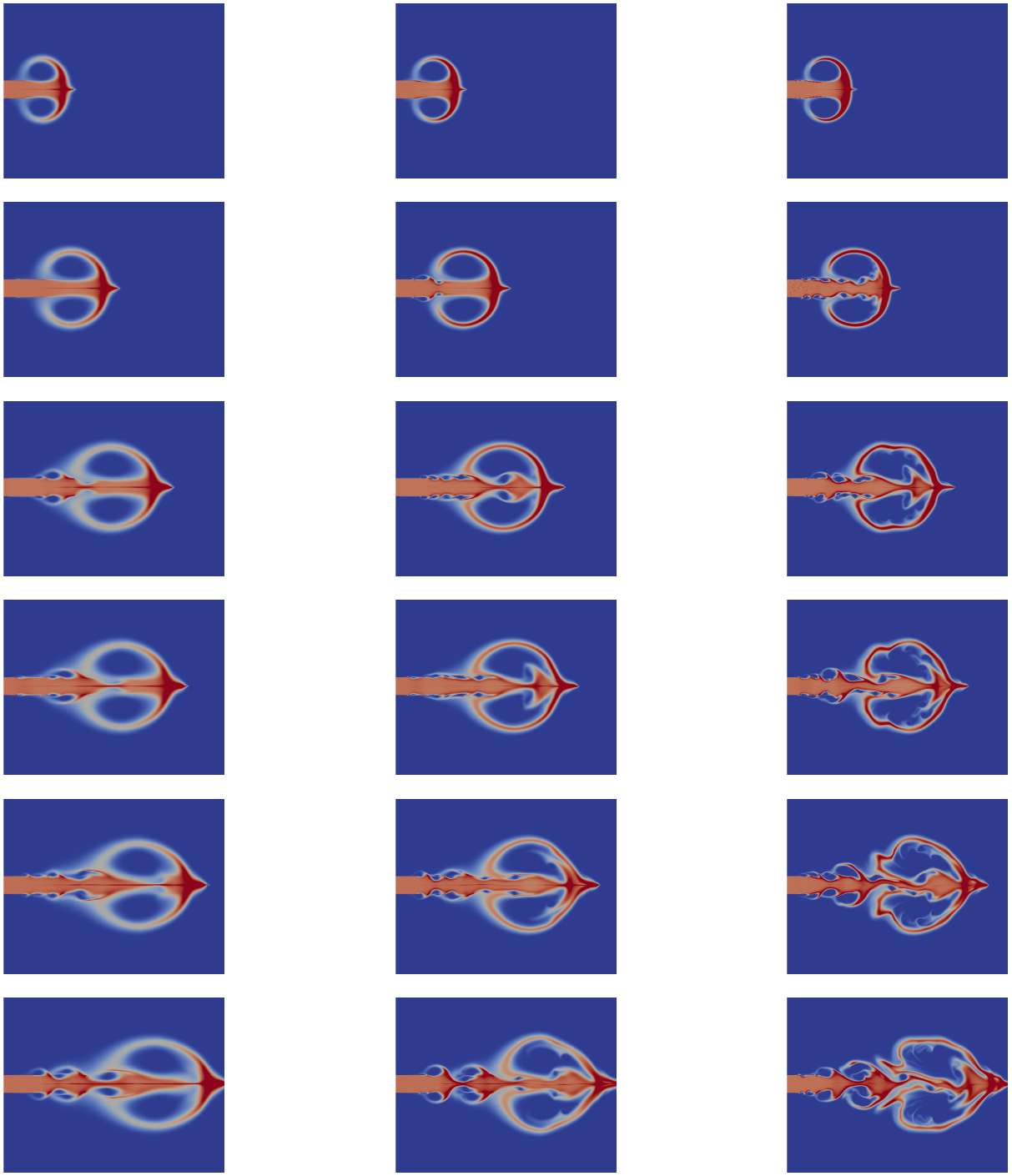

Figure D.3: *Results with Raptor and AG closure with several level of mesh refinement (number of cell in the injector,left:*32*, center:*64*, right:*128*) after* 3 μs*,* 5.1 μ*,* 7.5 μs*,* 8.1 μs*,* 9.0 μs*, and* 9.9 μs *(from top to bottom).*

References

Abdulle, A. 2002. "Fourth order Chebyshev methods with recurrence relation". *SIAM Journal on Scientific Computing* 23 (6): 2041–2054.

Abramzon, B., and W.A. Sirignano. 1989. "Droplet vaporization model for spray combustion calculations". *International journal of heat and mass transfer* 32 (9): 1605–1618.

Andrepont, W. C., and R. M. Felix. 1994. "The History of Large Solid Rocket Motor Development in the United States," in *30th AIAA AIAA/ASME/SAE/ASEE Joint Propulsion Conference*, papier N°94–3057.

Andries, P., P. Le Tallec, J.-Ph. Perlat, and B. Perthame. 2000. "The Gaussian-BGK model of Boltzmann equation with small Prandtl number". *European Journal of Mechanics-B/Fluids* 19 (6): 813–830.

Anthoine, J. 2000. "Experimental and numerical study of aeroacoustic phenomena in large solid propellant boosters". PhD thesis, Université libre de Bruxelles.

Arienti, M., X. Li, M. C. Soteriou, C. A. Eckett, M. Sussman, and R.J. Jensen. 2012. "Coupled level-set/volume-of-fluid method for simulation of injector atomization". *Journal of Propulsion and Power* 29 (1): 147–157.

Ashgriz, N, and JY Poo. 1990. "Coalescence and separation in binary collisions of liquid drops". *Journal of Fluid Mechanics* 221:183–204.

Baer, M.R., and J.W. Nunziato. 1986. "A two-phase mixture theory for the deflagration-to-detonation transition (DDT) in reactive granular materials". *International Journal of Multiphase Flow* 12 (6): 861–889.

Ballereau, S., F. Godfroy, J. Guéry, and D. Ribereau. 2003. "Assessment on analysis and prediction method applied on thrust oscillations of Ariane 5 solid rocket motor". *AIAA paper* 4675:2003.

Bandera, A., F. Maggi, and L.T. DeLuca. 2009. "Agglomeration of aluminized solid rocket propellants". *AIAA paper* 5439:2009.

Baraille, R. 1991. "Développement de schémas numériques adaptés à l'hydrodynamique. Une méthode numérique à pas fractionnaires. Application aux calculs d'écoulements hypersoniques réactifs non visqueux. Formulation du schéma MUSCL de van Leer pour une configuration axisymétrique." PhD thesis, Université Bordeaux I.

Barrere, M., A. Jaumotte, B. Fraeijs de Veubeke, and J. Vandenkerckhove. 1960. *Rocket propulsion*. Elsevier Pub. Co.

Bashforth, F. 1883. *An attempt to test the theories of capillary action by comparing the theoretical and measured forms of drops of fluid: with an explanation of the method of integration employed in constructing the tables which give the theoretical forms of such drops, by JC Adams*. University Press.

Basset, A. B. 1888. *A treatise on hydrodynamics: with numerous examples*. Vol. 2. Deighton, Bell / Company.

Batten, P., N. Clarke, C. Lambert, and D.M. Causon. 1997. “On the choice of wavespeeds for the HLLC Riemann solver”. *SIAM Journal on Scientific Computing* 18 (6): 1553–1570.

Beckstead, M. W. 2002. “Aluminium Combustion”. In *Internal aerodynamics in solid rocket propulsion*. RTO AVT/VKI Special Course. VKI.

Beckstead, M. W., K. Puduppakkam, P. Thakre, and V. Yang. 2007. “Modeling of combustion and ignition of solid-propellant ingredients”. *Progress in Energy and Combustion Science* 33 (6): 497–551.

Beddini, A.R. 1981. “Analysis of injection induced flows in porous walled duct with application to aerochemistry of solid propellant motor”. PhD thesis, University of New Brunswick.

Benson, D. J. 1992. “Computational methods in Lagrangian and Eulerian hydrocodes”. *Computer methods in Applied mechanics and Engineering* 99 (2-3): 235–394.

Berger, M. J., and J. Oliger. 1984. “Adaptive mesh refinement for hyperbolic partial differential equations”. *Journal of computational Physics* 53 (3): 484–512.

Berger, M., M. J. Aftosmis, and S. M. Murman. 2005. “Analysis of slope limiters on irregular grids”. *AIAA paper* 490.

Bernard-Champmartin, A., and F. De Vuyst. 2014. “A low diffusive lagrange-remap scheme for the simulation of violent air–water free-surface flows”. *Journal of Computational Physics* 274:19–49.

Berthon, C. 2005. “Stability of the MUSCL Schemes for the Euler Equations”. *Communications in Mathematical Sciences* 3, no. 2 (): 133–157. http://projecteuclid.org/euclid.cms/1118778272.

– . 2006a. “Numerical approximations of the 10-moment Gaussian closure”. *Mathematics of computation* 75 (256): 1809–1831.

– . 2006b. “Why the MUSCL–Hancock Scheme is L1-stable”. *Numerische Mathematik* 104 (1): 27–46.

Berthon, C., and R. Turpault. 2011. “Asymptotic preserving HLL schemes”. *Numerical methods for partial differential equations* 27 (6): 1396–1422.

Berzins, M., and J.M. Ware. 1995. “Positive cell-centered finite volume discretization methods for hyperbolic equations on irregular meshes”. *Applied Numerical Mathematics* 16 (4): 417–438.

Bhatnagar, P. L., E. P. Gross, and M. Krook. 1954. “A model for collision processes in gases. I. Small amplitude processes in charged and neutral one-component systems”. *Physical review* 94 (3): 511.

Binauld, Q. 2018. “Modélisation et simulation du rayonnement dans les jets de moteurs à propergol solide à haute altitude”. PhD thesis, Paris-Saclay University.

Bird, G.A. 1970. “Direct simulation and the Boltzmann equation”. *The Physics of Fluids* 13 (11): 2676–2681.

Blomshield, F. S. 2007. “Lessons learned in solid rocket combustion instability”. *AIAA Paper* 5803:2007.

Boileau, M., V. Dupif, F. Laurent, and M. Massot. 2017. “Modeling and numerical scheme of two-size moment Eulerian multi-fluid model describing statistical trajectory crossing”. *In preparation to International Journal on Multiphase Flow, IJMF*.

Boileau, M., J. Lagarde, V. Dupif, F. Laurent, and M. Massot. 2016. “Two-size moment Eulerian multi-fluid method describing the statistical trajectory crossing: modeling and numerical scheme”. In *9th International Conference on Multiphase Flow, ICMF*. Available at https://hal.archives-ouvertes.fr/hal-01543507. Firenze, Italy.

Boissonnat, J.-D. 1984. “Geometric structures for three-dimensional shape representation”. *ACM Transactions on Graphics (TOG)* 3 (4): 266–286.

Boivin, M., O. Simonin, and K. D. Squires. 2000. “On the prediction of gas–solid flows with two-way coupling using large eddy simulation”. *Physics of Fluids* 12 (8): 2080–2090.

Boris, J. P., and D. L. Book. 1997. “Flux-corrected transport”. *Journal of Computational Physics* 135 (2): 172–186.

Bouchut, F. 1994. “On zero pressure gas dynamics”. In *Advances in kinetic theory and computing*, 171–190. River Edge, NJ: World Sci. Publishing.

Bouchut, F., and F. James. 1999. “Duality solutions for pressureless gases, monotone scalar conservation laws, and uniqueness”. *Communications in partial differential equations* 24 (11-12): 2173–2189.

Bouchut, F., S. Jin, and X. Li. 2003. “Numerical approximations of pressureless and isothermal gas dynamics”. *SIAM Journal on Numerical Analysis* 41 (1): 135–158.

Boussinesq, J. 1885. “Sur la résistance qu’oppose un liquide indéfini en repos”. *CR Acad. Sci. Paris* 100:935–937.

Brenier, Y., and E. Grenier. 1998. “Sticky particles and scalar conservation laws”. *SIAM journal on numerical analysis* 35 (6): 2317–2328.

Brown, R.S., R. Dunlap, S.W. Young, and R.C. Waugh. 1981. “Vortex shedding as a source of acoustic energy in segmented solid rockets”. *Journal of Spacecraft and Rockets* 18 (4): 312–319.

Brown, S. L. 1996. “Approximate Riemann solvers for moment models of dilute gases”. PhD thesis, The University of Michigan.

Buckmaster, J., T.L. Jackson, L. Massa, and M. Ulrich. 2005. “Response of a burning heterogeneous propellant to small pressure disturbances”. *Proceedings of the Combustion Institute* 30 (2): 2079–2086.

Buffard, T., and S. Clain. 2010. “Monoslope and multislope MUSCL methods for unstructured meshes”. *Journal of Computational Physics* 229 (10): 3745–3776.

Burt, J., and I. Boyd. 2005. “A Monte carlo radiation model for simulating rarefied multiphase plume flows”. In *38th AIAA Thermophysics Conference*.

Butcher, J. C. 2016. *Numerical methods for ordinary differential equations*. John Wiley & Sons.

Capecelatro, J., and O. Desjardins. 2013. “An Euler-Lagrange strategy for simulating particle-laden flows”. *Journal of Computational Physics*, no. 238: 1–31.

Capecelatro, J., O. Desjardins, and R.O. Fox. 2016. “Strongly coupled fluid-particle flows in vertical channels. II. Turbulence modeling”. *Physics of Fluids* 28 (3): 033306.

Casalis, G., G. Avalon, and J-P. Pineau. 1998. “Spatial instability of planar channel flow with fluid injection through porous walls”. *Physics of Fluids* 10 (10): 2558–2568.

Casas-Vázquez, J., G. Lebon, and D. Jou. 2010. *Extended irreversible thermodynamics*. Springer.

Causon, D.M. 1989. “High resolution finite volume schemes and computational aerodynamics”. In *Nonlinear Hyperbolic Equations—Theory, Computation Methods, and Applications*, 63–74. Springer.

Cauty, F. 2000. “Ultrasonic method applied to full-scale solid rocket motors”. *Journal of Propulsion and Power* 16 (3): 523–528.

Cercignani, C. 1988. “The Boltzmann equation”. In *The Boltzmann Equation and Its Applications*, 40–103. Springer.

Cesco, N. 1997. “Etude et modélisation de l’écoulement diphasique à l’intérieur des propulseurs à poudre”. PhD thesis, ENSAE.

Chaisemartin, S. de. 2009. “Polydisperse evaporating spray turbulent dispersion: Eulerian model and numerical simulation”. Available on TEL: https://tel.archives-ouvertes.fr/tel-00443982. PhD thesis, Ecole Centrale Paris.

Chaisemartin, S. de, F. Laurent, L. Fréret, M. Massot, A-L. Birbaud, C. Lacour, S. Ducruix, and D. Durox. 2007. “Pulsated free jets with spray injection : Eulerian Multi-Fluid modelling and simulation versus experimental measurements”. In *Proceedings of the International Conference on Multiphase Flows, ICMF07, Leipzig*.

Chalons, C., R. O. Fox, F. Laurent, M. Massot, and A. Vié. 2017. "Multivariate Gaussian extended quadrature method of moments for turbulent disperse multiphase flow". *SIAM Multiscale Modeling & Simulation* 15 (4): 1553–1583.

Chalons, C., and S. Girardin M.and Kokh. 2016. "An all-regime Lagrange-Projection like scheme for the gas dynamics equations on unstructured meshes". *Communications in Computational Physics* 20 (1): 188–233.

Chalons, C., D. Kah, and M. Massot. 2012. "Beyond pressureless gas dynamics : Quadrature-based velocity moment models". *Communications in Mathematical Sciences* 10 (4): 1241–1272. https://hal.archives-ouvertes.fr/hal-00535782.

Chanteperdrix, G., P. Villedieu, and J.-P. Vila. 2002. "A compressible model for separated two-phase flows computations". In *ASME 2002 Joint US-European Fluids Engineering Division Conference*, 809–816. American Society of Mechanical Engineers.

Chapman, S., and T. G. Cowling. 1970. *The mathematical theory of non-uniform gases: an account of the kinetic theory of viscosity, thermal conduction and diffusion in gases*. Cambridge university press.

Charru, F. 2011. *Hydrodynamic instabilities*. Vol. 37. Cambridge University Press.

Chase, K. W. 2003. *Firearms: a global history to 1700*. Cambridge University Press.

Chen, Hudong, Steven A Orszag, Ilya Staroselsky, and Sauro Succi. 2004. "Expanded analogy between Boltzmann kinetic theory of fluids and turbulence". *Journal of Fluid Mechanics* 519:301–314.

Ciezki, Helmut K, K Naumann, and Volker Weiser. 2010. "Status of Gel Propulsion in the Year 2010 with a Special View on the German Activities". *Deutscher Luft-und Raumfahrtkongress 2010*.

Clain, S., and V. Clauzon. 2010. "L_∞ stability of the MUSCL methods". *Numerische Mathematik* 116 (1): 31–64.

Clain, S., D. Rochette, and R. Touzani. 2010. "A multislope MUSCL method on unstructured meshes applied to compressible Euler equations for axisymmetric swirling flows". *Journal of Computational Physics* 229 (13): 4884–4906.

Clain, Stéphane, Steven Diot, and Raphaël Loubère. 2011. "A high-order finite volume method for systems of conservation laws—Multi-dimensional Optimal Order Detection (MOOD)". *Journal of Computational Physics* 230 (10): 4028–4050.

Clauzon, V. 2008. "Analyse de schémas d'ordre élevé pour les écoulements compressibles. Application à la simulation numérique d'une torche à plasma." PhD thesis, Université Blaise Pascal-Clermont-Ferrand II.

Clavin, P. 1996. *Etude analytique de l'amortissement des ondes acoustiques longitudinales dans une chambre avec injection pariétale, programme ASSM 5 axe stabilité de fonctionnement*. Tech. rep. Technical report, IRPHE.

Cockburn, B., G. E. Karniadakis, and C.-W. Shu. 2000. "The development of discontinuous Galerkin methods". In *Discontinuous Galerkin Methods*, 3–50. Springer.

Cohen, A., S. M. Kaber, and M. Postel. 2003. "Adaptive multiresolution for finite volume solutions of gas dynamics". *Computers & fluids* 32 (1): 31–38.

Colella, P., and P. R. Woodward. 1984. "The piecewise parabolic method (PPM) for gas-dynamical simulations". *Journal of Computational Physics* 54 (1): 174–201.

Colin, O., and M. Rudgyard. 2000. "Development of high-order Taylor–Galerkin schemes for LES". *Journal of Computational Physics* 162 (2): 338–371.

Cordesse, P. 2019. "Study of combustion instabilities in liquid-propellant rocket engines: diffuse interface model and kinetic model coupling for primary atomization simulations". PhD thesis, Université Paris-Saclay, Polytechnique.

Costa, R., S. Clain, R. Loubère, and G. J. Machado. 2018. "Very high-order accurate finite volume scheme on curved boundaries for the two-dimensional steady-state convection–diffusion equation with Dirichlet condition". *Applied Mathematical Modelling* 54:752–767.

Cottet, G.-H., J.-M. Etancelin, F. Pérignon, and C. Picard. 2014. "High order semi-Lagrangian particle methods for transport equations: numerical analysis and implementation issues". *ESAIM: Mathematical Modelling and Numerical Analysis* 48 (4): 1029–1060.

Courant, R., K. Friedrichs, and H. Lewy. 1928. "Über die partiellen Differenzengleichungen der mathematischen Physik". *Mathematische annalen* 100 (1): 32–74.

Crowe, C. T. 2005. *Multiphase flow handbook*. Vol. 59. CRC press.

Crowe, C. T., J. D. Schwarzkopf, M. Sommerfeld, and Y. Tsuji. 2011. *Multiphase flows with droplets and particles*. CRC press.

Csanady, G.T. 1963. "Turbulent diffusion of heavy particles in the atmosphere". *Journal of the Atmospheric Sciences* 20 (3): 201–208.

Culick, F. E. C., and V. Yang. 1992. "Prediction of the stability of unsteady motions in solid-propellant rocket motors". In *Nonsteady Burning and Combustion Stability of Solid Propellants*, 143:719–779. Progress in Astronautics and Aeronautics. AIAA.

Culick, F.E.C. 1966. "Rotational axisymmetric mean flow and damping of acoustic waves in a solid propellant rocket". *AIAA Journal* 4 (8): 1462–1464.

Daniel, E. 2000. "Eulerian approach for unsteady two-phase solid rocket flows with aluminum particles". *J. of Propulsion and Power* 16 (2): 309–317.

Daniel, E., R. Saurel, M. Larini, and J.C. Loraud. 1993. "A comparison between centered and upwind schemes for two-phase compressible flows". In *AIAA/SAE/ASME/ASEE, Joint Propulsion Conference and Exhibit, 29th, Monterey, CA*.

– . 1994. "A multiphase formulation for two phase flows". *International Journal of Numerical Methods for Heat & Fluid Flow* 4 (3): 269–280.

Daru, V., and Ch. Tenaud. 2004. "High order one-step monotonicity-preserving schemes for unsteady compressible flow calculations". *Journal of computational physics* 193 (2): 563–594.

Davenas, A. 1995. "History of the development of solid rocket propellant in France". *Journal of Propulsion and Power* 11 (2): 285–291.

Davis, S.F. 1984a. "A rotationally biased upwind difference scheme for the Euler equations". *Journal of Computational Physics* 56 (1): 65–92.

– . 1984b. "TVD finite difference schemes and artificial viscosity". *ICASE Report No. 84-20*.

– . 1988. "Simplified second-order Godunov-type methods". *SIAM Journal on Scientific and Statistical Computing* 9 (3): 445–473.

Del Pino, S., and H. Jourdren. 2006. "Arbitrary high-order schemes for the linear advection and wave equations: application to hydrodynamics and aeroacoustics". *Comptes Rendus Mathematique* 342 (6): 441–446.

Delhaye, Jean-Marc. 2001. "Some issues related to the modeling of interfacial areas in gas–liquid flows I. The conceptual issues". *Comptes Rendus de l'Académie des Sciences-Series IIB-Mechanics* 329 (5): 397–410.

Delhaye, J.-M. 1974. "Jump conditions and entropy sources in two-phase systems. Local instant formulation". *International Journal of Multiphase Flow* 1 (3): 395–409.

Dellacherie, S. 2010. "Analysis of Godunov type schemes applied to the compressible Euler system at low Mach number". *Journal of Computational Physics* 229 (4): 978–1016.

DeLuca, L. T. 2017. "Highlights of solid rocket propulsion history". In *Chemical Rocket Propulsion*, 1015–1032. Springer.

DeLuca, L.T., L. Galfetti, G. Colombo, F. Maggi, A. Bandera, V.A. Babuk, and V.P. Sinditskii. 2010. "Microstructure effects in aluminized solid rocket propellants". *Journal of propulsion and power* 26 (4): 724–733.

Descombes, S., M. Duarte, and M. Massot. 2016. "Operator splitting methods with error estimator and adaptive time-stepping. Application to the simulation of combustion phenomena". In *Splitting Methods in Communication, Imaging, Science, and Engineering*, 627–641. Springer.

Descombes, S., and M. Massot. 2004. "Operator splitting for nonlinear reaction-diffusion systems with an entropic structure: singular perturbation and order reduction". *Numer. Math.* 97 (4): 667–698. ISSN: 0029-599X.

Desjardins, O., R. O. Fox, and P. Villedieu. 2008. "A quadrature-based moment method for dilute fluid-particle flows". *Journal of Computational Physics* 227 (4): 2514–2539.

Dette, H., and W.J. Studden. 1997. *The theory of canonical moments with applications in statistics, probability, and analysis*. Vol. 338. John Wiley & Sons.

Doisneau, F. 2013. "Modeling and simulation of polydisperse moderately dense coalescing spray flows with nanometric-to-inertial droplets: application to Solid Rocket Motors". TEL : HTTPS://TEL.ARCHIVES-OUVERTES.FR/TEL-01009896. PhD thesis, Ecole Centrale Paris.

Doisneau, F., M. Arienti, and J. Oefelein. 2017a. "On Multi-Fluid models for spray-resolved LES of reacting jets". *Proceedings of the Combustion Institute* 36 (2): 2441–2450.

Doisneau, F., M. Arienti, and J. C. Oefelein. 2017b. "A semi-Lagrangian transport method for kinetic problems with application to dense-to-dilute polydisperse reacting spray flows". *Journal of Computational Physics* 329:48–72.

Doisneau, F., F. Laurent, A. Murrone, J. Dupays, and M. Massot. 2013. "Eulerian Multi-Fluid models for the simulation of dynamics and coalescence of particles in solid propellant combustion". *Journal of Computational Physics* 234:230–262.

Doisneau, F., A. Sibra, J. Dupays, A. Murrone, F. Laurent, and M. Massot. 2014. "Numerical strategy for unsteady two-way coupled polydisperse sprays: application to solid-rocket instabilities". *Journal of Propulsion and Power* 30 (3): 727–748.

Donea, J. 1984. "A Taylor–Galerkin method for convective transport problems". *International Journal for Numerical Methods in Engineering* 20 (1): 101–119.

Donea, J., and A. Huerta. 2003. *Finite element methods for flow problems*. John Wiley & Sons.

Dormand, J. R., and P. J. Prince. 1980. "A family of embedded Runge-Kutta formulae". *Journal of Computational and Applied Mathematics* 6 (1): 19–26.

Drew, Donald A, and Stephen L Passman. 2006. *Theory of multicomponent fluids*. Vol. 135. Springer Science & Business Media.

Drui, F. 2017. "Eulerian modeling and simulations of separated and disperse two-phase flows: development of a unified modeling approach and associated numerical methods for highly parallel computations". PhD thesis, Université Paris-Saclay, prepared at CentraleSupélec.

Druzhinin, O.A. 1994. "Concentration waves and flow modification in a particle-laden circular vortex". *Physics of Fluids* 6 (10): 3276–3284.

– . 1995. "On the two-way interaction in two-dimensional particle-laden flows: the accumulation of particles and flow modification". *Journal of Fluid Mechanics* 297:49–76.

Duarte, M. 2011. "Adaptive numerical methods in time and space for the simulation of multi-scale reaction fronts". PhD thesis, Ecole Centrale Paris.

Duarte, M., M. Massot, S. Descombes, C. Tenaud, T. Dumont, V. Louvet, and F. Laurent. 2012. "New resolution strategy for multiscale reaction waves using time operator splitting, space adaptive multiresolution, and dedicated high order implicit/explicit time integrators". *SIAM Journal on Scientific Computing* 34 (1): A76–A104.

Duboc, F., C. Enaux, S. Jaouen, H. Jourdren, and M. Wolff. 2010. "High-order dimensionally split Lagrange-remap schemes for compressible hydrodynamics". *Comptes Rendus Mathematique* 348 (1-2): 105–110.

Dufour, G. 2005. “Modélisation Multi-Fluide eulérienne pour les écoulements diphasiques à inclusions dispersées”. PhD thesis, Université Paul Sabatier Toulouse III.

Dumbser, M., and D.S. Balsara. 2016. “A new efficient formulation of the HLLEM Riemann solver for general conservative and non-conservative hyperbolic systems”. *Journal of Computational Physics* 304:275–319.

Dupays, J. 1996. “Contribution à l’étude du rôle de la phase condensée dans la stabilité d’un propulseur à propergol solide pour lanceur spatial”. PhD thesis, Institut National Polytechnique de Toulouse.

Dupays, J., Y. Fabignon, P. Villedieu, G. Lavergne, and J. L. Estivalezes. 2000. “Some Aspects of Two-Phase Flows in Solid-Propellant Rocket Motors”. In *Solid Propellant Chemistry, Combustion, and Motor Interior Ballistics*, 185:859–883. Progress in Astronautics and Aeronautics. AIAA.

Dupays, J., F. Godfroy, O. Orlandi, P. Prevot, M. Prévost, S. Gallier, S. Ballereau, and Y. Fabignon. 2008. “Inert condensed phase driving effect of combustion instabilities in solid rocket motor”. In 5^{th} *International Spacecraft Propulsion Conference, Heraklion, Greece.*

Dupays, J., S. Wey, and Y. Fabignon. 2001. “Steady and unsteady reactive two-phase computations in solid rocket motors with Eulerian and Lagrangian approaches”. In *37th Joint Propulsion Conference and Exhibit.*

Dupif, V., J. Dupays, A. Larat, and M. Massot. 2018a. “Accurate and robust numerical strategy for axisymmetric Eulerian modeling of particles laden flows of moderate inertia”. *To be submitted to Journal of Computational Mathematics, SMAI-JCM.*

Dupif, V., M. Massot, J. Dupays, and F. Laurent. 2015a. “Eulerian models and related numerical schemes and parallel implementation for the simulation of polydisperse two-phase flows in solid rocket motors”. In *SimRace, International conference on numerical methods and High Performance Computing for industrial fluid flows.* Rueil-Malmaison, France.

– . 2017a. “A robust multislope MUSCL method formulation for two-phase flow simulations inside solid rocket motors”. In *8ème Congrès SMAI.* Ronce-les-Bains, France.

– . 2018b. “Euler-Euler simulation of an unsteady solid rocket motors with size polydispersion and local velocity dispersion”. *To be submitted to Journal of Propulsion and Power, JPP.*

Dupif, V., M. Massot, J. Dupays, F. Laurent, and C. Le Touze. 2015b. “Influence of numerical methods on the simulation of the steady and unsteady two-phase flow in solid rocket motors”. In *6th European Conference for Aeronautics and Space Sciences, EUCASS.* Krakow, Poland.

– . 2016. “On the influence of the numerical strategy on the predictive character of an Euler-Euler model for two-phase flow simulations in solid rocket motor instabilities”. In *9th International Conference on Multiphase Flow, ICMF.* Firenze, Italy.

– . 2017b. “A robust and accurate MUSCL multislope scheme for particle laden flow: application to solid rocket motor instabilities”. In *3rd International Conference on Numerical Methods in Multiphase Flows, ICNMMF-III.* Tokyo, Japan.

– . 2018c. “Predictive character of Euler-Euler model and numerical strategy for two-phase flow simulations of solid rocket motor instabilities”. *To be submitted to Journal of Computational Physics, JCP.*

Dupuy, M. 2012. “Etude par simulations numériques instationnaires de l’écoulement dans les moteurs à propergol solide”. PhD thesis, ISAE-ENSMA Ecole Nationale Supérieure de Mécanique et d’Aérotechique-Poitiers.

Duval, R. 2002. “Transferts radiatifs dans les chambres de combustions de propulseurs à propergol solide aluminisé”. PhD thesis, PhD thesis, École Centrale Paris.

Einfeldt, B. 1988. “On Godunov-type methods for gas dynamics”. *SIAM Journal on Numerical Analysis* 25 (2): 294–318.

Einfeldt, B., C.-D. Munz, P.L. Roe, and B. Sjögreen. 1991. "On Godunov-type methods near low densities". *Journal of Computational Physics* 92 (2): 273–295.

Elghobashi, S., and G.C. Truesdell. 1993. "On the two-way interaction between homogeneous turbulence and dispersed solid particles. I: Turbulence modification". *Physics of Fluids A: Fluid Dynamics* 5 (7): 1790–1801.

Emre, O. 2014. "Modeling of spray polydispersion with two-way turbulent interactions for high pressure direct injection in engines". PhD thesis, Ecole Centrale Paris.

Emre, O., D. Kah, S. Jay, Q.-H. Tran, A. Velghe, S. De Chaisemartin, R.O. Fox, F. Laurent, and M. Massot. 2015. "Eulerian moment methods for automotive sprays". *Atomization and Sprays* 25 (3): 189–254.

Esnault-Pelterie, R. 1913. "Considérations sur les résultats d'un allégement indéfini des moteurs". *Journal de physique theorique et appliquee* 3 (1): 218–230.

Essadki, M. 2018. "Contribution to a unified Eulerian modeling of fuel injection: from dense liquid to polydisperse evaporating spray". PhD thesis, Université Paris-Saclay, CentraleSupelec.

Essadki, M., S. de Chaisemartin, F. Laurent, and M. Massot. 2016. "High order moment model for polydisperse evaporating sprays towards interfacial geometry description". *submitted to SIAM Applied Mathematics*: 1–42.

Essadki, M., F. Drui, S. de Chaisemartin, A. Larat, T. Ménard, and M. Massot. 2017. "Statistical modeling of the gas-liquid interface using geometrical variables: toward a unified description of the disperse and separated phase flows". Available on HAL: https://hal.archives-ouvertes.fr/hal-01615076, *submitted to IJMF, arXiv preprint arXiv:1710.04585*.

Fabignon, Y., O. Orlandi, J.F. Trubert, D. Lambert, and J. Dupays. 2003. "Combustion of aluminum particles in solid rocket motors". In 39th AIAA/ASME/SAE/ASEE Joint Propulsion Conference and Exhibit , Huntsville, Tx, *AIAA Paper 2003-4807* ().

Fabignon, Y., J. Anthoine, D. Davidenko, R. Devillers, J. Dupays, D. Gueyffier, J. Hijlkema, N. Lupoglazoff, J.M. Lamet, L. Tessé, et al. 2016. "Recent Advances in Research on Solid Rocket Propulsion". *AerospaceLab* 1 (11): 15.

Falcone, M., and R. Ferretti. 1998. "Convergence analysis for a class of high-order semi-Lagrangian advection schemes". *SIAM Journal on Numerical Analysis* 35 (3): 909–940.

Fede, Pascal, Olivier Simonin, and Philippe Villedieu. 2015. "Monte-Carlo simulation of colliding particles or coalescing droplets transported by a turbulent flow in the framework of a joint fluid–particle pdf approach". *International Journal of Multiphase Flow* 74:165–183.

Ferry, J., and S. Balachandar. 2001. "A fast Eulerian method for disperse two-phase flow". *International Journal of Multiphase Flow* 27 (7): 1199–1226.

– . 2002. "Equilibrium expansion for the Eulerian velocity of small particles". *Powder Technology* 125 (2-3): 131–139.

– . 2005. "Equilibrium Eulerian approach for predicting the thermal field of a dispersion of small particles". *International Journal of Heat and Mass Transfer* 48 (3-4): 681–689.

Ferziger, J.H., and M. Peric. 2012. *Computational methods for fluid dynamics*. Springer Science & Business Media.

Fevrier, P., O. Simonin, and K.D. Squires. 2005. "Partitioning of particle velocities in a gas-solid turbulent flow into a continuous field and a spatially-uncorrelated random distribution : theoretical formalism and numerical study". *J. Fluid Mech.* 533:1–46.

Fialkow, L., and S. Petrovic. 2005. "A moment matrix approach to multivariable cubature". *Integral Equations and Operator Theory* 52 (1): 85–124.

Foissac, Arnaud, Jeanne Malet, Stéphane Mimouni, and François Feuillebois. 2010. "Binary water droplet collision study in presence of solid aerosols in air". In *7th International Conference on Multiphase Flow, ICMF*.

Fornberg, B. 1988. “Generation of finite difference formulas on arbitrarily spaced grids”. *Mathematics of computation* 51 (184): 699–706.

Fox, R. O. 2008a. “A quadrature-based third-order moment method for dilute gas-particle flow”. *Journal of Computational Physics* 227 (12): 6313–6350.

– . 2008b. “Optimal moment sets for multivariate direct quadrature method of moments”. *Industrial & Engineering Chemistry Research* 48 (21): 9686–9696.

Fox, R. O., F. Laurent, and M. Massot. 2008. “Numerical simulation of spray coalescence in an Eulerian framework : direct quadrature method of moments and Multi-Fluid method.” *Journal of Computational Physics* 227 (6): 2215–2222.

Frenklach, M. 2002. “Method of moments with interpolative closure”. *Chemical Engineering Science* 57 (12): 2229–2239.

Frenklach, M., and S. J. Harris. 1987. “Aerosol dynamics modeling using the method of moments”. *Journal of colloid and interface science* 118 (1): 252–261.

Gallier, S., and F. Godfroy. 2009a. “Aluminum combustion driven instabilities in solid rocket motors”. *Journal of Propulsion and Power* 25 (2): 509–521.

Gallier, S., F. Godfroy, and F. Plourde. 2004. “Computational study of turbulence in a subscale solid rocket motor”. *AIAA Paper* 4052:2004.

Gallier, Stany, and Franck Godfroy. 2009b. “Aluminum combustion driven instabilities in solid rocket motors”. *Journal of propulsion and power* 25 (2): 509.

Gander, M. J., and S. Vandewalle. 2007. “Analysis of the parareal time-parallel time-integration method”. *SIAM Journal on Scientific Computing* 29 (2): 556–578.

Gany, A., and I. Aharon. 1999. “Internal ballistics considerations of nozzleless rocket motors”. *J. Propul. Power* 15 (6): 866–873.

Garrigues, Jean. 2016. “Tensorial algebra and analysis for continuum mechanics”. Lecture, France. https://cel.archives-ouvertes.fr/cel-00679923.

Gautschi, Walter. 2004. *Orthogonal polynomials: computation and approximation*. Oxford University Press on Demand.

Gelfand, B.E. 1996. “Droplet breakup phenomena in flows with velocity lag”. *Progress in energy and combustion science* 22 (3): 201–265.

Genot, A. 2018. “Thermoacoustic instabilities in solid propellant motor”. PhD thesis, Université Paris-Saclay, CentraleSupelec.

Genot, A., S. Gallier, and T. Schuller. 2017. “A Numerical analysis of the aluminium combustion driven instability in solid rocket motors”. *7th European Conference for Aeronautics and Space Sciences, Milan (Italy)*. 10.13009/EUCASS2017-64.

Giovangigli, V., and M. Massot. 1998. “Asymptotic stability of equilibrium states for multicomponent reactive flows”. *Math. Models Methods Appl. Sci.* 8 (2): 251–297. ISSN: 0218-2025.

Goddard, R. H. 1920. “A method of reaching extreme altitudes”. *Nature* 105 (2): 809–811.

Godfroy, F., and J.-F. Guéry. 1997. “Unsteady eulerian two-phase flow analysis of solid rocket motor slag”. In *33rd AIAA/ASME/SAE/ASEE Joint Propulsion Conference and Exhibit*.

Godlewski, E., and P.-A. Raviart. 1996. *Numerical Approximation of Hyperbolic Systems of Conservation Laws*. Vol. 118. Springer Science & Business Media.

Godunov, Sergei K. 1961. “An interesting class of quasilinear systems”. In *Dokl. Akad. Nauk SSSR*, 139:521–523.

Godunov, Sergei Konstantinovich. 1999a. “Reminiscences about Difference Schemes”. *Journal of Computational Physics* 153 (1): 6–25. ISSN: 0021-9991. doi:http://dx.doi.org/10.1006/jcph.1999.6271. http://www.sciencedirect.com/science/article/pii/S002199919996271X.

– . 1999b. “Reminiscences about difference schemes”. See arXiv preprint arXiv:0810.0649, *Journal of Computational Physics* 153 (1): 6–25.

Godunov, S.K. 1959. “A difference method for numerical calculation of discontinuous solutions of the equations of hydrodynamics”. *Matematicheskii Sbornik* 89 (3): 271–306.

Gordon, S., and B. J. McBride. 1994. *Computer program for calculation of complex chemical equilibrium compositions and applications*. Vol. 1. National Aeronautics / Space Administration, Office of Management, Scientific / Technical Information Program.

Gossant, B. 1993. *Solid Propellant Combustion and Internal Ballistics of Motors in Solid Rocket Propulsion Technology*. Pergamon Pr (edited by A. Davenas).

Gottlieb, J.J., and C.P.T. Groth. 1988. “Assessment of Riemann solvers for unsteady one-dimensional inviscid flows of perfect gases”. *Journal of Computational Physics* 78 (2): 437–458.

Gottlieb, S. 2005. “On high order strong stability preserving Runge–Kutta and multi step time discretizations” [**inlang**English]. *Journal of Scientific Computing* 25 (1): 105–128. ISSN: 0885-7474. doi:10.1007/s10915-004-4635-5. http://dx.doi.org/10.1007/s10915-004-4635-5.

Gottlieb, S., D. I. Ketcheson, and C.-W. Shu. 2011. *Strong stability preserving Runge-Kutta and multistep time discretizations*. World Scientific.

Gottlieb, Sigal, Chi-Wang Shu, and Eitan Tadmor. 2001. “Strong stability-preserving high-order time discretization methods”. *SIAM review* 43 (1): 89–112.

Goudjo, A., and J.-A. Desideri. 1989. *Un schema de volumes-finis décentré pour la résolution des équations d’Euler en axisymétrique*. INRIA Report RR-1005. Institut National de Recherche en Informatique et en Automatique.

Grad, H. 1949. “On the kinetic theory of rarefied gases”. *Communications on pure and applied mathematics* 2 (4): 331–407.

Graille, B., T. Magin, and M. Massot. 2009. “Kinetic Theory of Plasmas : Translational Energy”. *Mathematical Models and Methods in Applied Sciences* 19 (04): 527–599.

Griffond, J. 2001. “Instabilité pariétale et accrochage aéro-acoustique dans les conduits à parois débitantes simulant les moteurs à propergol solide d’Ariane 5”. PhD thesis, Ecole Nationale Supérieure de l’Aéronautique et de l’Espace.

Griffond, J., and G. Casalis. 2001. “On the nonparallel stability of the injection-induced two-dimensional Taylor flow”. *Phys. Fluids* 13 (6): 1635–1644.

Griffond, J., G. Casalis, and J.-P. Pineau. 2000. “Spatial instability of flow in a semi-infinite cylinder with fluid injection through its porous walls”. *Eur. J. of Mech. B - Fluids* 19:69–87.

Grmela, Miroslav. 2010. “Multiscale equilibrium and nonequilibrium thermodynamics in chemical engineering”. *Advances in Chemical Engineering* 39:75–129.

Groth, C.P.T., and J.G. McDonald. 2009. “Towards physically realizable and hyperbolic moment closures for kinetic theory”. *Continuum Mechanics and Thermodynamics* 21 (6): 467.

Guardone, A., and L. Vigevano. 2007. “Finite element/volume solution to axisymmetric conservation laws”. *Journal of Computational Physics* 224 (2): 489–518.

Guery, J.-F., I.-S. Chang, T. Shimada, M. Glick, D. Boury, E. Robert, J. Napior, R. Wardle, C. Pérut, M. Calabro, et al. 2010. “Solid propulsion for space applications: An updated roadmap”. *Acta Astronautica* 66 (1): 201–219.

Guillard, H., and A. Murrone. 2004. “On the behavior of upwind schemes in the low Mach number limit: II. Godunov type schemes”. *Computers & fluids* 33 (4): 655–675.

Guillard, Hervé, and B Nkonga. 2017. “On the Behaviour of Upwind Schemes in the Low Mach Number Limit: A Review”. In *Handbook of Numerical Analysis*, 18:203–231. Elsevier.

Haider, F. 2009. “Discrétisation en maillage non structuré général et applications LES”. PhD thesis, Université Pierre et Marie Curie-Paris VI.

Haider, F., P. Brenner, B. Courbet, and J.-P. Croisille. 2014. “Parallel implementation of k-exact finite volume reconstruction on unstructured grids”. In *High Order Nonlinear numerical schemes for evolutionary PDEs*, 59–75. Springer.

Haider, F., J.-P. Croisille, and B. Courbet. 2009. "Stability analysis of the cell centered finite-volume M uscl method on unstructured grids". *Numerische Mathematik* 113 (4): 555–600.

Hairer, E., S. P. Nørsett, and G. Wanner. 1993a. *Solving ordinary differential equations. I.* xv+528. Nonstiff problems, second revised edition. Berlin: Springer-Verlag. ISBN: 3-540-56670-8.

Hairer, E., S.P. Nørsett, and G. Wanner. 1993b. *Solving Ordinary Differential Equations I: Nonstiff Problems*. Vol. 8. Springer Series in Computational Mathematics.

Hairer, E., and G. Wanner. 1996a. *Solving ordinary differential equations. II.* xv+614. Stiff and differential-algebraic problems, second revised edition. Berlin: Springer-Verlag. ISBN: 3-540-60452-9.

– . 1996b. *Solving Ordinary Differential Equations II: Stiff and Differential-Algebraic Problems*. Vol. 14. Springer Series in Computational Mathematics.

Harten, A. 1983. "High resolution schemes for hyperbolic conservation laws". *Journal of Computational Physics* 49 (3): 357–393.

– . 1994. "Adaptive multiresolution schemes for shock computations". *Journal of Computational Physics* 115 (2): 319–338.

Harten, A., B. Engquist, S. Osher, and S. R. Chakravarthy. 1987. "Uniformly high order accurate essentially non-oscillatory schemes, III". In *Upwind and high-resolution schemes*, 218–290. Springer.

Harten, A., and J. M. Hyman. 1983. "Self adjusting grid methods for one-dimensional hyperbolic conservation laws". *Journal of Computational Physics* 50 (2): 235–269.

Harten, A., P. D. Lax, and B. Van Leer. 1983. "On upstream differencing and Godunov-type scheme for hyperbolic conservation laws". *SIAM review* 25 (1): 35–61.

Henderson, C. B. 1976. "Drag coefficients of spheres in continuum and rarefied flows". *AIAA* 14 (6): 707–708.

Herrmann, M. 2010. "A parallel Eulerian interface tracking/Lagrangian point particle multi-scale coupling procedure". *Journal of Computational Physics* 229 (3): 745–759.

Hesthaven, J.S., and T. Warburton. 2007. *Nodal discontinuous Galerkin methods: algorithms, analysis, and applications*. Springer Science & Business Media.

Hill, P. G., and C. R. Peterson. 1992. "Mechanics and thermodynamics of propulsion". *Reading, MA, Addison-Wesley Publishing Co., 1992, 764 p.* 1.

Hirsch, C. 1990. *Numerical Computation of Internal and External Flows: Fundamentals of Numerical Discretization, Tome II*. John Wiley & Sons. ISBN: 0-471-924-520.

– . 2007. *Numerical computation of internal and external flows: The fundamentals of computational fluid dynamics*. Butterworth-Heinemann.

Hirschberg, L., T. Schuller, J. Collinet, C. Schram, and A. Hirschberg. 2018. "Analytical model for the prediction of pulsations in a cold-gas scale-model of a Solid Rocket Motor". *Journal of Sound and Vibration* 419C:452–468.

Hirt, C.W., A. A. Amsden, and J.L. Cook. 1974. "An arbitrary Lagrangian-Eulerian computing method for all flow speeds". *Journal of Computational Physics* 14 (3): 227–253.

Hoef, M. A. van der, and J.A.M. van Sint Annaland M .and Kuipers. 2004. "Computational fluid dynamics for dense gas–solid fluidized beds: a multi-scale modeling strategy". *Chemical Engineering Science* 59 (22-23): 5157–5165.

Holstad, A. 2001. "The Koren upwind scheme for variable gridsize". *Applied numerical mathematics* 37 (4): 459–487.

Holway, L.H. Jr. 1966. "New statistical models for kinetic theory: methods of construction". *The Physics of Fluids* 9 (9): 1658–1673.

Hölzer, A., and M. Sommerfeld. 2008. "New simple correlation formula for the drag coefficient of non-spherical particles". *Powder Technology* 184 (3): 361–365.

Hsiang, L-P, and Gerard M Faeth. 1993. "Drop properties after secondary breakup". *International Journal of Multiphase Flow* 19 (5): 721–735.

Hsiang, L-P, and G.M. Faeth. 1995. "Drop deformation and breakup due to shock wave and steady disturbances". *International Journal of Multiphase Flow* 21 (4): 545–560.

Hundsdorfer, W., and J.G. Verwer. 2003. *Numerical Solution of Time-Dependent Advection-Diffusion-Reaction Equations*. Springer-Verlag, Berlin.

Hylkema, J. J. 1999. "Modélisation cinétique et simulation numérique d'un brouillard dense de gouttelettes. Application aux propulseurs à poudre". PhD thesis, Ecole Nat. Supérieure de l'Aéronautique et de l'Espace.

Ishii, M., and T. Hibiki. 2010. *Thermo-fluid dynamics of two-phase flow*. Springer Science & Business Media.

Ishii, M., and N. Zuber. 1979. "Drag coefficient and relative velocity in bubbly, droplet or particulate flows". *AIChE Journal* 25 (5): 843–855.

Jabin, P.-E. 2002. "Various levels of models for aerosols". *Mathematical Models and Methods in Applied Sciences* 12 (7): 903–919.

Jackson, R., and B.J. Davidson. 1983. "An equation set for non-equilibrium two phase flow, and an analysis of some aspects of choking, acoustic propagation, and losses in low pressure wet steam". *International journal of multiphase flow* 9 (5): 491–510.

Jaisankar, S., and S.V.R. Rao. 2007. "Diffusion regulation for Euler solvers". *Journal of Computational Physics* 221 (2): 577–599.

Jameson, A. 1995a. "Analysis and design of numerical schemes for gas dynamics, 1: artificial diffusion, upwind biasing, limiters and their effect on accuracy and multigrid convergence". *International Journal of Computational Fluid Dynamics* 4 (3-4): 171–218.

– . 1995b. "Positive schemes and shock modelling for compressible flows". *International Journal for Numerical Methods in Fluids* 20 (8-9): 743–776.

Jameson, A., and T. J. Baker. July 1983. "Numerical solution of the Euler equations for complex configurations". *AIAA 6th Computational Fluid Dynamics Conference, Danvers, MA AIAA Paper 83-1929*.

Jameson, A., and W. Schmidt. 1985. "Some Recent Developments in Numerical Methods for Transonic Flow". *Computer Methods in Applied Mechanics and Engineering* 51:467–493.

Jameson, A., W. Schmidt, and E. Turkel. 1981. "Numerical solution of the Euler Equations by Finite Volume Methods Using Runge-Kutta Time-Stepping Schemes". *AIAA 1981-1259*.

Jiang, G.-S., and C.-W. Shu. 1996. "Efficient implementation of weighted ENO schemes". *Journal of computational physics* 126 (1): 202–228.

Johnson, E. A. 2011. "Gaussian-moment relaxation closures for verifiable numerical simulation of fast magnetic reconnection in plasma". Available at https://arxiv.org/abs/1409.6985. PhD thesis, University of Winsconsin - Madison.

Jordán, K. 1965. *Calculus of finite differences*. American Mathematical Soc.

Junk, M. 1998. "Domain of definition of Levermore's five-moment system". *Journal of Statistical Physics* 93 (5-6): 1143–1167.

Junk, M., and A. Unterreiter. 2002. "Maximum entropy moment systems and Galilean invariance". *Continuum Mechanics and Thermodynamics* 14 (6): 563–576.

Kah, D. 2010. "Taking into account polydispersity for the modeling of liquid fuel injection in internal combustion engines". Available on TEL https://tel.archives-ouvertes.fr/tel-00618786. PhD thesis, Ecole Centrale Paris.

Kah, D., O. Emre, Q. H. Tran, S. De Chaisemartin, S. Jay, F. Laurent, and M. Massot. 2015. "High order moment method for polydisperse evaporating sprays with mesh movement: application to internal combustion engines". *International Journal of Multiphase Flow* 71:38–65.

Kah, D., F. Laurent, M. Massot, and S. Jay. 2012. "A high order moment method simulating evaporation and advection of a polydisperse liquid spray". *Journal of Computational Physics*: 231(2):394–422.

Kaufmann, A., M. Moreau, O. Simonin, and J. Helie. 2008. "Comparison between Lagrangian and mesoscopic Eulerian modelling approaches for inertial particles suspended in decaying isotropic turbulence". *Journal of Computational Physics* 227 (13): 6448–6472.

Kay, D. 1988. *Schaum's Outline of Tensor Calculus*. McGraw Hill Professional.

Kleiber, C., and J. Stoyanov. 2013. "Multivariate distributions and the moment problem". *Journal of Multivariate Analysis* 113:7–18.

Kocamustafaogullari, Gunol. 1971. "Thermo-fluid dynamics of separated two-phase flow". PhD thesis, Georgia Institute of Technology.

Koren, B. 1993. *A robust upwind discretization method for advection, diffusion and source terms*. Centrum voor Wiskunde en Informatica Amsterdam.

Kourta, A. 1999. "Computation of vortex shedding in solid rocket motors using time-dependant turbulence model". *Journal of Propulsion and Power* 15 (3): 390–400.

Kraaijevanger, J. F. B. M. 1991. "Contractivity of Runge-Kutta methods". *BIT Numerical Mathematics* 31 (3): 482–528.

Krepper, Eckhard, Dirk Lucas, Thomas Frank, Horst-Michael Prasser, and Phil J Zwart. 2008. "The inhomogeneous MUSIG model for the simulation of polydispersed flows". *Nuclear Engineering and Design* 238 (7): 1690–1702.

Kuentzmann, P. 1973. "Contribution à l'étude des pertes d'impulsion specifique dans les fusees a propergol solide". PhD thesis, Paris VI University.

– . 1991. *Instabilités de combustion*. AGARD.

– . 1995. "Instabilités de fonctionnement des systèmes propulsifs". *La Recherche Aérospatiale* 5:341–351.

Kumar, A., and S. Hartland. 1985. "Gravity settling in liquid/liquid dispersions". *The Canadian Journal of Chemical Engineering* 63 (3): 368–376.

Kumar, J., M. Peglow, G. Warnecke, S. Heinrich, and L. Mörl. 2006. "Improved accuracy and convergence of discretized population balance for aggregation: The cell average technique". *Chemical Engineering Science* 61 (10): 3327–3342.

Kumar, Sanjeev, and D Ramkrishna. 1996a. "On the solution of population balance equations by discretization—I. A fixed pivot technique". *Chemical Engineering Science* 51 (8): 1311–1332.

– . 1996b. "On the solution of population balance equations by discretization—II. A moving pivot technique". *Chemical Engineering Science* 51 (8): 1333–1342.

Kuzmin, D. 2009. "Explicit and implicit FEM-FCT algorithms with flux linearization". *Journal of Computational Physics* 228 (7): 2517–2534.

Larson, W. J., and J. R. Wertz. 1992. *Space mission analysis and design*. Microcosm.

Laurent, F., and M. Massot. 2001. "Multi-fluid modeling of laminar poly-dispersed spray flames: origin, assumptions and comparison of the sectional and sampling methods". *Comb. Theory and Modelling* 5 (4): 537–572.

Laurent, F., M. Massot, and P. Villedieu. 2004. "Eulerian Multi-Fluid modeling for the numerical simulation of coalescence in polydisperse dense liquid sprays". *Journal of Computational Physics* 194 (2): 505–543.

Laurent, F., A. Sibra, and F. Doisneau. 2016. "Two-size moment multi-fluid model: a robust and high-fidelity description of polydisperse moderately dense evaporating sprays". *Communications in Computational Physics* 20 (4): 902–943.

Lax, P., and B. Wendroff. 1960. "Systems of Conservation". *Communications on pure and applied mathematics* 13:217–237.

Lax, Peter. 1971. “Shock waves and entropy”. In *Contributions to nonlinear functional analysis*, 603–634. Elsevier.

Lax, Peter D. 1954. “Weak solutions of nonlinear hyperbolic equations and their numerical computation”. *Communications on Pure and Applied Mathematics* 7 (1): 159–193.

Le Touze, C. 2015. “Couplage entre modèles diphasiques à «phases séparées» et à «phase dispersée» pour la simulation de l’atomisation primaire en combustion cryotechnique”. PhD thesis, Université Nice Sophia Antipolis.

Le Touze, C., A. Murrone, and H. Guillard. 2015. “Multislope MUSCL method for general unstructured meshes”. *Journal of Computational Physics* 284:389–418.

Lebas, R., G. Blokkeel, P.-A. Beau, and F.-X. Demoulin. 2005. *Coupling vaporization model with the Eulerian-Lagrangian Spray Atomization (ELSA) model in Diesel engine conditions*. Tech. rep. SAE Technical Paper.

Lebas, R., T. Menard, P.-A. Beau, A. Berlemont, and F.-X. Demoulin. 2009. “Numerical simulation of primary break-up and atomization: DNS and modelling study”. *International Journal of Multiphase Flow* 35 (3): 247–260.

Lebon, G., D. Lhuillier, and A. Palumbo. 2007. “A thermodynamic description of thermodiffusion in suspensions of rigid particles”. *The European Physical Journal-Special Topics* 146 (1): 3–12.

Leer, B. van. 1977. “Towards the ultimate conservative difference scheme IV. A new approach to numerical convection”. *Journal of Computational Physics* 23:276–299.

– . 1979. “Towards the ultimate conservative difference scheme V. A second order sequel to Godunov’s method”. *Journal of Computational Physics* 32:101–136.

Lerat, A. 1981. *Sur le calcul de solutions faibles des systèmes hyperboliques de lois de conservation à l’aide de schémas aux différences*. Office national d’études et de recherches aérospatiales.

Lerat, A., and R. Peyret. 1975. “Propriétés dispersives et dissipatives d’une classe de schémas aux différences pour les systèmes hyperboliques non linéaires”. *La Recherche Aérospatiale* 2:61–79.

Lestrade, J.-Y., J. Anthoine, O. Verberne, A. J. Boiron, G. Khimeche, and C. Figus. 2016. “Experimental demonstration of the vacuum specific impulse of a hybrid rocket engine”. *Journal of Spacecraft and Rockets*.

LeVeque, R. J. 1992. *Numerical methods for conservation laws*. Second. x+214. Basel: Birkhäuser Verlag. ISBN: 3-7643-2723-5.

LeVeque, R.J. 2002. *Finite volume methods for hyperbolic problems*. xx+558. Cambridge Texts in Applied Mathematics. Cambridge: Cambridge University Press.

– . 2007. *Finite difference methods for ordinary and partial differential equations: steady-state and time-dependent problems*. Vol. 98. Siam.

Levermore, C. D. 1996. “Moment closure hierarchies for kinetic theories”. *Journal of statistical Physics* 83 (5-6): 1021–1065.

Levermore, C.D., and W.J. Morokoff. 1998. “The Gaussian moment closure for gas dynamics”. *SIAM J. Appl. Math.* 59 (1): 72–96.

Ley, W. 1935. “Rocket Propulsion: A Résumé of Theory with an Account of the Practical Experiments made to Date”. *Aircraft Engineering and Aerospace Technology* 7 (9): 227–231.

Li, B. 1993. “The moment calculation of polyhedra”. *Pattern Recognition* 26 (8): 1229–1233.

Ling, Y., S. Zaleski, and R. Scardovelli. 2015. “Multiscale simulation of atomization with small droplets represented by a Lagrangian point-particle model”. *International Journal of Multiphase Flow* 76:122–143.

Lions, J.-L., Y. Maday, and G. Turinici. 2001. “Résolution d’EDP par un schéma en temps «pararéel»”. *Comptes Rendus de l’Académie des Sciences-Series I-Mathematics* 332 (7): 661–668.

Lions, P.-L., and N. Masmoudi. 1998. “Incompressible limit for a viscous compressible fluid”. *Journal de mathématiques pures et appliquées* 77 (6): 585–627.

Liu, G.-R., and Y.-T. Gu. 2005. *An introduction to meshfree methods and their programming*. Springer Science & Business Media.

Liu, X.-D., S. Osher, and T. Chan. 1994. “Weighted essentially non-oscillatory schemes”. *Journal of Computational Physics* 115 (1): 200–212.

Löhner, R., K. Morgan, J. Peraire, and M. Vahdati. 1987. “Finite element flux-corrected transport (FEM–FCT) for the euler and Navier–Stokes equations”. *International Journal for Numerical Methods in Fluids* 7 (10): 1093–1109.

Lupoglazoff, N., and F. Vuillot. 1991. *Ariane 5 MPS Combustion Stability Assessment: Subtask TN1. "Full Numerical Unsteady computations Of Vortx Shedding Phenomenon"*. Tech. rep. RT n°10/6133 EY. ONERA.

– . 1992a. “Numerical simulation of vortex-shedding phenomena in 2D test case solid rocket motors”. In *30th Aerospace and Sciences Meeting and Exhibit*.

Lupoglazoff, N, and F Vuillot. 1992b. “Simulation numérique bidimensionnelle des écoulements instationnaires dans les propulseurs à propergol solide”. *La Recherche Aérospatiale*, no. 2: 21–41.

Lupoglazoff, N., and F. Vuillot. 1993. “Comparison between firing tests and numerical simulation of vortex shedding in a 2-D test solid motor”. In *24th Fluid Dynamics Conference*, paper N°93–3066. AIAA.

– . 1994. *Application de modèles de turbulence de sous-maille aux cas test C1 et C1x et mise au point d'un module de combustion instaionnaire*. Tech. rep. RT 50/6133 EY. ONERA.

– . 1996. “Parietal vortex shedding as a cause of instability for long solid propellant motors - Numerical simulations and comparisons with firing tests”. In 34^{th}*th Aerospace Sciences Meeting and Exhibit*, papier N°96–0761. AIAA.

– . 1998. “Numerical simulations of parietal vortex-shedding phenomenon in a cold flow setup”. In *34th AIAA/ASME/SAE/ASEE Joint Propulsion Conference and Exhibit*.

– . 1999. “Simulations of solid propellant rocket motors instability including propellant combustion reponse”. In *6th Int. Congress on Sound and Vibration, Denmark*.

Lupoglazoff, N., F. Vuillot, J. Dupays, and Y. Fabignon. 2000. “Numerical simulations of the unsteady flow inside Ariane 5 P230 SRM booster with burning aluminum particles”. In 2^{nd} *European Conference on Launcher Technology*. Rome.

MacCormack, R. 1969. “The effect of viscosity in hypervelocity impact cratering”. (2003) reprinted from AIAA Paper 69-354, 1969, *Journal of spacecraft and rockets* 40 (5): 757–763.

Maggi, F., G. Gariani, L. Galfetti, and L. T. DeLuca. 2012. “Theoretical analysis of hydrides in solid and hybrid rocket propulsion”. *international journal of hydrogen energy* 37 (2): 1760–1769.

Majdalani, J. 2007. “On steady rotational high speed flows: the compressible Taylor–Culick profile”. In *Proceedings of the Royal Society of London A: Mathematical, Physical and Engineering Sciences*, 463:131–162. 2077. The Royal Society.

Majdalani, J., and W. K. Van Moorhem. 2001. “Laminar cold-flow model for the internal gas dynamics of a slab rocket motor”. *Aerospace science and technology* 5 (3): 193–207.

Majdalani, J., A.B. Vyas, and G.A. Flandro. 2001. “Higher mean-flow approximation for a solid rocket motor with radially regressing walls”. In *37th AIAA/ASME/SAE/ASEE Joint Propulsion Conference and Exhibit*.

Malina, F. J. 1968. “The Rocket Pioneers”. *Engineering and Science* 31 (5): 9–32.

Mandal, J.C., and S.M. Deshpande. 1994. “Kinetic flux vector splitting for Euler equations”. *Computers & fluids* 23 (2): 447–478.

Marble, F.E. 1970. “Dynamics of dusty gases”. *Ann. Rev. Fluid Mech.* 2:397–446.

Marble, F.E., and S. Candel. 1977. “Acoustic disturbance from gas non-uniformities convected through a nozzle”. *Journal of Sound and Vibration* 55 (2): 225–243.

Marchuk, G. I. 1968. “Some application of splitting-up methods to the solution of mathematical physics problems”. *Aplikace matematiky* 13 (2): 103–132.

– . 1990. “Splitting and alternating direction methods”. *Handbook of numerical analysis* 1:197–462.

Mashayek, F., F.A. Jaberi, R.S. Miller, and P. Givi. 1997. “Dispersion and polydispersity of droplets in stationary isotropic turbulence”. *International journal of multiphase flow* 23 (2): 337–355.

Masi, E. 2010. “Étude théorique et numérique de la modélisation instationnaire des écoulements turbulents anisothermes gaz-particules par une approche Euler-Euler”. PhD thesis, Institut National Polytechnique de Toulouse.

Masi, E., O. Simonin, and B. Bédat. 2011. “The mesoscopic Eulerian approach for evaporating droplets interacting with turbulent flows”. *Flow, Turbulence and Combustion* 86 (3): 563–583.

Masi, Enrica, and Olivier Simonin. 2012. “An algebraic-closure-based momentmethod for unsteady Eulerian modeling of non-isothermal particle-laden turbulent flows in very dilute regime and high Stokes number”. In *ICHMT DIGITAL LIBRARY ONLINE*. Begel House Inc.

Massot, M., and A. Larat. 2014. “Ecoulements Compressibles et Supersoniques”. ECP (2014).

Massot, M., F. Laurent, D. Kah, and S. de Chaisemartin. 2010. “A robust moment method for evaluation of the disappearance rate of evaporating sprays”. *SIAM J. Appl. Math.* 70 (8): 3203–3234. ISSN: 0036-1399. doi:10.1137/080740027. http://dx.doi.org/10.1137/080740027.

Maxey, MR. 1987. “The motion of small spherical particles in a cellular flow field”. *The Physics of fluids* 30 (7): 1915–1928.

McDonald, J. G., and C.P.T. Groth. 2005. “Numerical modeling of micron-scale flows using the Gaussian moment closure”. *AIAA Paper* 5035:2005.

McDonald, J., and M. Torrilhon. 2013. “Affordable robust moment closures for CFD based on the maximum-entropy hierarchy”. *Journal of Computational Physics* 251:500–523.

McGraw, R. 1997. “Description of aerosol dynamics by the quadrature method of moments”. *Aerosol Science and Technology* 27:255–265.

Mercier, D. 2018. “Large eddy simulation of disperse phase flows with inverse coupling”. PhD thesis, CentraleSupélec, Université Paris-Saclay.

Michal, A. D. 1947. *Matrix and tensor calculus*. Wiley New York.

Morfouace, V., and P.-Y. Tissier. 1995. “Two-phase flow analysis of instabilities driven by vortex-shedding in solid rocket motors”. In *31st AIAA/ASME/SAE/ASEE Joint Propulsion Conference and Exhibit*.

Muller, D. E. 1956. “A method for solving algebraic equations using an automatic computer”. *Mathematical Tables and Other Aids to Computation* 10 (56): 208–215.

Müller-Kirsten, H.J.W. 2013. *Basics of statistical physics*. World Scientific.

Munz, C.-D., S. Roller, R. Klein, and K. J. Geratz. 2003. “The extension of incompressible flow solvers to the weakly compressible regime”. *Computers & Fluids* 32 (2): 173–196.

Murrone, A., and P. Villedieu. 2011. “Numerical Modeling of Dispersed Two-Phase Flows”. Available at www.aerospacelab-journal.org/al2, *Aerospace Lab* 2:1–13.

Narasimha, R. 1985. “Rockets in Mysore and Britain, 1750-1850 AD”. *PD DU* 8503.

Naumann, K. W., H. K. Ciezki, R. Stierle, K. Schmid, and J. Ramsel. 2011. “Rocket propulsion with gelled propellants for sounding rockets”. In *Proceedings of the 20th symposium on European rocket and balloon programmes and related research, Fort Lauderdale, FL*.

Nguyen, T. T., F. Laurent, R. O. Fox, and M. Massot. 2016. "Solution of population balance equations in applications with fine particles: mathematical modeling and numerical schemes". *Journal of Computational Physics* 325:129–156.

Nicolis, C., and G. Nicolis. 1998. "Closing the hierarchy of moment equations in nonlinear dynamical systems". *Physical Review E* 58 (4): 4391.

Nielson, G. M. 1994. "Tools for Triangulations and Tetrahedrizations." In *Scientific Visualization*, 429–525.

Nievergelt, J. 1964. "Parallel methods for integrating ordinary differential equations". *Communications of the ACM* 7 (12): 731–733.

Nigmatulin, R. I. 1990. *Dynamics of multiphase media*. Vol. 2. CRC Press.

Nishikawa, H., and K. Kitamura. 2008. "Very simple, carbuncle-free, boundary-layer-resolving, rotated-hybrid Riemann solvers". *Journal of Computational Physics* 227 (4): 2560–2581.

Oberth, H. 1923. *Die Rakete zu den Planetenräumen*. Walter de Gruyter GmbH & Co KG.

Ohwada, T. 2002. "On the construction of kinetic schemes". *Journal of Computational Physics* 177 (1): 156–175.

Oliger, J., and A. Sundström. 1978. "Theoretical and practical aspects of some initial boundary value problems in fluid dynamics". *SIAM Journal on Applied Mathematics* 35 (3): 419–446.

O'Rourke, P. J. 1981. "Collective drop effects on vaporizing liquid sprays". PhD thesis, Los Alamos National Laboratory 87545, University of Princeton.

Oseen, C. W. 1927. *Neure methoden und ergebnisse in der hydrodynamik*. Akademische Verlagsgesellschaft.

Osher, S., and S. Chakravarthy. 1983. "Upwind schemes and boundary conditions with applications to Euler equations in general geometries". *Journal of Computational Physics* 50 (3): 447–481.

Öttinger, H. C. 1998. "General projection operator formalism for the dynamics and thermodynamics of complex fluids". *Physical Review E* 57 (2): 1416.

– . 2009. "On the stupendous beauty of closure". *Journal of Rheology* 53 (6): 1285–1304.

Öttinger, H. C., and H. Struchtrup. 2007. "The mathematical procedure of coarse graining: From Grad's ten-moment equations to hydrodynamics". *Multiscale Modeling & Simulation* 6 (1): 53–69.

Pai, M.G., and S. Subramaniam. 2012. "Two-way coupled stochastic model for dispersion of inertial particles in turbulence". *Journal of Fluid Mechanics* 700:29–62.

Park, S. H., and J. H. Kwon. 2003. "On the dissipation mechanism of Godunov-type schemes". *Journal of Computational Physics* 188 (2): 524–542.

Park, S. H., J. E. Lee, and J. H. Kwon. 2006. "Preconditioned HLLE method for flows at all Mach numbers". *AIAA journal* 44 (11): 2645–2653.

Parmar, M., A. Haselbacher, and S. Balachandar. 2011. "Generalized Basset-Boussinesq-Oseen equation for unsteady forces on a sphere in a compressible flow". *Physical review letters* 106 (8): 084501.

Peshkov, I., and E. Romenski. 2016. "A hyperbolic model for viscous Newtonian flows". *Continuum Mechanics and Thermodynamics* 28 (1-2): 85–104.

Peyret, R. 1979. "Numerical solution of hyperbolic systems. Application to gas dynamics". *NASA STI/Recon Technical Report N* 79:30524.

Pianet, G., S. Vincent, J. Leboi, J.P. Caltagirone, and M. Anderhuber. 2010. "Simulating compressible gas bubbles with a smooth volume tracking 1-fluid method". *International Journal of Multiphase Flow* 36 (4): 273–283.

Pickett, L. M., C. L. Genzale, G. Bruneaux, L.-M. Malbec, L. Hermant, C. Christiansen, and J. Schramm. 2010. "Comparison of diesel spray combustion in different high-temperature, high-pressure facilities". *SAE International Journal of Engines* 3 (2010-01-2106): 156–181.

Pilch, M, and CA Erdman. 1987. “Use of breakup time data and velocity history data to predict the maximum size of stable fragments for acceleration-induced breakup of a liquid drop”. *International journal of multiphase flow* 13 (6): 741–757.

Poinsot, T., and S. K. Lele. 1992. “Boundary conditions for direct simulations of compressible viscous flows”. *Journal of Computational Physics* 101 (1): 104–129.

Pottier, N. 2007. *Physique statistique hors d’équilibre - Processus irréversibles linéaires*. EDP Sciences.

Price, E. W. 1984. “Experimental observations of combustion instability”. Edited by K. Kuo and M. Summerfield, *in Fundamentals of Solid-Propellant Combustion, Progress in Astronautics and Aeronautics, AIAA* 90:733–790.

Qian, J., and C.K. Law. 1997. “Regimes of coalescence and separation in droplet collision”. *Journal of Fluid Mechanics* 331:59–80.

Rabe, C. 2009. “Study of coalescence in spray headers: application to the spray system of PWRs”. PhD thesis, Universite Pierre et Marie Curie.

Ranger, A.A., and J.A. Nicholls. 1968. “Aerodynamic shattering of liquid drops.” *AIAA Journal* 7 (2): 285–290.

Ranz, W.E., and W.R. Marshall. 1952. “Evaporation from drops”. *Chem. Eng. Prog* 48 (3): 141–146.

Raun, R.L., and M.W. Beckstead. 1993. “A numerical model for temperature gradient and particle effects on Rijke burner oscillations”. *Combustion and flame* 94 (1-2): 1–24.

Raviart, P.-A., and J.-M. Thomas. 1977. “A mixed finite element method for 2-nd order elliptic problems”. In *Mathematical aspects of finite element methods*, 292–315. Springer.

Reddy, J. N., and D. K. Gartling. 2010. *The finite element method in heat transfer and fluid dynamics*. CRC press.

Refloch, A., B. Courbet, A. Murrone, P. Villedieu, C. Laurent, P. Gilbank, J. Troyes, L. Tessé, G. Chaineray, J.B. Dargaud, E. Quémerais, and F. Vuillot. 2011. “CEDRE software”. Available at www.aerospacelab-journal.org/al2, *Aerospace Lab* 2:1–10.

Regert, T., and Ph. Planquart. 2015. “Cold flow tests for flow field and deformation characteristics of the PTF membrane from the PODX”. In *6th European Conference for Aeronautics and Space Sciences, EUCASS*. Krakow, Poland.

Reveillon, J., and L. Vervisch. 2005. “Analysis of weakly turbulent diluted-spray flames and spray combustion regimes”. *J. Fluid Mech.* 537:317–347.

Richardson, C. H. 1954. *An introduction to the calculus of finite differences*. Van Nostrand.

Rijke, P. L. 1859. “LXXI. Notice of a new method of causing a vibration of the air contained in a tube open at both ends”. *The London, Edinburgh, and Dublin Philosophical Magazine and Journal of Science* 17 (116): 419–422.

Riley, J. J, and G. S. Patterson. 1974. “Diffusion experiments with numerically intergrated isotropic turbulence”. *Physics of Fluids* 17:292–297.

Roe, P.L. 1981. “Approximate Riemann solvers, parameter vectors and difference schemes”. *Journal of Computational Physics* 43:357–372.

– . 1984. “Generalized formulation of TVD Lax-Wendroff schemes”. *ICASE 84-53*.

Roe, P.L., and J. Pike. 1985. “Efficient construction and utilisation of approximate Riemann solutions”. In *Proc. of the sixth int’l. symposium on Computing methods in applied sciences and engineering, VI*, 499–518. North-Holland Publishing Co.

Rohde, A. 2001. “Eigenvalues and eigenvectors of the Euler equations in general geometries”. In *15th AIAA Computational Fluid Dynamics Conference*, 2609.

Ropp, D. L., and J. N. Shadid. 2009. “Stability of operator splitting methods for systems with indefinite operators: Advection–diffusion–reaction systems”. *Journal of Computational Physics* 228 (9): 3508–3516.

Rusanov, V. V. 1961. "The calculation of the interaction of non-stationary shock waves with barriers". *Zhurnal Vychislitel'noi Matematiki i Matematicheskoi Fiziki* 1 (2): 267–279.

Rusche, H., and R.I. Issa. 2000. "The effect of voidage on the drag force on particles, droplets and bubbles in dispersed two-phase flow". In *Japanese European Two-Phase Flow Meeting, Tshkuba, Japan*.

Sabat, M. 2016. "Eulerian models and realizable numerical schemes for the description of low-to-medium inertia polydisperse sprays in turbulent two-phase flows". PhD thesis, Université Paris-Saclay, CentraleSupélec.

Sabat, M., A. Larat, A. Vié, and M. Massot. 2014. "On the development of high order realizable schemes for the Eulerian simulation of disperse phase flows: a convex-state preserving Discontinuous Galerkin method". *The Journal of Computational Multiphase Flows* 6 (3): 247–270.

Sabat, M., A. Vié, A. Larat, and M. Massot. 2018. "Statistical description of turbulent particle-laden flows in the very dilute regime using the Anisotropic Gaussian Moment Method". *International Journal of Multiphase Flow*.

Sabnis, J.S. 2003. "Numerical simulation of distributed combustion in solid rocket motors with metalized propellant". *Journal of Propulsion and Power* 19 (1): 48–55.

Sachdev, J.S., C.P.T. Groth, and J.J. Gottlieb. 2005. "A parallel solution-adaptive scheme for multi-phase core flows in solid propellant rocket motors". *International Journal of Computational Fluid Dynamics* 19 (2): 159–177.

– . 2007. "Numerical solution scheme for inert, disperse, and dilute gas-particle flows". *International journal of multiphase flow* 33 (3): 282–299.

Sachdev, P.L. 2016. *Shock Waves & Explosions*. CRC Press.

Saffman, P.G. 1962. "On the stability of laminar flow of a dusty gas". *J. Fluid Mech.* 13 (1): 120–128.

Saurel, R., E. Daniel, and J.-C. Loraud. 1994. "Two-phase flows-Second-order schemes and boundary conditions". *AIAA journal* 32 (6): 1214–1221.

Schiller, L., and A. Naumann. 1935. "A drag coefficient correlation". *V.D.I Zeitung* 77:318–320.

Sheng, W., and T. Zhang. 1999. *The Riemann problem for the transportation equations in gas dynamics*. Vol. 654. American Mathematical Soc.

Sheynin, S. A., and A. V. Tuzikov. 2001. "Explicit formulae for polyhedra moments". *Pattern Recognition Letters* 22 (10): 1103–1109.

Shraiber, A.A., A.M. Podvysotsky, and V.V. Dubrovsky. 1996. "Deformation and breakup of drops by aerodynamic forces". *Atomization and Sprays* 6 (6).

Shu, C.W., and S. Osher. 1988. "Efficient implementation of essentially non-oscillatory shock-capturing schemes". *Journal of Computational Physics* 77:439–471.

– . 1989. "Efficient implementation of essentially non-oscillatory shock-capturing schemes, II". In *Upwind and High-Resolution Schemes*, 328–374. Springer.

Sibra, A. 2015. "Modélisation et étude de l'évaporation et de la combustion de gouttes dans les moteurs à propergol solide par une approche eulérienne Multi-Fluide". Available on TEL https://tel.archives-ouvertes.fr/tel-01260314. PhD thesis, Université Paris-Saclay, préparée à CentraleSupélec.

Sibra, A., J. Dupays, A. Murrone, F. Laurent, and M. Massot. 2017. "Simulation of reactive polydisperse sprays strongly coupled to unsteady flows in solid rocket motors: Efficient strategy using Eulerian multi-fluid methods". *Journal of Computational Physics* 339:210–246.

Simoes, M. 2003. *Rapport de synthèse de l'année 1 de la thèse CIFRE sur le diphasique eulérien*. Tech. rep. 1151/2003/SME/DPS/CER. SME.

– . 2006. “Modélisation eulérienne de la phase dispersée dans les moteurs à propergol solide, avec prise en compte de la pression particulaire”. PhD thesis, Institut National Polytechnique de Toulouse.

Simonin, O., P. Fevrier, and J. Lavieville. 2002. “On the spatial distribution of heavy-particle velocities in turbulent flow : from continuous field to particulate chaos”. *Journal of Turbulence* 40.

Singer, M. H. 1993. “A general approach to moment calculation for polygons and line segments”. *Pattern Recognition* 26 (7): 1019–1028.

Sirignano, W. A. 1999. *Fluid Dynamics and Transport of Droplets and Sprays*. xvii+311. Cambridge: Cambridge Univ. Pr. ISBN: 0-521-63036-3.

– . 2010. *Fluid dynamics and transport of droplets and sprays*. Cambridge University Press.

Smagorinsky, J. 1963. “General circulation experiments with the primitive equations”. *Monthly Weather Review* 91 (3): 99–164.

Smith, G. D. 1985. *Numerical solution of partial differential equations: finite difference methods*. Oxford university press.

Snyder, W. H., and J.L. Lumley. 1971. “Some measurements of particle velocity autocorrelation functions in a turbulent flow”. *Journal of Fluid Mechanics* 48 (1): 41–71.

Sod, G. A. 1978. “A survey of several finite difference methods for systems of nonlinear hyperbolic conservation laws”. *Journal of Computational Physics* 27 (1): 1–31.

Spiteri, R. J., and S. J. Ruuth. 2002. “A new class of optimal high-order strong-stability-preserving time discretization methods”. *SIAM Journal on Numerical Analysis* 40 (2): 469–491.

Squires, K. D., and J. K. Eaton. 1991a. “Preferential concentration of particles by turbulence”. *Physics of Fluids* 3 (5): 1169–1178.

Squires, K.D., and J.K. Eaton. 1991b. “Measurements of particle dispersion obtained from direct numerical simulations of isotropic turbulence”. *J. Fluids Mech.* 226:1–35.

Stokes, George Gabriel. 1846. “Report on recent researches in hydrodynamics”. *Brit. Ass. Rep* 1:1–20.

Strang, G. 1963. “Accurate partial difference methods I: Linear Cauchy problems”. *Archive for Rational Mechanics and Analysis* 12 (1): 392–402.

– . 1968. “On the construction and comparison of difference schemes”. *SIAM Journal on Numerical Analysis* 5 (3): 506–517.

Subramaniam, S. 2001. “Statistical modeling of sprays using the droplet distribution function”. *Physics of Fluids* 13 (3): 624–642.

Swanson, R.C., and E. Turkel. 1991. “On central-difference and upwind schemes”. *Journal of computational physics 101,292-306*.

Sweby, P.K. 1984. “High resolution schemes using flux limiters for hyperbolic conservation laws”. *SIAM journal on numerical analysis* 21 (5): 995–1011.

Tambour, Y. 1980. “A sectional model for evaporation and combustion of sprays of liquid fuel”. *Isr. J. Technol.* 18:47–56.

Taylor, G. 1956. “Fluid flow in regions bounded by porous surfaces”. In *Proceedings of the Royal Society of London A: Mathematical, Physical and Engineering Sciences*, 234:456–475. 1199. The Royal Society.

Temkin, S., and R. A. Dobbins. 1966. “Attenuation and dispersion of sound by particulate-relaxation processes”. *The Journal of the Acoustical Society of America* 40 (2): 317–324.

Thomée, V. 1984. *Galerkin finite element methods for parabolic problems*. Vol. 1054. Springer.

Toro, E. F. 2009. *Riemann Solvers and Numerical Methods for Fluid Dynamics: A Practical Introduction*. Berlin, Heidelberg: Springer-Verlag Berlin Heidelberg.

Toro, E. F., M. Spruce, and W. Speares. 1994. “Restoration of the contact surface in the HLL-Riemann solver”. *Shock waves* 4 (1): 25–34.

Traineau, J.-C., and P. Kuentzmann. 1986. “Ultrasonic measurements of solid propellant burning rates in nozzleless rocket motors”. *Journal of Propulsion and Power* 2 (3): 215–222.

Traineau, J.-C., M. Prévost, F. Vuillot, P. Le Breton, J. Cuny, N. Preioni, and R. Bec. 1997. “A subscale test program to assess the vortex shedding driven instabilities in segmented solid rocket motors”. In 33^{rd} *Joint Propulsion Conference*. AIAA/ASME/SAE/ASEE.

Trotter, H.F. 1959. “On the product of semi-groups of operators”. *Proc. Am. Math. Soc.* 10:545–551.

Turkel, E. 1987. “Preconditioned methods for solving the incompressible and low speed compressible equations”. *Journal of Computational Physics* 72 (2): 277–298.

– . 1993. “Review of preconditioning methods for fluid dynamics”. *Applied Numerical Mathematics* 12 (1-3): 257–284.

Tuzikov, A.V., S.A. Sheynin, and P. V. Vasiliev. 2003. “Computation of volume and surface body moments”. *Pattern Recognition* 36 (11): 2521–2529.

Ugurtas, B., G. Avalon, N. Lupoglazoff, F. Vuillot, and G. Casalis. 2000. “Stability and acoustic resonance of internal flows generated by side injection, Solid Propellant Chemistry, Combustion and Motor Interior Ballistics”. *AIAA Progress in Astronautics and Aeronautics Series* 185:823–836.

Vallet, A., and R. Borghi. 1999. “Modélisation eulerienne de l’atomisation d’un jet liquide”. *Comptes Rendus de l’Académie des Sciences-Series IIB-Mechanics-Physics-Astronomy* 327 (10): 1015–1020.

Van Leer, B. 1973. “Towards the ultimate conservative difference scheme I. The quest of monotonicity”. In *Proceedings of the Third International Conference on Numerical Methods in Fluid Mechanics*, 163–168. Springer.

– . 1977. “Towards the ultimate conservative difference scheme III. Upstream-centered finite-difference schemes for ideal compressible flow”. *Journal of Computational Physics* 23 (3): 263–275.

van Leer, B. 1974. “Towards the ultimate conservative difference scheme. II. Monotonicity and conservation combined in a second-order scheme”. *Journal of Computational Physics* 14 (4): 361–370. ISSN: 0021-9991. doi:http://dx.doi.org/10.1016/0021-9991(74)90019-9. http://www.sciencedirect.com/science/article/pii/0021999174900199.

Varapaev, V.N., and V.I. Yagodkin. 1969. “Flow stability in a channel with porous walls”. *Fluid Dynamics* 4 (5): 60–62.

Verwer, J. G., E. J. Spee, J. G. Blom, and W. Hundsdorfer. 1999. “A second-order Rosenbrock method applied to photochemical dispersion problems”. *SIAM Journal on Scientific Computing* 20 (4): 1456–1480.

Verwer, J.G., J.G. Blom, M. Van Loon, and E.J. Spee. 1996. “A comparison of stiff ODE solvers for atmospheric chemistry problems”. *Atmospheric environment* 30 (1): 49–58.

Vetel, J. 2001. “Interaction des structures pariétales sur le développement instationnaire d’écoulements cisaillés en milieu confiné - Rôle de l’injection différentielle”. PhD thesis, Université de Poitiers.

Vié, A., F. Doisneau, and M. Massot. 2015. “On the Anisotropic Gaussian closure for the prediction of inertial-particle laden flows”. *Communications in Computational Physics* 17 (1): 1–46.

Vié, A., F. Laurent, and M. Massot. 2013. “Size-velocity correlations in high order moment methods for polydisperse evaporating sprays: modeling and numerical issues”. *Journal of Computational Physics* 237:177–210.

Vié, A., E. Masi, O. Simonin, and M. Massot. 2012. “On the Direct Numerical Simulation of moderate-Stokes-number turbulent particulate flows using Algebraic-Closure-Based and

Kinetic-Based Moment Methods". In *Proceedings of the summer program*, 355–364. Center for Turbulence Research.

Villedieu, P., J. J. Hylkema, G. Lavergne, B. Platet, Y. Fabignon, M. Vardelle, J.-F. Guéry, F. Godfroy, P. Le Helley, and L. Jacques. 2000. "Slag accumulation in solid propellant rocket motors with a submerged nozzle". In 2^{nd} *European Conference on Launcher Technology*. Rome.

Vincent, S., J.-P. Caltagirone, and P. Bonneton. 2001. "Numerical modelling of bore propagation and run-up on sloping beaches using a MacCormack TVD scheme". *Journal of hydraulic research* 39 (1): 41–49.

Vuillot, F. 1995. "Vortex-shedding phenomena in solid rocket motors". *J. Propulsion and Power* 11 (4): 626–639.

Vuillot, F., T. Basset, J. Dupays, E. Daniel, and N. Lupoglazoff. 1997. "2D Navier-Stokes computations for solid rocket motors : rotationnal combustion and two-phase flow effects". In *33rd AIAA/ASME/SAE/ASEE Joint Propulsion Conference and Exhibit*, paper N° 97–3326.

Vuillot, F., and N. Lupoglazoff. 1996. "Combustion and turbulent flow effects in 2D unsteady Navier-Stokes simulations of oscillatory solid rocket motors - First applications". In *34th Aerospace Sciences Meeting and Exhibit*.

Vuillot, F., and A. Refloch. 2014. "Some HPC challenges for multi-physics extended CFD computations". In *The 16th IEEE International Conference on High Performance Computing and Communications (HPCC 2014)*.

Vuillot, F., P.Y. Tissier, and R. De Amicis. 1996. "Stability prediction for large segmented solid propellant rocket motors". In *AAAF: 5ème Symposium International sur la propulsion dans les Transports Spatiaux*. Paris.

Wagner, W. 1992. "A convergence proof for Bird's direct simulation Monte Carlo method for the Boltzmann equation". *Journal of Statistical Physics* 66 (3): 1011–1044.

Warming, R.F., and R. M. Beam. 1976. "Upwind second-order difference schemes and applications in aerodynamic flows". *AIAA Journal* 14 (9): 1241–1249.

Warming, R.F., and B.J. Hyett. 1974. "The modified equation approach to the stability and accuracy analysis of finite-difference methods". *Journal of Computational Physics* 14 (2): 159–179.

Washburn, E., M. Gross, S. Smith, and S. Balachandar. 2010. "Fundamental simulation of aluminum droplet combustion". In *46th AIAA Joint Propulsion Conference, Number AIAA*, 6677:1–15.

Waterson, N. P., and H. Deconinck. 2007. "Design principles for bounded higher-order convection schemes–a unified approach". *Journal of Computational Physics* 224 (1): 182–207.

Will, J.B., N.P. Kruyt, and C.H. Venner. 2017. "An experimental study of forced convective heat transfer from smooth, solid spheres". *International Journal of Heat and Mass Transfer* 109:1059–1067.

Williams, F. A. 1958. "Spray Combustion and Atomization". *Phys. Fluids* 1:541–545.

– . 1985. *Combustion Theory (Combustion Science and Engineering Series)*. Ed. F. A. Williams (Reading, MA: Addison-Wesley).

Williams, F. A., M. Barrère, and N.C. Huang. 1969. *Fundamental aspects of solid propellant rockets*. Tech. rep. Advisory Group for Aerospace Research and Development Neuilly-Sur-Seine (FRANCE).

Wingborg, N., and M. Calabro. 2016. "Green Solid Propellants for Launchers". In *Space Propulsion conference, Rome, Italy*, 02–06.

Woodward, P., and P. Colella. 1984. "The numerical simulation of two-dimensional fluid flow with strong shocks". *Journal of Computational Physics* 54 (1): 115–173.

Xiu, D., and G. E. Karniadakis. 2001. “A semi-Lagrangian high-order method for Navier–Stokes equations”. *Journal of Computational Physics* 172 (2): 658–684.

Yanenko, N. N. 1971. *The method of fractional steps*. Springer.

Yee, H.C. 1987. “Construction of explicit and implicit symmetric TVD schemes and their applications”. *Journal of Computational Physics* 68 (1): 151–179.

Yuan, C., and R. O. Fox. 2011. “Conditional quadrature method of moments for kinetic equations”. *Journal of Computational Physics* 230 (22): 8216–8246.

Yuan, C., F. Laurent, and R.O. Fox. 2012. “An extended quadrature method of moments for population balance equations”. *Journal of Aerosol Science* 51:1–23.

Zaichik, L. I., V. M. Alipchenkov, and E. G. Sinaiski. 2008. *Particles in turbulent flows*. John Wiley & Sons.

Zaichik, L. I., O. Simonin, and V. M. Alipchenkov. 2003. “Two statistical models for predicting collision rates of inertial particles in homogeneous isotropic turbulence”. *Physics of Fluids* 15 (10): 2995–3005.

Zaichik, L.I., O. Simonin, and V.M. Alipchenkov. 2009. “An Eulerian approach for large eddy simulation of particle transport in turbulent flows”. *Journal of Turbulence*, no. 10: N4.

Zamansky, R., F. Coletti, M. Massot, and A. Mani. 2014. “Radiation induces turbulence in particle-laden fluids”. *Physics of Fluids* 26 (7): 071701.

Zhang, X.; and C.-W. Shu. 2010a. “On positivity-preserving high order discontinuous Galerkin schemes for compressible Euler equations on rectangular meshes”. *Journal of Computational Physics* 229 (23): 8918–8934.

Zhang, X., Y. Xia, and C.-W. Shu. 2012. “Maximum-principle-satisfying and positivity-preserving high order discontinuous Galerkin schemes for conservation laws on triangular meshes”. *Journal of Scientific Computing* 50 (1): 29–62.

Zhang, Xiangxiong, and Chi-Wang Shu. 2010b. “On maximum-principle-satisfying high order schemes for scalar conservation laws”. *Journal of Computational Physics* 229 (9): 3091–3120.

Ziolkovski, K. 1903. *Issledovaniye mirovykh prostranstv reaktivnymi priborami (Study of outer space by reaction devices)*.

université PARIS-SACLAY | École doctorale de mathématiques Hadamard (EDMH)

Titre : Modélisation et simulation de l'écoulement diphasique dans les moteurs-fusées à propergol solide par une approche eulérienne polydispersée en taille et en vitesse

Mots Clefs : Modélisation mathématique, méthodes numériques, écoulements diphasiques polydispersés, moteurs-fusées à propergol solide, croisement de trajectoires, HPC.

Résumé :
Les gouttes d'oxyde d'aluminium présentes en masse dans l'écoulement interne des moteurs-fusées à propergol solide ont tendance à influer de façon importante sur l'écoulement et sur le fonctionnement du moteur quel que soit le régime. L'objectif de la thèse est d'améliorer les modèles diphasiques eulériens présents dans le code de calcul semi-industriel pour l'énergétique de l'ONERA, CEDRE, en y incluant la possibilité d'une dispersion locale des particules en vitesse en plus de la dispersion en taille déjà présente dans le code, tout en gardant une structure mathématique bien posée du système d'équations à résoudre. Cette nouvelle caractéristique rend le modèle capable de traiter les croisements de trajectoires anisotropes, principale difficulté des modèles eulériens classiques pour les gouttes d'inertie modérément grande.
En plus de la conception et de l'analyse détaillée d'une classe de modèles basés sur des méthodes de moments, le travail se concentre sur la résolution des systèmes d'équations obtenus en configurations industrielles. Pour cela, de nouvelles classes de schémas précis et réalisables pour le transport des particules dans l'espace physique et l'espace des phases sont développées. Ces schémas assurent la robustesse de la simulation malgré différentes singularités (dont des chocs, δ-chocs, zones de pression nulle et zones de vide...) tout en gardant une convergence d'ordre deux pour les solutions régulières. Ces développements sont conduits en deux et trois dimensions, en plus d'un référentiel bidimensionnel axisymétrique, dans le cadre de maillages non structurés.
La capacité des schémas numériques à maintenir un niveau de précision élevé tout en restant robuste dans toutes les conditions est un point clé pour les simulations industrielles de l'écoulement interne des moteurs à propergol solide. Pour illustrer cela, le code de recherche SIERRA, originellement conçu durant les année 90 pour les problématiques d'instabilités de fonctionnement en propulsion solide, a été réécrit afin de pouvoir comparer deux générations de modèles et de méthodes numériques et servir de banc d'essais avant une intégration dans CEDRE. Les résultats obtenus confirment l'efficacité de la stratégie numérique choisie ainsi que le besoin d'introduire, pour les simulations axisymétriques, une condition à la limite spécifique, développée dans le cadre de cette thèse. En particulier, les effets à la fois du modèle et de la méthode numérique dans le contexte d'une simulation de l'écoulement interne instationnaire dans les moteurs-fusées à propergol solide sont détaillés. Par cette approche, les liens entre des aspects fondamentaux de modélisation et de schémas numériques ainsi que leurs conséquences pour les applications sont mis en avant.

Title : Eulerian modeling and simulation of two-phase flows in solid rocket motors taking into account size polydispersion and droplet trajectory crossing

Keys words : Mathematical modeling, numerical methods, polydisperse two-phase flow, solid rocket motors, particle trajectory crossing, high performance computing.

Abstract :
The massive amount of aluminum oxide particles carried in the internal flow of solid rocket motors significantly influences their behavior. The objective of this PhD thesis is to improve the two-phase flow Eulerian models available in the semi-industrial CFD code for energetics CEDRE at ONERA by introducing the possibility of a local velocity dispersion in addition to the size dispersion already taken into account in the code, while keeping the well-posed characteristics of the system of equations. Such a new feature enables the model to treat anisotropic particle trajectory crossings, which is a key issue of Eulerian models for droplets of moderately large inertia.
In addition to the design and detailed analysis of a class of models based on moment methods, the conducted work focuses on the resolution of the system of equations for industrial configurations. To do so, a new class of accurate and realizable numerical schemes for the transport of the particles in both the physical and the phase space is proposed. It ensures the robustness of the simulation despite the presence of various singularities (including shocks, δ-shocks, zero pressure area and vacuum...), while keeping a second order accuracy for regular solutions. These developments are conducted in two and three dimensions, including the two dimensional axisymmetric framework, in the context of general unstructured meshes.
The ability of the numerical schemes to maintain a high level of accuracy in any condition is a key aspect in an industrial simulation of the internal flow of solid rocket motors. In order to assess this, the in-house code SIERRA, originally designed at ONERA in the 90's for solid rocket simulation purpose, has been rewritten, restructured and augmented in order to compare two generations of models and numerical schemes, to provide a basis for the integration of the features developed in CEDRE. The obtained results assess the efficiency of the chosen numerical strategy and confirm the need to introduce a new specific boundary condition in the context of axisymmetric simulations. In particular, it is shown that the model and numerical scheme can have an impact in the context of the simulation of the internal flow of solid rocket motors and their instabilities. Through our approach, the shed light on the links between fundamental aspects of modeling and numerical schemes and their consequences on the applications.